METALS. SUPERCONDUCTORS

Phase segregation in the $Fe_{90}Zr_{10}$ amorphous alloy under heating

G. E. Abrosimova and A. S. Aronin

Institute of Solid State Physics, Russian Academy of Sciences, 142432 Chernogolovka, Moscow Region, Russia

(Submitted April 21, 1998)
Fiz. Tverd. Tela (St. Petersburg) **40**, 1769–1772 (October 1998)

A study of the changes in the structure of melt-quenched $Fe_{90}Zr_{10}$ amorphous alloys by x-ray diffraction, Auger spectroscopy, and transmission electron microscopy is reported. The samples were subjected to isochronous (for 1 h) and isothermal anneals at 100–650 °C. It is shown that an amorphous alloy annealed for one hour at 300–500 °C crystallizes with formation of a supersaturated solid solution of Zr in α Fe and the intermetallic compound Fe_3Zr. Isothermal anneal at 100 °C for up to 7000 h produces nanocrystallites 110–30 nm in size, with fuzzy interfaces between the grains. An alloy subjected to such an anneal contains two solid solutions of Zr in Fe, having a cubic and a weakly tetragonal lattice. Crystallization taking place during low-temperature anneals is preceded by phase segregation of the alloy within the amorphous state. The lattice periods of the solid solutions have been determined. The possibility of the alloy crystallizing by spinodal decomposition during prolonged annealing is discussed. [S1063-7834(98)00110-5]

Evolution of the structure of amorphous alloys is among the most intriguing problems in the physics of highly disordered systems. The nature of the processes occurring in the transition from the initial amorphous to an equilibrium crystalline state depends on a large number of both external and internal parameters. Any analysis of relevant experimental data must take into account two important points. First, during certain heat treatments the researcher can miss some stages in the evolution of a structure and detect only some steps in its development. Second, the actual nature of the structural changes in amorphous alloys can vary strongly depending on the specific heat treatment conditions, as well as on the internal parameters of the system, so that crystallization can result in the onset of different structural states. Because the properties of a material are mostly structure-sensitive, knowledge of the specific features of the structural evolution and of the possibility of attaining a given structural state is extremely important. The amorphous alloy $Fe_{90}Zr_{10}$ investigated in this work is of considerable interest from the standpoint of both an analysis of the structure and of studying its properties.[1–4]

It is known that crystallization from a disordered to an ordered phase can follow either the mechanism of nucleation and growth or proceed by spinodal decomposition.[5] The crystallization mechanism can, in its turn, be dominated both by heat treatment conditions and by the state of the amorphous phase immediately before the crystallization. This work deals with investigation of the effect of various heat-treatment conditions on the structure of the $Fe_{90}Zr_{10}$ amorphous alloy and on the character of its crystallization, as well as with development of a nanocrystalline structure in this material.

1. EXPERIMENTAL TECHNIQUES

The amorphous $Fe_{90}Zr_{10}$ alloy was prepared in the form of a 25-μm thick, 10-mm wide ribbon by rapid melt-quenching in a one-roller arrangement. The samples were subjected to isochronous (for 1 h) and isothermal anneals up to 7000 h long in an argon atmosphere at various temperatures. The annealing was done by placing a sample into a furnace preheated to the desired temperature. The initial and annealed samples were examined by x-ray diffraction, Auger spectroscopy, and transmission-electron microscopy. The x-ray diffraction patterns were obtained by the Debye–Scherrer method with Fe $K\alpha$ radiation, as well as with a DRON-3.0 diffractometer using Mo $K\alpha$ radiation. The TEM studies were performed on a JEM-100CX electron microscope. The samples for the electron microscopy were prepared by ion milling. The alloy composition was studied with a JAMP-10S Auger electron spectrometer, with the surface layers removed by an argon ion beam.

2. EXPERIMENTAL RESULTS

The influence of heat-treatment conditions on changes in the structure and the nature of crystallization was studied in a series of isothermal and isochronous anneals, and therefore it appears reasonable to divide the experimental results obtained into groups.

A. Crystallization of the amorphous $Fe_{90}Zr_{10}$ alloy under isochronous anneal

This series of experiments dealt with the changes in the structure of the amorphous alloy occurring after one-hour long anneals at 300–500 °C. Annealing the alloy below

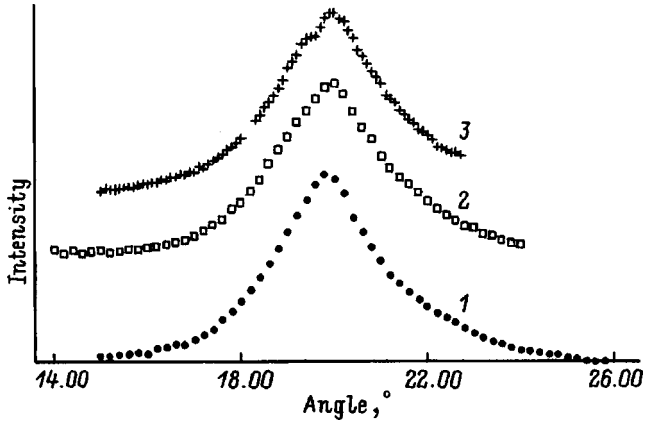

FIG. 1. Variation of the first maximum in the structure factor $S(Q)$ of the amorphous alloy under annealing at 100 °C. *1* — original sample, *2* and *3* — samples annealed for 1500 and 4000 h, respectively.

350 °C leaves it amorphous. After a one-hour long anneal at 350 °C, crystals of a supersaturated solid solution of Zr in α Fe with a lattice period $a=0.292$ nm form in the amorphous matrix. The lattice period of the α phase decreases with increasing anneal temperature to become equal to that of pure α Fe (0.286 nm) following an anneal at 600 °C. Annealing at 500 °C gives rise to the appearance in the samples, besides crystals of α Fe(Zr), of Fe_3Zr crystals as well.

B. Changes in the structure under isothermal annealing

We are going to deal here with the changes in the structure of amorphous $Fe_{90}Zr_{10}$ alloy induced by prolonged annealing. We shall have to separate the structural changes occurring within the amorphous state from those produced by crystallization.

Structural changes within the amorphous state. Figure 1 shows the change of the first maximum in the structure factor $S(Q)$ ($Q=4\pi\sin\theta/\lambda$ is the wave vector) occurring under annealing at 100 °C. For the sake of convenience the curves are displaced with respect to one another along the vertical axis; no changes in the integrated intensity of the maximum were observed within experimental error during the specified anneals. One readily sees the appearance of a shoulder in the first maximum on the side of smaller diffraction angles. As the anneal time increases, this shoulder shifts toward smaller diffraction angles, which is accompanied by an insignificant displacement of the maximum itself in the opposite direction. The amorphicity of the alloy in these anneals was monitored also by electron microscopy. For anneal durations above 5000 h, the curve retains its character in the early stages of crystallization, with only the intensity of the maxima increasing.

It should be noted that the same variations in the structure were observed in isothermal anneals performed above 250 °C, although in this case all processes occurred at a faster rate.

Crystallization of the $Fe_{90}Zr_{10}$ alloy under isothermal annealing. Figure 2a shows the structure of the alloy following an annealing at 100 °C for 6850 h. The photomicrograph reveals grains 10–30 nm in size with fuzzy boundaries. A

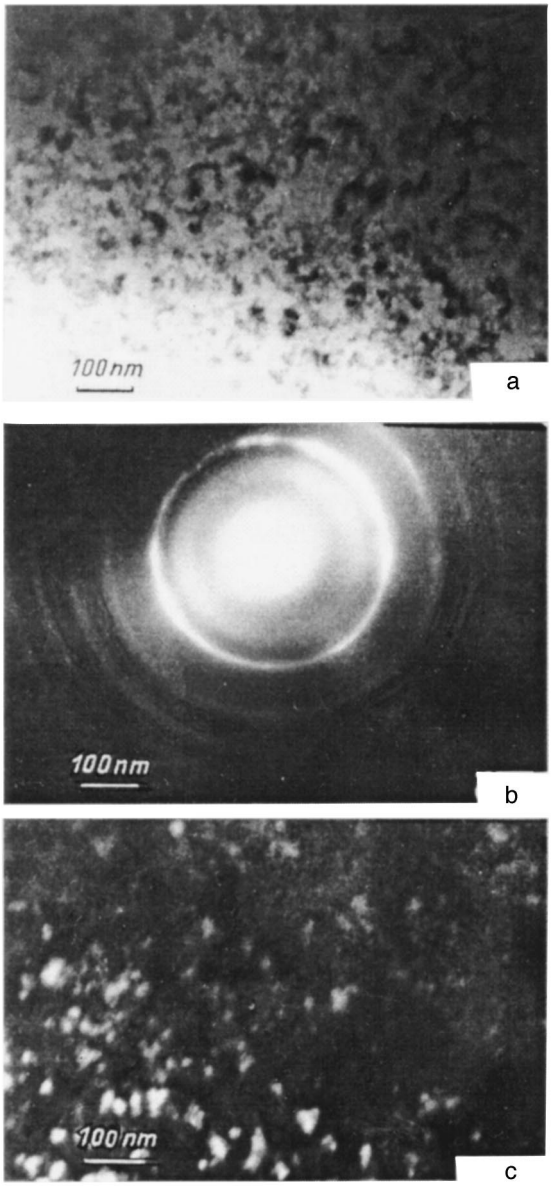

FIG. 2. Bright-field image (a), electron-diffraction pattern (b), and dark-field image (c) of a sample annealed at 100 °C for 6850 h.

microdiffraction pattern of this structure is presented in Fig. 2b. What is characteristic of such a structure? First, it is the fuzziness of the interfaces between the grains, which is not the result of poor image focusing. Second, the rings in the electron-diffraction patterns remain fuzzy to a certain extent after the crystallization. This fuzziness can hardly be accounted for solely by the small grain size, because in other cases grains 5–7 nm in size produce considerably sharper rings. For comparison, Fig. 3 shows an image of the structure and a microdiffraction pattern from a crystallized $Fe_{85}B_{15}$ alloy. The grain size in this case is 10–20 nm. Third, some of the electron-diffraction patterns obtained from the regions of the sample where the transformation progressed to a greater extent exhibit a splitting in the reflections (Fig. 4). The lines thus formed indicate segregation of two different solid solutions of Zr in Fe. The grain boundaries have become sharper. An analysis of these diffractograms suggests that the two

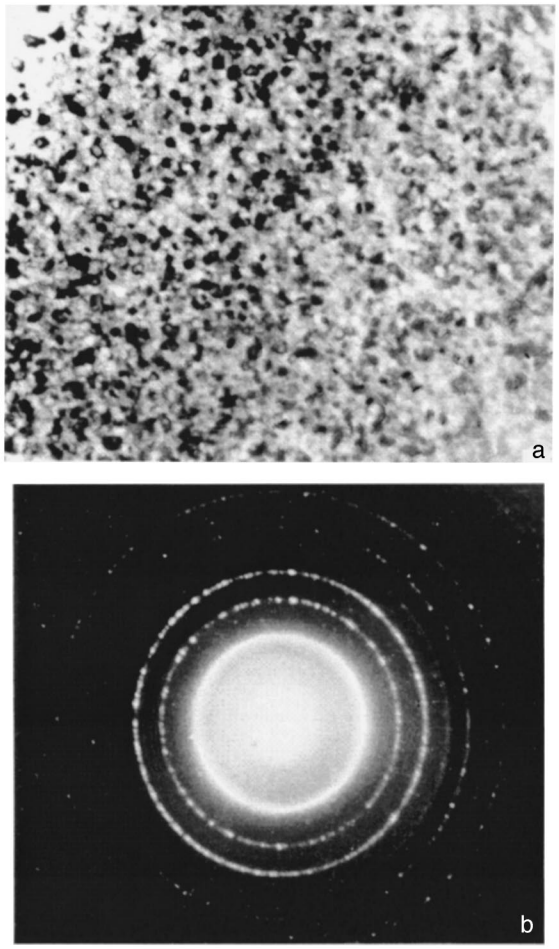

FIG. 3. Bright-field image (a) and electron-diffraction pattern (b) of a sample of crystallized $Fe_{85}B_{15}$ alloy.

solid solutions have a cubic and a weakly tetragonal lattice. The cubic-lattice parameter is 0.302 nm. The second solid solution has a close-to-cubic tetragonal lattice with parameters $a=0.292$ nm and $c=0.288$ nm.

Zirconium is known to be highly susceptible to oxidation. To check whether the oxides do indeed form and to see how they influence crystallization under prolonged heat treatment, the samples were studied by Auger spectroscopy. Figure 5 displays the distribution in depth of the alloy components, as well as of oxygen and of carbon, which is always present in the chamber because the instrument is evacuated by a diffusion pump. A small amount of oxygen was found on the sample surface, but it decreases down to the background level already at a depth of about 100 nm.

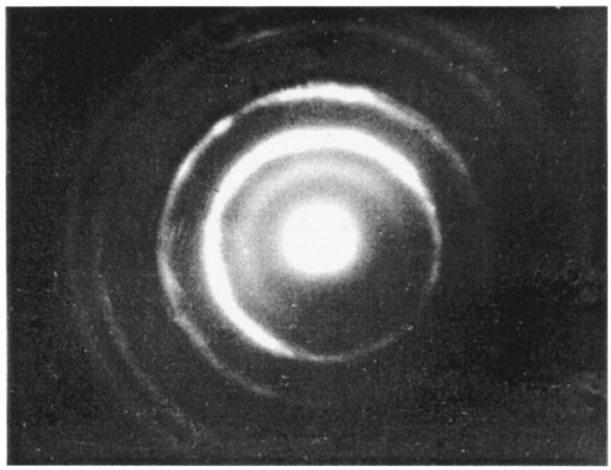

FIG. 4. Electron-diffraction pattern of a $Fe_{90}Zr_{10}$ sample annealed at 100 °C for 7000 h.

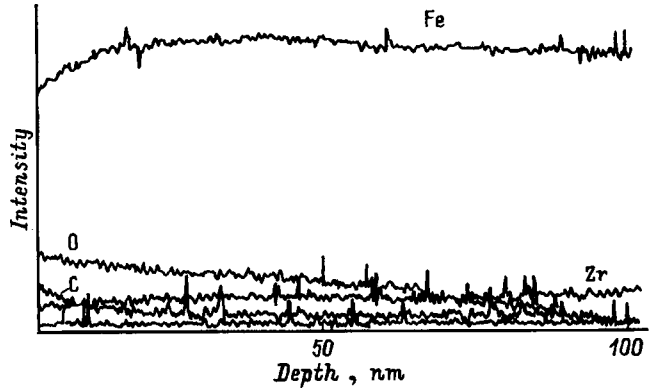

FIG. 5. Depth profile of the alloy components.

3. DISCUSSION OF RESULTS

As shown above, crystallization of the alloy under isochronous anneal starts with the formation of a supersaturated solid solution of Zr in α Fe, with the degree of supersaturation decreasing with increasing temperature. A similar situation was observed to occur also on other alloys [Fe–B (Ref. 6), Co–Fe–Si–B (Ref. 7), and others] in such treatments, where a sample was placed into a preheated furnace, and raised to the anneal temperature in 3–5 min. The formation of a supersaturated solid solution in the initial stage is obviously connected with nonequilibrium capture of Zr by the αFe lattice. Mass transport by diffusion increases with temperature, which reduces the degree of supersaturation. After the first stage of crystallization has ended, the amorphous matrix contains crystals of α Fe(Zr). In this case the crystallization obviously proceeds by the conventional mechanism of nucleation and growth. As the temperature increases, Fe_3Zr crystals appear next to α Fe(Zr), as was observed earlier[8]. No segregation of the $Fe_{23}Zr_6$ or ω phases (Refs. 9 and 10, respectively) was detected.

The pattern is different in the case of prolonged isothermal anneals. The formation and development of the shoulder at the first maximum of $S(Q)$ indicates phase segregation in the amorphous alloy into regions having different types of short-range order and composition. It is this process that results eventually in the formation of a nanocrystalline structure. As pointed out in Sect. 2B, a sequence of phase transformations takes place already in the early stage of crystallization. The first to form are two solid solutions of Zr in α Fe, to be followed by Fe_3Zr:

$$\alpha' \mathrm{Fe(Zr)} + \alpha'' \mathrm{Fe(Zr)} \rightarrow \alpha \mathrm{Fe} + \mathrm{Fe_3\,Zr}\,,$$

and this process is continuous. In the earliest stages of evolving crystalline structure from the amorphous state the inter-

face between the α' and α'' precipitates is fuzzy, and the corresponding reflections in the electron diffractograms, broad. The dimensions of the grains determined from dark-field images (Fig. 2c) are 10–30 nm. These observations can be explained by assuming that the precipitating particles are not uniform in composition and degree of order. Longer anneals at a higher temperature make the boundaries sharper, with the broad rings in the diffractograms splitting into several lines (Fig. 4).

It had been suggested earlier that crystallization of an amorphous $Fe_{90}Zr_{10}$ alloy can be accompanied by formation of iron oxides.[11] The results presented in Fig. 5 showing the distribution of components in depth indicate, however, that the observed structure cannot be associated with the formation of oxides (the foils for electron microscopy were prepared from a part of the sample equally distant from the end faces).

Let us try to estimate the composition of the two precipitating solid solutions of Zr in Fe assuming the lattice parameter to depend linearly on concentration in accordance with Vegard's law, and using for this purpose the parameter of the bcc lattice of Zr. We obtain approximately 4 at. % Zr for the first solution, and 20 at. % for the second. If we take into account that the alloy under study contains 10 at. % Zr, the phase with 4 at. % Zr should be present in a larger amount than the 20-at. % Zr phase. This correlates with the observed higher intensities of reflections from the phase with 4 at. % Zr. If the annealing is continued still longer, the Fe_3Zr phase appears. It probably forms from the solid solution containing 20 at. % Zr.

The nature of the phase transformations occurring under prolonged low-temperature anneal (continuous variation of the composition and degree of order, the absence of sharp interfaces between the precipitates in the initial stages of crystallization and the reduction of grain-boundary fuzziness with increasing anneal time, etc.) may be considered as typical of the group of continuous transformations (spinodal decomposition or continuous ordering), which can take place, in particular in the cases where the initial phase is not crystalline lattice.[12,13] Assumptions of a spinodal decomposition occurring in crystallization of amorphous alloys were put forward before.[13,14] The $Fe_{90}Zr_{10}$ alloy under study here has a close-to-eutectic composition and, therefore, it cannot be excluded that a spinodal region can also exist in the diagram of the concentration dependence of free energy for the amorphous state within the range of concentrations covered in this work.

In principle, one cannot rule out the possibility that the observed nanocrystalline structure can form under prolonged low-temperature anneal by the mechanism of nucleation and growth as well. In this case, however, it would be difficult to account for such specific features in the structure as the fuzziness of grain boundaries in the initial stages and its reduction under annealing, as well as the evolution of the diffraction patterns with increasing anneal time. While the data obtained are certainly not sufficient to warrant a conclusion on the mechanism of the low-temperature decomposition of amorphous $Fe_{90}Zr_{10}$, they do not conflict at any rate with the assumption that the transformations this alloy under certain conditions have a spinodal nature.

Support of the Russian Fund for Fundamental Research (Grant 96-02-19582) is gratefully acknowledged.

[1] K. H. J. Buschow, J. Less-Common Met. **79**, 243 (1981).
[2] K. Osamura, S. Ochiai, and S. Takayama, J. Mater. Sci. **19**, 1917 (1984).
[3] R. W. Cochrane, J. Destry, R. Legault, and M. Trudeau, J. Appl. Phys. **55**, 1939 (1984).
[4] L. F. Barquín, J. C. G. Sal, S. N. Kaul, J. M. Barandiarán, P. Gorria, J. S. Pedersen, and R. Heenan, J. Appl. Phys. **79**, 5146 (1996).
[5] J. W. Christian, *The Theory of Transformations in Metals and Alloys* [Pergamon Press, Oxford, 1975; Mir, Moscow, 1978].
[6] G. E. Abrosimova and A. V. Serebryakov, in *Physics of Amorphous Alloys* [in Russian] (UdGU, Izhevsk, 1984).
[7] G. E. Abrosimova, A. S. Aronin, and A. V. Serebryakov, **68**, 552 (1989).
[8] Z. Altounian, E. Batalla, and J. O. Strom-Olsen, J. Appl. Phys. **59**, 2364 (1986).
[9] D. P. Abraham, J. W. Richardson, Jr., and S. M. McDeavitt, Scr. Mater. **37**, 239 (1997).
[10] A. V. Dobromyslov and N. V. Kazantseva, Scr. Mater. **37**, 615 (1997).
[11] Y. Khan and M. Sostarich, J. Mater. Sci. Lett. **6**, 1223 (1987).
[12] *Physical Metallurgy*, edited by R. W. Cahn and P. Haasen [North-Holland, Amsterdam, 1983; Metallurgiya, Moscow, 1987].
[13] J. W. Martin and R. D. Doherty, *Stability of Microstructure in Metallic Systems* [Cambridge University Press, London, 1976; Atomizdat, Moscow, 1978].
[14] H. S. Chen and D. Turnbull, Acta Metall. **17**, 1021 (1969).

Translated by G. Skrebtsov

Mixed state and critical current in narrow semiconducting films

G. M. Maksimova*

N. I. Lobachevskiĭ Nizhniĭ Novgorod State University, 603000 Nizhniĭ Novgorod, Russia
(Submitted January 23, 1998; resubmitted April 3, 1998)
Fiz. Tverd. Tela (St. Petersburg) **40**, 1773–1777 (October 1998)

The mixed state of thin narrow superconducting films with an edge barrier placed in a transverse magnetic field is considered. The boundaries of the region for the existence of metastable mixed states with an assigned number of vortices N $[H_{\min}(N) \leqslant H \leqslant H_{\max}(N)]$ are found. The magnetic-field dependence of the critical field is found for the films. The transition from the Meissner state to the static mixed state is discussed. © *1998 American Institute of Physics.* [S1063-7834(98)00210-X]

The behavior of thin superconducting films in a perpendicular magnetic field has been the subject of numerous studies. It is known that a fairly strong magnetic field leads to the penetration of vortices into a film. If the bulk pinning is small, then these vortices, arising at the edges of a sample, are ''driven'' by Meissner currents into the central part of the film, where they form a mixed state. The stability of such a state is assured by the existence of a barrier to vortex entry (exit), which is similar to a Bean–Livingston surface barrier. An edge barrier also influences the transport properties, the magnetization, and other characteristics of thin current-carrying strips. The structure, stability region, and relaxation of the mixed state of broad films (with $d \ll \lambda_\perp \ll W$, where d is the thickness, W is the width of the film, $\lambda_\perp = 2\lambda^2/d$, and λ is the London length) in a transverse magnetic field was considered in Refs. 1 and 2. The influence of an edge barrier on the critical current of such films was discussed by Kupriyanov and Likharev.[3] The nucleation of vortices at edges and their penetration into a narrow film was considered in Ref. 4 by solving the non-steady-state Ginzburg–Landau equations.

In this paper we calculate the magnetic-field dependence of the critical current for a narrow film: $\xi \ll d \ll W \ll \lambda_\perp$ (ξ is the coherence length). In Sec. 1 we first consider the mixed state of a film with an assigned number of vortices N in a transverse magnetic field in the absence of a transport current. As a result of analyzing the Gibbs free energy of a test vortex ΔG we find the range of values of the external magnetic field $H_{\min}(N) \leqslant H \leqslant H_{\max}(N)$, which specifies the stability boundary of quasiequilibrium states with a given value of N. It is shown that the absolute boundary of the mixed state is the field $\tilde{H} = \Phi_0/(4\pi\xi^2)$, $\tilde{H} \propto H_{c2}$ (Φ_0 is the magnetic flux quantum).

In Secs. 2 and 3 we discuss the behavior of a current-carrying film in a magnetic field. The transport current I conveyed along the film alters the conditions for vortex entry and exit. Depending on the ratio between I and H, a film which is initially in the Meissner state can pass either into a resistive state [when $I > I_c(H)$] or into a static mixed state, which also becomes unstable when the current is increased further.

1. STRUCTURE OF THE MIXED STATE OF A NARROW FILM IN THE ABSENCE OF A TRANSPORT CURRENT

Let us consider a superconducting film of width $W(-W/2 \leqslant y \leqslant W/2)$ and thickness d $(0 \leqslant z \leqslant d,\ d \ll \lambda_\perp)$ immersed in a magnetic field $\mathbf{H} = (0,0,H)$. The distribution of the linear current density $i = i_x = j_x d$ is described by the generalized Maxwell–London equation

$$\frac{2\pi}{c}\lambda_\perp \frac{di}{dy} + \frac{2}{c}\int_{-W/2}^{W/2} \frac{i(t)\,dt}{t-y} = H - n(y)\Phi_0, \tag{1}$$

where $n(y)$ is the averaged vortex density, which is nonzero in the region of the film where $i(y) = 0$. In the general case the current density $i(y)$ is the sum of the densities of the transport current, the Meissner current, and the current of the vortices forming the mixed state. In the leading approximation with respect to $W/\lambda_\perp \ll 1$, from (1) we obtain

$$n(y) = \begin{cases} H/\Phi_0, & |y| \leqslant \theta, \\ 0, & |y| \geqslant \theta, \end{cases} \tag{2}$$

$$i(y) = \frac{cH}{2\pi\lambda_\perp} \begin{cases} y - \theta, & \theta \leqslant y \leqslant \dfrac{W}{2}, \\ 0, & |y| \leqslant \theta, \\ y + \theta, & \dfrac{-W}{2} \leqslant y \leqslant -\theta. \end{cases} \tag{3}$$

The parameter θ, which specifies the half-width of the region occupied by vortices, is related to the number of vortices which have entered the film: $N = 2H\theta/\Phi_0$.

Let us consider the Gibbs free energy of a test vortex in a film as a function of its coordinate y_0. As was shown in Refs. 1 and 6, $\Delta G(y_0, N)$ can be represented in the form

$$\Delta G(y_0, N) = E_0(y_0) + E_1(y_0), \tag{4}$$

where $E_0(y_0)$ is the self-energy of a vortex in a narrow film,[5]

$$E_0(y_0) = \frac{\Phi_0^2}{8\pi^2\lambda_\perp}\left\{\ln\frac{\lambda_\perp}{2\xi} + \sum_{n=1}^{k_0/2} \ln\left[\frac{(2n-1)^2}{2n^2} - \frac{y_0^2}{n^2 W^2}\right]\right\}, \tag{5}$$

and $k_0=\lambda_\perp/W\gg 1$. In the limit $k_0\gg 1$ this expression can be brought into a form which is more convenient for further calculations (see the Appendix)

$$E_0(y_0)=\frac{\Phi_0^2}{8\pi^2\lambda_\perp}\ln\left[\frac{W}{\pi\xi}\cos\left(\frac{\pi y_0}{W}\right)\right],\quad |y_0|\leqslant\frac{W}{2}-\xi. \tag{6}$$

The function $E_1(y_0,N)$ in Eq. (4) is the interaction energy of the test vortex with the current $i(y)$:

$$E_1(y_0)=\frac{\Phi_0}{2c}\left[\int_{-W/2}^{y_0} i\,dy-\int_{y_0}^{W/2} i\,dy\right]. \tag{7}$$

For specificity, we assume that $y_0>0$. From (3) and (7) we then obtain

$$E_1(y_0,N)=\frac{\Phi_0 H}{4\pi\lambda_\perp}\begin{cases}[(y_0-\theta)^2-(W/2-\theta)^2], & \theta\leqslant y_0\leqslant\dfrac{W}{1},\\ -(W/2-\theta)^2, & 0\leqslant y_0\leqslant\theta.\end{cases} \tag{8}$$

The mixed state described by (2) and (3) is stable (more precisely, metastable) as long as there are energy barriers to vortex entry into the film and vortex exit from it. The field $H_{\max}(N)$, at which the barrier to entry is suppressed, can be found from the condition

$$\left.\frac{\partial\Delta G(y,N)}{\partial y}\right|_{y=W/2-\xi}=0 \tag{9}$$

and, with allowance for (4), (6), and (8), equals

$$H_{\max}(N)=H_s+\frac{N\Phi_0}{W}(1+2\xi/W), \tag{10}$$

where H_s is the field for entry of the first vortex:[6]

$$H_s=\frac{\Phi_0}{2\pi\xi W}. \tag{11}$$

The field $H_{\min}(N)$, which corresponds to disappearance of the barrier to vortex exit from the film, specifies the lower stability boundary of the mixed state. This is equal to the total field at which the dependence of $\Delta G(y_0,N)$ on y_0 in the region $\theta\leqslant y_0\leqslant W/2-\xi$ becomes monotonic:

$$\begin{cases}\dfrac{d}{dy_1}\Delta G(y_1,N)=0,\\ \dfrac{d^2}{dy_1^2}\Delta G(y_1,N)=0,\end{cases} \tag{12}$$

or, in explicit form,

$$\frac{N\Phi_0}{4\pi\lambda_\perp}=P(y_1),\quad y_1=\frac{W}{2}\arccos\sqrt{\frac{H'}{H}}, \tag{13}$$

where

$$P(y)=\frac{H}{2\pi\lambda_\perp}y-\frac{\Phi_0}{8\pi\lambda_\perp W}\tan\left(\frac{\pi y}{W}\right), \tag{14}$$

$$H'=\frac{\pi\Phi_0}{4W^2}. \tag{15}$$

Solving this system of equations, we obtain the expression for determining $H=H_{\min}(N)$

$$\frac{\pi\Phi_0 N}{2HW}=\arccos\sqrt{\frac{H'}{H}}-\sqrt{\frac{H'}{H}}\sqrt{1-\frac{H'}{H}}. \tag{16}$$

It follows from (16) that H' can be called the exit field for one vortex ($N=0$): at $0<H<H'$ vortices are absolutely unstable in the film. In the range of values of H near H', as follows from (16),

$$H_{\min}(N)\approx H'\left[1+\left(\frac{3\pi\Phi_0 N}{4WH'}\right)^{2/3}\right]. \tag{17}$$

We note that $dH_{\min}/dN|_{N\to 0}\to\infty$. In the strong-field range $H\gg H'$ we have

$$H_{\min}(N)\approx\frac{\Phi_0 N}{W}+\frac{4}{\pi}\sqrt{\frac{H'\Phi_0 N}{W}}. \tag{18}$$

It must be noted that as H increases, the point of inflection y_1 in (13) shifts to the film edge. The maximum value $y_1\approx W/2-\xi$ is achieved when $H=\tilde{H}$, where

$$\tilde{H}=\frac{\Phi_0}{4\pi\xi^2}\propto H_{c2}. \tag{19}$$

Thus, the asymptotic expression (18) is valid when $H\leqslant\tilde{H}$. When $H>\tilde{H}$, $H_{\max}(N)=H_{\min}(N)$, i.e., $\tilde{H}$ is the maximum field in which the film is still in the mixed state [as follows from (19), in fields close to $\tilde{H}$ there is some overlapping of the vortex cores, which signifies an almost complete loss of superconductivity and a transition of the film to the normal state].

2. STABILITY OF THE MEISSNER STATE IN A CURRENT-CARRYING FILM

Let us now consider the problem of the stability of the superconducting state of a current-carrying film in a magnetic field. We assume that the current I flows in the positive direction of the x axis. At sufficiently low values of H the film is in the Meissner state, and the current distribution is given by the formula

$$i(y)=\frac{cH}{2\pi\lambda_\perp}y+\frac{I}{W}. \tag{20}$$

Under these circumstances the penetration of vortices into the film is prevented by the edge barrier at $y_0=W/2$. This barrier vanishes when $I=I_c(H)$, and then $\Delta G(y_0)$ [which is defined by (4), (6), (7), and (20)] becomes monotonic.[1)] The extremum points of the function $\Delta G(y_0)$ are given by the solution of the equation

$$P(y_0)=-I/(cW), \tag{21}$$

where the function $P(y)$ is defined by Eq. (14). The value of this function on the film edge equals

$$P\left(\frac{W}{2}-\xi\right)=\frac{W}{4\pi\lambda_\perp}(H-H_s). \tag{22}$$

In fields $H<H^*$ (the field H^* is defined below) the absolute value of $P(y_0)$ at the extremum point is less than the corresponding value on the edge. Thus, the solution of Eq. (21) vanishes at $I>I_c(H)$, where

$$I_c(H)=\frac{cW^2}{4\pi\lambda_\perp}(H_s-H), \quad H\leqslant H^*. \tag{23}$$

The current $I_c(H)$ can be called the suppression current of the barrier to vortex entry. The field H^*, which restricts the applicability of the last equation, is found from the condition of equality of $P(y_0)$ at the minimum point to its value at the film edge $y_0=W/2-\xi$. Considering the explicit form of $P(y_0)$ (14) we have

$$\frac{\pi}{2}\left(\frac{H_s}{H^*}-1\right)=\arccos\sqrt{\frac{H'}{H^*}}-\sqrt{\frac{H'}{H^*}\left(1-\frac{H'}{H^*}\right)}. \tag{24}$$

Assuming that $H^*\gg H'$, we hence find

$$H^*\approx\frac{H_s}{2}\left(1+Q\left(\sqrt{\frac{H'}{H_s}}\right)\right). \tag{25}$$

In fields $H>H^*$ the value of $P(y_0)$ at the minimum point is smaller than the corresponding values at the film edge. This means that solutions of Eq. (21) appear at the current $I_c(H)$ (23) (where the barrier to vortex entry is open). An analysis shows that the departure of vortices from the side of the film at $y_0=-W/2$ is prevented by an edge barrier, i.e., the appearance of a mixed state characterized by a number of trapped vortices N is possible. A further analysis of the behavior of the film at $I>I_c(H)$ and $H^*<H<H_s$ must be performed self-consistently using the Gibbs function of the test vortex for a film in the mixed state.[2)]

3. CRITICAL CURRENT OF A FILM IN THE MIXED STATE

The transport current I flowing along a film displaces the region occupied by vortices in the direction of negative values of y:

$$n(y)=\begin{cases}H/\Phi_0, & y\in[b,a],\\ 0, & y\in[b,a],\end{cases} \tag{26}$$

$$i(y)=\frac{cH}{2\pi\lambda_\perp}\begin{cases}y-a, & a\leqslant y\leqslant\dfrac{W}{2},\\ 0, & y\in[b,a],\\ y-b, & \dfrac{-W}{2}\leqslant y\leqslant b,\end{cases} \tag{27}$$

where

$$a=\Delta+\theta, \quad b=\Delta-\theta. \tag{28}$$

The total current I equals

$$I=-\frac{cH}{2\pi\lambda_\perp}\Delta(W-2\theta). \tag{29}$$

Thus, Δ determines the magnitude of the displacement of the region occupied by vortices under the action of the current, and θ, as before, is determined by the number of trapped vortices N. Let us now discuss the stability of the mixed state (26)–(29). We, first of all, note that for $N\neq 0$ the function $\Delta G(y_0,N)$ cannot be monotonic everywhere within the region $-W/2<y_0<W/2$. Therefore, we define the critical current I_c as the current at which vortices can enter the film (the barrier to entry is open) and leave it (the barrier to vortex exit is suppressed).

a) In the range of fields $H^*<H<H_s$ the condition under which the barrier to vortex entry into the film is open has the form

$$P\left(\frac{W}{2}-\xi\right)=\frac{Ha}{2\pi\lambda_\perp}. \tag{30}$$

Using (22), (28), and (29), we obtain an expression for the vortex entry current $I_{en}(N,H)$

$$\frac{4\pi\lambda_\perp}{cW}I_{en}(N,H)=-\frac{\Phi_0^2N^2}{WH}+\Phi_0N\left(2-\frac{H_s}{H}\right)+W(H_s-H). \tag{31}$$

Similarly, vortices leave the film when $I\geqslant I_{ex}(N,H)$, where the exit current $I_{ex}(N,H)$ is given by the equation

$$P(y_0^*)=\frac{Hb}{2\pi\lambda_\perp}, \tag{32}$$

or, in explicit form,

$$\frac{4\pi\lambda_\perp}{cW}I_{ex}(N,H)=-\left(1-\frac{\Phi_0N}{WH}\right)(\Phi_0N+4\pi\lambda_\perp P(y_0^*)), \tag{33}$$

where y_0^* is the minimum point of $P(y_0)$:

$$y_0^*\approx-\frac{W}{2}+\frac{W}{\pi}\sqrt{H'/H}. \tag{34}$$

When $N=0$, we have

$$I_{ex}(0,H)=\frac{cW^2H}{4\pi\lambda_\perp}, \tag{35}$$

$$I_{en}(0,H)=\frac{cW^2(H_s-H)}{4\pi\lambda_\perp}. \tag{36}$$

Plots of $I_{en}(N,H)$ and $I_{ex}(N,H)$ as functions of N for $H^*<H<H_s$ are shown in Fig. 1. As follows from Eq. (33), the exit current $I_{ex}(N_1,H)=0$ for $N=N_1$, which causes the expression in the second set of parentheses in (33) to vanish. Allowing for (14) and (34), we obtain

$$N_1=\frac{W}{\Phi_0}\left(H-\frac{4}{\pi}\sqrt{H'H}\right).$$

Let us now consider the passage of a film from the initial Meissner state, with $N=0$ in an assigned magnetic field (we shall consider $H<H_s$), to the static mixed state or the resistive state. Until we increase the current to the value of $I_{en}(N=0)$ (36), we remain in the stable Meissner state. When $I>I_{en}(N=0)$, vortices begin to enter the film, and N becomes nonzero, i.e., we enter the stability region of the mixed state (see Fig. 1). The situation will continue as such

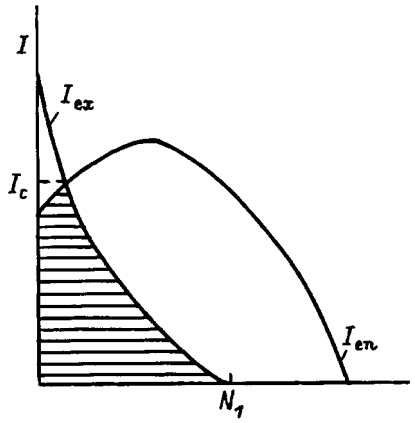

FIG. 1. Plots of $I_{en}(N)$ and $I_{ex}(N)$ as functions of the number of trapped vortices N for an assigned value of H. The hatched area corresponds to the stable mixed state. The point where the $I_{en}(N)$ and $I_{ex}(N)$ curves cross specifies the critical current I_c.

until I reaches $I_c(H)$, where $I_c(H)$ is the current at which the $I_{en}(N)$ and $I_{ex}(N)$ curves cross. When $I>I_c(H)$, vortices enter the film from the side at $y=W/2$ and leave at the other edge, i.e., the film is in a dynamic mixed (or resistive) state. The value of the critical current is found from formulas (31) and (33):

$$I_c(H)=\frac{cW^2}{16\pi\lambda_\perp}\frac{H_s^2}{H},\quad H^*<H<H_s. \tag{37}$$

This dependence coincides with the analogous expression for wide ($W\gg\lambda_\perp$) films.[3]

b) In fields $H_s<H<\tilde{H}$ the film is already in the mixed state when $I=0$. The passage of a weak current through it leads, first, to an increase in the number of trapped vortices and, second, to reorganization of their distribution (26). At currents larger than the critical value, the barrier to vortex exit is opened, and the film passes into the resistive state. The expression for the critical current in this range of magnetic fields has the form

$$I_c(H)=\frac{c}{16\pi\lambda_\perp}\frac{(H_sW-2H\xi)^2}{H},\quad H_s<H<\tilde{H}. \tag{38}$$

When $H\ll\tilde{H}=H_sW/(2\xi)$, Eq. (38) transforms into (37), and when $H=\tilde{H}$, $I_c(\tilde{H})=0$.

It is noteworthy that the matter of the stability of the current state of narrow thin strips in a transverse magnetic field considered here is identical to the analogous case for thin unbounded wafers of parallel geometry.[7] The characteristic magnetic fields H', H_{c1}, and H_s for films depend in an identical manner on the transverse scale, whose role is played by the film width W in our case and the wafer thickness d in the case in Ref. 7. This is apparently due to the small value of $W/\lambda_\perp$ and, accordingly of d/λ in Ref. 7: the Meissner currents depend linearly on the coordinate y, and the structures of Abrikosov and Pearl vortices practically coincide over small distances. The results that we obtained can be used for high-T_c superconducting films, in which the London depth λ is fairly large, and the condition $W\ll\lambda_\perp$ can be realized. The model considered here can be used to calculate the magnetic and dissipative characteristics of thin-film superconducting bridges.

We thank I. L. Maksimov for some useful discussions.

This work was performed with partial financial support from the Ministry of Education of the Russian Federation (Grant No. 95-0-7.3-178), as well as the Ministry of Science of the Russian Federation (Project No. 95057).

APPENDIX

Using Eq. (5), we represent dE_0/dy_0 in the form

$$\frac{dE_0}{dy_0}=-\frac{\Phi_0^2}{8\pi^2\lambda_\perp W}\left\{\frac{2y_0/W}{(y_0/W)^2-1/4}+\sum_{n=0}^{k_0/2}\frac{1}{n-1/2-y_0/W}-\sum_{n=0}^{k_0/2}\frac{1}{n-1/2+y_0/W}\right\}. \tag{A1}$$

The sums appearing in (A1) can be expressed in terms of $\Psi(z)=d\ \ln\Gamma(z)/dz$:

$$\sum_{n=0}^{k_0/2}\frac{1}{n-1/2\mp y_0/W}=\Psi\left(\frac{k_0}{2}+\frac{1}{2}\mp\frac{y_0}{W}\right)-\Psi\left(-\frac{1}{2}\mp\frac{y_0}{2}\right). \tag{A2}$$

Substituting (A2) into (A1) and using the asymptote of $\Psi(z)$ at $z\gg1$ [$\Psi(z)\approx\ln z$], as well as functional relations from Ref. 8, we obtain

$$\frac{dE_0}{dy_0}=\frac{-\Phi_0^2}{8\pi^2\lambda_\perp W}\ \pi\ \tan\frac{\pi y_0}{W}. \tag{A3}$$

The integration of (A3) allowing for the boundary condition $E_0(W/2-\xi)=0$ leads to Eq. (6).

*E-mail: ilmaks@phys.unn.runnet.ru

[1)] Similar calculations were performed by Shmidt to find the critical current of an unbounded film in a parallel magnetic field.[7]

[2)] In the paper cited,[7] whose results [pertaining to $I_c(H)$] coincide to within the notation with the results of this section, it was assumed for $H>H^*$ that the critical current is specified by an expression similar to (21). An analysis of this equation leads to a peak effect, which would be correct only if a mixed state does not form in the film.

[1] I. L. Maksimov and G. M. Maksimova, JETP Lett. **65**, 423 (1997).
[2] G. M. Maksimova and I. L. Maksimov, Physica C **282–287**, 2198 (1997).
[3] M. Yu. Kupriyanov and K. K. Likharev, Fiz. Tverd. Tela (Leningrad) **16**, 2829 (1974) [Sov. Phys. Solid State **16**, 1835 (1975)].
[4] I. Aranson, M. Gitterman, and B. Ya. Shapiro, Phys. Rev. B **51**, 3092 (1995).
[5] A. I. Larkin and Yu. N. Ovchinnikov, Zh. Éksp. Teor. Fiz. **61**, 1221 (1971) [Sov. Phys. JETP **34**, 651 (1972)].
[6] K. K. Likharev, Izv. Vyssh. Uchebn. Zaved. Radiofiz. **14**, 2095 (1971).
[7] V. V. Shmidt, Zh. Éksp. Teor. Fiz. **57**, 2095 (1969) [Sov. Phys. JETP **30**, 1137 (1970)].
[8] I. S. Gradshteyn and I. M. Ryzhik, *Table of Integrals, Series, and Products*, transl. of 4th Russ. ed., Academic Press, New York (1980), 959 pp.

Translated by P. Shelnitz

Influence of the superconducting state on the thermal instability of low-temperature plastic deformation in crystals

G. A. Malygin

A. F. Ioffe Physicotechnical Institute, Russian Academy of Sciences, 194021 St. Petersburg, Russia
(Submitted March 24, 1998)
Fiz. Tverd. Tela (St. Petersburg) **40**, 1778–1784 (October 1998)

The influence of the superconducting transition on the unstable, discontinuous nature of plastic deformation in crystals at low temperatures (<10 K) is discussed theoretically. It is established, within the mechanism of the thermal instability of low-temperature plastic deformation, that the superconducting state promotes the stabilization of deformation in a superconductor because of the positive sign of the temperature sensitivity coefficient of the flow stresses below the superconducting-transition temperature and the reduced level of energy dissipated by moving dislocations in comparison to the normal metal. The temperature-rate regions for stable and unstable deformation of a superconductor and the dependence of the stress-jump amplitudes on temperature and deforming stress are determined. © *1998 American Institute of Physics.* [S1063-7834(98)00310-4]

The superconducting state has a complex and uncertain influence on the characteristic instability (discontinuous nature) of plastic deformation in crystals at low deformation temperatures ($<10-20$ K). The transition to the superconducting state can initiate instability [Pb (Refs. 1 and 2)] or suppress it [Al (Ref. 3), Pb (Ref. 4), and Al–Mg (Ref. 5), Al–Li (Refs. 5 and 6), and Sn–Cd (Ref. 7) alloys], have no influence on it (the alloys just enumerated in the case of large strains[5–7]), or alter only its parameters, for example the stress-jump amplitudes.[6,7] Such an uncertain effect of the superconducting (S) state on the stability of low-temperature deformation indicates that the transition to this state has a significant influence not on one, but on several parameters, on which the stability of the low-temperature deformation of crystals depends.

The thermal (heat-induced) mechanism for the appearance of the instability of low-temperature deformation has been developed most thoroughly and is most consistent with experiment.[8–12] From the standpoint of the thermal mechanism, the transition to the superconducting state can influence such significant factors of this mechanism as the specific heat and thermal conductivity of the crystal, as well as, as was noted in Ref. 13, the sign of the temperature-sensitivity coefficient of the flow stresses below the critical superconducting-transition temperature T_c, caused by the softening effect associated with this transition.[14–20] When the sign of this coefficient is positive, an increase in the temperature of the crystal due to warming by plastic deformation will enhance, rather than weaken, the deforming stress, i.e., will increase the thermal stability of deformation.

The influence of the change in the specific heat (c) of a crystal accompanying the N–S transition on the stability of low-temperature deformation was analyzed in Ref. 13. The stabilizing role of the change in the sign of the temperature-sensitivity coefficient of the flow stresses near T_c in the development of thermomechanical instability in superconductors was discussed at a qualitative level in the same paper. In the present paper we shall examine this question at the quantitative level (Sec. 1). As for the thermal conductivity $\varkappa$, the decrease in it in the superconducting state should not significantly influence the stability of deformation, since the relaxation rate of heat in the bulk of a crystal is determined by the thermal diffusivity $a=\varkappa/c$, which changes only slightly upon the superconducting transition,[21] and the relaxation of heat as a result of surface heat transfer, which usually controls the thermal stability of low-temperature deformation,[11] does not depend on the state of the crystal.

One more factor which can play an appreciable stabilizing role in the plastic deformation of superconductors is the coefficient β of the conversion of the work of plastic deformation into heat, which is related to the energy dissipation by moving dislocations when they interact with electrons. As the calculations in Refs. 22 and 23 show, the viscous force of dislocations, i.e., their viscous damping coefficient B is appreciably lower in a superconductor than in a normal metal and depends strongly on temperature and dislocation velocity. In fact, according to the data in Ref. 24, all other conditions being equal, the stationary warming of an indium crystal is reduced by 1.5 fold following its passage into the superconducting state. From the standpoint of the thermal mechanism, a decrease in the energy dissipation rate should have a stabilizing influence on plastic deformation in superconductors. This question is discussed in Sec. 2. The influence of the superconducting state on the stress jump amplitudes is examined in Sec. 3.

1. TEMPERATURE SENSITIVITY OF FLOW STRESSES AND STABILITY OF DEFORMATION IN SUPERCONDUCTORS

The instability of low-temperature deformation usually develops at moderate and large degrees of strain; therefore, we shall henceforth assume that the thermal (τ^*) and ather-

mal (τ_μ) components of the flow stress τ are determined by the intersection of moving dislocations with stationary dislocations

$$\tau=\tau_0+\tau_\mu+\tau^*, \quad \tau^*=\frac{H_0-kT\ln(\nu/\dot{\varepsilon})}{V},$$

$$\tau_\mu=\alpha\mu b\rho^{1/2}, \tag{1}$$

where τ_0 is the flow stress for the interaction of dislocations with impurity atoms, $V=bsl$ is the activation volume, b is the Burgers vector, s is the barrier width, $l=\rho^{-1/2}$ is the distance between static dislocations, H_0 is the total activation energy for overcoming the barrier, T is the temperature, k is Boltzmann's constant, $\dot{\varepsilon}$ is the rate of plastic deformation, ν is the pre-exponential factor in the Arrhenius expression for the rate of deformation, α is the interdislocation interaction constant, μ is the shear modulus, and ρ is the dislocation density.

The transition to the superconducting state is accompanied by softening of the crystal $\Delta\tau_{ns}=\tau_n^*-\tau_s^*$.[14,15] According to Ref. 16, this softening is caused by partial undamping of dislocations in a superconductor, which results in an increase in the frequency factor ν in (1), and, therefore,

$$\Delta\tau_{ns}^*=\frac{kT}{V}\ln\frac{\nu_s}{\nu_n}, \quad \frac{\nu_s}{\nu_n}=\frac{B_n}{B_s}=\frac{1}{2}\,(1+e^{\Delta(T)/T}), \tag{2}$$

where B_s and B_n are the viscous damping coefficients in the superconducting (S) and normal (N) states, and $\Delta(T)$ is the superconducting energy gap. The frequency mechanism (2) is effective for distances between obstacles $l>l_0$, where $l_0=\pi(MC)^{1/2}/B_n$, M is the mass of a unit length of a dislocation, and C is its linear tension. If the distance between obstacles $l<l_0$, the dynamic mechanism,[17] which is associated with an increase in the contribution of the inertia of dislocations to their ability to overcome barriers becomes effective. In this case

$$\tau_s^*=\tau_n^*\,\frac{1+(8/\pi^2)e^{-Z_n}}{1+(8/\pi^2)e^{-Z_s}}, \quad Z_{n,s}=\frac{B_{n,s}l}{\pi(MC)^{1/2}}. \tag{3a}$$

When $Z_{n,s}\ll 1$, the degree of N–S softening has the form

$$\Delta\tau_{ns}=0.5Z_n\tau_n^*\,\frac{B_n-B_s}{B_n}, \quad \frac{B_n-B_s}{B_n}=\tanh\frac{\Delta(T)}{2kT}. \tag{3b}$$

Other mechanisms of softening accompanying the superconducting transition have been considered: a thermoinertial mechanism,[18] a thermal-activation mechanism,[19] which takes into account the influence of the superconducting state on the transit time of dislocations between potential wells, and a general mechanism for the influence of the viscosity of the electron gas on the ability of dislocations to overcome potential barriers with the aid of thermal fluctuations.[20] All these mechanisms specify a particular dependence of the pre-exponential (frequency) factor ν in (1) on the viscous damping coefficient B of dislocations. In a certain bounded range (with respect to stress and dislocation velocity) the degree of softening $\Delta\tau_{ns}$ associated with these mechanisms reduces, as can be shown, to expressions like (2) or (3b).

The curves in Fig. 1 demonstrate the temperature dependence of the flow stress according to relations (1)–(3b) in dimensionless coordinates, where $\tau^*(0)=H_0/V$, $T_c/T_\infty=0.04$, $T_\infty=H_0/k\ln(\nu/\dot{\varepsilon})$, $Z_n=4\times10^{-2}$, $\Delta(T)=1.76kT_c\Delta(t)$, and $t=T/T_c$. In the calculations here and below the energy gap was approximated by the expression $\Delta(t)=1-t^6$, which quite closely describes its variation with temperature according to the BCS theory. It can be seen from the figure that in the case of expression (3b) the temperature dependence of the flow stress (curve *3*) below T_c has a segment with a positive sign for the stress temperature sensitivity coefficient, $\partial\tau_s^*/\partial T>0$. There is no such segment on the analogous plot for expression (2) (curve *2*).

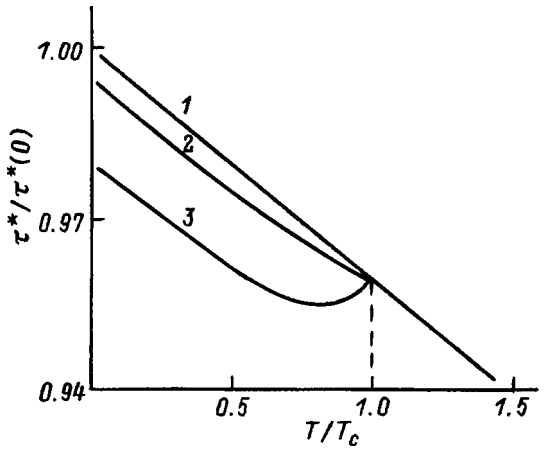

FIG. 1. Temperature dependence of the flow stress in the normal (*1*) and superconducting (*2*, *3*) states of a crystal: *2*—according to expression (2), *3*—according to expression (3b).

The criterion for the thermal instability in thermally activated plastic deformation has the form[10,25]

$$\left(S_T-\frac{c(K+\chi)}{\beta\tau}\right)(T-T_0)>S_{\dot{\varepsilon}}. \tag{4a}$$

Here $S_T=-(\partial\tau^*/\partial T)_{\dot{\varepsilon}}$ and $S_{\dot{\varepsilon}}=(\partial\tau^*/\partial\ln\dot{\varepsilon})_T$ are the temperature and rate sensitivity coefficients of the flow stresses, $c=c(T)$ is the specific heat of the crystal, K is the effective modulus of the crystal/loading-machine system, χ is the strain-hardening coefficient, T is the temperature to which the crystal is heated by plastic deformation, and T_0 is the temperature of the coolant. In the normal state $S_T=(k/V)\ln(\nu/\dot{\varepsilon})$, and $S_{\dot{\varepsilon}}=kT/V$. Substituting these expressions into (4a), we obtain the equation for determining the critical heating temperature as a function of the temperature of the coolant:

$$\left(1-\frac{c(T)}{c_k}\right)(T-T_0)>T/\ln(\nu/\dot{\varepsilon}), \tag{4b}$$

where $c_k=\beta\tau S_T/(K+\chi)$. The solution of this equation for a normal metal [$c=\gamma_eT$, $\ln(\nu/\dot{\varepsilon})=25$] and $T_0/T_k=0.1$ is illustrated by curve *1* and line *4* in Fig. 2 [the left-hand side $L(T)$ and the right-hand side $R(T)$ of Eq. (4b)]. The intersection of these curves at different values of T_0 specifies the upper $[T_2(T_0)]$ and lower $[T_1(T_0)]$ boundaries of the temperature range for unstable deformation (curves *1* in Figs. 3a and 3b), and their tangency specifies the maximum coolant tempera-

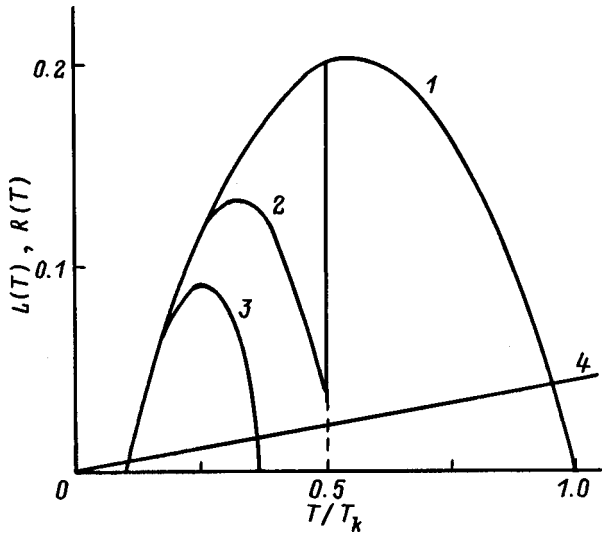

FIG. 2. Solution of Eqs. (4b) and (5a) for the normal (*1*) and superconducting (*2*, *3*) states of a crystal, *2*—in the case of expression (5b), *3*—in the case of expression (5c).

ture $T_{0k}=0.64T_k$, above which deformation becomes stable for any T_0, where $T_k=c_k/\gamma_e$, and γ_e is the electronic specific heat.

Substituting $\tau_s^*=\tau_n^*-\Delta\tau_{ns}$ and $c_s=c_s(T)$ into (4a) in the case of a superconductor, we obtain

$$\left(1-\frac{c_s(T)}{c_k}+\frac{1}{S_T}\frac{\partial\Delta\tau_{ns}}{\partial T}\right)(T-T_0)>T/\ln(\nu/\dot{\varepsilon}). \tag{5a}$$

In the superconducting state $c_s=c_c e^{-\delta(T_c/T)}$, $c_c=3\delta^2\gamma_e T_c$ and $\delta=1-1.8$ (Ref. 21). For expressions (2) and (3b), which describe the $N-S$ softening effect, we have, respectively,

$$\frac{1}{S_T}\frac{\partial\Delta\tau_{ns}}{\partial T}=\left(\ln\frac{B_n}{B_s}+\frac{\partial\ln(B_n/B_s)}{\partial\ln T}\right)\frac{1}{\ln(\nu/\dot{\varepsilon})}, \tag{5b}$$

$$\frac{1}{S_T}\frac{\partial\Delta\tau_{ns}^*}{\partial T}=0.5Z_n\left(-\frac{B_n-B_s}{B_n}+\frac{V\tau_n^*}{k\ln(\nu/\dot{\varepsilon})}\frac{\partial(B_n-B_s)/B_n}{\partial T}\right). \tag{5c}$$

Curves *2* and *3* (Fig. 2) show the character of the temperature dependences of the left-hand sides of Eq (5a) for the expressions under consideration. Here $c_c/c_k=3\delta^2(T_c/T_k)$, $\delta=1.35$, $T_c/T_k=0.5$, and the remaining parameters are the same as above. It is noteworthy that the critical temperature $T_2<T_c$ in the case of (3b).

The results of solving Eq. (5a) at all T_0 for mechanisms (2) and (3b), respectively, are illustrated by curves *2* and *3* in Fig. 3a. The dashed line demarcates the temperature region for the existence of the superconducting state in the crystal. It can be seen that the superconducting transition has practically no influence on the thermal stability of deformation in the case of mechanism (2), while for (3b) there is a considerable range of experimental temperatures ($0.54T_c<T_0<T_c$) and of warming temperatures ($0.72T_c<T<T_c$) where deformation is stable in the superconducting state, but not in the normal state. This is a consequence of the existence of

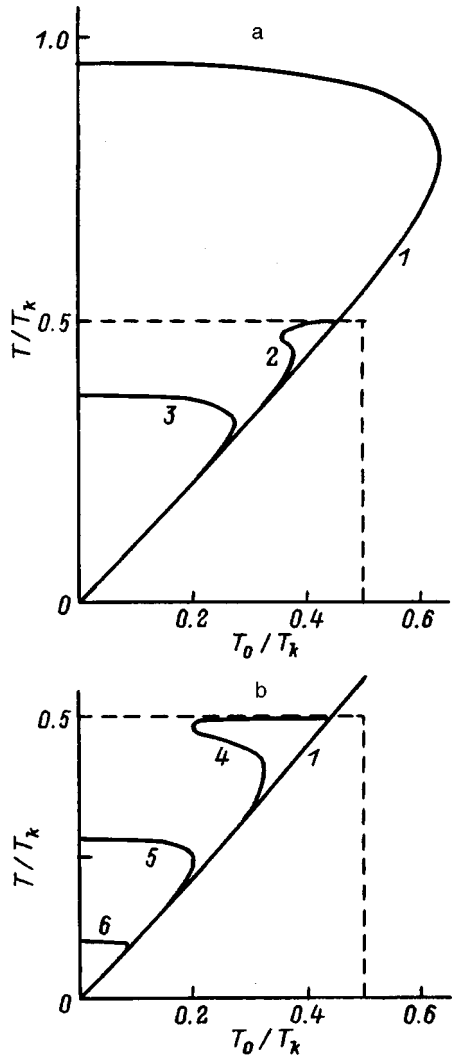

FIG. 3. Regions of critical temperatures for the appearance of the thermal instability of deformation in the normal (*1*) and superconducting (*2–6*) states of a crystal. *a*) For $\beta_s=\beta_n$: *2*—in the case of expression (5b), *3*—in the case of expression (5c); *b*) for $\beta_s\neq\beta_n$ and dislocation velocities $u/u_c=3$ (*4*), 1.5 (*5*), and 1.01 (*6*). The dashed line demarcates the region for the existence of the superconducting state.

positive temperature sensitivity of the flow stresses for this case below T_c and weakening of this sensitivity in the adjacent temperature range (curve *3* in Fig. 1).

The solutions of Eqs. (4b) and (5a) shown in Fig. 3a in the form of $T_n(T_0)$ and $T_s(T_0)$ curves enable us to determine the ranges of the rates of deformation $\dot{\varepsilon}_n$ and $\dot{\varepsilon}_s$ (and the stress τ, see Sec. 3) where deformation is unstable in the normal and superconducting states:[10,25]

$$\dot{\varepsilon}_{n,s}=\dot{\varepsilon}_h\frac{T_{n,s}-T_0}{T_k}\left(\frac{T_{n,s}}{T_k}\right)^p,\quad \dot{\varepsilon}_h=\frac{fT_k h(T_k)}{\beta\tau d}. \tag{6}$$

Here d is the characteristic transverse dimension of the crystal, f is a coefficient, which depends on the cross-sectional shape of the crystal, and h is the surface heat-transfer coefficient. The results of the calculation for $h(T)=h_m T^p$, where $p=2$ [deformation in liquid ^{3}He (Refs. 26 and 27)] are illustrated by curves *1–3* in Fig. 4. The dashed line shows the temperature dependence of the rate of deformation $\dot{\varepsilon}_c(T_0)$,

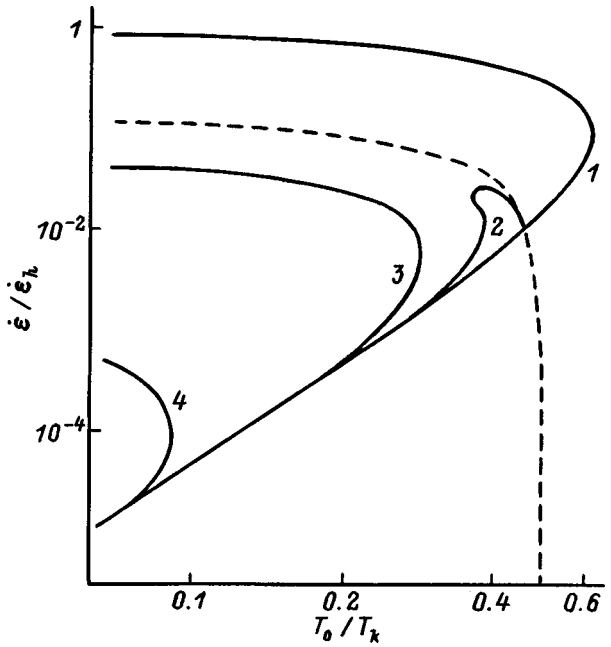

FIG. 4. Temperature-rate region for the appearance of the thermal instability of deformation in the normal (*1*) and superconducting (*2–4*) states of a crystal: *2, 3*—in the case of expressions (2) and (3b), respectively; *4*—according to (5b) and Eq. (9) for $\beta_s/\beta_n=10^{-2}$. The dashed line demarcates the region for the existence of the superconducting state.

above which the crystal passes from the superconducting state into the normal state as a consequence of warming:

$$\dot{\varepsilon}_c(T_0)=\frac{fh(T_c)}{\beta\tau d}(T_c-T_0). \tag{7}$$

As can be seen from Fig. 4, in the case of expression (3b) there is a region of rates of deformation $\dot{\varepsilon}$ and temperatures T_0 between this curve and curves *1* and *3* where deformation in the superconducting state is stable toward warming. The corresponding region for expression (2) (between curves *1* and *2*) is insignificant. Curve *4* in this figure shows how strongly the region for the thermal instability of deformation is reduced in size in response to a sharp decrease in the rate of energy dissipation in the superconductor (see the next section).

It was assumed in the calculations above that the critical superconducting transition temperature $T_c=0.5T_k$ is less than the maximum temperature $T_{0k}=0.64T_k$, above which deformation in the normal metal remains stable at any experimental temperature and rate of deformation (Figs. 3a and 4). Since $T_k=c_k/\gamma_e\sim\tau^n$, where $n=1-2$, such a situation is characteristic of superconductors with low values of T_c (Al, Sn, and In), as well as for superconductors which have high values of T_c, but are high-strength (Nb). For metals having a low strength, but relatively large values of T_c (Pb), it can turn out that $T_c>T_k$. In this case, as a calculation shows, regardless of the mechanism of the $\Delta\tau_{ns}$ effect, the normal region for the thermomechanical instability of deformation lies within the region for unstable deformation in the superconducting state.[13] This means that there is a region of temperatures T_0 and rates of deformation $\dot{\varepsilon}$, where the transition from the superconducting state to the normal state causes the load jumps to vanish [1.3–3.2 K, Pb (Refs. 1, 2, and 4)]. The opposite situation[4] observed in lead at a lower temperature (0.5 K) is possibly due to the influence of the residual normal phase remaining after the magnetic field is switched off, which is characteristic of plastically deformed type-II superconductors, such as lead. This question requires further study.

2. INFLUENCE OF THE ENERGY DISSIPATION LEVEL

The coefficient β of the conversion of the work of plastic deformation into heat is of the order of 0.4–0.6 at low temperatures.[24] The fraction of the energy dissipated that is related to the interaction of dislocations with electrons is presently unclear. The 1.5-fold decrease in the temperature to which indium crystals warm after the transition to the superconducting state[24] indicates that this fraction is significant.

When the dislocation motion is thermally activated, energy is dissipated mainly by the movement of dislocations having large velocities u between potential barriers. The mean energy-dissipation rate of a unit of length of a dislocation undergoing thermally activated motion with a velocity u_a equals $W_0=Fu_a$, where $F=Bu$ is the viscous force of the dislocations. For a density of mobile dislocations ρ_m, the energy dissipation rate $W=W_0\rho_m=\tau_F\dot{\varepsilon}$, where $\tau_F=F/b$ is the viscous damping stress and $\dot{\varepsilon}=b\rho_m u_a$ is the rate of plastic deformation. Assuming that the viscous damping stress of the dislocations amounts to a fraction β of the total deforming stress, $\tau_F=\beta\tau$, we find that the ratio between the rates of energy dissipation in the normal and superconducting states is $W_s/W_n=\beta_s/\beta_n=F_s/F_n$. At dislocation velocities $u\leqslant u_c$, where $u_c=10^2-10^3$ m·s^{-1} is the critical velocity, above which the Cooper electron pairs dissociate, $F_s/F_n=B_s/B_n=2(1+e^{\Delta(T)/T})^{-1}$. At large velocities $u>u_c$ the electronic dislocation damping force F_s is a complicated function of dislocation velocity and temperature, according to the calculations in Refs. 22 and 23. When $T/T_c<0.4$, it does not depend on temperature and increases with increasing dislocation velocity, so that at $u/u_c=1.5$, 2.5 and 3.0 the ratio F_s/F_n equals 0.2, 0.6, and 0.7, respectively.[23] In the calculations below the dependence of $\Gamma=F_s/F_n=\beta_s/B_n$ on u and $t=T/T_c$ at $u/u_c>1$ is approximated by the expression

$$\Gamma=1-e^{-0.6(u/u_c-1)}\left(1-t^{-1}e^{-1.76[\Delta(t)/t]}\right). \tag{8}$$

With consideration of the influence of the temperature and the dislocation velocity on the coefficient β_s, the condition (5) for the loss of the thermal stability of deformation in a superconductor takes the form

$$\left(1-\frac{\beta_n}{\beta_s(T,u)}\frac{c_s(T)}{c_k}+\frac{1}{S_T}\frac{\partial\Delta\tau_{ns}}{\partial T}\right)(T-T_0)>T/\ln\frac{\nu}{\dot{\varepsilon}}. \tag{9}$$

In Fig. 3b curves *4* and *6* show the results of a calculation of the temperature boundaries of the regions of thermal instability of deformation according to (8) and (9) in the case of expression (2) as the dislocation velocity decreases from $u/u_c=3$ to 1.01 when $F_s/F_n=\beta_s/\beta_n=0.01$ at $T=0$. It can be seen that lowering of the energy dissipation level leads to the appearance of a region of stable deformation for the su-

perconductor, which becomes increasingly broader as the value of β_s decreases. A strong drop in the energy dissipation level ($\beta_s/\beta_n=0.01$) causes a sharp reduction in the size of the temperature-rate region for the development of the thermal instability of deformation in a superconductor (curve *4* in Fig. 4). Clearly, in the case of expression (3b) a decrease in β_s will additionally expand the region of stable deformation of the crystal in the superconducting state.

3. STRESS-JUMP AMPLITUDES

As experiment has shown,[5–7] the instability of deformation usually develops during the plastic deformation of crystals in an earlier stage of deformation in the superconducting state than in a normal metal and with smaller jumps in the load amplitude. When the deforming stresses are increased further, the difference between the superconducting and normal states vanishes. The mechanism of thermal instability enables us to understand these points, which are fundamental for the discontinuous deformation of superconductors.

For this purpose, let us consider how the temperature T_0 and the stress τ influence the stress jump amplitudes in the normal ($\Delta\tau_n$) and superconducting ($\Delta\tau_s$) states of a crystal. According to the thermal mechanism, the stress-jump amplitude is defined by the expression[10]

$$\Delta\tau=\frac{kT_2}{V}\ln\frac{\nu}{\dot\varepsilon_2}-\frac{kT_1}{V}\ln\frac{\nu}{\dot\varepsilon_1}, \tag{10}$$

where T_1, T_2 and $\dot\varepsilon_1$, $\dot\varepsilon_2$ are, respectively, the lower and upper critical temperatures (Figs. 3a and 3b) and rates of deformation (Fig. 4) demarcating the regions for the appearance of the thermal instability of deformation. Since, according to (6), the critical rates of deformation are functions of the critical temperatures, the variation of the latter with T_0 (Fig. 3) and τ (see Fig. 6a below) specifies the dependence of the jump amplitudes on these factors.

Curves *1* and *2* in Fig. 5 show the results of a calculation of the dependence of the stress-jump amplitudes in the normal and superconducting states on the deformation temperature T_0 at a constant value of T_k, i.e., at a constant level of deforming stresses, in the case of expression (3b), $T_c=0.5T_k$, and $\ln(\nu/\dot\varepsilon_h)=17.4$. In fact, since $T_k=c_k/\gamma_e$, with consideration of (1), (4b), and the Cottrell–Stokes law for $S_T=S_0(\tau-\tau_0)$ we have

$$T_k=\frac{\beta S_0}{\gamma_e(K+\chi)}(\tau-\tau_0)\tau,\quad S_0=\frac{k\ln(\nu/\dot\varepsilon)}{\alpha\mu b^2 s}. \tag{11}$$

It is seen that instability appears at a lower temperature and with a smaller stress-jump amplitude in the superconducting state (curve *2*) than in the normal state (curve *1*). The dashed line in Fig. 5 denotes the temperature for passage of the crystal into the superconducting state. Curve *3* in that figure shows how strongly the stress jump amplitude decreases in response to dramatic lowering of the energy dissipation coefficient ($\beta_s/\beta_n=0.01$) in a superconductor.

To find the dependence of the critical temperatures on deforming stress in the normal and superconducting states we must solve Eqs. (4b) and (5a), respectively. Substituting

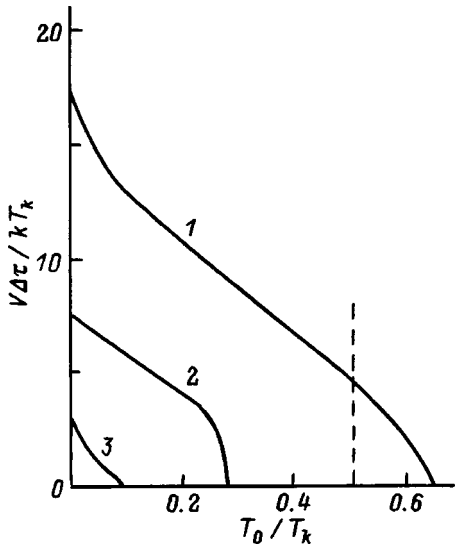

FIG. 5. Temperature dependence of the stress-jump amplitudes in a normal metal (*1*) and a superconductor (*2*, *3*): *2*—in the case of expression (3b), *3*—in the case of expression (2) and $\beta_s/\beta_n=10^{-2}$. Dashed line—temperature of the $N-S$ transition.

(5c), $c_k\sim T_k$ (11), and $S_T=S_0(\tau-\tau_0)$ into these equations and taking into account that, according to (3a), the temperature sensitivity coefficient of the softening stress $\Delta\tau_{ns}$ contains the parameter $Z_n\sim l\sim\rho^{-1/2}\sim(\tau-\tau_0)^{-1}$, we obtain expressions for determining the dependence of the critical temperatures $T_{1,2}$ on the stress τ for the normal and superconducting states of the crystal, respectively:

$$\left(1-\frac{w_c t}{(w-1)w}\right)(t-t_0)>t/\ln(\nu/\dot\varepsilon),$$

$$w_c=\frac{\gamma_e T_c(K+\chi)}{\beta S_0\tau_0^2}, \tag{12a}$$

$$\left(1-\frac{3\delta^2 w_c}{(w-1)w}e^{-1.35/t}+\frac{1}{S_T}\frac{\partial\Delta\tau_{ns}}{\partial T}\frac{1}{w-1}\right)(t-t_0)$$

$$>t/\ln(\nu/\dot\varepsilon), \tag{12b}$$

where $t=T/T_c$, $t_0=T_0/T_c$, and $w=\tau/\tau_0$.

The result of solving Eqs. (12a) and (12b) for $w_c=1$, $T_0/T_c=0.5$, and $Z_n=Z_n(0)/(w-1)$, where $Z_n(0)=4\times10^{-2}$, are illustrated by curves *1* and *2* in Fig. 6a. The dashed lines in the figure mark the positions of T_0 and T_c. It follows from the results of the solution that 1) the region of thermal instability of deformation in the superconductor up to $\tau/\tau_0=3.95$ comprises a small part of the region of unstable deformation in the normal metal; 2) as the deforming stress is increased, the instability of deformation appears first in the normal state ($\tau/\tau_0=1.5$) and then in the superconducting state ($\tau/\tau_0=1.85$); 3) there is a limiting stress ($\tau/\tau_0=3.95$ for the values of the parameters given), above which the upper critical temperature of the superconducting state becomes equal to the temperature of the superconducting transition (point *c* on curve *2*). This means that above this critical stress thermal instability develops in the superconductor as in the normal metal.

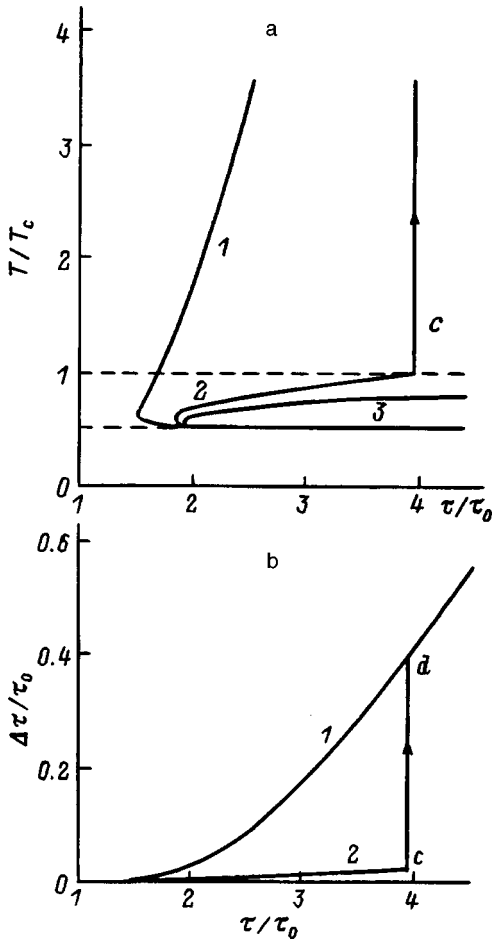

FIG. 6. Dependence of the critical temperatures (a) and the stress-jump amplitudes (b) on deforming stress in the normal (*1*) and superconducting (*2*, *3*) states of a crystal: *2*—for $Z_n \sim (\tau-\tau_0)^{-1}$, *3*—for $Z_n = \text{const}$. The dashed lines mark the temperatures T_c and T_0.

An analysis shows that such behavior of the upper boundary is related to the dependence of the dynamic parameter Z_n in (5c) and (12b) on $\tau-\tau_0$. In the absence of this dependence, the upper boundary of the superconducting region (curve *3* in Fig. 6a) is at a certain constant distance from the superconducting transition temperature and thus forms a ''forbidden zone'' separating the region of thermal instability of the superconductor from the normal metal. Passage through this zone can occur in this case only as a result of steady warming of the superconductor of sufficient magnitude:

$$T = T_0 + \frac{\beta\tau\dot{\varepsilon}d}{fh}. \tag{13}$$

In the notation in Fig. 6a, the dependence of the warming temperature (13) on the deforming stress τ can be written in the form $t = t_0 + pw$, where $p = \beta\tau_0\dot{\varepsilon}d/fhT_c$. Under ordinary deforming conditions ($\beta = 0.6$, $\tau_0 = 10$ MPa, $\dot{\varepsilon} = 10^{-4}$ s^{-1}, $d = 2\times10^{-3}$ m, $f = 2$) in liquid ^{3}He ($h \approx 100$ W·m^{-2}·K^{-1}, $T_c = 3$ K) the coefficient $p \approx 2\times10^{-3}$ is too small for the growth of the deforming stresses during deformation to be able to lead to passage of the entire volume of the superconductor into the normal state at $T_0/T_c < 0.9$. A higher rate of deformation (of the order of 10^{-3}–10^{-2} s^{-1}) is needed.

The results of calculating the dependence of the stress-jump amplitudes in the normal and superconducting states on deforming stress under the conditions indicated above are shown in Fig. 6b. As can be seen, in accordance with experiment,[5–7] after the onset of discontinuous deformation in the normal state the transition to the superconducting state at first leads to the stabilization of deformation ($\Delta\tau_s = 0$). As the stress (degree of strain) increases further, deformation of the superconductor also becomes unstable, but the jump amplitudes are smaller for it than for the normal metal. The ''fine-toothed'' course of the stress-strain diagrams is a characteristic feature of the deformation of superconductors.[6,7] Finally, at the critical stress corresponding to point *c* on curve *2* (Fig. 6b), the jump amplitudes increase sharply and reach the same values as in the normal metal (point *d* on curve *1*). This is also characteristic of the unstable deformation of crystals in the superconducting state.[7]

Thus, the results of this work show that the mechanism of the thermal instability of low-temperature deformation enable us to understand both the main fundamental points associated with influence of the superconducting state on the instability (discontinuous nature) of plastic deformation in superconductors and the fine details of this influence.

[1] Yu. A. Ossipyan and V. S. Bobrov, Cryst. Res. Technol. **19**, 825 (1984).
[2] E. Y. Gutmanas and Yu. Estrin, Phys. Status Solidi A **91**, 137 (1985).
[3] I. N. Kuz'menko and V. V. Pustovalov, Fiz. Nizk. Temp. **5**, 1433 (1979) [Sov. J. Low Temp. Phys. **5**, 676 (1979)].
[4] I. N. Kuz'menko and V. V. Pustovalov, Dokl. Akad. Nauk SSSR **282**, 599 (1985) [Sov. Phys. Dokl. **30**, 424 (1985)].
[5] V. V. Pustovalov, Mater. Sci. Eng., A **234–236**, 157 (1997).
[6] N. V. Isaev, V. V. Pustovalov, V. S. Fomenko, and S. É. Shumilin, Fiz. Nizk. Temp. **20**, 832 (1994) [Low Temp. Phys. **20**, 653 (1994)].
[7] G. I. Kirichenko, V. D. Natsik, V. V. Pustovalov, V. P. Soldatov, and S. É. Shumilin, Fiz. Nizk. Temp. **23**, 1010 (1997) [Low Temp. Phys. **23**, 758 (1997)].
[8] G. A. Malygin, Phys. Status Solidi B **61**, K45 (1974).
[9] L. P. Kubin and Yu. Estrin, Cryst. Res. Technol. **19**, 853 (1984).
[10] G. A. Malygin, Fiz. Met. Metalloved. **81(3)**, 5 (1996).
[11] O. V. Klyavin, G. A. Malygin, and Yu. M. Chernov, Fiz. Tverd. Tela (St. Petersburg) **38**, 191 (1996) [Phys. Solid State **38**, 105 (1996)].
[12] M. Zaiser and P. Hähner, Phys. Status Solidi B **199**, 267 (1997).
[13] G. A. Malygin, Fiz. Nizk. Temp. **12**, 849 (1986) [Phys. Status Solidi B **12**, 481 (1986)].
[14] V. I. Startsev, V. Ya. Il'ichev, and V. V. Pustovalov, *Plasticity and Strength of Metals and Alloys at Low Temperatures* [in Russian], Metallurgiya, Moscow (1975), 328 pp.
[15] H. Kojima, T. Moriya, and T. Suzuki, J. Phys. Soc. Jpn. **38**, 1032 (1975).
[16] V. D. Natsik, Zh. Éksp. Teor. Fiz. **61**, 2540 (1971) [Sov. Phys. JETP **34**, 1359 (1972)].
[17] A. V. Granato, Phys. Rev. B **4**, 2196 (1971).
[18] V. I. Dotsenko, A. I. Landau, and V. V. Pustovalov, *Current Problems in the Low-Temperature Plasticity of Materials* [in Russian], Naukova Dumka, Kiev (1987), 162 pp.
[19] R. Behrensmeir and J. M. Galligan, Phys. Status Solidi A **131**, 357 (1992).
[20] V. D. Natsik and P. P. Pal'-Val', Fiz. Nizk. Temp. **23**, 1229 (1997) [Low Temp. Phys. **23**, 922 (1997)].
[21] N. V. Zavaritskiĭ, Zh. Éksp. Teor. Fiz. **34**, 1116 (1958) [Sov. Phys. JETP **7**, 773 (1958)].
[22] G. P. Huffman and N. Louat, Phys. Rev. Lett. **24**, 1055 (1970).
[23] V. G. Bar'yakhtar, E. I. Druinskiĭ, and I. I. Fal'ko, Fiz. Met. Metalloved. **33**, 5 (1972).

[24] O. V. Klyavin, *Physics of the Plasticity of Crystals at Helium Temperatures* [in Russian], Nauka, Moscow (1987), 257 pp.
[25] G. A. Malygin, Fiz. Tverd. Tela (St. Petersburg) **39**, 1392 (1997) [Phys. Solid State **39**, 1235 (1997)].
[26] D. M. Lee and H. F. Fairbank, Phys. Rev. **116**, 1359 (1959).
[27] K. N. Zinov'eva, Zh. Éksp. Teor. Fiz. **60**, 2243 (1971) [Sov. Phys. JETP **33**, 1205 (1971)].

Translated by P. Shelnitz

Singlet-triplet model of cuprate magnetism

A. S. Moskvin* and A. S. Ovchinnikov

Institute of Physics and Applied Mathematics, Ural University, 620083 Ekaterinburg, Russia
(Submitted April 10, 1998)
Fiz. Tverd. Tela (St. Petersburg) **40**, 1785–1792 (October 1998)

A model for describing the spin subsystem of cuprates within a model of polar singlet-triplet Jahn–Teller centers is proposed. In this model spin ordering is described by two vector order parameters **S** (the total spin of a CuO_4 cluster) and **V** (the operator of the change in spin multiplicity per cluster). It is shown within a modified mean-field approximation that the formation of a noncollinear magnetic structure characterized by an antiferromagnetic wave vector, which, however, has a nontrivial temperature dependence of the order parameters, is possible along with the formation of ordinary collinear structures of the (anti)ferromagnetic type. The temperature dependences of the order parameters and the principal equilibrium thermodynamic characteristics, viz., the static susceptibility and the specific heat, are obtained.
 [S1063-7834(98)00410-9]

In recent years the problem of describing the static and dynamic magnetic properties of cuprates has been considered a central problem in high-temperature superconductivity. It has been firmly established by neutron-diffraction studies that the spin statics and dynamics of such cuprates as $La_{2-x}Sr_xCuO_4$ and $YBa_2Cu_3O_{6+x}$ in an insulating phase are described well by the Heisenberg Hamiltonian with spin $s=\frac{1}{2}$ for a CuO_2 plane or two planes.[1,2] Definite hopes for describing superconducting compositions have been placed in the $t-J$ model and the nearly antiferromagnetic Fermi liquid (nearly AFL) model; however, there are some fundamental difficulties in the correct microscopic substantiation of these theories. The serious constructive critical review of these two widely popularized approaches that was recently undertaken by Anderson[3] now, more than 10 years since the discovery of high-T_c superconductivity, raises the fundamental question of the choice of a reliable microscopic model of cuprate magnetism.

In our opinion, one of the most fruitful ideas, which might be the basis for the microscopic scenario of high-T_c superconductivity, is the special role of the Jahn–Teller effect or Jahn–Teller centers (polarons), which served as the starting point for Muller's pioneering work that culminated in the discovery of high-T_c superconductivity.[4,5] This idea has been repeatedly discussed in recent years and has been evoked to account for individual properties of cuprates.[6,7] In Refs. 8–11 it was formulated in the form of a novel model of singlet-triplet pseudo-Jahn–Teller centers, which was designed to describe the entire variety of properties of high-T_c superconductors. Below we shall consider the description of the spin subsystem of copper oxides within this model.

1. MODEL OF POLAR SINGLET-TRIPLET PSEUDO-JAHN–TELLER CENTERS

The model of polar singlet-triplet pseudo-Jahn–Teller (PJT) centers treats copper oxides based on CuO_4 clusters as systems that are unstable toward the disproportionation reaction

$$[CuO_4]^{6-}+[CuO_4]^{6-}\rightarrow[CuO_4]^{5-}_{PJT}+[CuO_4]^{7-}_{PJT} \qquad (1)$$

with the formation of a system of polar hole ($[CuO_4]^{5-}$) or electron ($[CuO_4]^{7-}$) PJT centers. The electron and hole PJT centers are distinguished by two electrons, which are paired in a completely filled molecular orbital of the CuO_4 cluster and form a local singlet boson. The new phase can be represented as a system of such local singlet bosons moving in a lattice of hole PJT centers with a boson concentration N_B close to 1/2. The Jahn–Teller structure of the polar centers provides for the high stability of the disproportionated phase, which coexists with the original antiferromagnetic parent matrix in the case of weakly doped compositions and has a small propensity to undergo the reverse recombination process.

The low level of the threshold of the disproportionation reaction ΔE_d is one of the unique properties of copper oxides. For weakly covalent oxides reaction (1) would reduce to the reaction

$$Cu^{2+}+Cu^{2+}\rightarrow Cu^{3+}+Cu^{1+},$$

whose threshold energy coincides with the correlation energy for intraatomic electrostatic repulsion $U_d\sim 10$ eV. In reality, the electronic configurations of the polar $[CuO_4]^{5-}$ and $[CuO_4]^{7-}$ centers in strongly covalent copper oxides differ appreciably from the simple ''ionic'' analogs Cu^{3+} and Cu^{1+}, respectively. For example, the electron density of the two holes in the ground state of the $[CuO_4]^{5-}$ hole center can have an approximately equal distribution between the copper and oxygen atoms, which formally corresponds to the ionic composition Cu^{2+} for copper. As a result, the threshold energy of the disproportionation reaction in copper oxides approaches the oxygen-copper electron-transfer energy, which amounts to only $1-2$ eV in nonconducting copper oxides.

The disproportionation reaction in 2-1-4, 1-2-3, and other systems is stimulated by nonisovalent substitution and is accompanied by the formation of a nucleus of a new

phase, which coexists in the general case with the old antiferromagnetic ''parent'' phase. Chemical or physical separation of the phases would be of major importance for explaining many features of the behavior of copper oxides with nonisovalent substitution or charge heterogeneity.

One remarkable property of the ground states of the polar $[CuO_4]^{5-}$ and $[CuO_4]^{7-}$ centers is their quasidegeneracy (closely positioned levels), under which the hole added to the original ''one-hole'' $[CuO_4]^{6-}$ cluster to form a $[CuO_4]^{5-}$ hole center can ''reside'' in the half-filled Cu $3d-$O $2p$ hybrid orbital of b_{1g} symmetry with the formation of a $(b_{1g}^2)^1A_{1g}$ Zhang–Rice singlet or, in the purely oxygen O $2p$ molecular orbital of e_u symmetry, with the formation of a singlet or triplet $(b_{1g}e_u)^{1,3}E_u$ term of similar energy.

The presence of quasidegeneracy with competition between the b_{1g}^2 and $b_{1g}e_u$ configurations and the $^1A_{1g}$ and $^{1,3}E_u$ terms, respectively, can lead to the realization of conditions for a strong pseudo-Jahn–Teller effect with active displacement modes for CuO_4 clusters of the Q_{e_u}, $Q_{b_{1g}}$, and $Q_{b_{2g}}$ types and the formation of a four-well adiabatic potential with two symmetry types, viz., E_uB_{1g} and E_uB_{2g}.

The unusual properties of the $^1A_{1g}$ and $^{1,3}E_u$ terms, which differ in parity, spin, and orbital multiplicity, shape the unusual properties of the ground state of $[CuO_4]^{5-}$ hole centers with an active role for orbital, spin, and local structural (more precisely, vibronic) modes.

A hole PJT center, with its high polarizability, can serve as a center for effective local pairing with the formation of a local singlet boson. Moreover, a $[CuO_4]^{5-}_{PJT}$ center with a local boson differs significantly from a primitive $[CuO_4]^{7-}$ center, which has a nondegenerate system of completely filled Cu $3d$ and O $2p$ orbitals.

The transition from a hole to an electron PJT center can be accompanied in the general case by alteration of the bare local parameters, such as, for example, the $A-E$ splitting $\Delta_{AE}=\varepsilon(^1E_u)-\varepsilon(^1A_{1g})$ or the singlet-triplet splitting $\Delta_{ST}=\varepsilon(^3E_u)-\varepsilon(^1E_u)$, as well as interchange of the fundamental Jahn–Teller mode $E_uB_{1g}\leftrightarrow E_uB_{2g}$.

As a whole, the unusual properties of cuprates are determined by the CuO_4 centers in the active CuO_2 planes. The environment of these planes, including the apical oxygen, creates appropriate conditions for the nucleation of a new phase of polar PJT centers and its structure.

Without dwelling in detail on the problem of experimentally substantiating the model of singlet-triplet PJT centers, we mention some recent NQR experiments on the $La_2Cu_{0.5}Li_{0.5}O_4$ system, in which Li^{1+} ions form an ordered superlattice using separated CuO_4^{5-} hole centers, making it possible to investigate the spin structure of a CuO_4 cluster in the doped-hole state.[12] This research experimentally demonstrated the existence, along with the Zhang–Rice ground spin singlet, of a low-lying spin triplet with an energy of the order of ~ 130 meV, which is close in value to the effective exchange-coupling constant between copper spins in undoped and weakly doped cuprates.

The model under consideration, like the familiar Aleksandrov–Mott bipolar model, is one of the variations of Schafroth's model of local bosons.[13] Unlike the bipolar model, which presupposes a fairly complicated structure for a local boson as a bound singlet or triplet pair of small polarons in a relatively simple ''rigid'' lattice, the model of PJT centers presupposes a relatively simple structure for a local singlet boson in the form of a pair of electrons in a filled molecular orbital, but a complicated PJT structure for the lattice.

2. SINGLET-TRIPLET MODEL OF CUPRATE MAGNETISM

In order to maximally simplify the description of the spin subsystem in a phase of polar Jahn–Teller centers, we confine ourselves to consideration of the singlet (^1E_u) and triplet (^3E_u) terms for the $b_{1g}e_u$ configuration, neglecting the orbital degeneracy and taking into account the isotropic spin exchange interaction between b_{1g} and e_u holes in neighboring CuO_4 centers. Such an approach leads to a two-component spin Hamiltonian

$$H_{ST}=\frac{1}{2}\sum_i I_{b_{1g}e_u}(ii)\mathbf{s}_{1i}\cdot\mathbf{s}_{2i}+\frac{1}{2}\sum_{ij} I_{b_{1g}b_{1g}}(ij)\mathbf{s}_{1i}\cdot\mathbf{s}_{1j}+\frac{1}{2}\sum_{ij} I_{b_{1g}e_u}(ij)\mathbf{s}_{1i}\cdot\mathbf{s}_{2j}+\frac{1}{2}\sum_{ij} I_{e_ub_{1g}}(ij)\mathbf{s}_{2i}\cdot\mathbf{s}_{1j}+\frac{1}{2}\sum_{ij} I_{e_ue_u}(ij)\mathbf{s}_{2i}\cdot\mathbf{s}_{2j}, \quad (2)$$

where $\mathbf{s}_{1i}$ and $\mathbf{s}_{2i}$ are spins localized in predominantly copper b_{1g} and purely oxygen e_u orbitals, respectively. The first term in Eq. (2) describes intracenter dp exchange, and the remaining terms describe intercenter dd, dp, and pp exchange interactions.

Introducing the total spin of the ith cluster $\mathbf{S}_i=\mathbf{s}_{1i}+\mathbf{s}_{2i}$ and the spin polarization (singlet-triplet mixing) operator

$$\mathbf{V}_i=\mathbf{s}_{1i}-\mathbf{s}_{2i}$$

with a nonzero matrix element of the type $\langle 00|V_z|10\rangle$, we can rewrite Eq. (2) in the form

$$H_{ST}=\frac{\Delta_{ST}}{2}\sum_i \mathbf{S}_i^2+\frac{1}{2}\sum_{ij} I_{ij}^{(1)}\mathbf{S}_i\cdot\mathbf{S}_j+\frac{1}{2}\sum_{ij} I_{ij}^{(2)}\mathbf{S}_i\cdot\mathbf{V}_j+\frac{1}{2}\sum_{ij} I_{ij}^{(3)}\mathbf{V}_i\cdot\mathbf{S}_j+\frac{1}{2}\sum_{ij} I_{ij}^{(4)}\mathbf{V}_i\cdot\mathbf{V}_j. \quad (3)$$

Here we have introduced the new exchange integrals

$$I_{ij}^{(1)}=\frac{1}{4}\{I_{b_{1g}b_{1g}}(ij)+I_{e_ue_u}(ij)+2I_{b_{1g}e_u}(ij)\},$$

$$I_{ij}^{(2)}=I_{ij}^{(3)}=\frac{1}{4}\{I_{b_{1g}b_{1g}}(ij)-I_{e_ue_u}(ij)\},$$

$$I_{ij}^{(4)}=\frac{1}{4}\{I_{b_{1g}b_{1g}}(ij)+I_{e_ue_u}(ij)-2I_{b_{1g}e_u}(ij)\},$$

and the singlet-triplet splitting parameter $\Delta_{ST}=I_{b_{1g}e_u}(ii)$. The first term in Eq. (3) explicitly takes into account the intracenter dp exchange, which corresponds to singlet-triplet splitting in each cluster, the second term describes the traditional Heisenberg exchange of triplets, which leads to the

TABLE I. Types of possible collinear structures at T=0 $\left(i_1=\frac{I^{(1)}}{\Delta},\ i_2=\frac{I^{(2)}}{\Delta},\ i_4=\frac{I^{(4)}}{\Delta}\right)$.

Spin configuration	Stability conditions	Free energy, $\varepsilon=\frac{E}{\Delta}$
Singlet $\langle S_z\rangle_A=\langle S_z\rangle_B=0$, $\langle V_z\rangle_A=\langle V_z\rangle_B=0$	$\lvert i_4\rvert<\frac{1}{2z}$	$\varepsilon=0$
Ferromagnetic *VV* phase $\langle S_z\rangle_A=\langle S_z\rangle_B=0$, $\langle V_z\rangle_A=\langle V_z\rangle_B=\pm\eta$ $\eta=\left(1-\frac{1}{4z^2i_4^2}\right)^{1/2}$	$i_4<0,\ \lvert i_2\rvert<i_4\frac{2zi_4-1}{\sqrt{4z^2i_4^2-1}}$	$\varepsilon=-\frac{1}{2}zi_4\eta^2+\frac{1}{2}+zi_4$
Antiferromagnetic *VV* phase $\langle S_z\rangle_A=\langle S_z\rangle_B=0$, $\langle V_z\rangle_A=-\langle V_z\rangle_B=\pm\eta$ $\eta=\left(1-\frac{1}{4z^2i_4^2}\right)^{1/2}$	$i_4>0,\ \lvert i_2\rvert<i_4\frac{2zi_4+1}{\sqrt{4z^2i_4^2-1}}$	$\varepsilon=\frac{1}{2}zi_4\eta^2+\frac{1}{2}-zi_4$
Triplet ferromagnetic *SS* phase $\langle S_z\rangle_A=\langle S_z\rangle_B=\pm1$, $\langle V_z\rangle_A=\langle V_z\rangle_B=0$	$i_1<-\frac{1}{2z}-\frac{1}{2z}\sqrt{1+4z^2i_2^2}$	$\varepsilon=1+\frac{z}{2}i_1$
Triplet antiferromagnetic *SS* phase $\langle S_z\rangle_A=-\langle S_z\rangle_B=\pm1$, $\langle V_z\rangle_A=\langle V_z\rangle_B=0$	$i_1>\frac{1}{2z}+\frac{1}{2z}\sqrt{1+4z^2i_2^2}$	$\varepsilon=1-\frac{z}{2}i_1$

formation of spin waves. The remaining terms are nontrivial and correspond to spin-polarized exchange with the possible formation of magnetic excitons (spin-multiplicity waves) and their hybridization with spin waves.

The numerical values and signs of the exchange parameters $I^{(1,2,3,4)}$ are determined by the competition between the $b_{1g}-b_{1g}$, $b_{1g}-e_u$, and e_u-e_u exchange interactions, and only the different signs of the $b_{1g}-e_u$ contributions to $I^{(1)}$ and $I^{(4)}$, on the one hand, and of the $b_{1g}-b_{1g}$ and e_u-e_u contributions to $I^{(2)}=I^{(3)}$, on the other hand, should be noted.

Unlike the well known weakly covalent and weakly correlated magnetic oxides of the ferrite type, the exchange interaction between two nearest-neighbor PJT centers in strongly covalent cuprates includes an unusually large ferromagnetic Hund contribution (for different orbitals) or antiferromagnetic correlation contributions (for identical orbitals) to the intraatomic O $2p$ exchange in the common oxygen ion, and, in addition, the relatively large ferromagnetic contribution due to Heisenberg Cu $3d-$O $2p$ exchange must be taken into account. In general, a detailed microscopic analysis of the exchange interactions in PJT centers is fairly complicated, especially when they are comparable to the magnitude of the singlet-triplet splitting $I\sim\Delta_{ST}\sim0.1$ eV.

The problem of singlet-triplet magnetism has been discussed fairly long ago and in detail in connection with the description of the magnetic behavior of rare-earth magnets with non-Kramers ions such as Pr^{3+}, Tb^{3+}, and Tm^{3+} (Refs. 14–16). Until recent times, there has been an unwavering opinion that singlet magnetism is characteristic only of compounds containing rare-earth elements. However, in the last few years a model of singlet-triplet magnetism was developed for oxides of the iron group, for example, for La_2NiO_4 (Ref. 17).

Hamiltonian (3) has the symmetry of the SO(4) group[18]

$$[S_i,S_j]=i\varepsilon_{ijk}S_k,\quad [S_i,V_j]=i\varepsilon_{ijk}V_k,\quad [V_i,V_j]=i\varepsilon_{ijk}S_k, \tag{4}$$

whose algebra has two invariant operators (Casimir operators)

$$C_1^{\mathrm{SO}(4)}=\mathbf{S}^2+\mathbf{V}^2=3\overline{I},\quad C_2^{\mathrm{SO}(4)}=\mathbf{S}\cdot\mathbf{V}=0. \tag{5}$$

These relations impose kinematic constraints on the values S and V of the order parameters and follow directly from the spin algebra of the operators **S** and **V**.

Let us consider Hamiltonian (3) within a modified two-sublattice mean-field approximation, which takes into account the interaction of nearest neighbors (to denote the sublattices we introduce the additional label $\gamma=A,B$). Hamiltonian (3) can be represented in the form

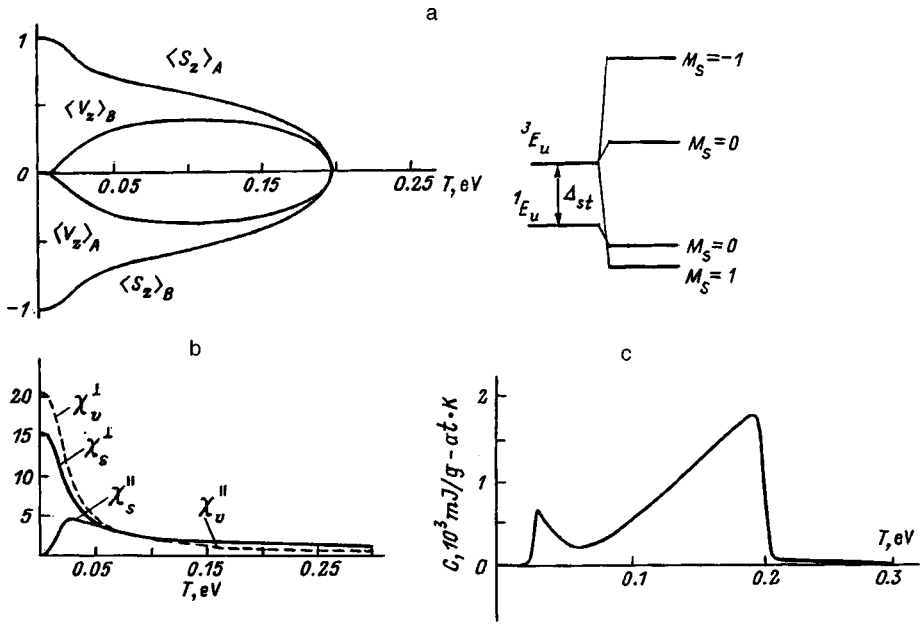

FIG. 1. Temperature dependence of the order parameters (a), the longitudinal and transverse magnetic susceptibilities χ_s (solid lines) and χ_v (dashed lines) (b), and the specific heat (c) for an *SS* phase ($\Delta=0.1$ eV, $zI^{(1)}=0.3$ eV, $zI^{(2)}=-0.2$ eV, $zI^{(4)}=0.1$ eV). The corresponding splitting diagram of the spin levels ($T=0$) is shown in the inset.

$$H_{\mathrm{MFA}}=\frac{\Delta}{2}\sum_{i\gamma}\mathbf{S}_{i\gamma}^2-\frac{1}{2}\sum_{i\alpha\gamma}h_{si\alpha\gamma}\langle S_{i\alpha}\rangle_\gamma-\frac{1}{2}\sum_{i\alpha\gamma}h_{vi\alpha\gamma}\langle V_{i\alpha}\rangle_\gamma$$
$$+\sum_{i\alpha\gamma}h_{si\alpha\gamma}S_{i\alpha\gamma}+\sum_{i\alpha\gamma}h_{vi\alpha\gamma}V_{i\alpha\gamma} \tag{6}$$

with the molecular fields

$$h_{si\alpha\gamma}=\sum_{i,\gamma'}(I_{ij}^{(1)}\langle S_{j\alpha}\rangle_{\gamma'}+I_{ij}^{(2)}\langle V_{j\alpha}\rangle_{\gamma'}), \tag{7}$$

$$h_{vi\alpha\gamma}=\sum_{i,\gamma'}(I_{ij}^{(2)}\langle S_{j\alpha}\rangle_{\gamma'}+I_{ij}^{(4)}\langle V_{j\alpha}\rangle_{\gamma'}), \tag{8}$$

where $\alpha=x,y,z$. We note that the standard treatment of Hamiltonians (2) and (3) in the mean-field approximation differs in the way the first term, which describes the intracenter exchange interaction, is taken into account. Unlike the usual approach, the SM_S representation of the total spin used in (3) ensures exact allowance for the intracenter exchange interaction. In the standard approximation of the molecular field for Hamiltonian (3), the averages $\langle\mathbf{S}\rangle$ and $\langle\mathbf{V}\rangle$ (which are usually denoted by **M** and **L**) correspond to the ferro- and antiferromagnetic vectors for a PJT center with the kinematic relations

$$\langle\mathbf{S}\rangle^2+\langle\mathbf{V}\rangle^2=4s_1^2=4s_2^2=1,\quad \langle\mathbf{S}\rangle\langle\mathbf{V}\rangle=0$$

instead of the operator relation (5), which, for the corresponding averages, is equivalent to

$$\langle\mathbf{S}^2\rangle+\langle\mathbf{V}^2\rangle=4s_1(s_1+1)=3,\quad \langle\mathbf{S}\cdot\mathbf{V}\rangle=0.$$

Thus, the singlet-triplet model within the modified mean-field approximation permits more exact allowance for quantum effects which are significant for a small spin $s_{1,2}=1/2$.

The appearance of two vector order parameters and the existence of kinematic relation (5) introduce significant changes into the analysis of the possible spin ordering. In the general case we are dealing with competition between exchange interactions of the *SS*, *VV*, and *SV* types, which ensures the appearance not only of simple collinear spin configurations, but also of two-sublattice multiparametric $|\langle\mathbf{S}\rangle|$, $|\langle\mathbf{V}\rangle|$, $\Theta_{AA}=\Theta_{BB},\Theta_{AB}$ canted spin configurations [here and below $\Theta_{AA,BB}$ is the angle between the vectors **S** and **V** of the site singled out in sublattice $A(B)$, and Θ_{AB} is the angle between $\mathbf{S}_A$ and $\mathbf{S}_B$].

3. COLLINEAR PHASES

Relatively simple collinear spin configurations, which are direct analogs of (anti)ferromagnetic ordering, are possible for the following relations between the signs of the exchange parameters: 1) $I^{(1,2,3,4)}<0$, $\Theta_{AA}=\Theta_{BB}=\Theta_{AB}=0$; 2) $I^{(1,4)}>0$, $I^{(2,3)}<0$, $\Theta_{AA}=\Theta_{BB}=\Theta_{AB}=\pi$; 3) $I^{(1,2,3,4)}>0$, $\Theta_{AA}=\Theta_{BB}=0$, $\Theta_{AB}=\pi$; 4) $I^{(1,4)}<0$, $I^{(2,3)}>0$, $\Theta_{AA}=\Theta_{BB}=\pi$, $\Theta_{AB}=0$. In the approximation of nearest-neighbor interactions, the free energy of the collinear spin structures per center is

$$\tilde{F}=\frac{F}{N}=-\frac{1}{4}\sum_{\gamma=A,B}(h_{sz\gamma}\langle S_z\rangle_\gamma+h_{vz\gamma}\langle V_z\rangle_\gamma)$$
$$+\frac{\Delta}{2}-\frac{1}{2\beta}\sum_{\gamma=A,B}\ln\left\{2\left(\cosh\left(\frac{\beta}{2}\alpha_\gamma\right)\right.\right.$$
$$\left.\left.+\exp\left(-\beta\frac{\Delta}{2}\right)\cosh(\beta h_{sz\gamma})\right)\right\}. \tag{9}$$

Here $\alpha_\gamma=\{\Delta^2+4h_{vz\gamma}^2\}^{1/2}$, and $\beta=\frac{1}{T}$ is the reciprocal temperature.

The self-consistent equations for the order parameters which minimize $\tilde{F}$ have the form

$$\langle S_z\rangle_\gamma=-\frac{\exp\left(-\beta\frac{\Delta}{2}\right)\sinh(\beta h_{sz\gamma})}{\cosh\left(\frac{\beta}{2}\alpha_\gamma\right)+\exp\left(-\beta\frac{\Delta}{2}\right)\cosh(\beta h_{sz\gamma})}, \tag{10}$$

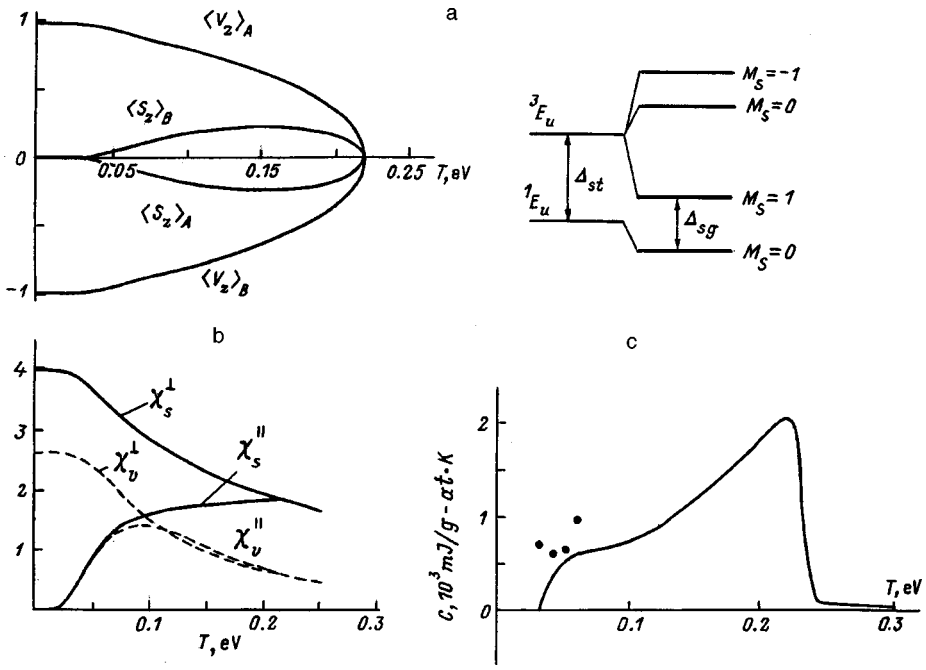

FIG. 2. Temperature dependence of the order parameters (a), the longitudinal and transverse magnetic susceptibilities χ_s (solid lines) and χ_v (dashed lines) (b), and the specific heat (c) for a *VV* phase ($\Delta=0.1$ eV, $zI^{(1)}=0.1$ eV, $zI^{(2)}=-0.2$ eV, $zI^{(4)}=0.3$ eV). The corresponding splitting diagram of the spin levels ($T=0$) and the effective spin gap are shown in the inset. The electronic contribution to the specific heat according to the data in Ref. 19 is indicated by filled circles.

$$\langle V_z\rangle_\gamma = -\frac{2\dfrac{h_{vz\gamma}}{\alpha_\gamma}\sinh\left(\dfrac{\beta}{2}\alpha_\gamma\right)}{\cosh\left(\dfrac{\beta}{2}\alpha_\gamma\right)+\exp\left(-\beta\dfrac{\Delta}{2}\right)\cosh(\beta h_{sz\gamma})}. \quad (11)$$

The mean-field equations (10) and (11) can be used to find the possible collinear spin configurations and the conditions for their existence. The main results of the analysis of Hamiltonian (6) in the mean-field approximation at $T=0$ for collinear spin configurations are listed in Table I. In the purely singlet, nonmagnetic phase each PJT center is characterized by the singlet ground state $|00\rangle$. In the triplet *SS* spin configuration one of the purely triplet states, $|11\rangle$ or $|1(-1)\rangle$, has the minimum energy in both the *A* and *B* sublattices (Fig. 1). The ground state of the phase of PJT centers in sublattices *A* and *B* for the *VV* phase is a quantum mixture of $|00\rangle$ and $|10\rangle$ states (Fig. 2), which corresponds to ordering of the spin density. The phase diagram of the ground state of a singlet-triplet magnet (Fig. 3) for the case of $I^{(2)}=0$, which rules out the appearance of a noncollinear spin configuration, gives a quantitative picture of the real magnetic behavior of a singlet-triplet system. Transitions between the *VV* and *SS* phases, like transitions between the singlet and triplet phases, correspond to first-order transitions. Transitions between the singlet phase and the mixed-spin *VV* phases are second-order transitions.

Pure *SS* and *VV* configurations are realized only at $T=0$, whereas at finite values of *T* we are dealing with nonzero values of both $\langle S_z\rangle$ and $\langle V_z\rangle$, i.e., with mixing of the phases.

The Curie (Néel) temperature T_c, which is defined as the temperature at which all the parameters vanish simultaneously, is obtained by expanding the system of equations (10) and (11) in the corresponding small order parameters, which leads to the pair of nonlinear equations

$$2\exp\left(\beta\frac{\Delta}{2}\right)\sinh\left(\beta\frac{\Delta}{2}\right)\{(2zI^{(2)})^2-4z^2I^{(1)}I^{(4)}\}$$
$$=(3+\exp(\beta\Delta))\left\{\frac{\Delta}{\beta}(3+\exp(\beta\Delta))\pm 2zI^{(1)}\Delta\right.$$
$$\left.\pm 4\frac{zI^{(4)}}{\beta}\exp\left(\beta\frac{\Delta}{2}\right)\sinh\left(\beta\frac{\Delta}{2}\right)\right\}, \quad (12)$$

whose solution gives $T_{1,2}$, and then $T_c=\max\{T_1,T_2\}$ (z is the number of nearest neighbors).

The presence of two spin order parameters leads to two types of spin susceptibilities: the ordinary susceptibility

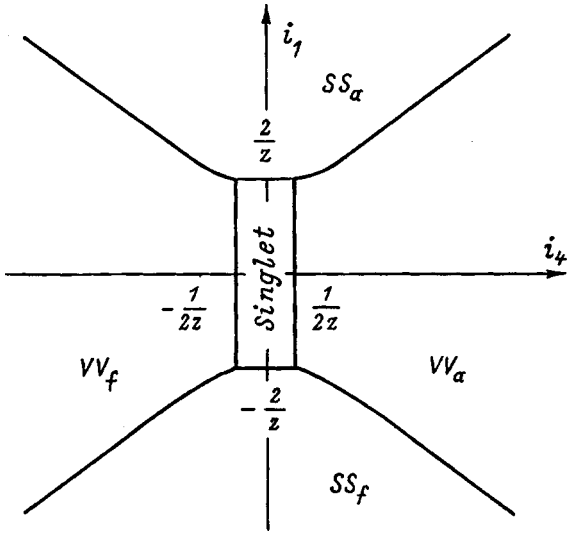

FIG. 3. Phase diagram of the collinear phases of a singlet-triplet magnet ($I^{(2)}=0$, $i_1=I^{(1)}/\Delta$, $i_4=I^{(4)}/\Delta$).

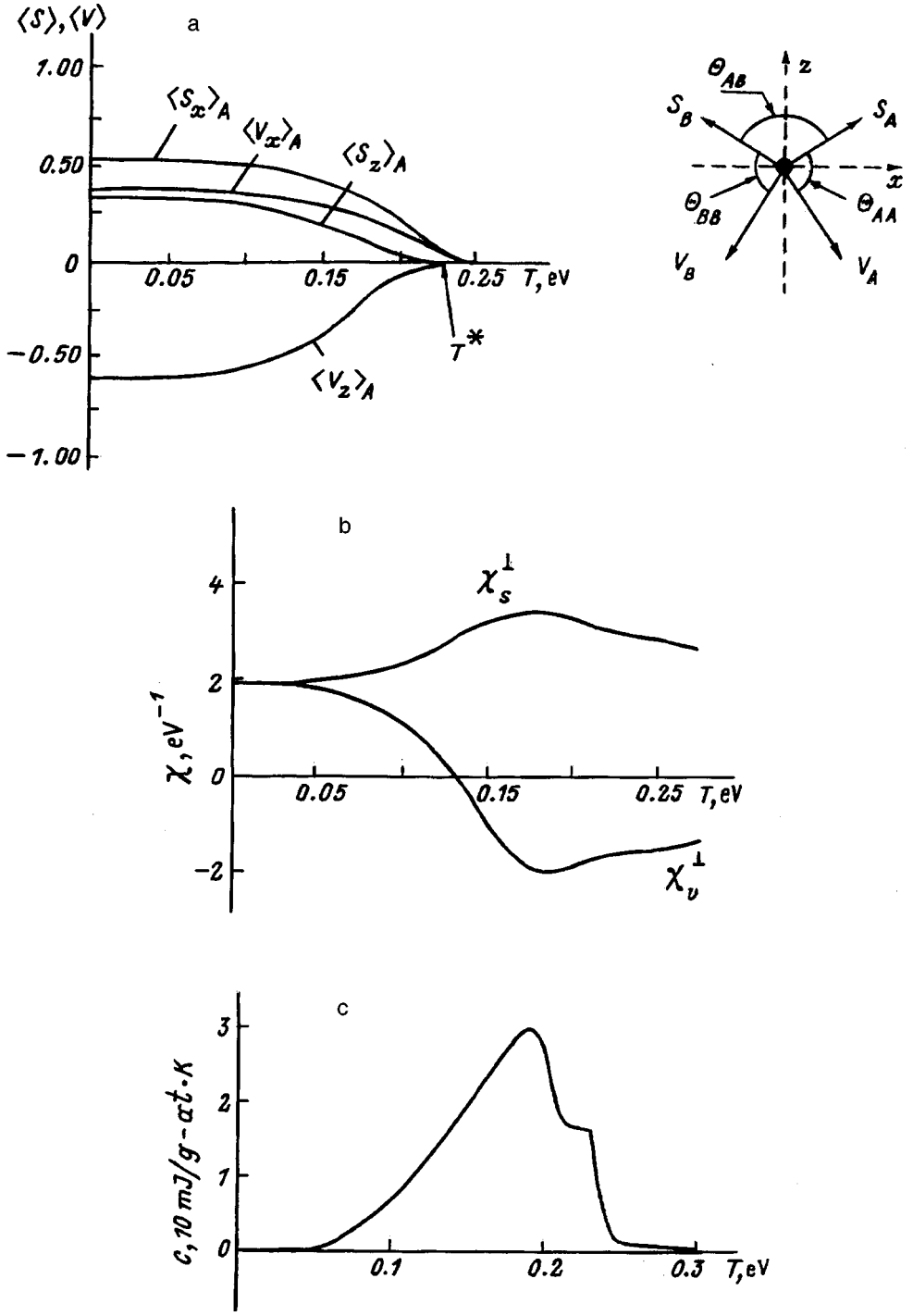

FIG. 4. Temperature dependence of the order parameters (a) (the values for sublattice A are shown), the transverse magnetic susceptibilities $\chi^{\perp}_{s,v}$ (b), and the specific heat (c) for the noncollinear phase ($\Delta = 0.1$ eV, $zI^{(1)} = 0.2$ eV, $zI^{(2)} = 0.3$ eV, and $zI^{(4)} = -0.1$ eV).

$\chi_s \sim \partial\langle \mathbf{S}\rangle/\partial \mathbf{h}$ and a new spin-polarization susceptibility $\chi_v \sim \partial\langle \mathbf{V}\rangle/\partial \mathbf{h}$ with different temperature behavior (Figs. 1b and 2b).

We note that consideration of the singlet-triplet mixing or the V terms leads to the appearance of S-type magnetism and the special, ''almost paramagnetic'' behavior of the system. This is manifested both in the behavior of the order parameter $\langle S_z\rangle$ and in the tendency of the longitudinal and transverse spin susceptibilities to coincide (Fig. 1b). The partial spin polarizations on copper and oxygen can have unusual temperature behavior for the phases considered due to antiferromagnetic exchange interactions of the SS and VV types. For example, in the SS phase for the case illustrated in Fig. 1a, crossover from intracenter ferromagnetic ordering ($\langle V_z\rangle \sin 0$) to a state with intense quantum suppression of the spin-polarization copper subsystem ($\langle V_z\rangle \sim -\langle S_z\rangle$) occurs as the temperature is increased. For the VV phase in the situation illustrated in Fig. 2a similar suppression occurs as soon as there is antiferromagnetic intracenter ordering. Both phases exhibit different types of behavior of the copper [χ_d

$=(\frac{1}{2})(\chi_s+\chi_v)]$ and oxygen $[\chi_p=(\frac{1}{2})(\chi_s-\chi_v)]$ susceptibilities. The similar values and identical signs of χ_s and χ_v in the *SS* phase lead to a large value for the former and almost complete disappearance of the latter.

Figures 1c and 2c present the results of a calculation of the spin specific heat for collinear phases. For convenience, all the data have been recalculated for $YBa_2Cu_3O_7$. Note the characteristic spin-gap behavior of the specific heat, as well as its numerical values. In the range $300<T<700$ K the latter are completely comparable to the electronic contribution estimated in Ref. 19, which was ascribed therein to the Fermi electronic subsystem. These results demonstrate the need for a more detailed analysis of the spin specific heat of copper oxides to correctly separate the different contributions to the experimentally observed value of the specific heat and to isolate the intrinsic contribution, whose analysis is widely used to draw conclusions regarding the applicability of a particular mechanism of high-T_c superconductivity.

4. NONCOLLINEAR PHASES

A fundamental feature of noncollinear spin configurations in the model under consideration is their two-sublattice character with combined ferro-antiferromagnetic ordering of the components of the vector order parameters $\langle \mathbf{S} \rangle$ and $\langle \mathbf{V} \rangle$ and, in the general case, with a characteristic wave vector of the structure $\mathbf{Q}_{\mathrm{AF}}=(\pi,\pi)$, which distinguish the structures considered here from noncollinear noncommensurate structures of the helicoidal type.

An analytical treatment of canted phases would be cumbersome and hardly productive; therefore, we shall discuss the results of a numerical solution. The behavior of different components of the order parameters, the susceptibilities, and the magnetic specific heat for one of the variants of the noncollinear phase is shown in Fig. 4. Unlike the collinear phases, in the situation under consideration both order parameters, $\langle \mathbf{S} \rangle$ and $\langle \mathbf{V} \rangle$, are simultaneously nonzero at $T=0$, although the orthogonality relation (5) holds for each site. As the temperature rises, there is a tendency for collinear ordering, i.e., $\langle \mathbf{S} \rangle_A \| \langle \mathbf{S} \rangle_B$ and $\langle \mathbf{V} \rangle_A \| \langle \mathbf{V} \rangle_B$, so that the system virtually goes over the collinear phase above a certain temperature T^*.

The noncollinear phase does not exhibit a clear difference between the longitudinal and transverse spin susceptibilities. Figure 4b presents the temperature dependence of the transverse (in the notation of Fig. 4a the applied field $\mathbf{H} \| Oz$ is perpendicular to the antiferromagnetic vector in its usual meaning) susceptibilities $\chi_s^{\perp}$ and $\chi_v^{\perp}$. Let us turn our attention to the anomalous temperature behavior of the spin-polarization susceptibility $\chi_v^{\perp}$. In the case shown in Fig. 4b with the natural positive sign for $\chi_s^{\perp}$, the sign of $\chi_v^{\perp}$ becomes negative at $T \sim 0.13$ eV.

The appearance of multiparametric canted spin configurations instead of ''rigid'' collinear (anti)ferromagnetic structures significantly expands the possibilities of the spin subsystem of cuprates in optimizing the total energy, especially under the conditions of strong inhomogeneity of the intracenter and intercenter exchange parameters. The magnetic structures formed, even in their static variant, will most probably resemble quasi-two-dimensional spin-glass systems without clearly expressed long-range order, but with the occurrence of clearly expressed spin fluctuations of the ferromagnetic and antiferromagnetic types. The magnetic structures will be pinned by inhomogeneity centers with a correlation length restricted either by the effective size of an inhomogeneity center or by the distance between such centers. We note that numerous manifestations of ferromagnetic fluctuations[20,21] in insulating and superconducting compositions of doped cuprates clearly point to fluctuations of noncollinear phases.

In summation, we note that we have proposed a singlet-triplet model for describing the spin subsystem of cuprates, within which we have calculated the main characteristics of the system in a modified version of the mean-field approximation. Further development of the model considered calls for taking into account the quasi-two-dimensional structure of cuprates and the strongly developed fluctuations of the intracenter and intercenter exchange parameters. As a whole, the proposed model provides a reliable basis for developing different alternatives for the phenomenological description of the spin statics and dynamics of cuprates.

*E-mail: alexandr.moskvin@usu.ru

[1] S. M. Hayden, G. Aeppli, H. A. Mook, T. G. Perring, T. E. Mason, S.-W. Cheong, and Z. Fisk, Phys. Rev. Lett. **76**, 1344 (1996).
[2] P. Bourges, L. P. Regnault, Y. Sidis, and C. Vettier, Phys. Rev. B **53**, 876 (1996).
[3] P. W. Anderson, Adv. Phys. **46**, 1 (1997).
[4] J. G. Bednorz and K. A. Muller, Z. Phys. B **64**, 189 (1986).
[5] K. A. Muller, in *Materials and Mechanisms of Superconductivity High-Temperature Superconductors. 5th International Conference M2S-HTSC-V, Abstract Book*, Beijing, China, 28 Feb.–4 Mar. 1997, p. 1.
[6] R. Englman, B. Halperin, and M. Weger, Physica C **169**, 314 (1990).
[7] M. Georgiev and M. Borisov, Phys. Rev. B **39**, 11624 (1989).
[8] A. S. Moskvin, Pis'ma Zh. Eksp. Teor. Fiz. **58**, 342 (1993) [JETP Lett. **58**, 345 (1993)].
[9] A. S. Moskvin, N. N. Loshkareva, Yu. P. Sukhorukov, M. A. Sidorov, and A. A. Samokhvalov, Zh. Éksp. Teor. Fiz. **105**, 967 (1994) [JETP **78**, 518 (1994)].
[10] A. S. Moskvin, Physica C **282–287**, 1807 (1997).
[11] A. S. Moskvin, A. S. Ovchinnikov, and O. S. Kovalev, Fiz. Tverd. Tela (St. Petersburg) **39**, 1948 (1997) [Phys. Solid State **39**, 1742 (1997)].
[12] Y. Yoshinari, P. C. Hammel, J. A. Martindale, E. Moshopoulou, J. D. Thompson, J. L. Sarrao, and Z. Fisk, Phys. Rev. Lett. **77**, 2069 (1996).
[13] M. R. Schafroth, Phys. Rev. **100**, 463 (1955).
[14] R. Birgeneau, J. Als-Nielsen, and E. Bucher, Phys. Rev. B **6**, 2724 (1972).
[15] Y. Kitano and G. Trammel, Phys. Rev. Lett. **16**, 572 (1966).
[16] Y. Y. Hsieh and M. Blume, Phys. Rev. B **6**, 2684 (1972).
[17] A. M. Oles, L. F. Feiner, and J. Zaanen, in *Abstracts of ICM-94*, Warsaw, 22–26 August 1994, p. 257.
[18] A. Bohm, *Quantum Mechanics: Foundations and Applications*, 2nd ed., [Springer-Verlag, New York (1986); Mir, Moscow (1990)].
[19] M. E. Reeves, D. A. Ditmars, S. A. Wolf, T. A. Vanderah, and V. Z. Kresin, Phys. Rev. B **47**, 6065 (1993).
[20] P. Wachter, B. Blucher, and R. Pittini, Phys. Rev. B **49**, 13164 (1994).
[21] E. L. Vavilova and N. N. Garif'yanov, Pis'ma Zh. Éksp. Teor. Fiz. **66**, 470 (1997) [JETP Lett. **66**, 498 (1997)].

Translated by P. Shelnitz

Valence states of copper atoms in cuprates determined from the change in the electron-capture constant of ^{64}Cu

S. I. Bondarevskiĭ, V. F. Masterov, F. S. Nasredinov, N. P. Seregin, and P. P. Seregin

St. Petersburg State Technical University, 195251 St. Petersburg, Russia
(Submitted April 16, 1998)
Fiz. Tverd. Tela (St. Petersburg) **39**, 1793–1794 (October 1998)

The change in the ^{64}Cu electron-capture constant for the compounds Cu_2O, $YBa_2Cu_3O_7$, $YBa_2Cu_3O_6$, Nd_2CuO_4, $Nd_{1.8}Ce_{0.2}CuO_4$, La_2CuO_4, $La_{1.7}Sr_{0.3}CuO_4$, $Tl_2Ba_2CaCu_2O_8$, and $Bi_2Sr_2CaCu_2O_8$ has been measured. It is concluded that the copper in $YBa_2Cu_3O_7$, Nd_2CuO_4, La_2CuO_4, $La_{1.7}Sr_{0.3}CuO_4$, $Tl_2Ba_2CaCu_2O_8$, and $Bi_2Sr_2CaCu_2O_8$ is exclusively divalent, whereas in Cu_2O, $YBa_2Cu_3O_6$, and $Nd_{1.8}Ce_{0.2}CuO_4$ univalent copper is present.
 [S1063-7834(98)00510-3]

Determination of the valence state of copper is an urgent problem in studies of the high-T_c superconductivity in cuprates. This work uses for this purpose measurement of the electron-capture (EC) constant of the ^{64}Cu isotope.

Radioactive decay of nuclei is described by the relation

$$N = N_0 \exp(-\lambda t),$$

where N is the number of nuclei at time t, N_0 is their initial number, $\lambda = \ln 2/T_{1/2}$ is the decay constant, and $T_{1/2}$ is the decay half-period.

In the case of electron capture, the quantity λ was experimentally shown to depend on the valence state of the radioactive atom.[1,2] The change in the probability of radioactive decay is usually characterized by the quantity $\Delta\lambda/\lambda = 2\Delta\lambda/(\lambda_1+\lambda_2)$, where $\Delta\lambda = \lambda_1 - \lambda_2$, and λ_1 and λ_2 are, respectively, the decay constants for the radioactive isotope in chemical states 1 and 2. While there is no rigorous theory at present relating $\Delta\lambda/\lambda$ to chemical parameters, interpretation of the above experimental dependence of λ on the atomic valence state takes into account the prominent part in the EC rate played by the electron density at the nucleus, so that in a general case

$$\Delta\lambda/\lambda \sim [|\Psi(0)_1|^2 - |\Psi(0)_2|^2],$$

where $|\Psi(0)_1|^2$ and $|\Psi(0)_2|^2$ are the electron densities at the radioactive nucleus in compounds 1 and 2, respectively.[2]

The ratio $\Delta\lambda/\lambda$ is determined experimentally, usually by studying the dependence of the normalized ratio R of the count rates of radioactive sources 1 and 2 on time (the quasi-differential method), which can be written

$$R(t) = R_{(t)}/R_0 = \exp(\Delta\lambda t),$$

where $R_t = C_1/C_2$, $C_1(t) = k\lambda_1 N_{01}\exp(-\lambda_1 t)$ and $C_2(t) = k\lambda_2 N_{02}\exp(-\lambda_2 t)$ are the count rates of sources 1 and 2, k is the count-rate coefficient, N_{01} and N_{02} are the numbers of nuclei in sources 1 and 2 at the initial instant of time, and R_0 is the count-rate ratio at the initial instant of time.

The ^{64}Cu isotope ($T_{1/2} = 12.88$ h) suits ideally the conditions of $\Delta\lambda/\lambda$ measurement by the quasi-differential method. There are three decay branches for ^{64}Cu: electron-capture (43%), β^+ (19%), and β^- (38%) (see inset to Fig. 1), and there is a wealth of experimental data on the dependence of $\Delta\lambda/\lambda$ on the chemical state of copper for this isotope.[1,2] This work reports determination of the valence state of copper atoms in cuprates (Cu_2O, CuO, $YBa_2Cu_3O_{7-x}$, $La_{2-x}Sr_xCuO_4$, $Nd_{2-x}Ce_xCuO_4$, $Tl_2Ba_2CaCu_2O_8$, and $Bi_2Sr_2CaCu_2O_8$) by measuring the radioactive-decay constant of ^{64}Cu.

The count rates of the radioactive sources were determined at room temperature by measuring the accompanying 511-keV annihilation radiation. The PM tube was coupled to a 76×76-mm NaI(Tl) crystal with a well (measuring 40 ×20 mm). The sample under study was placed at the center of the well. The 511-keV photopeak was cut out in the amplitude spectrum, and the discrimination thresholds were chosen so as to reduce to the minimum the effect of instrument drift on the count rate. The overall stability of this arrangement was monitored by measuring the count rates of the two samples under study alternately with intervals of 240 s. To maintain the PM tube in a constant operating regime, a ^{64}Cu source of the same activity was placed above the detector for the source replacement. The radioactive sources were prepared by diffusion doping the existing compound by a ^{64}Cu isotope.

Figure 1a–1d presents typical $R(t)$ dependences for the compared source pairs CuO–Cu_2O, $YBa_2Cu_3O_7$–$YBa_2Cu_3O_6$, Nd_2CuO_4–$Nd_{1.8}Ce_{0.2}CuO_4$, and La_2CuO_4–$La_{1.7}Sr_{0.3}CuO_4$, and Table I lists the measured values of $\Delta\lambda/\lambda$ relative to CuO for all the studied compounds. As seen from Table I and Fig. 1, the CuO–Cu_2O pair exhibits the maximum value of $\Delta\lambda/\lambda$. This observation has a trivial explanation, namely, that the copper in these compounds resides in two characteristic valence states with electronic configurations $3d^9$ (Cu^{2+}) and $3d^{10}$ (Cu^+), and that the transition from the former to the latter is accompanied by a decrease of $|\Psi(0)|^2$ and, consequently, by a decrease in the radioactive-decay rate of ^{64}Cu.

A comparison of the source pairs $YBa_2Cu_3O_7$–$YBa_2Cu_3O_6$ and Nd_2CuO_4–$Nd_{1.8}Ce_{0.2}CuO_4$ also reveals an obvious decrease of λ in going from $YBa_2Cu_3O_7$ to $YBa_2Cu_3O_6$ (Fig. 1b), and from Nd_2CuO_4 to

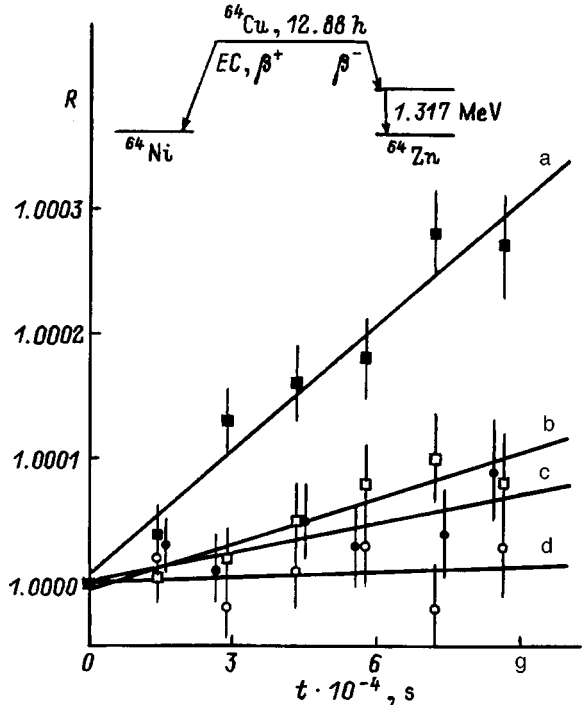

FIG. 1. $R(t)$ plot for the source pairs (a) CuO–Cu_2O, (b) $YBa_2Cu_3O_7$–$YBa_2Cu_3O_6$, (c) Nd_2CuO_4–$Nd_{1.8}Ce_{0.2}CuO_4$, and (d) La_2CuO_4–$La_{1.7}Sr_{0.3}CuO_4$. The inset shows the ^{64}Cu decay scheme.

$Nd_{1.8}Ce_{0.2}CuO_4$ (Fig. 1c), although in these cases the decrease of λ is not so significant as it is for the CuO–Cu_2O pair (see Table I). In other words, while in $YBa_2Cu_3O_7$ and Nd_2CuO_4 the copper is divalent [relative to CuO, $\Delta\lambda/\lambda = 0.0(1)\times 10^{-4}$], in $YBa_2Cu_3O_6$ and $Nd_{1.8}Ce_{0.2}CuO_4$ part of the copper atoms are univalent. Neglecting the effects of bond covalency and assuming the fraction of univalent copper to be proportional to $\Delta\lambda/\lambda$, we come to the result that in $YBa_2Cu_3O_6$ about 30%, and in $Nd_{1.8}Ce_{0.2}CuO_4$, ~20% of copper is univalent.

Finally, a comparison of the source pairs La_2CuO_4–$La_{1.7}Sr_{0.3}CuO_4$ (Fig. 1d), CuO-$Tl_2Ba_2CaCu_2O_8$, and CuO-$Bi_2Sr_2CaCu_2O_8$ (see Table I) does not reveal within experimental error any change in the magnitude of λ relative to CuO. This implies that in these compounds copper is divalent.

TABLE I. The values of $\Delta\lambda/\lambda$ (relative to CuO) for cuprates.

Compound	$(\Delta\lambda/\lambda)\times 10^4$
Cu_2O	23(1)
$YBa_2Cu_3O_7$	−0.05(10)
$Yba_2Cu_3O_6$	0.7(1)
Nd_2CuO_4	0.06(10)
$Nd_{1.8}Ce_{0.2}CuO_4$	0.5(1)
La_2CuO_4	−0.02(10
$Ls_{1.7}Sr_{0.3}CuO_4$	0.07(10)
$Tl_2Ba_2CaCu_2O_8$	0.05(10)
$Si_2Sr_2CaCu_2O_g$	0.04(10)

Note that our conclusions regarding the valence state of copper in the cuprates studied are in agreement with the results obtained by photoelectron spectroscopy for CuO, Cu_2O (Ref. 3), $YBa_2Cu_3O_{7-x}$ (Ref. 4), $Nd_{2-x}Ce_xCuO_4$ (Ref. 5), $La_{2-x}Sr_xCuO_4$ (Ref. 6), $Tl_2Ba_2CaCu_2O_8$ (Ref. 7), and $Bi_2Sr_2CaCu_2O_8$ (Ref. 8), as well as with the determination of the effective atomic charges in the above compounds by Mössbauer spectroscopy[9,10].

Support of the Russian Fund for Fundamental Research (Grant 97-02-16216) is gratefully acknowledged.

[1] A. G. Maddock, Radiochim. Acta **70-71**, 323 (1995).
[2] K. V. Makariunas, Izv. Akad. Nauk SSSR, Ser. Fiz. **47**, 18 (1983).
[3] J. Ghijsen, L. H. Tjeng, J. van Elp, H. Eskes, J. Westerink, G. A. Sawatzky, and M. T. Czyzyk, Phys. Rev. B **38**, 11322 (1988).
[4] H. Verweij, Solid State Commun. **64**, 1213 (1987).
[5] Y. Hwu, M. Marsi, A. Terrasi, D. Rioux, Y. Chang, J. T. McKinley, M. Onellion, G. Margaritondo, M. Capozi, C. Quaresima, A. Campo, C. Ottaviani, P. Perfetti, N. G. Stoffel, and E. Wang, Phys. Rev. B **43**, 3678 (1991).
[6] G. Jasiolek, A. Pajaczkowska, and P. Przyslupski, Z. Phys. B **72**, 7 (1988).
[7] I. Z. Kostadinov, V. G. Hadjiev, J. Tihov, M. Mateev, M. Mikhov, O. Petrov, V. Popov, E. Dinolova, Ts. Zheleva, G. Tyuliev, and V. Kojouharov, Physica C **156**, 427 (1988).
[8] F. U. Hillebrecht, J. Fraxedas, L. Ley, H. J. Trodahl, J. Zaanen, W. Braun, M. Mast, H. Petersen, M. Schaible, L. C. Bourne, P. Pinsukanjana, and A. Zettl, Phys. Rev. B **39**, 236 (1989).
[9] V. F. Masterov, F. S. Nasredinov, and P. P. Seregin, Fiz. Tverd. Tela (St. Petersburg) **37**, 1265 (1995) [Phys. Solid State **37**, 687 (1995)].
[10] V. F. Masterov, F. S. Nasredinov, N. P. Seregin, and P. P. Seregin, Fiz. Tverd. Tela (St. Petersburg) **39**, 1750 (1997) [Phys. Solid State **39**, 1559 (1997)].

Translated by G. Skrebtsov

Singlet-triplet pseudo Jahn–Teller centers in copper oxides

A. S. Moskvin and Yu. D. Panov

Ural State University, 620083 Ekaterinburg, Russia
(Submitted March 26, 1998; resubmitted April 20, 1998)
Fiz. Tverd. Tela (St. Petersburg) **40**, 1795–1804 (October 1998)

One of the most interesting attributes of a hole CuO_4^5 center in doped cuprates is the complexity of the ground state as a result of electronic pseudodegeneracy. An extra hole injected into the initial CuO_4^6 cluster with a b_{1g} hole can occupy not only the very same hybrid Cu $3d-$O $2p$ orbital state, producing a Zhang–Rice A_{1g} singlet, but also the pure oxygen e_u state, generating a singlet or triplet $^{1,3}E_u$ term, with close energies. The pseudo Jahn–Teller effect induced by pseudodegeneracy of the singlet $^1A_{1g}$ and ^1E_u terms is analyzed in detail.
 [S1063-7834(98)00610-8]

Intuitive notions about the special role of Jahn-Teller (JT) ions (polarons and centers) have provided the springboard for pioneering research that led Muller and Bednorz to the discovery of high-temperature (high-T_c) superconductivity in 1986.[1] Unfortunately, the passing years have not fully closed the gap in our understanding of this phenomenon. In many ways the situation has been complicated by a failure to fully appreciate the role of the Jahn–Teller effect—a typical shortcoming of the traditional description of the electronic structure of oxides by the ''metallic'' approach, which is the foundation of the majority of popular high-T_c superconductivity scenarios. On the other hand, a wealth of facts has been amassed in these years, attesting to the existence of Jahn–Teller copper-oxygen centers with very strong electron-vibration correlations.

The subject of the Jahn–Teller effect in cuprates is usually framed either within the entrenched concept of the JT ion $Cu^{2+}(3d^9)$, an outgrowth of the well-known problem of the JT effect for the $Cu^{2+}(3d^9)$ ion in an octahedral or cubic environment,[2] or in terms of phenomena associated with extreme anharmonicity of apical oxygen vibrations (double-well potential).[3,4] However, these phenomena are not of a universal nature spanning a broad class of cuprates and in most cases do not have direct bearing on their extraordinary properties.

A common element of the crystal and electronic structure of various copper oxide high-T_c superconducting systems is found in the almost square CuO_4 clusters that form the superconducting planes of CuO_2. The occurrence of the pseudo Jahn–Teller effect in the presence of hole or electron doping in the CuO_2 plane is the basis of the previously proposed[5–11] model of pseudo JT centers. Within the context of this model copper oxides based on CuO_4 clusters are regarded as systems that are unstable against a reaction of the disproportionation type

$$2CuO_4^6 \rightarrow [CuO_4^{5-}]_{JT} + [CuO_4^{7-}]_{JT} \quad (1)$$

with the formation of a system of polar pseudo JT centers CuO_4^{5-} (hole center) and CuO_4^{7-} (electron center), which differ by a pair of electrons bound in the completely filled molecular shell, i.e., a ''local boson'' (Anderson bipolaron).[6–8] The phase of the polar centers can be regarded as a system of local bosons moving in a lattice of hole polar JT centers—a generalized quantum lattice Bose gas. The low threshold of the disproportionation reaction and the JT nature of the polar centers (in particular, the energy of JT stabilization and high polarizability) tend to stabilize them. The centers of nucleation of the new phase of polar centers, in general, are local potential inhomogeneities formed by nonisovalent substitution ($La^{3+} \rightarrow Ba^{2+}$, Ca^{2+}, Sr^{2+} in $La_{2-x}M_xCuO_4$ and $Nd^{3+} \rightarrow Ce^{4+}$ $Nd_{2-x}Ce_xCuO_4$, interstitial oxygen in $La_2CuO_{4+\delta}$, and oxygen ions and (or) oxygen vacancies in CuO_x chains in $YBa_2Cu_3O_{6+x}$, which serve as unique nucleation centers or a center of charge inhomogeneity (CI center).

In regard to superconductivity, the model of pseudo JT centers, like the Alexandrov–Mott bipolaron model,[12] is in fact a variant on the Schafroth local-boson model. In contrast with bipolarons, which have a rather complex structure of paired polarons and move in a relatively simple rigid lattice, the local bosons in the model of pseudo JT centers have the simpler structure of a pair of electrons that form a filled molecular shell but move in a complex pseudo JT lattice.

According to quantum-chemical calculations, the ground state of the one-hole square CuO_4^{6-} cluster is the nondegenerate symmetry state $b_{1g}(d_{x^2-y^2})$. The nearest excited symmetry states e_g, b_{2g}, a_{1g}, e_u, and a_{2g} are separated by a large gap $\sim 1.5-2.5$ eV, which governs the fundamental absorption edge $b_{1g} \rightarrow e_u$ in copper oxides. One universal feature of the optical absorption spectra of oxides based on CuO_4^{6-} clusters—the exciton-band structure of the fundamental absorption spectral band in the interval 1.5–3.0 eV (Ref. 13), associated with the $b_{1g} \rightarrow e_u$ transition—deserves special attention. The doublet structure of the transition with charge transfer from the Cu $3d \rightarrow$ O $2p$ hybrid b_{1g} state to the O $2p$ pure oxygen e_u state indicates the existence of two types of e_u states: one weakly correlated and one strongly correlated. This anomalous feature of the e_u states is associated with their relatively high density of O $2p$ holes and the well-known dependence of the oxygen O $2p$ states on the density of holes in the $2p$ shell. To describe this correlation effect of a ''nonrigid anionic background,'' Hirsch and

Tang[14] have proposed the introduction of two types of oxygen states (conditionally localized and delocalized, i.e., strongly correlated and weakly correlated), which are identified with two components of the ''correlation pseudospin'' $s=1/2$. This effect produces a special kind of correlation splitting of the oxygen orbitals and invests the states with a doublet ''exciton'' structure; it also leads to formal doubling of the number of molecular orbitals: In particular, there emerge two types of orthogonal (!) states b_{1g} (upper correlation half-level) and b_{1g}^* (lower correlation half-level), which differ by the value of the projection of the correlation pseudospin. The increase in the density of O $2p$ holes in the transition $CuO_4^{6-}\rightarrow CuO_4^{5-}$ to a hole cluster produces a sharp increase in the correlation e_u splitting at the CuO_4^{5-} hole centers and imparts pseudodegeneracy to the b_{1g}^{*2} and $b_{1g}^* e_u^*$ configurations with the formation of a multiplet of closely spaced terms: $(g_{1g}^{*2})^1A_{1g}$ (Zhang–Rice singlet) and $(b_{1g}^* e_u^*)^{1,3}E_u$, where b_{1g}^* and e_u^* are the corresponding lower correlation half-levels. The energy spectrum of the original (''one-hole'') CuO_4^{6-} cluster and the ''two-hole'' CuO_4^{5-} cluster (hole polar center) is shown schematically in Fig. 1, taking into account the correlation splitting for pure oxygen e_u orbitals. Also observed on the part of the CuO_4^{5-} center is a correlation effect of purely electrostatic origin,[6] which has the effect of bringing the $^1A_{1g}$ and $^{1,3}E_u$ terms of the (respectively) b_{1g}^{*2} and $b_{1g}^* e_u^*$ configurations still closer together.

The net effect of the two operative correlation effects is pseudodegeneracy in the ground state of a hole center. The optical portrait of a polaron center is the $b_{1g}^{*2}\rightarrow b_{1g}^* e_u^*$ absorption band in the mid-infrared (MIR) band. Such bands are actually observed in copper oxides in the interval 0.1–0.5 eV and are an important argument for the existence of pseudo JT centers.[6]

The pseudodegeneracy in the ground state of the two-hole center of CuO_4^{5-} terms having different parities and an orbital and spin multiplet character imparts unique properties to the copper oxides, including the pseudo Jahn–Teller effect, which manifests itself at many levels. Our objective in this paper is to investigate in detail the vibronic nature of the CuO_4^{5-} center. We consider the problem of the pseudo Jahn–Teller effect in a square CuO_4 cluster on the basis of two-particle states of the pseudodegenerate $^1A_{1g}$ and ^1E_u terms over a wide range of values of the initial electron splitting parameter and vibronic interaction constants. We investigate the adiabatic potential of a polar CuO_4 cluster and tunnel states in the case of a strong pseudo Jahn–Teller effect, and we derive expressions for the vibronic reduction factors.

1. ADIABATIC POTENTIAL

In the ensuing discussion we adopt the $|\Gamma\gamma\rangle$ states of the $^1A_{1g}$ and ^1E_u terms as the electronic basis. Here $\Gamma\gamma=(A_{1g},E_u^x,E_u^y)$ is the irreducible representation and its row expansion in the D_{4h} symmetry group of the square CuO_4 cluster, under which the orbital part of the wave function is transformed. In the linear approximation the active JT coordinates on the adopted electronic basis are the vibrational modes of symmetry a_{1g}, ba_{1g}, b_{2g}, and e_u.

The vibronic interaction for the isolated ^1E_u term has the well-known form of the $E-b_1-b_2$ problem,[2] and the singlet $^1A_{1g}$ and ^1E_u terms are mixed with the vibronic interaction

$$\langle A_{1g}|\hat{V}_{\rm vib}|E_u^i\rangle=\sum_{e_u} V_e Q_{e_u^i} \tag{2}$$

by means of the active $Q_{e_u^x}$ and $Q_{e_u^y}$ vibrational modes. For the square CuO_4 cluster there are three modes of symmetry e_u, but we shall confine the ensuing discussion to just one pair of e_u-type coordinates; we denote the corresponding linear vibronic constant by V_e.

The sum of the electron operator $\hat{V}_{\rm el}$, the elastic energy $\hat{V}_Q$, and the vibronic interaction operator $\hat{V}_{\rm vib}$ for the singlet states of the $^1A_{1g}$ and ^1E_u terms with initial distribution Δ_{AE} (Fig. 1), given the appropriate choice of coordinate origin $Q_{a_{1g}}$, has the form

$$\hat{U}(Q)=\sum_i \frac{\omega_i^2 Q_i^2}{2}\hat{I} + \begin{pmatrix} -\Delta+V_z Q_z & V_e Q_x & V_e Q_y \\ V_e Q_x & V_\alpha Q_\alpha & V_\beta Q_\beta \\ V_e Q_y & V_\beta Q_\beta & -V_\alpha Q_\alpha \end{pmatrix}, \tag{3}$$

where the indices distinguishing the linear vibronic constants and the normal coordinates are denoted as follows: $a_{1g}\rightarrow z$, $e_u^x\rightarrow x$, $e_u^y\rightarrow y$, $b_{1g}\rightarrow\alpha$, $b_{2g}\rightarrow\beta$, and the following notation has been introduced: $\Delta=\Delta_{AE}-V_z q_z^{(0)}$, $V_z=V_z^{A_{1g}}-V_z^{E_u}$, $q_i^{(0)}=V_i/\omega_i^2$.

Important information about the system can be obtained by investigating the sheets of the adiabatic potential $\varepsilon(Q)$, which are the roots of the characteristic equation for $\hat{U}(Q)$. It is most important to know the coordinates of the minima Q^0, their depth, the curvature of the energy surface in the vicinity of Q^0, and the composition of the wave functions at the minima of the adiabatic potential. Such information can be obtained in the Opik–Pryce method,[15] where the eigenvalue problem is solved only for extrema of the adiabatic potential. The conditions underlying the occurrence of minima of a specific type are found by analyzing the curvature of the energy surface of the adiabatic potential $\varepsilon(Q)$ in the vicinity of Q^0.

The eigenvalue problem for $\hat{V}_{\rm vib}$ at the extrema of the adiabatic potential has the form

$$\begin{pmatrix} -\Delta-2E_{\rm JT}^z z^2 & -4E_{\rm JT}^e zx & -4E_{\rm JT}^e zy \\ -4E_{\rm JT}^e zx & -2E_{\rm JT}^\alpha(x^2-y^2) & -4E_{\rm JT}^\beta xy \\ -4E_{\rm JT}^e zy & -4E_{\rm JT}^\beta xy & 2E_{\rm JT}^\alpha(x^2-y^2) \end{pmatrix}\begin{pmatrix} z \\ x \\ y \end{pmatrix} = \lambda\begin{pmatrix} z \\ x \\ y \end{pmatrix}, \tag{4}$$

where $E_{\rm JT}^i=V_i^2/2\omega_i$ is a characteristic JT energy, and z, x, and y denote the coefficients of the expansion of the electron wave function in the basis $|A_{1g}\rangle$, $|E_u^x\rangle$, $|E_u^y\rangle$. The system (4) in conjunction with the normalization condition $x^2+y^2+z^2=1$ admits 13 solutions, which are summarized in Table I;

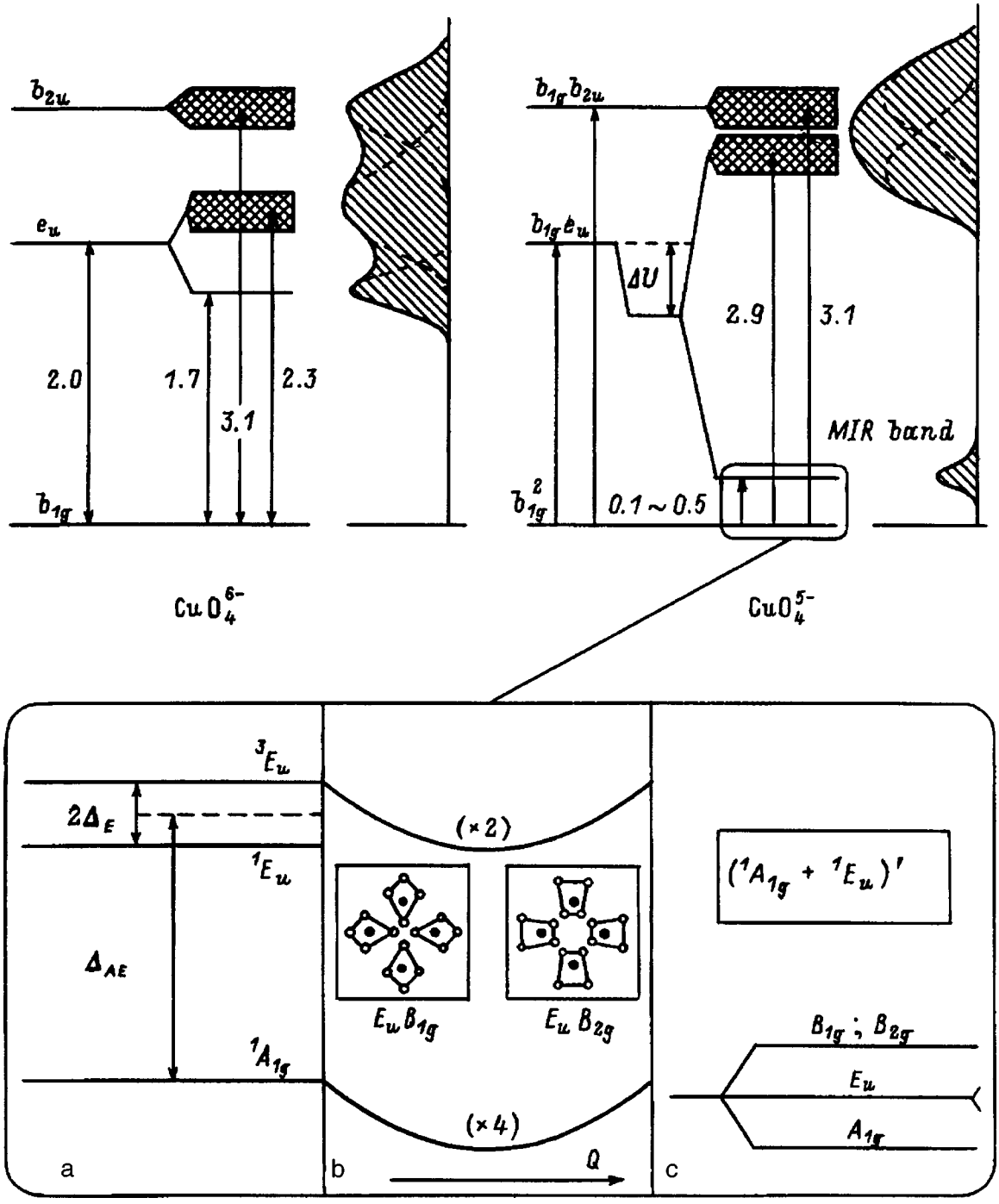

FIG. 1. Correlation effects in the energy spectrum of an initial CuO_4^{6-} center and a hole CuO_4^{5-} center with characteristic numerical quantities (eV) for oxides of the CuO type. On the right is shown the formation of the fundamental absorption spectrum for the parent and doped oxides with the occurrence of a characteristic MIR band in the latter case. The lower part of the figure shows the schematic form of the energy spectrum of a CuO_4^{5-} center: a) fragment of the initial electron spectrum; b) strong pseudo JT effect without spin-orbital interaction; c) tunnel splitting of the ground state in the case of the strong pseudo Jahn–Teller effect. Inset: distortions of a CuO_4 cluster, corresponding to different minima of the adiabatic potential.

the last column of the table gives expressions for the expansion of the surface of the adiabatic potential near the extrema up to and including squared terms. The solutions are divided into three groups according to their properties.

1) The first group, NJT, consists of one solution. The wave functions at the extrema coincide with $|A_{1g}\rangle$. The NJT extremum is a minimum on the lower sheet of the adiabatic potential, $b<0$ $(b=-\Delta+4E^e_{\rm JT}-2E^z_{\rm JT})$; for $(\Delta+2E^z_{\rm JT})<0$ the minimum is situated on the upper sheet of the adiabatic potential. A weak pseudo JT effect prevails in both cases; because of the weakness of vibronic interaction in comparison with Δ, there is no distortion of the CuO_4 cluster with a change of symmetry. All that happens as a result of vibronic interaction is renormalization of the frequency of the local e_u mode (see Table I).

2) The second group, JT_i $(i=\alpha,\beta)$, comprises four so-

TABLE I. Coordinates of extrema of the adiabatic potential and expansion coefficients of the electronic wave functions at the extremum points.

Type	z	x	y	Q_z^0	Q_α^0	Q_β^0	Q_x^0	Q_y^0	$2\varepsilon(q)-2\varepsilon_0^\sigma-\Sigma_i\omega_i^2q_i^2$
NJT	1	0	0	$-q_z^{(0)}$	0	0	0	0	$-\omega_e^2\eta_z(q_x^2+q_y^2)$
JT_α	0	0	1	0	$q_\alpha^{(0)}$	0	0	0	$-\omega_e^2\varkappa_\alpha q_y^2-\omega_\beta^2\lambda_\alpha q_\beta^2$
	0	1	0	0	$-q_\alpha^{(0)}$	0	0	0	$-\omega_e^2\varkappa_\alpha q_x^2-\omega_\beta^2\lambda_\alpha q_\beta^2$
JT_β	0	$\frac{-1}{\sqrt{2}}$	$\frac{1}{\sqrt{2}}$	0	0	$q_\beta^{(0)}$	0	0	$-\omega_e^2\varkappa_\beta q_2^2-\omega_\alpha^2\lambda_\beta q_\alpha^2$
	0	$\frac{1}{\sqrt{2}}$	$\frac{1}{\sqrt{2}}$	0	0	$-q_\beta^{(0)}$	0	0	$-\omega_e^2\varkappa_\beta q_1^2-\omega_\alpha^2\lambda_\beta q_\alpha^2$
PJT_α	c_α	0	d_α	$-q_z^{(0)}c_\alpha^2$	$q_\alpha^{(0)}d_\alpha^2$	0	0	$-q_e^{(0)}2c_\alpha d_\alpha$	$-(\omega_e v_\alpha q_x+\omega_\beta\rho_\alpha q_\beta)^2$ $-(\omega_z\tau_\alpha q_z+\omega_\alpha\mu_\alpha q_\alpha-\omega_e\nu_\alpha q_y)^2$
	c_α	d_α	0	$-q_z^{(0)}c_\alpha^2$	$-q_\alpha^{(0)}d_\alpha^2$	0	$-q_e^{(0)}2c_\alpha d_\alpha$	0	$-(\omega_e v_\alpha q_y+\omega_\beta\rho_\alpha q_\beta)^2$ $-(\omega_z\tau_\alpha q_z-\omega_\alpha\mu_\alpha q_\alpha-\omega_e\nu_\alpha q_x)^2$
	c_α	0	$-d_\alpha$	$-q_z^{(0)}c_\alpha^2$	$q_\alpha^{(0)}d_\alpha^2$	0	0	$q_e^{(0)}2c_\alpha d_\alpha$	$-(\omega_e v_\alpha q_x-\omega_\beta\rho_\alpha q_\beta)^2$ $-(\omega_z\tau_\alpha q_z+\omega_\alpha\mu_\alpha q_\alpha+\omega_e\nu_\alpha q_y)^2$
	c_α	$-d_\alpha$	0	$-q_z^{(0)}c_\alpha^2$	$-q_\alpha^{(0)}d_\alpha^2$	0	$q_e^{(0)}2c_\alpha d_\alpha$	0	$-(\omega_e v_\alpha q_y-\omega_\beta\rho_\alpha q_\beta)^2$ $-(\omega_z\tau_\alpha q_z-\omega_\alpha\mu_\alpha q_\alpha+\omega_e\nu_\alpha q_x)^2$
PJT_β	c_β	$\frac{-d_\beta}{\sqrt{2}}$	$\frac{d_\beta}{\sqrt{2}}$	$-q_z^{(0)}c_\beta^2$	0	$q_\alpha^{(0)}d_\beta^2$	$q_e^{(0)}\sqrt{2}c_\beta d_\beta$	$-q_e^{(0)}\sqrt{2}c_\beta d_\beta$	$-(\omega_e v_\beta q_1-\omega_\alpha\rho_\beta q_\alpha)^2$ $-(\omega_z\tau_\beta q_z+\omega_\beta\mu_\beta q_\beta-\omega_e\nu_\beta q_2)^2$
	c_β	$\frac{d_\beta}{\sqrt{2}}$	$\frac{d_\beta}{\sqrt{2}}$	$-q_z^{(0)}c_\beta^2$	0	$-q_\alpha^{(0)}d_\beta^2$	$-q_e^{(0)}\sqrt{2}c_\beta d_\beta$	$-q_e^{(0)}\sqrt{2}c_\beta d_\beta$	$-(\omega_e v_\beta q_2-\omega_\alpha\rho_\beta q_\alpha)^2$ $-(\omega_z\tau_\beta q_z-\omega_\beta\mu_\beta q_\beta-\omega_e\nu_\beta q_1)^2$
	c_β	$\frac{d_\beta}{\sqrt{2}}$	$\frac{-d_\beta}{\sqrt{2}}$	$-q_z^{(0)}c_\beta^2$	0	$q_\alpha^{(0)}d_\beta^2$	$-q_e^{(0)}\sqrt{2}c_\beta d_\beta$	$q_e^{(0)}\sqrt{2}c_\beta d_\beta$	$-(\omega_e v_\beta q_1+\omega_\alpha\rho_\beta q_\alpha)^2$ $-(\omega_z\tau_\beta q_z+\omega_\beta\mu_\beta q_\beta+\omega_e\nu_\beta q_2)^2$
	c_β	$\frac{-d_\beta}{\sqrt{2}}$	$\frac{-d_\beta}{\sqrt{2}}$	$-q_z^{(0)}c_\beta^2$	0	$-q_\alpha^{(0)}d_\beta^2$	$q_e^{(0)}\sqrt{2}c_\beta d_\beta$	$q_e^{(0)}\sqrt{2}c_\beta d_\beta$	$-(\omega_e v_\beta q_2+\omega_\alpha\rho_\beta q_\alpha)^2$ $-(\omega_z\tau_\beta q_z-\omega_\beta\mu_\beta q_\beta+\omega_e\nu_\beta q_1)^2$

Note. The following notation is introduced in the table: $q_i^{(0)}=V_i/\omega_i^2$, $q_1=(q_x+q_y)/\sqrt{2}$, $q_2=(-q_x+q_y)/\sqrt{2}$, $q_i=Q_i-Q_i^0$, $c_\sigma=\sqrt{a_\sigma/(a_\sigma+b)}$, $d_\sigma=\sqrt{b/(a_\sigma+b)}$, $\eta_z=4E_{JT}^e/(\Delta+2E_{JT}^z)$, $\lambda_\sigma=E_{JT}^{\sigma'}/E_{JT}^\sigma$, $\varkappa_\sigma=4E_{JT}^e/(-\Delta+2E_{JT}^\sigma)$, $v_\sigma=\sqrt{E_{JT}^e a_\sigma/(E_{JT}^e a_\sigma+E_{JT}^\sigma b)}$, $\rho_\sigma=\sqrt{E_{JT}^{\sigma'}b/(E_{JT}^e a_\sigma+E_{JT}^\sigma b)}$, $\tau_\sigma=\sqrt{E_{JT}^z a_\sigma b/[E_{JT}^e(a_\sigma+b)^2]}$, $\mu_\sigma=\sqrt{E_{JT}^\sigma a_\sigma b/[E_{JT}^e(a_\sigma+b)^2]}$, $\nu_\sigma=(a_\sigma-b)/(a_\sigma+b)$, $\varepsilon_0^{\sigma,NJT}=-\Delta-E_{JT}^z$, $\varepsilon_0^{\sigma,JT}=-E_{JT}^\sigma$, $\varepsilon_0^{\sigma,PJT}=-E_{JT}^\sigma-(1/2)c_\sigma^2 a_\sigma$.

lutions, which are analogous to the results of the $E-b_1-b_2$ problem. The wave function at the extrema of the adiabatic potential consists of functions of the E_u type. From now on we shall use the phrase ''strong'' σ in application to the rhombic mode for which the JT energy is higher, and ''weak'' σ' for the rhombic mode having lower JT energy: $E_{JT}^\sigma>E_{JT}^{\sigma'}$ $(\sigma,\sigma'=\alpha,\beta)$; in the case of the $E-b_1-b_2$ problem E_{JT}^σ is the energy of JT stabilization. Of the four extrema, only the two JT_α are minima, which are situated on the lower sheet of the adiabatic potential if $a_\sigma<0$ $(a_\sigma=\Delta+4E_{JT}^e-2E_{JT}^\sigma)$, or on the middle sheet of the adiabatic potential if $(\Delta-2E_{JT}^\sigma)>0$. We note that the pair of solutions $JT_{\sigma'}$ corresponds to saddle points, and for $E_{JT}^\sigma=E_{JT}^{\sigma'}$ we have an equipotential ravine of minima. The wave functions at the minima are mutually orthogonal. The frequency of the σ mode is invariant, and the frequency of the σ' mode is renormalized by vibronic interaction (see Table I).

It should be noted that the type (B_{1g} or B_{2g}) of fundamental JT mode plays a principal role in the physics of copper oxides. It is determined by competition between the vibronic parameters for Cu $3d-$O $2p$ and O $2p-$O $2p$ bonds minimizing the B_{1g} or B_{2g} mode, respectively.

For the e_u mode the JT_i solutions correspond to the weak pseudo JT effect: Vibronic interaction merely induces renormalization of the frequencies of local e_u modes. If the α mode is strong, the coordinates of the minima determine the distortion of the CUO_4 cluster in the form of a rhombus stretched along the x axis or along the y axis (Fig. 2a). One of the local modes, either e_u^x or e_u^y, is softened accordingly (see Table I); however, since the two minima are equivalent, the frequencies of the local e_u modes remain twofold degenerate. For the case of a strong β mode with rectangular distortion of the cluster at the points of the adiabatic potential minima (Fig. 2b), we encounter renormalization of the e_u mode codirectional with this distortion.

3) The third group, PJT_i $(i=\alpha,\beta)$, comprises eight solutions and corresponds to the most complex case of the strong pseudo JT effect. Here the wave functions at the extrema are hybrid $A_{1g}-E_u$ states, where the coefficients of the linear combination depend on the initial splitting Δ and the JT energies. Of the eight extrema, only the four PJT_σ (σ denotes the strong rhombic mode) are minima if $a_\sigma>0$ and $b>0$. All the PJT_σ minima are equivalent and are situated on the lower sheet of the adiabatic potential. The wave functions at the points of the minima are not mutually orthogonal, this being a characteristic attribute of the strong pseudo JT effect.

The distortion of a CuO_4 cluster with a nonzero quadrupole moment is accompanied by codirectional distortion of the e_u mode, causing a dipole moment to appear. The alter-

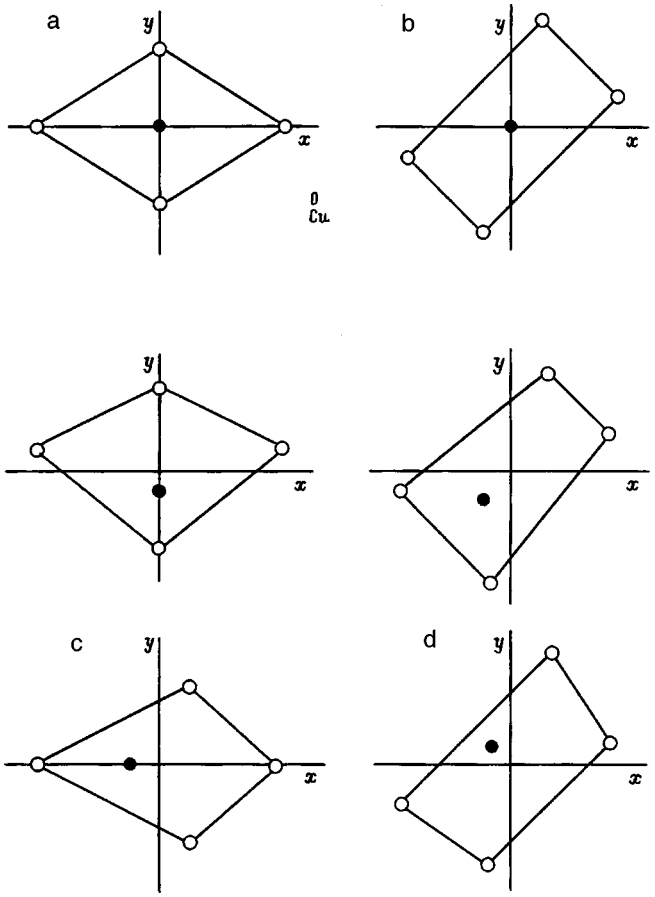

FIG. 2. Illustration of the possible distortion of a CuO_4 cluster. a) At a JT_α minimum; b) at a JT_β minimum; c) at a PJT_β minimum (the dipole moment can be directed along one of the diagonals of the rhombus); d) at a PJT_β minimum (the possible directions of the dipole moment are rotated through the angle $\phi=\pi/4$ relative to the directions for the PJT_α minima.

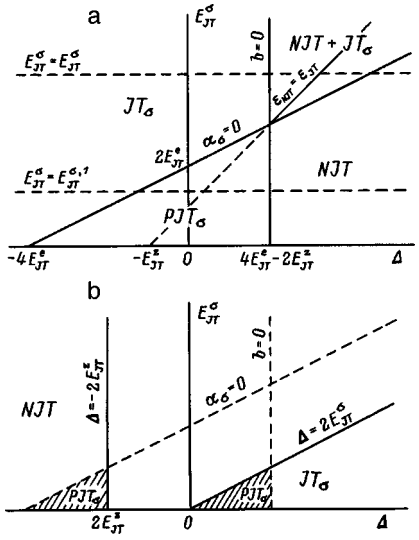

FIG. 3. a) State diagram of the lower sheet of the adiabatic potential on the plane of parameters $(\Delta, E^{\sigma}_{\mathrm{JT}}$ for fixed E^{z}_{JT} and E^{e}_{JT}. The figure shows the boundaries of domains with different types of minima of the lower sheet of the adiabatic potential ($a_\sigma=0$ and $b=0$). The lines $E^{\sigma}_{\mathrm{JT}}=E^{\sigma,1}_{\mathrm{JT}}$ and $E^{\sigma}_{\mathrm{JT}}=E^{\sigma,2}_{\mathrm{JT}}$ correspond to different relative intensities of vibronic interaction with the σ and e_u modes. b) State diagram of the upper sheets of the adiabatic potential on the plane of parameters $(\Delta, E^{\sigma}_{\mathrm{JT}}$ for fixed E^{z}_{JT} and E^{e}_{JT}. In the parameter domain to the left of the line $\Delta=2E^{\sigma}_{\mathrm{JT}}$ an NJT minimum exists on the upper sheet of the adiabatic potential; only a trivial, nonanalytical minimum exists on the middle sheet. In the parameter domain to the right of the line $\Delta=2E^{\sigma}_{\mathrm{JT}}$ minima exist on the middle sheet of the adiabatic potential. If $E^{z}_{\mathrm{JT}}<2E^{e}_{\mathrm{JT}}$, parameter domains exist in which an NJT minimum of the upper sheet or JT_σ minima exist simultaneously with PJT_σ minima on the lower sheet of the adiabatic potential. It is impossible for all three types of minima to coexist on different sheets of the adiabatic potential. In the parameter domain between the lines $\Delta=-2E^{z}_{\mathrm{JT}}$ and $\Delta=2E^{\sigma}_{\mathrm{JT}}$ only trivial, nonanalytical minima exist on the upper and lower sheets of the adiabatic potential.

native distortions of the cluster in this case are shown in Figs. 2c and 2d. As a result, the σ mode is mixed with a codirectional e_u mode and an a_{1g} mode, generating three local hybrid modes, and the σ' mode is hybridized with the remaining e_u mode and generates two more local hybrid modes. The mode mixing coefficients are proportional to the corresponding vibronic constants, and the frequencies of the new local modes can be determined from the corresponding expressions for the expansion of the adiabatic potential surface in the vicinity of the extrema (see Table I). Inasmuch as the minima are equivalent, the local frequencies at all four minima coincide.

The conditions for minima of one type or another to exist on the lower sheet of the adiabatic potential are determined by the quantities

$$a_\sigma=\Delta+4E^{e}_{\mathrm{JT}}-2E^{\sigma}_{\mathrm{JT}},\quad b=-\Delta+4E^{e}_{\mathrm{JT}}-2E^{z}_{\mathrm{JT}}. \tag{5}$$

The minima are of type a) NJT if $a_\sigma>0$ and $b<0$; b) JT_σ if $a_\sigma<0$ and $b>0$; c) PJT_σ if $a_\sigma>0$ and $b>0$; d) NJT and JT_σ if $a_\sigma<0$ and $b<0$.

A cross section of the domain of the parameters Δ, E^{σ}_{JT}, and E^{e}_{JT} for set values of E^{e}_{JT} and $E^{z,0}_{\mathrm{JT}}$ is shown in Fig. 3a. In the limit $\Delta\to+\infty$ the lower $^1A_{1g}$ term is well isolated, and the corresponding sheet of the adiabatic potential has a trivial NJT minimum. In the limit $\delta\to-\infty$ the ^1E_u term is lower, and we have the usual $E-b_1-b_2$ problem with two JT_σ minima on the lower sheet of the adiabatic potential. As the $^1A_{1g}$ and ^1E_u terms come closer together, they begin to interact through the agency of the e_u mode, whose frequency is then renormalized. The merging of the terms is accompanied either by the advent of four PJT_σ minima or by the advent of three ($NJT+JT_\sigma$) minima, depending on the value of E^{σ}_{JT}. In Fig. 3a these two possibilities correspond to the lines $E^{\sigma}_{\mathrm{JT}}=E^{\sigma,1}_{\mathrm{JT}}$ and $E^{\sigma}_{\mathrm{JT}}=E^{\sigma,2}_{\mathrm{JT}}$.

In motion along the line $E^{\sigma}_{\mathrm{JT}}=E^{\sigma,1}_{\mathrm{JT}}$ from $-\infty$ to $+\infty$ the curvature of the JT_σ minima along the e_u directions decreases, vanishing at $a_\sigma=0$. Each of the two JT_σ in this case changes into a saddle point with the formation of two PJT_σ minima (one of the JT_σ minima divides along the coordinate Q_1, and the other divides along Q_2). Next, between the lines $a_\sigma=0$ and $b=0$ the value of the rhombic coordinate of the PJT_σ minima decreases to zero at the line $b=0$. The value of the e_u coordinate of the minima increases at first and then decreases to zero, attaining a maximum at the line $\Delta=(E^{z}_{\mathrm{JT}}-E^{\sigma}_{\mathrm{Jt}})$. The coordinate Q_z increases linearly ($\sim a_\sigma$) from zero to $-q^{(0)}_z$ at the line $B=0$, where the four PJT_σ minima merge into a single NJT minimum. Next, as $\Delta\to+\infty$, the A_{1g} and E_u terms interact to an ever-diminishing degree, and the renormalized frequency tends to its initial value.

The PJT_σ minima appear in the presence of efficient interaction of the A_{1g} and E_u terms through e_u modes. If $E^\sigma_{JT} > (4E^e_{JT} - E^z_{JT})$ (e.g., if $E^\sigma_{JT} = E^{\sigma,2}_{JT}$, Fig. 3a), interaction through the σ mode is far more efficient. In this case, for $b=0$ an NJT minimum also appears on the lower sheet of the adiabatic potential in addition to JT_σ minima. On the line $\Delta = (E^z_{JT} = E^\sigma_{JT})$ all three minima have the same energy. The JT_σ minima then flatten out more and more without changing their positions, until only the NJT minimum is left when $a_\sigma = 0$.

Figure 3b also shows the state diagram of the upper sheets of the adiabatic potential.

2. TUNNEL SPLITTING

The most complex and interesting case of the strong pseudo JT effect can be treated within the framework of the tunneling Hamiltonian,[16] when the motion of the system represents localized vibrations at the adiabatic potential minima, accompanied by tunneling between them. We assume in this case that the depth of the adiabatic potential minima is greater than the characteristic elastic quantum and that the tunneling frequency is low.

We consider the problem of minimizing the complete energy functional $E[\Psi] = \langle |\hat{H}\Psi\rangle$ with the Hamiltonian

$$\hat{H} = \hat{T}_Q + \hat{V}_{\rm el} + \hat{V}_Q + \hat{V}_{\rm vib}, \tag{6}$$

where $\hat{T}_Q$ is the kinetic energy of the nuclei, and the trial function

$$\Psi = \sum_{M=1}^{4} c_M \varphi_M^{(\sigma)} \chi_M^{(\sigma)}, \tag{7}$$

where $\varphi_M^{(\sigma)}$ and $\chi_M^{(\sigma)}$ are the electron and vibrational wave functions centered at the $PJT_\sigma^{(M)}$ minimum.

The variation of $E|\Psi|$ yields a matrix equation of the form

$$\begin{pmatrix} H & H_q & H_d & H_q \\ H_q & H & H_q & H_d \\ H_d & H_q & H & H_q \\ H_q & H_d & H_q & H \end{pmatrix} \begin{pmatrix} c_1 \\ c_2 \\ c_3 \\ c_4 \end{pmatrix} = E \begin{pmatrix} 1 & S_q & S_d & S_q \\ S_q & 1 & S_q & S_d \\ S_d & S_q & 1 & S_q \\ S_q & S_d & S_q & 1 \end{pmatrix} \begin{pmatrix} c_1 \\ c_2 \\ c_3 \\ c_4 \end{pmatrix}, \tag{8}$$

where three matrix elements are present by virtue of the equivalence of the PJT_σ minima in the matrices of the Hamiltonian $\hat{H}$ (6) and overlap. Equation (8) can be used to find the tunneling states and tunneling energy levels. The eigenvectors of (8) have the form

$$\mathbf{c}_1 = \frac{1}{2}(1,1,1,1), \quad \mathbf{c}_2 = \frac{1}{2}(1,-1,1,-1),$$

$$\mathbf{c}_3 = \frac{1}{\sqrt{2}}(-\sin\theta, \cos\theta, \sin\theta, -\cos\theta),$$

$$\mathbf{c}_4 = \frac{1}{\sqrt{2}}(\cos\theta, \sin\theta, -\cos\theta, -\sin\theta). \tag{9}$$

The vectors $\mathbf{c}_3$ and $\mathbf{c}_4$ are degenerate, introducing arbitrariness into the choice of the phase θ. For $\theta = 0$ we have

$$|\Psi_{A_{1g}}\rangle = c_\sigma |A_{1g}\rangle \chi_{a_{1g}} + \frac{d_\sigma}{\sqrt{2}} \{|E_u^{(1)}\rangle \chi_{e_u^{(1)}} + |E_u^{(2)}\rangle \chi_{e_u^{(2)}}\},$$

$$|\Psi_\Sigma\rangle = -c_\sigma |A_{1g}\rangle \chi_\Sigma - \frac{d_\sigma}{\sqrt{2}} \{|E_u^{(1)}\rangle \chi_{e_u^{(1)}} - |E_u^{(2)}\rangle \chi_{e_u^{(2)}}\},$$

$$|\Psi_{E_u^{(1)}}\rangle = c_\sigma |A_{1g}\rangle \chi_{e_u^{(1)}} + \frac{d_\sigma}{\sqrt{2}} |E_u^{(1)}\rangle \{\chi_{a_{1g}} + \chi_\Sigma\},$$

$$|\Psi_{E_u^{(2)}}\rangle = c_\sigma |A_{1g}\rangle \chi_{e_u^{(2)}} + \frac{d_\sigma}{\sqrt{2}} |E_u^{(2)}\rangle \{\chi_{a_{1g}} - \chi_\Sigma\}, \tag{10}$$

where the functions $\{|E_u^{(1)}\rangle, |E_u^{(2)}\rangle\}$ have the form $\{|E_u^x\rangle, |E_u^y\rangle\}$ for $\sigma = \alpha$ or $\{(|E_u^x\rangle + |E_u^y\rangle)/\sqrt{2}, (-|E_u^x\rangle + |E_u^y\rangle)/\sqrt{2}\}$ for $\sigma = \beta$. The symmetrized combination s of the vibrational wave functions

$$\chi_{a_{1g}} = \frac{1}{2}(\chi_1^{(\sigma)} + \chi_2^{(\sigma)} + \chi_3^{(\sigma)} + \chi_4^{(\sigma)}),$$

$$\chi_{e_u^{(1)}} = \frac{1}{\sqrt{2}}(\chi_2^{(\sigma)} - \chi_4^{(\sigma)}),$$

$$\chi_\Sigma = \frac{1}{2}(-\chi_1^{(\sigma)} + \chi_2^{(\sigma)} - \chi_3^{(\sigma)} + \chi_4^{(\sigma)}),$$

$$\chi_{e_u^{(2)}} = \frac{1}{\sqrt{2}}(\chi_1^{(\sigma)} - \chi_3^{(\sigma)}), \tag{11}$$

and the Σ symmetry of the vibronic and vibrational wave functions coincides with the symmetry of the σ mode. The expressions for the tunneling-energy levels have the form

$$E_{A_{1g}} = \frac{H + 2H_q + H_d}{1 + 2S_q + S_d}, \quad E_{E_u} = \frac{H - H_d}{1 - S_d},$$

$$E_\Sigma = \frac{H - 2H_q + H_d}{1 - 2S_q + S_d}. \tag{12}$$

The pattern of the tunneling spectrum is shown in Fig. 4. The tunnel splittings are related to the frequencies of tunneling transitions between distorted configurations of the CuO_4 cluster, and in the case of deep minima the tunneling frequencies become much lower than the characteristics phonon frequencies. We note that in the case of the pseudo JT effect the symmetry of the vibronic ground state and the initial lower electron state do not necessary coincide, contrary to the case of the ordinary JT effect (Ham's law).[17] It is evident from Fig. 4 that regions exist with $\delta < 0$ (the electronic $^1A_{1g}$ term lies above the ^1E_u term) and $E_{A_{1g}} < E_{E_u}$. In the case of the pseudo JT effect vibronic interaction mixes different to electron terms, in contrast to the ordinary JT effect, where the electron functions belong to a degenerate level. On the whole, however, in our case the transformed properties of the

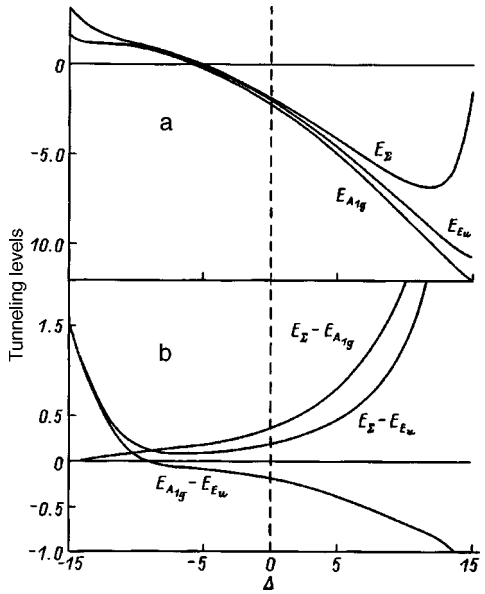

FIG. 4. Lower tunneling energy levels (a) and tunnel splittings (b) versus Δ for $k_e=3$, $k_\sigma/k_e=0.5$, $k_{\sigma'}/k_\sigma=0.5$, and $k_{z=0}$ (where $k_i=\sqrt{2E^i_{\rm JT}/\hbar\omega_i}$). A characteristic elastic quantum is adopted as the unit of energy. The upturn of the energy of tunneling states at the ends of the interval of possible values of Δ is attributable to the inappropriate basis choice in the case of shallow minima.

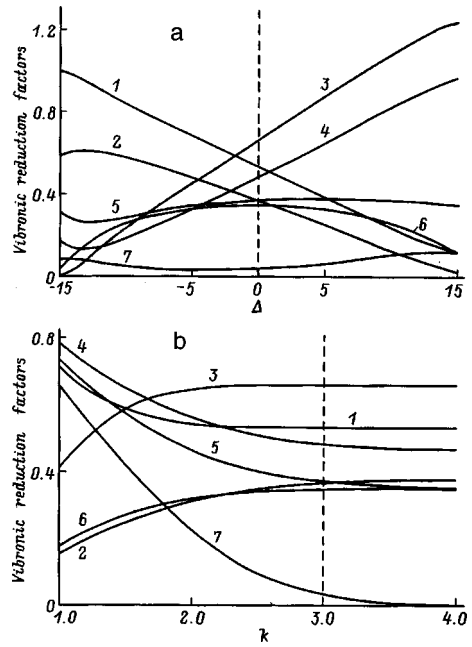

FIG. 5. Vibronic reduction factors as functions of Δ for $k_e=3$, $k_\sigma/k_e=0.5$, $k_{\sigma'}/k_\sigma=0.5$, and $k_{z=0}$ (where $k_i=\sqrt{2E^i_{\rm JT}/\hbar\omega_i}$) (a) and as functions of the parameter k for $k_e=k$, $k_\sigma/k_e=0.5$, $k_{\sigma'}/k_\sigma=0.5$, and $k_{z=0}$ (b). *1* — $K_{A_{1g}}\binom{E_u\ \ E_u}{E_u\ \ E_u}$, *2* — $K_{A_{1g}}\binom{A_{1g}\ \ A_{1g}}{E_u\ \ E_u}$, *3* — $K_{A_{1g}}\binom{E_u\ \ E_u}{A_{1g}\ \ A_{1g}}$, *4* — $K_{A_{1g}}\binom{A_{1g}\ \ A_{1g}}{A_{1g}\ \ A_{1g}}$, *5* — $K_{E_u}\binom{A_{1g}\ \ E_u}{A_{1g}\ \ E_u}$, *6* — $K_{E_u}\binom{A_{1g}\ \ E_u}{E_u\ \ A_{1g}}$, *7* — $K_{\Sigma'}\binom{E_u\ \ E_u}{E_u\ \ E_u}$.

lower vibronic states are the same as for a function of the initial electronic basis: the Σ level always lies above the A_{1g} and E_u levels.[18]

3. VIBRONIC REDUCTION FACTORS

The concept of vibronic reduction factors is used in the investigation of vibronic phenomena. A vibronic reduction factor is equal to the ratio of a reduced matrix element of the electron operator to the wave functions of the vibronic ground level and to the initial electron wave functions. In application to the pseudo JT effect, in general, the reduced vibronic matrix element is a linear combination of reduced electron matrix elements.

In a tight-binding scheme the vibronic wave function has the form

$$\Psi_{\Gamma\gamma}=\frac{1}{N_\Gamma}\sum_{\Gamma_1} c(\Gamma\Gamma_1)\sum_{\gamma_1\Gamma_2\gamma_2}\varphi_{\Gamma_1\gamma_1}\chi_{\Gamma_2\gamma_2}\langle\Gamma_1\gamma_1\Gamma_2\gamma_2|\Gamma\gamma\rangle, \tag{13}$$

where $\Gamma_2\in\Gamma\times\Gamma_1$ N_Γ is a normalization factor, $c(\Gamma\Gamma_1)$ is the amplitude of the vibronic function Γ generated by the electron representation Γ_1, $\chi_{\Gamma_2\gamma_2}$ is a linear combination of vibrational wave functions of equivalent minima, and $\langle\Gamma_1\gamma_1\Gamma_2\gamma_2|\Gamma\gamma\rangle$ is a Clebsch–Gordan coefficient.

Applying the Wigner–Eckart theorem to the vibronic matrix element, we obtain

$$\langle\Psi_\Gamma\|\hat V_{\tilde\Gamma}\|\Psi_{\Gamma'}\rangle=\sum_{\Gamma_1\Gamma_1'}K_{\tilde\Gamma}\begin{pmatrix}\Gamma & \Gamma'\\ \Gamma_1 & \Gamma_1'\end{pmatrix}\langle\varphi_{\Gamma_1}\|\hat V_{\tilde\Gamma}\|\varphi_{\Gamma_1'}\rangle, \tag{14}$$

where

$$K_{\tilde\Gamma}\begin{pmatrix}\Gamma & \Gamma'\\ \Gamma_1 & \Gamma_1'\end{pmatrix}=\frac{\sqrt{g_\Gamma g_{\Gamma'}}}{N_\Gamma N_{\Gamma'}}(-1)^{\Gamma+\tilde\Gamma+\Gamma_1}c(\Gamma\Gamma_1)c(\Gamma'\Gamma_1')\times\sum_{\Gamma_2}(-1)^{\Gamma_2}\langle\chi^2_{\Gamma_2}\rangle\begin{bmatrix}\Gamma & \tilde\Gamma & \Gamma'\\ \Gamma' & \Gamma_2 & \Gamma_1\end{bmatrix}. \tag{15}$$

Here $[\cdots]$ denotes the 6Γ symbol of the point group G (Ref. 19), and $\langle\chi^2_{\Gamma_2}$ is the integral of normalization of the vibrational wave function. The factor $(-1)^\Gamma$ is equal to unity for all representations of the group D_{4h} except $(-1)^{A_{2g}}=-1$ (Ref. 20). In the case of the Jahn–Teller effect Eq. (15) gives the well-known result for a vibronic reduction factor.[21] It follows from Eq. (15) that

$$K_{\tilde\Gamma}\begin{pmatrix}\Gamma & \Gamma'\\ \Gamma_1 & \Gamma_1'\end{pmatrix}=(-1)^{\Gamma+\Gamma'+\Gamma_1+\Gamma_1'}K_{\tilde\Gamma}\begin{pmatrix}\Gamma' & \Gamma\\ \Gamma_1' & \Gamma_1\end{pmatrix}. \tag{16}$$

For the given problem $\Gamma_1,\Gamma_1'=A_{1g},E_u$ and $\Gamma,\Gamma',\Gamma_2,\Gamma_2'=A_{1g},\Sigma,E_u$. The nonzero matrix elements have symmetry operators $\tilde\Gamma=A_{1g},A_{2g},B_{1g},B_{2g},E_u$. Figure 5a shows the vibronic reduction factors as functions of Δ. Clearly, the symmetry operators Σ' are highly suppressed. When vibronic interaction is intensified, the vibronic reduction factors tend to their limiting values (Fig. 5b), which can be obtained from Eq. (15) by making the substitutions $N_\Gamma\to1$ and $\langle\chi^2_{\Gamma_2}\rangle\to1$.

The components of the external electric field parallel to the plane of the CuO_4 cluster ($\mathbf{E}\perp C_4$) induce electric-dipole transitions between tunneling states of symmetry A_{1g} and E_u. The reduced vibronic matrix element of the E_u operator has the form

$$\langle \Psi_{A_{1g}} \| \hat{V}_{E_u} \| \Psi_{E_u} \rangle = \frac{c_\sigma d_\sigma}{N_{A_{1g}} N_{E_u}} (\langle \chi^2_{A_{1g}} \rangle + \langle \chi^2_{E_u} \rangle) \langle A_{1g} \| \hat{V}_{E_u} \| E_u \rangle. \tag{17}$$

For strong vibronic interaction ($N_\Gamma \to 1, \langle \chi^2_{\Gamma_2} \rangle \to 1$) and for $c_\sigma = d_\sigma = 1/\sqrt{2}$ the electric-dipole transition matrix element is not renormalized.

For E_u states the orbital Zeeman contribution associated with the z-component of the magnetic field is nonvanishing; this condition can be described by means of the well-known effective spin Hamiltonian for a non-Kramers doublet.[22] Vibronic interaction leads to strong renormalization of the reduced matrix element of the z component of the orbital angular momentum:

$$\langle \Psi_{E_u} \| \hat{V}_{A_{2g}} \| \Psi_{E_u} \rangle = \frac{\sqrt{2} d^2_\sigma S^n_q}{N^2_{E_u}} \langle E_u \| \hat{V}_{A_{2g}} \| E_u \rangle. \tag{18}$$

The vibronic reduction factor in this case is proportional to the overlap integral S^n_q of the vibrational states in adjacent wells of the adiabatic potential. When vibronic interaction is intensified, we have $S^n_q \to 0$, causing the orbital angular momentum to be completely frozen.

4. DISCUSSION OF THE RESULTS

We have given a detailed analysis of the pseudo Jahn–Teller effect for the electronic states of $^1A_{1g}$ and ^1E_u terms of a hole or electron CuO_4 centers in doped cuprates. We have sidestepped problems associated with the onset of pseudo JT centers, in particular, the effects of strong coupling between centers due to the presence of shared oxygen and coupling with rotational modes of the CuO_4 cluster (tilting or buckling). Pseudo JT centers are responsible for numerous manifestations of short-range and long-range JT orderings observed in cuprates; some of them have been discussed previously.[10,23]

An important problem has to do with the influence of pseudo JT centers on the kinetics of local bosons and superconductivity. On the whole, this topic warrants separate consideration, although certain vibronic reduction effects and the isotropic effect have been briefly discussed in the past.[8]

We close with an enumeration of several experimental factors which, in our opinion, lend support to the above-proposed scenario of pseudo JT centers in cuprates: 1) the occurrence of MIR bands in the absorption spectra for all cuprate high-T_c superconducting systems;[6] 2) the observation of singlet-triplet pseudodegeneracy near the ground state for hole centers according to NQR data;[24] 3) from EPR data the detection of a copper-oxygen JT center possessing a low triplet state in compounds $LaSrAl_{1-x}Cu_xO_4$ isostructural to $La_{2-x}Sr_xCuO_4$ (Refs. 25 and 26); 4) the observation of anomalously strong anharmonicity of low-temperature thermal motion of a copper ion as part of the hybrid copper-oxygen Q_{e_u} mode by the ''entropy maximum method'' (Ref. 27); 5) the observation of ferroelectric anomalies;[28] 6) the unusual character of the isotope effect with respect to copper in superconducting cuprates;[8] 7) the observation of characteristic phonon anomalies;[4,10,29,30] 8) the detection of tunneling paramagnetic centers.[7]

The tunneling paramagnetic effect is a consequence of the unusual singlet-triplet structure of a pseudo JT center with the localization of different spin states in different minima of the adiabatic potential. The spin dynamics and relaxation for tunneling paramagnetic centers exhibit an anomalously strong dependence on the magnitude and orientation of the external magnetic field. These centers can be reduced with comparative ease to a metastable state. The existence of tunneling paramagnetic centers in phase nucleations of pseudo JT centers has previously[7] been regarded as the cause of magnetization and magnetostriction anomalies in the oxide CuO. The extraordinary magnetic resonance properties of the cuprate Eu_2CuO_4 (Ref. 31) might well be of the same nature.

In this paper we do not boast an exhaustive survey of all experimental evidence of the pseudo Jahn–Teller nature of CuO_4 clusters in doped cuprates or the comparison of such data with our model; such an undertaking is a topic for separate discussion. At the same time, it should be noted that the model of pseudo JT centers is based on a vast inventory of experimental facts. The results of the present study should be viewed as a first step toward the formulation of theory of the pseudo Jahn–Teller lattice in doped cuprates.

The authors are grateful to M. V. Eremin, B. I. Kochelaev, S. Yu. Shashkin, E. E. Nikiforov, A. S. Ovchinnikov, V. Ya. Mitrofanov, and A. Ya. Fishman for profitable discussions.

[1] J. G. Bednorz and K. A. Muller, Z. Phys. B **64**, 189 (1986); K. A. Muller, Physica C **282–287**, 3 (1997).
[2] I. B. Bersuker and V. Z. Polinger, *Vibrational Interactions in Molecules and Crystals* [in Russian], Nauka, Moscow (1983), 336 pp.
[3] M. Georgiev and M. Borissov, Phys. Rev. B **39**, 11624 (1989); L. Mikhailov, M. Georgiev, A. Manov, A. Vavrek, M. Dimitrova, and M. Borissov, Physica C **235–240**, 2377 (1994).
[4] N. M. Plakida, *High-Temperature Superconductors* [in Russian], International Education Program, Moscow (1996), 288 pp.
[5] A. S. Moskvin, JETP Lett. **58**, 345 (1993).
[6] A. S. Moskvin, N. N. Loshkaeva, Yu. P. Sukhorukov, M. A. Sidorov, and A. A. Samokhvalov, Zh. Éksp. Teor. Fiz. **105**, 967 (1994) [JETP **78**, 518 (1994)].
[7] A. S. Moskvin, I. B. Krynetskiĭ, R. Shimchak, Yu. D. Panov, S. V. Naumov, and A. A. Samokhvalov, Fiz. Tverd. Tela (St. Petersburg) **39**, 474 (1997) [Phys. Solid State **39**, 412 (1997)].
[8] A. S. Moskvin and Yu. D. Panov, Zh. Éksp. Teor. Fiz. **111**, 644 (1997) [JETP **84**, 354 (1997)].
[9] A. S. Moskvin, Physica C **282–287**, 1807 (1997).
[10] A. S. Moskvin, A. S. Ovchinnikov, and O. S. Kovalev, Fiz. Tverd. Tela (St. Petersburg) **39**, 1948 (1997) [Phys. Solid State **39**, 1742 (1997)].
[11] A. S. Moskvin, Physica B (in press).
[12] A. S. Alexandrov and N. F. Mott, *Polarons and Bipolarons* (World Scientific, Singapore, 1995), 169 pp.
[13] M. J. Rice and Y. R. Yang, Phys. Rev. B **36**, 8794 (1988).
[14] J. E. Hirsch and S. Tang, Phys. Rev. B **40**, 2179 (1989).
[15] U. Opik and M. H. L. Pryce, Proc. R. Soc. London, Ser. A **238**, 425 (1957).
[16] I. B. Bersuker, Zh. Éksp. Teor. Fiz. **43**, 1315 (1962) [Sov. Phys. JETP **16**, 933 (1962)].
[17] F. S. Ham, Phys. Rev. **138**, 1727 (1965).
[18] G. F. Koster, Phys. Rev. **109**, 227 (1958).
[19] D. T. Sviridov, Yu. F. Smirnov, and V. E. Troitskiĭ, Kristallografiya **9**, 807 (1964) [Sov. Phys. Crystallogr. **9**, (1964)].
[20] M. Hamermesh, *Group Theory and Its Applications to Physical Problems* [Addison-Wesley, Reading, Mass., 1962; Mir, Moscow, 1966, 587 pp.].
[21] R. Englman, S. Caner, and S. Toaff, J. Phys. Soc. Jpn. **29**, 306 (1970).

[22] S. A. Altshuler and B. M. Kozyrev, *Electronic Paramagnetic Resonance in Compounds of Transition Elements* [Halstead, New York, 1975; Nauka, Moscow, 1972, 672 pp.].
[23] M. D. Kaplan and D. I. Khomskiĭ, JETP Lett. **47**, 730 (1988); M. A. Ivanov, V. Ya. Mitrofanov, A. Ya. Fishman, and A. A. Fotiev, Fiz. Nizk. Temp. **19**, 364 (1993) [Low Temp. Phys. **19**, 255 (1993)].
[24] Y. Yoshinari, P. C. Hammel, J. A. Martindale, E. Moshopoulou, and J. D. Thompson, Phys. Rev. Lett. **77**, 2069 (1996).
[25] T. A. Ivanova, E. F. Kukovitskiĭ, E. N. Nabiulina, V. E. Petrashen', A. E. Usachev, Yu. V. Yayulokov, and V. V. Zelentsov, JETP Lett. **57**, 63 (1993).
[26] A. S. Moskvin and Yu. D. Panov, Magn. Reson. Solids **2**, 2 (1998).
[27] M. Takata, E. Nishibori, T. Takayama, M. Sakata, K. Kodama, M. Sato, and C. J. Howard, Physica C **263**, 176 (1996)..
[28] V. Muller, C. Hucho, K. de Groot, D. Winau, D. Maurer, and K. M. Rieder, Solid State Commun. **72**, 997 (1989).
[29] I. Pintschovius and W. Reichardt, *Physical Properties of High Temperature Superconductors IV*, edited by D. M. Ginzberg (World Scientific, Singapore, 1994), 295 pp.
[30] S. Lupi, M. Capizzi, P. Calvani, B. Ruzicka, P. Maselli, P. Dore, and A. Paolone, Phys. Rev. B **57**, 12548 (1998).
[31] D. C. Vier, S. Schultz, C. Rettori, D. Rao, S. B. Oseroff, M. Tovar, Z. Fisk, and S.-W. Cheong, J. Appl. Phys. **69**, 4872 (1991).

Translated by James S. Wood

SEMICONDUCTORS AND INSULATORS

Stationary hopping photoconduction among multiply charged impurity atoms in crystals

N. A. Poklonskiĭ* and S. Yu. Lopatin

Belarus State University, 220050 Minsk, Belarus
(Submitted March 3, 1998)
Fiz. Tverd. Tela (St. Petersburg) **40**, 1805–1809 (October 1998)

A derivation of the equation for the hopping current of electrons and holes (electron vacancies) among impurities of a single species in three charge states [(−1), (0), and (+1)] is given in the continuum approximation. The screening length of an electrostatic field and the diffusion length of charge carriers are calculated. The dependence of the effective lifetime of electrons hopping among impurities relative to $(-1)\rightarrow(+1)$ transitions [and of holes relative to $(+1)\rightarrow(-1)$ transitions] on the degree of compensation and the rate of interimpurity photoexcitation, which stimulates the formation of ions, is obtained. The calculations of the dependence of the hopping photoconductivity on photoexcitation rate are consistent with known experimental data, which have not previously found a theoretical explanation. © *1998 American Institute of Physics.* [S1063-7834(98)00710-2]

1. Many phenomena in crystalline semiconductors are caused by impurity atoms of a single species in the (-1), (0), and $(+1)$ charge states. The research on crystals with such defects was summarized in Refs. 1–4. In particular, the stabilization of the position of the Fermi level in the band gap of numerous crystalline materials during exposure to ionizing radiation has been associated with the introduction of intrinsic lattice defects in the (-1), (0), and $(+1)$ charge states.[5]

Processes in semiconductors having defects in the (-1), (0), and $(+1)$ charge states are often interpreted using models in which the energy levels of these defects form two energy bands in the forbidden band of the crystal. For example, the influence of charge exchange between immobile impurities in the (-1), (0), and $(+1)$ charge states on the concentration of electrons in the c band was considered in Ref. 6. At the same time, at low temperatures, where the concentrations of electrons in the c band and of holes in the v band are negligibly small, charge transfer is governed by electron (hole) hopping between impurities.

The study of steady-state hopping photoconduction in Refs. 7 and 8, where neutral impurity atoms of a single species pass into the $(+1)$ and (-1) charge states as a result of impurity photoexcitation of the crystal, is important not just for applications.[9] Since its discovery,[10,11] hopping photoconduction has been actively studied, but a theory for this phenomenon has not been developed even at a phenomenological level, which would permit, say, estimation of the concentration and mobility of hopping electrons.[7]

The purpose of the present work is to calculate the screening length of an external electrostatic field and the diffusion length of electrons and holes (electron vacancies) by means of hops between immobile impurity atoms in the (-1), (0), and $(+1)$ charge states with consideration of interimpurity photoexcitation, which stimulates the formation of ions from neutral impurities.

2. Let us consider a crystalline semiconductor, in which impurity atoms of a single species randomly distributed in space exist in three charge states [(−1), (0), and (+1)] with a total concentration $N=N_{-1}+N_0+N_{+1}$. We assume that the exchange of electrons and electron vacancies between impurities takes place by means of thermally activated tunneling (hopping) and that no exchange takes place through the c or v band.

Electron hops between different charge states are fundamentally different. The ionization of neutral states of two defects $(0)\rightarrow(0)$, like the recombination of charge states $(-1)\rightarrow(+1)$, is accompanied by a considerably larger change in electron energy than are $(0)\rightarrow(+1)$ and $(-1)\rightarrow(0)$ hops. Therefore, we shall assume that the energy levels of the impurity atoms in the (-1), (0), and $(+1)$ charge states form two impurity bands. In the case of hydrogenic donors in covalent crystals they are called the D^- and D^0 bands, and in the case of acceptors they are called the A^+ and A^0 bands; the A^+ bands are analogs of the upper Hubbard band in unordered systems.[1]

To fix ideas we consider the transfer of charges between the D^- and D^0 bands. In addition, we assume that the impurity atoms have a positive Hubbard correlation energy, i.e., the D^- band is closer to the c band than is the D^0 band.

Interimpurity $(0)\rightarrow(0)$ electron transitions correspond to the thermal ''generation'' of carriers in the D^- band from the D^0 band, and $(-1)\rightarrow(+1)$ transitions correspond to ''recombination.'' Charge transfer is accomplished by means of $(-1)\rightarrow(0)$ hops of electrons in the D^- band and $(0)\rightarrow(+1)$ hops of electron vacancies in the D^0 band. Such a division makes sense, if the energy gap between the D^- and

D^0 impurity bands is much greater than the activation energy for charge transfer in these bands.

Let us find the expression for the density of the stationary hopping current involving the k and $k+1$ charge states of an impurity, where $k=-1,0$. We assume that electrons (holes) hop between nearby impurity atoms. Under this charge-transfer regime the mean hopping distance $R_{k,k+1}$ of an electron is determined mainly by the total impurity concentration $N=N_{-1}+N_0+N_{+1}$.

Let an electrostatic field be applied to a homogeneous crystalline sample in a thermostat so that the electric intensity within the sample $E=-d\varphi/dx$ is directed along the OX axis. We arbitrarily select two points with coordinates $x_2>x_1$ such that $(x_2-x_1)=R_{k,k+1}$. We construct two planes perpendicular to the electric field through these points so that the field would be directed from the first plane to the second.

We use $N_k(x_1)$ and $N_{k+1}(x_2)$ to denote the concentrations of the impurity in charge state k in plane 1 and in charge state $k+1$ in plane 2, respectively. Let $\Gamma_{k,k+1}(x_1,x_2)$ be the probability of the passage of an electron from plane 1 to plane 2 per unit time. Then the hopping-current density between impurities in charge states k and $k+1$ can be written in the form

$$J_{k,k+1}=qR_{k,k+1}\left[N_k(x_2)\,\frac{N_{k+1}(x_1)}{N}\Gamma_{k,k+1}(x_2,x_1)-N_k(x_1)\,\frac{N_{k+1}(x_2)}{N}\Gamma_{k,k+1}(x_1,x_2)\right], \quad (1)$$

where $-q<0$ is the charge of the electron, $N_{k+1}(x_1)/N$ is the probability that an arbitrarily selected impurity atom in plane 1 is in charge state $k+1$; for plane 2 the probability equals $N_{k+1}(x_2)/N$. In the absence of an external field $N_k(x_1)=N_k(x_2)$, and $N_{k+1}(x_1)=N_{k+1}(x_2)$; $\Gamma_{k,k+1}(x_1,x_2)=\Gamma_{k,k+1}(x_2,x_1)$ is the hopping frequency of electrons in one direction along the OX axis.

In the continuum approximation we can write

$$N_k(x_2)\approx N_k(x_1)+\frac{dN_k(x_1)}{dx}R_{k,k+1},$$

$$N_{k+1}(x_2)\approx N_{k+1}(x_1)+\frac{dN_{k+1}(x_1)}{dx}R_{k,k+1},$$

$$\Gamma_{k,k+1}(x_2,x_1)-\Gamma_{k,k+1}(x_1,x_2)\approx\frac{d\Gamma_{k,k+1}}{dx}R_{k,k+1}=-\frac{d\Gamma_{k,k+1}}{d\varphi}ER_{k,k+1}, \quad (2)$$

where $\Gamma_{k,k+1}$ depends on x through the electrostatic potential $\varphi(x)$ of the external field in the crystal.

Substituting (2) into (1) and confining ourselves to terms linear in the gradient at $x_1=x$, we obtain the hopping current density

$$J_{k,k+1}=qN_{k,k+1}\left[M_{k,k+1}E+D_{k,k+1}\frac{d}{dx}\ln\left(\frac{N_k}{N_{k+1}}\right)\right], \quad (3)$$

where $N_{k,k+1}(x)=N_k(x)N_{k+1}(x)/N$ is the effective concentration of electrons hopping between impurities in charge states k and $k+1$, $D_{k,k+1}=\Gamma_{k,k+1}R_{k,k+1}^2$ is the diffusion coefficient of the hopping electrons, and $M_{k,k+1}=-R_{k,k+1}^2\,d\Gamma_{k,k+1}/d\varphi$ is the hopping mobility.

We note that, according to (3), the hopping current has both drift and diffusion components and that the hopping conductivity $\sigma_{k,k+1}=qN_{k,k+1}M_{k,k+1}$. When $N_{-1}=N_{+1}$, the maximum concentrations of electrons hopping in the D^- band and of holes hopping in the D^0 band are $N_{-1,0}=N_{0,+1}=N/8$.

According to Refs. 12 and 13 the ratio of the mobility to the diffusion coefficient of hopping electrons $M_{k,k+1}/D_{k,k+1}=q/\xi k_BT$, where k_BT is the thermal energy and $\xi\geqslant 1$ characterizes the influence of fluctuations of the electrostatic potential in the crystal on the electron states in the impurity D^- and D^0 bands. When the width of the impurity bands is less than or of the order of the thermal energy, $\xi\approx 1$. Under the regime of electron (hole) hopping between nearby impurity atoms in charge states k and $k+1$, the mobility $M_{k,k+1}\propto\Gamma_{k,k+1}R_{k,k+1}^2$ is determined by the total impurity concentration $N=N_{-1}+N_0+N_{+1}$.

3. The continuity equations for charge states of immobile impurity atoms migrating through a crystal have the form (compare Ref. 6)

$$\frac{\partial N_{-1}}{\partial t}=-\alpha N_{-1}N_{+1}+\beta N_0^2+\frac{1}{q}\frac{\partial}{\partial x}J_{-1,0},$$

$$\frac{\partial N_0}{\partial t}=2(\alpha N_{-1}N_{+1}-\beta N_0^2)+\frac{1}{q}\frac{\partial}{\partial x}(J_{0,+1}-J_{-1,0}),$$

$$\frac{\partial N_{+1}}{\partial t}=-\alpha N_{-1}N_{+1}+\beta N_0^2-\frac{1}{q}\frac{\partial}{\partial x}J_{0,+1}, \quad (4)$$

where $N_k(x,t)$ is the nonequilibrium concentration of the impurity in charge state $k=-1,0,+1$, which depends on the coordinate x and the time t; $J_{0,+1}$ and $J_{-1,0}$ are the hopping current densities between impurities in $(0)\rightarrow(+1)$ and $(-1)\rightarrow(0)$ transitions, respectively; α is the coefficient for the ''trapping'' of an electron from a negatively charged impurity in a positively charged impurity, i.e., the $(-1)\rightarrow(+1)$ transition; β is the coefficient for the thermal ionization of neutral impurities $2N_0\rightarrow N_{+1}+N_{-1}$, i.e., the passage of an electron from the D^0 band to the D^- band.

When an external electric field is applied to a crystal, the electronic processes determined by impurities in the (-1), (0), and $(+1)$ charge states are described with consideration of (3) and (4) by the system of equations

$$\frac{dN_0}{dx}=\frac{N_0(N_{-1}-N_{+1})}{N}\frac{qE}{\xi k_{\mathrm{B}}T}-\frac{J_{-1,0}}{qD_{-1,0}}+\frac{J_{0,+1}}{qD_{0,+1}},$$

$$\frac{dN_{+1}}{dx}=\frac{N_{+1}(2N_{-1}+N_0)}{N}\frac{qE}{\xi k_{\mathrm{B}}T}-\frac{J_{-1,0}N_{+1}}{qD_{-1,0}N_0}+\frac{J_{0,+1}(N_{+1}-N)}{qD_{0,+1}N_0},$$

$$\frac{dE}{dx}=\frac{q}{\varepsilon}[N_{+1}(x)-N_{-1}(x)],$$

$$\frac{d}{dx}J_{-1,0}=q(\alpha N_{-1}N_{+1}-\beta N_0^2),$$

$$\frac{d}{dx}J_{0,+1}=q(\beta N_0^2-\alpha N_{-1}N_{+1}), \tag{5}$$

where $\varepsilon=\varepsilon_r\varepsilon_0$ is the static dielectric constant of the crystal lattice.

Since the total impurity concentration N does not depend on x, the concentration gradients of only two charge states appear in (5) (N_0 and N_{+1}were chosen as the independent variables).

We represent the nonequilibrium concentration of defects in the charge states $k=-1,0,+1$ as $N_k(x)=N_k+\delta N_k(x)$. Here and in the following, N_k is the equilibrium value of the concentration and $\delta N_k(x)$ is the deviation from N_k resulting from the effect of the external electrostatic field on the hopping electrons (holes). The equilibrium concentrations of the ionized impurities satisfy the electroneutrality equation

$$N_{-1}=N_{+1}+ZKN, \tag{6}$$

where KN is the concentration of a completely ionized impurity of another species with a charge Zq, which does not participate in charge-exchange processes. Here $Z\geqslant+1$ for donors whose energy levels are closer to the c band than is the center of the D^- band, $Z\leqslant-1$ for acceptors whose energy levels are closer to the v band than is the center of the D^0 band, and $0<|Z|K<1$.

At a low excitation level ($\delta N_0/N_0\ll1$, $\delta N_{+1}/N_{+1}\ll1$) the system of equations (5) is linearized. Taking into account that the relation $\alpha N_{-1}N_{+1}=\beta N_0^2$ follows from the principle of detailed equilibrium, we obtain the general solution of the linearized system in the form

$$\begin{pmatrix}\delta N_0\\ \delta N_{+1}\\ E\\ J_{-1,0}\\ J_{0,+1}\end{pmatrix}=C_1\begin{pmatrix}ZKN_0\\ (1+ZK)N_{+1}\\ \lambda_1\xi k_{\mathrm{B}}T/q\\ 0\\ 0\end{pmatrix}\exp(\lambda_1x)+C_2\begin{pmatrix}ZKN_0\\ (1+ZK)N_{+1}\\ -\lambda_1\xi k_{\mathrm{B}}T/q\\ 0\\ 0\end{pmatrix}\exp(-\lambda_1x)+C_3\begin{pmatrix}A_1\\ A_2\\ A_3\\ A_4\\ A_5\end{pmatrix}\exp(\lambda_3x)+C_4\begin{pmatrix}-A_1\\ -A_2\\ A_3\\ A_4\\ A_5\end{pmatrix}\times\exp(-\lambda_3x)+C_5\begin{pmatrix}0\\ 0\\ N\xi k_{\mathrm{B}}T/q^2\\ N_{-1}N_0D_{-1,0}\\ N_0N_{+1}D_{0,+1}\end{pmatrix}, \tag{7}$$

where C_1, C_2, C_3, C_4, and C_5 are determined from the boundary conditions

$$A_1=ZK\lambda_3\left(\frac{D_{0,+1}+D_{-1,0}}{qD_{0,+1}D_{-1,0}}-\frac{2qN_0}{\alpha\varepsilon\xi k_{\mathrm{B}}TN}\right),$$

$$A_2=ZK\lambda_3\left[\frac{N_{+1}D_{0,+1}+(N_{+1}-N)D_{-1,0}}{qN_0D_{0,+1}D_{-1,0}}+\frac{qN_0}{\alpha\varepsilon\xi k_{\mathrm{B}}TN}\right],$$

$$A_3=ZKN\frac{D_{0,+1}(1-ZK)-D_{-1,0}(1+ZK)}{\varepsilon N_0D_{0,+1}D_{-1,0}},$$

$$A_4=-A_5=ZK(\lambda_1^2-\lambda_3^2);$$

the nontrivial eigenvalues equal

$$\lambda_1=-\lambda_2=q\left(\frac{N_0N_{+1}+N_{-1}N_0+4N_{-1}N_{+1}}{\varepsilon\xi k_{\mathrm{B}}TN}\right)^{1/2},$$

$$\lambda_3=-\lambda_4=\left(\alpha N\frac{N_{+1}D_{0,+1}+N_{-1}D_{-1,0}}{N_0D_{0,+1}D_{-1,0}}\right)^{1/2}.$$

We note that, since the eigenvalues include real, nonzero numbers, the solutions of the original and linearized system of differential equations coincide in the vicinity of the equilibrium point.[14]

When $J_{-1,0}=J_{0,+1}=0$, we can use (7) with allowance for (6) to find the screening length L_s (the penetration depth of an electrostatic field into the semiconductor)

$$L_s=\frac{1}{\lambda_1}=\frac{1}{q}\left\{\frac{\varepsilon\xi k_{\mathrm{B}}T}{N[1-(ZK)^2]-N_0}\right\}^{1/2}, \tag{8}$$

which coincides with the expression for L_s obtained in Ref. 13 from the solution of the electrostatic Poisson equation in the Debye–Hückel approximation.

When $J_{-1,0}+J_{0,+1}\neq0$, the diffusion length of the hopping electrons from (7) is

$$L_d=\frac{1}{\lambda_3}=\left[\frac{N_0 D}{\alpha N(N-N_0)}\right]^{1/2}, \tag{9}$$

where $D=D_{0,+1}D_{-1,0}(N_{+1}+N_{-1})/(N_{+1}D_{0,+1}+N_{-1}\times D_{-1,0})$ is the bipolar diffusion coefficient[15] of the charge carriers in the D^- and D^0 bands.

The effective ''recombination'' time of the (-1) and $(+1)$ charge states (the lifetime of electrons in the D^- band relative to trapping on electron vacancies in the D^0 band[7,8]) equals

$$\tau_d=L_d^2/D=\frac{N_0}{\alpha N(N-N_0)}. \tag{10}$$

4. Uniform irradiation of a crystal throughout its volume by light that causes $(0)\rightarrow(0)$ transitions of electrons between neutral impurities alters the filling of the D^- and D^0 bands with electrons and thus plays the role of ''photogeneration.'' We assume that interimpurity illumination does not cause heating of the crystal, i.e., does not increase the thermal impurity ionization coefficient $\beta=\alpha N_{+1}N_{-1}/N_0^2$. Then, in the scheme for solving the system of equations (5) it is sufficient to replace the equilibrium values of N_{+1}, N_0, and N_{-1}, by the nonequilibrium values $N_{+1}(\gamma)$, $N_0(\gamma)$, and $N_{-1}(\gamma)$, which can be determined from the relations

$$\alpha\frac{N_{+1}N_{-1}}{N_0^2}+\gamma=\alpha\frac{N_{+1}(\gamma)N_{-1}(\gamma)}{N_0^2(\gamma)},$$

$$N_{-1}(\gamma)=N_{+1}(\gamma)+ZKN,$$

$$N_{-1}(\gamma)+N_0(\gamma)+N_{+1}(\gamma)=N, \tag{11}$$

where γ is the photoionization coefficient of the neutral impurities, which is proportional to the intensity of the stationary illumination causing transitions of electrons from the D^0 band to the D^- band.

Thus, to find the screening length $L_s(\gamma)$ and the diffusion length $L_d(\gamma)$ under the conditions of interimpurity illumination, the replacements $N_0\rightarrow N_0(\gamma)$ and $N_{+1}\rightarrow N_{+1}(\gamma)$ must be made in (8) and (9).

When $\gamma/\beta\ll 1$ (interimpurity photogeneration is small in comparison to thermal generation), it follows from (8) and (9) with consideration of (11) that $L_s(\gamma)<L_s$ and $L_d(\gamma)<L_d$. At low temperatures $N_0(\gamma)\approx N(1-|Z|K)-2\gamma N(1-|Z|K)^2/\alpha|Z|K$, and from (10) we then have

$$\tau_d(\gamma)\approx\tau_d-2\gamma(1-|Z|K)^2/\alpha^2N(|Z|K)^3,$$

i.e., the lifetime of nonequilibrium electrons in the D^- band and electron vacancies in the D^0 band decreases as their concentrations increase.

When $\gamma/\beta\gg 1$, i.e., when the rate of interimpurity photoexcitation is high, $N_0(\gamma)\rightarrow 0$, and $N_{+1}(\gamma)+N_{-1}(\gamma)\rightarrow N$, so that from (8) and (9) we have $L_s^2(\gamma)\rightarrow\varepsilon\xi k_BT/q^2\times[1-(ZK)^2]N$, and $L_d(\gamma)\rightarrow 0$. In particular, if $K\ll 1$, then $N_{+1}(\gamma)\approx N_{-1}(\gamma)$, and the character of the decrease in $L_d(\gamma)$ with increasing γ can be described as follows:

$$L_d^2(\gamma)/D=\tau_d(\gamma)\approx(1/2)N\sqrt{\alpha\gamma},$$

where in this case $D\approx 2D_{0,+1}D_{-1,0}/(D_{0,+1}+D_{-1,0})$.

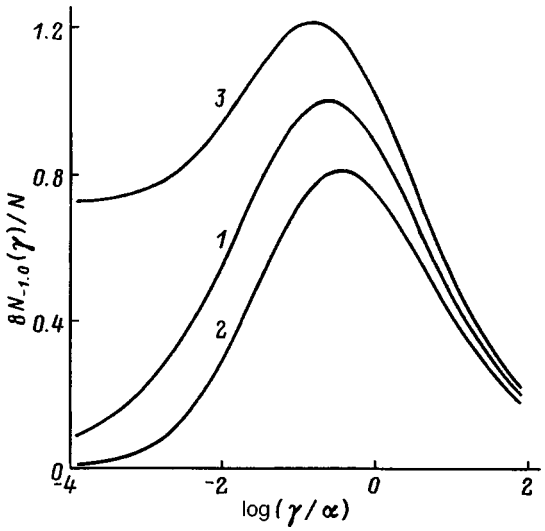

FIG. 1. Variation of the concentration $N_{-1,0}$ of electrons in the D^- band as a function of the ratio of the interimpurity photoionization coefficient γ, which is proportional to the illumination intensity, to the trapping coefficient α of electrons from the D^- band in the D^0 band. *1*—$K=0$, *2*—$K=0.1$, $Z=-1$, *3*—$K=0.1$, $Z=+1$.

5. At low temperatures $(T\rightarrow 0)$ the values of N_{-1} and/or N_{+1} are small, so that $\beta=\alpha N_{-1}N_{+1}/N_0^2\rightarrow 0$. In this case the degree of photoexcitation is determined by the relation between γ, which is proportional to the illumination intensity, and the trapping coefficient α of an electron from a negatively charged impurity in a positively charged impurity.

The mobility $M_{-1,0}$ of electrons in the D^- band significantly surpasses the mobility $M_{0,+1}$ of holes (electron vacancies) in the D^0 band.[1] At the same time, when $K\ll 1$, the concentration of photoexcited carriers (hopping electrons or holes) in both bands are approximately equal. Therefore, the change in the hopping photoconductivity $\Delta\sigma_h(\gamma)$ in response to an increase in the interimpurity illumination intensity will be considered with allowance for electron transfer only in the D^- band, i.e., under the assumption that $\Delta\sigma_h(\gamma)\approx\sigma_{-1,0}(\gamma)$.

According to Eq. (3), the hopping conductivity $\sigma_{-1,0}(\gamma)$ can be represented in the factored form $\sigma_{-1,0}(\gamma)=qM_{-1,0}N_{-1,0}(\gamma)$, where $N_{-1,0}(\gamma)=N_{-1}(\gamma)N_0(\gamma)/N$ is the concentration of electrons hopping in the D^- band. In the regime of electron hopping between nearby impurities in the (-1) and (0) charge states, the character of the dependence of the hopping conductivity $\sigma_{-1,0}(\gamma)$ on illumination intensity is determined by the variation of $N_{-1,0}(\gamma)$ (see Fig. 1). When $K=0$ (curve *1*) and the semiconductor contains defects of only one species in the (-1), (0), and $(+1)$ charge states, the maximum value of the concentration of electrons hopping in the D^- band and holes in the D^0 band equals $N/8$ [this value was chosen for normalizing $N_{-1,0}(\gamma)$]. When compensating acceptors that trap electrons from the D^- and D^0 bands are introduced into the semiconductor (curve *2*), the character of the dependence of $N_{-1,0}(\gamma)$ on illumination intensity remains unchanged, but the value of $N_{-1,0}(\gamma)$ decreases with increasing compensation (all other conditions being equal). Curve *3* corresponds to the case where the compensating impurities are completely ionized donors,

whose energy levels are closer to the c band than is the D^- band,[16] and, as a result, the D^- and D^0 bands are filled with electrons. When $\gamma=0$, in this case $N_{-1,0}=K(1-K)N$.

It can be seen from Fig. 1 that $N_{-1,0}(\gamma)$ reaches a maximum at $\gamma\approx\alpha$ and depends weakly on the rate of interimpurity photoexcitation, i.e., γ. When $\gamma/\alpha\gg1$, the dependence of the concentration of hopping electrons on illumination intensity is identical for uncompensated and compensated crystals: $N_{-1,0}(\gamma)\propto1/\sqrt{\gamma}$.

The equations presented above are equally applicable to the description of hopping photoconductivity in the A^+ band, where the hops of holes between the $(+1)$ and (0) states determine $\Delta\sigma_h(\gamma)\approx\sigma_{+1,0}(\gamma)$. For example, when $\gamma/\alpha\gg1$, from (11) we obtain $\sigma_{+1,0}(\gamma)\propto N_{+1,0}(\gamma)\propto1/\sqrt{\gamma}$ (Fig. 1). This corresponds to the results of the measurements of $\sigma_{+1,0}(\gamma)$ at $T\approx4.2$ K in Si:B crystals ($N=7.8\times10^{16}$ cm^{-3}, $K=3\times10^{-4}$, $Z=+1$; $N=9\times10^{16}$ cm^{-3}, $K=2\times10^{-3}$, $Z=+1$), where a fourfold increase in the illumination intensity caused a twofold decrease in the hopping photoconductivity of holes in the A^+ band.[7]

6. Thus, an expression for the hopping current among defects (impurity atoms) of a single species in the (-1), (0), and $(+1)$ charge states in a crystalline semiconductor with an energy gap between the D^- and D^0 bands much greater than the activation energies for charge transfer via these bands has been obtained here for the first time. Continuity equations for the (-1), (0), and $(+1)$ charge states of immobile impurity atoms migrating through a crystal have been given. The screening length an electrostatic field L_s and the diffusion length of charge carriers L_d, as well as the character of their variation upon interimpurity illumination, have been calculated. Expressions have been obtained for the bipolar diffusion coefficient and the lifetime τ_d of electrons in the D^- band relative to recombination with electron vacancies in the D^0 band. It has been shown that τ_d decreases with increasing concentration of electrons hopping in the D^- band and holes in the D^0 band (i.e., with increasing illumination intensity).

It has been shown that the concentration of electrons hopping in the D^- band is proportional to the product of the concentrations of impurities in the (-1) and (0) states and depends nonmonotonically on the rate of interimpurity photoexcitation. The hopping conductivity depends weakly on illumination in the regime of hops between nearby impurity atoms. The decrease in the hopping photoconductivity with increasing photoexcitation rate in weakly compensated Si:B, where energy levels of the boron atoms form the impurity A^+ and A^0 bands, has been interpreted in this framework.

*E-mail: Poklonski@phys.bsu.unibel.by

[1] E. M. Gershenzon, A. P. Mel'nikov, R. I. Rabinovich, and N. A. Serebryakova, Usp. Fiz. Nauk **132**(2), 353 (1980) [Sov. Phys. Usp. **23(10)**, 684 (1980)].
[2] I. A. Drabkin and B. Ya. Moĭzhes, Fiz. Tekh. Poluprovodn. **15**, 625 (1981) [Sov. Phys. Semicond. **15**, 357 (1981)].
[3] N. V. Agrinskaya and T. V. Mashovets, Fiz. Tekh. Poluprovodn. **28**, 1505 (1994) [Semiconductors **28**, 843 (1994)].
[4] V. I. Kaĭdanov, S. A. Nemov, and Yu. I. Ravich, Fiz. Tekh. Poluprovodn. **28**, 369 (1994) [Semiconductors **28**, 223 (1994)].
[5] V. N. Brudnyi, S. N. Grinyaev, and V. E. Stepanov, Physica B **212**, 429 (1995).
[6] V. L. Bonch-Bruevich, Pis'ma Zh. Éksp. Teor. Fiz. **41**(2), 58 (1985) [JETP Lett. **41**, 69 (1985)].
[7] E. M. Gershenzon, F. M. Ismagilova, L. B. Litvak-Gorskaya, and A. P. Mel'nikov, Zh. Éksp. Teor. Fiz. **100**, 1029 (1991) [Sov. Phys. JETP **73**, 568 (1991)].
[8] E. M. Gershenzon, Yu. A. Gurevich, A. P. Mel'nikov, and L. N. Shestkov, Zh. Éksp. Teor. Fiz. **100**, 1547 (1991) [Sov. Phys. JETP **73**, 856 (1991)].
[9] V. N. Aleksandrov, E. M. Gershenzon, A. P. Mel'nikov, and N. A. Serebryakova, Fiz. Tekh. Poluprovodn. **11**, 532 (1977) [Sov. Phys. Semicond. **11**, 306 (1977)].
[10] V. P. Dobrego and S. M. Ryvkin, Fiz. Tverd. Tela (Leningrad) **6**, 1203 (1964) [Sov. Phys. Solid State **6**, 928 (1964)].
[11] V. P. Dobrego, Fiz. Tekh. Poluprovodn. **3**, 1665 (1969) [Sov. Phys. Semicond. **3**, 1400 (1970)].
[12] N. A. Poklonski and V. F. Stelmakh, Phys. Status Solidi B **117**, 93 (1983).
[13] N. A. Poklonski, V. F. Stelmakh, V. D. Tkachev, and S. V. Voitikov, Phys. Status Solidi B **88**, K165 (1978).
[14] P. Hartman, *Ordinary Differential Equations*, Wiley, New York (1964); Mir, Moscow (1970).
[15] V. L. Bonch-Bruevich and S. G. Kalashnikov, *Physics of Semiconductors* [in Russian], Nauka, Moscow (1990).
[16] V. I. Kaĭdanov and Yu. I. Ravich, Usp. Fiz. Nauk **145**, 51 (1985) [Sov. Phys. Usp. **28**, 31 (1985)].

Translated by P. Shelnitz

Optical bistability, switching, and self-pulsing in direct-gap semiconductors upon the binding of two excitons in a biexciton

A. Kh. Rotaru and V. Z. Tronchu

Institute of Applied Physics, Moldovan Academy of Sciences, MD-2028 Kishinev, Moldova
(Submitted March 24, 1998)
Fiz. Tverd. Tela (St. Petersburg) **40**, 1810–1816 (October 1998)

A system of nonlinear differential equations describing the dynamic evolution of coherent excitons, photons, and biexcitons is derived in the geometry of a ring cavity. Nonlinearity is caused by the direct binding of two excitons in a biexciton as a result of their Coulomb interaction, which was first predicted by Ivanov, Keldysh, and Panashchenko. The equation of state of the theory of optical bistability is obtained for the stationary case. The stability of stationary states is studied, and the switching times between the branches of the optical bistability curve are determined. It is shown that the appearance of nonlinear periodic and chaotic self-pulsations with the creation of a system of limit cycles and strange attractors in phase space is possible in the unstable portions of the equation of state. Dynamic optical bistability is studied, and the possibility of experimentally detecting the phenomena studied is discussed. © *1998 American Institute of Physics.* [S1063-7834(98)00810-7]

The study of nonlinear optical phenomena is of great interest both theoretically and from the standpoint of current experimentation in connection with the employment of nonlinear optical devices in the formation, processing, transmission, and analysis of information, as well as in the creation of a new generation of computers with neurocomputer optical logic.

Theoretical and experimental problems concerning optical nonlinear phenomena were studied in Ref. 1. In particular, aspects of the study of semiconductor nonlinear materials and their use in creating optical bistable elements were considered, the design of the first digital optical computing circuits was analyzed, and other questions were examined. The importance of finding new media with large nonlinearities for creating optical bistable elements was noted.

There is special interest in the study of the optical bistability (OB) caused by excitons and biexcitons in condensed media owing to the giant optical nonlinearities on the long-wavelength fundamental absorption edge of a crystal, short relaxation times, and small switching energies and times between the branches of the optical bistability curve. In addition, the appearance of regular and chaotic self-pulsations is possible in the unstable portions of the OB curve in a system of excitons, photons, and biexcitons. All this opens up tremendous prospects for studying fundamentally new optical phenomena involving excitons and biexcitons for various purposes, including their practical application.

In Refs. 2–12 we devised a theory of optical bistability, optical switching, and regular and stochastic fluctuations with the formation of classical and strange attractors in a phase space of excitons, photons, and biexcitons. The possibility of noise-induced optical multistability in a system of coherent excitons and biexcitons was predicted in Refs. 13 and 14.

It should be noted that OB was investigated in Refs. 2, 3, 9, and 10 only under the conditions of a giant oscillator strength for the exciton-biexciton transition,[15–17] i.e., only the creation of a biexciton $\mathbf{p}$ as a result of the absorption of a photon $\mathbf{p}-\mathbf{q}$ by an exciton $\mathbf{q}$ was taken into account. Nevertheless, Ivanov, Keldysh, and Panashchenko[18,19] showed, for the first time, that there is another process, which is defined by the term $(1/\sqrt{V})M(\mathbf{p},\mathbf{q})b_{\mathbf{p}}^{+}a_{\mathbf{q}}a_{\mathbf{p}-\mathbf{q}}$ and which involves the direct binding of two excitons, $\mathbf{p}-\mathbf{q}$ and $\mathbf{q}$, in a biexciton $\mathbf{p}$ due to the Coulomb attraction between them. Actually, a fundamentally new mechanism for the exciton-biexciton transformation of the spectra of a semiconductor due to the binding of two excitons in a biexciton as a result of their Coulomb interaction was proposed in those papers. In particular, it was shown that just this mechanism leads to effective long-wavelength displacement of both the exciton and biexciton levels.

This paper is devoted to a study of a new cooperative phenomenon: stationary and nonstationary OB, optical autooscillations, and switching with consideration of exciton-photon coupling and the Coulomb binding of two excitons in a biexciton proposed in Refs. 18 and 19. A system of nonlinear differential equations describing the dynamic evolution of the system is derived using the Heisenberg equations of motion for excitons and biexcitons and the wave equation for the field. The equation of state of the theory of optical bistability is obtained in the stationary case. The stability of the stationary solutions is investigated. The possibility of the formation of regular and chaotic self-pulsations is predicted. A scenario is found for the transition to optical dynamic chaos and the possibility of the appearance of optical turbulence. The switching times between the branches of the OB curve and dynamic OB in the case where the external pump field is a function of time having a parabolic form are studied. The possibility of experimentally detecting the phenomena studied is discussed.

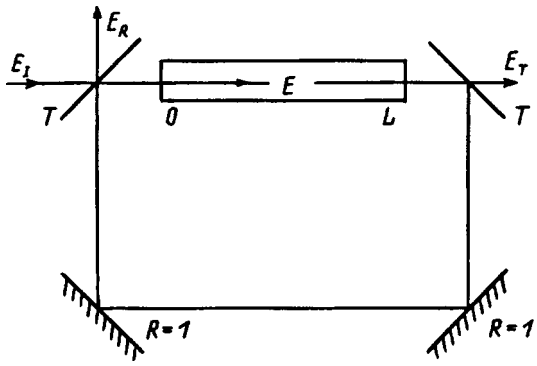

FIG. 1. Schematic representation of a ring cavity: E_I, E_R, and E_T are the amplitudes of the incident, reflected, and transmitted fields, respectively, and T is the transmission coefficient of the cavity mirrors.

1. DERIVATION OF BASIC EQUATIONS

The present stage of the study of OB is characterized by the fact that it is treated in a specific experimental geometry. Let a monochromatic coherent electromagnetic wave impinge on a ring cavity containing a semiconductor of length L. The boundary conditions for the ring cavity have the form

$$E(0,t)=\sqrt{T}E_I+RE(L,t-\Delta t)e^{iF}, \quad E_T=\sqrt{T}E(L,t),$$

where E_I is the amplitude of the incident field at the cavity entrance (the pump field), E_T is the amplitude of the transmitted field at the cavity exit, $R=1-T$ is the reflectivity of the cavity mirrors, Δt is the feedback delay time, i.e., $\Delta t=L+2l/c_0$, c_0 is the speed of light in free space, $F=kL+k_0(2l+L)$ is the phase shift of the field in the cavity, and k_0 is the wave vector of the field in free space (Fig. 1).

Bogolyubov-coherent excitons are excited in the semiconductor. According to Refs. 18 and 19, these excitons can bind in a biexciton owing to their Coulomb interaction. This process, which ensures the nonlinearity of the problem, is specified by the term $(1/\sqrt{V})Db^+aa$.

The Hamiltonian of the problem consists of a sum of the Hamiltonians of free excitons, biexcitons, and a field, as well as the Hamiltonian of the interaction of coherent excitons with an electromagnetic field and with coherent biexcitons, which, in the model adopted, has the form

$$H_{\rm int}=i\hbar g(aE^+-a^+E)+i\hbar D(ba^+a^+-b^+aa), \qquad (1)$$

where a^+ (b^+) is the exciton (biexciton) creation operator, g is the exciton-photon coupling constant, D is the constant for the direct binding of two excitons in a biexciton, and E^+ is the positive-frequency part of the electric field of the electromagnetic wave. Here and in the following we assume that the volume of the system is equal to unity, and we omit the labels of the wave vectors.

The equations of motion for the exciton (a) and biexciton (b) amplitudes have the form

$$\frac{da}{dt}=-i\omega_{\rm ex}a-gE+2Dba^+-\gamma_{\rm ex}a, \qquad (2)$$

$$\frac{db}{dt}=-i\omega_{\rm biex}b-Daa-\gamma_{\rm biex}b, \qquad (3)$$

where $\hbar\omega_{\rm ex}$ ($\hbar\omega_{\rm biex}$) is the energy of formation of an exciton (biexciton), and $\gamma_{\rm ex}$ and $\gamma_{\rm biex}$ are the exciton and biexciton damping constants, respectively, which determine the rate of escape of the quasiparticles from coherent modes into incoherent modes. The latter were introduced into the equation of motion phenomenologically. We note that these equations can be obtained rigorously within the quantum theory of fluctuations and damping from the flux part of the corresponding Fokker–Planck equation.[20]

The equation of motion for the component E of the electromagnetic field is equivalent to the wave equation

$$c_1^2\frac{\partial^2E}{\partial z^2}-\frac{\partial^2E}{\partial t^2}=-i4\pi\hbar g\,\frac{\partial^2a}{\partial t^2}, \qquad (4)$$

where c_1 is the propagation velocity of the field in the semiconductor.

We represent the amplitudes of the excitons, biexcitons, and field in the form of modulated plane waves:

$$a(z,t)=A'(z,t)e^{i(kz-\omega t)}, \quad b(z,t)=B'(z,t)e^{2i(kz-\omega t)},$$

$$E(z,t)=E'(z,t)e^{i(kz-\omega t)}, \qquad (5)$$

where ω and k are the carrier frequency and wave vector, and $A'(z,t)$, $B'(z,t)$, and $E'(z,t)$ are slowly varying amplitudes.

For the further treatment it is convenient to go over to dimensionless quantities. We introduce

$$X=\frac{E'}{E_s}, \quad B=\frac{B'}{B_s}, \quad A=\frac{A'}{A_s},$$

$$E_s=\frac{\gamma_{\rm biex}^2}{gD}, \quad A_s=B_s=\frac{\gamma_{\rm biex}}{D},$$

$$C=\frac{\alpha L}{4T}, \quad \alpha=\frac{4\pi\hbar g^2\omega^2}{c_1k\gamma_{\rm ex}}, \quad d=\frac{\gamma_{\rm ex}}{\gamma_{\rm biex}},$$

$$\delta_0=\frac{2\omega_{\rm ex}-\omega_{\rm biex}}{\gamma_{\rm biex}}, \quad \delta_1=\frac{\omega-\omega_{\rm ex}}{\gamma_{\rm biex}},$$

$$\sigma=\frac{C_1^2kT}{L\gamma_{\rm biex}\omega}, \quad \tau=\gamma_{\rm biex}t,$$

$$\Delta_1=\frac{\omega^2-c_1^2k^2}{2\omega\gamma_{\rm biex}}.$$

Introducing the dimensionless amplitudes of the incident and transmitted fields $E_I=YE_s\sqrt{T}$ and $E_T=XE_s\sqrt{T}$, for the normalized amplitudes we obtain the following boundary conditions:

$$TY+R[X_1(L,\tau-\Delta\tau)\cos F-X_2(L,\tau-\Delta\tau)\sin F]=X_1(0,\tau),$$

$$R[X_1(L,\tau-\Delta\tau)\sin F+X_2(L,\tau-\Delta\tau)\cos F]=X_2(0,\tau), \qquad (6)$$

where X_1 and X_2 are the real and imaginary parts of the field.

Substituting (5) into (2)–(4) in the slowly-varying envelope approximation[7,22] and neglecting the effects of the spatial dispersion of the excitons and biexcitons, which are insignificant in the relevant region of the spectrum, as well as

using the mean-field approximation[8,21,22] and the boundary conditions (6), we obtain a system of nonlinear differential equations, which describes the temporal evolution of coherent photons, excitons, and biexcitons:

$$\frac{dX_1}{d\tau}=-\Delta_1 X_2-\frac{\sigma(1-R\cos F)}{T}X_1 - \frac{\sigma R\sin F}{T}X_2+2C\sigma A_1+\sigma Y, \tag{7}$$

$$\frac{dX_2}{d\tau}=\Delta_1 X_1-\frac{\sigma(1-R\cos F)}{T}X_2 + \frac{\sigma R\sin F}{T}X_1+2C\sigma A_2, \tag{8}$$

$$\frac{dA_1}{d\tau}=-dA_1-\delta_1 A_2-X_1+2(B_1A_1+B_2A_2), \tag{9}$$

$$\frac{dA_2}{d\tau}=-dA_2+\delta_1 A_1+X_2+2(B_2A_1-B_1A_2), \tag{10}$$

$$\frac{dB_1}{d\tau}=-(2\delta_1+\delta_0)B_2-B_1-A_1^2+A_2^2, \tag{11}$$

$$\frac{dB_2}{d\tau}=(2\delta_1+\delta_0)B_1-B_2-2A_1A_2, \tag{12}$$

where the complex nature of X, A, and B has been taken into account: $X_1=\mathrm{Re}\,X$, $X_2=\mathrm{Im}\,X$, $A_1=\mathrm{Re}\,A$, $A_2=\mathrm{Im}\,A$, $B_1=\mathrm{Re}\,B$, and $B_2=\mathrm{Im}\,B$.

The evolution of the solutions of Eqs. (7)–(12) depends largely on the evolution of a small region of the phase space of this system. Treating the motion of points in phase space as the motion of a fluid with the divergence

$$\frac{\partial\dot X_1}{\partial X_1}+\frac{\partial\dot X_2}{\partial X_2}+\frac{\partial\dot A_1}{\partial A_1}+\frac{\partial\dot A_2}{\partial A_2}+\frac{\partial\dot B_1}{\partial B_1}+\frac{\partial\dot B_2}{\partial B_2} =-2\left[1+d+\frac{\sigma(1-R\cos F)}{T}\right],$$

we arrive at the conclusion that any small volume of the phase space of the system of equations (7)–(12) tends to zero as $\tau\to\infty$ at the rate $[2+2d+2\sigma(1-R\cos F)/T]^{-1}$. If the stationary states of the system are unstable, any limit cycle, torus, or strange attractor can be attractors in the phase space. They correspond to nonlinear periodic, quasiperiodic, and stochastic auto-oscillations in the system.

In the stationary case, from (7)–(12) we obtain equations which relate the densities of coherent excitons and biexcitons to the field amplitude,

$$Z_e\left[\left(d+\frac{2Z_e}{1+\delta_2^2}\right)^2+\left(\frac{2\delta_2 Z_e}{1+\delta_2^2}-\delta_1\right)^2\right]=X_{\mathrm{st}}^2, \tag{13}$$

$$Z_b=\frac{Z_e^2}{1+\delta_2^2}, \tag{14}$$

and the equation of state of the theory of optical bistability, which relates the amplitudes of the fields at the entrance and exit of the cavity,

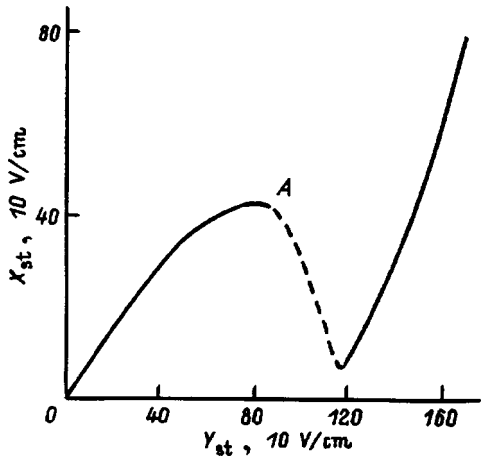

FIG. 2. Stationary dependence of the amplitude of the transmitted field X_{st} on the amplitude of the incident field Y_{st} for $\delta_0=5$, $C=5$, $F=2\pi n$, $\Delta_1=0$, and $\delta_1=10$.

$$Y_{\mathrm{st}}^2=X_{\mathrm{st}}^2\left\{\left[\frac{1-R\cos F}{T}+\frac{2CQ_1}{Q}\right]^2 +\left[\frac{\Delta_1}{\sigma}+\frac{R}{T}\sin F-\frac{2CQ_2}{Q}\right]^2\right\}, \tag{15}$$

where $Z_e=A_1^2+A_2^2$ is the exciton density, $Z_b=B_1^2+B_2^2$ is the biexciton density, $X_{\mathrm{st}}=\sqrt{X_1^2+X_2^2}$, $\delta_2=2\delta_1+\delta_0$, $Q_1=d+2Z_e/1+\delta_2^2$, $Q_2=\delta_1-2\delta_2 Z_e/1+\delta_2$, and $Q=Q_1^2+Q_2^2$.

Expression (15) is the equation of state of the theory of optical bistability in a system of coherent excitons and biexcitons in the case of the binding of two excitons in a biexciton as a result of their Coulomb interaction. It is an analog of the equations of state in the theory of two-level media and the excitonic region of the spectrum[3,8,21] and differs significantly from the latter. Unlike Eqs. (13) and (14), which define the nonlinear relationship between the densities of the coherent excitons and biexcitons and the electromagnetic field and lead to density–light bistabilities, Eq. (15) describes the dependence of the radiation emerging from the crystal on the incident radiation. Under certain conditions it leads to the appearance of light–light bistability.

2. OPTICAL BISTABILITY AND SELF-PULSING

There is great interest in the investigation of the stability of stationary states in connection with the possibility of the appearance of optical nonlinear self-pulsations in a system of coherent quasiparticles. It was shown using the Routh–Hurwitz criterion that part of the plot of the stationary dependence of the amplitude of the radiation emerging from the cavity X_{st} on the amplitude of the incident radiation Y_{st} for $\delta_0=5$, $C=5$, $F=2\pi n$, $\Delta_1=0$, and $\delta_1=10$ is unstable (Fig. 2). The instability window appearing is denoted by the dashed line. At point A, which corresponds to the beginning of the region of instability, nonlinear periodic self-pulsations appear in the system of coherent quasiparticles, and the phase trajectory follows the limit cycle (Fig. 3a). As the image point moves toward the center of the instability window, the oscillations become more complicated. A period-

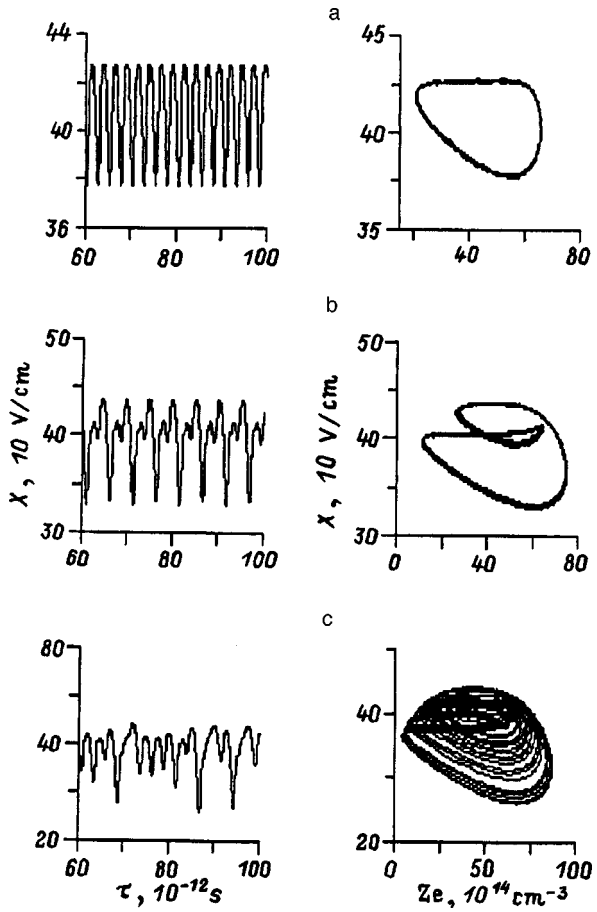

FIG. 3. Oscillations in a ring cavity (on the left) and their phase portraits in the $X-Z_e$ plane (on the right) for $\delta=5$, $C=5$, $F=2\pi n$, $\Delta_1=0$, $\delta_1=10$, $\sigma=1$, $d=0.1$, $T=0.01$, and various values of the external pump field Y: a—85, b—90, c—100.

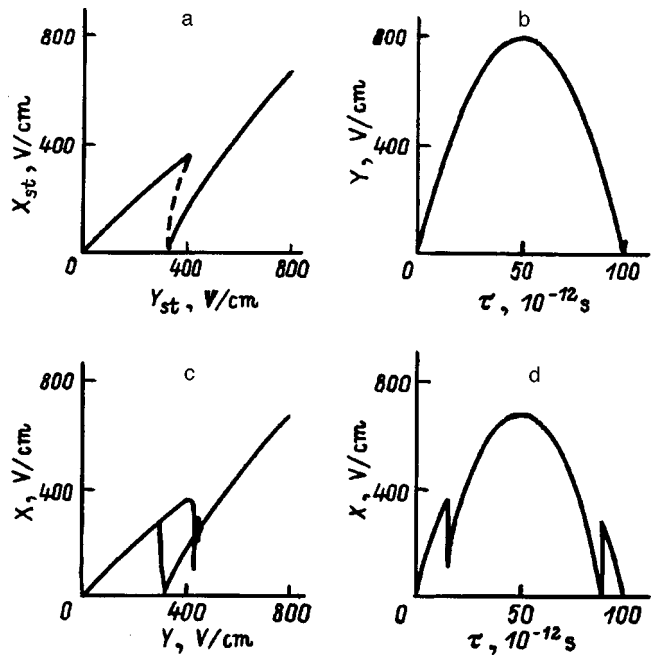

FIG. 4. a) Stationary dependence of the amplitude of the transmitted field $X_{\rm st}$ on the amplitude of the incident field $Y_{\rm st}$ for $\delta_0=5$, $C=5$, $F=2\pi n$, $\Delta_1=0$, $\delta_1=30$, $\sigma=1$, $d=0.1$, and $T=0.01$; b) form of the incident pulse; c) dynamic optical bistability; d) form of the pulse at the exit from the cavity.

doubling bifurcation sequence is observed (Fig. 3b), and, as a result, a stochastic auto-oscillatory regime is established in the central part of the instability window. Optical turbulence appears in the system of coherent excitons, photons, and biexcitons. Figure 3c shows a stochastic self-modulation process and the corresponding projections of the phase trajectories onto the $X-Z_e$ plane in the presence of an external pump field $Y=100$ ($E_I=1000$ V/cm). The surface in phase space toward which the phase trajectories converge varies with the external pump field. As the external pump field is increased further, the strange attractor becomes unstable and transforms into a stable limit cycle, and nonlinear regular periodic self-pulsations are established in the system.

As the resonance mismatch between the frequency of the external electromagnetic field and the exciton frequency δ_1 increases, the stationary dependence of the amplitude of the radiation emerging from the cavity $X_{\rm st}$ on the amplitude of the incident radiation $Y_{\rm st}$ changes significantly. At small values of $Y_{\rm st}$ there is a linear single-valued relationship between $X_{\rm st}$ and $Y_{\rm st}$. As $Y_{\rm st}$ is increased, this relationship becomes nonlinear, and at a certain relation between the parameters it becomes multivalued. Figure 4a presents the stationary dependence of the amplitude of the radiation transmitted through the cavity on the amplitude of the incident field for cos $F=1$, $C=5$, $\Delta_1=0$, $\delta_1=30$, $\delta_0=5$, and $\sigma=10$. As can be seen, clockwise OB appears for these values of the parameters. The dashed line denotes the unstable part of the $X_{\rm st}(Y_{\rm st})$ curve. Thus, unlike the model of two-level atoms, where counterclockwise OB is realized, clockwise OB occurs in the present case. The investigation shows that both the upper and lower branches of the OB curve are stable with these values of the parameters. Therefore, it would be interesting to study the switching time between them. The basis for investigating the switching time is the system of equations (7)–(12). We performed a computer experiment, in which the initial conditions were selected so that they would correspond to a value of the pump field $Y_{\rm st}$ near the downward switching threshold. At the time $\tau=0$ an abrupt change is imparted to the pump field $Y_{\rm st}$ so that $Y_{\rm st}+\Delta Y$ drops on the other side of the corresponding switching threshold. The optical switching times in a system of coherent excitons and biexcitons lie in the picosecond range ($\tau_\uparrow\sim 2\times 10^{-12}$ s, $\tau_\downarrow \sim 4\times 10^{-12}$ s), making it possible to use the mechanism of optical bistability studied here in designing high-speed optical memory cells.

As the Q factor of the cavity decreases, switchings are accompanied by oscillations, which lead to deterioration of the operation of a bistable element.

Experimental investigations of OB often reveal dynamic, rather than stationary, OB, which is obtained as a result of a comparison of the time-dependent external pump field with the system response corresponding to it. Optical bistability of this kind was first considered in Ref. 23. The behavior of a nonlinear Fabry–Pérot interferometer filled with a Kerr medium under the action of pulses of different shape was examined theoretically and experimentally. Excellent agreement between theory and experiment was obtained.

We solved the system of nonlinear differential equations (7)–(12) numerically with consideration of the boundary conditions for a ring cavity, where the external pump field $Y(\tau)$ is a function of time having a parabolic form. The results of the computer experiment are presented in Figs. 4b–4d for $F=2\pi n$, $C=5$, $\Delta_1=0$, $\delta_1=30$, $\delta_0=5$, $\sigma=1$, $d=0.1$, and $T=0.01$. Figures 4b and 4d show the forms of the electromagnetic fields impinging on the cavity and emerging from it, respectively, as functions of time in the case where the pulse duration $\tau=100$ ($t=100\times10^{-12}$ s). It is seen from Fig. 4d that the pulse transmitted through the cavity is deformed. Figure 4c shows the dependence of the amplitude of the radiation emerging from the cavity on the amplitude of the incident radiation. As we see, in this case dynamic clockwise optical bistability appears in the system of coherent excitons, photons, and biexcitons. If the pulse duration is diminished, the system does not manage to respond to its passage, and the latter takes place without any changes.

As a final step, let us discuss the possibility of the experimental observation of the effects predicted. We present numerical estimates for CdS crystals, where $\hbar D=10^{-9}$ eV·cm$^{3/2}$, $\hbar g=0.1$ eV/(cm$^{1/2}$·V), $\hbar\omega=2$ eV, $\hbar c_0 k_0\approx 2$ eV, $\hbar\gamma_{ex}=1.38\times10^{-10}$ s, $\hbar\gamma_{biex}=1.38\times10^{-11}$ s,[24] $T=0.01$, $L=10^{-6}$ m, and $\hbar(2\omega-\omega_{biex})=-0.04$ eV. The critical intensity at which the nonlinear phenomena that we studied can be observed is $I\sim1.5\times10^6$ W/cm^2. The exciton and biexciton concentrations are of the order of 10^{16} and 10^{14} cm^{-3}, respectively; the upward switching time $\tau_\uparrow\sim2\times10^{-12}$ s, the downward switching time $\tau_\downarrow\sim4\times10^{-12}$ s, and the switching energies are of the order of 50×10^{-12} J. Our results can be qualitatively compared to the results of the experimental studies in Refs. 1, 25, and 26, where clockwise OB was observed in a CdS crystal and the switching times and switching energies were determined. Thus, the numerical estimates that we have presented allow us to conclude that there is a real possibility for observing optical hysteresis, switching, and self-pulsing in systems of coherent excitons and biexcitons in semiconductors when two excitons bind in a biexciton. We note that the chaotic autooscillations studied here, which appear as a result of the instability of the stationary states, provide another example of the appearance of temporal structures in nonlinear dynamic systems. Nevertheless, the original equations are nonlinear equations in partial derivatives, which describe the spatiotemporal evolution of coherent quasiparticles in condensed media. As has been reported,[27] the development of spatial turbulence is possible for equations of this type. A new class of order-chaos transitions in the form of moving transition fronts was discovered in Ref. 27. Similar phenomena can also occur in a system of coherent excitons, photons, and biexcitons. Along with dynamic optical turbulence, the development of turbulence in space and the appearance of order-chaos and chaos-order structures are possible.

[1] H. M. Gibbs, G. Khitrova, and N. Peghambarian, *Nonlinear Photonics (Springer Series in Electronics and Photonics, Vol. 30)*, Springer-Verlag, Berlin (1990), 210 pp.
[2] A. Kh. Rotaru and V. A. Zalozh, *Optical Self-Organization of Excitons and Biexcitons in Semiconductors* [in Russian], Shtiintsa, Kishinev (1990).
[3] P. I. Khadzhi, G. D. Shibarshina, and A. Kh. Rotaru, *Optical Bistability in Systems of Coherent Excitons and Biexcitons in Semiconductors* [in Russian], Shtiintsa, Kishinev (1988).
[4] A. H. Rotaru and G. D. Shibarshina, Phys. Lett. **109**, 292 (1985).
[5] A. Kh. Rotaru, Fiz. Tverd. Tela (Leningrad) **29**, 3282 (1987) [Sov. Phys. Solid State **29**, 1883 (1987)].
[6] A. I. Bobrysheva, V. A. Zalozh, and A. Kh. Rotaru, Fiz. Tverd. Tela (Leningrad) **33**, 915 (1991) [Sov. Phys. Solid State **33**, 518 (1991)].
[7] V. A. Zalozh, S. A. Moskalenko, and A. Kh. Rotaru, Zh. Éksp. Teor. Fiz. **95**, 601 (1989) [Sov. Phys. JETP **68**, 338 (1989)].
[8] B. Sh. Parkanskiĭ and A. Kh. Rotaru, Zh. Éksp. Teor. Fiz. **99**, 899 (1991) [Sov. Phys. JETP **72**, 499 (1991)].
[9] V. A. Zalozh, A. N. Rotaru, and V. Z. Tronchu, Zh. Éksp. Teor. Fiz. **103**, 994 (1993) [JETP **76**, 487 (1993)].
[10] V. A. Zalozh, A. N. Rotaru, and V. Z. Tronchu, Zh. Éksp. Teor. Fiz. **105**, 260 (1994) [JETP **78**, 138 (1994)].
[11] A. N. Rotaru and S. V. Shura, Zh. Éksp. Teor. Fiz. **107**, 450 (1995) [JETP **80**, 240 (1995)].
[12] V. R. Mis'ko, S. A. Moskalenko, A. Kh. Rotaru, and Yu. M. Shvera, Zh. Éksp. Teor. Fiz. **99**, 1215 (1991) [Sov. Phys. JETP **72**, 676 (1991)].
[13] A. E. Barbéroshie, I. I. Gontsya, Yu. N. Nika, and A. Kh. Rotaru, Zh. Éksp. Teor. Fiz. **104**, 2655 (1993) [JETP **77**, 211 (1993)].
[14] A. Kh. Rotaru and K. V. Shura, Fiz. Tverd. Tela (Leningrad) **33**, 1973 (1991) [Sov. Phys. Solid State **33**, 1111 (1991)].
[15] A. A. Gogolin and É. I. Rashba, JETP Lett. **17**, 478 (1973).
[16] É. I. Rashba, Fiz. Tekh. Poluprovodn. **8**, 1241 (1974) [Sov. Phys. Semicond. **8**, 807 (1975)].
[17] E. Hanamura, Solid State Commun. **12**, 951 (1973).
[18] A. L. Ivanov and V. V. Panashchenko, JETP Lett. **49**, 39 (1989).
[19] A. L. Ivanov, L. V. Keldysh, and V. V. Panashchenko, Zh. Éksp. Teor. Fiz. **99**, 641 (1991) [Sov. Phys. JETP **72**, 359 (1991)].
[20] S. A. Moskalenko, A. Kh. Rotaru, and Yu. M. Shvera, Theor. Math. Phys. **75**, 295 (1988).
[21] R. Bonifacio and L. Lugiato, Lett. Nuovo Cimento **21**, 510 (1978).
[22] H. M. Gibbs, *Optical Bistability: Controlling Light with Light* [Academic Press, Orlando, 1985; Mir, Moscow, 1988].
[23] T. Bischoferger and Y. Shen, Phys. Rev. A **19**, 1169 (1979).
[24] C. C. Sung, C. M. Bowden, J. M. Haus, and W. K. Chi, Phys. Rev. **30**, 1873 (1984).
[25] M. Dagenais and H. Winful, in *Optical Bistability 2*, C. M. Bowden, H. M. Gibbs, and S. L. McCall (Eds.), Plenum Press, New York (1984), p. 267.
[26] M. Dagenais and H. Winful, Appl. Phys. Lett. **44**, 574 (1984).
[27] I. S. Aranson, A. V. Gapanov-Grekov, M. I. Rabinovich, and N. M. Starobinets, Zh. Éksp. Teor. Fiz. **90**, 1707 (1986) [Sov. Phys. JETP **63**, 1000 (1986)].

Translated by P. Shelnitz

Electrical properties of plastically deformed silicon crystals

M. A. Aliev, Kh. O. Alieva, and V. V. Seleznev

Institute of Physics, Dagestan Scientific Center, Russian Academy of Sciences, 367003 Makhachkala, Russia
(Submitted April 6, 1998)
Fiz. Tverd. Tela (St. Petersburg) **40**, 1816–1817 (October 1998)

The influence of the nature of the interaction of deformation and impurity defects on the scattering of majority carriers is investigated in silicon single crystals. © *1998 American Institute of Physics.* [S1063-7834(98)00910-1]

Our preceding study[1] disclosed features of the behavior of a silicon crystal during electroplastic deformation (the EPD regime) with the simultaneous diffusion of indium impurity atoms. The occurrence of both processes resulted in the discovery of plasticization and the accelerated migration of impurity atoms. It is natural to theorize that the effects discovered are governed by the nature of the structural evolution of deformation defects in the crystals and that these defects should influence all of their structure-sensitive properties, including their electrical properties.

Although various investigators[2,3] have studied the electrical properties of crystals containing dislocations introduced by thermoplastic deformation (the TPD regime), i.e., by heating the sample from an external source, the question of the responsibility of specific defects remains unresolved.[4,5] Therefore, the present work to study the influence of the evolutionary processes in the defect structure of a crystal, on its electrical properties, which has undergone treatment by the technological process described above, are of unquestionable interest.

In the present work we investigated samples of single-crystal p-type silicon, which were initially doped with gallium to a hole concentration of 10^{16} cm^{-3} at room temperature. Samples in the form of parallelepipeds measuring $12\times10\times5$ mm, whose edges coincided with the [112], [111], and [110] crystallographic directions, respectively, were stacked in pairs and clamped between the grips of a deformation machine after thermal sputtering of the impurity onto the broad faces. The constant current passing through the sample served simultaneously to heat the sample and to create a constant electric field. The samples were compressed in the [110] direction under conditions allowing the simultaneous occurrence of diffusion and deformation processes in a regime of stationary creep under a shear stress of 12 MPa at a temperature of 973 K and a residual pressure of 13×10^{-4} Pa for 30 min. At the conclusion of the testing, the anode and cathode parts of the samples were separated mechanically. To measure the electrical characteristics, $9\times3\times1$-mm strips were cut from them. The measurements of the Hall coefficient and the conductivity were performed by the compensation method under dc conditions in a 7620-G magnetic field in the temperature range 77–300 K within a metal cryostat with automatic regulation and maintenance of the temperature to within ±1 K.

Figure 1 (curves *1–5*) shows the experimental results of the temperature dependence of the hole mobility in the temperature range 77–300 K in log-log coordinates. As can be seen from the figure, the magnitude and temperature dependence of the mobility of all the deformed samples differ from another, and this difference appears at temperatures below 200 K. The strongest scattering is observed in a sample which has undergone treatment in the TPD regime, and the weakest scattering is observed in a sample which has undergone treatment in the EPD regime, but was cut from its anode part (curves *5* and *2*). It should be noted that the samples from the EPD and TPD series were deformed to the same degree ($\sim1\%$). However, according to the data from electron-microscopic investigations, the dislocation density is almost two orders of magnitude smaller in the samples which underwent treatment in the EPD regime than in the samples from the TPD regime. Among the samples from the EPD regime (curves *2–4*), the largest scattering is observed

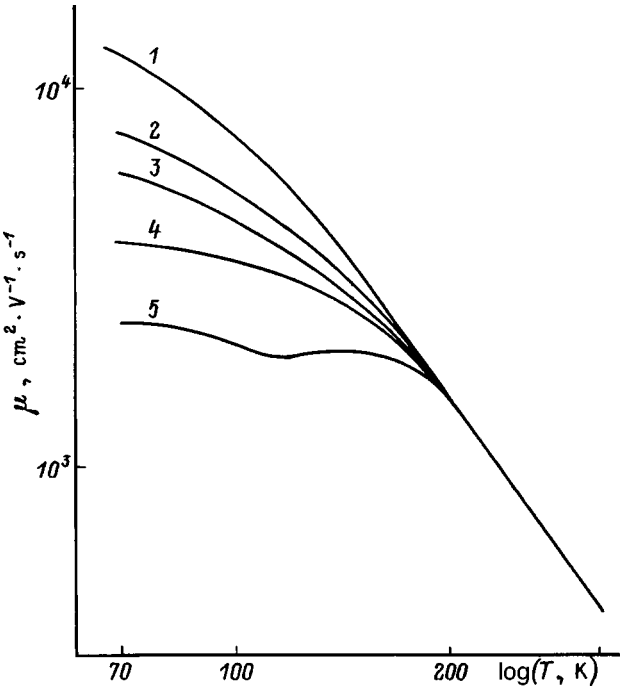

FIG. 1. Temperature dependence of the Hall conductivity of holes in the control sample (*1*), in samples of p-type silicon crystals deformed in the EPD (*2–4*) and TPD (*5*) regimes: *2*—anode part, *3*—cathode part, *4*—diffusionless part of the crystal. The degree of strain is 1.2%.

in the sample cut from the part of the crystal where impurity diffusion was not observed (curve *4*).

We attribute the picture of the temperature dependence of the mobility, and the differences observed in the figure for different samples, to details of the formation and behavior of deformation defects in the structure of the crystals investigated. For example, the largest scattering in the sample from the TPD regime is explained by the higher dislocation density and the greater misorientation of the dislocation tubes in comparison to the other samples deformed in the electroplastic regime. As for the difference between the mobility values for the samples from the anode and cathode parts of a crystal which underwent treatment in the EPD regime, with the simultaneous electrical migration of indium impurity atoms, it is caused by the interaction of the diffusing impurity with mobile dislocations. Since the most scattering is observed in the sample into which the diffusing impurity did not manage to penetrate, we have direct evidence of the compensating role of the indium impurity in these processes. It is also known that impurities have a tendency to settle at dislocations as a consequence of both elastic and electrostatic attraction and,[6] once present in a dislocation core, they can alter significantly the spectrum of states bound to them. Such mutual influences and interconversions of deformation defects result in charge exchange and neutralization, and significant compensation of the combined (dislocation and impurity) electrostatic interaction with the carriers is consequently possible. Thus, we presume that the indium ions are not only prevented from being effective scatterers to a considerable extent, but also markedly weaken the scattering properties of the dislocations. The replacement of a silicon atom at the edge of the axial plane by an impurity atom can be offered as a model for the compensating role of such an atom. In this case, the indium ions are neutralized and, since there is no possibility for the creation of a fourth covalent bond, the dislocation simultaneously loses the unpaired valence bond of the silicon atom which previously participated in the formation of the charge.

Since there is less scattering in the anode part of the sample than in the cathode part, such an interpretation agrees well with the previously observed preferential transfer of indium impurity ions toward the anode.

[1] M. A. Aliev, Kh. O. Alieva, and V. V. Seleznev, Fiz. Tverd. Tela (St. Petersburg) **38**, 3372 (1996) [Phys. Solid State **38**, 1839 (1996)].
[2] T. Alezander and H. Teichler, Mater. Sci. Technol. **4**, 249 (1991).
[3] V. G. Eremenko, V. I. Nikitenko, E. B. Yakimov, and N. A. Yarykin, Fiz. Tekh. Poluprovodn. **12**, 273 (1978) [Sov. Phys. Semicond. **12**, 157 (1978)].
[4] V. I. Sokolov, Fiz. Tekh. Poluprovodn. **29**, 842 (1995) [Semiconductors **29**, 436 (1995)].
[5] T. Suzuki, S. Takeuchi, and H. Yoshinaga, *Dislocation Dynamics and Plasticity* [Springer-Verlag, Berlin–New York, 1991; Moscow, 1989, 294 pp.].
[6] I. A. Ryzhkin, Fiz. Tverd. Tela **20**, 3612 (1978) [Sov. Phys. Solid State **20**, 2087 (1978)].

Translated by P. Shelnitz

Electron paramagnetic resonance of defects with metastable properties in crystalline GaN

P. G. Baranov, I. V. Il'in, E. N. Mokhov, and V. A. Khramtsov

A. F. Ioffe Physicotechnical Institute, Russian Academy of Sciences, 194021 St. Petersburg, Russia
(Submitted April 8, 1998)
Fiz. Tverd. Tela (St. Petersburg) **40**, 1818–1823 (October 1998)

An EPR study of GaN revealed the presence of defects exhibiting metastable properties. EPR spectra of two centers ($ii1a$ and $ii1b$) with axial symmetry along the hexagonal axis of the crystal, which have strongly anisotropic g factors, were observed. The anisotropy of the spectra decreases, and the line shape changes, with increasing temperature. The spectra of the $ii1a$ and $ii1b$ centers disappear at 25 and 50 K, respectively. Subsequent cooling of the samples does not restore the EPR signals, which implies that one observes here phenomena inherent in defects with metastable states. To restore EPR signals, one has to warm the samples to room temperature under very specific conditions. The possible microstructure of the discovered defects is discussed. © *1998 American Institute of Physics.* [S1063-7834(98)01010-7]

GaN is one of the most promising semiconductor materials for developing high-efficiency optoelectronic devices, in particular, blue- and violet-emitting diodes, as well as short-wavelength lasers intended for use in optical-storage systems.[1] This has become possible, however, only quite recently, after one succeeded in obtaining GaN-based low-resistance p-type layers and high-quality n-p transitions.[2]

GaN layers are usually grown on sapphire substrates, despite the large (15%) lattice mismatch between GaN and sapphire. Silicon carbide substrates appear preferable for this purpose, because in this case the lattice mismatch is only 3.5%.

A sublimation sandwich technique[3,4] has been developed for growing GaN layers,[3,4] and one of its modifications is used successfully[5] to prepare single-crystal SiC. The specific features of the mechanism of SiC and GaN film growth on polar {0001} faces are discussed in Ref. 6. Later, the optical properties of these layers were studied, and their high crystal perfection demonstrated.[7] At the same time the large defect concentration in available crystals is a major problem on the way to producing GaN-based devices, e.g. lasers, capable of stable operation. The most effective method of studying the microstructure of intrinsic and extrinsic defects in semiconducting materials is EPR. The elements making up the III–V compounds typically have high concentrations of isotopes with large nuclear spins. On the one hand, this interferes with obtaining EPR spectra because of the strong line broadening caused by hyperfine interactions of unpaired spins with the crystal nuclei and, as a consequence, degrades the sensitivity of measurements. On the other, observation of hyperfine interactions provides a wealth of information about defect structure.

Information available presently from EPR studies of defects in GaN crystals is scarce. The interest here is focused primarily on donors in GaN,[8] but there is no reliable information on the microstructure of donor centers, because one has observed to date only one line with a practically isotropic g factor, which was found to be slightly smaller than that of the free electron. More specific data were obtained in EPR investigation of a number of transition elements in GaN from EPR spectra of Fe^{3+},[9,10] Mn^{2+},[10–12] and Ni^{3+} (Refs. 11 and 12).

This work reports a study of a new type of defects in GaN crystals, which exhibit properties of metastable defects in semiconductors. If a defect in a solid has two (or more) different atomic configurations separated by an energy barrier, the higher-energy configuration is metastable. The electronic and optical properties of such defects are different for each configuration, and this may result in technological problems with the starting semiconductor materials, because any application presupposes reproducibility of these properties. It is believed at present that metastability is a common phenomenon in semiconductors,[13] but until recently it was not observed in such wide-gap materials as GaN and SiC. Nevertheless it is in wide-gap semiconductors that manifestations of metastability may give rise to nonreproducibility of reproducibility of characteristics even at high enough temperatures and, in this way, affect the performance of devices based on these materials.

1. EXPERIMENTAL METHODS AND CRYSTAL PREPARATION

Thick epitaxial GaN layers were prepared on a SiC substrate by the sublimation sandwich technique at different temperatures (1100–1250 °C), with elemental gallium or polycrystalline GaN used as sources. GaN layers were grown in an rf-heated horizontal quartz reactor.[4] The substrates were SiC single crystals of the 6H polytype grown by the Lely method, with basal (0001)C and (0001)Si planes. The Ga vapor was produced from elemental gallium or preliminarily synthesized GaN powder. GaN was deposited at 1000–1300 °C. The process lasted from five min to 1 h, and the GaN layer thickness varied from 20 to 500 μm.

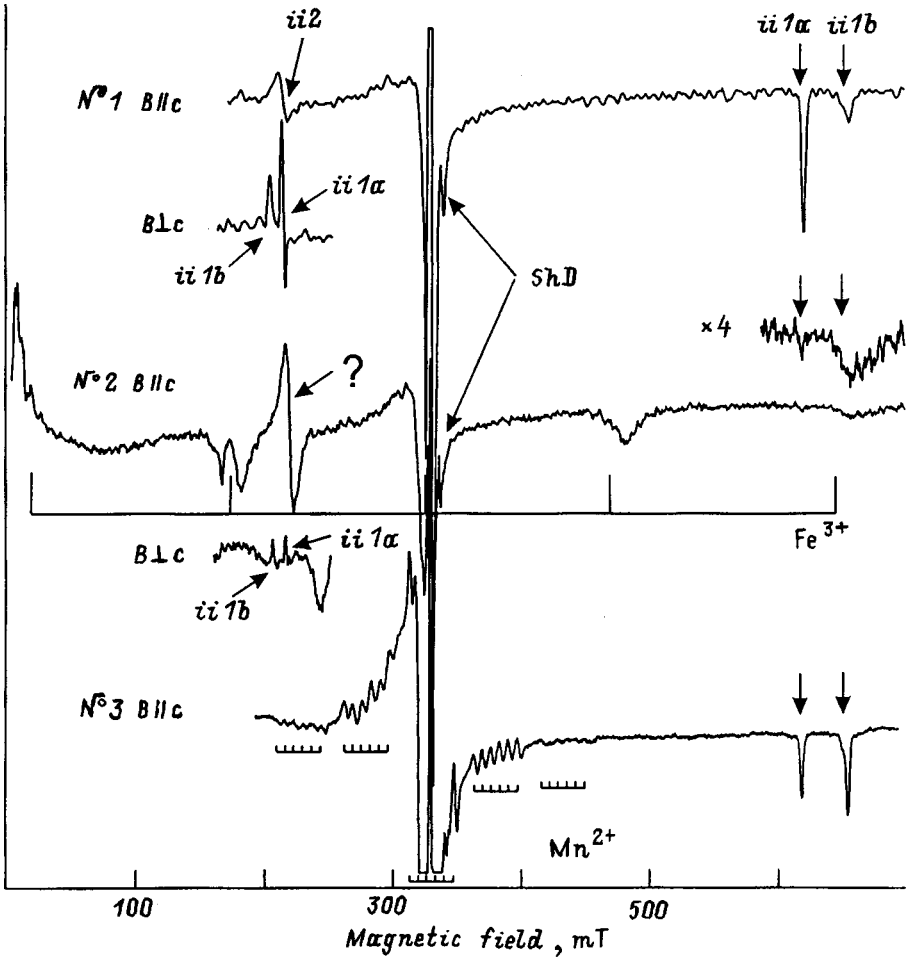

FIG. 1. EPR spectra of three GaN samples (1, 2, 3) recorded at 4 K in identical conditions in the X range in the $B\|c$ orientation. Fragments of $B\perp c$ spectra for samples 1 and 2 are presented. EPR spectra of shallow donors (shD), Fe^{3+} and Mn^{2+} ions are identified.

We studied in this work three types of GaN samples grown on SiC. Sample 1 — GaN crystal thickness 100 μm, SiC substrate 120 μm thick; sample 2 — GaN crystal thickness 250 μm, SiC substrate completely removed; sample 3 — GaN crystal thickness 150 μm, SiC substrate 200 μm thick.

The EPR spectra were measured on a standard JEOL instrument operating in the 3-cm (X) range. The magnetic fields used ranged from 0 to 1.6 T. A laboratory-built cryostat allows varying the sample temperature smoothly within the 3.5–300 K range by varying properly the flow of liquid helium or nitrogen. Facilities were provided for rotating the sample in a magnetic field in different planes of the specially oriented crystal.

2. EXPERIMENTAL RESULTS

Figure 1 shows EPR spectra of three GaN samples (1, 2, and 3) taken at 4 K under identical conditions in the X range in the $B\|c$ orientation. Consider first the EPR spectra of known centers studied earlier in GaN crystals (see Fig. 1). The spectra of samples 1 and 2 contain EPR signals of shallow donors denoted by shD and representing practically isotropic single lines with a g factor slightly smaller than that of a free electron. Sample 2 exhibits additional strong signals due to Fe^{3+} ions (five broad lines caused by fine-structure transitions between the levels of the system with electron spin $S=5/2$), and sample 3, Mn^{2+} signals (likewise a system with an electron spin $S=5/2$, but with an additional splitting of each fine-structure component into six lines produced in hyperfine interaction with the manganese nuclear spin $I=5/2$). Iron and manganese are present in GaN crystals as residual impurities.

Besides the above-mentioned signals, all crystals exhibit new EPR signals of the centers denoted by $ii1a$ and $ii1b$. Preliminary results on the observation of these centers were reported earlier.[14] The signals of the $ii1a$ and $ii1b$ centers possess a number of unusual properties. First of all, they exhibit a strong anisotropy in their g factors, which vary by about three times as the magnetic-field orientation relative to the hexagonal axis c of the crystal changes from $B\|c$ to $B\perp c$. Typical orientation dependences of the $ii1a$ and $ii1b$ centers measured in sample 3 in the X range at 4 K are displayed in Fig. 2 The magnetic field was swept in the $\{11\bar{2}0\}$ plane of the crystal.

The spectra of the $ii1a$ and $ii1b$ centers can be described by an axially symmetric spin Hamiltonian with the symmetry axis along the hexagonal direction in the crystal

$$H=\mu_B[g_\parallel B_Z S_Z+g_\perp(B_X S_X+B_Y S_Y)], \quad (1)$$

where $S=1/2$, and μ_B is the Bohr magneton. The local axis

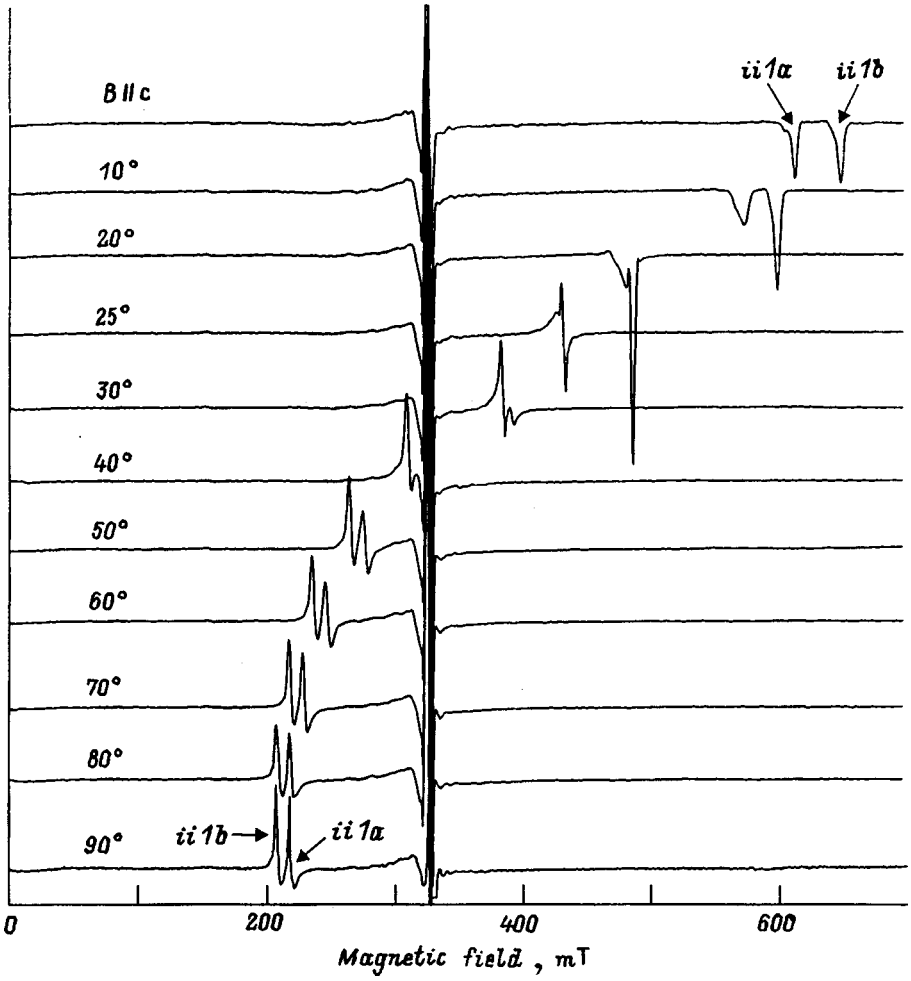

FIG. 2. Orientation dependence of EPR spectra of the $ii1a$ and $ii1b$ centers measured in the X range on GaN sample 3 at 4 K. The scan was done in the $\{11\bar{2}0\}$ plane of the crystal.

z coincides with the c axis of the crystal. We obtained the following values of the g factor for the $ii1a$ centers: $g_{\parallel}=1.07, g_{\perp}=3.00$, and for the $ii1b$ centers: $g_{\parallel}=1.015$, $g_{\perp}=3.12$.

A remarkable feature besides the high anisotropy is the unusual shape of the EPR signals in the form of an absorption line in orientations close to $B\|c$ and $B\perp c$, where they are in opposite phase. It should be pointed out that the shape of the EPR lines does not depend on microwave power, and the lines retain their shape down to the minimum power levels at which the signal is still detectable. As seen from Fig. 2, the EPR line shape varies strongly also with orientation, and at an angle of about 25°, where the lines due to the $ii1a$ and $ii1b$ centers practically coincide, it is close to the derivative form.

Another feature of the new EPR signals is the strong temperature dependence of these spectra. Figure 3 shows a typical temperature behavior of the $ii1a$ and $ii1b$ spectra observed with sample 3 and detected in the X range for two orientations, (a) $B\perp c$ and (b) $B\|c$. The g factors for $B\|c$ are seen to increase substantially, while for $B\perp c$ one observes the opposite trend. The temperature behavior of the g factors obtained for the two orientations is presented in Fig. 4a. The anisotropy in the $ii1a$ and $ii1b$ signals is seen to decrease substantially with increasing temperature.

Besides a strong temperature dependence of the g factors in the EPR spectra of the $ii1a$ and $ii1b$ centers, we observed hysteresis in the temperature-induced EPR intensity variation. As evident from Fig. 3a and 3b, as the temperature increases, the EPR line intensity decreases, until at about 25 K the $ii1b$ line, and at approximately 50 K, the $ii1a$ EPR line disappear. In the 20–30 K interval, the $ii1a$ line takes on the derivative shape typical of the EPR, and it becomes substantially more narrow. Subsequent cooling from the temperature at which the $ii1b$ (or $ii1a$) centers disappeared does not restore the EPR signals, i.e. one observes here a hysteresis effect. This phenomenon is clearly seen in Fig. 4b showing the dependence of the integrated intensities of the $ii1a$ and $ii1b$ EPR lines on the temperature of pulsed heating of the crystal for five min to various temperatures, followed by cooling down to 4 K. The arrows in Fig. 4b specify the direction of temperature variation. It should be added that cooling the crystals from 20–35 K, the temperatures at which the $ii1a$ EPR line became narrow and took on the shape of the derivative form, to 4 K restores the line in shape and width, but at the same time the line intensity drops, as seen from Fig. 4b. This phenomenon is demonstrated by Fig. 3a presenting several EPR spectra of the $ii1a$ and $ii1b$ centers, which were recorded at 4 K following a number of pulsed heatings illustrated in Fig. 4b.

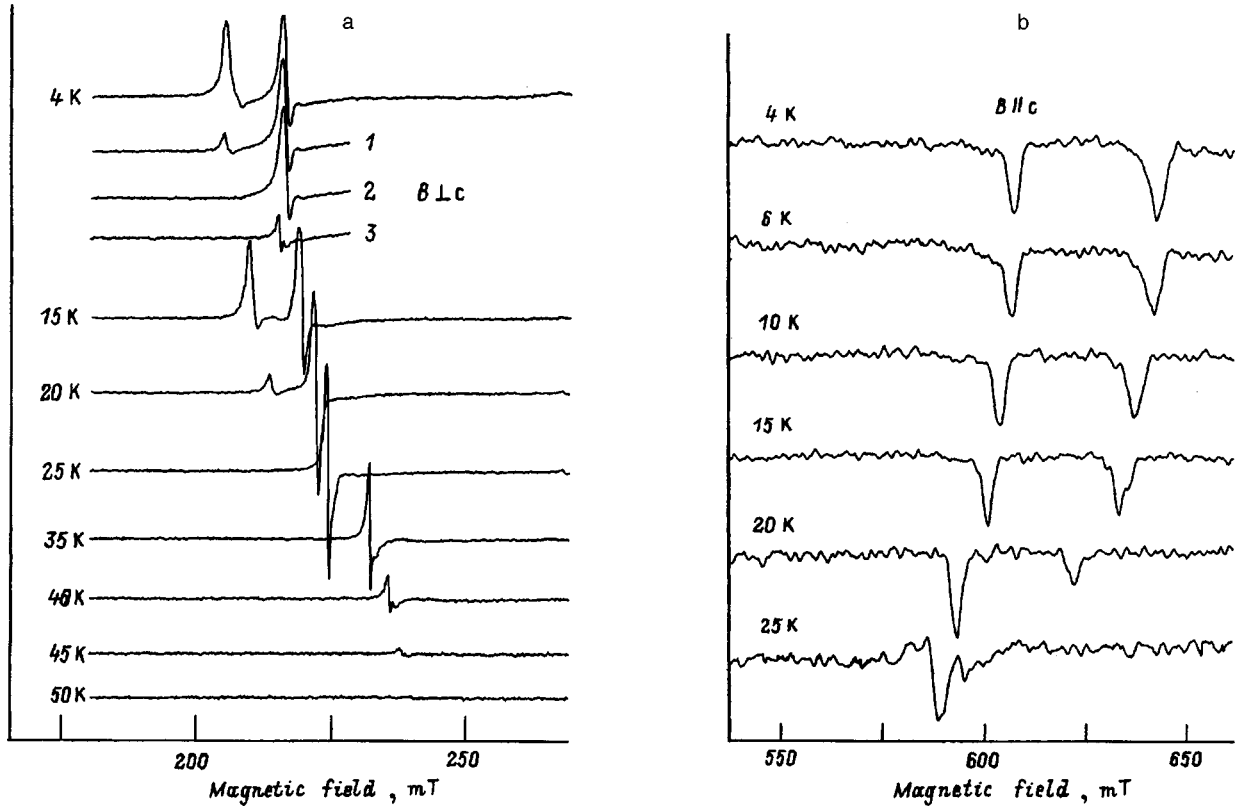

FIG. 3. Temperature dependence of EPR spectra of the $ii1a$ and $ii1b$ centers measured in the X range on sample 3 in two orientations, (a) $B\perp c$ and (b) $B\|c$. Also shown for the $B\perp c$ orientation are EPR spectra taken at 4 K and at subsequent coolings of this sample to 4 K from three temperatures (K): *1* — 20, *2* — 25, and *3* — 40, at which the sample was maintained for five min.

3. DISCUSSION OF RESULTS

Irreversible changes occur in the $ii1$ centers within the 25–50 K interval and, as a result, either these centers lose their paramagnetic properties or their spectra transform in such a way that the corresponding EPR signals can no longer be observed in our experimental conditions. Subsequent cooling of the samples from the temperatures of 25 and 50 K, at which the EPR spectra of the $ii1b$ and $ii1a$ centers disappear, respectively, does not restore the EPR signals. To recover the EPR signals, one has to warm the samples to room temperature under very specific conditions, in particular, in the dark. When recovered for the second time, however, the absolute and relative intensities of the $ii1b$ and $ii1a$ signals are found to depend in a random way on the conditions in which this was done. There are, apparently, other specific conditions as well (for instance, cooling rate in different temperature intervals), on which the $ii1a$ and $ii1b$ signals and the ratio of their intensities after recovery depend. Additional studies supplemented by other experimental techniques are required to reveal these conditions. The observed effects are typical of defects in semiconductors which exhibit metastable properties.

One can make only a few conjectures concerning the microstructure of the defects. An important point is the narrowness of the EPR lines, which, considering that all isotopes in GaN have nonzero nuclear magnetic moments, implies weakness of hyperfine interactions. The linewidth in some conditions is smaller than 1 mT, which is comparable only with that of shallow donors, but, in contrast to the latter, the $ii1a$ and $ii1b$ centers have a strongly anisotropic g factor. One can draw also a certain analogy in the temperature behavior of EPR linewidth between the $ii1a$ center and a shallow donor, namely, in both cases the EPR lines undergo substantial narrowing at about 20 K (EPR spectra of the $ii1b$ centers disappear at these temperatures) with increasing temperature, and for shallow donors this narrowing is due to motional averaging of hyperfine interactions with GaN nuclei[8]. Thus there are grounds to assume that the $ii1a$ and $ii1b$ centers are actually fairly shallow donor centers. Interestingly, for the $ii1a$ and $ii1b$ centers $g_\perp/g_\| \cong 3$, a ratio typical of the orientational dependence of a center with an effective spin $S=1/2$ for a system with a real spin of 5/2, and a large fine-structure splitting. We have not succeeded in detecting any hyperfine structure, despite the fact that the signal/noise ratio in some of our experiments was as high as 100. One may recall in this connection observation of some complexes of transition metals (TM) with an electron (e) or hole (h), i.e. (TM,e,h) complexes, which were studied in wurtzite-type crystals, including GaN, by optical techniques.[15,16] The absence of hyperfine structure and the probability of the presence in the system of a large electronic spin suggests that the $ii1$ structure can contain iron. Metastability could in this case be due to either the mutual arrangement of the components of the complex or its different charge states. It may be added that the different phases of the EPR signals produced by the $ii1a$ and $ii1b$ centers in the

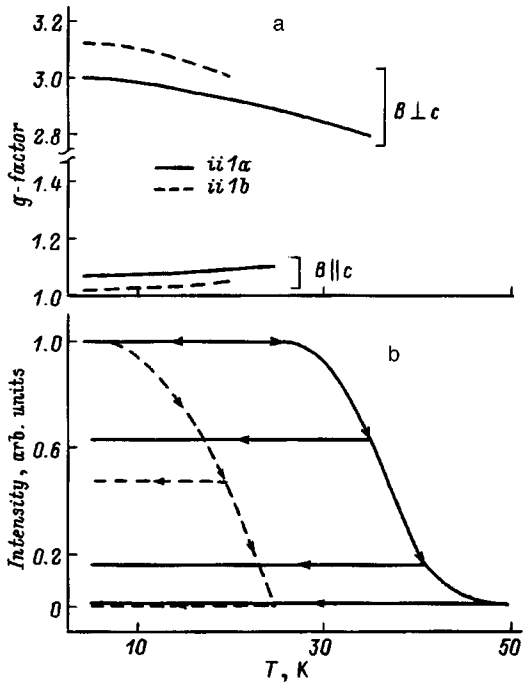

FIG. 4. Temperature dependence of EPR signals of the $ii1a$ and $ii1b$ centers. (a) g factors for two orientations: $B\|c$ and $B\perp c$; (b) EPR intensity. The direction of temperature variation is shown with arrows. The horizontal lines specify the fixed temperatures from which the sample was cooled to 4 K.

$B\|c$ and $B\perp c$ orientations (Figs. 1–3) could also be considered as an argument for the high spin state of the centers.

The large degree of anisotropy of the $ii1a$ and $ii1b$ EPR lines and their comparatively narrow width permit high-precision determination of the quality of GaN in the region of the crystal where these signals are observed. Indeed, considering that the EPR lines can shift by ~ 10 mT with the crystal turned in a magnetic field by 1°, and taking 0.5 mT for the minimum linewidth, it becomes clear that the angular spread around the c axis of the crystal cannot exceed 0.05°.

Some of the crystals exhibited other centers as well, which were denoted by us by $ii2$ and had $g_{\|}=3.17$ and $g_{\perp} \cong 2.0$.[14] The $ii2$ line is seen in the $B\|c$ orientation for sample 1 in Fig. 1. The magnitude of $g_{\|}$ and the linewidth of the $ii2$ centers depend on temperature, so that as the temperature rises above 25 K, the line becomes broader, and the g factor decreases and approaches 2. This behavior of EPR signals was observed by us for deep boron, deep aluminum, and deep gallium acceptors.[17] By analogy, we can assign the $ii2$ signals to some acceptor centers in GaN. Sample 2 in Fig. 1 exhibits an additional strong line about 220 mT, whose intensity drops sharply with changing orientation. This line was not studied in detail in this work.

The authors express their gratitude to Yu. A. Vodakov and A. D. Roenkov for fruitful discussions.

Partial support of the Russian Fund for Fundamental Research (Grant 98-02-18241) is gratefully acknowledged.

[1] H. Morkoç, S. Strite, G. B. Gao, M. E. Lin, B. Sverdlov, and M. Burns, J. Appl. Phys. **76**, 1363 (1994).
[2] S. Nakamura, N. Iwasa, M. Seno, and T. Mukai, J. Appl. Phys. **31**, 1258 (1992).
[3] Yu. A. Vodakov, M. I. Karklina, E. N. Mokhov, and A. D. Roenkov, Izv. Akad. Nauk SSSR, Neorg. Mater. **16**, 537 (1980).
[4] Yu. A. Vodakov, E. N. Mokhov, A. D. Roenkov, M. E. Boiko, and P. G. Baranov, J. Cryst. Growth **183**, 10 (1998).
[5] Yu. A. Vodakov, E. N. Mokhov, M. G. Ramm, and A. D. Roenkov, Krist. und Techn. **14**, 729 (1979).
[6] Yu. A. Vodakov, E. N. Mokhov, A. D. Roenkov, and D. T. Saidbekov, Phys. Status Solidi A **51**, 209 (1979).
[7] C. Wetzel, D. Volm, B. K. Meyer, K. Pressel, S. Nilsson, E. N. Mokhov, and P. G. Baranov, Appl. Phys. Lett. **65**, 1033 (1994).
[8] W. E. Carlos, J. A. Freitas, M. Asif Khan, D. T. Olson, and J. N. Kuznia, Phys. Rev. B **48**, 17878 (1993-II).
[9] K. Maier, M. Kunzer, U. Kaufmann, J. Schneider, B. Monemar, I. Akasaki, and H. Amano, Mater. Sci. Forum **143-147**, 93 (1994).
[10] P. G. Baranov, I. V. Ilyin, E. N. Mokhov, and A. D. Roenkov, Semicond. Sci. Technol. **11**, 1843 (1996).
[11] P. G. Baranov, I. V. Ilyin, and E. N. Mokhov, Solid State Commun. **101**, 611 (1997).
[12] P. G. Baranov, I. V. Ilyin, E. N. Mokhov, and A. D. Roenkov, in *Proceedings of the 23rd International Symposium on Compound Semiconductors* (St. Petersburg, Russia, 1996), Inst. Phys. Conf. Ser., No. 155 (1997), Ch. 12, p. 985.
[13] G. D. Watkins, Mater. Sci. Forum **38-41**, 39 (1989).
[14] P. G. Baranov, I. V. Ilyin, and E. N. Mokhov, Mater. Sci. Forum **258-263**, 1167 (1997).
[15] R. Heitz, A. Hoffmann, and I. Broser, Phys. Rev. B **48**, 8672 (1993).
[16] R. Heitz, P. Maxim, L. Eckey, P. Thurian, A. Hoffmann, I. Broser, K. Pressel, and B. K. Meyer, Phys. Rev. B **55**, 4382 (1997- I).
[17] P. G. Baranov, I. V. Ilyin, and E. N. Mokhov, Solid State Commun. **100**, 371 (1996).

Translated by G. Skrebtsov

EPR spectrum of donors in 6*H* SiC in a broad temperature range

E. N. Kalabukhova, S. N. Lukin, and Yu. S. Gromovoĭ

Institute of the Physics of Semiconductors, National Academy of Sciences of Ukraine, 252028 Kiev, Ukraine

E. N. Mokhov

A. F. Ioffe Physicotechnical Institute, Russian Academy of Sciences, 194021 St. Petersburg, Russia
(Submitted April 16, 1998)
Fiz. Tverd. Tela (St. Petersburg) **40**, 1824–1828 (October 1998)

An EPR study of donors in 6*H* SiC crystals with an uncompensated donor concentration (N_D-N_A) of 2×10^{18} to 1×10^{16} cm^{-3} performed in the temperature range 4.2 to 160 K at frequencies of 9 and 140 GHz showed that 6*H* *n*-SiC samples have two donor states in the gap. One of them originates from nitrogen occupying three inequivalent lattice sites with ionization energies of 150 and 80 meV, and the second is connected with a structural defect lying deeper in the gap than nitrogen. The temperature dependences of donor EPR line intensities have been found to deviate from the Curie law. The observed EPR line-intensity peaks of donors are produced in a temperature-driven successive redistribution of donor electrons between the donor levels. The temperature dependences of EPR line intensities obtained from samples with low donor concentrations were used to determine the valley-orbit splitting of nitrogen in cubic sites. © *1998 American Institute of Physics.* [S1063-7834(98)01110-1]

Nitrogen is a major paramagnetic donor impurity in silicon carbide polytypes. It remains, however, unknown, whether nitrogen is the only donor impurity responsible for the *n* conduction in SiC crystals.

Indeed, an EPR study of donors in 3*C* SiC with a donor concentration of 10^{17} cm^{-3}, carried out within the temperature interval from 10 to 40 K, resolved two spectra, namely, a hyperfine triplet associated with nitrogen and a single line coinciding at 9 GHz with the central line of the nitrogen triplet, whose origin was not established.[1] The EPR spectrum of nitrogen in 6*H* SiC with donor concentrations of 1×10^{17} to 6×10^{18} cm^{-3} measured from 80 to 125 K suggests that the additional line coinciding with the central nitrogen-triplet line at 9 GHz is due to nonlocalized electrons. The energy characteristics of this additional line were also derived from the temperature dependence of EPR line intensities.

The narrow temperature interval within which the measurements were carried out considerably limited, however, the information on donors which could be extracted from EPR data.

Besides, determination of the donor energy characteristics from the temperature dependences of EPR line intensities[2,3] was done without normalizing the measured EPR signal to the intensity of a reference signal varying with temperature according to the Curie law, which resulted in substantial errors in the donor energy.

To determine the number of donor centers responsible for the *n*-type conduction of SiC, as well as to obtain their energy characteristics, we have studied donor EPR spectra in 6*H* silicon carbide samples with uncompensated donor concentrations (N_D-N_A) ranging from 2×10^{18} to 1×10^{16} cm^{-3} within a temperature interval of 4.2 to 160 K and at frequencies of 9 and 140 GHz.

1. SAMPLES AND EXPERIMENTAL TECHNIQUE

We studied samples of the 6*H* silicon carbide polytype grown by the Lely and sublimation-sandwich methods at 2173 K, with an uncompensated donor concentration varying from 2×10^{18} to 1×10^{16} cm^{-3}.

The measurements were carried out on an EPR radiospectrometer within a 20–160 K interval at 9 GHz, and at $T=4.2$ K at 140 GHz.

To take into account the variation of radiospectrometer sensitivity and of sample magnetization with temperature, the EPR signal from Cr^{3+} ions in MgO powder, whose intensity varies according to the Curie law, was measured simultaneously with the EPR spectrum under study. The *g* factor of the reference resonant line, 1.9799, was close to that of nitrogen in silicon carbide, which made possible its measurement simultaneously with the EPR signal of the sample under study, without overlap of the two spectra.

The temperature was varied by passing gaseous helium through the evacuated system mounted in the radiospectrometer resonator. The sample temperature was measured with a germanium transducer. The temperature was maintained constant to within 0.3 K.

2. TEMPERATURE DEPENDENCE OF DONOR EPR SPECTRA IN 6*H* SIC

Figures 1 and 2 display EPR spectra in 6*H* SiC taken within a broad temperature range at 9 GHz, and at 140 GHz at $T=4.2$ K. At high temperatures, samples with concentrations from 2×10^{18} to 3×10^{17} cm^{-3} exhibit a single broad line, whereas at low temperatures the spectrum consists of

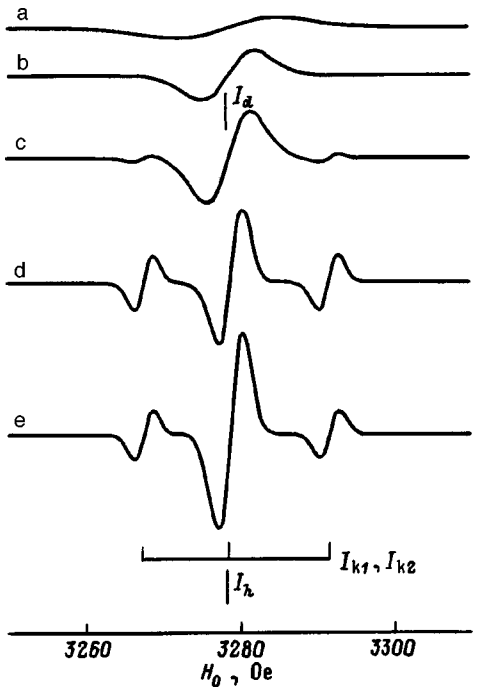

FIG. 1. Temperature dependence of a donor EPR spectrum of 6*H* SiC with uncompensated donor concentration $(N_D-N_A)\approx 2\times 10^{18}$ cm^{-3}, T(K): (a) 140, (b) 103, (c) 95, (d) 60, (e) 20. ν=9.2 GHz.

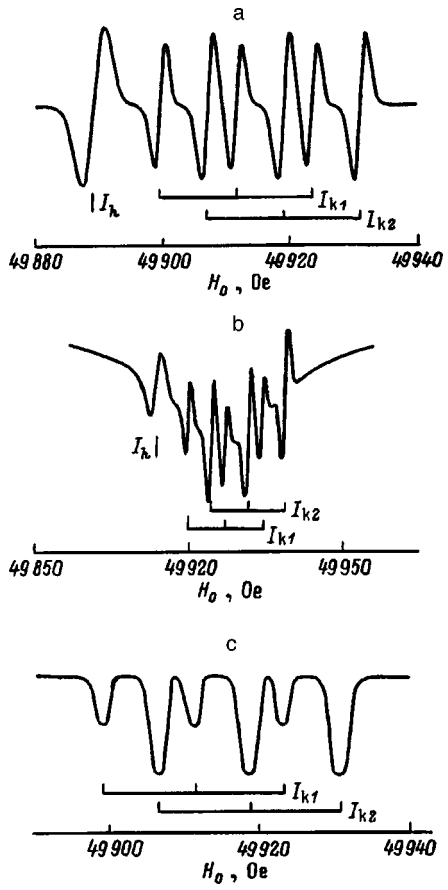

FIG. 2. Donor EPR spectrum of 6*H* SiC with uncompensated donor concentration (N_D-N_A) (cm^{-3}): (a) 2×10^{18}, (b) 3×10^{17}, (c) 1×10^{16}; ν=140 GHz, T=4.2 K.

TABLE I. Temperature characteristics of donor EPR spectra of 6*H* SiC polytypes with different uncompensated donor concentrations (N_D-N_A).

	(N_D-N_A), cm^{-3}			
	2×10^{18}	8×10^{17}	3×10^{17}	1×10^{16}
ΔT_k, K	110–4.2	140–4.2	140–4.2	150–4.2
$T_k^{\max}$, K	60	80	85	92
ΔT_h, K	85–4.2	45–4.2	45–4.2	30–4.2
$T_h^{\max}$	15	15	15	15
ΔT_d, K	160–4.2	160–4.2	160–4.2	160–4.2
$T_d^{\max}$, T	110	140	—	—

Note. ΔT_i - temperature interval of observation of the EPR spectra I_c, I_h, I_d; $T_i^{\max}$ - the temperatures at which the I_c, I_h, I_d EPR lines have maxima.

two triplets of hyperfine EPR lines due to nitrogens sitting at two cubic lattice positions I_{c1} and I_{c2}, which coincide in g factor at 9 GHz, and of a single line I_h originating from nitrogens in the hexagonal positions, which coincides at 9 GHz with the central nitrogen-triplet line.[4] In the sample with concentration 1×10^{16} cm^{-3} one also observes at high temperatures a single broad line, while in the low-temperature domain (Fig. 2) the spectrum consists of two hyperfine nitrogen EPR lines due to the two cubic positions with an intensity ratio $I_{c1}/I_{c2}=1/2$, with no line originating from the hexagonal nitrogen position, which implies a high degree of compensation in the sample.

The temperature behavior of the nitrogen EPR spectra and of the single line coinciding with the central triplet line changes with the donor concentration varied from 2×10^{18} to 1×10^{16} cm^{-3}.

Table I lists the temperature characteristics of the donor EPR spectra in samples with the donor concentration varying

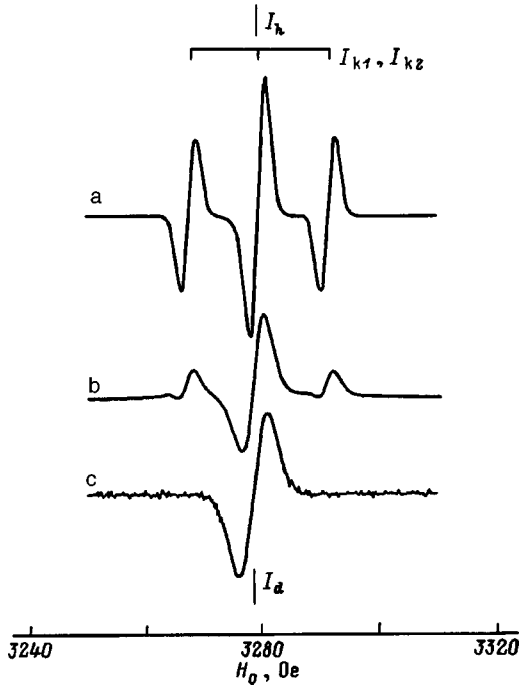

FIG. 3. Donor EPR spectrum of 6*H* SiC with uncompensated donor concentration 3×10^{17} cm^{-3} at three microwave power levels differing by 30 dB, with $P_a<P_b<P_c$. ν=9.2 GHz, T=4.2 K.

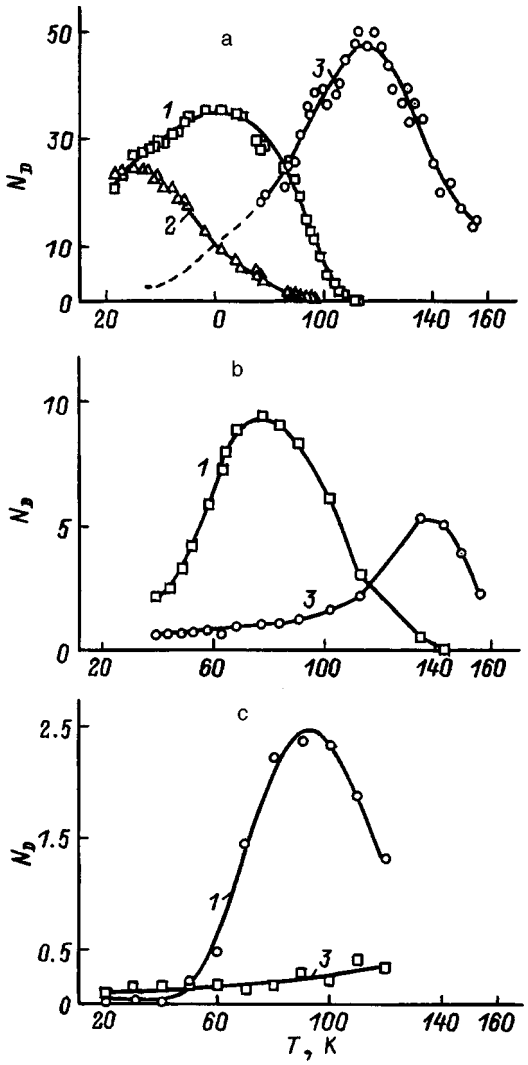

FIG. 4. Temperature dependence of the relative integrated EPR absorption line intensities of donors in 6*H* SiC with uncompensated donor concentration (N_D-N_A) (cm^{-3}) (a) 2×10^{18}, (b) 8×10^{17}, (c) 1×10^{16}. *1* — I_{c1}, I_{c2}; *2* — I_h, *3* — I_d.

from 2×10^{18} to 1×10^{16} cm^{-3}. As seen from Table I, the region where the nitrogen EPR lines are observed and the positions of their maxima depend on donor concentration. This region and the EPR line intensity maxima due to the nitrogen cubic positions, I_{ci}, and the single line I_d shift toward higher temperatures with decreasing donor concentration. At low temperatures their intensity decreases, and the nitrogen EPR spectra show signs of saturation (see Figs. 2 and 3). This permitted us, by properly increasing microwave power at 9 GHz, to isolate the single EPR line I_d coinciding in g factor with the central nitrogen-triplet line, which has substantially shorter spin-lattice relaxation times.

An analysis of low-temperature EPR spectra made at 9.2 and 140 GHz (Figs. 1 and 2) shows that the region of observation of EPR spectra due to hexagonal nitrogens shifts with decreasing donor concentration toward lower temperatures, with the maximum in intensity occurring about $T=15$ K.

3. ENERGY CHARACTERISTICS OF DONOR CENTERS

Figure 4 displays the temperature dependences of relative integrated intensities of the nitrogen EPR lines and of the additional resonant line due to an unidentified donor center I_d obtained on samples with the donor concentration varying from 2×10^{18} to 1×10^{16} cm^{-3}. The absorption-line intensity due to the hexagonal nitrogen (I_h) was found as the difference between the intensities of the central and side lines in the nitrogen triplet (at these temperatures the intensity of the additional line I_d is low and does not contribute noticeably to that of the central line of the triplet).

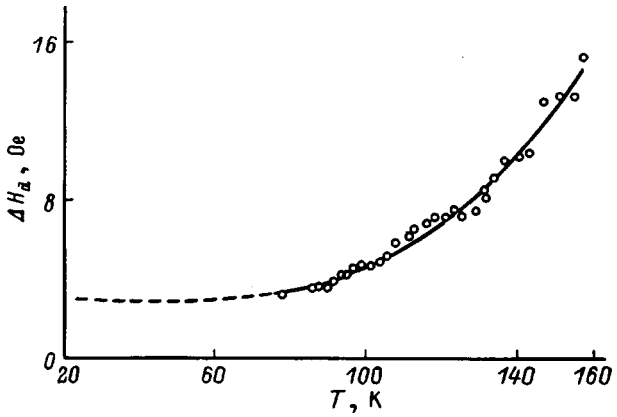

FIG. 5. Temperature dependence of the width of the single EPR line I_d in 6*H* SiC with uncompensated donor concentration $(N_D-N_A)\approx2\times10^{18}$ cm^{-3}. $\nu=9.2$ GHz.

The widths of the nitrogen EPR lines do not depend on temperature, and that of the single line I_d grows with temperature (Fig. 5).

An analysis of the temperature dependences of integrated EPR intensities permitted determination of the activation and ionization energies of the donor centers. The temperature dependences of the donor EPR line intensities, which are proportional to the concentration of paramagnetic donor centers N_D, are given by the expression

$$N_D=\frac{I_D(T)}{I_{\mathrm{ref}}(T)}\,\frac{1}{T}(\Delta H_D)^2\approx\exp\left(-\frac{E_D}{kT}\right),$$

where $I_D(T)$ and $I_{\mathrm{ref}}(T)$ are the donor center and reference sample line intensities, respectively, and ΔH_D is the peak-to-peak width of the first derivative of the absorption line due to donor centers.

As seen from this relation, one can determine the donor-center energy characteristics from the slope of the straight-line part in $\ln N_D$ curves drawn *vs* inverse temperature (Fig. 6).

The ionization energies E_i of the nitrogen occupying the cubic and hexagonal lattice positions derived from the high-temperature slope of these relations for samples with the donor concentration of 2×10^{18} cm^{-3} are in agreement with those obtained from Hall effect measurements[5,6] (see Table II).

The high- and low-temperature slopes of the curve due to the unidentified donor center yield the energies $E_i=60$ and 16 meV, respectively.

The low-temperature slope of the curves corresponding to nitrogen in cubic sites was used to determine the thermal

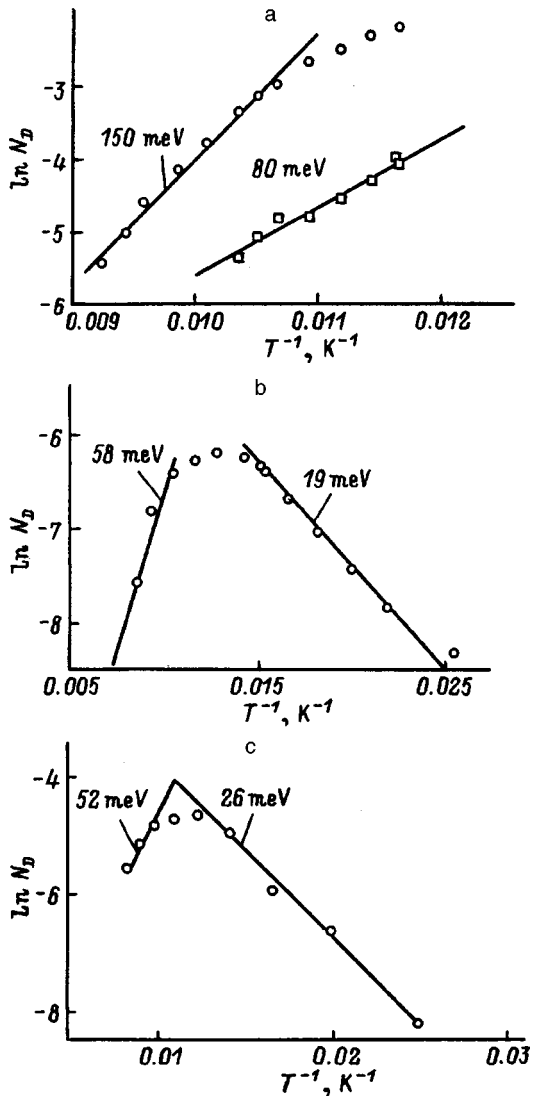

FIG. 6. Temperature dependences of the nitrogen paramagnetic-center concentration in 6*H* SiC with (N_D-N_A) (cm^{-3}): (a) 2×10^{18}, (b) 3×10^{17}, (c) 1×10^{16}. The high-temperature and low-temperature slopes of the curves can be approximated with $\exp(E_D/kT)$, where E_D: (a) 150 meV for $I_{c1,c2}$ and 80 meV for I_h, (b) 19 and 58 meV for $I_{c1,c2}$, and (c) 26 and 52 meV for I_{c2}.

activation energy of nitrogen, which was found to increase with decreasing donor concentration.

For samples with a low donor concentration, where $(N_D-N_A)\leqslant 3\times10^{17}$ cm^{-3}, the high-temperature slope yields an ionization energy coinciding with the valley-orbit splitting of nitrogen sitting at cubic sites, which is known from Raman scattering data[7] (Table II).

TABLE II. Energies of ionization E^i, activation E^a, and valley-orbit splitting E^{v-o} derived from EPR data of 6*H* SiC with different uncompensated donor concentrations (N_D-N_A).

	(N_D-N_A), cm^{-3}				
	4×10^{18}	2×10^{18}	8×10^{17}	3×10^{17}	1×10^{16}
E_k^i, meV	—	150	125	125 [5]	120 [5]
E_h^i, meV	—	80,80 [6]	—	85.5–83 [5]	80 [5]
E_k^{v-0}, meV	60.2, 63.6 [7]	—	—	58	52
E^a, meV	—	16	—	19	26

The different energies of valley-orbit splitting, $E_{v-o}=58$ and 52 meV, and of thermal nitrogen activation at the cubic sites, $E_c^a=19$ and 26 meV, obtained for samples with concentrations of 3×10^{17} and 1×10^{16} cm^{-3} are associated with the different EPR line intensity ratio for nitrogen residing in the two cubic sites in the lattice and, hence, are due to the different occupation of their levels in these crystals. This is seen particularly well from the EPR spectra measured at 140 GHz.

While, in a sample with the concentration of 3×10^{17} cm^{-3}, the two cubic nitrogen sites provide comparable contributions to the intensity of the hyperfine triplet at 9 GHz, in the sample with 1×10^{16} cm^{-3} the contribution due to one of the nitrogen cubic sites, I_{c1}, to the nitrogen triplet will be negligible at a high temperature. Therefore the energy characteristics determined in the first case actually will be an averaged characteristic of the two cubic positions, while in the second case they will relate to the nitrogen cubic position I_{c2} lying deeper in the gap. This can account for the small discrepancy between the valley-orbit splittings obtained by EPR and that derived from Raman data.

The above studies permit the following conclusions:

1) Samples with uncompensated donor concentration of 2×10^{18} to 1×10^{16} cm^{-3} exhibit donor EPR spectra of two types in the temperature region from 4.2 to 160 K, namely, three EPR spectra due to nitrogen occupying three nonequivalent lattice sites, with activation energies of 150 and 80 meV, and an additional single line;

2) The difference in the temperature dependence of the additional line for different donor concentrations permits a conclusion that this line is produced by a donor center rather than by nonlocalized electrons, as this was universally accepted[2] thus far. This also follows from the temperature dependence of the width of the single line which increases with temperature, a feature not typical of lines due to exchange interaction[8];

3) The observed second donor center can be associated with an intrinsic defect, which are known to form[9,10] in nonstoichiometric silicon carbide. The ionization energy of 60 meV derived from the high-temperature slope of the curve due to an intrinsic defect may disagree with its ionization energy, because the single EPR line is observed at higher temperatures than the nitrogen EPR spectrum, and, hence, the level of the intrinsic defect lies deeper than those of nitrogen;

4) The temperature dependence of donor EPR line intensities was found to deviate from the Curie law. The peaks observed in donor EPR line intensities can be interpreted as due to successive population redistribution in the multilevel donor system induced by temperature variation. Indeed, as follows from Fig. 4, there is a correlation between the temperature at which donor electrons are ionized at one level and the temperature at which their concentration reaches a maximum at another level;

5) The temperature dependence of donor EPR spectra has been found to correlate with the concentration of uncompensated donors in 6*H* SiC crystals. As seen from Table I,

the intensity maxima of the EPR lines due to nitrogen in cubic sites and to the intrinsic defect shift toward higher temperatures with the concentration decreasing from 2×10^{18} to 1×10^{16} cm^{-3}, whereas the EPR spectrum originating from the hexagonal nitrogen site moves toward lower temperatures, and the position of the intensity maximum does not change with temperature;

6) The thermal activation energy of donor electrons has been determined from the low-temperature slope of EPR line intensities and was found to increase with decreasing donor concentration from 16 to 26 meV. This result is in agreement with conductivity measurements[2] performed on samples in the same concentration region;

7) An important result of the study is that, at low donor concentrations, where all donor states are localized, one can determine the valley-orbit splitting for the nitrogen occupying cubic lattice sites from the temperature dependence of EPR line intensities.

Support of the Fund for Fundamental Research of the Ministry for Science and Technology of Ukraine and of Deutsche Forschungsgemeinschaft is gratefully acknowledged.

[1] W. E. Carlos, in *Properties of Silicon Carbide*, edited by G. L. Harris (IEE, London,1995), p. 42.
[2] A. I. Veĭnger, Fiz. Tekh. Poluprovodn. **1**, 20 (1967) [Sov. Phys. Semicond. **1**, 14 (1967)].
[3] C. Kiselowski, K. Maier, J. Schneider, and V. Oding, Mater. Sci. Forum **83-87**, 1171 (1992).
[4] E. N. Kalabukhova, N. N. Kabdin, S. N. Lukin, E. N. Mokhov, and B. D. Shanina, Fiz. Tverd. Tela (Leningrad) **31**, 50 (1989) [Sov. Phys. Solid State **31**, 378 (1989)].
[5] W. Suttrop, G. Pensl, W. J. Choyke, R. Stein, and S. Leibenzeder, J. Appl. Phys. **72**, 3708 (1992).
[6] A. O. Evwaraye, S. R. Smith, and W. C. Mitchel, J. Appl. Phys. **75**, 3472 (1994).
[7] P. J. Colwell and M. V. Klein, Phys. Rev. B **6**, 498 (1972).
[8] E. N. Kalabukhova, V. S. Kiselev, and S. N. Lukin, in *Proceedings of the 6th International Conference on Silicon Carbide and Related Materials* (Kyoto, 1995); Inst. Phys. Conf. Ser. **142**, 405 (1996).
[9] E. N. Kalabukhova, S. N. Lukin, E. N. Mokhov, J. Reinke, S. Greulich-Weber, and J.-M. Spaeth, in *Proceedings of the 6th International Conference on Silicon Carbide and Related Materials* (Kyoto, 1995); Inst. Phys. Conf. Ser. **142**, 333 (1996).
[10] E. N. Kalabukhova, S. N. Lukin, B. D. Shanina, Yu. A. Vodakov, A. A. Lepneva, and E. N. Mokhov, in *Proceedings of the 5th International Conference on Silicon Carbide and Related Materials*; Springer Proc. in Phys. **71**, 149 (1992).

Translated by G. Skrebtsov

Thermal expansion of crystal lattices of germanium with different isotopic compositions

A. P. Zhernov

Kurchatov Institute Russian Scientific Center, 123182 Moscow, Russia;
Institute of Superconductivity and Solid-State Physics, 123182 Moscow, Russia
(Submitted March 11, 1998)
Fiz. Tverd. Tela (St. Petersburg) **40**, 1829–1831 (October 1998)

The linear thermal expansion coefficient of crystal lattices of germanium with different isotopic compositions is analyzed. © *1998 American Institute of Physics.* [S1063-7834(98)01210-6]

Many problems in the theory of the thermal expansion of crystal lattices have been thoroughly studied (see, for example, the monograph in Ref. 1 and the review in Ref. 2). However, as far as we know, the question of the nature of the behavior of the thermal-expansion coefficient α for crystals having different isotopic compositions has not been studied. For this reason, the first-order effects for α with respect to the isotopic mass difference are discussed in this paper.

We note that in the case of classical statistics the value of the coefficient of thermal expansion is insensitive to the isotopic composition. The variation of $\alpha(T)$ in response to variation of the content of different isotopes in a crystal is a quantum effect.[3]

The standard quasiharmonic approximation is employed in this paper. In other words, the dependence of the lattice parameter a on the temperature T is taken into account. Actually, because of the anharmonicity of the interatomic interaction energy, the associated dynamic force parameters and the frequencies of the phonon modes ω_l (the subscript l labels the modes) depend on $a(T)$. In the harmonic approximation the frequencies ω_l do not depend on $a(T)$. In the quasiharmonic approach under consideration the terms above second order are discarded from the expansion of the potential energy in displacements. In addition, some of the anharmonic effects are taken into account because of the dependence of a on T and of ω_l on a.

As a concrete example we shall discuss the features of the variation of the values of α in response to variation of the isotopic composition over a broad temperature range for germanium crystals.

This research was initiated by the studies of the properties of chemically pure and isotopically highly enriched germanium crystals performed by V. I. Ozhogin's research group. Measurements of the thermal conductivity were performed elsewhere.[4,5] Other properties are investigated here.

1. THERMAL EXPANSION AND GRÜNEISEN PARAMETER IN THE LINEAR APPROXIMATION WITH RESPECT TO THE ISOTOPIC MASS DIFFERENCE

In the quasiharmonic approach and the linear approximation with respect to the isotopic mass difference in cubic crystals, the linear thermal-expansion coefficient α is given by the relations (c.f., Refs. 3, 6, and 7)

$$\alpha(T)=\frac{1}{3\Omega_0 B_0}\sigma(T), \tag{1}$$

$$\sigma(T)=\sum_l \gamma(l)C_l(T),$$

$$C_j(T)=\frac{1}{T^2}\omega^2(l)n(\omega(l))[n(\omega(l))+1]. \tag{1a}$$

Here $\omega(l)$ is the photon frequency of the lth mode with quasimomentum f and polarization j, i.e., $l=\{\mathbf{f},j\}$, $n(\omega)$ is the Planck distribution, and $\gamma(l)$ is the partial Grüneisen parameter. By definition

$$\gamma(l)=-\{\partial \ln \omega(l)/\partial \ln \Omega\}_{\Omega=\Omega_0}.$$

This relation is used to take into account the fact that the dependence of the frequencies of different modes on the volume $\Omega(T)\sim a^3(T)$ varies. The parameter C_l is the specific heat of the lth mode. In addition, it was assumed above that Ω_0 is the equilibrium unit-cell volume of the lattice, and B_0 is the bulk modulus at $T=0$. In order to simplify the notation, the Boltzmann and Planck constants are assumed to be equal to unity.

We note that the equilibrium unit-cell volume (and parameter) at $T=0$ due to the zero-point vibrations of the atoms depends on the mean mass of the mixture of isotopes. It can be shown that the corresponding correction to Ω_0 is described by

$$\delta\Omega_0=\Omega_0-\Omega_0'\approx\frac{\Sigma_l\gamma(l)\omega(l)}{2B_0}. \tag{2}$$

In (2) Ω_0' is the unit-cell volume determined only by the elastic energy of the crystal.

We also note that in any isotopic composition the equality

$$M_c\omega^2(l)=\varphi(l)$$

holds for a specific mode and that the effective force factor $\varphi(l)$ does not depend on the value of the mean mass M_c. In this case

$$M_c=\sum_i c_i M_i, \tag{3}$$

where c_i is the concentration and M_i is the mass of the isotopes of the ith kind.

We define a specific isotopic composition using the label c_0. Then, with consideration of (3) for an arbitrary isotopic composition, which we label c, we have a universal relation of the form

$$\alpha_c(T)=\alpha_{c_0}(T'), \quad T'=T\sqrt{M_c/M_{c_0}}\,.$$

If $\gamma(l)$ is close to a certain mean value $\gamma_a=\text{const}$ at small and large frequencies, then instead of (1), we obtain an expression for the coefficient of thermal expansion of the form

$$\alpha(T)\approx\frac{1}{3\Omega_0 B_0}\gamma_a C_L(T), \tag{4}$$

where C_L is the lattice specific heat.

Along with $\alpha(T)$ we also consider the Grüneisen parameter $\gamma(T)$, which is a weighted-mean function of the contributions of the individual modes. By definition (c.f., Refs. 1 and 7)

$$\gamma(T)=\frac{\sigma(T)}{C_L(T)}=\frac{\Sigma_l\gamma(l)C_l(T)}{\Sigma_l C_l(T)}. \tag{5}$$

We recall that, since the range of frequencies excited narrows with decreasing temperature, a dependence of γ on temperature (5) appears because of the difference between the partial parameters $\gamma(l)$ at low and high frequencies.

As we have already noted, the temperature dependence of the coefficient of thermal expansion is determined in many cases by the temperature dependence of the specific heat, i.e., Eq. (4). This is because the Grüneisen parameter usually displays a comparatively weak dependence on temperature. In the general case the dependence of γ on T is very significant.

Let us now consider the situation where there are two crystals with mean masses M_c and $M_{c1}=M_c+\Delta M$. According to (1) and (2), the relative change in the coefficient of thermal expansion $\Delta\alpha_c(T)=\alpha(M_{c1})-\alpha(M_c)$ in the case of $|\Delta M|\ll M_c$ can be represented in the form

$$\Delta\alpha_c\approx\alpha^{(1)}(M_c)+\alpha^{(2)}(M_c),$$

where

$$\alpha^{(1)}(M_c)=\alpha(M_c)\left(\frac{\Delta\gamma_c}{\gamma(M_c)}+\frac{\Delta C_c}{C_L(M_c)}\right),$$

$$\Delta\gamma_c(T)=\gamma(M_{c1})-\gamma(M_c),$$

$$\Delta C_c(T)=C_L(M_{c1})-C_L(M_c), \tag{6}$$

$$\alpha^{(2)}(M_c)=\alpha(M_c)\left(\frac{Z(M_c)}{Z(M_{c1})}-1\right), \quad Z=\Omega_0 B_0. \tag{6a}$$

In this case

$$\alpha^{(2)}(M_c)\sim-\alpha(M_c)\rho\frac{\Delta M}{M_c},$$

where

$$\rho=\left(\frac{\Sigma_l\gamma(l)\omega(l)}{2B_0\Omega_0}\right)_{M=M_0}.$$

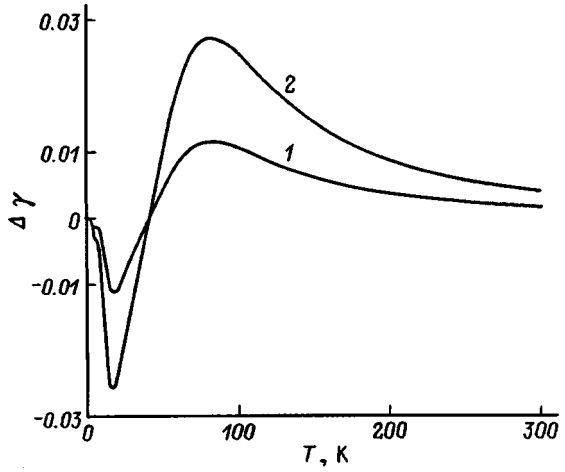

FIG. 1. Dependence of $\Delta\gamma=\gamma(M_{c1})-\gamma(M_{c2})$ on T. *1*—$M_{c1}=72.6$, $M_{c2}=70$; *2*—$M_{c1}=76$, $M_{c2}=70$.

Let us comment on relations (6) and (6a). First, the character of the dependence of $\Delta\alpha_c^{(1)}$ on T is determined by the difference between the phonon spectra of the crystals with the masses M_c and M_{c1}. If the partial Grüneisen parameters $\gamma(l)$, as a whole, differ only slightly from some mean values, the first term can be neglected. In the general case both $\Delta\gamma_c$ and ΔC_c are significant. Second, for germanium $\rho\approx 2\times10^{-3}$, and $\Delta M/M_0$ can amount to several hundredths. Thus, the changes in the unit-cell volume at $T=0$ due to variation of the isotopic composition amount to $\sim10^{-5}$ in relative units. As concrete estimates show, in the case of germanium $\alpha^{(2)}$ can be neglected in comparison to $\alpha^{(1)}$.

2. ISOTOPIC DEPENDENCES OF THE COEFFICIENT OF THERMAL EXPANSION ON THE GRÜNEISEN PARAMETER FOR GERMANIUM

The isotopic dependences of $\alpha(T)$ and $\gamma(T)$ for germanium. The frequencies $\omega(l)$ of the phonon modes were calculated were determined within the Born–von Kármán theory. The value of the parameters of the force interaction found by fitting the data from the inelastic-neutron-scattering experiment in Ref. 8 were used. Furthermore, the values of the partial isotope-shift factors for Ge were analyzed theoretically in Ref. 9 within the microscopic bond-charge model. This model is based on the idea that the electronic charge concentrated at the center of a chemical bond can be regarded as a dynamic quantity which influences the interatomic interaction. The application of this model to Ge is enabled by the fact that it can be used to simulate the large flat portion of the dispersion curve for transverse-acoustic phonons.

As for the calculations of $\alpha(T)$ and $\gamma(T)$, since the partial isotope shift factors were determined in Ref. 9 only along symmetry directions, the integration was performed along symmetry directions using Houston's relation (c.f., Ref. 10) instead of over the Brillouin zone. The following values were taken for the parameters appearing in the theory: the lattice constant $a_0=5.658$ Å and the bulk modulus $B_0=0.772\times10^{12}$ dyn/cm^2 (see, for example, Ref. 5).

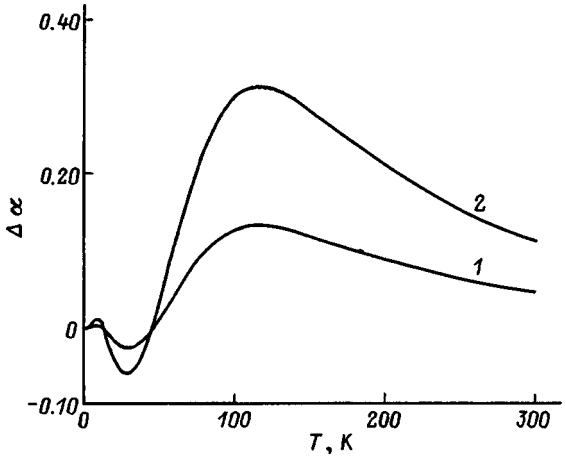

FIG. 2. Dependence of $\Delta\alpha=\alpha(M_{c1})-\alpha(M_{c2})$ on T. *1*—$M_{c1}=72.6$, $M_{c2}=70$; *2*—$M_{c1}=76$, $M_{c2}=70$.

The results of the calculations are presented in Figs. 1 and 2. These figures show plots of the temperature dependence which illustrate the scale of the isotope effects for $\alpha(T)$ and $\gamma(T)$. Difference plots of $\Delta\gamma=\gamma(M_{c1})-\gamma(M_{c2})$ and $\Delta\alpha=\alpha(M_{c1})-\alpha(M_{c2})$ for germanium crystals with masses M_{c1} and M_{c2} equal to 76 and 70 (highly enriched samples) and to 72.6 and 70, respectively, are presented. The case of $M=72.6$ corresponds to the natural composition. The behavior of $\Delta\alpha(T)$ is qualitatively specified by the values of $\Delta\gamma(T)$. However, since, according to (6), the isotope effect for the linear thermal expansion coefficient is dictated simultaneously by renormalizations of both the Grüneisen parameter and the lattice specific heat C_L, the relative changes are generally more pronounced for $\alpha(T)$ than for $\gamma(T)$.

We further note that, in the temperature intervals of the order of several degrees, where the Grüneisen parameter changes sign, the value of $\Delta\alpha/\alpha$ is of the order of 0.1. At other temperatures the corresponding values of $\Delta\alpha/\alpha$ do not exceed a few hundredths.

In summation, the influence of the isotopic composition on the coefficient of thermal expansion of crystals with respect to the isotopic mass difference has been considered in this paper in a quasiharmonic approach in the linear approximation. The effect on $\alpha(T)$ and $\gamma(T)$ of varying the value of the mean mass has been estimated qualitatively for germanium over a broad temperature range. It has been shown that, in contrast to standard crystals, the behavior of α as a function of T is determined to a significant extent by renormalization of the Grüneisen parameter.

We are indebted to S. M. Stipov and the referee for some valuable comments, as well as D. A. Zhernov for his assistance. We thank Y. M. Kagan for discussing the results.

This work was carried out with support from V. I. Ozhogin.

[1] S. I. Novikova, *Thermal Expansion of Solids* [in Russian], Nauka, Moscow (1979), 285 pp.
[2] T. H. Barron, J. G. Collins, and G. K. White, Adv. Phys. **29**, 609 (1980).
[3] G. Leibfried, ''Gittertheorie der mechanischen und thermischen Eigenschaften der Kristalle,'' in *Handbuch der Physik, Vol. 7/1*, edited by S. F. Flügge [Springer-Verlag, Berlin–Göttingen–Heidelberg (1955), pp. 105–324; GIL, Moscow (1963), 312 pp.].
[4] V. I. Ozhogin, A. V. Inyushkin, A. N. Toldenkov, G. É. Popov, E. Haller, and K. Itoh, JETP Lett. **63**, 490 (1996).
[5] M. A. Asen-Palmer, N. Bartcovsky, E. Gmellin, M. Cardona, A. P. Zhernov, A. V. Inushkin, A. N. Toldenkov, V. I. Oghogin, K. M. Iton, and E. E. Haller, Phys. Rev. B **56**, 9431 (1997).
[6] G. Leibfried and W. Ludwig, ''Theory of anharmonic effects in crystals,'' in *Solid State Physics, Vol. 12*, F. Seitz and D. Turnbull (Eds.) [Academic Press, New York–London (1961), pp. 276–444; IL, Moscow (1963), 212 pp.].
[7] V. G. Vaks, E. V. Zarochentsev, S. P. Kravchuk, V. P. Safronov, and A. V. Trefilov, Phys. Status Solidi **85**, 749 (1978).
[8] A. D. Zdetsis and C. S. Wang, Phys. Rev. **19**, 2999 (1979).
[9] Resul Eryiğit and I. P. Herman. Phys. Rev. B **53**, 7775 (1996).
[10] A. A. Maradudin, E. W. Montroll, and G. H. Weiss, *Theory of Lattice Dynamics in the Harmonic Approximation* (Solid State Physics, Suppl. 3), Academic Press, New York (1963) Mir, Moscow (1965), 384 pp.].

Translated by P. Shelnitz

Observation of stimulated gamma emission in MgO:^{123m}Te

V. F. Masterov, S. I. Bondarevskiĭ, V. B. Eremin, F. S. Nasredinov, and P. P. Seregin

St. Petersburg State Technical University, 195251 St. Petersburg, Russia
(Submitted March 6, 1998)
Fiz. Tverd. Tela (St. Petersburg) **39**, 1832–1834 (October 1997)

The radioactive-decay rate of impurity ^{123m}Te atoms in MgO was observed to decrease with the temperature lowered from 295 to 80 K. It is assumed that this phenomenon is connected with stimulated gamma emission of the long-lived isomer ^{123m}Te, whose probability should increase with decreasing temperature due to the increase of the Mössbauer factor for 88-keV gamma photons. A phenomenological description of the effect of stimulated gamma radiation (SGR) on the radioactive-decay rate is proposed, and a parameter is introduced which characterizes the SGR intensity such that, as this parameter approaches one, a single-pass laser-shot mode should set in. It is shown that in the geometry used this critical mode for MgO:^{123m}Te can be initiated by increasing the specific activity by two orders of magnitude.
 [S1063-7834(98)01310-0]

Investigation of stimulated gamma radiation (SGR) of nuclei is a promising problem in physics of the solid state, because this phenomenon can be used to develop a gamma-ray laser based on long-lived nuclear isomers. Despite theoretical estimates casting doubt on the actual feasibility of such a laser,[1] attempts at SGR observation do not cease [see, e.g., a review Ref. (2)]. The available results of nuclear experiments are, however, poorly reproducible and therefore can be questioned.

One of the most obvious manifestations of SGR should be an increase in the isomer decay rate. The traditional method of measuring the decay rate consists in studying the normalized ratio R of the count rates of two sources having the same isotope composition as a function of time. This relation can be written

$$R(t)=R/R_0=\exp(\Delta\lambda t), \tag{1}$$

where $R=C_1/C_2$; $C_1(t)=k\lambda_1 N_{01}\exp(-\lambda_1 t)$ and $C_2(t)=k\lambda_2 N_{02}\exp(-\lambda_2 t)$ are the count rates of sources 1 and 2, k is the detector efficiency, N_{01} and N_{02} are the numbers of radioactive nuclei in sources 1 and 2 at the initial instant of time, R_0 is the count-rate ratio at the initial instant of time, $\Delta\lambda=\lambda_2-\lambda_1$, λ_1 and λ_2 are the decay constants of the nucleus under study in sources 1 and 2, $\lambda=\ln 2/T_{1/2}=1/\tau_0$, $T_{1/2}$ is the decay half-period, and τ_0 is the lifetime of the nucleus.

This method was used in this work to detect the SGR of the long-lived isomer ^{123m}Te ($T_{1/2}=119.7$ d, $\tau_0=1.47\times10^7$ s, $\lambda=6.81\times10^{-8}$ s^{-1}). The ^{123m}Te decay scheme is shown in Fig. 1. The decay rate of ^{123m}Te is determined by the intensity of the 88-keV isomeric transition, where the spontaneous emission should be accompanied by a stimulated component. If the latter is detectable, the decay rate should be temperature dependent because of the temperature dependence of the Mössbauer factor entering the cross section of stimulated emission.

The radioactive isotope ^{123m}Te was produced on a cyclotron in the ^{123}Sb$(p,n)^{123m}$Te reaction. The MgO:^{123m}Te sources were obtained by sintering a carrier-free ^{123m}Te preparation with MgO at 900 °C for 2 h in air. The MgO matrix was chosen because ^{125}Te Mössbauer spectroscopy shows[3] MgO:^{123m}Te sources to have an unsplit radiation line and a high Mössbauer factor. Two MgO:^{123m}Te sources were prepared; one of them was subsequently kept at room temperature, and the second, in liquid nitrogen, from where it was taken out only for the duration of measurements. The count-rate measurements were performed once every 20–30 days for seven months. The radiation source was pressed into a narrow quartz-glass ampoule. The radionuclide activity was 6 MBq, the active part of the ampoule was 8 mm long with a diameter of 0.6 mm. The counter measured gamma photons emitted from the end face of the source normal to the detector window.

The count rates of the sources were measured at room temperature using the 159-keV radiation following in the cascade the 88-keV transition in the ^{123m}Te isomer. A DGR-type semiconductor detector was employed for gamma-radiation measurement. The 159-keV photopeak in the amplitude spectrum was isolated with the discrimination levels

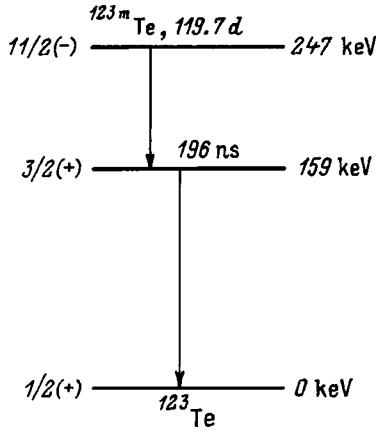

FIG. 1. Decay scheme of the ^{123m}Te isotope.

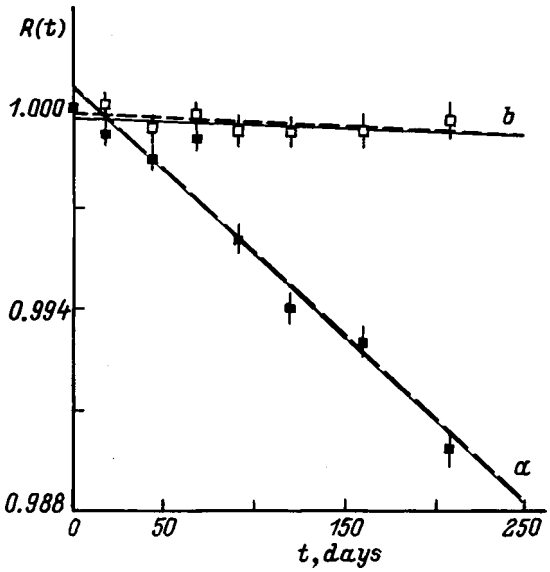

FIG. 2. $R(t)$ relations for the sources (a) MgO:^{123m}Te (80 K) – MgO:^{123m}Te (295 K) and (b) $H_2{}^{123m}TeO_4$ – $H_2{}^{123m}TeO_3$.

chosen such as to reduce to a minimum the effect of electronics drift on the count rate. The stability of the set-up was monitored by measuring the count rates of the two samples alternately once every 3000 s.

Figure 2a presents the $R(t)$ plot obtained for the two MgO:^{123m}Te sources. The experimental data fit onto a straight line representing the initial portion of exponential (1). The slope of the line yields the value $\Delta\lambda/\lambda = 8.6(2) \times 10^{-3}$, and its sign indicates an increase in the ^{123m}Te count rate of the source kept in liquid nitrogen compared to that maintained at room temperature.

It was of interest to compare the temperature λ dependence of ^{123m}Te in MgO observed by us with its dependence on the valence state of tellurium atoms. ^{123m}Te decays by an isomeric conversion transition, and the intensity of the conversion channel, i.e., of the decay path in which the energy of the isomeric transition is transferred to an electron in the atom, depends on the electron density at the decaying nucleus, $|\Psi(0)|^2$. For this reason the variations in the decay constant are related, as a rule, to those of the electron density in an approximate expression $\Delta\lambda/\lambda = \Delta|\Psi(0)|^2/|\Psi(0)|^2$.[4] The variations in $|\Psi(0)|^2$ are most noticeable at changes in the valence state of the parent atom, and are the strongest when the number of *s* electrons undergoes a change.

Figure 2b shows the $R(t)$ dependence for two ^{123m}Te sources in H_2TeO_4 and H_2TeO_3. In contrast to the sources described above, these had different chemical compositions but were stored together at room temperature between measurements. We readily see that the transition from H_2TeO_4 to H_2TeO_3 is accompanied by an increase in the ^{123m}Te decay rate, and that $\Delta\lambda/\lambda = 3.5(5) \times 10^{-4}$. This is in accord with the change in the tellurium valence state from Te^{6+} (electron configuration $4d^{10}$) to Te^{4+} ($4d^{10}5s^2$). This is accompanied by an increase of $|\Psi(0)|^2$ and, as a result, an increase in the ^{123m}Te decay rate.

It is essential that the value of $\Delta\lambda/\lambda$ produced by a change in temperature of the MgO:^{123m}Te source exceeds by a factor 25 that caused by the two 5*s* electrons of tellurium. For this reason we interpreted the temperature dependence of λ in MgO:^{123m}Te as resulting from the temperature dependence of SGR, which, in its turn, is related to that of the Mössbauer factor for the 88-keV transition.

This interpretation is supported also by the observation that measurements of the $R(t)$ dependence for a pair of ^{123m}Te sources in the form of elemental tellurium (with one of the sources kept at room temperature, and the other, in liquid nitrogen) yielded $|\Delta\lambda/\lambda| < 5 \times 10^{-5}$. Mössbauer spectroscopy shows that the ^{123m}Te source in the form of elemental tellurium has a small Mössbauer factor both at 295 and at 80 K,[3] and therefore this source should not exhibit any temperature dependence of λ.

Discussions of the feasibility of SGR are usually based on estimates of the effective cross section of the elementary event in this process. At present, however, there is no common opinion on this problem.[1,2] We shall attempt therefore to put forward a phenomenological description of the effect of SGR on the decay rate of a long-lived isomer and to compare the relations thus obtained with the results of our experiments.

The rate of decrease of the concentration N of radioactive nuclei in a source can be described approximately by a differential equation

$$dN/dt = -\lambda N + bn\, dn/dt\,, \tag{2}$$

where b is a proportionality coefficient depending on the properties of the nucleus, gamma-photon energy, size and shape of the source, properties of the matrix material and so on. The first term on the right corresponds to spontaneous decay and, the second, to the SGR-induced depletion of the long-lived isomeric state. The rate of the second process is proportional to the concentration of radioactive nuclei N and the gamma-ray flux while the latter, in its turn, is proportional to the concentration-decay rate dN/dt. After simple manipulations we come to

$$dN/dt = -\lambda N(1 - bN)\,. \tag{3}$$

The solution of this equation has the form

$$N \exp(-bN) = N_0 \exp(-bN_0)\exp(-\lambda t)\,, \tag{4}$$

where N_0 is the initial concentration of radioactive nuclei.

For small values of parameter bN the dependence of the concentration on time differs only slightly from that in the case of spontaneous decay, $N = N_0 \exp(-\lambda t)$, and one can look for the solution in the form $N = N_0 \exp[-(\lambda + \Delta\lambda)\, t]$. In this case one obtains

$$\Delta\lambda/\lambda = bN_0\,. \tag{5}$$

Thus data on the temperature dependence of the decay rate of the MgO:^{123m}Te source permit one to determine the parameter bN_0 characterizing the SGR intensity in the 88-keV transition. This parameter has a direct bearing on empirical estimation of the possibility of lasing. According to Eq. (3), the decay rate tends to infinity as the bN parameter approaches one. This critical regime corresponds to the one-pass laser shot.

The value $\Delta\lambda/\lambda = bN_0 = 8.6\times 10^{-3}$ obtained by us suggests that the critical regime for ^{123m}Te can be reached by increasing the specific activity by two orders of magnitude for the same source geometry. Such an increase of specific activity appears technically feasible while very expensive. Another way of approaching the critical regime lies in increasing the parameter b. Its precise determination requires a special analysis, but it is clear that this parameter having the dimension of volume is the product of some effective cross section characterizing the properties of the nucleus by a characteristic length, which is the smaller of two quantities, namely, the sample size and the gamma-ray mean-free path in the source material. In our case they were approximately 1 and 3 cm, whence it is seen that one cannot reach the critical regime by increasing the dimensions of the source.

Finally, it should be pointed out that our estimates are of a purely qualitative character because they are based on the approximate relation (3). One can point out at least two phenomena which are disregarded in this equation; they are, first, the nonuniformity of the gamma-radiation field in the source, i.e., a coordinate dependence of parameter b, and second, nonlinear phenomena associated with approaching the critical regime.

Nevertheless the interpretation of our experimental data as a manifestation of SGR far from the critical regime appears fully substantiated. The current theoretical estimates of the smallness of SGR cross section[1] stem from the concept of a giant inhomogeneous broadening of the emission line. The same estimates prohibited observation of the Mössbauer effect on the long-lived level in ^{109}Ag. The recent observation of this phenomenon by two groups[5,6] casts doubt on the universal character of these estimates.

[1] V. I. Gol'danskiĭ, R. N. Kuz'min, and V. A. Namiot, in *Mössbauer Spectroscopy* [in Russian], Mir, Moscow (1983), p. 65.
[2] A. A. Zadernovsky, Laser Phys. **5**, 362 (1995).
[3] W. Bresser, M. Zhang, L. Koudelka, J. Wells, P. Boolchand, G. J. Ehrhart, and P. Miller, Phys. Rev. B **47**, 11663 (1993).
[4] A. G. Maddock, Radiochim. Acta **70-71**, 323 (1995).
[5] S. Rezaie-Serej, G. R. Hoy, and R. D. Taylor, Laser Phys. **5**, 240 (1995).
[6] V. G. Alpatov, A. V. Davydov, G. R. Kartashov, M. M. Koratkov, V. E. Rad'ko, A. A. Sadovskiĭ, and V. M. Samoĭlov, Izmerit. Tekhn. **38**, 52 (1995).

Translated by G. Skrebtsov

DEFECTS. DISLOCATIONS. PHYSICS OF STRENGTH

Migration of molecules in *p*-bromochlorobenzene with vacancies in its structure

V. F. Shabanov and M. A. Korshunov[1)]

L. V. Kirenskiĭ Institute of Physics, Russian Academy of Sciences, Siberian Branch, 660036 Krasnoyarsk, Russia

(Submitted March 10, 1998; resubmitted March 24, 1998)
Fiz. Tverd. Tela (St. Petersburg) **40**, 1835–1838 (October 1998)

Based on polarization measurements of the low-frequency Raman spectra of *p*-bromochlorobenzene and calculations of the frequency spectra of lattice vibrations by the Dean method it is shown that the structure may contain vacancies. Their presence affects the appearance of additional lines in the low-frequency spectrum, particularly in the vicinity of $70\ \mathrm{cm}^{-1}$, and their positions depend weakly on the orientational disorder of the molecules with respect to the *para* substituents. The activation energies for diffusion in a randomly disordered *p*-bromochlorobenzene crystal with vacancies in the structure is calculated from atom-atom potentials. It is shown that the value of the activation energy varies along a selected direction and depends on the arrangement of the *p*-bromochlorobenzene molecules with respect to the *para* substituents, in contrast to the results for ordered *p*-dibromobenzene and *p*-dichlorobenzene. © *1998 American Institute of Physics.* [S1063-7834(98)01410-5]

Low-symmetry organic crystals have become promising materials in molecular electronics, particularly for recording and processing information in optical computers.[1] In practice, crystals whose structure is not described by an ideal three-dimensional lattice are used. The presence of vacancies in the crystal causes the emergence of diffusion. This prevents a reduction in the size of the area needed to record information, since an increase in the recording density depends on the fact that the distance between two light beams passing through a sample can be reduced only as long as independent responses are observed. Gibbs noted in his book[2] that the occurrence of diffusion can lead to a need for increased separation of the light beams. In addition, a migrating molecule can alter the recorded information. This calls for an investigation of diffusion in molecular crystals.

Low-frequency Raman scattering can be used to determine the presence of vacancies in a crystal (whose presence is responsible for diffusion), since the presence of vacancies in a crystal affects the lattice vibrations and is thus manifested in the spectra.

The manifestations of vacancies in low-frequency spectra have heretofore been studied in molecular crystals consisting of centrosymmetric molecules.[3] However, crystals consisting of noncentrosymmetric molecules, such as, for example, *p*-bromochlorobenzene, are often employed in molecular electronics, yet the migration of molecules in a crystal of this compound has not been investigated.

p-Bromochlorobenzene is isomorphous with *p*-dibromobenzene and the α modification of *p*-dichlorobenzene, in which the migration of molecules has been studied.[3]

According to x-ray structural[4] and NQR[5] data, *p*-bromochlorobenzene crystallizes in the centrosymmetric $P2_1/a$ space group with two molecules in the unit cell owing to the statistically disordered arrangement of the molecules with respect to the *p*-substituted halogen atoms.

The spectrum of lattice vibrations of similar crystals should display six intense lines associated with orientational vibrations and three lines associated with translational vibrations.

The polarization measurements of the spectra of lattice vibrations of *p*-bromochlorobenzene showed that the spectrum contains a series of additional lines, whose intensity does not decrease significantly as the temperature is lowered to 77 K. Table I presents the values of the frequencies of the additional lines of *p*-bromochlorobenzene at room temperature and 77 K. The two lines with frequencies equal to 35 and $60\ \mathrm{cm}^{-1}$ at 77 K can be assigned to translational vibrations, in agreement with the data from the IR absorption spectra [36 and $59\ \mathrm{cm}^{-1}$ at 80 K (Ref. 6)]. Figure 1a shows the spectrum of *p*-bromochlorobenzene (the XY component of the scattering tensor) at 293 K. The additional lines in the spectrum of *p*-bromochlorobenzene can be caused both by the presence of disorder with respect to the *para* positions and the presence of vacancies. Manifestations of vacancies in the spectrum of lattice vibrations can be found by comparing the experimental spectra with spectra obtained from computer calculations with and without consideration of the presence of vacancies in the structure.

In the calculations of the spectra of lattice vibrations, the structure of the molecules was assumed to be absolutely rigid. The interaction between molecules was described by atom-atom potentials.[7] The coefficients in the interaction potential were the same as in the calculations of the spectra of the frequencies of *p*-dibromobenzene and *p*-dichlorobenzene in Ref. 3.

The spectra of the disordered crystals were calculated by the Dean method.[8] It permits finding the eigenvalues for

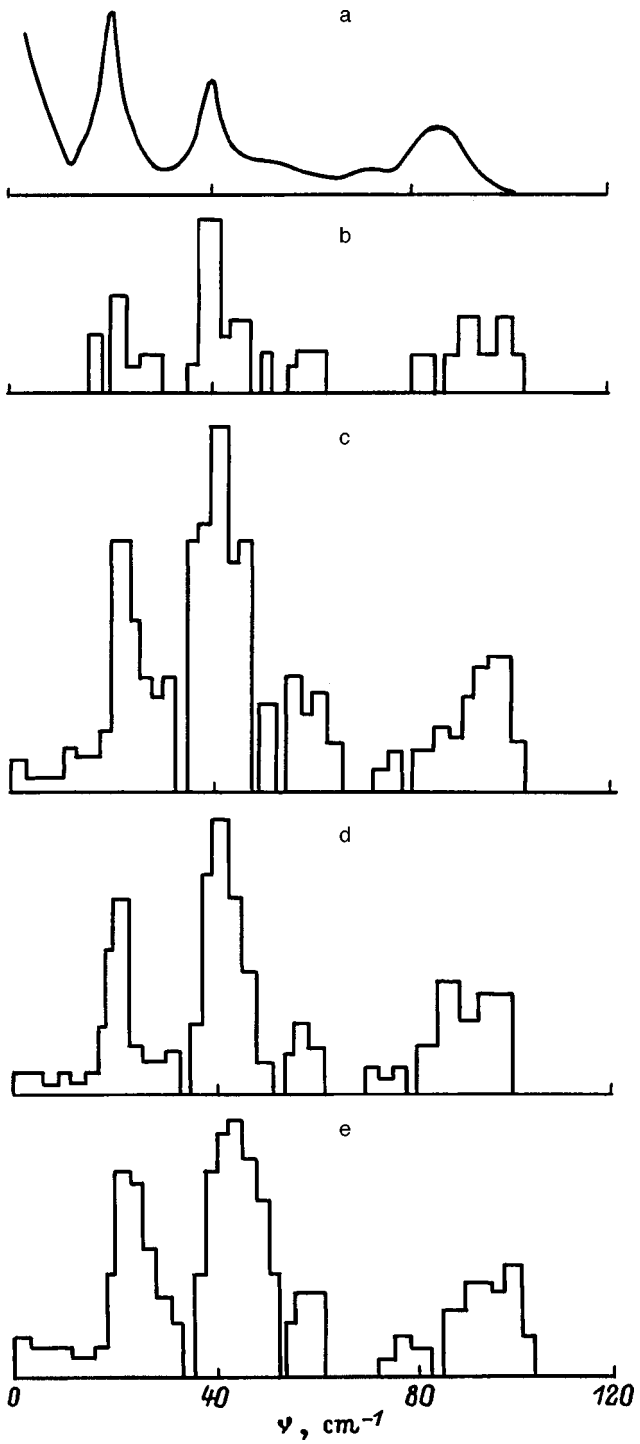

FIG. 1. Experimental low-frequency spectrum of *p*-bromochlorobenzene at 293 K (the *XY* component of the scattering tensor) (a) and histograms obtained from calculations with (c, d, e) and without (b) vacancies in the structure.

high-order matrices. The calculations yielded histograms, which show the probability of the appearance of spectral lines in a selected frequency range.

The histogram of the frequency spectrum of lattice vibrations without vacancies, but with consideration of disorder in the structure with respect to the *para* positions of *p*-bromochlorobenzene is presented in Fig. 1b. As can be seen, no lines are observed in the vicinity of 70 cm^{-1}, but additional peaks caused by disorder appear.

TABLE I. Experimental frequency values (in cm^{-1}) of the additional lines of *p*-bromochlorobenzene at 293 and 77 K.

293 K	77 K
19.5	20.0
-	35.0
-	60.0
72.0	73.0
-	80.0
-	90.0

The arrangement of the molecules in a crystal lattice with vacancies was found at the free-energy minimum. The minimization was carried out with respect to the orientations and displacements of the centers of gravity of the molecules taken into consideration.

Figure 1c shows the histogram of the spectrum of lattice vibrations of *p*-bromochlorobenzene with vacancies in the structure. As can be seen, additional lines appear in the vicinity of 70 cm^{-1}.

There can be differences in the arrangement of the molecules (with respect to the *para* substituents) surrounding a migrating molecule, which affect the migration energy of the molecule. They can also be reflected in the low-frequency spectra. Figures 1d and 1e show histograms of the spectra of lattice vibrations calculated for two energetically stable arrangements of the molecules. Each of the arrangements is assigned by a dominant arrangement in the structure of the crystal whose histogram is presented in Fig. 1c. As is seen from the histograms, although the positions of the maxima vary somewhat, the lines in the vicinity of 70 cm^{-1} caused by the presence of vacancies in the structure appear in both cases.

Thus, it can be concluded that an unordered crystal of *p*-bromochlorobenzene contains vacancies, which give rise to diffusion in the crystal. The position of the lines in the vicinity of 70 cm^{-1} associated with the presence of vacancies in the structure depends weakly on the orientational disorder of the molecules with respect to the *para* substituents.

Using the same coefficients in the interaction potential as in the calculation of the spectra of lattice vibrations, we calculated the lattice energy, the energy of vacancy formation, and the migration energy of *p*-bromochlorobenzene molecules.

The lattice energy E_L for the molecular arrangement in the structure of *p*-bromochlorobenzene used to obtain the histogram in Fig. 1c is $E_L = 16.7$ kcal/mol.

In the calculations of the structure the positions of the vacancies were assigned, and the equilibrium configuration was found. When the molecules relaxed, the energy of *p*-bromochlorobenzene varied by the amount E_R. For the arrangement of molecules chosen it amounts to $E_R = 0.6$ kcal/mol. The formation energy of vacancies E_f in this case amounts to $E_f = 16.1$ kcal/mol.

When the migration of molecules was considered, a molecule was displaced from the position at (0,0,0) in 0.2-Å steps along a chosen direction toward a vacancy. The energy

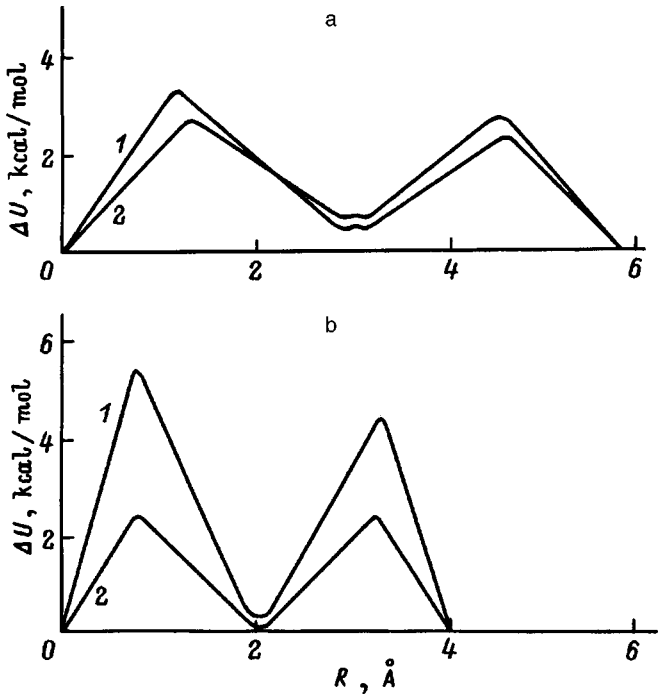

FIG. 2. Variation of the potential energy upon displacement of a migrating *p*-bromochlorobenzene molecule toward a vacancy in the [010] (a) and [001] (b) crystallographic directions: *1*—for a disordered (with respect to the *para* positions) arrangement of the surrounding molecules, *2*—for an ordered arrangement.

was minimized in each step. Figure 2 presents plots of the variation of the potential energy as a *p*-bromochlorobenzene molecule is displaced along the crystallographic directions [001] (b) and [010] (a).

As a consequence of the different arrangements of *p*-bromochlorobenzene molecules (with respect to the *para* positions), the environment of the migrating molecule is different for different points in the crystal. Depending on the arrangement of the molecules around a vacancy, the plots of the variation of the potential as the molecules are displaced can be either symmetric or asymmetric relative to the middle of the plot. Examples of this are presented in Fig. 2. Curves *1* (in Fig. 2) for the [001] and [010] crystallographic directions are asymmetric. These curves were obtained for one of the possible disordered (with respect to the *para* positions) arrangements of the molecules surrounding the migrating molecule. The curves are asymmetric because the arrangement of the molecules (and their interaction with the migrating molecule) for the point from which the molecule migrates differs from the environment around the point where the vacancy is located. Curves *2* in Fig. 2 were obtained for an ordered arrangement of the molecules.

Thus, it is seen that, unlike the case of ordered *p*-dibromobenzene with centrosymmetric molecules, the value of the migration energy can differ from cell to cell for the same migrating molecule.

In the cases considered the migration energy along the [010] crystallographic direction has the values $E_{m1}^{[010]}=3.3$ kcal/mol and $E_{m2}^{[010]}=2.8$ kcal/mol. The positions of the maxima (along the horizontal axis) for them are different. After passing the maximum on curves *2*, there is sharper variation of the orientation of the migrating molecule. The angle between the planes of the undisplaced and displaced molecules after passage of the maximum equals about 60° in all the cases considered.

The migration energy of *p*-bromochlorobenzene molecules along the [001] crystallographic direction has the values $E_{m1}^{[001]}=5.5$ kcal/mol and $E_{m2}^{[001]}=2.5$ kcal/mol in the cases considered. The positions of the maxima for both cases scarcely changed.

The results of the calculations of the activation energy show that its value also varies. The values for the [010] crystallographic direction are $E_{d1}^{[010]}=19.4$ kcal/mol and $E_{d2}^{[010]}=18.9$ kcal/mol. In the [001] direction the values are $E_{d1}^{[001]}=21.6$ kcal/mol and $E_{d2}^{[001]}=18.6$ kcal/mol, respectively.

Therefore, unlike centrosymmetric *p*-dibromobenzene, whose activation energy is larger along the [001] crystallographic direction than along the [010] direction, in *p*-bromochlorobenzene the activation energy can vary as a function of the arrangement of the molecules with respect to the *para* substituents. In this case variation of the direction of diffusion from cell to cell is possible [either the molecule can migrate along the (001) or (010) direction, or the directions are equally preferable]. Apparently, when the experimental results on the activation energy in *p*-bromochlorobenzene are compared with the calculated values, the averaged values of the energy along the respective direction should be considered.

Thus, it has been shown that there are vacancies in the structure of *p*-bromochlorobenzene. Their presence affects the appearance of the additional lines in the vicinity of 70 cm^{-1} in the spectrum of lattice vibrations, in agreement with the data on *p*-dibromobenzene and *p*-dichlorobenzene. The positions of the lines in the vicinity of 70 cm^{-1} depend weakly on the orientational disorder of the molecules with respect to the *para* substituents. Calculations of the activation energy in *p*-bromochlorobenzene have shown that, in contrast to the case of *p*-dibromobenzene, it is not a constant along the crystallographic direction selected, but depends on the arrangement of the *p*-bromochlorobenzene molecules with respect to the *para* substituents.

[1)]E-mail: mspec@iph.krasnoyarsk.su

[1] *New Physical Principles of the Optical Processing of Information*, edited by S. A. Akhmanov and M. A. Vorontsov [in Russian], Moscow (1990), p. 399.
[2] H. M. Gibbs, *Optical Bistability: Controlling Light with Light*, Academic Press, Orlando (1985); Mir, Moscow (1988).
[3] V. F. Shabanov and M. A. Korshunov, Fiz. Tverd. Tela (St. Petersburg) **37**, 3463 (1995) [Phys. Solid State **37**, 1902 (1995)].
[4] A. I. Kitaĭgorodskiĭ, *X-Ray Structural Analysis* [in Russian], Moscow (1950), 650 pp.
[5] V. S. Grechishkin, *Nuclear Quadrupole Coupling in Solids* [in Russian], Nauka, Moscow (1973), 263 pp.
[6] M. B. Wincke, A. Hadni, and X. Gerbaux, J. Phys. (Paris) **31**, 893 (1970).
[7] A. I. Kitaĭgorodskiĭ, *Molecular Crystals* [in Russian], Moscow (1971), 424 pp.
[8] P. Dean, Rev. Mod. Phys. **44**, 127 (1972).

Translated by P. Shelnitz

Influence of temperature and strain on the amplitude-dependent internal friction of high-purity aluminum

S. N. Golyandin, K. V. Sapozhnikov, Yu. A. Emel'yanov, A. B. Sinani, and S. P. Nikanorov

A. F. Ioffe Physicotechnical Institute, Russian Academy of Sciences, 194021 St. Petersburg, Russia

S. B. Kustov

Institute de Génie Atomique, Département de Physique, École Polytechnique Fédérale de Lausanne, CH-1015 Lausanne, Switzerland

W. H. Robinson

Penguin Engineering Ltd. (PEL), P.O. Box 33, 093 Petone, New Zealand
(Submitted April 10, 1988)
Fiz. Tverd. Tela (St. Petersburg) **40**, 1839–1844 (October 1998)

The dislocation amplitude-dependent friction (ADIF) of high-purity (99.999%) polycrystalline aluminum is investigated in the temperature range 7–300 K at vibrational strain amplitudes of $10^{-7}-10^{-4}$ for samples in the annealed and deformed (by quasistatic, shock, and ultrasonic loading) states. The ADIF is a multistage effect in the indicated temperature and vibration amplitude ranges. Analysis of the amplitude-temperature spectra of the ADIF permits separation of components attributable to: interaction between dislocations, the interaction of dislocations with pinning points, and pure dislocation relaxation (the interaction of dislocations with the Peierls relief). ADIF is observed to depend nonmonotonically on the initial quasistatic strain determined by strain hardening and recovery processes. © *1998 American Institute of Physics.* [S1063-7834(98)01510-X]

Metals having a face-centered cubic lattice are classical objects for research in the dynamics of materials in high-velocity impact tests.[1] From a practical standpoint pure fcc metals having a low melting point also have promising seismic safety applications as the working medium of extrusion dampers.[2] The internal friction method is widely used in studying the dynamics of crystal defects. Here we report an investigation the influence of quasistatic, shock, and ultrasonic loading on the amplitude-dependent internal friction (ADIF) of high-purity (99.999%) aluminum. Investigations of aluminum of various purities frequently indicate that ADIF has a multistage character resulting from the contributions of diverse microstructural mechanisms.[3–6] Unfortunately, the roles and interconnection of the various microstructural mechanisms have never really been examined. To obtain a clearer picture of the micromechanisms of ADIF and the dynamics of defects in fcc metals, we have undertaken a study of ADIF in high-purity aluminum subjected to various mechanical effects over a wide range of temperatures and vibrational strain amplitudes.

1. EXPERIMENTAL PROCEDURE

The internal friction was measured by means of a sectional, longitudinal-mode piezoelectric vibrator[7] operating at a frequency of approximately 100 kHz. Automated equipment[8] was used in conjunction with a helium cryostat to facilitate simultaneous recording of the temperature spectra of the amplitude-dependent and amplitude-independent internal friction and the effective Young's modulus in the temperature range 7–300 K, and also so that the internal friction and modulus defects could be measured at arbitrary temperatures as functions of the vibrational strain amplitude in the range $10^{-7}-10^{-4}$. The rate of change of the temperature in the measurements was approximately 0.02 K/s.

Polycrystalline samples of approximate dimensions $2\times3\times25$ nm were cut from an ingot of Mark A3 high-purity aluminum (99.999% pure with an average grain diameter of 1 mm) by electric-spark cutting. After removing the rough surface layer to a thickness of approximately 0.2 mm in a concentrated Keller reagent (100 ml HNO_3, 50 ml HCl, and 1.5 ml HF), the samples were annealed for 7200 s at 420 K.

The samples were subjected to quasistatic deformation by compression along the shortest axis in an Instron 1341 hydraulic testing machine with the clamps moving at a rate of 0.002 mm/s. High-velocity loading of the samples by a plane shock wave was performed under conditions such as to preserve the shape of the samples. Stress pulses having a duration of approximately 2×10^{-6} s and amplitudes in the range $\sigma_{pls}=0.4-3.7$ GPa were generated by a projectile accelerated in a light-gas gun.[9] The acoustical procedure permitted ultrasonic loading of the samples at a vibrational strain amplitude in excess of 10^{-4}. For high-purity aluminum this strain amplitude falls within the range where microplastic deformation and fatigue phenomena occur.[3]

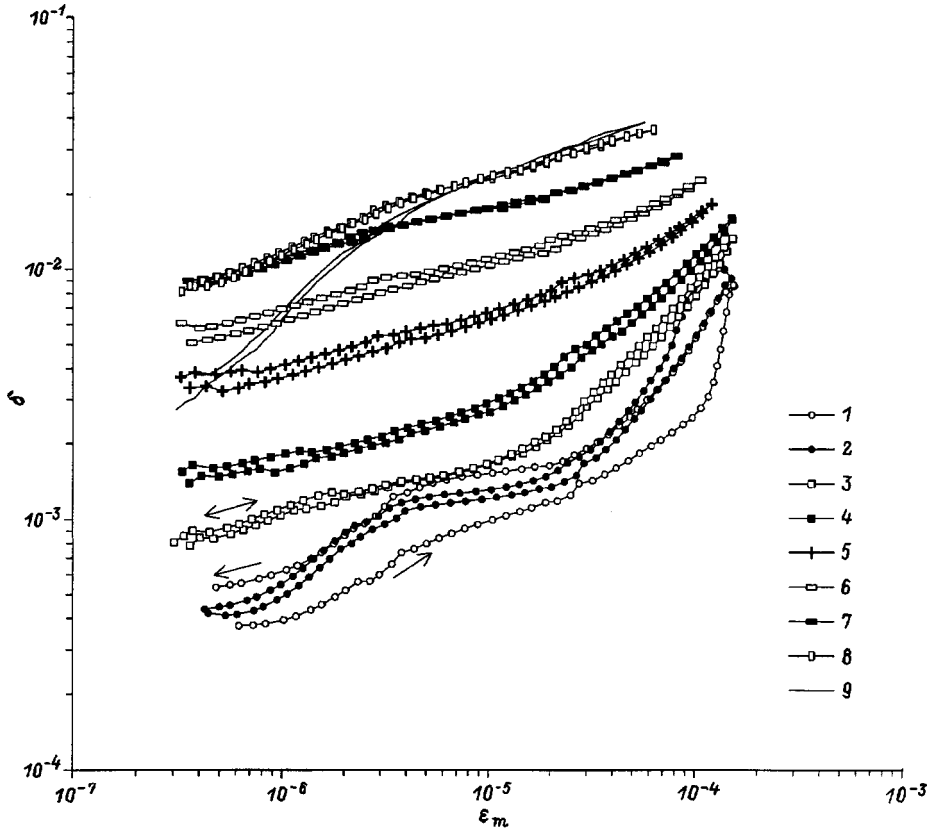

FIG. 1. Logarithmic decrement of the vibrations of an aluminum sample versus vibrational strain amplitude, measured during heating to various temperatures after ultrasonic deformation at a temperature of 10 K. *1* — $T=10$ K; *2* — 24 K; *3* — 56 K; *4* — 86 K; *5* — 124 K; *6* — 154 K; *7* — 194 K; *8* — 255 K; *9* — 309 K.

2. INFLUENCE OF TEMPERATURE ON THE AMPLITUDE-DEPENDENT INTERNAL FRICTION OF ALUMINUM

Figure 1 shows the logarithmic decrement of a high-purity aluminum sample as a function of the vibrational strain amplitude ε_m, measured in an annealed sample at 10 K and during subsequent heating. The high-amplitude ultrasonic loading of annealed aluminum crystals is accompanied by a sudden increase in the ADIF at $\varepsilon_m > 10^{-4}$ and amplitude hysteresis of the ADIF (which is lower when the amplitude increases than when it is subsequently decreased). An example of this behavior is presented by curve *1* in Fig. 1 measured at 10 K. At temperatures $T<180$ K amplitude hysteresis of the ADIF is all but nonexistent if the maximum value of ε_m in the measurements does not exceed the value attained in the preceding low-temperature measurements. This result attests to the stability of the ADIF-inducing defect structure formed by high-amplitude loading at low temperatures.

Analyzing the data in Fig. 1, we discern three distinct temperature intervals. At low temperatures ($T<60$ K) ADIF exhibits a multistage behavior. The saturation observed in the growth of ADIF at $\varepsilon_m = 10^{-6} - 10^{-5}$ is superseded by an abrupt increase in the ADIF at higher amplitudes $\varepsilon_m \sim (2-3)\times 10^{-5}$. At moderate temperatures ($T=60-180$ K) and moderate vibration amplitudes the ADIF depends strongly on the temperature, but only slightly on ε_m, revealing a more or less well-defined microplastic stage at high vibration amplitudes ($\varepsilon_m > 10-5$). At high temperatures ($T>180$ K) the ADIF tends to abate as the temperature rises, though only at low to moderate vibration amplitudes.

An analysis of the data obtained at low and moderate temperatures enables us to discriminate the components δ_1, δ_2, and δ_3 responsible for the formation of the ADIF amplitude-temperature spectra. Figure 2 shows the strain-amplitude dependence of the internal friction, measured as the vibration amplitude is increased (except for curve *1*, which has been measured at $T=10$ K with decreasing ε_m). Background amplitude-independent internal friction is not observed in the investigated range of ε_m. At moderate temperatures and vibration amplitudes (curves *4–6* in Fig. 2) the ADIF curves are well approximated over a wide range ($\varepsilon_m = 5\times 10^{-7} - 2\times 10^{-5}$) by an exponential function:

$$\delta_1 = \varepsilon_m^n f_1(T), \tag{1}$$

where n is a temperature-independent coefficient, and $f_1(T)$ is a certain function of the temperature. These functions are represented by dashed lines in Fig. 2. At higher vibration amplitudes we observe a microplastic stage, which is more pronounced at low temperatures. In this amplitude range the temperature dependence of the ADIF subsides considerably as ε_m increases. We can assume therefore that the high-amplitude ADIF has a common asymptote, which is essentially independent of the temperature. To test this assump-

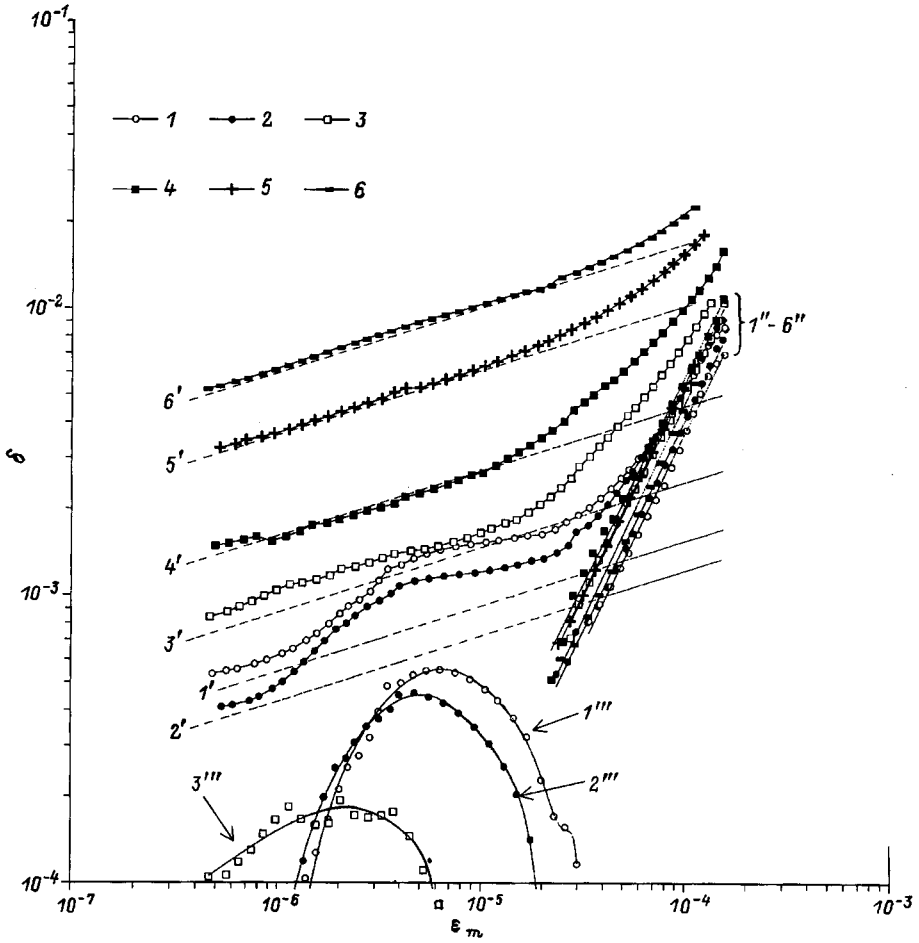

FIG. 2. Separation of the amplitude curves of the logarithmic decrement of an aluminum sample, measured at low and moderate temperatures, into components attributable to: interaction between dislocations, the interaction of dislocations with pinning points, and pure dislocation relaxation (interaction of dislocations with the Peierls relief). *1* — $T=10$ K; *2* — 24 K; *3* — 56 K; *4* — 86 K; *5* — 124 K; *6* — 154 K. The dashed lines *1′–6′* represent the approximation $\delta_1=\varepsilon_m'' f_1(T)$ at the temperatures of curves *1–6*, with n evaluated from curves *4–6*. Lines *1″–6″* correspond to $\delta_2=\delta-\delta_1$ for the temperatures of curves *1–6*. Curves *1‴–3‴* correspond to $\delta_3=\delta-(\delta_1+\delta_2)$ at low temperatures for the temperatures of curves *1–3*.

tion, we have separated the ADIF as follows: a) The ADIF at moderate temperatures (curves *4–6* in Fig. 2 is approximated by the exponential functions (1); b) the microplastic ADIF component is obtained by subtracting the functions (1) from the initial experimental curves. The resulting microplastic ADIF component is also well approximated by an exponential function

$$\delta_2=\varepsilon_m^k f_2(T), \tag{2}$$

where the exponent $k\gg n$, and $f_2(T)$ is a very weak function of the temperature.

It is difficult to determine the values of $f_1(T)$ at $T<80$ K, because the ADIF is a multistage effect in this temperature range, even at moderate amplitudes ε_m. However, since the low-temperature microplastic ADIF component is much more pronounced (note the logarithmic scale of Fig. 2), the choice of values of $f_1(T)$ affects only the initial stage of the resulting amplitude dependence of the microplastic component. Assuming then that n and k remain constant down to the lowest temperatures, we can separate the ADIF into components, achieving the best approximation of the microplastic component of the exponential function (2) with a single exponent k at all temperatures. The results of the separation are shown in Fig. 2 (curves *1–3*). They reveal the existence of three ADIF components,

$$\delta_3=\delta-(\delta_1+\delta_2), \tag{3}$$

which are responsible for the distinctive features of the ADIF at low temperatures ($T<60$ K) and moderate amplitudes ε_m. The third ADIF component given by Eq. (3) discloses a maximum in its dependence on ε_m. We note that, strictly speaking, the ADIF should be scaled from the sample to the material. However, this kind of adjustment does not qualitatively alter the results. Especially noteworthy is the strong temperature dependence of the position of the maximum of the third ADIF component on the amplitude scale and its height, observed under conditions when the defect structure responsible for ADIF is stable (i.e., when the ADIF does not exhibit amplitude hysteresis). These details are consistent with theoretical inferences[10] as to the nonlinear process of pure dislocation relaxation (the interaction of dislocations with the Peierls relief). They are observed at temperatures much lower than the Bordoni relaxation temperature ($\sim$150 K in aluminum at a frequency of approximately 100

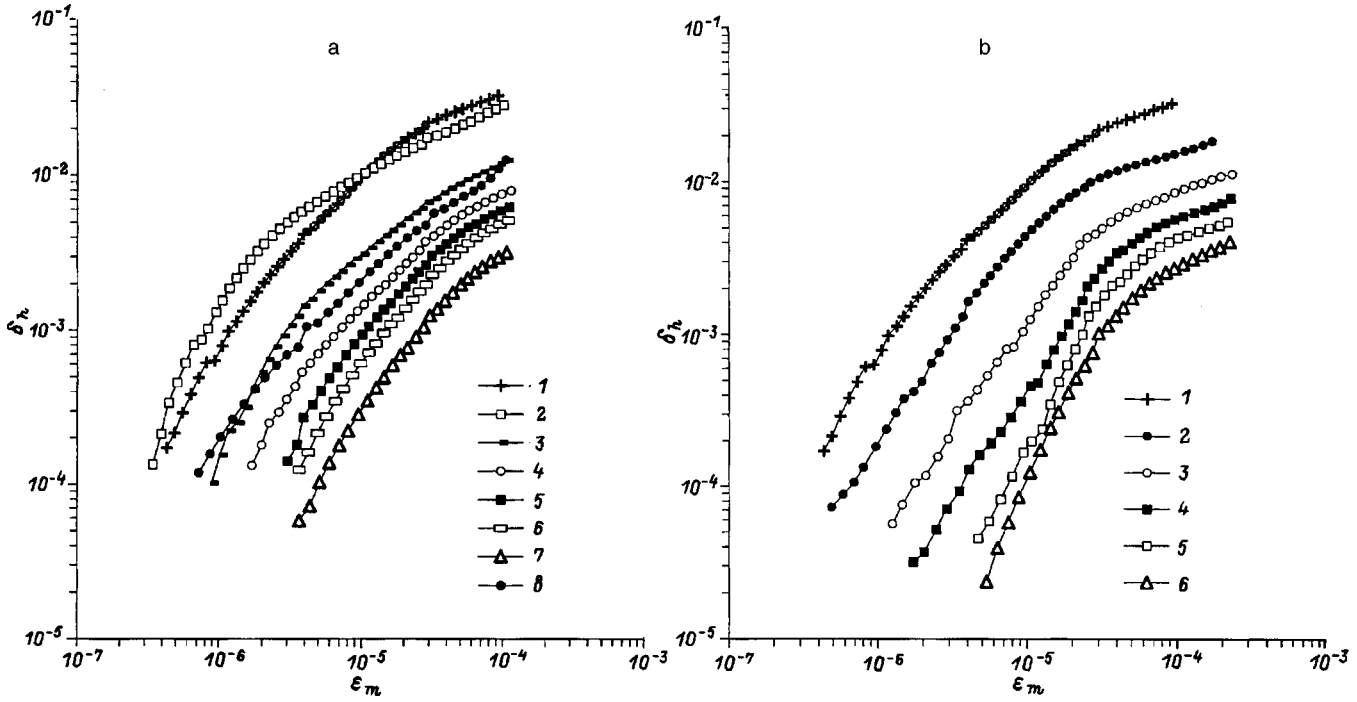

FIG. 3. Influence of quasistatic (a) and shock (b) loading on the amplitude-dependent part of the logarithmic decrement of aluminum samples. a) True strain: *1* — 0; *2* — 0.01; *3* — 0.02; *4* — 0.046; *5* — 0.091; *6* — 0.223; *7* — 0.328; *8* — 0.693; b) Stress pulse amplitude: *1* — 0; *2* — 0.4 GPa; *3* — 0.6 GPa; *4* — 1.2 GPa; *5* — 2.9 GPa; *6* — 3.7 GPa.

kHz), consistent with the mechanism underlying the formation of paired kinks in the presence of point defects (vacancies).[11] In our tests an excess density of vacancies in aluminum was formed as a result of microplastic deformation of the sample by high-amplitude ultrasound at 10 K.

The multistage behavior of the ADIF indicates a change of ADIF mechanisms as the temperature or the vibration amplitude or both are varied. In the first high-amplitude ultrasonic loading at low temperature fresh dislocations are formed as a result of either dislocation multiplication or the unpinning of older dislocations from pinning Cottrell atmospheres. The evolved dislocation structure remains stable during subsequent loading up to $T \approx 180$ K. At $T > 180$ K the ADIF acquires a time dependence and amplitude hysteresis simultaneously with the onset of ADIF abatement at low and moderate amplitudes ε_m. This effect indicates the formation of atmospheres of mobile point defects around dislocations that contribute to ADIF. It is reasonable to assume, therefore, that the highly temperature-dependent ADIF component approximated by Eq. (1) in Fig. 2 corresponds to the motion of dislocations without pinning atmospheres. The exponential function $\delta(\varepsilon_m)$ does not become straight in Granato-Lücke coordinates; this feature is typical of a ''nonlocalized'' friction mechanism.[12] We can therefore conclude that this ADIF component is attributable to thermally activated dislocation motion in the fields of pinning points randomly distributed in the dislocation glide planes.

Inasmuch as dislocation multiplication does not occur in low-temperature measurements after the first high-amplitude loading of an aluminum crystal, the microplastic ADIF component can be identified, as in polycrystalline lead,[13] with interaction between dislocations. The very weak temperature dependence of the this component is in good agreement with the athermal nature of long-range interactions between dislocations (strictly speaking, the temperature dependence of Young's modulus should be taken into account).

The thermally activated ADIF component induced by the interaction of dislocations with point defects precedes the athermal microplastic component on the ε_m scale. It is important to note that the substantial temperature variations of the thermally activated component do not influence the microplastic component. Consequently, these components are essentially independent at ultrasonic frequencies. Hence, the microplastic ADIF component is most pronounced at low temperatures, when the thermally activated component is suppressed.

3. INFLUENCE OF QUASISTATIC AND SHOCK LOADING ON THE AMPLITUDE-DEPENDENT INTERNAL FRICTION OF ALUMINUM

Figure 3 illustrates the influence of quasistatic and shock loading at room temperature on the ADIF of high-purity aluminum. Quasistatic loading took place by subjecting a single sample to incremented compression. The influence of shock loading was investigated on several samples stressed by pulses of various amplitudes. Two stages are discernible in the strain-amplitude curves of the internal friction in Fig. 3. The internal friction increases fairly quickly as the vibration amplitude is increased at $\varepsilon_m < (2-3)\times 10^{-5}$. At higher amplitudes ε_m the increase in the ADIF becomes smoother. A comparison of Figs. 3a and 3b shows that the first stage shifts toward higher values of ε_m in shock-loaded samples.

The dependence of ADIF on the true strain in quasistatic

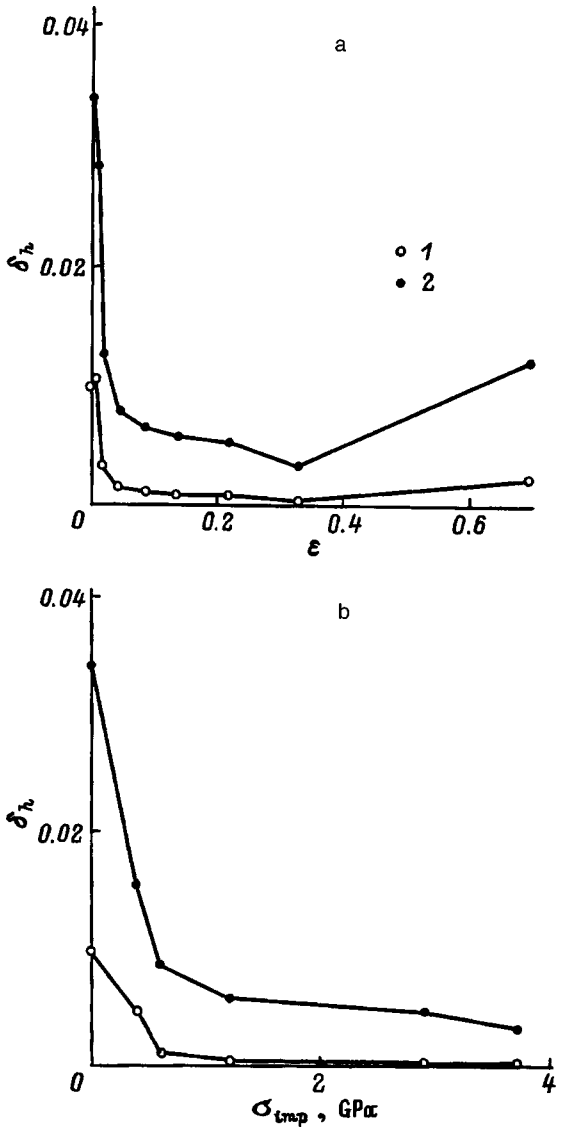

FIG. 4. Amplitude-dependent internal friction of aluminum samples at fixed vibrational strain amplitudes equal to 10^{-5} (*1*) and 10^{-4} (*2*) versus true strain in quasistatic loading (a) and versus stress pulse amplitude in shock loading (b).

loading or on the amplitude of the stress pulse in shock loading at two fixed amplitudes ε_m is shown in Fig. 4. ADIF depends monotonically on the initial quasistatic strain (Fig. 4a). For a not-too-large initial strain ($\sim 1\%$) an ADIF maximum is recorded, but only at moderate values of ε_m (see also curves *1* and *2* in Fig. 3a). Upon further deformation the ADIF is observed to drop considerably over the entire range of ε_m (Figs. 3a and 4a) and then, at the maximum initial strain, it rises again. As the stress pulse in shock loading is increased, the ADIF decreases monotonically over the entire investigated range of $\sigma_{\rm pls}$ (Figs. 3b and 4b).

Our analysis of the influence of temperature on ADIF in high-purity aluminum in Sec. 2 helps to explain the multistage character of the ADIF, observed at room temperature. The distinctive characteristics of the ADIF at $T>180$ K leads to the conclusion that the initial ADIF stage ($\varepsilon_m<5\times10^{-5}$) at room temperature corresponds to the interaction of dislocations with Cottrell vacancy atmospheres. Stage III recovery of the electrical resistance due to the bulk diffusion of vacancies is known to be observed at these temperatures in aluminum. The saturation of the ADIF at high amplitudes ε_m is attributable to the transition of dislocations into the atmosphere-free state observed in newly deformed samples at $T<180$ K.

The observed dependence of ADIF on the initial quasistatic strain in the case of aluminum is qualitatively similar to the dependence obtained for lead.[13] The suppression of ADIF with rising initial deformation is explained by growth in the dislocation density lowering their mobility.[13] The growth of the ADIF at large strains, accompanied by lowering of the elastic limit of the crystals, has been associated with the transition to a more inhomogeneous dislocation structure due to the formation of dislocation cells.[13] An ADIF minimum has been observed for lead[13] at lower strains, fully consistent with its lower homological temperature relative to aluminum.

The influence of shock loading on the ADIF is qualitatively similar to the influence of quasistatic deformation. ADIF exhibits a clearly visible tendency to diminish as the stress pulse is increased. However, there are also qualitative differences. The first ADIF stage is steeper and shifted toward higher amplitudes ε_m in shock-loaded samples (see Fig. 3). The slope of the second ADIF stage is identical for shock- and quasistatically deformed samples. Consequently, the difference between the first ADIF stages can be attributed to the formation of denser Cottrell vacancy atmospheres in the shock-loaded samples.

This work has received financial support from the Russian Fund for Fundamental Research (Grant 96-01-01207a).

[1] *Shock Waves and High-Strain Rate Phenomena in Metals*, edited by M. A. Meyers and L. A. Murr (Plenum Press, New York–London, 1981).
[2] R. I. Skinner, W. H. Robinson, and G. H. McVerry, *An Introduction to Seismic Isolation* (Wiley, Chichester, 1993).
[3] W. P. Mason, J. Acoust. Soc. Am. **28**, 1207 (1956).
[4] T. S. Hutchison and D. H. Rogers, J. Appl. Phys. **33**, 792 (1962).
[5] D. Gelli, Phys. Status Solidi **12**, 829 (1965).
[6] P. Peguin, J. Perez, and P. Gobin, Trans. Metall. Soc. AIME **239**, 438 (1967).
[7] W. H. Robinson and E. Edgar, IEEE Trans. Sonics Ultrason. **SU-21**, 98 (1974).
[8] S. B. Kustov, B. K. Kardashev, V. I. Ivanov, S. N. Golyandin, Yu. A. Burenkov, S. P. Nikanorov, V. M. Chernov, H. Lüft, G. Mattauch, E. Hegenbarth, and Ü. Schreiber, Preprint FÉI-2141 [in Russian], Physics and Power Institute, Obninsk (1990), 22 pp.
[9] N. A. Zlatin, S. M. Mochalov, G. S. Pugachev, and A. M. Bragov, Zh. Tekh. Fiz. **45**, 681 (1975) [Sov. Phys. Tech. Phys. **20**, 428 (1975)].
[10] G. Fantozzi, C. Esnouf, W. Benoit, and I. G. Ritchie, Prog. Mater. Sci. **27**, 311 (1982).
[11] W. Benoit, G. Gremaud, and B. Quenet, Mater. Sci. Eng., A **164**, 42 (1993).
[12] G. Gremaud, J. Phys. Colloq. **48**, C8-15 (1987).
[13] S. Kustov, S. Golyandin, K. Sapozhnikov, and W. H. Robinson, Mater. Sci. Eng., A **237**, 191 (1997).

Translated by James S. Wood

Low-temperature photoluminescence determination of dislocation slip systems in CdSe single crystals

N. I. Tarbaev

Institute of Semiconductor Physics, Academy of Sciences of Ukraine, 252650 Kiev, Ukraine
(Submitted March 16, 1998)
Fiz. Tverd. Tela (St. Petersburg) **40**, 1845–1848 (October 1998)

The transformation of the low-temperature emission spectrum of cadmium selenide crystals during plastic deformation by a point load and by uniaxial compression is investigated. A one-to-one correspondence is established between the occurrence of photoluminescence bands in the vicinity of 1.765 eV and the motion of dislocations in the prismatic slip system, on the one hand, and the emergence of a 1.792-eV band as a result of dislocation slip in the basal plane, on the other. © *1998 American Institute of Physics.* [S1063-7834(98)01610-4]

Bulk cadmium selenide single crystals are used in all-optical actuator elements. Moreover, owing to the nonlinear absorption of light in the exciton region of the spectrum, this material has a promising potential for the development of resonant and nonresonant high-speed optical switches capable of implementing basic logic operations, and also for the design of optical computers.[1] For this reason, the investigation of structure defects that contribute to the formation of density-of-state tails near the fundamental absorption edge and the development of methods for such investigations are timely issues. In the majority of technological operations, semiconductor single crystals are subjected to some degree of mechanical effects, which can lead to local plastic deformation, i.e., the generation of dislocations and deformation point defects.[2]

Characteristic bands have been discovered comparatively recently in the emission and optical absorption spectra of cadmium sulfide crystals, which have the same crystal structure (wurtzite) as cadmium selenide. The bands are formed during dislocation slip in the prismatic slip system.[3,4] Like CdS crystals, a series of bands associated with plastic deformation have been observed in the photoluminescence spectra of CdSe crystals plastically deformed at a low temperature[5] and in CdTe (sphalerite) crystals.[6]

The objective of the present study is to investigate the correlation of the low-temperature (4.2–77 K) photoluminescence spectrum and the active dislocation slip system. Two dislocation slip systems appear at a temperature lower than half the melting point of CdSe crystals: one in the basal (0001) plane and one in the prismatic {1010} plane with exactly the same Burgers vector $\mathbf{b}=1/3\langle 1120\rangle$ (Ref. 2). Indentation of the {0001} and {1010} faces was chosen as the method to initiate slip in either system. A comparative analysis of the spectra is useful in this case, because the deformed regions of the crystal and the regions undistorted by plastic deformation are situated on one surface of the same sample.

THE EXPERIMENT

Special undoped cadmium selenide single crystals grown by the Bridgman technique were investigated. The samples were cut from x-ray oriented ingots, mechanically ground, polished with diamond paste, and then polished chemically in a bromine-methyl alcohol solution to remove the contaminated outer layer. Plastic deformation took place either by local indentation with a Vickers pyramid under a 30-g load for 60 s or by uniaxial compression; the temperature was 77 K in both cases. To achieve an overall increase in the photoluminescence signal from the deformed regions, the indentation was performed in 4×4 series, i.e., in a pattern of 16 square impressions 150 μm on a side. The photoluminescence was recorded by an FÉU-62 photomultiplier through an MDR-23 grating monochromator (1200 lines/mm). Photoluminescence was excited by an LGN-215 632.8-nm helium-neon laser focused to a spot diameter of 50 μm.

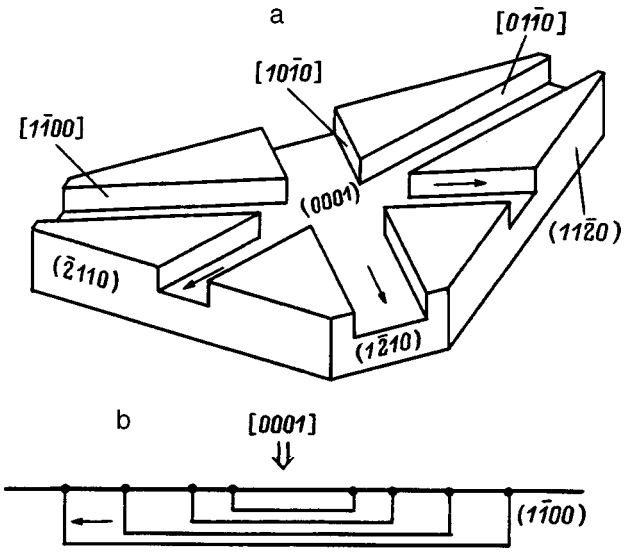

FIG. 1. Schematic diagram of slip forming a dislocation rosette in indentation of the {0001} face. The arrows indicate equivalent orientations of the Burgers vector. a) dislocation slip system; b) positions of half-loops of dislocations slipping in the prismatic plane. The broad vertical arrow indicates the indentation site. The dots represent outcroppings of dislocations on the top face.

INDENTATION OF THE {0001} FACE.

The slip around the indentor impression can be nominally divided into two processes: dislocation slip with the Burgers vectors parallel to the indented surface, i.e., rosette slip, and with the Burgers vectors canted relative to the surface, i.e., volume slip. Since the radiation used for excitation is strongly absorbed, only regions near the surface contributed to the photoluminescence signal, so that the discussion can be confined to rosette slip only. Rosette slip on the {0001} face is characterized by the formation of rays in the directions +/−[1120], +/−[2110], and +/−[1210]. The rosette slip pattern is shown schematically in Fig. 1. Here dislocation half-loops slipping in equivalent prismatic planes break out directly on the top face of the crystal (Fig. 1b), whereas dislocations slipping in the basal (0001) plane move parallel to the top face at a certain depth from it (Fig. 1a).

We now consider the transformation of the low-temperature photoluminescence spectrum after indentation. The initial photoluminescence spectrum of CdSe in the vicinity of the fundamental absorption edge at 4.2 K consists of a group of narrow lines representing exciton-impurity complexes (EICs) in the vicinity of 1.824 eV and their phonon replicas (curve *1* in Fig. 2), and a series of bands separated by the lattice *LO*-phonon energy with the nonphonon 1.728-eV line, which are associated with radiative recombination through donor-acceptor pairs.[7] The photoluminescence spectrum at 4.2 K from the region of indentations on the {0001} face exhibit three strong bands: 1.7645 eV, 1.7731 eV, and 1.792 eV, which do not exist in the as-grown crystals (curve *2* in Fig. 3). In the figure the bands are labeled *a*, *b*, and *c*, respectively. The emergence of the new photoluminescence bands is observed against the background of a slight decrease in the photoluminescence intensity through donor-acceptor pairs (10–20%) and a sizable (severalfold) drop of the intensity and broadening of the EIC lines. The latter effect is probably attributable to the large

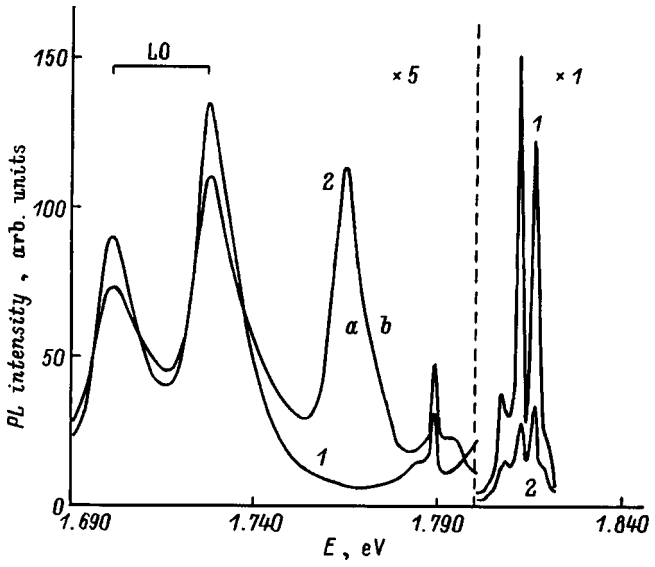

FIG. 2. Photoluminescence spectra of CdSe single crystals at 4.2 K before deformation (*1*) and after low-temperature plastic deformation by uniaxial compression (*2*), observed along a direction normal to the **C** axis.

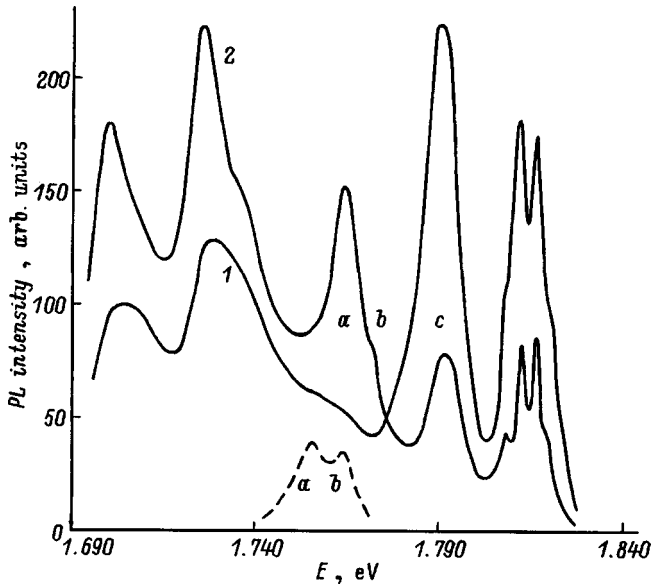

FIG. 3. Photoluminescence spectra from the zone of indentation of the {1010} face (*1*) and the {0001} face (*2*) at 4.2 K. The dashed curve represents the position of the band group *a b* at 77 K.

cross section of inelastic scattering of the excitations by dislocations.[8] The bands associated with plastic deformation have a relatively small half-width (approximately 9 meV), which is approximately one half the half-width of the 1.728-nm nonphonon band of recombination through donor-acceptor pairs.

As the temperature increases, the plastic deformation-induced emission bands *a*, *b*, and *c* shift toward the long-wavelength end as does the fundamental absorption edge of the crystal. Their half-widths remain essentially unchanged in the process. An increase in the temperature also drives up band *b* but has little influence on the intensity of band *a*, so that at 77 K their intensities are almost comparable (Fig. 3, dashed curve). The positions of these bands in the spectrum are 1.756 eV and 1.764 eV at 77 K. The identical temperature shift of bands *a* and *b* has enabled us to establish the precise position of band *b* at 4.2 K, because it appears only in the form of a kink on the short-wavelength slope of band *a*. Band *c*, which already begins to smooth out at 40 K, is scarcely perceptible in the spectrum at 77 K.

The ratio between the intensities of bands *a* and *b* is constant at a given temperature, whereas the intensity ratio of bands *a* and *c* varies with the position of the exciting light spot; however, the intensity of band *a* is always dominant over that of band *c* when the {0001} face is indented. It follows, therefore, that bands *a* and *b* most likely correspond to radiative transitions in the same multilevel electronic system, while band *c* is associated with some other, independent system.

An important characteristic of the deformation-induced bands is the fact that, after the sample is held at room temperature for several hours, bands *a* and *b* completely disappear from the low-temperature photoluminescence spectrum (i.e., they degrade), whereas band *c* remains essentially unaltered. At a low temperature, liquid-nitrogen for example, the emission spectrum of the deformed regions does not

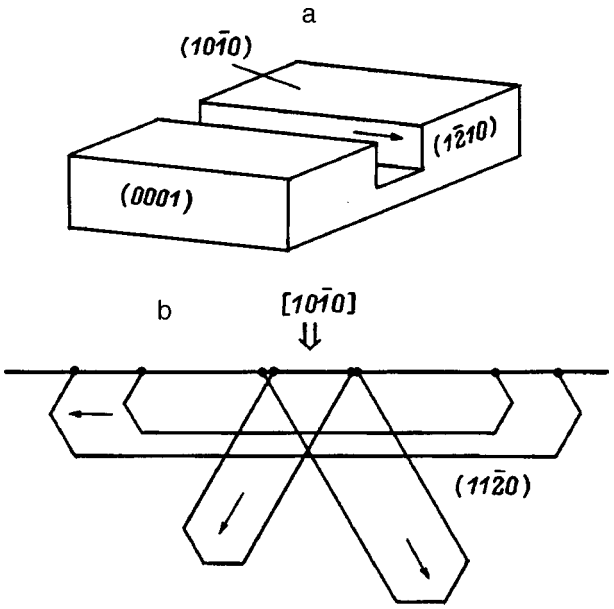

FIG. 4. Diagram of slip forming a dislocation rosette for indentation of the {1010} face. a) Dislocation slip system; b) dislocation half-loops slipping in the basal plane.

change within the actual duration of the experiment.

INDENTATION OF THE {10$\bar{1}$0} FACE.

In this case dislocation slip results in a double-ray rosette with rays along $+/-\langle 1210\rangle$, as shown schematically in Fig. 4. In contrast with the case shown in Fig. 1, now only the half-loops of dislocations slipping in the basal plane of the crystal break out on the top face, while dislocations (or segments thereof) slipping in the prismatic {1010} plane are situated at a certain depth. The indentation of the prismatic face with the same load produces a strong line in the interval 1.779–1.792 eV (band *c*), while the emission bands of group *a b* are either weak or not observed at all (curve *2* in Fig. 3). In this case the observed floating spectral position or broadening of band *c* as the position of the photoexcitation spot varies relative to the indentation is obviously associated with the action of the stress component along the **C** axis of the crystal (when the piezoelectric displacement constant is high). This conjecture is confirmed by the presence of EIC lines exhibiting the same shift (and/or broadening).

The above-described orientation dependence must obviously be identified with a difference in the way defects are formed depending on the slip system in which plastic deformation predominantly evolves.

Indeed, the emergence of the photoluminescence bands *a* and *b* must be attributed to slip in the prismatic system $\langle 1210\rangle\{1010\}$, because the rosette around the indentation on the {0001} surface is formed by outcroppings of the slip bands of this particular system on the top face. The photoluminescence band *c* must be attributed to slip in the system $\langle 1\bar{2}10\rangle\{0001\}$, because the dislocation rosette for indentation on the {1010} surface is formed by outcroppings of the slip bands in the basal plane. The existence of the weak bands *a* and *b* bands in the latter case and the strong band *c* in both cases is explained by the fact that basal slip in crystals having a wurtzite structure is the easiest. As a result, in the optimal experimental geometry for basal slip, prismatic slip evolves only regions of the crystal farther removed in depth from the surface and scarcely contributes at all to photoluminescence with the highly absorbed photoexcitation used in our work (curve *2* in Fig. 3), whereas in the optical geometry for prismatic slip, basal slip occurs fairly close to the surface and still contributes significantly to photoluminescence (curve *1* in Fig. 3). Consequently, for indentation in either the {0001} face or the {1010} face slip actually takes place in both systems, but in different quantitative proportions.

To confirm the validity of the proposed explanation of the orientation dependence of the defect photoluminescence, a CdSe sample was deformed uniaxially in the $\langle 10\bar{1}0\rangle$ direction at 77 K in compression to 3 kbar in the stress-relaxation regime. Only prismatic slip is possible in this geometry since the displacement load in the (0001) plane equals zero. Figure 2 (curve *2*) shows the photoluminescence spectrum after stress relief. As postulated, the spectrum acquires only the group of bands *a b* as a result of plastic deformation in the slip system $\langle 1\bar{2}10\rangle\{10\bar{1}0\}$. It has also been found that bands *a* and *b* are polarized the same as radiative recombination through donor-acceptor pairs (perpendicular to the **C** axis), but to a far lesser extent.

Dislocation emission induced by low-temperature plastic deformation has been well studied in cadmium sulfide (wurtzite) single crystals, where it is attributed to the formation of metastable clusters of point defects by moving dislocations.[5] The group of bands *a b* of cadmium selenide is probably their analog. When the temperature is raised at least to room temperature, interaction between defects leads to decomposition of the metastable clusters and degradation of bands *a* and *b* in the photoluminescence spectra. The stable band *c* must be identified with the electron states of dislocations not directly decorated by the defect atmosphere, i.e., ''fresh'' dislocations slipping in the basal plane and structurally far more stable than clusters of point defects.

From the results and their discussion, therefore, it can be stated that the prismatic slip of dislocations in the slip system $\langle 1\bar{2}10\rangle\{10\bar{1}0\}$ during low-temperature plastic deformation is accompanied by the appearance of the group of bands *a b* in the low-temperature photoluminescence spectrum, whereas basal slip (system $\langle 1\bar{2}10\rangle\{0001\}$) is accompanied by the appearance of band *c*. The observed correlation of the dislocation slip system and the photoluminescence spectra can be used to expose and discriminate slip directly in a low-temperature experiment associated with the deformation of cadmium selenide single crystals. Owing to the high sensitivity of the method, it should be particularly useful for investigating the initial stages of plastic flow of a semiconductor crystal (violation of Hooke's law) during macroscopicscale plastic deformation.

The author is grateful to G. A. Shepel'skiĭ for a profitable discussion of the work and for critical remarks.

[1] S. W. Koch, N. Peyghambarian, and H. M. Gibbs, J. Appl. Phys. **63**, K1 (1988).

[2] J. P. Hirth and J. Lothe, *Theory of Dislocations* [McGraw-Hill, New York/St. Louis/San Francisco/Toronto/London/Syndney, 1968; Atomizdat, Moscow, 1972, 600 pp.].
[3] E. A. Sal'kov, N. I. Tarbaev, G. A. Shepel'skiĭ, and M. K. Sheĭnkman, Fiz. Tekh. Poluprovodn. **17**, 1835 (1983) [Sov. Phys. Semicond. **17**, 1170 (1983)].
[4] V. D. Negry, Yu. A. Osipyan, and N. V. Lomak, Phys. Status Solidi A **126**, 49 (1991).
[5] N. I. Tarbaev, J. Schreiber, and G. A. Shepelskii, Phys. Status Solidi A **110**, 97 (1988).
[6] N. I. Tarbaev, G. A. Shepel'skiĭ, and Yu. Shraĭber, Fiz. Tverd. Tela (Leningrad) **31**(8), 127 (1989) [Sov. Phys. Solid State **31**, 1348 (1989)].
[7] *Physics and Chemistry of II and VI Compounds* [North-Holland Publ., Amsterdam, 1967; Mir, Moscow, 1970, 624 pp.].
[8] Yu. A. Osip'yan and É. A. Shteĭnman, Izv. Akad. Nauk SSSR, Ser. Fiz. **37**, 718 (1973).

Translated by James S. Wood

Resistance of zinc crystals to shock deformation and fracture at elevated temperatures

A. A. Bogach, G. I. Kanel', S. V. Razorenov, and A. V. Utkin

Institute of Problems in Chemical Physics, Russian Academy of Sciences, 142432 Chernogolovka, Moscow Region, Russia

S. G. Protasova and V. G. Sursaeva

Institute of Solid-State Physics, Russian Academy of Sciences, 142432 Chernogolovka, Moscow Region, Russia

(Submitted March 31, 1998)
Fiz. Tverd. Tela (St. Petersburg) **40**, 1849–1854 (October 1998)

Velocity profiles of the free surface of shock-loaded zinc crystals are measured in two different orientations. The test temperature is varied from room temperature to 410 °C. The results of the measurements show that the high-velocity deformation and fracture are athermal processes and that the fracture stresses are influenced by the preceding plastic deformation. © *1998 American Institute of Physics.* [S1063-7834(98)01710-9]

The effect on solids from plane shock waves generated by explosions, high-velocity impact, or laser pulses affords a unique possibility for studying extremely high-velocity deformation and fracture processes under well-regulated load conditions. The most informative experiments in this regard are those involving single crystals,[1–6] because they are capable of yielding information on the elementary mechanisms and dynamics of deformation and fracture without complications from the influence of grain boundaries, impurities and other structural irregularities. An important and fascinating issue, in particular, is the influence of temperature on the elastoplastic and strength characteristics of metals in high-velocity deformation.

It is generally known that the yield point and the tensile strength decrease as the temperature increases at low and moderately high strain rates. This trend is attributable to the fact that under the conditions of low-velocity deformation dislocations overcome obstacles under the combined influence of the applied stress and thermal fluctuations.[7] Higher stresses need to be applied in the case of high-velocity deformation. At a strain rate above $\sim 10^4\ s^{-1}$ the active stresses are high enough to overcome obstacles without any addition contribution from thermal fluctuations. In other words, as the strain rate is increased, there is a transition from thermal-fluctuation to athermal overbarrier dislocation slip. Since fracture is always associated with plastic deformation in the vicinity of growing discontinuities, one should also expect the dynamic strength of solids to be athermal at high strain rates.[8]

The resistance of materials to deformation and fracture in shock loading is investigated by analyzing the structure and evolution of the compression and rarefaction waves. Because the longitudinal compressibility changes in transition through the yield point, a shock wave in a solid becomes unstable, breaking up into an elastic precursor and a plastic compression wave propagating behind it. The amplitude of the elastic precursor is determined by the dynamic yield point of the material. When the compression pulse is reflected from the free surface of the solid, tensile stresses are generated in its interior, resulting in cleavage fracture. Studies of cleavage phenomena provide information about the strength of materials in loading with durations $\sim 10^{-9} - 10^{-5}$ s (Ref. 9).

Until recently there have been scarcely any measurements of the yield point and especially the tensile strength in shock loading at elevated temperatures. In this paper we give the results of such measurements for zinc single crystals in various orientations in the temperature range from room temperature to just short of the melting point. Zinc has a highly anisotropic hexagonal-close-packed crystal structure, with a ratio of the distance between the basal planes to the minimum interatomic distance $c/a = 1.856$. The melting point of zinc is 419.5 °C. The principal dislocation slip system of hcp crystals is the basal (0001) plane; slip and twinning in the pyramidal (1122) planes require much higher stresses. At a temperature above 225 °C in zinc slip is also activated in the (1101) planes.[10]

The high-velocity deformation of hcp metal single crystals — beryllium and zinc — has been investigated previously.[2,11] Recording of the structure of shock waves in beryllium single crystals[2] has shown that the elastic precursors of compression waves are generated for all orientations of the crystal relative to the direction of the load. The amplitude of the elastic precursor was $\sim 6.9-7.2$ GPa in compression along the hexagonal c axis of the crystal and 0.64 GPa in compression along the a axis. It has been determined from the results of experiments using shock compression in directions at 33° and 45° angles relative to the hexagonal axis of the crystal that the shear stress of basal slip under these conditions is 120–140 GPa, which is an order of magnitude larger than the slip stress in quasistatic loading (10 MPa). The ratio of the dynamic to the quasistatic stress of plastic deformation along the prismatic planes is equal to 250 MPa and 70 MPa; the values of these quantities obtained for the pyramidal planes are 3.35 GPa and 1 GPa, respectively. In shock compression along the a and c axes the elas-

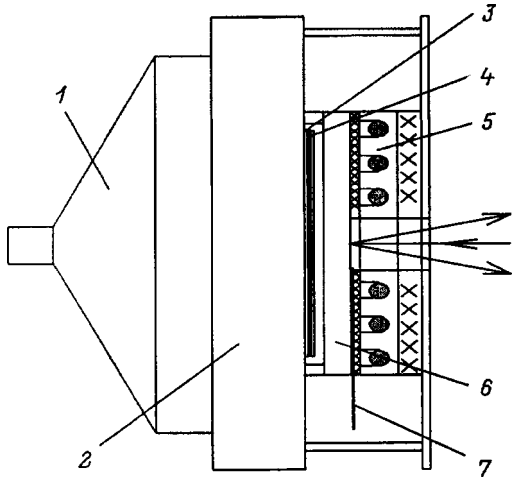

FIG. 1. Experimental arrangement for measuring the velocity profiles of the free surface of shock-compressed samples at elevated temperature. *1* — Plane-wave explosive lens; *2* — steel attenuator; *3* — Teflon spacer; *4* — striker; *5* — heater; *6* — sample; *7* — thermocouple.

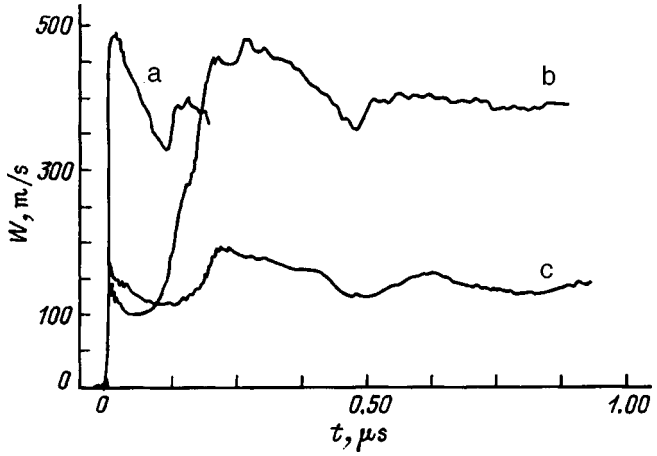

FIG. 2. Typical profiles of the surface velocity for two sample orientations relative to the direction of shock loading and for two striker thicknesses. a) Loading along [0001], striker thickness 0.4 mm; b) [1010], 0.85 mm; c) [1010], 0.4 mm.

tic precursors of shock waves in a beryllium single crystal has a characteristic peak, which is explained by vigorous dislocation multiplication and, associated with it, the acceleration of relaxation of shear stresses. A metallographic analysis of the samples after shock loading has shown that the cleavage fracture of beryllium single crystals is initiated at a stress of approximately 1 GPa in loading either along or perpendicular to the hexagonal axis of the crystal, whereas the quasistatic cleavage stresses for these two orientations differ sixfold.

The high-velocity deformation of zinc single crystals at elevated temperatures has been investigated previously[11] by a Hopkinson pressure bar method. It was found that at strain rates $>0.5\times10^4\,s^{-1}$ the shear stress in the basal plane is independent of the temperature up to the melting point, leading to the conclusion that by far the dominant contribution is from overbarrier dislocation slip controlled by viscous drag. The stress-strain diagram of slip in the pyramidal planes contains a ''yield drop,'' whose relative amplitude increases with the strain rate; here the lower yield point is approximately an order of magnitude higher than the yield point for the basal plane. At a strain rate $\sim0.5\times10^4\,s^{-1}$ the upper yield point is approximately twice the lower yield point.

1. EXPERIMENTAL MATERIAL AND APPARATUS

The experiments were carried out using 99.999% pure zinc single crystals grown by directional crystallization from the melt in high-purity graphite molds.[11] During the growth process flat single crystals having areal dimensions of 10 $\times$15 mm and thicknesses from 0.5 mm to 2.2 mm were oriented normal to the plane in the crystallographic [1000] and [1010] directions. Three or four samples were cut from each single crystal grown. The samples were etched electrochemically to remove surface defects.

The experimental arrangement is shown in Fig. 1. The samples were impacted by an aluminum plate of thickness 0.4 mm or 0.85 mm at a rate of 650–700 m/s either in the basal (0001) plane or in the prismatic (1010) plane, which is perpendicular to the basal plane. Explosive devices described in detail in Ref. 9 were used to drive the striker plates. At a resistance-heater power of approximately 1 kW the time for the sample to be heated to the prescribed temp did not exceed 10 min. The heater was turned off approximately 1 min prior to blast time. The temperature was monitored continuously within $\pm5°$ error limits by means of a Chromel-Alumel thermocouple mounted in the immediate vicinity of a check point on the back surface of the sample; the sensing beam of a laser Doppler velocimeter (VISAR — Velocity Interferometer System for Any Reflector[12,13]) was focused onto this surface. The focal spot had a diameter $\sim$0.1 mm. A digital oscilloscope was used to record the interference beats, with the recorded signal digitized at a frequency of 0.5 GHz. The frequency response characteristics of the apparatus were such that the signals could be recorded with a rise time at the level of 2–3 ns.

2. MEASUREMENT RESULTS

Figure 2 shows typical velocity profiles $W(t)$ of the free surface of differently oriented single-crystal samples shock-compressed to a pressure $\sim$7 GPa.

In loading along the hexagonal axis of the crystal, a shock wave with a maximum rise time of 2 ns is recorded, followed by a rarefaction wave. The duration of the compression pulse is determined by the wave reverberation time in the striker, i.e., its thickness. The second velocity rise is caused by the arrival at the surface of a compression wave (cleavage pulse) formed by relaxation of the tensile stresses in cleavage fracture. The drop of the velocity from its maximum to the level just before the leading edge of the cleavage pulse is determined by the fracture stress in cleavage.

For shock loading in the [1010] direction the compression wave acquires a double-wave structure: A separate elastic precursor emerges, propagating at a velocity equal to the velocity of longitudinal elastic waves and greater than the velocity of the plastic compression wave following it, which is equal to the ''bulk'' sound velocity c_b. Since the rarefac-

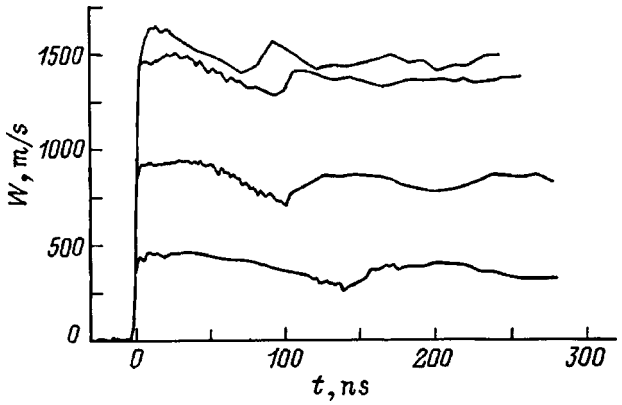

FIG. 3. Velocity profiles of the free surface of single crystals loaded in the [0001] direction by aluminum strikers of thickness 0.4 mm at velocities from 0.7 km/s to 2.2 km/s.

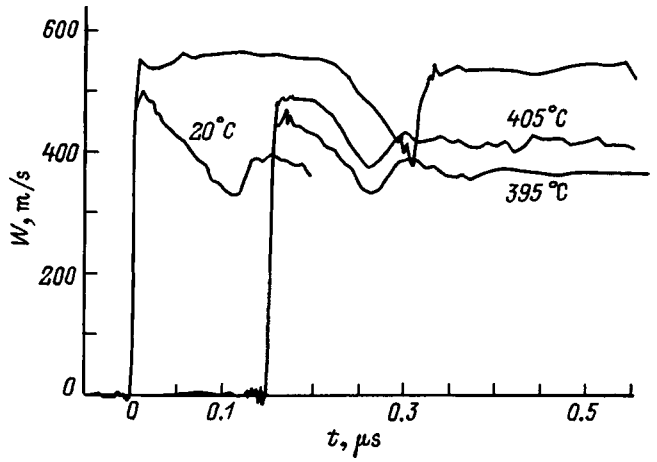

FIG. 4. Velocity profiles of the free surface of zinc crystals loaded in the [0001] direction by the impact of an aluminum plate of thickness 0.4 mm or 0.85 mm with a velocity of 650–700 m/s at room and higher temperatures.

tion wave front also propagates at the ''longitudinal'' sound velocity in the shock-compressed material, the compression pulses in this direction begin to decay if the thickness of the sample is more than three times the thickness of the striker. The rise time in the plastic wave in this case is 80–90 ns, which corresponds to a strain rate $\sim 5\times 10^5\,\mathrm{s}^{-1}$.

Inasmuch as the shear and bulk viscosities of a solid in the elastic strain region are insignificant, the steepness of the leading edge of the elastic precursor stays within the resolution limits of the measurements (2–3 ns).

In tests where the direction of shock compression is parallel or perpendicular to the basal plane of the crystal the shear stresses in this easy-glide plane are equal to zero, so that the only way plastic deformation can take place is by slip in the pyramidal planes. In this light one would expect the resistance to plastic deformation and the steepness of the plastic shock wave to be identical for these two orientations. The start of plastic deformation and the separation of the elastic precursor occur when the deviator stress in the compression wave $S_x=\sigma_x-p=\sigma_x(1-c_b^2/c_l^2)$ (where σ_x is the normal stress in the direction of compression, p is the spherical component of the stress tensor, or pressure, and c_b and c_l are the bulk and longitudinal sound velocities) reaches 2/3 of the yield point σ_T.

The bulk sound velocity in zinc at room temperature and zero pressure is $c_b=3.03$ km/s. The longitudinal sound velocity in the direction perpendicular to the hexagonal axis of the crystal is $c_l=4.73$ km/s, while in the axial direction the longitudinal elastic wave velocity is very close to the bulk sound velocity[14] (a formal calculation using the elastic constants in Ref. 14 gives the longitudinal sound velocity even lower than the bulk sound velocity, but this result is obviously a consequence of errors in the elastic constants and the analytical equations). With regard to the steep slope of the leading edge of the compression wave, it is natural to conclude that a shock wave of intensity 7 GPa propagating in the axial direction is wholly elastic. Figure 3 shows the results of tests using a higher impact velocity, for which signs of the onset of plastic deformation appear only in the axial direction above 21 GPa (the velocity of the free surface is 1.43 km/s), confirming the above-stated conclusion experimentally.

Figures 4 and 5 show free-surface-velocity profiles measured at standard and elevated sample temperatures. Heating of the single crystals to temperatures very close to the melting point does not produce any significant changes in the structure of the compression and rarefaction waves either for basal orientation of the samples or for shock compression in the direction perpendicular to the hexagonal axis of the crystal.

The cleavage fracture stresses and the dynamic elastic limit for the differently oriented samples have been determined from the resulting free-surface velocity profiles. The fracture stress, or ''cleavage strength'' σ^*, has been calculated from the drop ΔW of the velocity from its maximum to the level just before the leading edge of the cleavage pulse[9]:

$$\sigma^*=0.5\rho_0 c_b(\Delta W+\delta),$$

where ρ_0 is the density of the material, c_b is the bulk sound velocity in it at zero pressure, and δ is a correction for distortion of the wave profile by the difference in the propagation velocities of the unloading side of the incident pulse

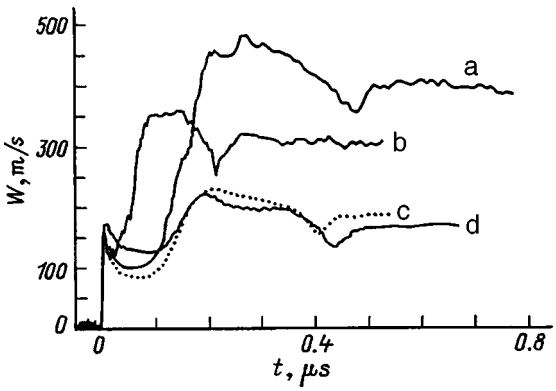

FIG. 5. Velocity profiles of the free surface of a zinc single crystal loaded in the [1010] direction by an aluminum striker of thickness 0.4 mm (b–d) or 0.85 mm (a) with a velocity of 650–700 m/s at room temperature (a, b, d) and at an elevated temperature (410 °C) (c).

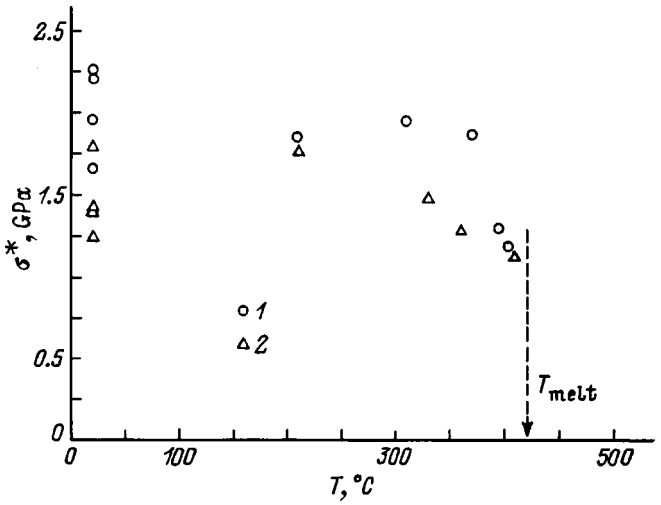

FIG. 6. Cleavage-strength dependence of differently oriented zinc single crystals on test temperature. *1* — Loading direction [0001]l; *2* — [1010].

(c_b) and the leading edge of the cleavage pulse(c_l). Taking into account the velocity gradient of the free surface ahead of the leading edge of the cleavage pulse $\dot{u}_1$ and the gradient in the leading edge $\dot{u}_2$, we can estimate this correction as

$$\delta=\left(\frac{h}{c_b}-\frac{h}{c_l}\right)\frac{|\dot{u}_1\dot{u}_2|}{|\dot{u}_1|+\dot{u}_2},$$

where h is the thickness of the cleavage plate, determined from the wave reverberation time in it. The introduction of a correction factor is pointless for axial-loading tests, because the longitudinal and bulk sound velocities are very close for this orientation. The given technique for determining the strength of the material from the free-surface velocity profiles is actually based exclusively on fundamental conservation laws and does not involve any assumptions about the mechanism, rate, or degree of fracture. The values obtained for the fracture stresses in samples of two different orientations at standard and elevated temperatures are summarized in Fig. 6. The cleavage thickness in these tests was 0.2–0.5 mm, and the strain rate was $(2-5)\times10^5\,\mathrm{s}^{-1}$.

Most of the measurements were performed at room temperature. The results have considerable scatter, which is generally typical of such measurements with high space-time resolution and reflects the microinhomogeneity of the samples. Variations of the fracture stresses, even within a single sample, have been observed in experiments on molybdenum single crystals.[15] All the same, the measurement results definitely show that when a zinc single crystal is loaded in the direction of the hexagonal c axis, cleavage fracture takes place at higher stresses than in tests with loading in the perpendicular direction. At room temperature the average fracture stresses in the axial and transverse directions are 2.1 ± 0.2 GPa and 1.33 ± 0.3 GPa, respectively. Fracture develops more rapidly in loading along the crystal axis; this fact is manifested on the free-surface profiles by the steeper slope of the cleavage pulses. For comparison, the fracture strength of industrial aluminum and aluminum alloys under similar load conditions is 1–1.4 GPa, and the strength of soft steels is 1.5–3 GPa (Ref. 9). It is important to note that experiments with less anisotropic fcc copper[5] and bcc molybdenum[6] single crystals have not demonstrated any influence of the load direction on the magnitude of the cleavage fracture stress. Under loading conditions closely approximating those in the present study copper and molybdenum single crystals have dynamic strengths of 4 ± 0.5 GPa and 5 ± 0.5 GPa, respectively, which are approximately three times the dynamic strengths of these metals in the polycrystalline state. It is interesting to note that estimates of the maximum tensile stresses, which correspond to the minimum of the $p(V)$ isotherm, are ~23 GPa, 55 GPa, and 10.5 GPa for copper, molybdenum, and zinc, respectively. In other words, the fracture resistance of single crystals in the submicrosecond loading-time range is commensurate with the theoretical limit.

The basal (0001) planes are known to be easy-cleavage surfaces, owing to the relatively large interplanar spacing.[16] In the reported experiments the resistance to cleavage fracture is found to be higher for the most favorable orientation of the weakest planes of the crystal. Generally speaking, a change in the direction of shock loading should not produce any major changes in the fracture stress. In plane shock waves the stress tensor is close to the spherical stress, so that cleavage fracture is initiated when the stressed state is close to hydrostatic tension, irrespective of the loading direction. A more likely assumption is that the influence of orientation on the resistance to cleavage fracture is the result of a difference in the defect structure formed at the onset of fracture for different shock loading directions.

It is a well-known fact that various kinds of irregularities (grain boundaries, micropores, and brittle inclusions) in polycrystalline materials or more microscopic imperfections such as twins, dislocation pileups, or point defects in single crystals are fracture nucleation centers in solids. The occurrence of higher fracture stresses in tests where the basal planes in loading by plane shock waves have the most favorable orientation for crack propagation can be attributed to the fact that plastic deformation of the material did not occur in these tests, and its defect structure was therefore left unchanged; consequently, fracture could only be initiated at defects already present in the original material. In experiments with the shock load oriented perpendicular to the crystal axis plastic deformation did occur and was accompanied by an increase in the density of dislocations and other deformation defects capable of serving as fracture nucleation centers and, hence, of reducing the fracture stresses.

When the temperature is increased from room temperature to 350–370 °C, the cleavage strength of zinc single crystals with two different orientations remains essentially unchanged but, with a further increase in temperature, the difference between the cleavage strengths and the cleavage strengths themselves decrease, the latter having a value of 1.1–1.2 GPa at a temperature of 405–410 °C. This temperature is only 2% below the absolute melting point. It should be noted that a much larger drop in the cleavage strength as the initial temperature of the samples approached the melting point has been reported for polycrystalline materials.[17]

The results of the measurements do not show any influ-

ence of temperature on the dynamic elastic limit of zinc. For loading in the (1010) plane elastic precursors with a characteristic ''yield drop'' are recorded over the entire temperature range. This structure of the elastic precursor is usually a consequence of the acceleration of stress relaxation due to dislocation multiplication as plastic deformation develops. In our experiments the scatter of the measured precursor amplitudes attained $\pm 10\%$ of the average peak value of 2.5 GPa and $\pm 20\%$ at the point of the minimum between the elastic and plastic wave fronts. Such a large data scatter is partially explained by the fact that even a small deviation of the direction of compression from a given crystallographic direction can produce sufficient shear stresses in the basal plane to activate easy dislocation glide.

The measurements do not show any appreciable influence of temperature on the steepness of the plastic shock wave, which is determined by the viscosity of the material. These data indicate the athermal nature of the high-velocity plastic deformation in shock waves. The inadequate reproducibility of the samples and the loading conditions have made it impossible to determine the amplitude decay of the precursor as it propagates over distances from 0.5 mm to 2 mm. Moreover, a detailed comparison of the wave profiles at distances of 0.5 mm to 2 mm from the impact surface has shown that the evolution of the elastic precursor is very nearly self-similar. Given the existing scatter of the experimental data, this odd result is very likely fortuitous; not to be ruled out, however, is the possibility of contributions to stress relaxation from overlooked effects such as, for example, rotation of the crystallographic planes during plastic deformation and, as a result, the possible activation of easy-glide systems.

The authors are grateful to L. G. Ermolov for assistance in setting up and running the experiments.

This work has been carried out as a part of projects of the Russian Fund for Fundamental Research Nos. 97-02-17701 and 96-02-17483.

[1] W. J. Murri and G. D. Anderson, J. Appl. Phys. **41**, 3521 (1970).
[2] L. E. Pope and A. L. Stevens, in *Metallurgical Effects at High Strain Rates*, edited by R. W. Rohde *et al.* (Plenum Press, New York–London, 1973), p. 349.
[3] J. N. Johnson, J. Phys. Chem. **35**, 609 (1974).
[4] G. Meir and R. J. Clifton, J. Appl. Phys. **59**, 124 (1986).
[5] S. V. Razorenov and G. I. Kanel', Fiz. Met. Metalloved. **78** 141 (1992).
[6] G. I. Kanel, S. V. Razorenov, A. V. Utkin, V. E. Fortov, K. Baumung, H. U. Karow, D. Rush, and V. Licht, J. Appl. Phys. **74**, 7162 (1993).
[7] A. Kumar and R. G. Kumble, J. Appl. Phys. **40**, 3475 (1969).
[8] L. A. Merzhievskiĭ and V. M. Titov, Dokl. Akad. Nauk SSSR **286**, 109 (1986) [Sov. Phys. Dokl. **73** 31 (1986)].
[9] G. I. Kanel', S. V. Razorenov, A. V. Utkin, and V. E. Fortov, *Shock-Wave Phenomena in Condensed Media* [in Russian], Yanus-K, Moscow (1996), 408 pp.
[10] R. Berner and H. Kronmüller, *Plastic Deformation of Single Crystals* (Mir, Moscow, 1969), 272 pp.
[11] P. L. Studt, E. Nidick, F. Uribe, and A. K. Mukherjee, in *Metallurgical Effects at High Strain Rates*, edited by R. W. Rohde *et al.* (Plenum Press, New York–London, 1973), pp. 379–398.
[12] A. Antonov, S. V. Kopetskiĭ, L. S. Shvindlerman, and V. Sursaeva, Dokl. Akad. Nauk SSSR **213**, 318 (1973) [Sov. Phys. Dokl. **18**, 736 (1974)].
[13] J. R. Asay and L. M. Barker, J. Appl. Phys. **45**, 2540 (1974).
[14] *Physical Acoustics, Vol. 3B: Lattice Dynamics*, edited by W. P. Mason [Academic Press, New York–London (1965); Mir, Moscow (1968), 392 pp.].
[15] K. Baumung, G. I. Kanel, S. V. Razorenov, D. Rusch, J. Singer, and A. V. Utkin, J. Phys. Colloq. **7**, C3-927 (1997).
[16] F. A. McClintock and A. S. Argon, *Mechanical Behavior of Materials* [Addison-Wesley, Reading, Mass. (1966); Mir, Moscow (1970), 444 pp.].
[17] G. I. Kanel, S. V. Razorenov, A. A. Bogatch, A. V. Utkin, V. E. Fortov, and D. E. Grady, J. Appl. Phys. **79**, 8310 (1996).

Translated by James S. Wood

MAGNETISM AND FERROELECTRICITY

Macroscopic quantum resonance tunneling of domain walls

V. V. Makhro

Bratsk Industrial Institute 665728 Bratsk, Russia
(Submitted February 3, 1998; resubmitted April 9, 1998)
Fiz. Tverd. Tela (St. Petersburg) **40**, 1855–1860 (October 1998)

Results are presented of a theoretical investigation of the tunneling of magnetic domain walls, taking account of the interaction of the walls with the thermal system of the crystal. It is shown that thermal stimulation increases considerably the transmittance of the potential barriers during propagation of walls through a crystal. © *1998 American Institute of Physics.* [S1063-7834(98)01810-3]

The importance of taking account of tunneling in magnetodynamics was first pointed out in 1971 by Egami.[1] He investigated the tunneling of extremely narrow (several lattice constants wide) domain walls in hard ferromagnets through potential barriers formed by the ''intrinsic'' coercivity. The relatively small mass of such walls and the width of the potential barriers result in appreciable tunneling probabilities. In any case, the experimental data on the spontaneous demagnetization of hard ferromagnets agree very well with Egami's results.[1]

A new burst of interest in wall tunneling arose in the 1990s as part of a general increase in interest in macro- and mesoscopic quantum effects. This is completely explainable, since the tunneling of magnetic domain walls, together with superconductivity, superfluidity, and the Josephson effect, is one of the few examples of macroscopic quantum processes.

A great deal of attention has been devoted, first and foremost, to tunneling of walls in ordinary ferromagnets (c.f., Ref. 2). In general, tunneling is considered in this case because of the observed anomalous behavior of magnetization relaxation processes at low temperatures: For many magnetic materials, as temperature decreases, the relaxation rates tend not to zero but rather a certain finite value.[3] The tunneling explanation of this circumstance seems fully justified.

However, attempts to perform quantitative calculations encounter unexpected difficulties. Indeed, estimates of the characteristics of potential barriers in terms of the parameters of hysteresis loops and magnetic-noise data lead to the conclusion that we are dealing in ferromagnets, in most cases, with high and thick barriers as pinning centers. For this reason (especially taking account of the appreciable ''massiveness'' of walls in these materials), negligibly small values are obtained for the transmittances (of the order of 10^{-80} and lower).

The situation is somewhat better in weak ferromagnets, where the mass of domain walls is usually an order of magnitude smaller than in ferromagnets. The theory of tunneling for walls in these materials is more complicated, since here quasirelativistic effects must be taken into account. A successful theory for weak ferromagnets was recently proposed by Zvezdin and Dobrovitskiĭ.[4,5] But, even in the case of weak ferromagnets, tunneling alone cannot give effective depinning, required to explain the temperature dependence of relaxation processes at both low and high temperatures.

In this connection it is important to explain the mechanisms that are capable of producing an appreciable probability of depinning of magnetic domain walls in magnetization reversal processes. All such mechanisms can be divided conventionally into three groups: The first group consists of thermally activated depinning, in which the wall overcomes a potential barrier by means of energy obtained directly from the thermal system of the crystal. Another type of thermally activated depinning materializes for defects modeled by the combination ''well + barrier.'' We place this type in the second group. If the wall in front of the barrier is in a potential well with a characteristic frequency of the order of at least 10^{11} s^{-1}, then its interaction with thermal excitations of the crystal can have a resonance character as a function of temperature and it can undergo efficient depinning in a narrow temperature range, even in very weak advancing fields.[6] Finally, the third group consists of tunneling depinning. Here, however, as indicated above, at the present time the situation is extremely ambiguous. The experimental data on magnetization relaxation processes, internal friction, and electric conductivity show that in most cases pinning centers are characterized by energies of the order of $10^{-13}-10^{-14}$ ergs. However, successful tunneling depinning (other conditions being equal) is possible only for barriers with three to four orders of magnitude lower amplitude energy. On the other hand, low-temperature depinning cannot be explained by anything other than tunneling. In the present paper it will be shown that in a certain sense the cooperation of the mechanisms in the first and third groups and also the second and third groups has a considerable effect on the nature of tunneling depinning. In the first case, this has the effect that a wall, absorbing thermal energy from the crystal, ''rises'' in front of barrier, lowering its effective height and, correspondingly, increasing the transmittance in a very wide tem-

perature range. In the second case, the transmittance increases resonantly only in a narrow temperature region (specifically, for ferromagnets at liquid-helium temperatures).

1. PREBARRIER THERMAL STIMULATION OF BLOCH WALLS

Let us consider the first of the mechanisms named above. We note that because of the interaction with the thermal system of the crystal a domain wall in front of a barrier of height U_0 will possess an additional energy w and the effective barrier height will now be lower for such a wall: U_0-w. It can be expected that in this case the probability of tunneling depinning should indeed increase.

Let us consider a 180° Bloch-type domain wall in a uniaxial crystal. The equation of motion for the unit vector of uniform magnetization (Landau–Lifshitz equation[7]) has the form

$$\frac{d\boldsymbol{\alpha}}{dt}=\gamma[\alpha\times\mathbf{H}], \tag{1}$$

where $\gamma=ge/2mc$ is the gyromagnetic ratio and $\mathbf{H}$ is the effective field calculated from the exchange and anisotropy energies, the stray fields, and the external field. In spherical coordinates

$$\boldsymbol{\alpha}=(\sin\theta\sin\phi,\sin\theta\cos\phi,\cos\theta)$$

Eq. (1) reduces to the following pair of equations:

$$\dot{\theta}=-\frac{\gamma}{I_S}\frac{1}{\sin\theta}\delta_\phi e_g, \quad \sin\phi=\frac{\gamma}{I_S}\delta_\theta e_g, \tag{2}$$

where e_g is the total-energy functional and I_S is the saturation magnetization. Stray fields are induced in a moving wall. The additional energy due to these fields can be represented in a form which quadratic in the velocity v and the kinetic energy of the wall can be represented as[8]

$$K=\frac{v^2 m_D}{2},$$

where the constant $m_D=E_0/8\pi A\gamma^2\sin^2\theta$ is the effective or Doring mass of the wall (per unit surface area of the wall), A and K_1 are, respectively, the exchange and anisotropy constants, and $E_0=\sqrt{AK_1}$ is the rest energy (also per unit area) of the wall. The equation of motion for a Bloch wall thus has the Newtonian form (which is why the wall can be treated as a classical particle)

$$m_D\frac{d^2x}{dt^2}=2I_S H.$$

Here x is the coordinate of the center of the wall along an axis perpendicular to the plane of the wall. The interaction of a wall with defects is taken into account by introducing the interaction potential energy function $U(x)$

$$m_D\frac{d^2x}{dt^2}=2I_S H-\frac{d}{dx}U(x).$$

Let a moving domain wall with kinetic energy K reach a potential barrier of height U_0, modeling the interaction with one or another defect of the crystal. If $K<U_0$, the section of the wall immediately adjacent to the defect is localized in a metastable minimum in front of the barrier. Let the external field be very weak

$$H\ll\frac{1}{I_S}\frac{dU}{dx},$$

so that it cannot influence depinning significantly, but by forming a metastable minimum in front of the barrier it produces an asymmetry between the positions of the particle in front of and behind the barrier.

For the calculations we shall use the following values of the parameters (these are the standard values for ferromagnets): barrier height $U_0=10^{-14}$ ergs and defect area 10^{-13} cm^2, which corresponds to the measured coercive force of 100 Oe. We take the thickness of a defect $a=10^{-6}$ cm and the mass of the tunneling section of the wall $m=10^{-25}$ g. For the chosen parameter values, the energy spectrum of a quasiparticle can be assumed to be quasicontinuous, and the classic Maxwellian distribution can be used in the analysis.

We shall consider a particle (i.e. a tunneling section of the wall) in a state of thermal equilibrium with the crystal. Let there be an ensemble of N such particles. We divide the entire energy interval from zero to U_0 into subintervals of identical width δw. The number of particles in the ensemble which have energies in one subinterval is

$$N_w=\int_{w-\delta w/2}^{w+\delta w/2}\frac{2N}{\sqrt{\pi}}(kT)^{-3/2}w^{1/2}\exp\left(-\frac{w}{kT}\right)dw. \tag{3}$$

We shall calculate for each subinterval the corresponding transmittance D. To calculate D we attach to all particles in a given subinterval the same energy w. The correctness of this procedure was checked numerically. More accurately, the number N was chosen so that on the whole the computational scheme would be stable. The product of D and N_w is the number N_{w0} of particles from a given subinterval which find themselves on the other side of the barrier. The sum of all N_{w0} over all subintervals is the total number N_0 of particles from an ensemble which find themselves on the other side of the barrier. Then $F=N_0/N$ will be the effective barrier transmittance for a given quasiparticle.

The calculations show that any sufficiently smooth barrier can be chosen to simulate a defect. Only the height U_0 and width a of the barrier are important. In our computational scheme, we used the well-known potential

$$U(x)=U_0\cosh^{-2}\left(\frac{x}{a}\right), \tag{4}$$

for which the transmittance coefficient is given by the expression[9]

$$D=\frac{\sinh^2(\pi\theta a)}{\sinh^2(\pi\theta a)+\cosh^2\left(\frac{\pi}{2}\sqrt{\frac{32\pi^2U_0ma^2}{h^2}-1}\right)},$$

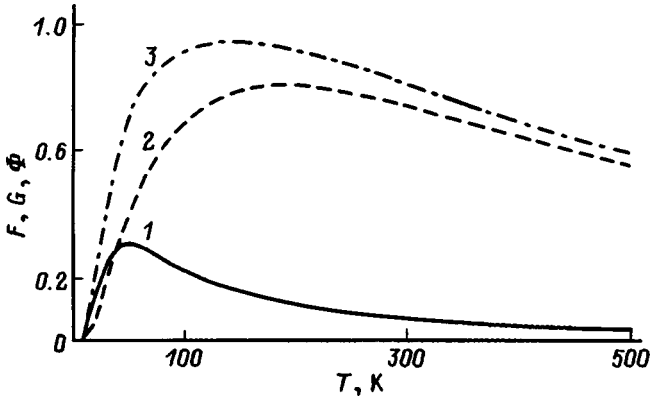

FIG. 1. Temperature dependences of the probability F of thermally stimulated tunneling (*1*), the probability G of thermally activated depinning (*2*), and the total depinning probability Φ (*3*) for a Bloch domain wall.

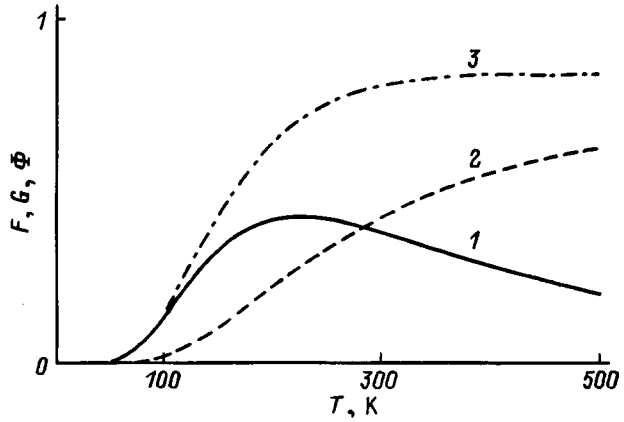

FIG. 2. Probability F of thermally stimulated tunneling (*1*), probability G of thermally activated depinning (*2*), and total depinning probability Φ (*3*) for a domain wall in a weak ferromagnet as a function of temperature.

$$\frac{32\pi^2 m U_0 a^2}{h^2} > 1,$$

$$D = \frac{\sinh^2(\pi\theta a)}{\sinh^2(\pi\theta a) + \cos^2\left(\frac{\pi}{2}\sqrt{1 - \frac{32\pi^2 m U_0 a^2}{h^2}}\right)},$$

$$\frac{32\pi^2 m U_0 a^2}{h^2} < 1,$$

where $Q = \frac{\sqrt{2mw}}{\hbar}$. The probability G of thermally activated depinning can be calculated by simply determining the fraction of particles from an ensemble which have energy higher than U_0, i.e.

$$G = \int_{U_0}^{\infty} \frac{2}{\sqrt{\pi}} (kT)^{-3/2} w^{1/2} \exp\left(-\frac{w}{kT}\right) dw. \tag{5}$$

The computational results for the temperature dependences of the effective transmittance F, the probability G of thermally activated depinning, and the total depinning probability Φ, which were all calculated in the interval from 0 to 500 K, are presented in Fig. 1. As one can see from this figure, right up to 100 K the thermally activated depinning and thermally stimulated tunneling make the same contribution to the probability of total depinning of a wall. But even at higher temperatures taking account of tunneling remains a pressing problem.

The situation is even better for thermally stimulated tunneling in weak ferromagnets. For these materials an important feature is the quasirelativistic character of the dynamics. In accordance with the results obtained in Ref. 10 , the Lagrangian for a unit surface area of the wall, in terms of the so-called ''abbreviated description'' of the dynamics, has the form

$$L = -mc_0^2\sqrt{1 - v^2/c_0^2} - U(x), \tag{6}$$

where x is the coordinate of the center of the wall, c_0 is the maximum velocity of the wall, and $U(x)$ describes the potential relief formed by defects in the presence of an external field. The quasirelativistic character of the Lagrangian (6) requires to calculate Eq. (3) the use of not the Maxwellian distribution but rather a corresponding ''relativistic'' distribution. The latter can be obtained easily on the basis of the Gibbs canonical distribution

$$dz_p = a^0 \exp(-K(p)/kT)\, dp,$$

where a^0 is determined from the normalization

$$\int_{-\infty}^{\infty} dz_p = 1,$$

and taking for the kinetic energy of the wall $K = c_0 p$ ($p = mv/\sqrt{1 - v^2/c_0^2}$ is the canonical momentum). Finally,

$$z(w) = \frac{1}{2(kT)^3} w^2 \exp\left(-\frac{w}{kT}\right). \tag{7}$$

The numerical procedure used to calculate the thermally stimulated tunneling of Bloch walls was also used in calculations for weak ferromagnets. However, the numerical calculations of D in this case were performed by the procedure proposed in Refs. 4 and 5 . The results, which are presented in Fig. 2, show that in weak ferromagnets thermally stimulated tunneling should be more pronounced than for Bloch walls. Indeed, the contribution of tunneling to the depinning probability is greater than the contribution of thermal activation right up to 280 K. This circumstance, apparently, will require that the existing experimental data on depinning at high temperatures be analyzed in a new way.

2. SUBBARRIER RESONANCE THERMAL STIMULATION OF WALLS

We shall discuss one other possible mechanism whereby the barrier transmittance can increase for a domain wall, specifically, pumping of energy in the process of ''subbarrier motion'' of the wall. Strictly speaking, the passage of a particle through a potential barrier, accompanied by a change in the energy of the particle, cannot be viewed as tunneling in the traditional sense. However, the requirement that dissipa-

tion processes be taken into account and that interactions of the wall with other quasiparticles of the crystal be taken into account in a more general form makes it important to consider this mechanism.

In the preceding section, in studying the prebarrier behavior of a particle, we implicitly assumed the particle to be classical. There were sufficient grounds for doing so. Indeed, an external field applied to the crystal forms in front of the barrier a metastable minimum for the potential energy of the wall — a wide and shallow potential well. Simple estimates show that the energy spectrum in such a well is quasicontinuous, which makes it possible to use the classical approach to describe the prebarrier motion of the wall and its interaction with thermal excitations of the crystal. However, the ''subbarrier motion,'' since it is local, requires a substantially quantum approach.

Let the particle have energy w in front of the barrier (domain wall). Since it predominates, we shall confine our analysis to the interaction of a wall with an ideal gas of thermal magnons. Different types of interactions between a wall and the thermal magnons are described in the classical approximation in an integral manner by introducing a phenomenological friction with constant λ.

The friction can be interpreted as a perturbation

$$f(t)=-\Lambda(t)e^{-\lambda t}. \tag{8}$$

The expression (8) is additive and can be represented in the form

$$f(t)=\sum_i \Lambda_i e^{-\lambda_i t}, \tag{9}$$

where the summation extends over all relaxation processes, and the weights Λ_i are determined by the probabilities of the corresponding processes. Treating a wall as a collection of magnons[1] with a quadratic dispersion law and confining attention to three-magnon processes only (thus, in weak ferromagnets their amplitude is an order of magnitude higher than the four-magnon processes because of the high intensity of dipole-dipole interactions), we obtain for the rate of removal of energy by magnons of the type i with energy ε_i

$$\frac{d}{dt}E_i=P_i\frac{1}{\exp(\varepsilon_i/kT)-1}N^{\langle e\rangle}, \tag{10}$$

where

$$P_i=\frac{kT}{\pi}\varepsilon_i^{5/2}\frac{\Delta a}{U_0 h^{5/2}}$$

is the probability of generation of a magnon with energy ε_i per unit time, and $N^{\langle e\rangle}$ is the total number of bound magnons in the wall. On the other hand, the rate of removal of energy by magnon of type i can be expressed in terms of the phenomenological constant λ as

$$\frac{d}{dt}E_i=-2\lambda_i e^{-2\lambda_i t}. \tag{11}$$

Comparing the expressions (10) and (11) we find

$$\lambda_i=-\frac{1}{2}\frac{W\left(\dfrac{1}{\exp(\varepsilon_i/kT)-1}P_i N^{\langle e\rangle}t\right)}{t}, \tag{12}$$

where $W(x)$ is the function inverse to xe^x.

In thermodynamic equilibrium the dependence of Λ on t is weak, so that the expansion of the expression (12) in terms of t can be limited to zeroth order and we can write

$$\lambda_i=-\frac{1}{2}P_i\frac{N^{\langle e\rangle}}{\exp(\varepsilon_i/kT)-1}. \tag{13}$$

Therefore, taking account of Eq. (13) we have for Λ_i

$$\Lambda_i=\lambda_i\sqrt{\frac{2\varepsilon_i}{m_i^{\langle e\rangle}}},$$

where $m_i^{\langle e\rangle}$ is the mass of the magnon emitted in a process of the i-th type.

We introduce once again an ensemble of particles — domain walls with a Maxwellian energy distribution

$$dN(w)=\frac{2N}{\sqrt{\pi}}(kT)^{-3/2}w^{1/2}\exp\left(-\frac{w}{kT}\right)dw.$$

We write the wave functions of the particles in the ensemble in the subbarrier region in the quasiclassical approximation

$$\psi_j=\frac{1}{2\sqrt{|p|}}\exp\left(-\frac{2\pi}{h}\left|\int_{b_j}^{x}p\,dx\right|\right), \tag{14}$$

where b_j is the corresponding turning point, determined by the condition

$$U(b_j)=w_j.$$

We make the substitution $t\to it$ i.e. we switch formally to a problem in imaginary time. Here the particle is localized in the potential well — ''inverted potential'' (4)

$$U(x)=-U_0\cosh^{-2}\left(\frac{x}{a}\right), \tag{15}$$

where it will possess a discrete spectrum[9]

$$w_n=-\frac{h^2}{32ma^2\pi^2}\left[-(1+2n)+\sqrt{1+\frac{32mU_0a^2\pi^2}{h^2}}\right], \tag{16}$$

and the maximum number of levels is determined by the condition

$$n\leqslant s=\frac{1}{2}\left(-1+\sqrt{1+\frac{32mU_0\pi^2a^2}{h^2}}\right).$$

The particle with energy w in front of the barrier will occupy one of the levels in the ''inverted potential'' (15) with probability determined by the squared modulus of the matrix element

$$c_n=\int\psi(x)\psi_n(x)dx,$$

where ψ_n are the eigenfunctions for a particle in the potential (15). Calculation of $|c_n|^2$ in the quasiclassical approximation gives

$$B_n=|c_n|^2\simeq\frac{1}{s}\exp\left(\frac{|w_n-w|}{sw}\right).$$

Then the number of particles in the ensemble that are in the n-th eigenstate in the potential (15) will be $N_n=B_nN$.

Let us now return to the perturbation (8). After switching to imaginary time, it acquires the periodic form

$$f(t)=\sum_i f_i(t),$$

where $f_i(t)=\Lambda_i e^{-i\lambda_i t}$.

The probability of transitions in the spectrum (16) under the influence of a periodic perturbation $f_i(t)$ is determined mainly by the frequencies

$$\lambda_i=\lambda_{\nu n}=\frac{w_\nu-w_n}{\hbar}$$

and is found from the expression

$$dW_{n\nu}=\frac{1}{\hbar}(|\Phi_{\nu n}|^2\delta(w_\nu-w_n-\hbar\lambda_{\nu n})), \tag{17}$$

where w_n and w_ν are the energies of the stationary states between which a transition occurs and $\Phi_{\nu n}$ is the corresponding transition matrix element. The presence of a δ function in Eq. (17) signifies that a transition between neighboring levels occurs almost definitely if at least one λ_i equals $\lambda_{\nu n}$. For this reason, since the probability that a corresponding λ_i materializes in a given ensemble is given by the ratio Λ_i/Λ, the probabilities of transitions in the spectrum (16) can be calculated. Next, using the method described in Sec. 1, we calculate numerically the number of particles of an ensemble which after a series of transitions occupy the zeroth energy level. Then we make the reverse substitution $it\rightarrow t$ and calculate in the quasiclassical approximation the squared modulus of the wave function behind the barrier, determining ultimately the barrier transmittance for each particle of the ensemble. The product of this coefficient and the number of particles in the zeroth state determines the number of particles which find themselves on the other side of the barrier. The ratio of this number to the initial number of particles in the ensemble gives the effective transmittance of the barrier in the presence of subbarrier thermal stimulation Q.

The results obtained by using the above-described numerical method for calculating the tunneling depinning for Bloch walls and walls in a weak ferromagnet of the type terbium orthoferrite are presented in Figs. 3 and 4, respectively. One can see that the effect is indeed of a resonant (with respect to temperature) nature. The maximum of the distribution $Q(T)$ for ferromagnets falls at a temperature of about 7 K and has a width of about 10 K, while for weak ferromagnets the corresponding maximum is shifted to 50 K and is approximately two times wider.

In summary, the present paper examined mechanisms that can increase the probability of tunneling depinning of magnetic domain walls in ferromagnets and weak ferromagnets. In one case, this effect is achieved by obtaining a wall in a metastable minimum in front of the barrier, an additional energy from the thermal system of the crystal, and a consequent decrease of the effective height of the potential barrier. In another case the effect is due to the ''subbarrier'' resonance interaction of the wall with the thermal-magnon system of the crystal.

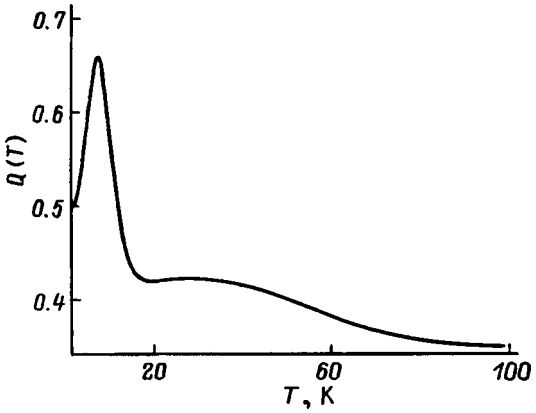

FIG. 3. Barrier transmittance Q in resonance tunneling of Bloch walls as a function of temperature.

The effect of the first mechanism is to increase the depinning in a very wide temperature range (with a width of several hundreds of K) and can influence considerably the processes which are sensitive to the dynamics of walls (internal friction, electrical conductivity, magnetic aftereffect). This effect can apparently be checked empirically by comparing the computed and experimental temperature dependences for the indicated processes in wide temperature intervals. For such a comparison the character of the dependences will be important, while agreement of the absolute values is less important. The latter is so because the values of the barrier heights and widths are determined indirectly on the basis of one or another model. They are essentially adjustable parameters. The values adopted for the parameters in the present work are the standard values for the materials discussed, but they were not attached to any specific material. Actually, they were chosen so that the effects described would be readily apparent. Unfortunately, we know only of experimental works performed at low temperatures (as a

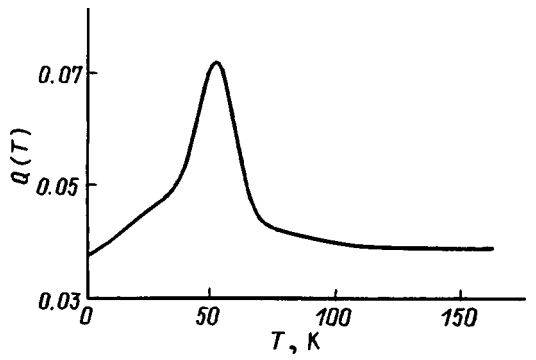

FIG. 4. Temperature dependence $Q(T)$ for walls in a weak ferromagnet.

rule, liquid-helium temperatures).[2,3,11,12] It is important to extend the experimental investigations of tunneling into the high-temperature region.

The check of the second mechanism described above is more encouraging. Taking for the parameters of pinning centers (comparatively high potential barriers), for whose transmittance vanishingly small values are obtained, the values mentioned above and using the experimental data attesting to tunneling depinning at low temperatures, subbarrier resonance thermal stimulation can indeed be recognized as the mechanism that gives the observed values of the transmittance. In any case, here, in contrast to prebarrier pumping, where the influence of ordinary thermal activation was superimposed, the effect can be manifested in a pure form. For this reason, it can be identified by simply comparing the calculations and the experimental data for samples for which reliable values of the parameters of the potential relief of the defects have been determined. The latter problem appears to be most conveniently solved by magnetic-noise methods.

I thank A. K. Zvezdin for helpful discussions of this work and for valuable remarks.

[1] T. Egami, Phys. Status Solidi B **57**, 211 (1973).
[2] E. M. Chudnovski, O. Iglesias, and P. C. E. Stamp, Phys. Rev. B **46**, 5392 (1992).
[3] Kiming Hong and N. Giordano, J. Phys.: Condens. Matter **8**, L301 (1996).
[4] V. V. Dobrovitskiĭ, Zh. Éksp. Teor. Fiz. **109**, 1420 (1996) [J. Exp. Theor. Phys. **82**, 766 (1996)].
[5] V. V. Dobrovitski and A. K. Zvezdin, J. Magn. Magn. Mater. **157/158**, 419 (1996).
[6] A. M. Tishin and V. V. Makhro, Phys. Lett. A **189**, 331 (1994).
[7] L. D. Landau and E. M. Lifshitz, Phys. Z. UdSSR **8**, 153 (1935).
[8] W. Doring, Z. Naturforsch. A **3a**, 373 (1948).
[9] L. D. Landau and E. M. Lifshitz, *Quantum Mechanics* [Pergamon Press, N. Y.; Nauka, Moscow, 1989].
[10] A. K. Zvezdin, JETP Lett. **29**, 553 (1979).
[11] B. Barbara and E. Chudnovski, Phys. Lett. A **145**, 205 (1990).
[12] E. M. Chudnovski and L. Gunther, Phys. Rev. Lett. **60**, 661 (1988).

Translated by M. E. Alferieff

Role of the oxygen subsystem in the double-exchange mechanism

S. M. Dunaevskiĭ

St. Petersburg Nuclear Physics Institute, Russian Academy of Sciences, 188350 Gatchina, Russia
(Submitted February 6, 1998)
Fiz. Tverd. Tela (St. Petersburg) **40**, 1861–1864 (October 1998)

The paper is an attempt at unraveling the role of $p-d$ hybridization in perovskites exhibiting giant magnetoresistance by performing a semiclassical calculation of single-particle eigenenergies of electrons in the triatomic system Mn–O–Mn for arbitrarily oriented manganese-ion magnetic moments. It is shown that, in the most interesting case of the system having three electrons, the hopping integral in the Zener double-exchange model is modified in such a way that it does not vanish for any mutual orientation of the manganese magnetic moments. The ferromagnetic state remains the ground state of the system. For an even number of electrons, the antiferromagnetic (G-type) ordering of the nearest manganese magnetic moments corresponds to the minimum total energy of the system.
[S1063-7834(98)01910-8]

1. Qualitative interpretation[1] of the temperature dependence of resistivity and negative magnetoresistance of the substituted perovskite $La_{1-x}Ca_xMnO_3$ is based on the Zener double-exchange model.[2] The term "double" indicates here that an electron transfers from one ion to another through exchange interaction with the two electrons of the oxygen ion located between the manganese ions. Ferromagnetic ordering of magnetic moments of the manganese ions Mn^{3+} ($S=2$) and Mn^{4+} ($S=3/2$) increases the electron hopping probability and favors the onset of metallic conduction in the system. The double-exchange model was subsequently refined in Refs. 3–5 and some other publications. Some authors take into account also, besides the double exchange, electron-phonon[6,7] or electron-electron interaction.[8] All these studies consider, however, only the manganese subsystem and disregard the effect exerted by oxygen, transition-metal, and rare-earth atoms on the transport properties of the perovskites.

2. In considering the double exchange in $LaMnO_3$-type compounds, one usually assumes the outer electrons of lanthanum and manganese to transfer to oxygen, thus making this compound an insulator (dielectric) with a formula $La^{3+}Mn^{3+}O_3^{2-}$. Cubic environment splits the d level into a triply degenerate t_{2g} and a doubly degenerate e_g sublevel. In octahedral environment, the energy of the t_{2g} level is less than that of the e_g level, and therefore, in accordance with the first Hund's rule, the three d electrons with the same spin orientation fill the lower t_{2g}, and the fourth electron with the same spin occupies the e_g level. The t_{2g} electrons are assumed to be strongly localized and not to take part in the transfer process. When lanthanum in $LaMnO_3$ is partially replaced by divalent atoms of calcium or strontium, the Mn^{3+} and Mn^{4+} ions will occupy equivalent crystallographic positions. If the extent of substitution is large enough, the e_g electron will acquire a probability of hopping from one manganese ion to another, a process which can be denoted by Mn^{3+}, $Mn^{4+} \leftrightarrow Mn^{4+}$, Mn^{3+}. Anderson and Hasegawa[3] were the first to show that the hopping integral has in this case the following form

$$t_{ij}^* = t^* \cos(\theta_{ij}/2),$$

$$\cos(\theta_{ij}/2) = \frac{(S_i + S_j\sigma + 1/2)}{2S+1} \equiv \frac{S_0 + 1/2}{2S+1}, \tag{1}$$

where θ_{ij} is the angle between vectors S_i and S_j, and $S=3/2$. In the general case of arbitrary mutual orientation of spins S_i and S_j, one can readily obtain from Eq. (1), using the well-known rules[9] of spinor component transformation under reference-frame rotation (see Ref. 10), more general expressions for the hopping integral and write the following simple relation for the effective double-exchange Hamiltonian:

$$H_{DE} = -\sum_{ij} (t_{ij}^* d_i^+ d_j + \text{h.c.}),$$

$$t_{ij}^* = t^*(R_{ij}) \left\{ \cos\left(\frac{\theta_i}{2}\right)\cos\left(\frac{\theta_j}{2}\right) + \sin\left(\frac{\theta_i}{2}\right)\sin\left(\frac{\theta_j}{2}\right) \times \exp[i(\varphi_i - \varphi_j)] \right\},$$

$$d_i = \cos\left(\frac{\theta_i}{2}\right) c_{i\uparrow} + i \sin\left(\frac{\theta_i}{2}\right) \exp(i\varphi_i) c_{i\downarrow}. \tag{2}$$

Here $t^*(R_{ij})$ is the hopping integral in the tight-binding approximation, which depends on the position vector R_{ij} connecting the nearest-neighbor manganese ions, θ_i and φ_i are the angles specifying the direction of the local spin S_i relative to the quantization axis common for ions i and j, t_{ij}^* is the e_g-electron hopping integral between two nearest-

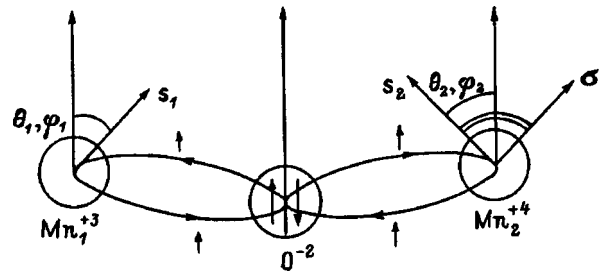

FIG. 1. Triatomic double-exchange model for arbitrary orientation of the atomic magnetic moments of manganese ions with inclusion of six *p* and *d* orbitals.

neighbor manganese ions of different valency, $c^{+}_{i\sigma}(c_{i\sigma})$ are the electron creation (annihilation) operators for position i in the local reference frame, and d^{+}_{i} (d_i) are the creation (annihilation) operators for a spin-up electron in position i in the common reference frame. The double-exchange Hamiltonian is obtained using the condition $J_H > |t^*_{ij}|$, where J_H is a (positive) parameter of the intratomic Hund's interaction of the spin operator σ of this electron with the atomic spin moment S_i. This condition requires that the electron spin be always parallel to the local atomic-spin moment both before and after the transfer. Equations (1) and (2) were derived by considering the two-level, two-center problem with one electron. The intermediate oxygen ion, which is simulated by a doubly filled energy level, acts in such an approach only on the absolute value of parameter $t^*(R_{ij})$. The filled oxygen level is implicitly assumed to lie below the e_g level $(E_p < E_d)$. The latter assumption has to be dropped, because the e_g level in free transition-metal ions lies always below the oxygen-ion p level $(E_p > E_d)$, and in a solid usually $E_p \sim E_d$, if one understands by these parameters the centers of the corresponding bands. In order to take into account hybridization between the p states of the oxygen ion and the nondegenerate e_g state of the transition-metal ion in double exchange, one has to consider the three-center problem with six atomic orbitals and three electrons (two transition-metal ions sandwiching an oxygen ion). A similar problem was first treated in Ref. 11, but only for the p states of an oxygen ion with two electrons in the system.

This work reports a semiclassical calculation of single-particle eigenenergies of electrons in the triatomic Mn-O-Mn system for the case of arbitrary orientation of manganese magnetic moments. The odd number of electrons results in the energy of the system becoming dependent on the half-angle between the local atomic moments, a situation characteristic of double exchange. The ground state of the system for an even number of electrons is always antiferromagnetic.

3. To determine the eigenvalues of the system in Fig. 1 within the above assumptions, one has to solve a sixth-order secular equation $\det(H-EI)=0$, where the Hamiltonian matrix taken in the basis $(d^{\uparrow}_1, d^{\downarrow}_1, d^{\uparrow}_2, d^{\downarrow}_2, p^{\uparrow}, p^{\downarrow})$, with only interaction among the nearest neighbors included, has the form

$$H=\begin{pmatrix} E_d-JS & 0 & 0 & 0 & a_1 & b_1 \\ 0 & E_d-J(S+1) & 0 & 0 & c_1 & a_1 \\ 0 & 0 & E_d-JS & 0 & a_2 & b_2 \\ 0 & 0 & 0 & E_d-J(S+1) & c_2 & a_2 \\ a_1 & c_1^* & a_2 & c_2^* & E_p & 0 \\ b_1^* & a_1 & b_2^* & a_2 & 0 & E_p \end{pmatrix}, \tag{3}$$

where $a_k = t\cos(\theta_k/2)$, $b_k = i^*t\sin(\theta_k/2)\exp(-i\varphi_k)$, and $c_k = i^*t\sin(\theta_k/2)\exp(i\varphi_k)$ $(k=1,2)$ are the coefficients of the binary spinor-component transformation, t is the Hamiltonian matrix element between the oxygen p orbital and the manganese d orbital which have the same spin index with respect to the quantization axis common for all atoms, $J(J_H)$ is the intratomic exchange integral, and $S=3/2$ is the manganese-ion spin. A Hartree-Fock self-consistent relativistic calculation using programs of Ref. 12 yields $J=0.25$ eV for the value of this integral for a free manganese ion Mn^{3+}, which can be larger than t^* but less than $t \geqslant 1$ eV.[13] Matrix (3) is a generalization of the expression (4×4 matrix) considered earlier,[3] which did not contain dependence on the azimuthal angle. Following some cumbersome calculations, the secular equation can be reduced to the form

$$\begin{aligned} &[(E'_d-E)^2 - J^2(S+1/2)^2]^2(E_p-E)^2 \\ &\quad -4t^2[(E'_d-E)^2 - J^2(S+1/2)^2](E'_d-E)(E_p-E) \\ &\quad +4t^4[(E'_d-E)^2 - J^2(S+1/2)^2\cos^2(\theta_{12}/2)] = 0, \\ &E'_d = E_d + J/2. \end{aligned} \tag{4}$$

Here θ_{12} is the angle between the local spins of the nearest-neighbor manganese ions. Introducing the parameter $\Delta^2 = J^2(S+1/2)^2$, one readily comes to

$$E = E_p - 2t^2\frac{(E'_d-E) \pm \Delta\cos(\theta_{12}/2)}{(E'_d-E)^2-\Delta^2}. \tag{5}$$

If we substitute now E_p for E on the right-hand side of Eq. (5) and neglect magnetic interactions, so that $\Delta=0$, these energies will coincide with the values obtained in first-order perturbation theory. To find approximate values of the roots of Eq. (4), one can, following Ref. 11, look for solutions close to the unperturbed atomic levels in the form

$$E_i \sim E_{d(p)} - \xi t^2 + \eta t^4. \tag{6}$$

Of particular interest are the solutions obtained for d levels, which were not considered earlier. The solutions for the two lowest energy levels can be written

$$\begin{aligned} &\xi^d_{\pm} = \frac{1 \pm \cos(\theta_{12}/2)}{(E_p - E_d + JS)}, \\ &\eta^d_{\pm} = \frac{\xi^d_{\pm}[\xi^d_{\pm}(E_p-E_d+JS) + 2\xi^d_{\pm}\Delta - 2]}{2\Delta(E_p-E_d+JS)}. \end{aligned} \tag{7}$$

The solutions for the two upper d levels have a similar form, and those for the p levels coincide with the ones derived in Ref. 11.

3.1. In the case of strong intratomic exchange interaction, where

$$JS,\Delta \gg |t|, \quad |(E_p - E_d)|, \tag{8}$$

one can limit oneself in Eq. (6) to the first term, which is proportional to the square of the interatomic matrix element, and write the following expressions for the eigenenergies of a triatomic system in their ascending order

$$\begin{aligned}
E_1 &= E_d - JS - t^2 \frac{1+\cos(\theta_{12}/2)}{E_p - E_d + JS}, \\
E_2 &= E_d - JS - t^2 \frac{1-\cos(\theta_{12}/2)}{E_p - E_d + JS}, \\
E_3 &= E_p - 2t^2 \frac{E_d' - E_p - \Delta\cos(\theta_{12}/2)}{(E_d' - E_p)^2 - \Delta^2}, \\
E_4 &= E_p - 2t^2 \frac{E_d' - E_p + \Delta\cos(\theta_{12}/2)}{(E_d' - E_p)^2 - \Delta^2}, \\
E_5 &= E_d + J(S+1) - t^2 \frac{1-\cos(\theta_{12}/2)}{E_p - E_d - J(S+1)}, \\
E_6 &= E_d + J(S+1) - t^2 \frac{1+\cos(\theta_{12}/2)}{E_p - E_d - J(S+1)}.
\end{aligned} \tag{9}$$

These expressions permit the following two important conclusions: (a) For an even number of filled levels, the energy of the system does not depend on the mutual orientation of local magnetic moments; (b) the levels corresponding to the oxygen-ion p orbitals (E_3, E_4) lie above the electronic levels of positive spin-up manganese ions (E_1, E_2), which are first to become filled. Therefore in a three-electron system the initially degenerate p level of oxygen will split into two, of which only the lowest one will be filled. The hybridization-induced change in the total energy of one d and two p electrons in this system can be written

$$\begin{aligned}
\Delta E &= E_1 + E_2 + E_3 - 2E_p - E_d + JS \\
&= E_d - E_p - JS + 2t^2\Delta \frac{1+\cos(\theta_{12}/2)}{(E_d' - E_p)^2 - \Delta^2},
\end{aligned} \tag{10}$$

which implies that the total energy of the system will be minimum for ferromagnetic ordering of the manganese atomic magnetic moments [$\theta_{12}=0$, and the denominator in Eq. (10) is assumed to be less than zero]. If the number of filled levels is even, the dependence of the total energy of the system on magnetic ordering can be found by taking into account in the expressions for the eigenvalues terms with t^4. As follows from Eq. (7), the energy of a two-electron system ($CaMnO_3$) will be minimum in the case of antiferromagnetic (G-type) ordering of magnetic moments of the manganese ions with all its nearest neighbors. This statement applies equally to the four-electron case (undistorted $LaMnO_3$ structure), because the antiferromagnetic contribution of the two oxygen electrons to the energy of our system was found[11] earlier. The twofold degeneracy of the e_g level in $LaMnO_3$ gives rise to Jahn-Teller distortions, whose effect on the magnetic structure of perovskites is not considered here.

3.2. In the more realistic case of weak intratomic exchange coupling (compared to the interatomic hopping integral), where

$$JS,\Delta \ll |t|, \quad |(E_p - E_d)| \quad \text{and} \quad E_p > E_d, \tag{11}$$

the sequence of the levels will change in such a way that the upper filled level in a three-electron system will be

$$E_6 = E_d + J(S+1) - t^2 \frac{1+\cos(\theta_{12}/2)}{E_p - E_d - J(S+1)}. \tag{12}$$

4. The above pattern of orbital filling in a triatomic system with strong intratomic exchange coupling and three electrons, which models the situation in substituted perovskites $La_{1-x}Ca_xMnO_3$, results in the appearance of a "hole" at the oxygen ion, which differs from the usual pattern of double exchange in perovskites postulating the existence of "holes" at manganese ions. It is buttressed, however, by electronic band calculations of the $La_{1-x}Ca_xMnO_3$ system and data obtained by photoemission and x-ray spectroscopy on $La_{1-x}Sr_xMnO_3$ (Refs. 14 and 15). The conventional Zener double-exchange scenario for which model Hamiltonian (2) was introduced is possible only for $E_p \ll E_d$, a condition which is hardly realistic for perovskites. Nevertheless, Eq. (10) indicates the formation in a solid of a partially filled band (derived from the broadened E_3 and E_4 levels), whose width should depend on magnetic ordering. The width of this band will grow, and the perovskite resistance (in the low-temperature domain), decrease with increasing external magnetic field or decreasing temperature. The same results are obtained for the case which in our opinion is more realistic, namely, where the oxygen p level lies considerably above all split manganese d levels, and it is here that the hole appears.

Thus in all the cases considered here calculations yield the same results as those obtained within the double-exchange model, but with a modified hopping integral

$$t_{ij}^* = t^2(\alpha + \beta\cos(\theta_{ij}/2)), \tag{13}$$

which never vanishes. In the case of strong intratomic exchange coupling, coefficients α and β can be found in an explicit form from Eq. (9) for E_3, and for weak coupling (compared to the interatomic hopping integral) $\alpha = \beta = 1/[E_p - E_d - J(S+1)]$. An analysis of the effect of the oxygen subsystem on the transport properties of perovskites, with inclusion of the twofold degeneracy of the e_g level, will be carried out in a separate publication.

Support of the Russian Fund for Fundamental Research (Grant 96-02-18143) is gratefully acknowledged.

[1] G. H. Jonker and J. H. van Santen, Physica **16**, 337 (1950).
[2] C. Zener, Phys. Rev. **82**, 403 (1951).
[3] P. W. Anderson and H. Hasegawa, Phys. Rev. **100**, 675 (1955).
[4] P. G. de Gennes, Phys. Rev. **118**, 141 (1960).
[5] K. Kubo and N. Ohata, J. Phys. Soc. Jpn. **33**, 21 (1972).
[6] A. J. Millis, P. B. Littlewood, and B. I. Shrainman, Phys. Rev. Lett. **74**, 5144 (1955).
[7] J. D. Lee and B. I. Min, Phys. Rev. B **55**, 12454 (1997).
[8] S. Ishibara, J. Inoue, and S. Maekawa, Phys. Rev. B **55**, 8280 (1997).
[9] L. D. Landau and E. M. Lifshits, *Quantum Mechanics* [Pergamon Press, Oxford (1974); Nauka, Moscow (1963), 246 pp.].
[10] E. Müller-Hartmann and E. Dagotto, Phys. Rev. B **54**, R6819 (1996).

[11] T. Oguchi, K. Terakura, and A. R. Williams, Phys. Rev. B **28**, 6443 (1983).
[12] I. M. Band and M. B. Trzhaskovskaya, *Tables of Eigenenergies of Electrons, Densities near Zero, and Mean Values in Self-Consistent Fields of Atoms and Ions* [in Russian], Preprint No. 91, LNPI AN SSSR (Leningrad, 1974).
[13] L. F. Mattheis, Phys. Rev. B **5**, 290 (1972).
[14] W. E. Pickett and D. J. Singh, Europhys. Lett. **32**, 759 (1995).
[15] T. Saitoh, A. E. Bocquet, T. Mizokawa, H. Namatame, A. Fujimori, M. Abbate, Y. Takeda, and M. Takano, Phys. Rev. B **51**, 13942 (1995).

Translated by G. Skrebtsov

Three-dimensional diagrams of the regions occupied by induced Anger states in a multidomain magnetic medium

G. S. Kandaurova and A. A. Rusinov

Ural State University, 620083 Ekaterinburg, Russia
(Submitted February 9, 1998)
Fiz. Tverd. Tela (St. Petersburg) **40**, 1865–1870 (October 1998)

The regions of existence of Anger states in an iron garnet film are plotted and investigated for the first time in a space of three controlling parameters: the frequency and amplitude of the alternating field and the magnitude of the static bias field. It is shown that the dynamic spiral domains differ significantly in their configuration and properties in different regions. A quantitative parameter involving the velocity of the domain walls and the ''looseness'' (sparseness) of the dynamic array of magnetic domains is introduce to characterize the favorability of conditions for the formation of spiral domains. © *1998 American Institute of Physics.* [S1063-7834(98)02010-3]

A new phenomenon, essentially the onset of stable, ordered, dynamic domain structures in the form of spiral or ring domains in polydomain magnetic films under the influence of a spatially homogeneous, continuous, low-frequency ($f=10^2-10^4$ Hz) alternating magnetic field, has been reported previously.[1,2] A state in which dynamic self-organization takes place in a chaotically moving system of magnetic domains has been given the name Anger state.[3] The amplitude-frequency ($f-H_0$) region in which ordered structures are formed, i.e., the region of existence of an Anger state exists, was first constructed in Ref. 2. The influence of a static magnetizing field (bias field H_b) on dynamic spiral domains (DSDs) in an Anger state of iron garnet films has been investigated.[3] It has been established that the field H_b, which comprises a relatively small part of the amplitude H_0 of the alternating field (10–20%) completely eradicates the Anger state. However, it has been shown[4] that stronger magnetizing fields H_b are capable of creating new Anger states and DSDs of a kind that are not observed for zero field H_b. Consequently, a static bias magnetic field H_b, together with the amplitude H_0 and the frequency f of the alternating field, emerges as a third controlling parameter of an open thermodynamic system — the investigated sample. This fact dictates the need for analyzing the three-dimensional $f-H_0-H_b$ state diagrams of the dynamic system of magnetic domains. In this paper we map the first such diagrams for magnetically uniaxial iron-garnet films characterized by perpendicular anisotropy. We distinguish the regions of the Anger state and investigate the properties of spiral domains in these states.

The samples were epitaxial films having the usual labyrinth structure described by the Kittel model. The alternating field $H_{\sim}=H_0 \sin 2\pi ft$ and the static field H_b were oriented along the normal to the films, i.e., along their easy magnetization axis. The controlling parameters were varied within the following ranges: $f=0-140$ kHz; $H_0=0-100$ Oe; $H_b=0-80$ Oe. The important characteristic of each sample is the static saturation field H_s. It was determined in practice as the field in which the majority of the magnetic-bubble domains collapse during quasistatic magnetization.[1)] The few remaining bubbles (those ''stuck'' at defects, or ''hard'' bubbles) were ignored. The domains were exposed by means of the Faraday magnetooptical effect and were photographed with an exposure time $\tau_{ex}=1$ ms.

The $f-H_0-H_b$ diagrams were plotted as follows. To establish a uniform initial state, the samples were demagnetized by an alternating field having a frequency $f=50$ Hz and an amplitude that decreased smoothly to zero from $H_0>H_s$. A certain bias field H_b was then set, and the two-dimensional $f-H_0$ region of existence of the Anger state was determined at $H_b=\text{const}$ by the technique described in Ref. 2. The procedure was subsequently repeated several times for different constant fields H_b. The field H_b was varied in half-oersted (0.5 Oe) steps.

In the example of a $(YLuBi)_3(FeCa)_5O_{12}$ film having a thickness $L=0.95$ μm, the results obtained after computer processing of the experimental data reveal a static saturation field $H_s=50$ Oe, a saturation magnetization $J_s=11$ G, an anisotropy field $H_A=13$ kOe, and a stripe domain period in the initial domain structure $P_0=33$ μm. These results are shown in Fig. 1. It is evident that in the space $R(f-H_0-H_b)$ for a positive bias field H_b there are four spatial figures,[2)] i.e., regions in which the Anger state exists. Here chaos$\leftrightarrow$order transitions take place, DSDs appear, survive with a certain lifetime T_g, vanish, and reappear, and this process continues as long as the pump field operates and the temperature remains constant. These regions, labeled R_0, R_1, R_2, and R_3 in Fig. 1, are far apart on the frequency scale. In the case of negative bias fields ($-H_b$) a pattern similar to that in Fig. 1 is observed, but now as its mirror image about the plane $H_b=0$. Thus, when both signs of the field H_b are taken into account, we have seven Anger state regions for the given sample. Only in one of them, R_0, does the Anger state exist without a bias field; in the others, R_1, R_2, and R_3, it exists only in the presence of the field H_b. Consequently, the first region is naturally called the ground Anger state, and the others are called induced Anger states.

The spiral domains in regions R_0, R_1, R_2, and R_3 are very different in configuration and dynamic behavior. Fig-

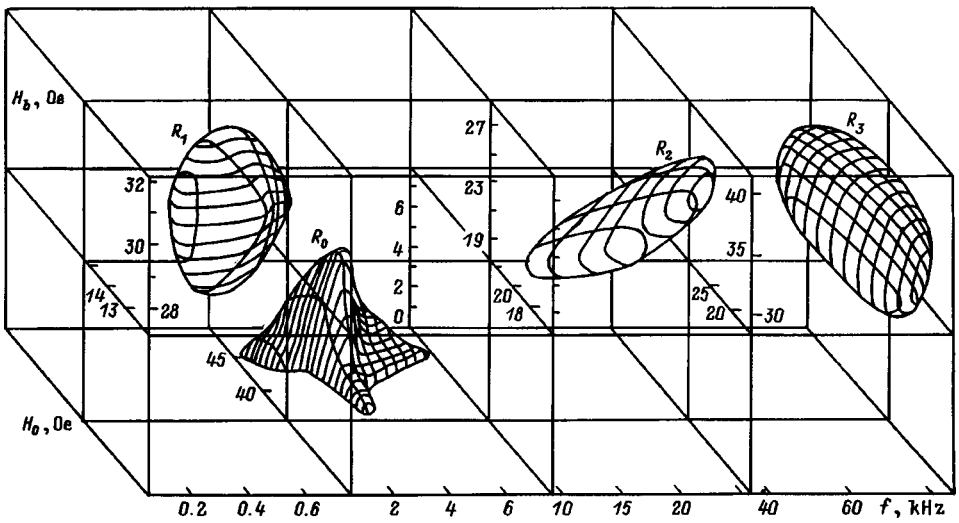

FIG. 1. Regions of existence of dynamic spiral domains in the ground (R_0) and bias field-induced (R_1, R_2, R_3) Anger states of an iron garnet film.

ures 2a–2d show photographs of spiral domains typical of the regions R_0, R_1, R_2, and R_3. In accordance with these patterns, Figs. 3a–3d illustrate schematically the relations between the fields H_s, H_b, and the total field ($H=H_b+H_0\sin 2\pi ft$) and also between the exposure time τ_{ex} and the period of the alternating field T. It follows from a comparison of T and τ_{ex} that Figs. 2a, 2c, and 2d show time-averaged patterns of the dynamic domain structures. In the case of Fig. 2b (see the schematic diagram in Fig. 3b) the illumination interval τ_{ex} can lie on different parts of the sine curve $H(t)$. If τ_{ex} is associated with the upper (or lower) part of the sine curve, a total magnetization effect is visible in the photographs of the domain structure, i.e., the area of the ''black'' (or ''white'') domains is larger than the area of domains with opposite polarity. If τ_{ex} lies in an interval where $H_\sim$ changes sign, a noticeable third contrast — gray — is added.[3] It is associated with wall oscillations in the DSDs and with lengthening and shortening of the ends of stripe domains during the time τ_{ex}.

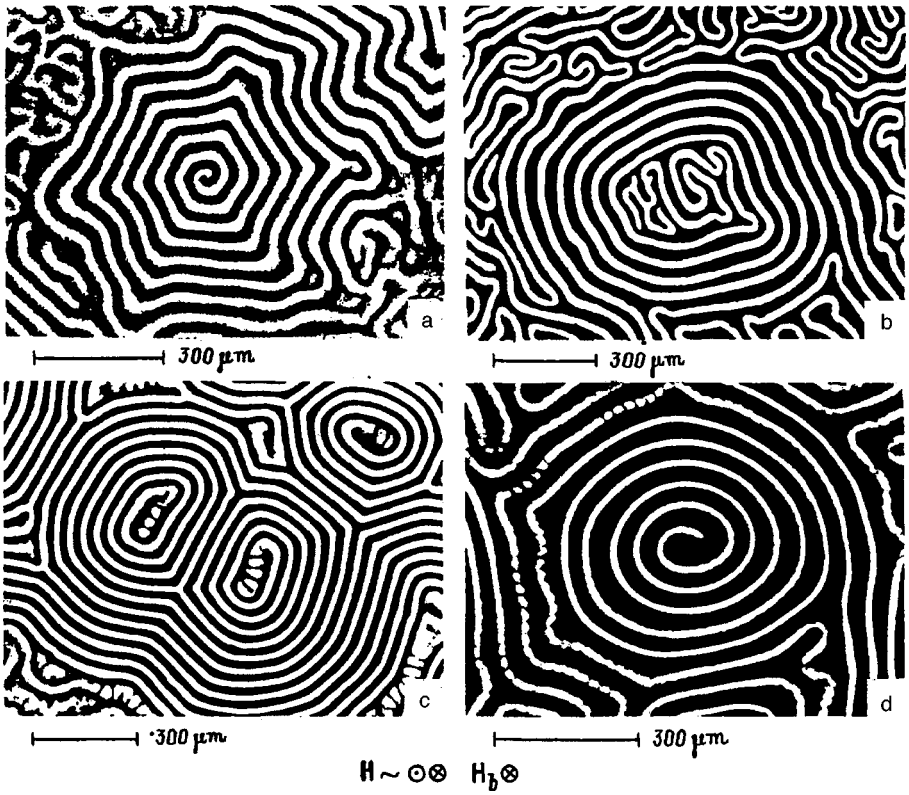

FIG. 2. Dynamic spiral domains in the ground (a) and bias field-induced (b–d) Anger states. a) $f=3$ kHz, $H_0=43$ Oe, $H_b=1.5$ Oe; b) 0.3 kHz, 14 Oe, 30 Oe; c) 20 kHz, 19 Oe, 24 Oe; d) 60 kHz, 18 Oe, 35 Oe. The magnetization in adjacent domains is directed toward the reader and away from the reader.

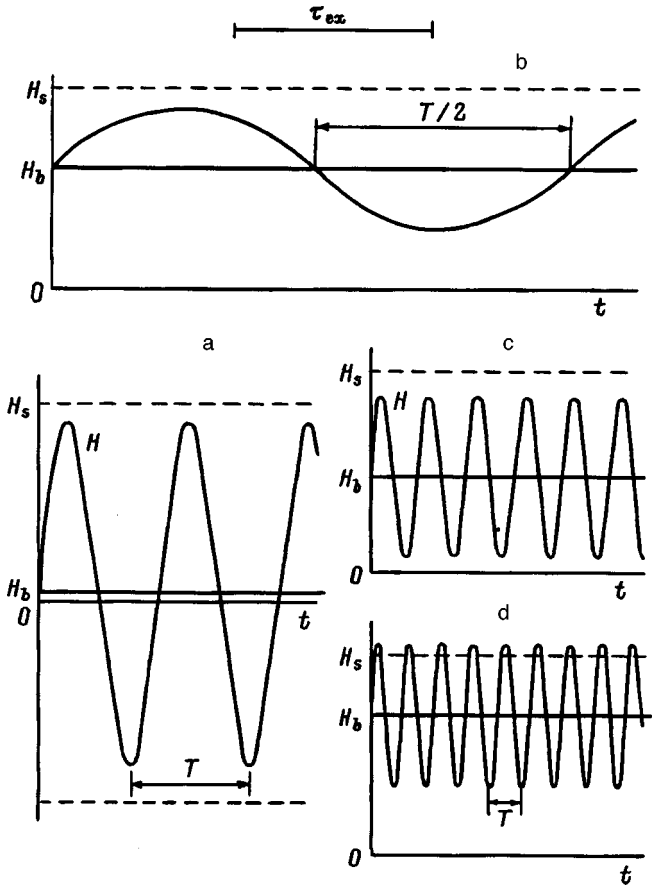

FIG. 3. Diagrams illustrating the relations between the period of the alternating field T, the exposure time τ_{ex} used in photographing the dynamic domain structure, the static bias field H_b, and the alternating field $H_\sim$. Graphs a–d correspond to photographs a–d in Fig. 2.

In R_0 (Fig. 1) the multiturn spirals have a small core ($D_n<80$ μm) in comparison with the outside diameter of the DSDs (Fig. 2a), which can attain 1.5 mm. The period of the stripe domains in the turns is $P=1.3P_0=4.2$ μm. It is evident that the turns of the DSDs have kinks. They are similar to polygons. Spirals of this kind have been studied in detail.[6] The kink effect is possibly attributable to the fact that a weak natural cubic anisotropy becomes superimposed onto strong induced perpendicular anisotropy under the experimental conditions corresponding to Fig. 2a. The wall-energy density[7] and the coercivity of the domain walls can acquire an azimuth dependence in that case, more or less reflecting the crystallographic symmetry of the film. The average lifetime of a given DSDs is 1.5 s, the spirals moving on average with a velocity of 2 mm/s.

In R_1 (Fig. 1) large-scale, long-lived (T_g attains 2 min) DSDs with large cores and smooth turns are formed (Fig. 2b). The maximum core diameter can be ~ 300 μm. The outside diameter of the spirals is 0.7–1.2 mm. The turns have an average period $P=1.4P_0=47$ μm. Such DSDs essentially stay in place during their lifetime T_g, but rapid chaotic motion of the free end of the spiral domain is now visually observed in the core, including its branching into several arms (Fig. 2b). The time for this end to make any appreciable change in position is much longer than τ_{ex} and the period of the alternating field T, so that a sharp domain structure pattern is seen inside the core of the DSD in Fig. 2b.

Region R_2 (Fig. 1) is typified by the formation of dense systems of spiral domains (Fig. 2c). Consequently, both the spirals and their cores are deformed. On the other hand, as observed in Refs. 1 and 3, no compression of the turns is noticeable here. Such DSDs have a maximum outside diameter of approximately 0.7 mm. On average, the core has dimensions of 0.2 mm. The turns of the DSDs have a smooth configuration, are densely packed, and are separated by a distance $P=1.1P_0=37$ μm. The DSDs in R_2 are more mobile than in R_1 and have a shorter lifetime ($T_g<2$ s). They move chaotically (''swim'') with a velocity of the order of 1 mm/s. Periodic distortions in the width of the stripe domain are visible in the core and at the outermost turns. This property indicates irregular or undulating motion of the domain walls during the exposure time τ_{ex}, or it indicates the formation of chains of bubble domains.

A ''bottleneck'' effect is also visible in R_3 (Fig. 2d). This effect can be induced by the occurrence of higher harmonics in the oscillations of the domain walls or the formation of Bloch lines.[8] Now DSDs having an outside diameter smaller than 0.7 mm and a small core ($D_n=0.1$ mm) are formed in R_3. The period of the turns of the DSDs is $P=1.4P_0=47$ μm. Since H_b is much greater than H_0 [$H_b=(1.5-2)H_0$; see the diagram in Fig. 3d), the time-averaged pattern of the domain structure corresponds to a partially magnetized state (the total area of the ''black'' domains is definitely greater than the area of the ''white'' domains, and vice versa for $H_b<0$]. As for the spiral dynamics, these ''loose'' DSDs are the most mobile structures of all those described above. They have a shorter life ($T_g<1$ s), move more vigorously, and rotate at random. The average translational velocity of the DSDs, on the whole, is ~ 1.5 mm/s.

We know[3] that for $H_b=0$ dynamic spiral domains twisted clockwise (topological charge $+q$) or counterclockwise ($-q$) occur with equal probability in the ground Anger state (Fig. 1, region R_0). The application of a bias field H_b leads to the predominance of DSDs with one sign of q. For example, more of the DSDs have $+q$ for $+H_b$, and the opposite is true for $-H_b$. In the case of induced Anger states (Fig. 1, regions R_1, R_2, and R_3) we have not noticed any appreciable predominance of DSDs with either sign of q.

We should mention that in all the situations described above, mainly one-armed DSDs are formed in the given sample; two-armed DSDs are encountered far less frequently. The outer turns of the spirals, as a rule, transform to stripe domains of the surrounding domain chaos. A distinct link has not been observed between the core of a DSD and visible microscopic defects in the sample. We note, in addition, that, when the alternating field is suddenly removed, the spiral domains persist in the static field $H=H_b$, but when this field is changed, they behave like ordinary static spiral structures.[9] This means that the induced Anger states, like the Anger states previously studied in detail in Refs. 1–5, may indeed be identified with states of the autowave type, but the DSDs are not identical to spiral autowaves.[10]

Analyzing the results of the observations, we can make

assumptions about the conditions for the formation of DSDs. It is evident from Fig. 3 that in every case where Anger states, induced Anger states, and DSDs appear, the amplitude values of $H_\sim$ are close to the saturation field H_s. It has been shown previously[9,11] that DSDs are formed in the field interval between the collapse of magnetic bubble domains (during magnetization) and the field required for the nucleation and formation of an array of stripe domains (as the field is decreased). This is the region of the triangular part of the tips of the dynamic hysteresis loops.[12,13] Dynamic spiral domains are most likely formed in the transition of hard bubble domains into strip domains.

The ''head'' of this domain moves with a velocity **V** and is acted upon by a gyrotropic force $\mathbf{F}_g$ perpendicular to the velocity. Following Ref. 14, for the case of not too high velocities we write $\mathbf{F}_g$ in the form

$$\mathbf{F}_g = Js[\mathbf{G}\cdot\mathbf{V}]/\gamma, \tag{1}$$

where γ is the gyromagnetic ratio, **G** is the resultant gyrotropic vector, equal to $\mathbf{G}=\int \mathbf{g}\cdot\mathbf{V}$. Here $\mathbf{g}=-\sin\theta[\nabla\theta\cdot\nabla\varphi]$ is the density of the gyrotropic vector, and $\nabla\theta$ and $\nabla\varphi$ are the gradients of (respectively) the polar and azimuth angles defining the orientation of the vectors $\mathbf{J}_s$ in a moving magnetic inhomogeneity, i.e., the domain wall. Setting either gradient equal to zero, we obtain $\mathbf{F}_g=0$. Conversely, the larger the value of **G**, the larger $\mathbf{F}_g$ is. The quantity **G** depends on the torsion of the wall and on the number and sign of Bloch lines and Bloch points in it. For a closed domain of arbitrary configuration **G** (and, hence, $\mathbf{F}_g$) is directly related to the effective number of complete turns J_s in the domain wall.

We lack information on the internal structure of the domain walls in investigated DSDs. The fact that the domain walls in iron garnet films in an alternating magnetic field can contain various types of Bloch lines is inferred from numerous experimental and theoretical papers (see, e.g., Ref. 8). It can be assumed that the DSDs do in fact evolve from hard bubble domains having a complex internal structure of the domain walls and a large vector **G**. A domain of this type exists in a metastable state, and when the field is decreased, the domain begins to change over to a stripe domain before the ordinary ''soft'' magnetic bubbles do. It is possible to have a symmetrical distribution of Bloch lines and symmetrical ''stretching'' of a bubble domain into a stripe domain with the formation of a two-armed DSD. However, asymmetrical distortion, the stretching of bubble domains, and the formation of one-armed DSDs are more probable.

We now consider the role of the second factor in Eq. (1) for $\mathbf{F}_g$: the velocity V of the domain and its wall. If the frequency f of the field is not too high Fig. 1, regions R_0, R_1, and R_2; Figs. 2a, 2b, and 2c), it is reasonable to assume that the variation of the domain wall will track the variation of the magnetic field dH/dt. Hence, $V=V_0\cos 2\pi ft$. At the times when the field $H_\sim$ reaches its amplitude value the velocity V becomes equal to zero (so that $\mathbf{F}_g=0$) and changes sign. The maximum velocities $V=V_0$ and, hence, the maximum gyrotropic forces correspond to the zero crossings of the field. However, this is the most favorable situation for the formation of DSDs, because a dense array of magnetic domains is present in the sample at this time. Consequently, the formation of a multiturn DSD requires a fairly high velocity V and a sufficiently sparse, or ''loose,'' domain environment around it.

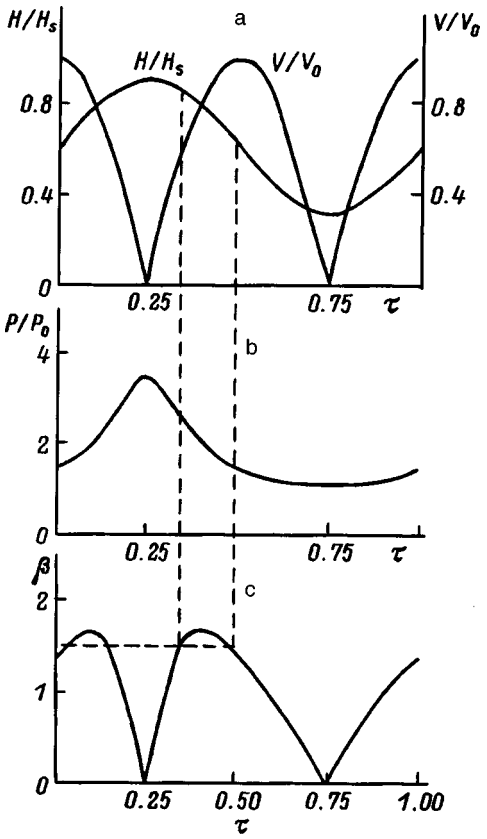

FIG. 4. Variation of the relative quantities H/h_s, and V/V_0 (a), P/P_0 (b), and the parameter β (c) with the time τ during one period T of the alternating field $H_\sim$.

As a first approximation we adopt the effective period P of the dynamic domain structure as a quantitative characteristic of its sparseness. We assume that as $H_\sim$ varies from zero to H_0 (in one quarter period the field $H_\sim = H_0\sin 2\pi ft$), the period P of the dynamic domain structure varies in the same way as in quasistatic magnetization, and the $P(H_\sim)$ curve coincides with the theoretical function $P(H)$ calculated in Ref. 15. Next we introduce the following parameter characterizing the favorability toward the formation of DSDs:

$$\beta(H/H_0)=[P(H)/P_0][V(H)/V_0], \tag{2}$$

where P_0 is the period of the domain structure at $H=0$, and V_0 is the amplitude value of the velocity.

The variations of V/V_0 and the total field $H=H_0+H_\sim$ normalized to H_s as functions of the time $\tau=t/T$ are shown in Fig. 4a. Figure 4b shows the $P_0(\tau)$ curve plotted in accordance with the function $P(H)$ in Ref. 15. The maximum value of the parameter $\beta_{\max}=1.7$, representing the most favorable conditions for the formation of DSDs, occurs for a relative alternating field $H_\sim/H_0=0.9$. We assume that these conditions are preserved in the vicinity of $\beta_{\max}$, for example, for $\beta=1.5-1.7$ (Fig. 4c). Hence it follows that DSDs are most likely to be formed at times when the alternating field decreases from $0.85H_s$ to $0.60H_s$ (Fig. 4a). Here the period

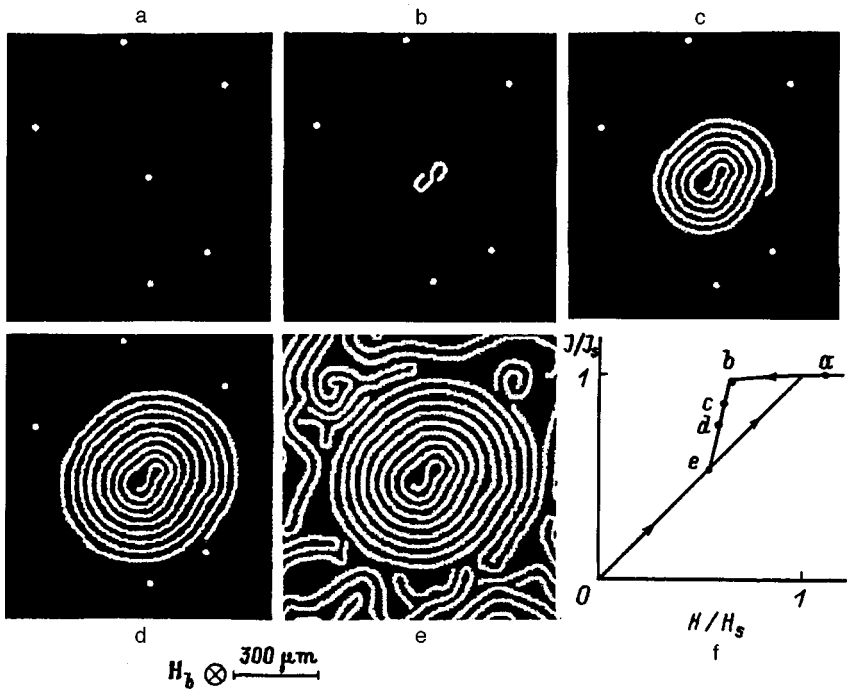

FIG. 5. Evolution of the formation of a spiral domain as the static bias field is decreased. a) $H_b=55$ Oe; b) 32 Oe; c) 31 Oe; d) 30 Oe; e) 28 Oe; f) here the lettered points correspond to the preceding patterns of the domain structure.

of the domain structure varies from $2.5P_0$ to $1.5P_0$ in the interval $\Delta H_{\sim}=(0.85-0.60)H_s$ (Fig. 4b). If $P<1.5P_0$, conditions become less favorable for the formation of DSDs, owing to the increase in the density of the domain array in the sample.

Remarkably, the field interval favoring for the formation of DSDs, normalized to $4\pi J_s$, essentially coincides with the theoretically calculated[11] interval of stability of static spiral domains. In the experiment we have determined the interval ΔH_0 of existence of static spiral domains by direct observation of the nucleation and growth of such domains from ''hard'' bubble domains surviving in fields higher than H_s (Fig. 5). We have found that $\Delta H_b=(0.77-0.62)H_s$. The upper limit in ΔH_b is somewhat lower than the same limit in $\Delta H_{\sim}$ (probably because of hysteresis effects), whereas the lower limits in ΔH_b and $\Delta H_{\sim}$ are almost the same.

The above-noted correspondences most likely indicate that the quasistatic approximation with the introduction of the parameter β is valid up to frequencies ~ 20 kHz. At higher frequencies the variation of the velocity of the domain walls can lag the variation of the field. This property should not be overlooked as the factor responsible for the observed excess of the maximum amplitude values of the alternating field over the value of H_s (Fig. 3d) at a frequency of 60 kHz.

In closing, we emphasize that a theory of Anger states and especially a theory of induced Anger states are nonexistent at the present time. A theory of static spiral domains has been developed,[11] but there is no theory of dynamic spiral domains. In the first[16] and as yet only attempt to provide a theoretical foundation for DSDs the calculations have been carried out only for small deviations of the magnetization vector from the homogeneous state, i.e., what has actually been demonstrated is the possibility of the existence of stable, small-amplitude magnetization waves (spiral solitons). In experimental work, however, judging from the observed high contrast of such patterns like in Fig. 2, the magnetization vectors in adjacent domains are oriented antiparallel to each other and perpendicular to the plane of the film. In reality the formation and lifetime of DSDs can be influenced by a whole set of factors: the velocity, internal structure, and coercivity of the domain walls; the density of the dynamic domain array and the form of the stable dynamic domain structures (in regard to the diversity of these structures see, e.g., the complete dynamic domain phase diagram in Ref. 5); the interaction of ordered and chaotic structures; the relaxation time of the magnetic moments to the equilibrium state, etc. The correct incorporation of these factors into a theory of dynamic spiral domains and the Anger state of a multidomain magnetic medium presents a complex problem.

[1)]Systems of magnetic bubble domains have been created in the sample by exposing it to a field $H_{\sim}$ whose frequency and amplitude correspond to the $(f-H_0)$ region of existence of an array of bubble domains in the dynamic-domain phase diagram (see Ref. 5). If H_s is defined as the field corresponding to disappearance of the last surviving stripe domains, whose tips are generally pinned to defects or the edges of the sample, H_s is obtained 10% higher than the field H_s determined from collapse of the bubble domains.

[2)]To aid visualization, minor bends on the surfaces of the figures are not shown in detail.

[1] G. S. Kandaurova and A. É. Sviderskiĭ, JETP Lett. **47**, 490 (1988).
[2] G. S. Kandaurova and A. É. Sviderskiĭ, Pis'ma Zh. Tekh. Fiz. **14**, 777 (1988) [Sov. Tech. Phys. Lett. **14**, 346 (1988)].
[3] G. S. Kandaurova and A. É. Sviderskiĭ, Zh. Éksp. Teor. Fiz. **97**, 1218 (1990) [Sov. Phys. JETP **70**, 684 (1990)].
[4] G. S. Kandaurova and A. A. Rusinov, JETP Lett. **65**, 63 (1997).

[5] G. S. Kandaurova and A. A. Rusinov, Dokl. Akad. Nauk **340**, 610 (1995) [Phys. Dokl. **40**, 53 (1995)].
[6] G. S. Kandaurova, V. Kh. Osadchenko, A. A. Rusinov, and E. A. Rusinova, JETP Lett. **63**, 478 (1996).
[7] G. S. Kandaurova, L. A. Pamyatnykh, M. A. Shamstudinov, and B. N. Filippov, Fiz. Met. Metalloved. **78**(4), 26 (1994).
[8] V. A. Bokov and V. V. Volkov, Fiz. Tverd. Tela (St. Petersburg) **39**, 660 (1997) [Phys. Solid State **39**, 577 (1997)].
[9] Yu. A. Gobov and G. A. Shmatov, Fiz. Met. Metalloved. **78**(1), 39 (1994).
[10] A. Yu. Loskutov and A. S. Mikhaĭlov, *Introduction to Synergetics* [in Russian], Nauka, Moscow, 1990.
[11] A. B. Borisov and Yu. I. Yalyshev, Fiz. Met. Metalloved. **79**(5), 18 (1995).
[12] I. E. Dikshteĭn, F. V. Lisovskiĭ, E. G. Mansvetova, and E. S. Chizhik, Zh. Éksp. Teor. Fiz. **100**, 1606 (1991) [Sov. Phys. JETP **73**, 888 (1991)].
[13] G. S. Kandaurova and V. Kh. Osadchenko, Pis'ma Zh. Tekh. Fiz. **21**(20), 11 (1995) [Tech. Phys. Lett. **21**, 819 (1995)].
[14] A. P. Malozemoff and J. C. Slonczewski, *Magnetic Domain Walls in Bubble Materials* [Academic Press, New York, 1979; Mir, Moscow, 1982].
[15] C. Kooy and U. Enz, Philips Res. Rep. **15**, 7 (1960).
[16] A. B. Borisov, V. A. Feĭgin, and B. N. Filippov, Fiz. Tverd. Tela (Leningrad) **33**, 2316 (1991) [Sov. Phys. Solid State **33**, 1304 (1991)].

Translated by James S. Wood

Phenomenological theory of the giant magnetoresistance of ferromagnet–nonmagnetic metal granular media

K. Yu. Guslienko

Institute of Magnetism, Academy of Sciences of Ukraine, 252680 Kiev, Ukraine
(Submitted February 24, 1998)
Fiz. Tverd. Tela (St. Petersburg) **40**, 1871–1875 (October 1998)

A phenomenological model is developed for the giant magnetoresistance of granular media comprising ferromagnetic granules in a nonmagnetic metal matrix. Both volume and surface spin-dependent scattering by the ferromagnetic granules are taken into account. The internal electric fields are inhomogeneous because of the different conductivities of the granules and the matrix. The dependence of the effective conductivity of the medium on the average magnetization is calculated and used to explain the giant magnetoresistance effect. The magnetoresistance is plotted as a function of the volume concentration of ferromagnetic granules and the granule radius. Experiments on Co–Cu and Co–Ag granular films are discussed.
 [S1063-7834(98)02110-8]

1. Research on the galvanomagnetic properties of metals (including magnetically ordered metals) today constitutes a vast area of solid-state physics. The magnetoresistance phenomenon, i.e., the dependence of the resistivity of a sample ρ on the external magnetic field, has intrigued researchers for years. Interest in this phenomenon rose considerably toward the end of the eighties following the discovery of giant magnetoresistance (GMR) in inhomogeneous magnetic fields. Characterized by the ratio $\Delta\rho/\rho=[\rho(H)-\rho(0)]/\rho(0)$, the GMR usually attains ten percent or more, is negative and isotropic, and approaches saturation as the magnetic field H increases. Typical of GMR is a dependence on the degree of inhomogeneity in the magnetic order at distances comparable to the mean-free path of conduction electrons. Large GMR is not expected in granular films, but they are simpler to prepare than other GMR systems (multilayer films, spin valves, etc.). By the same token, despite a relatively extensive list of papers on GMR models, the description of the magnetic and transport properties of granular media containing small-scale structural and magnetic inhomogeneities is far from complete. Various types of magnetic behavior are possible as the temperature and the concentration of the ferromagnetic phase vary, *viz.*: superparamagnets, spin glasses, superferromagnets, etc. It is clear only that the cause of GMR is spin-dependent scattering on the surface or in the volume (or both) of ferromagnetic granules of a 3*d* metal (Co, Fe, or FeNi) contained in a highly conducting nonmagnetic matrix (Cu, Ag, or Au). The granule and matrix metals are not very soluble in each other and scarcely intermix.

Kinetic effects are usually described on the basis of the quasiclassical Boltzmann equation or the Kubo quantum formalism. Here we attempt to construct a model of GMR in a heterogeneous medium (film) of the system ferromagnet–nonmagnetic metal on the basis of a spin-dependent effective conductivity of the medium (a modification of the first approach). This dependence is a consequence of the assumption that two subbands of electrons having ''up'' and ''down'' spins with different conductivities are present in the ferromagnetic granules. The analysis is based on a calculation of the distribution of local electric fields in a piecewise-homogeneous medium[1] consisting of ferromagnetic granules and a nonmagnetic matrix. Essential to the calculation of the GMR is the difference between the directions of the local magnetization (granule magnetic moment) and the average magnetization of the medium. The GMR is expressed in terms of the magnetization of the medium, the fraction of ferromagnetic phase, and the size of the granules.

The results of a similar model,[2] particularly the prediction of GMR$=50\%$ when the conductivity of the granules is much lower than that of the matrix, cannot be deemed satisfactory. Nor do we find much validity in the results of calculations of the phenomenological model in Ref. 3, where the GMR is proportional to the temperature average of the quantity $(1+\cos\theta)^2$ (θ is the angle between the magnetizations of adjacent granules). Also, the model of Ref. 3 does not predict the dependence of the GMR on the concentration and size of the granules. The dependence of the GMR on the radius of granules of a heterogeneous alloy has been calculated[4] on the basis of a nonlocal conductivity described by the Kubo equation and a subsequent calculation of effective local conductivities. This approach can be used to take into account both the GMR contribution associated with the difference in the granule and matrix conductivities and the dependence on the average magnetization. In the typical granular systems Co–Ag and Co–Cu the granule and matrix conductivities differ substantially (roughly threefold). Consequently, the use of the ''effective medium'' approximation, which is acceptably accurate only for a statistical mixture of alloy phases having close conductivities, to calculate the GMR in Ref. 4 leads one to believe that the GMR is calculated only qualitatively.

The present model is based on the hypothesis of a local (with mean-free path smaller than the scale of structural inhomogeneities of the medium) spin-dependent conductivity

and its subsequent volume averaging for the simple case of unconnected spherical granules. This scenario enables us to express the GMR directly in terms of the experimentally measured effective conductivity. A quantum GMR model[5] has been constructed in the opposite limit where the mean-free path is much larger than the inhomogeneity scale. Here the reciprocal-mean-free path (resistance) is self-averaging, a property that breaks down in the local treatment.

2. We consider a heterogeneous medium consisting of ferromagnetic granules with magnetic moments μ distributed in a nonmagnetic metal matrix. Let the granules be spherical with radius R and, on average, let them be separated by equal distances. We also assume that the spin-diffusion length (the distance traversed by an electron without its spin changing direction) is much larger than both the distance between the granules and the mean-free path. This assumption is equivalent to the approximation of two independent spin currents. We assume that the sizes of the granules and the distance between them are comparable with or larger than the mean-free path. Since the relaxation time of the conduction electrons is $\sim 10^{-12}$ s and the typical relaxation (rotation) time of the magnetic moment of a superparamagnetic granule is three or four orders of magnitude longer, the moving electrons in effect ''see'' a frozen pattern of granule magnetic moments. We assume that the charge carriers in the ferromagnetic granules are electrons belonging to two subbands: those with up-spin and those with down-spin relative to the granule magnetic moment. We denote the corresponding conductivities by σ_+ and σ_-. The conductivity of a granule is σ_+ or σ_- according to whether the electron spin is parallel or antiparallel to its magnetic moment. The conductivity of the matrix σ_N also depends on the direction of the spin of the conduction electrons, owing to their polarization by the magnetizing field of the granules. We calculate the effective conductivity of the medium on the assumption that the magnetic moments of the individual granules, generally speaking, are not parallel to the applied magnetic field. The effective conductivity σ^{ef} of the heterogeneous medium is defined as the ratio of the volume-average current density to the electric field.[1]

The steady-state current density $\mathbf{j}$ and the electric field $\mathbf{E}$ satisfy the equations $\operatorname{curl}\mathbf{E}=0$, $\operatorname{div}\mathbf{j}=0$, and $\mathbf{j}(\mathbf{r})=\sigma(\mathbf{r})\mathbf{E}(\mathbf{r})$, where $\sigma(\mathbf{r})$ is the local conductivity. The internal field of a granule and the field acting on the granule differ from each other and from the external field because of the difference between the conductivities of the granules ($\sigma_\pm$) and the matrix. To within the substitution $\mathbf{j}\to\mathbf{D}$ ($\mathbf{D}$ is the electric displacement), $\sigma\to\varepsilon$, the problem of determining the current and electric field distributions is analogous to the problem of the field distribution in a piecewise-homogeneous dielectric medium having a permittivity $\varepsilon(\mathbf{r})$ (Ref. 1). The solution of the equation for the electrostatic potential $\Delta\varphi=0$ with the appropriate boundary conditions on the granule surface can be used to find the electric field internal to (i) and external to (e) the granule. The assumption of spherical granules greatly simplifies the calculation of the distributions of the field and the effective conductivity of the medium. We note that the ''effective medium'' approximation, which is often used for a two-phase system, yields satisfactory results only when the difference between the conductivities of the phases is very slight or when the concentration of one of the phases is small.

We adopt the direction of the external magnetic field as the z axis of a spherical coordinate system. The average magnetization of the medium, defined as

$$\langle \mathbf{M}_z\rangle_V=\frac{1}{V}\sum_i \mu_{zi}=\frac{\mu}{V}\sum_i \langle\cos\theta_i\rangle_T=\frac{N\mu}{V}\langle\langle\cos\theta\rangle_T\rangle_V, \tag{1}$$

is also directed along the z axis and is the quantization axis for the spins of the matrix conduction electrons. Here N is the number of granules in a sample of volume V, and the indices T and V signify thermodynamic averaging for one granule and averaging over different granules in the volume V. The summation is carried out over all granules in the volume V.

We consider the current of $\uparrow$-spin electrons. Let us suppose that one of these electrons encounters in its path a granule with the magnetic moment directed along the unit vector $\mathbf{n}$ with probability $P(\mathbf{n})$. The direction of $\mathbf{n}$ is described by the spherical angles θ and φ. The probability of entering the subband with conductivity σ_+ (spin parallel to μ) is then determined both by the function $P(\mathbf{n})$ and by the projection of the spin part of the electron wave function $|+1/2\rangle_z$ onto $|+1/2\rangle_{\mathbf{n}}$. The probability of spin $+1/2$ occurring along the $\mathbf{n}$ axis is calculated by means of the two-dimensional representation of the rotation group $O(3)$ and is equal to $|{}_{\mathbf{n}}\langle+1/2|+1/2\rangle_z|^2=\cos^2(\theta/2)$. For the subband with conductivity σ_-, accordingly, we obtain $\sin^2(\theta/2)$. The current through a ferromagnetic granule for a given $\mathbf{n}$ is $j_f^{\uparrow}(\mathbf{n})=P(\mathbf{n})\times[\cos^2(\theta/2)j_f^{\uparrow}(\sigma_+)+\sin^2(\theta/2)j_f^{\uparrow}(\sigma_-)]$. From now on the spin indices $\uparrow$ and $\downarrow$ characterize the direction of the electron spin relative to the average magnetization (external field), while the indices $\pm$ indicate the direction of the spin relative to the local magnetization of a given granule. The average current through the sample and the average field are

$$\langle j^{\uparrow}\rangle_V=f\langle j_f^{\uparrow}\rangle_\mu+(1-f)j_N^{\uparrow},$$

$$\langle E^{\uparrow}\rangle_V=f\langle E_{\uparrow}^{i}\rangle_\mu+(1-f)E_{\uparrow}^{e},\quad j_N^{\uparrow}=\sigma_N^{\uparrow}E_{\uparrow}^{e}. \tag{2}$$

Here f is the volume fraction of ferromagnetic granules, and $\langle\ldots\rangle_\mu$ signifies averaging over the possible directions of the magnetic moment μ of the given granule (local) with the probability density function $P(\mathbf{n})$ and averaging over the magnetic moments of granules contained in the volume V. The form of the function $P(\mathbf{n})$ is determined both by the magnetic anisotropy of the individual granule and by the interaction of the granule moments. Without interaction between granules we have $P(\mathbf{n})\sim\exp[-(E_A(\mathbf{n})-\mu H\cos\theta/T)]$, where E_A is the granule anisotropy energy. In particular, for isotropically positioned spherical granules (without intrinsic anisotropy) it is sufficient to parametrize by the angle θ only:

$$\langle j_f^{\uparrow}\rangle_\mu=p_+j_f^{\uparrow}(\sigma_+)+p_-j_f^{\uparrow}(\sigma_-),$$

$$\langle E^{\uparrow}\rangle_\mu=p_+E_{\uparrow}^{i}(\sigma_+)+p_-E_{\uparrow}^{i}(\sigma_-), \tag{3}$$

where the total probabilities p_+ and p_- are equal to

$$p_+ = \int d\theta P(\theta)\cos^2\frac{\theta}{2}, \quad p_- = \int d\theta P(\theta)\sin^2\frac{\theta}{2}.$$

The effective conductivity for ↑-spin electrons $\sigma_\uparrow^{\text{ef}} = \langle j^\uparrow\rangle_V / \langle E^\uparrow\rangle_V$, according to Eqs. (2) and (3), is

$$\sigma_\uparrow^{\text{ef}} = \frac{f(p_+\sigma_+ k_\uparrow^+ + p_-\sigma_- k_\uparrow^-) + (1-f)\sigma_N^\uparrow}{f(p_+ k_\uparrow^+ + p_- k_\uparrow^-) + (1-f)}, \tag{4}$$

where the coefficients $k_\uparrow^\pm = E_\uparrow^i(\sigma_\pm)/E_\uparrow^e$ characterize the difference between the electric fields interior and exterior to the granules. Their calculation for zero surface resistance of the granules gives

$$k_\uparrow^\pm = \frac{3\sigma_N^\uparrow}{\sigma_\pm + 2\sigma_N^\uparrow} \tag{5}$$

and the analogous expression for ↓-spin.

We introduce the parametrization $p_\pm = (1/2) \pm \xi$, where it is evident from the definition of the probabilities that the temperature average $\xi = (1/2)\int d\theta\, P(\theta)\cos\theta = \langle\cos\theta\rangle_T$ has the significance of the relative volume average of the magnetization if all the granules are identical, and we can assume that $\langle\cos\theta\rangle_T = \langle\langle\cos\theta\rangle_T\rangle_V$. Even when the granules do not have intrinsic magnetic anisotropy, this average differs from the Langevin function by virtue of interaction (exchange and dipole-dipole) of the granule magnetic moments.

The total current through the sample is equal to the sum of the currents of the two spin channels, or since $\langle E^\uparrow\rangle_V = \langle E^\downarrow\rangle_V$, the total effective conductivity is equal to the sum of the effective conductivities of the parallel channels:

$$\sigma^{\text{ef}}(\xi) = \sigma_\uparrow^{\text{ef}}(\xi) + \sigma_\downarrow^{\text{ef}}(\xi),$$

$$\xi = \frac{1}{2}\frac{M}{M_s}, \quad M = \langle M_z\rangle_V, \tag{6}$$

where M is the magnetization in the field H, and M_s is the saturation magnetization.

The dependence of the effective conductivity on the relative magnetization ξ also governs the GMR of the granular medium. This dependence occurs as a result of the difference in the directions of the local and average magnetizations. By the definition of the GMR effect we can write the relative magnetoresistance in the form

$$G(\xi) = \frac{\rho^{\text{ef}}(\xi) - \rho^{\text{ef}}(0)}{\rho^{\text{ef}}(0)} = -\frac{\sigma^{\text{ef}}(\xi) - \sigma^{\text{ef}}(0)}{\sigma^{\text{ef}}(\xi)}. \tag{7}$$

To describe the dependence of the GMR on the granule radius R, we also take into account scattering by the granule surfaces (surface resistance). It can be caused, for example, by a contact potential difference at the granule-matrix interface. We incorporate the surface resistance, which depends on the spin in this case, into the boundary conditions of the electrostatic problem as a potential jump at $r = R$:

$$\Phi_\pm^e = \Phi_\pm^i = r_s^\pm j_f^{\uparrow,\downarrow}(\sigma_\pm). \tag{8}$$

A detailed calculation shows that in the coefficients $k_\uparrow^\pm$, $k_\downarrow^\pm$ (5), which characterize the effective conductivity of the spin channels $\sigma_{\uparrow,\downarrow}^{\text{ef}}$, it is necessary to make the substitutions

$$\sigma_N^\uparrow \to \sigma_N^{\pm\uparrow} = \sigma_N^\uparrow(1 + r_s^\pm\sigma_\pm/R)$$

and

$$\sigma_N^\downarrow \to \sigma_N^{\pm\downarrow} = \sigma_N^\uparrow(1 + r_s^\pm\sigma_\pm/R)$$

in the denominators of the expressions for $\sigma_{\uparrow,\downarrow}^{\text{ef}}$ and in the denominators of $k_\uparrow^\pm$ and $k_\downarrow^\pm$.

We disregard the polarization of the matrix conduction electrons, $\sigma_N^\uparrow = \sigma_N^\downarrow = \sigma_N$; making the necessary transformations, we obtain the expression for the GMR effect

$$G(\xi) = -\frac{3f^2\xi^2(\Delta k)^2}{[(1+f\gamma)(1-2f\gamma) + 2\xi^2 f^2(\Delta k)^2][1+f\gamma]}, \tag{9}$$

where the parameters of the model are

$$\Delta k = -\frac{3\sigma_N}{(\sigma_+ + 2\sigma_N^+)(\sigma_- + 2\sigma_N^-)}\left(\Delta\sigma - \frac{\Delta r_s}{R}\sigma_+\sigma_-\right),$$

$$\gamma = \frac{1}{2}\frac{(4\sigma_N^+\sigma_N^- - \sigma_N^+\sigma_- - \sigma_N^-\sigma_+ - 2\sigma_+\sigma_-)}{(\sigma_+ + 2\sigma_N^+)(\sigma_- + 2\sigma_N^-)},$$

$$\sigma_N^\pm = \sigma_N\left(1 + \frac{r_s^\pm\sigma_\pm}{R}\right),$$

$$\Delta\sigma = \sigma_+ - \sigma_-, \quad \Delta r_s = r_s^+ - r_s^-, \quad \Delta k = k^+ - k^-.$$

Here $\gamma = k - 1 = (k^+ + k^-)/2 - 1$ has the significance of the granule polarization factor averaged over the spin direction and takes values from -1 to 1/2, depending on the granule/matrix conductivity ratio. The magnitude of the GMR (9) depends on two parameters of the model: γ and Δk. We note that $\Delta k \sim (\Delta\rho + \Delta r_s/R)$ and $\Delta\rho = \rho_+ - \rho_-$, i.e., the GMR contributions from spin-dependent volume and surface scattering by the ferromagnetic granules are additive and can compete with one another.

The GMR given by Eq. (9) is negative, proportional to the square of the difference in the coefficients of penetration of the field into the granule, k^+ and k^- (which have nonzero values only for $\sigma_+ \neq \sigma_-$ or $r_s^+ \neq r_s^-$), and is a decreasing even function of the magnetization. In the limit of small granules or high surface resistance $r_s^\pm\sigma_\pm/R \gg 1$ the GMR tends to zero according to the law $\sim(R/r_s^\pm\sigma_\pm)^2$ (see Fig. 1) for any signs of $\Delta\sigma$ and Δr_s. This limit corresponds to the case where current does not flow in the granules as the surface resistance increases, and it is impossible to have granule spin subbands with conductivities $\sigma_\pm$. As the granules grow in size, $R \to \infty$, for $\Delta\sigma = 0$ the GMR also tends to zero according to the $1/R^2$ law (see Fig. 1a) by virtue of the decrease in the relative fraction of the granule surface, i.e., owing to the classical size effect.[4] Consequently, the dependence of the modulus of the GMR on the granule radius has a maximum. For $R/r_s^\pm\sigma_\pm \gg 1$ and $\Delta\sigma \neq 0$ the GMR tends to a finite limit, and the dependence of the modulus of the GMR on R retains the maximum and exceeds the magnitude of the GMR for $R/r_s^\pm\sigma_\pm \to \infty$ only under the condition $\Delta\sigma\Delta r_s < 0$ (see Fig. 1a). In the opposite case $\Delta\sigma\Delta r_s > 0$, as a result of competition between the surface and volume contributions to Δk, the modulus of the GMR as a function of R exhibits a slight maximum, reverts to zero, and then increases with R to saturation (see Fig. 1b). For $\Delta r_s = 0$ the

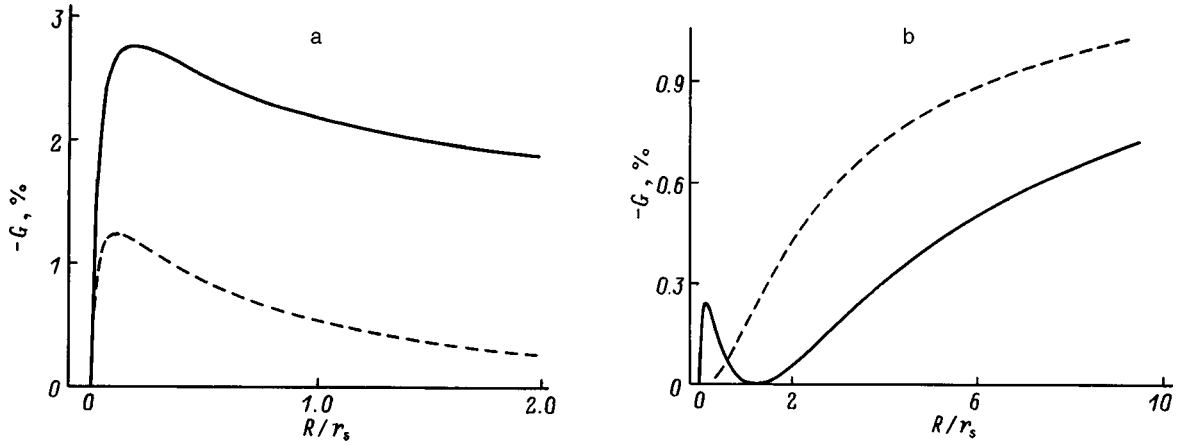

FIG. 1. Relative magnetoresistane G versus granule radius R. All the conductivities are given in units of σ_N. a — Solid curve: $\sigma_+=2$, $\sigma_-=0.5$, $r_s^+=0.1$ nm, $r_s^-=15$ nm; dashed curve: $\sigma_+=1$, $\sigma_-=1$, $r_s^+=0.1$ nm, $r_s^-=15$ nm; b — solid curve: $\sigma_+=2$, $\sigma_-=0.5$, $r_s^+=2$ nm, $r_s^-=0.1$ nm; dashed curve: $\sigma_+=2$, $\sigma_-=0.5$, $r_s^+=1$ nm, $r_s^-=1$ nm. $r_s=(r_s^++r_s^-)/2$, $f=0.3$, $\xi=0.5$.

modulus of the GMR increases monotonically with R to saturation (see Fig. 1b). In every case, for $\Delta\sigma\neq 0$ the saturation value is $G(r_s^{\pm}=0)$.

The modulus of the GMR (9) increases monotonically as the concentration of the ferromagnetic phase f increases. This behavior is a result of disregarding interaction between the granule magnetic moments, which is significant for $f\approx 0.2-0.3$, i.e., Eq. (9) has in fact been obtained in the one-granule approximation, when the influence of all surrounding granules on the designated granule is assumed to be proportional to the average magnetization M. The simplest way to take into account interaction between granules is to include in Eq. (9) the remanent magnetization $M_r=M(H=0)$, which occurs when the concentration of the ferromagnetic phase exceeds a critical value f_c (the ferromagnetic percolation concentration[6]). The remanent magnetization M_r increases monotonically as f increases. However, the calculation of the function $M_r(f)$ poses a complex percolation problem beyond the scope of the present study. When M_r is taken into account, the GMR assumes the form

$$G(\xi)=-\frac{3f^2(\Delta k)^2(1+f\gamma)(\xi^2-\xi_r^2)}{[(1+f\gamma)(1-2f\gamma)+2\xi^2f^2(\Delta k)^2][(1+f\gamma)^2-\xi_r^2f^2(\Delta k)^2]}, \tag{10}$$

where $\xi_r=M_r/2M_s$.

3. According to Eq. (10), the GMR increases as f increases (according to the f^2 law for $f\ll 1$). This trend corresponds to an increase in the number of ferromagnetic granules. The monotonic increase of the GMR with increasing concentration (with the appearance of ferromagnetic correlations of the granule magnetic moments and subsequent ferromagnetic percolation) is then superseded by a decrease at sufficiently large values of f, i.e., the GMR has a maximum at $f\approx f_c$. We note that f_c can be much lower than the concentration $f_c'=0.52$ at which identical spherical particles come into contact (agglomerate); this concentration is determined as the root of the equation $(4\pi/3f)^{1/3}=2$. When the concentration attains f_c, a tightly bound ferromagnetic cluster is formed, encompassing the entire sample.[6] With a further increase in f this cluster grows in size, the number of granules weakly bound to it diminishes, and the GMR goes over to the ordinary anisotropic magnetoresistance. This behavior of the modulus of the GMR as a function of the concentration, passing through a maximum, has been observed a number of times experimentally in granular films, for example, CoCu (Ref. 7 and CoAg (Refs. 8–10). In one experiment[10] a special technique for the preparation of films by the cluster beam method has yielded a medium in which all the Co granules had approximately the same radius. In an experiment on CoAg granular films,[9] in the superparamagnetic state the GMR depended approximately on the granule radius as $\Delta\rho\sim R^3$ and on the granule concentration as $\Delta\rho\sim\exp(-c/f^{1/3})$, where c is a positive constant. This result is in qualitative agreement with the GMR equations (9) and (10), where the magnetoresistance obeys the laws $\Delta\rho\sim R^2$ and $\Delta\rho\sim f^2$ in the superparamagnetic limit. The model of Ref. 5 does not predict the nonlinear and nonmonotonic concentration dependence given by Eq. (10).

The dependence of the GMR on the granule radius can be traced experimentally by varying the anneal temperature (or time) of the alloy — a supersaturated solid solution. A maximum of the modulus of the GMR as a function of these parameters has been observed in experiments (see the literature cited in Ref. 2). This fact indicates the decisive contri-

bution to GMR from spin-dependent surface scattering. We note that in the quantum model[5] the GMR increases monotonically as the granule size decreases, in conflict with the conclusions drawn from Eq. (9). The maximum of the GMR as a function of R (Ref. 5) is predicted in Ref. 5 only with the additional assumption that the granules have a size distribution $F(V)\sim 1/V$ [$F(V)$ is the distribution function). This assumption yields far too large a fraction of small supermagnetic granules, which are not saturated in a fixed magnetic field, causing the GMR to drop abruptly for small radii R. In Ref. 2 the GMR increases monotonically with R for $\Delta\sigma = 0$, again contradicting Eq. (9). The difference in the GMR after isothermal and isochronous anneals in FeCo–Cu and Co–Cu films[7] is explained by the fact that primarily ferromagnetic granules grow (R increases) in the first case, whereas in the second case new granules emerge from the supersaturated solid solution (f increases). The increase in the concentration of the ferromagnetic phase is what causes the GMR to increase monotonically to saturation. Both in Ref. 7 and on Co–Ag films in Refs. 8 and 11 the dependence of the GMR on the anneal temperature has a maximum. But the solubility of Co (FeCo) in Cu is significantly higher than that of Co in Ag. As a result, good phase segregation occurs even in as-deposited CoAg films, and isochronous annealing merely increases the size of the granules. This statement is corroborated by direct electron-microscope observations of the evolution of Co granules in the annealing of CoAg films.[11] The GMR attains its maximum at an average granule diameter $2R = 11$ nm, so that the surface resistance of the {Co granule–Ag matrix} interface can be estimated from (9) as $r_s = 10^{-11}\,\Omega\cdot\mathrm{cm}^2$. Experiments[10,12] have shown that the granule sizes approximately fit a log-normal distribution.

The magnitude of the MGR is determined by the ratio of the conductivities of the ferromagnetic granules to the nonmagnetic matrix, the spin asymmetry of the volume and surface contributions to the resistance of the ferromagnetic granules, and the concentration of the ferromagnetic phase (granules).

A maximum occurs in the dependence of the GMR on the concentration of the ferromagnetic phase when the remanent magnetization is taken into account. The advent of remanent magnetization (opening of a hysteresis loop) as the concentration increases produces a corresponding hysteresis in the GMR effect and shifts the maximum of the GMR curve as a function of the field. In addition, for $f > f_c$ not only the GMR, but also ordinary anisotropic magnetoresistance contributes to the resultant magnetoresistance. The dependence of the magnitude of the GMR on the magnetization (magnetic field) departs considerably from the $\sim M^2$ law at higher concentrations f and in the presence of pronounced spin asymmetry Δk of the volume and surface resistance of the ferromagnetic granules.

Owing to the presence of a surface contribution to the resistance, the GMR depends on the granule size R of the ferromagnetic phase in the nonmagnetic matrix. This dependences exhibits a maximum both for $\Delta\sigma\Delta r_s > 0$ and for $\Delta\sigma\Delta r_s < 0$. The GMR becomes a maximum when the signs of the spin asymmetry parameters of the conductivities (resistances) obey the relation $\Delta\sigma\Delta r_s < 0$.

The author is grateful to B. A. Ivanov for a discussion of the results.

This work has received partial support form the Ukrainian Science and Technology Center under Grant No. 300.

[1] L. D. Landau and E. M. Lifshitz, *Electrodynamics of Continuous Media*, 2nd ed. [Pergamon Press, Oxford–New York, 1984; Nauka, Moscow, 1982, 620 pp.].
[2] M. Rubinstein, Phys. Rev. B **50**, 3830 (1994).
[3] N. Wiser, J. Magn. Magn. Mater. **159**, 119 (1996).
[4] A. Vedyayev, B. Mevel, N. Ryzhanova, M. Tshiev, B. Dieny, A. Chamberod, and F. Brouers, J. Magn. Magn. Mater. **164**, 91 (1996).
[5] S. Zhang and P. M. Levy, J. Appl. Phys. **73**, 5315 (1993).
[6] B. I. Shkovskiĭ and A. L. Éfros, Usp. Fiz. Nauk **117**, 401 (1975) [Sov. Phys. Usp. **18**, 845 (1975)].
[7] S. H. Ge, Y. Y. Lu, Z. Z. Zhang, C. X. Li, T. Xu, and J. Z. Zhao, J. Magn. Magn. Mater. **168**, 35 (1997).
[8] W. Zhang, I. W. Boyd, M. Elliott, and W. Herrenden-Harkerand, J. Magn. Magn. Mater. **165**, 330 (1997).
[9] S. Honda, T. Okada, and M. Nawate, J. Magn. Magn. Mater. **165**, 326 (1997).
[10] F. Parent, J. Tuaillon, L. B. Stern *et al.*, Phys. Rev. B **55**, 3683 (1997).
[11] H. Sang, N. Xu, J. H. Du *et al.*, Phys. Rev. B **53**, 15023 (1996).
[12] O. Redon, J. Pierre, B. Rodmacq, B. Mevel, and B. Dieny, J. Magn. Magn. Mater. **149**, 398 (1995).

Translated by James S. Wood

Effect of doping on the magnetic properties of the low-dimensional antiferromagnet CuO

T. I. Arbuzova, I. B. Smolyak, S. V. Naumov, and A. A. Samokhvalov

Institute of Metal Physics, Urals Branch of the Russian Academy of Sciences, 620219 Ekaterinburg, Russia

(Submitted March 11, 1998)
Fiz. Tverd. Tela (St. Petersburg) **40**, 1876–1880 (October 1998)

The effect of doping with Li^{+}, Zn^{2+}, Ni^{2+}, and Ga^{3+} ions on the magnetic susceptibility of the low-dimensional antiferromagnet CuO ($T_N = 230$ K) has been studied within a broad temperature range of 77–600 K. The solubility of impurity ions in the CuO lattice is low, $\leqslant 3\%$. Impurity ions, similar to intrinsic defects, distort antiferromagnetic coupling and can shift the long- and short-range magnetic-order regions toward lower T. © *1998 American Institute of Physics.* [S1063-7834(98)02210-2]

Considerable attention is focused presently on low-dimensional systems. Cupric oxide and the perovskite-like cuprates La_2CuO_4 and $YBa_2Cu_3O_6$ can be assigned to this class. Although these compounds have different lattice symmetry, they contain the same structural cluster CuO_4, which accounts for the similarity between their magnetic, electrical, and optical properties. CuO, La_2CuO_4, and $YBa_2Cu_3O_6$ are semiconductors with low-mobility carriers of the type of small-radius polarons and low-dimensional (1D or 2D) antiferromagnets with strong spin correlations above T_N. The current interest in the properties of CuO is due also to the fact that tenorite may be considered as a building block of the high-T_c cuprate superconductors. The perovskite-like cuprates exhibit a broad homogeneity region. While their electrical conductivity can be increased considerably, up to the metallic level by doping or by changing properly the oxygen content, this results in a weakening of the antiferromagnetic spin correlations. CuO has a narrow homogeneity region,[1] and therefore annealing in the corresponding ambient or doping cannot change significantly the electrical resistance.[2] The antiferromagnetic order in CuO is due to the exchange interaction between localized Cu^{2+} ions ($S = 1/2$) via O^{2-} ions. By substituting heterovalent or heterospin ions for part of the copper ions one can affect the exchange coupling and magnetic order. This study reports on the effect of doping with the ions of Li, Ni, Zn, and Ga on the magnetic susceptibility of CuO within a broad temperature range.

1. SAMPLES

Polycrystalline samples of $Cu_{1-x}Li_xO$, $Cu_{1-x}Ni_xO$, $Cu_{1-x}Zn_xO$, and $Cu_{1-x}Ga_xO$ were prepared from powders of CuO, Li_2CO_3, NiO, ZnO, and Ga_2O_3 (all OSCh type) by sintering the starting components at 900 °C for 12 h. After this, the powder was ground and pressed into pellets, which were subsequently annealed at 900 °C for 24 h. The samples thus prepared were examined by x-ray structural and phase analysis. The studies were carried out on a DRON-2.0 diffractometer with Cr $K\alpha$ radiation. The error in the lattice-parameter determination did not exceed 0.1%.

Pure CuO has a monoclinic lattice with the parameters $a = 4.681$ Å, $b = 3.424$ Å, $c = 5.129$ Å, and $\beta = 99.55°$. The solubility of impurity ions in the CuO lattice is fairly low, for Li and Ga it is $\approx 1\%$. Ni ions have the highest solubility, up to 3%. The lattice parameters for $Cu_{0.99}Li_{0.01}O$ are $a = 4.681$ Å, $b = 3.416$ Å, $c = 5.129$ Å, $\beta = 99.55°$, and for $Cu_{0.99}Ga_{0.01}O$, $a = 4.686$ Å, $b = 3.426$ Å, $c = 5.137$ Å, $\beta = 99.36°$. The lattice parameters for various compositions of $Cu_{1-x}Ni_xO$ are given in Table I, and those for $Cu_{1-x}Zn_xO$, in Table II. Two lots of $Cu_{1-x}Zn_xO$ samples were prepared, namely, slowly cooled together with the furnace and quenched from $T = 950$ °C to liquid nitrogen.

The magnetic measurements were performed with a magnetic balance in the 77–600 K range and magnetic fields $H \leqslant 13$ kOe. The balance sensitivity permits susceptibility measurements up to 10^{-8} cm^3/g. The temperature dependence of the susceptibility was studied primarily at $H = 9$ kOe. The measurement error was less than 3%.

2. EXPERIMENTAL RESULTS

The temperature dependence of the magnetic susceptibility of CuO is typical of low-dimensional systems undergoing a phase transition to the 3D state with decreasing T.[3] Below $T = 213$ K, CuO is a collinear antiferromagnet, within the $T = 213-230$ K interval its magnetic structure is noncollinear, and above $T_N = 230$ K short-range order is retained due to strong spin correlations.[4] The susceptibility of polycrystalline CuO practically does not vary within the region $T = 77-140$ K. As the temperature increases, magnetic susceptibility χ grows, passes through a broad maximum near

TABLE I. Lattice parameters for $Cu_{1-x}Ni_xO$ solid solutions.

Parameter	$Cu_{0.99}Ni_{0.01}O$	$Cu_{0.97}Ni_{0.03}O$	$Cu_{0.9}Ni_{0.1}O$ (NiO present)
a, Å	4.676	4.658	4.659
b, Å	3.437	3.447	3.450
c, Å	5.131	5.133	5.133
β, °	99.42	99.10	99.08

TABLE II. Lattice parameters for $Cu_{1-x}Zn_xO$ solid solutions.

	$Cu_{0.99}Zn_{0.01}O$		$Cu_{0.98}Zn_{0.02}O$		$Cu_{0.97}Zn_{0.03}O$	
Parameter	Slow cooled	Annealed	Slow cooled	Annealed	Slow cooled	Annealed
a, Å	4.691	4.700	4.700	4.700	4.702	4.704
b, Å	3.415	3.410	3.414	3.405	3.413	3.406
c, Å	5.132	5.131	5.129	5.127	5.130	5.132
β, °	99.67	99.73	99.77	99.92	99.80	99.86

550 K, and falls off subsequently.[5,6] In the vicinity of T_N there is no susceptibility peak characteristic of Néel- type ferromagnets, and only the slope of $\chi(T)$ changes, which indicates preservation of short-range magnetic order.

The oxygen content in a sample can be varied by heat treating it in an appropriate ambient. Oxygen ions take part in exchange interactions so that a change in their concentration should affect the magnetic properties. Figure 1 shows temperature dependences of the susceptibility of polycrystalline CuO before and after annealing in an oxygen flow at 500 °C for 20 h. For high temperatures, $T>270$ K, the susceptibility of the sample is seen not to change. In the magnetic-ordering region an increase in the oxygen content reduces χ, while the character of $\chi(T)$ and the temperature of the break in χ are retained.

Single-crystal CuO exhibits an anisotropy in the susceptibilities $\chi_\parallel$ and $\chi_\perp$ both for $T<T_N$ and above T_N.[3,7] Parallel susceptibility in a collinear antiferromagnet should tend to zero for $T\to 0$, but in CuO one observes always a finite $\chi_\parallel$ along one of the major axes, $H\parallel b$. The $\chi_\parallel(T)$ relation behaves qualitatively similar to the $\chi(T)$ dependence for polycrystals, where $\chi=\frac{2}{3}\chi_\parallel+\frac{1}{3}\chi_\perp$. The susceptibilities χ_a and χ_c making up the component $\chi_\perp$ remain nearly constant and close in magnitude within the temperature region studied. For $H\parallel c$, a small minimum in χ was observed close to $T=213$ K, which corresponds to a phase transition to the noncollinear state. Oxygen vacancies in single crystals practically do not produce any influence on $\chi_a(T)$ while affecting strongly the absolute values of χ_b and χ_c. In defected single crystals, χ_b increases below T_N and decreases above it, i.e. the variation of $\chi_b(T)$ in absolute magnitude becomes weaker. The most pronounced effect of oxygen vacancies in single crystals is a slowing down of the low-temperature growth of χ and an increase of the minimum value of χ_b for $T<140$ K (see Fig. 1 and Ref. 8).

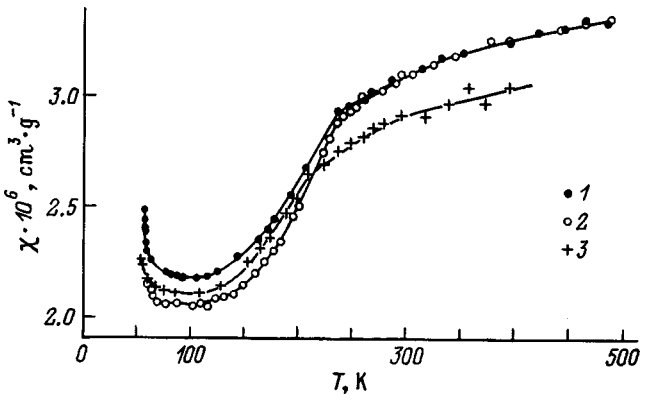

FIG. 1. Temperature dependence of magnetic susceptibility for polycrystal samples: (*1*) CuO before annealing, (*2*) CuO after annealing in oxygen flow, (*3*) $Cu_{0.99}Li_{0.01}O$.

The increase of the susceptibility for $T<65$ K is an unexpected feature in the behavior of $\chi(T)$ of CuO. This increase was believed to be caused by Cu^{3+} ions appearing due to the presence of cation vacancies.[9] Doping CuO with univalent Li ions should result in the appearance of Cu^{3+} ions to preserve charge neutrality and enhancement of this anomaly. Figure 1 presents the temperature dependence of the susceptibility of $Cu_{0.99}Li_{0.01}O$. We see that the temperature of the break in $\chi(T)$ corresponding to T_N shifts toward lower T, but doping with Li^+ does not bring about any enhancement in the growth of χ. Thus the low-temperature anomaly in χ is apparently connected not with the Cu^{3+} ions but rather with frustration of the exchange interactions. Copper ions bound in compounds reside usually in univalent or divalent states. There is presently no experimental evidence for the existence of Cu^{3+} ions in copper-containing oxides. The lowering of the Néel temperature in $Cu_{0.99}Li_{0.01}O$ is caused by diamagnetic dilution.

When CuO is doped with divalent ions Zn^{2+} and Ni^{2+}, the electronic state of the outer shells of oxygen and copper is preserved. The Zn^{2+} ions have a completely filled $3d$ shell ($S=0$), similar to the Cu^{2+} ions, while the $3d$ shell of Ni^{2+} ions contains eight electrons ($S=1$). In solid solutions, either the concentration of magnetically active ions or their spin change. Figure 2 shows the temperature dependence of the susceptibility of slowly cooled $Cu_{1-x}Zn_xO$ samples for $x=0, 0.01, 0.015$. We readily see that doping affects only weakly the $\chi(T)$ dependence. These samples exhibit inversion of χ with increasing x. The susceptibility of quenched doped $Cu_{1-x}Zn_xO$ samples is smaller throughout the temperature region studied than that of pure CuO: $\chi(\mathrm{CuO}) > \chi(Cu_{1-x}Zn_xO)$. On the whole, however, the variations of the susceptibility with zinc substituting for a part of Cu^{2+} ions are fairly small and are similar to those observed in CuO with various oxygen deficiencies. The temperature of the break in χ shifts slightly toward lower T, and short-range order persists up to high temperatures.

It has been mentioned that Ni^{2+} ions enter the CuO lattice up to high concentrations. Figure 3 displays the $\chi(T)$ relation for $Cu_{0.97}Ni_{0.03}O$. In contrast to pure CuO with different oxygen contents, $Cu_{1-x}Zn_xO$, and $Cu_{1-x}Li_xO$, the susceptibility of $Cu_{1-x}Ni_xO$ in the region of short-range order begins to decrease with increasing temperature already for $T\geqslant 470$ K. The narrowing of the short-range order region

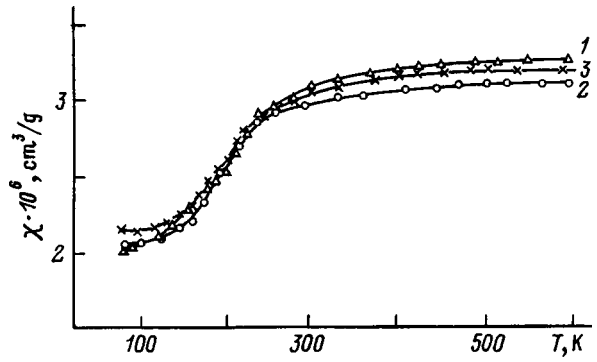

FIG. 2. Temperature dependence of magnetic susceptibility for $Cu_{1-x}Zn_xO$ solid solutions. x: *1*—0, *2*—0.01, *3*—0.015.

cannot be accounted for by the second phase NiO, which is a 3D antiferromagnet with $T_N = 523$ K, and whose susceptibility should increase up to T_N.[10]

The most pronounced changes in magnetic properties were revealed when doping CuO with Ga^{3+} ions. The susceptibility of $Cu_{0.99}Ga_{0.01}O$ passes near T_N through a maximum characteristic of Néel antiferromagnets (Fig. 4). Above T_N, the susceptibility falls off with increasing T, but the large effective magnetic moment $\mu_{\text{eff}} = 2.13\ \mu_B$ of Cu^{2+} ions for $T > 300$ K compared to the theoretical value $\mu_{\text{eff}} = 1.73\ \mu_B$ evidences persistence of short-range order at high temperatures. It should be pointed out that single-crystal La_2CuO_4 follows a similar $\chi(T)$ relation (Fig. 4). Neutron diffraction measurements show La_2CuO_4 to be a 3D collinear antiferromagnet below $T_N = 226$ K, while above T_N it retains two-dimensional antiferromagnetic spin correlations.[11] The magnetic properties of the 1D and 2D compounds are qualitatively similar, but different models yield different relations for the maximum susceptibility, temperature of the susceptibility maximum, and the exchange parameter.[12] $Cu_{0.99}G_{0.01}O$ differs also from the preceding solid solutions in a higher susceptibility. It may be conjectured that Ga^{3+} impurity ions give rise to diamagnetic dilution and a partial rupture of exchange bonds. As a result, part of the Cu^{2+} ions are in paramagnetic state and provide a contribution $\chi = C/T$ (C is the Curie constant) to the total susceptibility.

Doping brings about a weak change in both magnetic and electrical properties of CuO. For instance, in $Cu_{0.97}Ni_{0.03}O$ the electrical resistivity decreases from $\rho = 1.7 \times 10^3$ to 80 $\Omega \cdot$ cm at room temperature. The absence of radical changes in the properties of tenorite stems from the impossibility of incorporating significant amounts of defects into the CuO lattice.

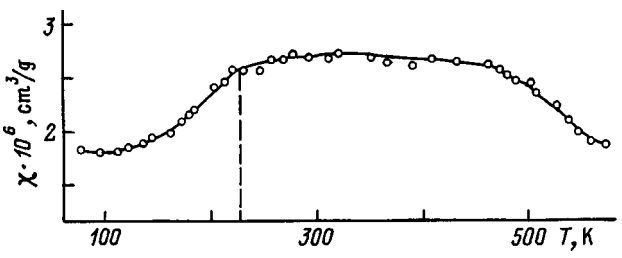

FIG. 3. Temperature dependence of magnetic susceptibility for polycrystalline $Cu_{0.97}Ni_{0.03}O$.

3. DISCUSSION

The magnetic structure of CuO is determined by competition between the antiferromagnetic and ferromagnetic exchange couplings. Antiferromagnetic order along $[10\bar{1}]$ is due to superexchange via the O^{2-} ions, because the Cu–O–Cu angle is the closest to 180°. In all the other directions the Cu–O–Cu angle is close to 90° and favors ferromagnetic coupling. The distance between the nearest Cu^{2+}–Cu^{2+} ions (2.90 Å) is much less than that between the Cu^{2+} ions along $[10\bar{1}]$ (3.74 Å). The $3d$ orbitals do not overlap, however, and ferromagnetic coupling between the nearest Cu^{2+} ions is mediated by O^{2-} ions. The magnetic structure of CuO can be conceived in the form of $[10\bar{1}]$-oriented antiferromagnetic chains of ferromagnetically coupled Cu^{2+} ions. The Cu^{2+} ions in the chains oriented in the perpendicular direction [101] are ferromagnetically ordered, but the chains themselves are ferromagnetically coupled only pairwise.[4]

The low-dimensional (1D and 2D) and three-dimensional (3D) systems differ in the nature of long-range magnetic order. The low dimensionality manifests itself in a noticeable decrease of the saturation magnetic moment, which is inversely proportional to the spin and number of interacting neighbors, from its theoretical value, as well as in a broad susceptibility maximum for $T > T_N$.[13] These properties are well pronounced in CuO. The close values of the competing antiferromagnetic and ferromagnetic exchange constants and the presence of residual or intentionally introduced defects result in frustration of magnetic order in CuO. The parallel and perpendicular susceptibilities in frustrated 3D antiferromagnets can increase with decreasing temperature. The low-temperature growth of χ observed in CuO (Fig. 1) can be explained for by frustration of interactions in the long-range order region.

Defects in CuO affect the magnetic properties and change the regions of long- and short-range order. The long-range order region can be estimated from the value of T_N, and the short-range order region, from the position of the maximum in χ above T_N and the effective magnetic moment. As follows from our results, in all the solid solutions the temperature of the break in χ (or T_N) shifts toward lower T, which implies narrowing of the long-range order region. The decrease of T_N was the strongest when doping with lithium, and the weakest, for doping with zinc. Both ions are nonmagnetic. Because the concentrations of the impurity ions Li and Zn are close, the decrease of T_N due to diamagnetic dilution should be the same in both cases. There are, apparently, other factors as well which are capable of affecting T_N. The Néel temperature is a measure of exchange coupling, which depends on the distance between magnetic ions. In solid solutions with Li and Zn the lattice parameters b are the same, whereas parameters a and c are larger in $Cu_{1-x}Zn_xO$ than in pure or lithium-doped CuO (see Table I and II). Hence the decrease in T_N cannot be explained as due only to the increasing Cu–O–Cu distance and decreasing

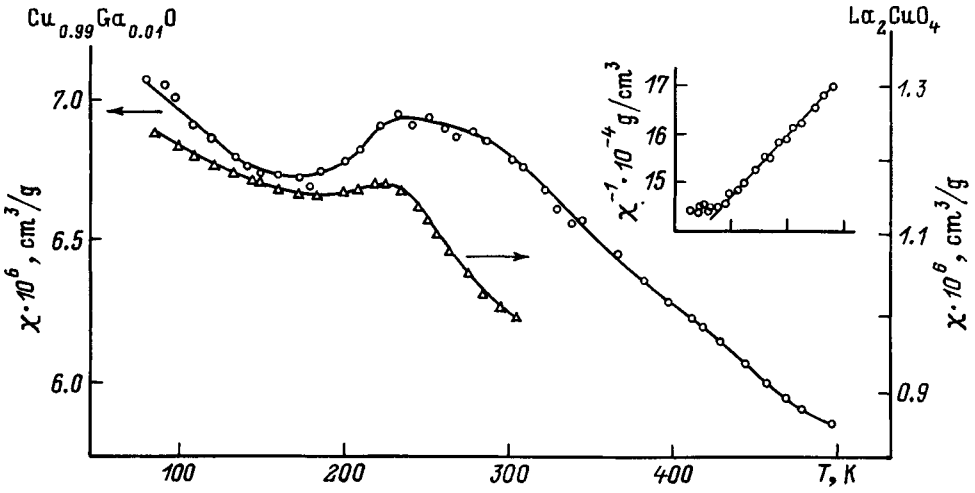

FIG. 4. Temperature dependence of magnetic susceptibility for polycrystalline $Cu_{0.99}Ga_{0.01}O$ and single-crystal La_2CuO_4 ($H\|[110]$). The inset shows the temperature dependence of inverse magnetic susceptibility for $Cu_{0.99}Ga_{0.01}O$.

concentration of magnetoactive ions. It may be assumed that the presence of electrons in the $3d$ shell of the impurity, similar to the case of Zn^{2+}, is an important factor favoring the persistence of long-range order. The region of short-range order in $Cu_{1-x}Li_xO$ and $Cu_{1-x}Zn_xO$ remains as it is in pure CuO. Doping with Ni and Ga results in destruction not only of long- but also of short-range order at lower temperatures. Although the Ni^{2+} ion has a larger magnetic moment compared to Cu^{2+}, it is a defect, and it changes the relation between the exchange parameters. The Cu^{2+}–Ni^{2+} exchange coupling is apparently ferromagnetic. It destroys the antiferromagnetic Cu–O–Cu coupling and narrows the regions of long- and short-range antiferromagnetic order.

The changes in the behavior of $\chi(T)$ were most pronounced for $Cu_{1-x}Ga_xO$. The stronger destruction of magnetic order observed under Ga doping can be due to the increase of all the lattice parameters, a, b, and c, in contrast to the other systems, and to the diamagnetic dilution. Note that when doping with trivalent gallium ions the real concentration of Cu^{2+} magnetoactive ions may be less than the nominal value, because charge neutrality requires that part of the copper ions be univalent.

Thus the monoclinic lattice of CuO allows incorporation only of a limited amount of impurities ($\leqslant 3\%$). CuO is a low-dimensional antiferromagnet, where below T_N collinear antiferromagnetic order sets in, and above T_N, short-range order persists in $[10\bar{1}]$-oriented Cu–O–Cu chains. Intrinsic defects do not affect the Néel temperatures and the susceptibility maximum near 550 K, with only the absolute values of χ changing. Impurity ions (both nonmagnetic and magnetic) distort antiferromagnetic coupling and cause decrease of T_N with the short-range order region left unaffected (doping with Li^+ and Zn^{2+}) or shift the regions of long- and short-range order toward lower T (Ni^{2+}, Ga^{3+}).

Support of the Russian State Program 0.12 ''Surface Atomic Structures'' (Grant 95-2.10) is gratefully acknowledged.

[1] Yu. V. Levinskiĭ, *Phase Diagrams of Binary Metal Systems: A Handbook* [in Russian], Metallurgiya, Moscow (1990), Vol. I.
[2] A. A. Samokhvalov, N. A. Viglin, B. A. Gizhevskiĭ, N. N. Loshkareva, V. V. Osipov, N. I. Solin, and Yu. P. Sukhorukov, Zh. Éksp. Teor. Fiz. **103**, 951 (1993) [Sov. Phys. JETP **76**, 463 (1993)].
[3] B. X. Yang, T. R. Thurston, J. M. Tranquada, and G. Shirane, Phys. Rev. B **39**, 4343 (1989).
[4] T. I. Arbuzova, A. A. Samokhvalov, I. B. Smolyak, B. V. Karpenko, N. M. Chebotaev, and S. V. Naumov, J. Magn. Magn. Mater. **95**, 168 (1991).
[5] M. O'Keefe and F. S. Stone, J. Phys. Chem. Solids **23**, 261 (1962).
[6] T. I. Arbuzova, A. A. Samokhvalov, I. B. Smolyak, N. M. Chebotaev, and S. V. Naumov, JETP Lett. **50**, 34 (1989).
[7] U. Köbler and T. Chattopadhyay, Z. Phys. B **82**, 383 (1991).
[8] T. I. Arbuzova, I. B. Smolyak, A. A. Samokhvalov, and S. V. Naumov, Zh. Éksp. Teor. Fiz. **113**, 1026 (1998) [JETP **86**, 559 (1998)].
[9] M. S. Seehra, Z. Feng, and R. Gopalakrishnan, J. Phys. C **21**, L1051 (1988).
[10] M. F. Trombe, J. Phys. (France) **12**, 170 (1951).
[11] G. Shirane, Y. Ehdoh, R. J. Birgeneau, M. A. Kasther, Y. Hidaka, M. Oda, M. Suzuki, and T. Murakami, in *Brookhaven High-T_c Superconductivity Papers* (1987).
[12] L. Y. de Jongh and A. R. Miedema, Adv. Phys. **23**, 1 (1974).
[13] R. L. Karlin, *Magnetochemistry* [Springer, Berlin, 1986; Mir, Moscow, 1989].

Translated by G. Skrebtsov

Role of surface phenomena in the magnetoresistivity of polycrystalline manganites $La_{1-x}Ca_xMnO_3$

N. I. Solin, A. A. Samokhvalov, and S. V. Naumov

Institute of Metal Physics, Ural Branch of the Russian Academy of Sciences, 620219 Ekaterinburg, Russia
(Submitted March 25, 1998)
Fiz. Tverd. Tela (St. Petersburg) **40**, 1881–1884 (October 1998)

The dc electrical resistivity and magnetoresistivity of polycrystalline manganites $La_{1-x}Ca_xMnO_3$ ($x=0-0.3$) are investigated as functions of the temperature, magnetic field and electric field, along with the microwave surface resistance. The investigations show that the dc electrical resistivity and magnetoresistivity are governed by the surface properties of the intergranular boundaries. The dc electrical resistivity is observed to decrease substantially (tenfold) for a comparatively small electric field ($E\cong 100$ V/cm). Estimates are obtained for the internal electrical resistivity of the granules, the thickness of the contact layer (which depends on the temperature and the magnetic field), and the height of the potential barrier between the interfaces separating the surface layer and inner layer of a granule. © *1998 American Institute of Physics.* [S1063-7834(98)02310-7]

Effects that originate in the bulk of an investigated sample and phenomena associated with the properties of its surface or an interface separating different kinds of substances are clearly distinguished in semiconductors and ferrites.[1–4] The role of the surface is especially powerful in the electrical properties of polycrystalline materials; the latter have been the object of most studies of manganites having a perovskite structure, which exhibit giant magnetoresistance (GMR).[5]

So far the role of boundaries and surface phenomena in the nature of the GMR of manganites has never really been clarified. Comparative studies of polycrystalline media and single crystals indicate that their influence is real. Polycrystalline materials exhibit a stronger magnetoresistivity and do so over a broader range of temperatures than single crystals.[6,7] As the size of the granules increases, the electrical resistivity ρ_0 of a polycrystalline manganite film approaches the value of ρ_0 for a single-crystal film.[7] The resistivity in the interior of a granule can be estimated from measurements of the microwave surface resistance R_s of a polycrystalline film by the induction method.[8] However, the measurements of R_s for manganites[9,10] have been qualitative in nature, so that the internal properties of the granules and the properties of the surface (interfacial) layer between granules could not be determined.

1. PROCEDURE AND SAMPLES

Here we report results obtained in investigations of the dc electrical resistivity ρ_0 and the dc magnetoresistivity $MR=[\rho(H)-\rho(H=0)]/\rho(H=0)$ of polycrystalline manganites $La_{1-x}Ca_xMnO_{3+\delta}$ ($x=0-0.3$) as functions of the temperature and the electric field, along with their surface resistance R_s at frequencies of 9 GHz and 32 GHz in the temperature range 77–300 K and in magnetic fields H up to 1.8 T. The samples were prepared by solid-phase reaction at $T=1200$ °C, and x-ray examinations showed them to be single-phase. According to measurements of the magnetic susceptibility χ_{ac} at 1 kHz in weak magnetic fields, all the samples had magnetic order below the Curie temperature $T_C=160-215$ K, depending on the calcium concentration x.

The dc resistivity ρ_0, including its values in strong (pulsed) electric fields, was measured by the standard four-contact method. To determine R_s, a polished wafer of thickness t and surface S was placed at an antinode of the microwave magnetic field h of an open resonator.[8] The resonance frequency ω and the pass band $\delta\omega$ of the resonator containing the magnetic material are determined not only by the resistivity,[8] but also by the influence of the complex magnetic permeability $\mu=\mu'+i\mu''$ (Ref. 11). Following Refs. 3, 8, and 11, we can show that for $\tau=t/\delta\gg 1$

$$(\delta\omega^L-\delta\omega^0)/\omega^0=R_sSC_1/V_r+\mu''2\,\delta SC_2/V_r, \tag{1}$$

$$(\omega^L-\omega^0)/\omega^0=(V_s-2\,\delta S)C_3/V_r - (\mu'-1)2\,\delta SC_4/V_r. \tag{2}$$

For arbitrary τ, including $\tau\leqslant 1$, and without regard for magnetic losses we have

$$(\delta\omega^L-\delta\omega^0)/\omega^0=2(V_s/V_r)(1/\tau)(\sinh\tau-\sin\tau)/(\cosh\tau+\cos\tau). \tag{3}$$

Here $R_s=\rho_{mw}/\delta$, $\delta=\sqrt{2\rho_{mw}/\omega\mu}$ is the skin depth, V_s and V_r are the volumes of the sample and the resonator, C_1-C_4 are constants, and the superscripts 0 and L identify the parameters of the empty and sample-loaded resonator, respectively. We have estimated the magnetic loss contributions by performing measurements at various frequencies and with longitudinal magnetization ($\mathbf{h}\|\mathbf{H}$). The values of the microwave resistivity ρ_{mw} are determined from R_s (1) and refined from (3) with measurements on samples of different thicknesses. Equation (2) is used to estimate the skin depth, thereby providing an additional check on the results of the measurements of ρ_{mw}.

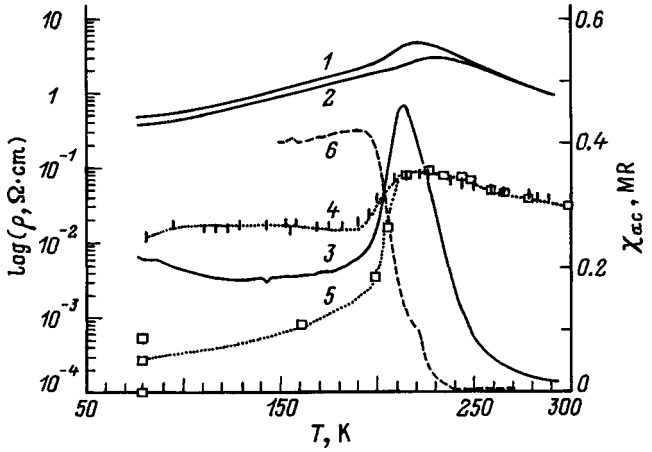

FIG. 1. Temperature dependence of the dc electrical resistivity in magnetic fields of 0.005 T (*1*) and 1.6 T (*2*), the dc magnetoresistivity MR (*3*), the microwave electrical resistivities at frequencies of 9 GHz (*4*) 32 GHz (*5*), and the magnetic susceptibility χ_{ac} at 1 kHz (in arbitrary units) (*6*) of polycrystalline $La_{0.7}Ca_{0.3}MnO_3$.

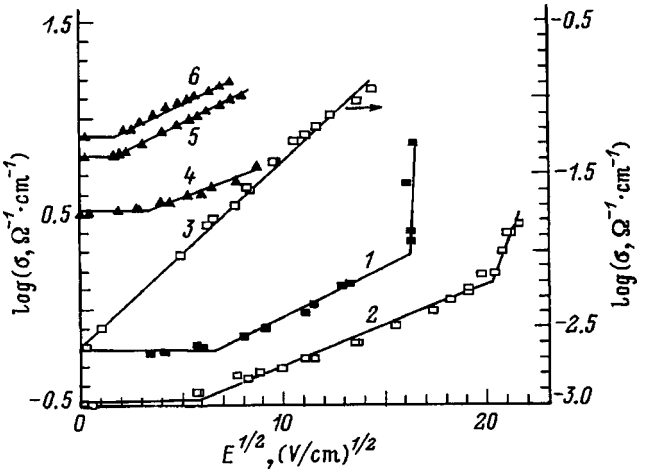

FIG. 2. Electrical conductivity of polycrystalline $La_{1-x}Ca_xMnO_3$ versus electric field at temperatures of 285 K (*1, 2, 4*) and 77 K (*3,5,6*) for samples with $x=0$ (*1*), 0.1 (*2, 3*), and 0.3 (*4–6*) for $H=0$ (*1–5*) and 1.7 T (*6*).

2. RESULTS

The investigated crystals have typical dc properties for manganites (Fig. 1): a maximum of ρ_0 and a peak of the relative magnetoresistivity MR (up to -0.5 in a magnetic field $H=1.8$ T) in the vicinity of T_C. The temperature dependences of ρ_{mw} and ρ_0 are approximately identical, the temperature dependence exhibiting semiconductor behavior in the paramagnetic temperature range and metal behavior in the ferromagnetic range. However, the values of ρ_{mw} are two or three orders of magnitude smaller than the corresponding values of the dc resistivity ρ_0. We note a sharp drop in ρ_{mw} around T_C and the fact that the microwave activation energy in the parametric range is approximately 0.05 eV lower than the dc activation energy: 0.11 eV and 0.16 eV, respectively. The values of $\rho_{mw}(T)$ at 9 GHz and 32 GHz (curves *4* and *5*) are approximately identical in the paramagnetic range, but differ considerably below T_C. It is evident that the values of ρ_{mw} are small ($\cong 0.3-0.8\,m\Omega\cdot cm$ at 77 K and 32 GHz) and roughly coincide with the values of ρ_0 for a $La_{0.7}Ca_{0.3}MnO_3$ single-crystal film.[7] We note that the character of the qualitative variations of $R_s(T)$ (Ref. 10) of conducting perovskites is in good agreement with our quantitative data as opposed to R_s for poorly conducting samples. The explanation for the apparent ''inversion'' of $R_s(\rho)$ for poorly conducting samples as reported in Ref. 10 follows from Eq. (3): $R_s \sim (\delta\omega^L-\delta\omega^0)$ for $\tau \gg 1$, and $R_s \sim (\delta\omega^L-\delta\omega^0)^{-1/2}$ for $\tau \ll 1$.

Investigations of ρ_{mw} (as a function of the dimensions and position of the sample in the resonator and the magnetic field) and estimates suggest that the reported values of ρ_{mw} are too high, especially at 9 GHz, because of the proximity of the frequency to natural ferromagnetic resonance,[12] whose maximum frequency $\omega_{max} \cong 10$ GHz can be estimated from the saturation magnetization of the investigated crystals. In manganites we have observed variations, similar to those in Ref. 9, of the microwave absorption as a function of the magnetic field. We have yet to be convinced, however, that this is a consequence of the onset of GMR and not of magnetic losses, because the variations of $\omega(H)$ according to Eq. (2) do not agree with the postulated variation of $R_s(H)$ determined from Eq. (1). Investigations of $R_s(H)$ in magnetic fields of 3–5 T could resolve this issue.

Our data therefore show that the dc values of ρ_0 and MR in the investigated polycrystalline films are determined entirely by their intergranular properties. Our investigations of the resistivity of polycrystalline manganites as a function of the electric field enable us to determine certain intergranular interaction parameters.

According to Frenkel',[13] in semiconductors an electric field of magnitude E lowers the activation energy E_a by the amount

$$\Delta U = 2e\sqrt{2eE/\varepsilon_e}, \tag{4}$$

so that the conductivity $\sigma_0 \equiv 1/\rho_0$ increases:

$$\sigma_0(E) = \sigma_0(E=0)\exp(2e\sqrt{2eE/\varepsilon_e}/kT), \tag{5}$$

where e is the electron charge, and ε_e is the electronic part of the dielectric permittivity. Switching (breakdown) effects, which set in at $E_a = \Delta U$ (Ref. 13), can take place in polycrystalline manganites, as in ferrites,[2] for small values of E because, as a result of the high intergranular resistance, the entire voltage drop takes place across a thin contact layer L_c, and the effective field in it is large: $E_{eff} = EL_{gr}/L_c$, where L_{gr} is the granule diameter. The investigations have confirmed our expectations.

It is evident from Fig. 2 that Ohm's law is violated by the action of the Frenkel' law (5) for very small fields $E \geqslant 1-30$ V/cm in both the ferromagnetic and the paramagnetic temperature range. The variations of $\sigma(E)$ are very large. For example, for $x=0.1$ at 77 K the conductivity σ_0 increases almost two orders of magnitude in a field $E \cong 250$ V/cm. At room temperature, switching (breakdown) to a more highly conducting state is observed at $E_p = 0.3-0.5$ kV/cm. The variations of $\sigma(E)$ are reproducible and hysteresis-free for $E < E_p$.

From the linear function $\log\sigma(\sqrt{E})$ (Fig. 2) for $\varepsilon_e = 8$ we estimate the values of L_c/L_{gr}, which vary from

TABLE I. Relative thickness of the contact layer L_c/L_{gr} of manganites $La_{1-x}Ca_xMnO_3$ as a function of the calcium concentration at two temperatures.

x	285 K	77 K
0.	6.6×10^{-3}	4.6×10^{-2}
0.1	1.4×10^{-2}	2.1×10^{-2}
0.2	1.3×10^{-2}	–
0.3	1.4×10^{-2}	9.6×10^{-2}

6×10^{-3} to 0.1 as the temperature and Ca concentration vary (see Table I). For average granule diameters $L_{gr}=3$ μm this result corresponds to a contact layer of thickness $L_c=200-3000$ Å. The estimates of L_c/L_{gr} fall within approximately 10% error limits. It can be stated within these limits that in a magnetic field at 77 K (curves *5* and *6* in Fig. 2), σ increases by $\cong 25\%$ for a 20% increase in L_c/L_{gr}. This means that the magnetoresistivity is attributable either to a decrease in the resistance of the contact layer in the continuous contact model[7,14] or to an increase in the contact volume in the point (bridge-type[15]) contact model.

The height of the potential barrier between granules, estimated from the breakdown voltage E_p (4) with allowance for L_c, is identical ($\Delta U_{gr}\cong 0.05$ eV) for samples with $x=0$ and $x=0.1$ and coincides with the difference between the activation energies, estimated from ρ_{mw} and ρ_0 for a sample with $x=0.3$. This result shows that a dc barrier of the order of 0.05 eV exists between the granules, regardless of composition.

3. DISCUSSION OF THE RESULTS

The influence of intergranular surface phenomena on the electrical properties of polycrystalline material came to light about half a century ago in studies of the frequency dependence of the dielectric permittivity of ferrites at low frequencies.[2,14] It was observed that comparatively highly conducting regions in ferrites were separated by thin layers of poorly conducting material. The same layers probably exist in polycrystalline manganites.[7] Such a layer is usually formed[2] as a result of nonequilibrium between the atmosphere and the sample during its preparation (e.g., during cooling). The relative thickness of the surface layer in ferrites is of the same order of magnitude ($\approx 10^{-2}$) as the thickness of the contact layer in our investigated manganites (see Table I). However, a simple model resting on the assumption that the high dc-resistivities ρ_0 of polycrystalline manganites are attributable to high surface-layer resistivities ρ cannot account for the observed variations of the thickness of the contact layer as a function of temperature (see Table I) and the magnetic field or for the high magnetoresistivity of polycrystalline manganites over a broader temperature range than for single crystals.[6,7]

The high values of ρ for polycrystalline films can be attributed to the presence of an additional potential barrier between the granules. In manganites, because of their high spin polarization, a barrier of this kind can occur in the ferromagnetic region when the magnetic moments of adjacent grains are not mutually parallel[6] or when an air gap exists between granules.[16] Certain features of the electrical resistivity and magnetoresistivity of manganites have been successfully explained[6,16] by carrier tunneling effects through these potential barriers. The large thickness of the contact layer probably renders the role of tunneling inconsequential in our case.

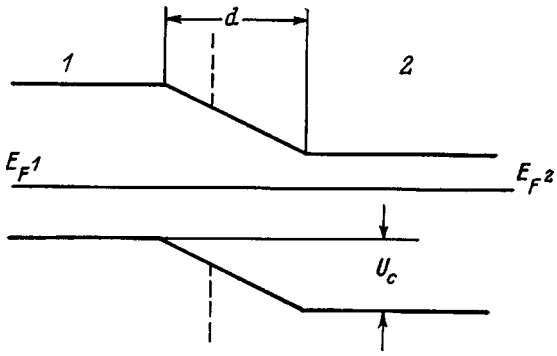

FIG. 3. Energy diagram of contact between two materials *1* and *2* in the equilibrium state.

However, such a barrier can occur not only between granules, but also within an individual granule. We assume that the anomalies of the microwave and dc electrical properties of manganites can also be attributed to the presence of a surface layer whose properties differ somewhat from those of the material inside the granules. The comparatively slow decline in the magnetic permeability (curve *6* in Fig. 1) in a 20–30 K interval around T_C is most likely caused by the magnetic inhomogeneity of the granules or the influence of a surface layer.

Let us consider the energy diagram of the contact between two dissimilar materials in the equilibrium state (Fig. 3).[1,4] Depending on the type and properties of the contact structure (metal-semiconductor or p–n junction), a potential barrier appears in the boundary layers, a semiconductor surface layer of substantial thickness d (up to 1000 atomic layers) can be depleted of electrons, and a barrier layer can form. This contact potential difference $\Delta U_{gr}\equiv U_C=E_F^1-E_F^2$ is determined by the difference in the thermoelectronic work functions or in the Fermi energies E_F^1 and E_F^2 of these materials, and the space-charge region is determined by the densities of carriers, donors, and acceptors, making up the structure of semiconductors.[1,4] The transition of a carrier from one region to the other requires that the potential barrier be overcome at the expense of the thermal energy kT. As a result, in the paramagnetic region the electrical resistivity of the contact structure {inner layer–surface layer–air gap–surface layer–inner layer} increases as the temperature is lowered. In the presence of magnetic order, the conduction band splits, an effect that probably causes U_C to decrease in manganites and, accordingly, causes the electrical resistivity to decrease upon transition to the ferromagnetic region.

Optical studies of manganites[17] indicate a sensitivity of their band structure to magnetic order and to a magnetic field in the ferromagnetic region. Different behaviors of the carrier concentration and mobility and the Fermi energies in the surface layer and in the granule as functions of the magnetic field in polycrystalline manganites can be elicited by varia-

tions in the contact-potential difference and the thickness and resistance of the barrier layer as functions of the magnetic field. On the basis of the exponential behavior of the electrical conductivity for a barrier layer of considerable thickness, small variations of the granule characteristics ΔU_{gr} and σ_0 can be expected to induce large values of MR in a magnetic field. Investigations of magnetic semiconductors[18] have shown that the magnetic field sensitivity of their band structure is a maximum in the vicinity of T_C, but is also very strong both above and below T_C. This fact could account for the magnetoresistivity peak of polycrystalline manganites around T_C and the persistence of high values of MR above and below T_C.

The proposed model thus explains the main features of the variation of the electrical resistivity of polycrystalline manganites as functions of the temperature, magnetic field, and electric field.

In closing, we note that the role of the surface and intergranular boundaries in the electrical properties of magnetic semiconductors of the type EuO and $HgCr_2Se_4$ also has been little studied. The role can be very large (especially in polycrystalline media[19]), in particular, because of a change in the magnetic state on the surface of magnetic semiconductors[20] and a strong magnetic order dependence of their carrier parameters.[21] Undoubtedly one should not overlook the fact that certain experiments on giant magnetoresistance in magnetic semiconductors and manganites (particularly in films) relate to surface phenomena.

We are grateful to A. V. Trefilov and M. I. Katsnel'son for the derivation of the equation (3) used to calculate R_s.

This work has received financial support from the Federal program ''Surface Atomic Structures'' (Project No. 95.2-10).

[1] R. A. Smith, *Semiconductors*, 2nd ed. [Cambridge Univ. Press, Cambridge, 1978; Mir, Moscow, 1982].
[2] J. M. Smit and H. P. J. Wijn, *Ferrites* [Wiley, New York, 1959; IL, Moscow, 1962].
[3] L. D. Landau and E. M. Lifshitz, *Electrodynamics of Continuous Media*, 2nd ed. (rev. and enl., with L. P. Pitaevskii) [Pergamon Press, Oxford–New York, 1984; Nauka, Moscow, 1982].
[4] V. L. Bonch-Bruevich and S. G. Kalashnikov, *Physics of Semiconductors* [in Russian], Nauka, Moscow, 1977.
[5] É. L. Nagaev, Usp. Fiz. Nauk **165**, 529 (1995); Usp. Fiz. Nauk **166**, 833 (1996).
[6] H. Y. Hwang, S.-W. Cheong, N. P. Ong *et al.*, Phys. Rev. Lett. **77**, 2041 (1996).
[7] A. Gupta, G. Q. Gong, Gang Xiao *et al.*, Phys. Rev. B **54**, R15629 (1996).
[8] N. I. Solin, A. B. Davydov, G. L. Shtrapenin *et al.*, Defektoskopiya, No. 2, 77 (1991).
[9] M. Dominguez, S. M. Bhagat, S. E. Lottand *et al.*, Europhys. Lett. **32**, 349 (1995).
[10] S. E. Lofland, P. H. Kim, P. Dahiroc *et al.*, J. Phys.: Condens. Matter **9**, 6697 (1997).
[11] S. A. Shmulevich, Pribory Tekh. Éksp., No. 2, 170 (1971).
[12] A. G. Gurevich and G. A. Melkov, *Magnetic Oscillations and Waves* [in Russian], Nauka, Moscow, 1994.
[13] Ya. I. Frenkel', Zh. Éksp. Teor. Fiz. **8**, 1292 (1971).
[14] C. G. Koops, Phys. Rev. **83**, 121 (1951).
[15] R. R. Heikes and W. D. Johnston, J. Chem. Phys. **26**, 582 (1957).
[16] N. Zhang, W. Ding, W. Zhong, D. Xing, and Y. Du, Phys. Rev. B **56**, 8138 (1997).
[17] N. N. Loshkareva, Yu. P. Sukhorukov, B. A. Gizhevskii *et al.*, Phys. Status Solidi A **164**, 863 (1997).
[18] É. L. Nagaev, *Physics of Magnetic Semiconductors* [in Russian], Nauka, Moscow, 1979.
[19] A. P. Ramirez, R. J. Cava, and J. Krajewski, Nature (London) **386**, 156 (1997).
[20] A. M. Ionov, Phys. Low-Dimens. Semicond. Struct. **1–2**, 27 (1996).
[21] N. I. Solin, A. A. Samokhvalov, and S. V. Naumov, Fiz. Tverd. Tela (St. Petersburg) **37**, 2100 (1995) [Phys. Solid State **37**, 1142 (1995)]; Fiz. Tverd. Tela (St. Petersburg) **39**, 848 (1997) [Phys. Solid State **39**, 54 (1997)].

Translated by James S. Wood

Self-localized nonlinear surface magnetic polaritons in a ferromagnetic medium

I. E. Dikshteĭn and S. A. Nikitov[a)]

Institute of Radio Engineering and Electronics, Russian Academy of Sciences, 103907 Moscow, Russia

D. S. Nikitov

Moscow Physicotechnical Institute, 141700 Dolgoprudnyiĭ, Moscow Region, Russia

(Submitted April 2, 1994)
Fiz. Tverd. Tela (St. Petersburg) **40**, 1885–1889 (October 1998)

The properties of electromagnetic waves propagating in a semibounded, nonlinear, ferromagnetic medium are investigated. It is shown that under certain conditions the interaction between the spin and electromagnetic waves results in the localization of volume polaritons near the surface. Self-localization of surface polaritons due to the nonlinear properties of the medium occurs thereby. The nonlinear Schrödinger equation for nonlinear surface and volume polaritons is derived, and the conditions under which solitons of these waves exist are determined. The wave intensity required to observe the predicted effects is estimated.
 [S1063-7834(98)02410-1]

Surface magnetostatic waves (MSWs) possess a number of distinguishing features that could be very important for designing microwave devices.[1,2] The use of ferromagnetic crystals with a large uniaxial magnetic anisotropy makes it possible to extend the working frequency interval of these devices into the millimeter range. An investigation of traveling MSWs in the frequency range 35–55 GHz and their amplitude-frequency characteristics in plates of barium hexaferrite, which possesses a high uniaxial anisotropy, were reported in Refs. 3–5. To determine the spectrum of excitations in such plates it is necessary to take account of the interaction of magnetostatic and electromagnetic waves.[5] New types of linear surface waves can arise from such an interaction. Specifically, a surface magnetic polariton due to the interaction of an electromagnetic wave with a Damon–Eshbach wave was studied in Refs. 5–7. A linear surface polariton can decay even in the absence of dissipative terms in the Landau and Lifshitz equations of motion and Maxwell's equations as a result of the emission of spin waves into the interior region of the crystal.[6]

The generation of surface magnetic polaritons by an ac magnetic field near the surface of a magnetic crystal can produce a high energy density of the magnetic wave and stimulate as a result large magnetic and electric field amplitudes at the surface. In such a case, the nonlinearity of the magnet can lead to different interesting effects. Specifically, it can induce nonlinear spin and electromagnetic waves which have no analogs in the case of linear waves and become delocalized at zero amplitude. Polaritons localized at the boundary of a self-focusing nonlinear isotropic magnetic (or dielectric) medium in vacuum are now well known.[8–10] Thus, self-localized nonlinear exchange[11,12] and dipole-exchange[13] spin waves and three-dimensional precessional surface solitons[14,15] in ferromagnets were recently investigated. Self-localized nonlinear surface polaritons near the interface of a linear ferromagnetic (ferrimagnetic) medium and a nonlinear isotropic material were also studied in Ref. 7.

In the works cited above, surface polaritons in optically isotropic materials were considered as being a consequence of the nonlinearity of the materials. However, the dispersion of electromagnetic waves in gyrotropic (optically active) ferromagnets can be very substantial and it can be controlled by varying the magnitude of the applied magnetic field. Hybridization of magnetostatic and electromagnetic waves can result in the appearance of new types of nonlinear self-localized surface polaritons.

In the present paper nonlinear self-localized surface polaritons propagating near the surface of a ferromagnet as well as the damping of these waves due to the radiation of the second harmonic into the interior region of the crystal are studied. A system consisting of a metallized, semibounded, ferromagnetic crystal (as shown in Fig. 1) with easy axis perpendicular to the surface $\mathbf{n} \| \mathbf{e}_z$ in an external magnetic field $\mathbf{H}_0 \| \mathbf{e}_z$ is studied. Linear surface polaritons do not exist in the model considered.

1. BASIC EQUATIONS

The system investigated consists of a ferromagnetic dielectric occupying the half-space $z<0$ whose surface is coated with an ideal metal (no losses), as shown in Fig. 1. The dynamics of the ferromagnet is described by the Landau and Lifshitz equations for the magnetization vector $\mathbf{M}$

$$\dot{\mathbf{M}} = -\gamma[\mathbf{M} \times \mathbf{H}_{\text{eff}}], \tag{1}$$

where the effective magnetic field $\mathbf{H}_{\text{eff}}$ is determined by the functional derivatives $\mathbf{H}_{\text{eff}} = -\delta W/\delta \mathbf{M}$ of the total energy of the ferromagnet[16]

$$W = \int dv \left[w_a(\mathbf{M}) + \frac{1}{8\pi}(\mathbf{H}_m^2 + \mathbf{E}\cdot\mathbf{D}) - \mathbf{H}_0 \cdot \mathbf{M} \right], \tag{2}$$

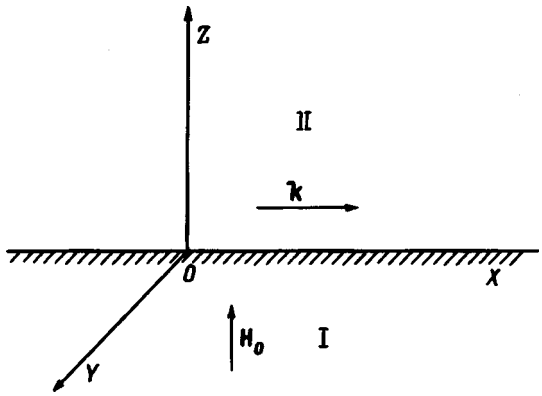

FIG. 1. Geometry of the problem. I — Ferromagnet, II — vacuum. The polariton propagates along the OX axis.

$\gamma>0$ is the gyromagnetic ratio, $w_a(M)=-\beta M_z^2/2$ is the uniaxial magnetic anisotropy energy density, $\beta>0$ is the anisotropy constant, $\mathbf{H}_m$ is the magnetic field minus the external magnetic field, $\mathbf{E}$ is the electric field, $\mathbf{D}=\varepsilon\cdot\mathbf{E}$ is the electric induction, and $\varepsilon=$ const is the permittivity of the magnet. In order to neglect in Eq. (2) the spatial dispersion due to the nonuniform exchange the inequality $k\ll k_{\rm ex}\equiv(\beta M/a^2J)^{1/2}$ must be satisfied. Here $1/k_{\rm ex}$ is the characteristic spatial dispersion length, J is an exchange integral, equal in order of magnitude to the Curie temperature, and a is the lattice constant.

The equations (1) together with Maxwell's equations

$$\text{curl } \mathbf{E}=-\partial\mathbf{B}/\partial t, \quad \text{div } \mathbf{B}=0,$$

$$\text{curl } \mathbf{H}_m=\frac{1}{c^2}\frac{\partial\mathbf{D}}{\partial t}, \quad \text{div } \mathbf{D}=0 \tag{3}$$

($\mathbf{B}=\mathbf{H}_m+4\pi\mathbf{M}$ — magnetic induction, c — velocity of light in vacuum) and the electrodynamic boundary conditions at the ferromagnet–metal surface

$$B_z=0, \quad E_x=E_y=0 \tag{4}$$

determine the spectrum of nonlinear polaritons in the ferromagnet. The magnetization and magnetic field of the ground state of a ferromagnet, for which $H=H_0+\beta M-4\pi M>0$, equal, respectively,

$$\mathbf{M}_0=M\mathbf{e}_z, \quad \mathbf{H}_{m0}=-4\pi M\mathbf{e}_z. \tag{5}$$

Since here we are interested in nonlinear processes with small amplitude, the total temporal and spatial dependence of the magnetization and magnetic field will be represented as a sum of the equilibrium part (M_0, H_{0m}) and small corrections $\overline{M}$ and $\overline{H}_m$ which depend on the coordinates and time, i.e.

$$M_\perp=\overline{M}_\perp, \quad M_z=M-\overline{M}_\perp^2/2M,$$

$$H_m=H_{m0}+\overline{H}_m, \quad M_\perp=\{\overline{M}_x,\overline{M}_y\}, \tag{6}$$

where $|\overline{M}_\perp|\ll M$ and $|\overline{H}_m|\ll|H_{m0}|$.

Taking into consideration the relations (5) and (6) and, for convenience, dropping the overbar, we represent the effective field $\mathbf{H}_{\rm eff}$ in the form

$$\mathbf{H}_{\rm eff}=(H-\beta M_\perp^2/2M)\mathbf{e}_z+\mathbf{H}_m, \tag{7}$$

with $H=(\beta-4\pi)M+H_0$. Substituting the expression (7) into Eq. (1) and retaining terms up to third order in $M_\perp$ and H_m inclusively, we obtain

$$-\frac{1}{\omega_0}\frac{\partial m_x}{\partial t}-hm_y+h_{my}=m_yh_{mx}-\frac{m_\perp^2}{2}(\beta m_y-h_{my}), \tag{8}$$

$$-\frac{1}{\omega_0}\frac{\partial m_y}{\partial t}+hm_x-h_{mx}=-m_xh_{my}+\frac{m_\perp^2}{2}(\beta m_x-h_{mx}), \tag{9}$$

where $\omega_0=\gamma M$. Here we have introduced the dimensionless variables $\mathbf{m}=\mathbf{M}/M$, $h_m=H_m/M$, $\mathbf{h}=\mathbf{H}/M$, and $h_0=H_0/M$. Eliminating the electric field from Maxwell's equations we obtain the equation

$$\boldsymbol{\nabla}^2h_m-\nabla\cdot(\nabla h_m)=\frac{\varepsilon}{c^2}\frac{\partial^2\mathbf{b}}{\partial t^2}, \tag{10}$$

where $\mathbf{b}=\mathbf{B}/M$. For surface waves we introduce the damping condition for $m_\perp$, h_m, and E as $z\to-\infty$ in the form of the boundary conditions

$$|m_\perp|, |h_m|, |E|\to 0. \tag{11}$$

The axial symmetry of the system makes it possible to limit without loss of generality the analysis to polaritons propagating along the **x** axis.

2. LINEAR POLARITONS

Using the linear approximation $\exp[i(kx-\omega t)+qz]$ for $m_\perp$ and h_m, we obtain from Eqs. (8)–(10) the characteristic equation

$$q^4-2Q_1q^2+Q_2=0. \tag{12}$$

Here

$$Q_1=\frac{\varepsilon}{c^2}\left(\frac{\mu+1}{2}\omega_{ck}^2-\mu\omega^2\right)$$

$$=\frac{\varepsilon}{c^2}\frac{(\omega^2-\omega_{3k}^2)(\omega^2-\omega_{4k}^2)}{\omega-\omega_s^2}, \tag{13}$$

$$Q_2=\frac{\varepsilon^2}{c^2}[(\mu^2-\nu^2)\omega^2-\mu\omega_{ck}^2](\omega^2-\omega_{ck}^2)$$

$$=\frac{\varepsilon^2}{c^4}\frac{(\omega^2-\omega_{1k}^2)(\omega^2-\omega_{2k}^2)(\omega^2-\omega_{ck}^2)}{\omega^2-\omega_s^2}, \tag{14}$$

$$\omega_{1,2k}^2=\frac{1}{2}(\omega_{1s}^2+\omega_{ck}^2\mp\sqrt{(\omega_{1s}^2+\omega_{ck}^2)^2-4\omega_{2s}^2\omega_{ck}^2}), \tag{15}$$

$$\omega_{3,4k}^2=\frac{1}{2}(\omega_{2s}^2+\omega_{ck}^2\mp\sqrt{(\omega_{2s}^2+\omega_{ck}^2)^2-4\omega_{3s}^2\omega_{ck}^2}), \tag{16}$$

where $\mu=1+\omega_s\omega_M/(\omega_s^2-\omega^2)$ and $\nu=\omega\omega_M/(\omega_s^2-\omega^2)$ are the components of the magnetic permeability tensor

$$\omega_{ck}=ck/\sqrt{\varepsilon}, \quad \omega_s=h\omega_0, \quad \omega_{1s}=\omega_s+\omega_M,$$

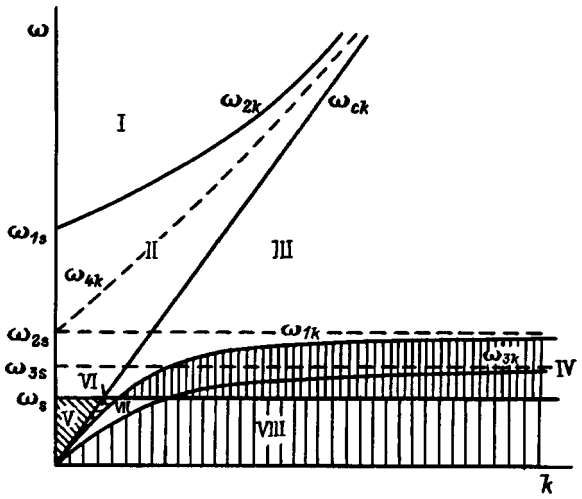

FIG. 2. Dispersion curves of electromagnetic waves in a ferromagnet. In the regions I–III Eq. (12) has four imaginary roots; in the regions IV–VI — two real and two imaginary roots; in the regions VII and VIII — four real roots. $\omega_{1s}=\omega_s+\omega_M$, $\omega_{2s}=\sqrt{\omega_s(\omega_s+\omega_M)}$, $\omega_{3s}=\sqrt{\omega_s(\omega_s+\omega_M/2)}$.

$$\omega_{2s}=\sqrt{\omega_s(\omega_s+\omega_M)}, \quad \omega_{3s}=\sqrt{\omega_s(\omega_s+\omega_M/2)},$$

$$\omega_M=4\pi\omega_0.$$

The roots of the characteristic equation (12) are

$$q_{1,2}=\pm(Q_1+\sqrt{Q_1^2-Q_2})^{1/2}, \tag{17}$$

$$q_{3,4}=\pm(Q_1-\sqrt{Q_1^2-Q_2})^{1/2} \tag{18}$$

in the (ω,k) plane, with the exception of the curves $\omega=\omega_{1k}$, ω_{2k}, ω_{ck}, and ω_s.

The behavior of the solutions of Eq. (12) in the (ω,k) plane is illustrated in Fig. 2. This plane is divided into eight regions. In the regions I ($\omega_{2k}<\omega$), II ($\omega_{ck}<\omega<\omega_s$), and III ($\omega_{3k}<\omega$, $\omega<\omega_{1k}$, $\omega<\omega_s$) Eq. (12) possesses four imaginary roots (q_1,q_2,q_3,q_4). In the regions IV ($\omega_s<\omega$, $\omega_{ck}<\omega$, $\omega<\omega_{2k}$), V ($\omega_s<\omega<\omega_{1k}$), and VI ($\omega_{1k}<\omega$, $\omega<\omega_{ck}$, $\omega<\omega_s$) it possesses two real roots (q_1,q_2) and two imaginary roots (q_3,q_4). In the regions VII ($\omega_{1k}<\omega$, $\omega_s<\omega$, $\omega<\omega_{ck}$) and VIII ($\omega<\omega_{3k}$, $\omega<\omega_s$) it possesses four real roots. Therefore the first three regions correspond to volume waves. In the present model of a metallized ferromagnet there are no surface waves in the linear approximation. In the nonlinear regime surface solutions (if they exist) must be sought in the regions IV–VIII, and in the regions VII–VIII they will be purely surface waves, while in the regions IV–VI they will be quasisurface (leaking) waves.

3. NONLINEAR SURFACE AND VOLUME POLARITONS

We seek the solution of the nonlinear equations (8)–(10), together with the boundary conditions (4) and (11), for the fundamental harmonic of the upper polariton branch ($\omega\leqslant\omega_{2k}$) in the following form:

$$m_{x,y}=\frac{1}{2}A_{x,y}(x,z,t)\exp i(kx-\omega t)+\text{c.c.}, \tag{19}$$

$$h_m=\frac{1}{2}B(x,z,t)\exp i(kx-\omega t)+\text{c.c.}, \tag{20}$$

$$e=\frac{E}{M}=\frac{1}{2}C(x,z,t)\exp i(kx-\omega t)+\text{c.c.} \tag{21}$$

Here the amplitudes $A_{x,y}(x,z,t)$, $B(x,z,t)$, and $C(x,z,t)$ are slowly varying compared with the fast oscillations of the carrying wave

$$\left|\frac{\partial G}{\partial t}\right|\ll\omega_2|G|, \quad \left|\frac{\partial G}{\partial z}\right|\ll K|G|, \quad G=\{A_{x,y},B,C\}. \tag{22}$$

For weakly localized nonlinear surface waves with low amplitude, substituting the solutions (19)–(21) into Eqs. (8)–(10) and using Eq. (22) gives

$$i\frac{\partial B_y}{\partial t}+\frac{1}{2}D_2\frac{\partial^2 B_y}{\partial z^2}+N_2|B_y|^2B_y=0, \tag{23}$$

$$A_x=[(\mu-1)(B_x+\Gamma_x)-i\nu(B_y+\Gamma_y)]/(4\pi), \tag{24}$$

$$A_y=[i\nu(B_x+\Gamma_x)+(\mu-1)(B_y+\Gamma_y)]/(4\pi), \tag{25}$$

$$B_x=-[(\mu-1)\Gamma_x-i\nu(B_y+\Gamma_y)]/(4\pi), \tag{26}$$

$$B_z=\frac{i\omega_{ck}^2}{\omega^2-\omega_{kc}^2}\frac{\partial}{\partial z}B_x, \tag{27}$$

$$D_n=(-1)^n\frac{4\omega_{ck}^2(\omega_{nk}^2-\omega_{3k}^2)(\omega_{nk}^2-\omega_{4k}^2)}{k^2\omega_{nk}(\omega_{2k}^2-\omega_{1k}^2)(\omega_{nk}^2-\omega_{ck}^2)} \quad (n=1,2), \tag{28}$$

$$\begin{aligned}N_n=&\frac{(-1)^n}{2048\pi^3\mu_n^3}\frac{\omega_{nk}}{(\omega_{2k}^2-\omega_{1k}^2)(\omega_{nk}^2-\omega_s^2)^3}\\&\times\{\beta\omega_M^4(3\omega_{1s}^4+2\omega_{1s}^2\omega_{nk}^2+\omega_{nk}^4)\\&+4\pi\omega_M^3[(4\omega_s+\omega_M)\omega_{nk}^4\\&+2\omega_{1s}^2(\omega_s+2\omega_M)\omega_{nk}^2-3\omega_s\omega_{1s}^4]\},\end{aligned} \tag{29}$$

$$\Gamma_x=-\frac{i|A_y|^2A_y}{1024\pi^3\mu^3}(\beta+4\pi)[(\mu_n^2-\nu_n^2-\mu_n)^2+3\nu_n^2], \tag{30}$$

$$\begin{aligned}\Gamma_y=&\frac{|A_y|^2A_y}{1024\pi^3\mu_n^3}[3(\mu_n^2-\nu_n^2-\mu_n)^2-\nu_n^2]\\&\times[\beta(\mu_n^2-\nu_n^2-\mu_n)-4\pi\mu_n],\end{aligned} \tag{31}$$

$$\mu_n=\mu(\omega=\omega_{nk}), \quad \nu_n=\nu(\omega=\omega_{nk}).$$

From Eqs. (3) we obtain $\partial E_x/\partial t=M\nabla_z h_{my}$. Taking account of this relation, the boundary conditions (4) for the amplitudes of the fundamental harmonic assume the form

$$\frac{\partial B_y}{\partial z}=\frac{\partial B_x}{\partial z}=0. \tag{32}$$

The ferromagnet under study possesses a self-focusing type nonlinearity ($D_2>0$, $N_2>0$). Introducing the dimensionless variables $b=B_y/B_{y0}$, $\tau=t/T$, and $\xi=z/z_0$ with

$$T^{-1}=N_2b_{y0}^2, \quad z_0^{-1}=b_{y0}N_2^{1/2}/D_2^{1/2}, \tag{33}$$

where h_{y0} is the maximum amplitude of the oscillations, we obtain from Eq. (23) the following nonlinear Schrödinger equation:

$$i\frac{\partial b}{\partial \tau}+\frac{1}{2}\frac{\partial^2 b}{\partial \xi^2}+|b|^2 b=0. \tag{34}$$

This equation must be solved for the half-space $0>z>-\infty$ under the following conditions:

$$\left|\frac{\partial b}{\partial \xi}\right|_{\xi=0}=0, \quad b|_{\xi=-\infty}=0, \tag{35}$$

which characterize a surface wave. A one-soliton solution of the NES that satisfies the boundary conditions (35) has the form

$$b(\xi,\tau)=\sinh(\xi)\exp[i(\tau/2+\Phi_0)], \tag{36}$$

where Φ_0 is an arbitrary phase. From Eqs. (19)–(21), (24)–(27), and (36) we obtain the following solution for the nonlinear surface polariton:

$$h_{my}=\frac{1}{2}b_{y0}\,\mathrm{sech}(z/z_0)\times\exp i\{kx-[\omega_2-(2T)^{-1}]t+\Phi_0\}+\text{c.c.}, \tag{37}$$

$$h_{mx}=-\frac{i\nu}{8\pi}h_{y0}\,\mathrm{sech}(z/z_0)\times\exp i\{kx-[\omega_2-(2T)^{-1}]t+\Phi_0\}+\text{c.c.}, \tag{38}$$

$$m_x=[(\mu-1)h_{mx}-i\nu h_{my}]/(4\pi),$$

$$m_y=[i\nu h_{mx}+(\mu-1)h_{my}]/(4\pi). \tag{39}$$

Then from Eq. (37) we obtain the dispersion relation for the nonlinear surface polariton

$$\omega=\omega_{2k}-N_2 b_{y0}^2/2. \tag{40}$$

The penetration depth $z_0\approx b_{y0}^{-1}$ of the surface polariton tends to infinity, where the amplitude decreases.

According to Lighthill's criterion,[17] the nonlinear stationary solution (37)–(39) is modulationally stable if

$$(\partial^2\omega/\partial k^2)/(\partial\omega/\partial b^2)>0. \tag{41}$$

Since $\partial^2\omega/\partial k^2>0$ and $\partial^2\omega/\partial b_{y0}^2=-N_2/2<0$, which hold for a surface polariton, are satisfied, the standard analysis shows that the stationary wave solutions (37)–(39) examined above are unstable with respect to small fluctuations with wave vector k_1 as soon as the amplitude of the wave exceeds the threshold

$$|b_{y0}|^2=\frac{k_1^2}{2N_2}\frac{\partial^2\omega_2}{\partial k^2}. \tag{42}$$

This modulation instability of a nonlinear surface polariton can lead to the formation of a three-dimensional ($3D$) surface soliton. Such $3D$ surface solitons for exchange spin waves were previously studied in Refs. 14 and 15.

Besides the nonlinear surface polariton solution (36), Eq. (34) also possesses a nonlinear stationary solution in the form

$$B_y=b_{y0}\exp(iN_2|b_{y0}|^2 t). \tag{43}$$

This solution simply describes a nonlinear exchange polariton, which is uniform over the thickness of the crystal and satisfies the boundary conditions (32). Then, we obtain from Eq. (43) the dispersion relation

$$\omega=\omega_{2k}-N_2|b_{0y}|^2, \tag{44}$$

where b_{0y} is the maximum amplitude. Since the inequalities $\partial\omega^2/\partial k^2>0$ and $\partial\omega/\partial b_{0y}^2=-N_2<0$ hold for a nonlinear volume polariton, the solution (44) is modulationally unstable relative to the formation of a train of solitons in the direction of propagation.

We shall now seek the solution of the nonlinear equations (8)–(10) near the lower polariton branch. Once again, we employ the envelope method. For the fundamental harmonic, we find a solution in the form (19)–(21) by replacing the subscript 2 by 1 for ω. We obtain $\omega=\omega_1$. When the inequalities (22) hold, the equations for the amplitudes of the envelopes **A** and **B** will have the same form as Eqs. (23)–(27). For the lower polariton branch, the index 1 is used for ω, D, and N in Eqs. (23)–(27).

It follows from Eqs. (28) and (29) that the inequalities $D_1<0$ and $N_1>0$ hold in the exchange-free approximation employed here. For this reason, a stationary volume polariton is stable with respect to localization in the transverse direction. As shown earlier, nonlinear self-localized surface spin waves can exist in a volume-dipole region.[13]

Thus, we have presented a theory of nonlinear surface polaritons in a semibounded ferromagnet taking account of the interaction of electromagnetic and spin waves. In the problem considered here, a ferromagnet with a metallized surface was chosen. Of course, it is very difficult to screen completely the electromagnetic radiation from the surface of a ferromagnet. This can be accomplished by using a screen made of a HTSC film. Screening is possible if the penetration depth of the electromagnetic field into the superconductor exceeds the London depth λ_L (for HTSC $\lambda_L\approx 10^{-4}-10^{-7}$ cm).

Of course, as a result of the weak nonlinearity of a ferromagnetic medium at high frequencies, localization of nonlinear surface polaritons requires a high power level of the order of 1 MW/m [see Eq. (33)]. Such power can be achieved only with pulsed excitation of a surface polariton.

We thank the Russian Fund for Fundamental Research (Grants 96-02-16168a, 96-02-16872a) and the Ministry of Science and Technology (program ''Surface Atomic Structures'') for partial financial support.

[a)]E-Mail: nikitov@open.cplire.ru

[1] D. D. Stansil, *Theory of Magnetostatic Waves* (Springer-Verlag, N. Y., 1993), 214 pp.
[2] A. G. Gurevich and G. A. Melkov, *Magnetostatic Oscillations and Waves* [in Russian], Nauka, Moscow (1994), 462 pp.
[3] V. S. Stal'makhov, A. A. Ignat'ev, and M. I. Kulikov, Radiology **26**, 2389 (1981).
[4] A. A. Ignat'ev and A. N. Lepestkin, Zh. Tekh. Fiz. **56**, 1829 (1986) [Sov. Phys. Tech. Phys. **31**, 1091 (1986)].
[5] Yu. F. Ogrin, S. V. Meriakri, and I. I. Petrova, Zh. Tekh. Fiz. **60**, 130 (1990) [Sov. Phys. Tech. Phys. **35**, 828 (1990)].

[6] M. I. Kaganov and T. I. Shalaeva, Zh. Tekh. Fiz. **96**, 2185 (1989) [Sov. Phys. Tech. Phys. **69**, 1237 (1989)].
[7] R. F. Wallis, A. D. Boardman, and M. Shabat, in *Nonlinear Waves In Solid State Physics*, NATO Advanced Study Institute, Vol. 47, edited by A. D. Boardman *et al.* [Plenum, N. Y., 1990, p. 51; Phys. Rev. B **41**, 717 (1990)].
[8] A. A. Maradudin, Z. Phys. B **41**, 341 (1981).
[9] A. A. Akhmediev, Zh. Eksp. Teor. Fiz. **83**, 545 (1982) [Sov. Phys. JETP **56**, 299 (1982)].
[10] A. D. Boardman and P. Egan, IEEE J. Quantum Electron. **QE-21**, 1701 (1985).
[11] Yu. I. Bespyatykh and I. K. Dikshteĭn, Fiz. Tverd. Tela (St. Petersburg) **35**, 1175 (1993) [Phys. Solid State **35**, 598 (1993)].
[12] A. S. Kovalev, Fiz. Tverd. Tela (St. Petersburg) **35**, 1935 (1993) [Phys. Solid State **35**, 966 (1993)].
[13] Yu. I. Bespyatykh, I. E. Dikstein, S. A. Nikitov, and A. D. Boardman, Phys. Rev. B **50**, 13435 (1994).
[14] Yu. I. Bespyatykh, I. E. Dikstein, and S. A. Nikitov, Phys. Lett. A **184**, 198 (1994).
[15] Yu. I. Bespyatykh, A. D. Bordman, I. E. Dikshteĭn, and S. A. Nikitin, Fiz. Tverd. Tela (St. Petersburg) **38**, 295 (1996) [Phys. Solid State **38**, 166 (1996)].
[16] A. I. Akhiezer, V. G. Bar'yakhtar, and S. V. Peletminskiĭ, *Spin Waves*, [North-Holland, Amsterdam, 1968; Nauka, Moscow, 1967, 368 pp.].
[17] M. J. Lighthill, J. Inst. Appl. Math. **1**, 269 (1965).

Translated by M. E. Alferieff

Magnetic phases of $Fe_xV_{1-x}S$ and their electronic structure

G. V. Loseva, S. G. Ovchinnikov, É. K. Yakubaĭlik, N. I. Kiselev

L. V. Kirenskiĭ Institute of Physics, Siberian Branch of the Russian Academy of Sciences, 660036 Krasnoyarsk, Russia

T. A. Gaĭdalova

Institute of Chemistry, Far-Eastern Branch of the Russian Academy of Sciences, 690022 Vladivostok, Russia
(Submitted April 6, 1998)
Fiz. Tverd. Tela (St. Petersburg) **40**, 1890–1893 (October 1998)

A study has been made of the $Fe_xV_{1-x}S$ solid solutions with $0<x<0.5$. For the compounds with $x>0.1$, x-ray diffraction analysis discloses a V_5S_8 superstructure. Samples with $x>0.1$ are magnetically ordered at room temperature. The concentration dependences of resistivity and magnetization exhibit sharp peaks for $x=0.1$ and $x=0.2$, respectively. The main features of the structure and electronic properties have been qualitatively explained in terms of the three-band exciton-insulator model, and the maxima in resistivity and magnetization are assigned to the formation of localized magnetic moments with $S=1$, which become delocalized with increasing x. © *1998 American Institute of Physics.* [S1063-7834(98)02510-6]

Vanadium compounds undergoing a metal-insulator (M-I) transition comprise, besides the well-known oxide series V_nO_{2n-1}, (Ref. 1) also sulfide systems, e.g., V_nS (Ref. 2) and $V_xMn_{1-x}S$ (Ref. 3). The M-I transition in transition-metal oxides and sulfides is accompanied frequently by formation of superstructures in the crystal and magnetic lattices, which are described as charge- or spin-density waves (CDW and SDW, respectively). The CDWs and SDWs are produced also in the course of transformation to the exciton-insulator phase.[4] For instance, the mechanism of the high-temperature M-I transition in vanadium monosulfide VS was considered within the exciton-insulator model.[2]

This work reports on electrical and magnetic measurements and x-ray diffraction and differential thermal analysis (DTA) studies of compounds in the $Fe_xV_{1-x}S$ system with $0<x<0.5$. The electronic structure of these compounds is analyzed.

1. STRUCTURAL DATA

Samples of the $Fe_xV_{1-x}S$ system were obtained by firing a mixture of pure elements at 1200 K for three days in evacuated quartz ampoules. The $Fe_xV_{1-x}S$ compositions prepared by cation substitution of iron for vanadium are as follows: $x=0.01$; 0.02; 0.05; 0.1; 0.2; 0.3; 0.4; 0.5.

X-ray diffraction analysis of the compounds obtained by isomorphic substitution V→Fe in the $Fe_xV_{1-x}S$ system with $0.1\leqslant x\leqslant 0.5$ showed them to be isostructural with V_5S_8 at 300 K.

This served as a starting point in finding the unit cell parameters of our samples. The determination was done by least-squares fitting of 15–30 unambiguously indexed and sufficiently intense reflections chosen throughout the diffraction pattern. The results of the determination are listed in Table I.

DTA curves of $Fe_xV_{1-x}S$ samples placed in evacuated ampoules of a special shape were measured in a MOM derivatograph with a rate of 10 K/min within the 300–1300 K range. All compounds with $0<x\leqslant 0.5$ exhibited two reversible and stable endothermal effects within the 800–900 K interval, which were found earlier[2] to exist in the vicinity of the high-temperature M-I transition in vanadium monosulfide.

The crystal structures formed in the $VS-V_5S_8$ system are based on the high-temperature NiAs hexagonal structure ($B8$ type), which is characterized by the presence on the cation sublattice of randomly distributed vacancies. As the sulfur content progressively increases in going from VS to V_5S_8, one observes an increase in the concentration of vacancies and in the extent of their ordering on the alternating cation layers. The superstructure symmetry changes at 300 K from orthorhombic ($Pmcn$-D_{2h}^{16}) for VS to monoclinic ($F2/m$-C_{2h}^{3}) for V_5S_8.[5]

According to the above x-ray diffraction data, progressive increase of iron concentration in the $Fe_xV_{1-x}S$ system produced from VS brings about formation of a V_5S_8-type monoclinic superstructure for $0.1\leqslant x\leqslant 0.5$, as this is observed in the $V_{1-x}S$ as well.

2. CONCENTRATION DEPENDENCE OF THE MAGNETIC AND ELECTRICAL PROPERTIES

It should be pointed out that the V_5S_8 antiferromagnet ($T_N=30$ K) exhibits metallic conduction, which can occur

TABLE I. Unit cell parameters of $Fe_xV_{1-x}S$ compounds.

Composition	Unit cell parameters, Å			
	a	*b*	*c*	β, °
$Fe_{0.1}V_{0.9}S$	11.60	6.61	11.30	90.98
$Fe_{0.2}V_{0.8}S$	11.56	6.60	11.29	91.0
$Fe_{0.3}V_{0.7}S$	11.72	6.62	11.35	91.7
$Fe_{0.4}V_{0.6}S$	11.80	6.60	11.28	91.85
$Fe_{0.5}V_{0.5}S$	11.71	6.60	11.23	92.02
V_5S_8[6]	11.396	6.645	11.293	91.45

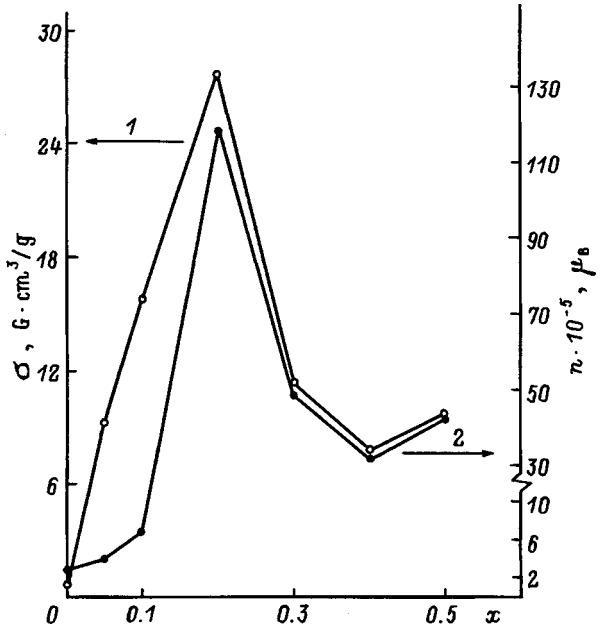

FIG. 1. Concentration dependence of the magnetization σ (curve *1*) and of the average magnetic moment n (curve *2*) per formula unit for the $Fe_xV_{1-x}S$ compounds ($0<x\leqslant 0.5$) measured at 300 K.

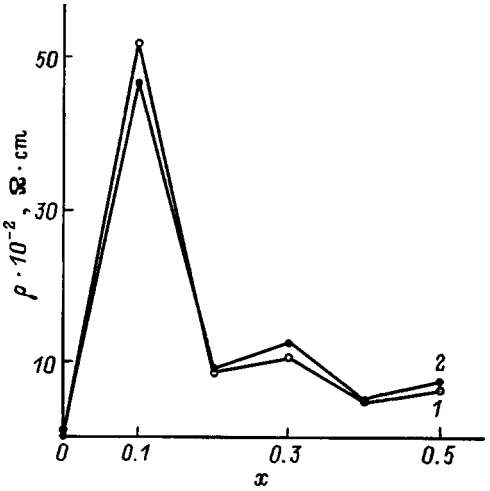

FIG. 2. Concentration dependence of the electrical resistivity $\rho(x)$ of $Fe_xV_{1-x}S$ samples ($0<x\leqslant 0.5$) measured at 300 K (curve *1*) and 80 K (curve *2*).

with vanadium atoms of two types, namely, with localized and delocalized electrons. The magnetic order is here intermediate between an itinerant antiferromagnet and an antiferromagnet with a localized magnetic moment.[6] Besides, the exciton-insulator model allowing formation of CDWs and SDWs was used to consider compounds with interband electron-hole pairing including the vanadium sulfides and selenides VS, V_3X_4, V_5X_8(X=S, Se).[7]

Figure 1 shows a concentration dependence of the magnetization σ of $Fe_xV_{1-x}S$ samples with $0<x\leqslant 0.5$ (curve *1*) obtained at 300 K. The magnetization was measured on a magnetic balance at room temperature in a field of 13.0 kOe. One readily sees an increase in sample magnetization with increasing iron concentration up to 27.85 $G\cdot cm^3/g$ for $x=0.2$. Subsequent increase of iron concentration in the system for $x>0.2$ results in a decrease of the magnetization to 7.77 $G\cdot cm^3/g$ for $x=0.4$, to be followed by an increase of σ to 9.91 $G\cdot cm^3/g$ for $x=0.5$.

Curve *2* in Fig. 1 plots the concentration dependence of the average magnetic moment in units of μ_B (μ_B is the Bohr magneton) calculated for the formula unit of $Fe_xV_{1-x}S$. A comparison of curves *1* and *2* in Fig. 1 leads to the same conclusion for compounds with $x>0.1$. Besides, assuming the magnetic state of the $Fe_xV_{1-x}S$ samples to be connected only with iron atoms, one has to analyze the concentration dependence of the magnetic moment M per Fe atom in units of μ_B. Reduction of σ (in units of $G\cdot cm^3/g$) to M (in units of μ_B) showed that the maximum magnetic moment of 2.06 μ_B is observed in this case for the $x=0.2$ composition, with its subsequent decrease to 0.3 μ_B with x increasing to 0.5.

Figure 2 shows the concentration dependence of the electrical resistivity $\rho(x)$ of $Fe_xV_{1-x}S$ samples with $0<x\leqslant 0.5$ measured at room temperature (curve *1*) and liquid nitrogen temperature (curve *2*). The resistivity measurements were made by the four-probe dc potentiometric method within the 80–300 K interval on parallelepiped-shaped samples annealed at 1000 K in evacuated quartz ampoules. The resistivity is seen to increase steeply at $x=0.1$, followed by a decrease with x increasing to 0.5. At $x=0.1$, the value of $\rho_{300\,K}$ is $50\times10^{-2}\ \Omega\cdot cm$, and for $x=0.5$ it is $5\times10^{-2}\ \Omega\cdot cm$, so that the resistivity decreases by an order of magnitude with increasing iron concentration compared to its value at $x=0.1$.

3. ANALYSIS OF THE ELECTRONIC STRUCTURE OF THE $Fe_xV_{1-x}S$ SYSTEM

The analysis starts with the high-temperature hexagonal α phase of VS, which can be successively distorted to obtain both the β VS and V_5S_8 structures. The diagram of one-electron levels of the $V^{2+}(3d^3)$ ion in the hexagonal phase is shown in Fig. 3. The a_1 orbitals are directed along the C axis, and the e_g orbitals lie primarily in the hexagonal plane, where they overlap to a considerable extent with the p orbit-

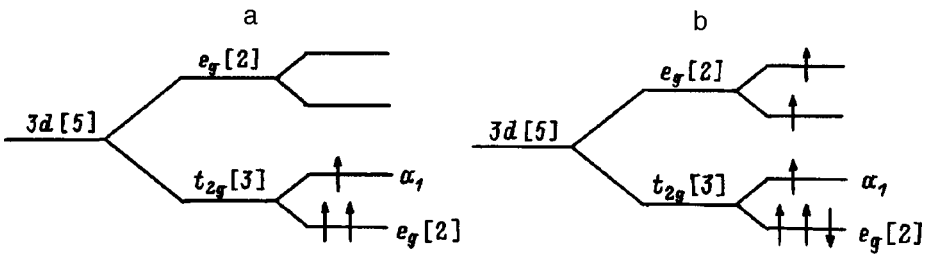

FIG. 3. Diagram of d levels in a crystal field of uniaxially distorted cubic symmetry. The arrows identify the filling of levels for (a) $V^{2+}(d^3)$ and (b) $Fe^{2+}(d^6)$.

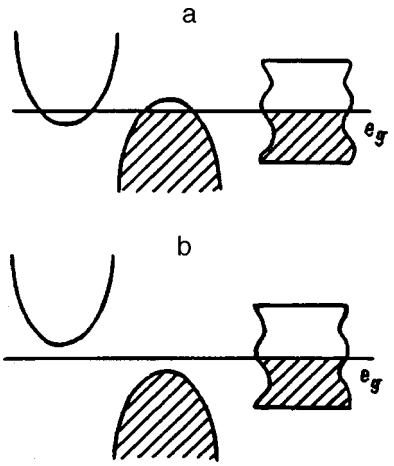

FIG. 4. Electronic structure of VS in (a) hexagonal α phase and (b) orthorhombic β phase.

als of sulfur to form a partially filled e_g band.[8] The overlap along the C axis creates the quasi-one-dimensional a_1 band possessing a nesting property, and it is this that accounts for the electronic transformations observed to occur with decreasing temperature or deviation from stoichiometry. This pattern is supported by Fermi surface calculations[9] which revealed two nearly congruent pieces, an electronic one at the Γ point and a hole one at zone edge (the M point) with a nesting vector $\mathbf{Q}\approx\mathbf{G}/2$, where $\mathbf{G}$ is the reciprocal lattice vector. The e_g band plays the part of an electron reservoir and accounts for conduction in the exciton-insulator phase (Fig. 4).[2]

Because the structure existing for $0.1<x<0.5$ in the $Fe_xV_{1-x}S$ system was found to be close to V_5S_8, consider the electronic structure of the latter in terms of the three-band model of Fig. 4. All nonstoichiometric $V_{1-x}S$ structures form α VS through ordering of successive cation-vacancy layers, including V_5S_8, which has a superstructure with $A=2a$, $B=2b$, and $C=2c$. The cation vacancies affect most strongly the specific a_1 band by breaking the quasi-one-dimensional chains and, to a lesser extent, the electron reservoir, i.e., the e_g band, because of the featureless character of its dispersion. NMR data suggest two types of electronic states for V_5S_8, localized and itinerant.[6]

Considered from a structural viewpoint, the $Fe_xV_{1-x}S$ system has a common feature with $V_{1-x}S$ in that the former has impurity Fe atoms, and the latter, V vacancies. Our data on the structural similarity between these two systems permit a conjecture that Fe atoms order on successive cation planes as the vanadium vacancies do. In electronic structure, however, it should not be close to V_5S_8, because in place of the vacancies it has the a^6 states of Fe^{2+} (Fig. 3b). The partially filled a_1 and e_g orbitals of iron combine with the other orbitals of V and S to form a band structure close to α VS (at high temperatures, in the praphase). The partially filled e_g doublet of the Fe^{2+} ion creates a localized magnetic moment with spin $S=1$. For small x, where impurity Fe atoms may be considered independent, this moment $\mu_{Fe}=2\mu_B$. A paramagnetic metal with local magnetic impurities could be a suitable model to describe the electronic and magnetic systems. As x increases, however, interaction among the impurities (both RKKY type and superexchange mediated by nonmagnetic cations) will result in their magnetic ordering. Besides, an increase of x entails also increasing overlap of the Fe e_g wave functions, which will give rise to delocalization and reduce the magnetic moment. The increase in magnetization per cell observed by us to occur for small x with a peak at $x=0.2$ corresponding to $\mu_{Fe}\approx2\mu_B$ can be assigned apparently to the regime of local magnetic impurities. The decrease of magnetization for $x>0.2$ can be associated with delocalization of the iron e_g doublet. This pattern of the concentration dependence of the magnetic properties correlates also qualitatively with the data on electrical conductivity (Fig. 2), which show the strongest localization of electrons to occur at $x=0.1$.

To conclude, our combined structural, magnetic, and electrical measurements have revealed the $Fe_xV_{1-x}S$ solid-solution system with $0<x<0.5$ to be structurally close to the V_5S_8 superstructure. The concentration dependences of magnetization and resistivity exhibit sharp maxima at $x\sim0.1$. The three-band exciton-insulator model provides a qualitative explanation for the structural features and electronic properties.

[1] A. A. Bugaev, B. P. Zakharchenya, and F. A. Chudnovskiĭ, *The Metal-Insulator Transition and its Applications* [in Russian], Nauka, Leningrad (1979), 183 pp.
[2] G. V. Loseva, G. M. Abramova, and S. G. Ovchinnikov, Fiz. Tverd. Tela (Leningrad) **25**, 3165 (1983) [Sov. Phys. Solid State **25**, 1824 (1983)]; G. V. Loseva, G. M. Mukoed, and S. G. Ovchinnikov, IFSO Preprint (Krasnoyarsk, 1987).
[3] G. V. Loseva, L. I. Ryabinkina, S. S. Aplesnin, A. D. Balaev, A. M. Vorotynov, A. F. Bovina, and K. I. Yanushkevich, Fiz. Tverd. Tela (St. Petersburg) **39**, 1428 (1997) [Phys. Solid State **39**, 1267 (1997)].
[4] Yu. V. Kopaev, Trudy FIAN **86**, 3 (1975).
[5] I. Kawada, M. Nakano-Onoda, M. Ishii, M. Saeki, and M. Nakahira, J. Solid State Chem. **15**, 246 (1975).
[6] A. B. de Vries and C. Haas, J. Phys. Chem. Solids **34**, 651 (1973).
[7] N. I. Kulikov and V. V. Tugushev, Usp. Fiz. Nauk **144**, 643 (1984) [Sov. Phys. Usp. **27**, 954 (1984)].
[8] G. V. Loseva, S. G. Ovchinnikov, and G. A. Petrakovskiĭ, *The Metal-Insulator Transition in 3d-Metal Sulfides* [in Russian], (Nauka, Novosibirsk, (1983), 144 pp.
[9] S. H. Liu, W. B. England, and H. W. Myron, Solid State Commun. **14**, 1003 (1977).

Translated by G. Skrebtsov

Magnetic anisotropy of a system of nanocrystalline $BaO \cdot 6Fe_2O_3$ particles

Z. V. Golubenko, L. P. Ol'khovik, Yu. A. Popkov, Z. I. Sizova

Khar'kov State University, Khar'kov, Ukraine

A. S. Kamzin

A. F. Ioffe Physicotechnical Institute, Russian Academy of Sciences, 194021 St. Petersburg, Russia
(Submitted February 13, 1998; resubmitted April 7, 1998)
Fiz. Tverd. Tela (St. Petersburg) **40**, 1894–1897 (October 1998)

The anisotropy of a system of barium ferrite particles with an average diameter of 60 nm has been studied. The effective anisotropy constant has been determined in the temperature range from 4.2 K to T_c by the law governing approach to saturation magnetization. The observed deviation from the magnetocrystalline anisotropy constant is explained as due to a negative contribution of the ''surface'' anisotropy constant. An estimate is made of this contribution as a function of particle size. © *1998 American Institute of Physics.* [S1063-7834(98)02610-0]

The hexagonal barium ferrite $BaO \cdot 6Fe_2O_3$ has a collinear five-sublattice magnetic structure and uniaxial magnetocrystalline anisotropy with an easy-magnetization axis parallel to the hexagonal axis c.

The magnetocrystalline anisotropy energy of a uniaxial crystal can be written

$$E_a = K_1 \sin^2 \theta + K_2 \sin^4 \theta + \ldots, \tag{1}$$

where K_1 and K_2 are the anisotropy constants, and θ is the angle between the magnetic moment and the easy axis. The K_1 constant of barium ferrite is positive and substantially larger than K_2.

Besides magnetocrystalline, two other types of magnetic anisotropy can play a significant part in single-domain particles, namely, the ''surface'' and shape anisotropies.

For the shape-anisotropy energy per unit volume one can write

$$E_a^{sh} = K_{sh}, \tag{2}$$

where the shape-anisotropy constant K_{sh} for a uniaxial crystal is $NI_{\text{sat}}^2/2$ (here I_{sat} is the saturation magnetization, and N is the demagnetizing factor equal to the difference between those along the axis, $N_\parallel$, and perpendicular to it, $N_\perp$). For a hexagonal platelet of barium hexaferrite approximated by an oblate ellipsoid with the minor axis coinciding with the hexagonal axis c

$$N(R) = N_\parallel - N_\perp = 2\pi \left\{ \left[\frac{3R^2}{R^2-1} \right] \left[1 - \frac{1}{\sqrt{R^2-1}} \times \arccos\left(\frac{1}{R} \right) \right] - 1 \right\}, \tag{3}$$

where $R = d/h$, d is the diameter of the particle, and h is its thickness.[1]

The surface anisotropy originates from the presence of a structurally defective open surface, whose effect is the stronger the smaller is the particle. By the surface anisotropy one understands the magnetic anisotropy of a near-surface zone of finite thickness.[2] It can be characterized by a constant K_{surf}.

The effective anisotropy constant can be written as a sum of the above three contributions

$$K_{\text{ef}} = K_1 - K_{sh} + K_{\text{surf}} \frac{V_{\text{surf}}}{V}, \tag{4}$$

where V is the particle volume, and V_{surf} is the volume of the near-surface layer.

The constants of magnetocrystalline and shape anisotropy for the particles under study have opposite signs, the sign of the surface-anisotropy constant and the magnitude of the corresponding contribution can be established only from an experimental study of the effective anisotropy.

This work reports an investigation of the magnetic anisotropy of a system of nanocrystalline barium ferrite particles with unsubstituted magnetic matrix.

The powder to be studied was prepared by a nontraditional cryochemical technology.[3]

The starting ferrite-forming components were the water-soluble compatible salts $Fe(NO_3)_3 \cdot 9H_2O$ and $Ba(NO_3)_2$. A complex-forming Cit-ion was used to stabilize the chemical homogeneity of the nitrate system. The sublimed ferrite-forming mixture was subjected to thermal treatment at a temperature ($T \leqslant 800$ °C) which is relatively low for the barium ferrite but was found high enough to achieve practically complete ferritization. The single-domain platelet-shaped particles thus obtained ranged in size from 20 to 160 nm (Fig. 1). Mössbauer studies performed at 300 K did not reveal any impurity phases as well as any paramagnetic fraction.

The effective magnetic-anisotropy constant was determined from the law governing approach to saturation magnetization in the form[4]

$$I(H) = I_{\text{sat}}(1 - A/H - B/H^2 - \ldots). \tag{5}$$

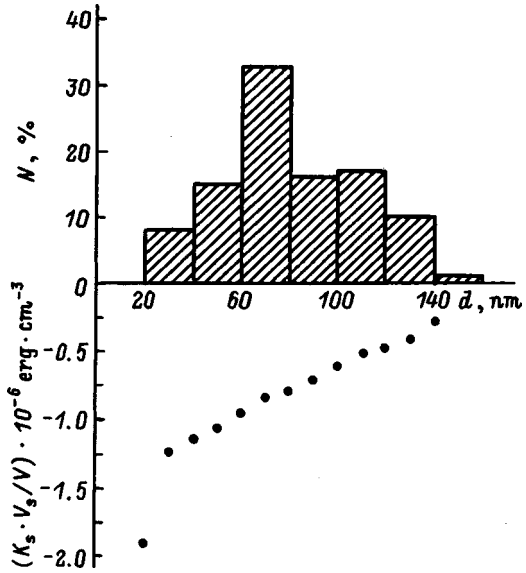

FIG. 1. Dependence of the surface-anisotropy contribution to the effective constant on particle size at 300 K.

The A/H term accounts for the inhomogeneities which can interfere with magnetization processes. This study did not deal with this aspect.

Coefficient B in expansion (5) is associated with magnetic anisotropy. For a uniaxial hexagonal crystal[5]

$$B=\frac{4}{15}\frac{K_{\rm ef}^2}{I_{\rm sat}}. \tag{6}$$

Figure 2 displays magnetization curves $\sigma(H)$ for several temperatures measured in a thermally demagnetized, close-packed powder sample, and the corresponding relations $\Delta\sigma \cdot H^2=f(H)$ [$\Delta\sigma=\sigma_{\rm sat}-\sigma(H)$, and σ is the specific magnetization]. The rectilinear portion ab of the $\Delta\sigma\cdot H^2=f(H)$ relation adjoining saturation extrapolates to the vertical axis to give an intercept of $B\cdot\sigma_{\rm sat}$. Note the pattern of the magnetization curve, which is not characteristic of a macroobject (a polycrystal or powder consisting of larger particles) and manifests itself particularly clearly in the $\Delta\sigma\cdot H^2=f(H)$ relations. The linear portion ab adjoining saturation is preceded by a region with a distinct maximum, which flattens out with increasing temperature to vanish at 694 K. The observed feature is apparently associated with the specific magnetization processes occurring in a system of ultrafine particles.

Figure 3 compares the temperature dependence of the effective anisotropy constant of the powder under study with the $K_1(T)$ relation[6] for a polycrystal. Within the interval from 4.2 K to T_c, $K_{\rm ef}$ is seen to be smaller than K_1. Estimates showed that the shape-anisotropy contribution alone, which is considered to be dominant, for instance, in Ref. 7, cannot account for the difference observed in our case. Indeed, at 300 K even for particles with the maximum values $d/h=4$, $K_{sh}=-0.3\times10^6$ erg·cm^{-3}, which is only 10% of K_1. One can thus conclude that surface anisotropy provides a negative contribution to $K_{\rm ef}$.

It was shown[8] that the deviation from stoichiometry ($n\neq6$) at the open surface of the basal plane of $BaO\cdot6Fe_2O_3$

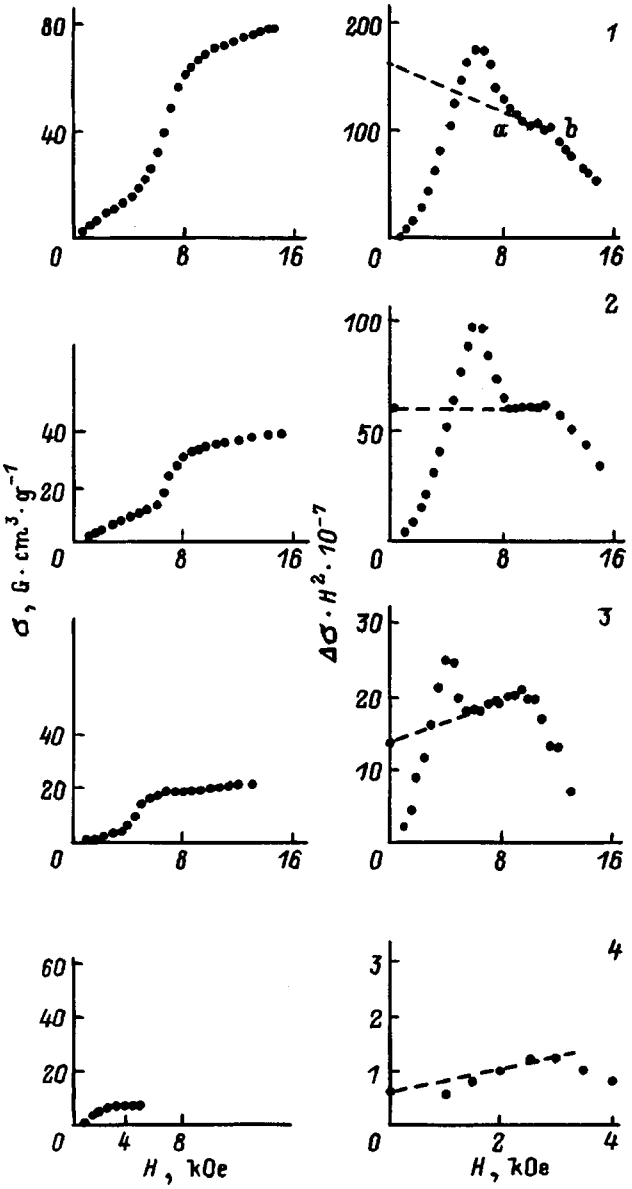

FIG. 2. Magnetization curves of nanocrystalline powder (experimental and derived from the law governing approach to saturation). T(K): *1*—4.2, *2*—474, *3*—620, *4*—694.

microcrystals is less than 20%, and that the associated structure defects propagate in decreasing numbers into the neighboring layers. The formation of a vacancy structure in the near-surface region gives rise to a local rearrangement of ions surrounding the Fe^{3+} ions and, hence, to a lowering of symmetry of the crystallographic sites they occupy. Accordingly, the single-ion contributions of Fe^{3+} ions to magnetic anisotropy should change.

As already pointed out, the magnitude of the effect increases with decreasing particle size. Because in our powder, like in any real system, there is a distribution of particles in size, an estimate of the integrated contribution due to surface anisotropy (17% of $K_{\rm ef}$ at 300 K) does in no way reflect its true significance. In connection with this, we calculated the dependence of the surface-anisotropy contribution to $K_{\rm ef}$ on particle distribution in size. The field dependence of remanence was used to derive the particle distribution in effective

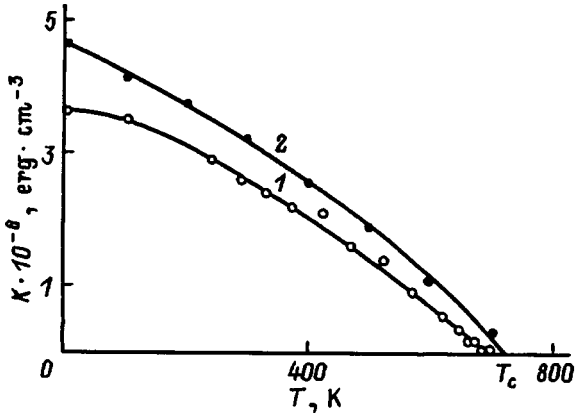

FIG. 3. Temperature dependence of the anisotropy constants of barium ferrite. *1*—$K_{ef}(T)$, the nanocrystalline system under study; *2*—$K_1(T)$, polycrystal.[6]

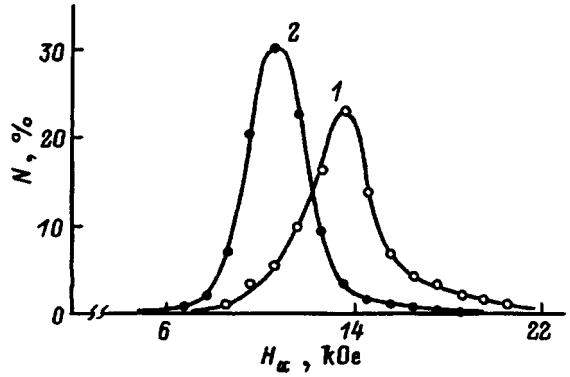

FIG. 4. Particle distribution of the nanocrystalline system in anisotropy fields. T(K): *1*—300, *2*—600.

magnetic-anisotropy fields, H_a^{ef}, by the method developed in Ref. 9 (Fig. 4). The upper limit of the H_a^{ef} distribution relates to the largest particles, for which the negative relative contributions of the shape and surface anisotropy are the smallest. The lower limit corresponds to the smallest particles ($d \sim 20$ nm), which feel most strongly a structurally perturbed surface layer. The upper limit of the H_a^{ef} distribution is overevaluated compared to the magnetocrystalline anisotropy field[6] by 20% for 300 K, and by 10% for 600 K. The possibility of such a discrepancy was admitted in Ref. 10, which pointed out that calculation of a distribution in anisotropy fields by differentiating the field dependence of remanence yields only a first approximation. A comparison of the particle distributions in anisotropy fields and size permitted one to calculate K_{sh} as a function of particle size and, using Eq. (4), to obtain the dependence of the surface-anisotropy contribution to K_{ef} on particle size (Fig. 1). As seen from the figure, the contribution of surface anisotropy for particles with $d \sim 20$ nm at 300 K is about 60% of the magnetocrystalline anisotropy. This contribution decays slowly within the 40–160-nm interval by practically an order of magnitude.

Because the thickness of the smallest particles in the system ($d \approx 20$ nm) may be as small as a few (down to two) lattice parameters c, one may safely assume that the distortion of the crystal lattice and perturbation of the magnetic structure extend throughout the particle volume. In this case $V_{surf}/V \sim 1$, and the surface-anisotropy contribution (-1.9×10^6 erg·cm^{-3}) is comparable to the K_{surf} constant. For the largest particles ($d \approx 160$ nm) the volume of the near-surface region is small compared to particle volume ($V_{surf}/V \ll 1$) and, hence, the contribution of surface anisotropy to K_{ef} tends to zero. For 600 K, $K_{surf} = -0.6 \times 10^6$ erg·cm^{-3}, which means that within the 300–600 K range K_{surf}, similar to K_1, decreases by a factor three. This suggests that the surface and magnetocrystalline anisotropies have the same nature, and that the variation of the surface-anisotropy contribution $K_{surf}V_{surf}/V$ to K_{ef} with particle size is determined only by the variation of the fraction of the volume occupied by the near-surface region.

To conclude, it has been established that surface anisotropy in the nanocrystalline barium-ferrite particle system under study provides a negative contribution to the effective constant relative to the magnetocrystalline anisotropy, which correlates with the existence[10] of a canted magnetic structure in the near-surface layer. It has been shown that in a highly anisotropic ferrite material the surface anisotropy is comparable to the magnetocrystalline one only in the nanometer-size range.

One of the authors, A.S.K., thanks the Russian Fund for Fundamental Research for support under Grant No. 98-02-18279.

[1] A. H. Morrish, *The Physical Properties of Magnetism* (Wiley, New York, 1965).
[2] J. M. D. Coey, Phys. Rev. Lett. **27**, 1140 (1971).
[3] L. P. Ol'khovik, N. M. Borisova, T. G. Kuz'micheva, and V. P. Shabanin, Funct. Mater. **3**, 84 (1996).
[4] S. Tikazumi, *The Physics of Ferromagnetism: Magnetic Characteristics and Applications* [Transl. into Russian from Japanese], Mir, Moscow (1987), 420 pp.
[5] R. Grössinger, Phys. Status Solidi A **66**, 665 (1981).
[6] J. Smith and H. P. G. Wijn, *Ferrites* [Wiley, New York, 1959; IL, Moscow, 1987, 504 pp.].
[7] H. Pfeiffer and W. Schüppel, Phys. Status Solidi A **119**, 259 (1990).
[8] A. S. Kamzin, V. L. Rozenbaum, L. P. Ol'khovik, and E. D. Kovtun, J. Magn. Magn. Mater. **161**, 139 (1996).
[9] E. Kneller, in *Handbuch der Physik*, Bd. XVIII/2, edited by S. Flügge and H. Wijn (Springer-Verlag, Berlin/Heidelberg/New York, 1996).
[10] K. Haneda and A. H. Morrish, IEEE Trans. Magn. **25**, 2597 (1989).

Translated by G. Skrebtsov

Longitudinal complex magnetic susceptibility of superparamagnetic particles with cubic anisotropy

Yu. P. Kalmykov and S. V. Titov

Institute of Radio Engineering and Electronics, Russian Academy of Sciences, 141120 Fryazino, Moscow Region, Russia

(Submitted April 14, 1998)
Fiz. Tverd. Tela (St. Petersburg) **40**, 1898–1899 (October 1998)

The dynamic susceptibility spectrum of single-domain particles with cubic anisotropy has been calculated within the continuous diffusion model throughout the total range of anisotropy- and damping-parameter variation. © *1998 American Institute of Physics.*
[S1063-7834(98)02710-5]

Studies of thermal fluctuations and relaxation of magnetization in single-domain particles are presently attracting considerable attention in connection with attempts to improve the characteristics of magnetic carriers.[1] To simplify mathematic calculations, theoretical consideration of the relaxation processes deals usually with uniaxial, uniformly magnetized particles.[2–5] Although using a uniaxial-anisotropy potential simplifies considerably the analysis, the results obtained with this approach have only limited applicability.[6] For other types of anisotropy, such as cubic, one uses either the discrete orientation approximation or asymptotic solutions for the diffusion model.[6–9] Both these approaches are, however, inapplicable to the most interesting case when the anisotropy energy is comparable to the thermal energy kT.

In the diffusion model, the dynamics of the magnetization vector $\mathbf{M}(t)$ of a single-domain particle are similar to the Brownian rotation of a macromolecule in a liquid and are described by Gilbert's equation[9] with fluctuating field. For a cubic-anisotropy potential of the type[7,9]

$$\frac{U}{kT}=\sigma(\sin^4\vartheta\,\sin^2 2\varphi+\sin^2 2\vartheta), \tag{1}$$

where σ is a dimensionless anisotropy constant, and ϑ and φ are the polar and azimuthal angles, respectively, the Gilbert stochastic vector equation can be formally solved similar to the way this is done[5,10] for uniaxial particles. This approach reduces the problem to solving an infinite system of coupled equations for equilibrium correlation functions $c_{n,m}(t)=\langle\cos\vartheta(0)Y_{n,m}(t)\rangle_0$:

$$\tau_N\frac{d}{dt}c_{n,m}(t)=\sum_{s=-1}^{1}\sum_{r=-4}^{4}d_{nmrs}c_{n+r,m+4s}(t), \tag{2}$$

where τ_N is the characteristic thermal-fluctuation time,[11] $Y_{n,m}$ are spherical harmonics,[12] and the angular brackets $\langle\rangle_0$ denote the equilibrium mean (the coefficients d_{nmrs} depend on the anisotropy parameter σ and damping parameter α and can be found in Ref. 11). Unfortunately, the methods usually employed to solve coupled equations (2) in the weak-damping case ($\alpha<0.1$) characteristic of single-domain particles[6] are hardly applicable here, because one would have to deal in the calculations with of the order of 10^4 equations or even more. For this reason no calculation and analysis of the dynamic susceptibility spectrum for the case of cubic anisotropy has been carried out within the diffusion model up to now. The problem allows, however, considerable simplification if one uses matrix-continuous fractions.[10,13]

Equation (2) can be reduced by Laplace transform to a matrix recurrence equation

$$\mathbf{Q}_n^-\tilde{\mathbf{C}}_{n-1}(s)+[\mathbf{Q}_n-\mathbf{I}s\tau_N]\tilde{\mathbf{C}}_n(s)+\mathbf{Q}_n^+\tilde{\mathbf{C}}_{n+1}(s)+\tau_N\mathbf{C}_n(0)=\mathbf{0},\quad n=1,2,3..., \tag{3}$$

where $\mathbf{I}$ is the identity matrix, the tilde denotes the Laplace transform, and

$$\tilde{\mathbf{C}}_n(s)=\begin{pmatrix}\tilde{\mathbf{c}}_{4n}(s)\\ \tilde{\mathbf{c}}_{4n-1}(s)\\ \tilde{\mathbf{c}}_{4n-2}(s)\\ \tilde{\mathbf{c}}_{4n-3}(s)\end{pmatrix},$$

$$\tilde{\mathbf{c}}_{4n-i}(s)=\begin{pmatrix}\tilde{\mathbf{c}}_{4n-i,-4(n-1+\delta_{i0})}(s)\\ \tilde{\mathbf{c}}_{4n-1i,-4(n-2+\delta_{i0})}(s)\\ \vdots\\ \tilde{\mathbf{c}}_{4n-i,4(n-1+\delta_{i0})}(s)\end{pmatrix},\quad i=0,1,2,3.$$

Vector $\tilde{\mathbf{C}}_n(s)$ contains $8n-2$ elements, and $\tilde{\mathbf{C}}_0(s)=0$. The dimensions of the $\mathbf{Q}_n$, $\mathbf{Q}_n^+$, and $\mathbf{Q}_n^-$ matrices are, respectively, $(8n-2)\times(8n-2)$, $(8n-2)\times(8n+6)$, and $(8n-2)\times(8n-10)$. An exception is $\mathbf{Q}_1^-$, which degenerates into a six-dimensional vector. Each of the $\mathbf{Q}_n$, $\mathbf{Q}_n^+$, and $\mathbf{Q}_n^-$ matrices consists, in its turn, of 16 submatrices, part of which has a tridiagonal form, and some of $\mathbf{Q}_n^+$ and $\mathbf{Q}_n^-$ are null submatrices.

Using the general method[13] for solving matrix recurrence equations of type (3), we obtain an exact solution for $\tilde{\mathbf{C}}_1(s)$:

$$\tilde{\mathbf{C}}_1(s)=\tau_N[\tau_N s\mathbf{I}-\mathbf{Q}_1-\mathbf{Q}_1^+\mathbf{S}_2(s)]^{-1}\left\{\mathbf{C}_1(0)+\sum_{n=2}^{\infty}\left[\prod_{k=2}^{n}\mathbf{Q}_{k-1}^+\mathbf{S}_k(s)(\mathbf{Q}_k^-)^{-1}\right]\mathbf{C}_n(0)\right\}, \tag{4}$$

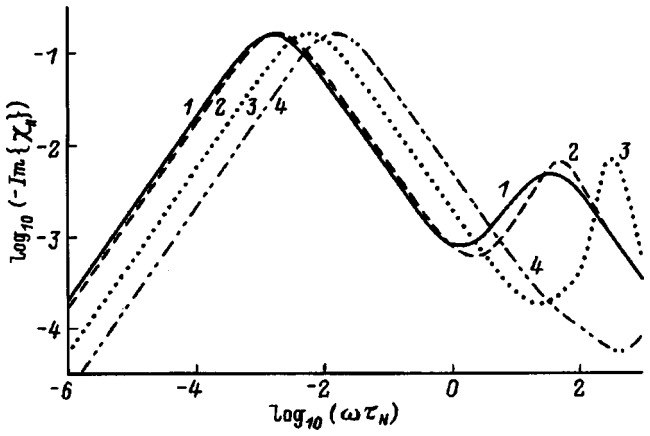

FIG. 1. $\log_{10}(\chi_\parallel'')$ plotted *vs* $\log_{10}(\omega\tau_N)$ for $\sigma=10$ and various values of the damping parameter α: (*1*) $\alpha\to\infty$, (*2*) 1, (*3*) 0.1, and (*4*) 0.01.

where the matrix-continuous fraction $\mathbf{S}_n(s)$ is defined by

$$\mathbf{S}_n(s)=[s\tau_N\mathbf{I}-\mathbf{Q}_n+\mathbf{Q}_n^+\mathbf{S}_{n+1}(s)]^{-1}\mathbf{Q}_n^-\ ,$$

[$\mathbf{C}_n(0)$ in Eq. (4) can also be expressed[12] through $\mathbf{S}_n(0)$].

Figures 1 and 2 display spectra of the imaginary part $\chi_\parallel''(\omega)$ of the complex susceptibility

$$\chi_\parallel(\omega)=\chi_\parallel'(\omega)-i\chi_\parallel''(\omega)=\chi_\parallel\{1-i\omega\tilde{c}_{1,0}(i\omega)/c_{1,0}(0)\},\tag{5}$$

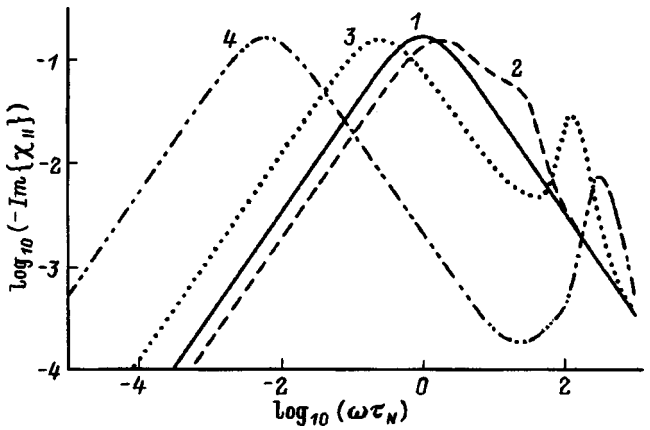

FIG. 2. $\log_{10}(\chi_\parallel'')$ plotted *vs* $\log_{10}(\omega\tau_N)$ for $\alpha=0.1$ and various values of the anisotropy parameter σ: (*1*) 0, (*2*) 1, (*3*) 5, and (*4*) 10.

($\chi_\parallel$ is the static susceptibility) calculated from Eqs. (4) and (5) for various values of parameters σ and α. Two peaks are seen in the loss spectrum. The first, low-frequency peak appears at frequencies of the order of the mean reorientation frequency of the particle magnetization vector $\mathbf{M}$.[9] The position of the maximum and the halfwidth of this low-frequency band are dominated by the lowest-frequency relaxation mode, which is characterized by the smallest eigenvalue λ_1 of the Focker-Planck equation for the density of probability of the distribution $W(\{\mathbf{M}\},t)$ of magnetization $\mathbf{M}$.[9] Taken in the low-temperature limit ($|\sigma|\gg1$), our calculations are in full agreement with asymptotic estimates of λ_1 for both strong[7,9] ($\alpha\geqslant1$) and weak[6] ($\alpha\leqslant0.01$) damping. The second, substantially weaker peak is due to the contribution of transverse and longitudinal high-frequency intrawell modes. In contrast to uniaxial particles, however, in the case of cubic anisotropy $\chi_\parallel(\omega)$ depends strongly on α due to the coupling between the longitudinal and transverse modes.

These results will be discussed in more detail in a separate publication.

Support of the Russian Fund for Fundamental Research (Grant 96-02-16762-a) is gratefully acknowledged.

[1] H.-B. Braun and H. N. Bertran, J. Appl. Phys. **75**, 4609 (1994).
[2] Yu. L. Raĭkher and M. I. Shliomis, Zh. Éksp. Teor. Fiz. **67**, 1060 (1974) [Sov. Phys. JETP **40**, 526 (1974)].
[3] D. A. Garanin, V. V. Ishchenko, and L. V. Panina, Teor. Mat. Fiz. **82**, 242 (1990) [Theor. Math. Phys. **82**, 169 (1990)].
[4] É. K. Sadykov and A. G. Isavnin, Fiz. Tverd. Tela (St. Petersburg) **38**, 2104 (1996) [Phys. Solid State **38**, 1160 (1996)].
[5] Yu. P. Kalmykov and W. T. Coffey, Phys. Rev. B **56**, 3325 (1997).
[6] I. Klik and L. G''unther, J. Stat. Phys. **60**, 473 (1990).
[7] D. A. Smith and F. A. de Rosario, J. Magn. Magn. Mater. **3**, 219 (1976).
[8] I. Eisenstein and A. Aharoni, Phys. Rev. B **16**, 1278 (1977).
[9] W. F. Brown, Jr., IEEE Trans. Magn. **15**, 1196 (1979).
[10] Yu. P. Kalmykov and S. V. Titov, Fiz. Tverd. Tela (St. Petersburg) **40**, 1642 (1998) [Phys. Solid State **40**, 1492 (1998)].
[11] L. J. Geoghegan, W. T. Coffey, and B. Mulligan, Adv. Chem. Phys. **100**, 475 (1997).
[12] D. A. Varshalovich, A. N. Moskalev, and V. K. Khersonskiĭ, *Quantum Theory of Angular Momentum* [World Scientific, Singapore, 1988; Nauka, Leningrad (1975)].
[13] W. T. Coffey, Yu. P. Kalmykov, and J. T. Waldron, *The Langevin Equation* (World Scientific, Singapore, 1996)

Translated by G. Skrebtsov

Natural ferromagnetic resonance in the disordered alloy Pd_2AuFe

D. N. Kourov and N. I. Kourov

Institute of Metal Physics,[a] *Ural Branch of the Russian Academy of Sciences, 620219 Ekaterinburg, Russia*

L. N. Tyulenev

Ural State Technical University, 620002 Ekaterinburg, Russia

(Submitted December 22, 1997; resubmitted April 20, 1998)
Fiz. Tverd. Tela (St. Petersburg) **40**, 1900–1904 (October 1998)

A contribution to electromagnetic power losses, additional to the losses due to eddy currents and exhibiting a resonance frequency dependence with the main maximum near 1 GHz, has been observed for the ferromagnetic alloy Pd_2AuFe in the frequency range 0.9 MHz–10 GHz in the absence of an external constant magnetic field. Investigations performed in a dc magnetic field show that this effect is a natural ferromagnetic resonance due to intradomain magnetization precession in the effective magnetic-anisotropy field.
[S1063-7834(98)02810-X]

1. Ferromagnetic resonance (FMR) is ordinarily investigated at a fixed frequency ν of the electromagnetic field, by varying the magnitude of the external dc magnetic field H_{dc}.[1,2] Together with induced FMR of this kind, a so-called natural ferromagnetic resonance (NFR) is also distinguished. The latter is observed for $H_{dc}=0$ in the form of a resonance frequency dependence of electromagnetic power absorption as ν tends to the frequency of uniform precession of the magnetization of the ferromagnet in an external effective magnetic-anisotropy field H_a.[3,4]

NFR was first studied, as a phenomenon due to magnetic anisotropy, by Landau and Lifshitz in 1935 for plastically deformed nickel.[5] It has now been investigated in detail experimentally in ferromagnets with a low current-carrier density — ferrites (see, for example, Refs. 3, 4, and 6), where this effect is ordinarily observed in the microwave range 100 MHz–100 GHz[3,4] in the form of the frequency dispersion of the complex magnetic susceptibility $\mu' - i \cdot \mu''$.

At the same time, according to the best known reviews and monographs (see, for example, Refs. 1–3 and 6–9), where questions concerning ferromagnetic resonance are considered, NFR has still not been observed in metallic ferromagnets. Investigations of the frequency dependences of the effective magnetic permeabilities $\mu_R=(\mu'^2+\mu''^2)^{1/2}+\mu''$ and $\mu_L=(\mu'^2+\mu''^2)^{1/2}-\mu''$, performed with $H_{dc}=0$ back in the first half of the 20th century, for the classical ferromagnetic metals — iron and nickel — demonstrate[10] a continuous decrease of these quantities from μ_R, $\mu_L \sim 50-100$ at $\nu \approx 100$ MHz to μ_R, $\mu_L \sim 1-5$ at $\nu \approx 10$ GHz. The resonance features in the frequency dependences of μ_R and μ_L have not been observed[10] either for iron or nickel, though simple estimates of the field H_a[3] which is due to the magnetocrystalline anisotropy show that for these metals the EFR should occur in the frequency range 100 MHz–10 GHz.[1)]

To explain the continuous decrease of the effective magnetic permeabilities observed in the case of iron and nickel with increasing frequency from μ_R, $\mu_L \sim \mu_a$ (μ_a — initial magnetic permeability) to several units, Kittel proposed a model[10] which employs the specific nature of the interaction of metals with an external electromagnetic field (existence of a thin skin layer δ) and explains the experimental results for Fe and Ni quite well. The essential feature of this model is that the processes causing the displacement of domain walls and making the main contribution to μ_a in weak fields become ineffective when the skin layer depth (which decreases with increasing frequency) becomes less than the sizes of the ferromagnetic domains.

Despite the fact that the absence of NFR for iron and nickel has been noted in works in the last 40 to 50 years, this experimental fact has not been convincingly explained either then[6,10] or now. It is possible that the lack of understanding of the reasons for the absence of NFR in the spectra of iron and nickel, together with certain methodological difficulties in measuring the frequency dependences of electromagnetic power absorption in metals in a wide range of microwave frequencies, are the reasons why NFR has not been observed in metallic ferromagnets to date.

2. It is known that the intensity of electromagnetic losses in metals is determined by the real part of the surface impedance R_s.[12] In the present work, to observe NFR the frequency dependence of R_s was investigated in detail for a metallic ferromagnet — the atomically disordered alloy Pd_2AuFe — in two frequency ranges — 0.9–120 MHz and 2.26–9.40 GHz. The measurements were performed in the absence of a constant magnetic field, at room temperature ($T \sim 295$ K), on cylindrical samples with height $h \approx 0.25$ cm and diameter $d \approx 0.275$ cm.

According to x-ray crystallographic analysis, the disordered alloy Pd_2AuFe possesses a fcc structure in which atoms of different kind are randomly distributed over the crystal lattice sites[13] and exhibits a temperature-dependence of the resistivity ρ that is typical for metals.[14] The choice of this particular alloy as the object for investigation was made

for the following reasons: 1) The Curie temperature of the disordered Pd_2AuFe alloy is $T_c = 460$ K and, therefore, at room temperature, the alloy is in a ferromagnetic state; 2) a quite high (for metals) resistivity $\rho = 0.83\ \mu\Omega \cdot$ m is observed at $T \sim 295$ K, ensuring the required measurement accuracy (the measured values are proportional to $\sqrt{\rho}$); and, 3) in contrast to iron and nickel, the disordered alloy Pd_2AuFe is characterized by a quite low initial magnetic permeability ($\mu_a \approx 4.5$). The latter circumstance leads to the expectation that NFR will be masked to a lesser degree (than, possibly, in the case of iron and nickel) by a strong change in the magnetic permeability due to the ''Kittel'' mechanism.[10] Moreover, using the disordered Pd_2AuFe as the experimental ferromagnetic metal makes it possible to exclude quite simply possible effects due to extraneous factors, which are not associated with the magnetic state of this alloy, on the measured value of R_s, such as the state of the surface of the sample (quality of mechanical working, impurity consisting of parasitic phases) and instrumental errors.

It is well known that when the degree of atomic order in the initially disordered alloy Pd_2AuFe changes, the magnetic properties of the alloy also change. Specifically, for low-temperature ($T = 270$ K) annealing times $\tau_{ann} \geqslant 15$ min the sample is no longer magnetically ordered at room temperature.[15] For this reason, in the present work we also investigated the frequency dependences of R_s for three partially ordered alloys with $\tau_{ann} = 15$ min, 30 min, and 5 h, which, on the one hand, have the same surface state as the disordered alloy and, on the other, are paramagnets at room temperature and therefore should not exhibit any features in the high-frequency response that are associated with the deviation of the magnetic permeability from 1.

The method used to prepare the alloys is described in detail in Ref. 16. The initial disordered state of the experimental cylindrical samples was obtained by cold plastic deformation (rolling, drawing). The degree of deformation was inadequate to produce an amorphous state. According to x-ray crystallographic data, the increase in the dislocation density accompanying plastic deformation resulted only in a random redistribution of atoms of different kinds over the sites of the fcc lattice.[13]

To measure R_s in the frequency range 0.9–120 MHz, cylindrical samples with the dimensions indicated above were placed in the coil of an oscillatory circuit and, for measurements in the frequency range 2.26–9.40 GHz, the samples were placed at the antinodes of the magnetic field inside cylindrical resonators excited on TE_{01p} oscillations. In both cases the surface resistance was determined from the change appearing in the width of the transmission band when a copper sample (with the same shape and size as the experimental sample) is replaced by the experimental sample inside the resonator or coil, according to equation[17]

$$R_s = R_s^{Cu} + \frac{G}{2S}(\Delta f = \Delta f_{Cu}), \tag{1}$$

where Δf and Δf_{Cu} are the widths of the transmission bands of the resonator or coil, respectively, with the experimental and copper samples; S is the surface area of the sample; R_s^{Cu} is the surface resistance of copper; and, G is a geometric factor (a formula for G is presented in Ref. 17). In the region where the samples are inserted the amplitude of the ac magnetic field was $H_0 \leqslant 0.5$ Oe.

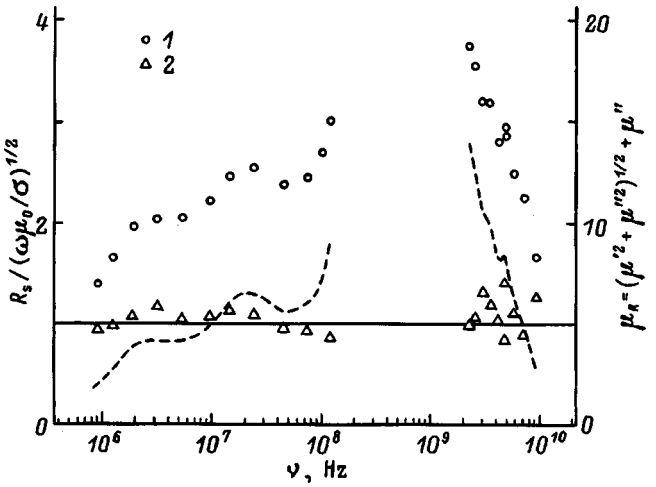

FIG. 1. Frequency dependence of $r = R_s/\sqrt{\omega\mu_0/2\sigma}$ at $T = 295$ K and $H_{dc} = 0$. *1* — Disordered alloy Pd_2AuFe, *2* — alloy Pd_2AuFe annealed for 5 h at $T = 720$ K. The solid line corresponds to $r = 1$. The dashed line shows the frequency dependence of the effective magnetic permeability $\mu_R = (\mu'^2 + \mu''^2)^{1/2} + \mu''$ for the disordered alloy Pd_2AuFe.

3. It is well known[12] that in the most general case the complex surface impedance Z_s of a homogeneous and isotropic conductor is a function of its relative magnetic permeability μ and permittivity ε (here and below all relations are written in the international system of units SI, the complex temporal factor is taken in the form $e^{i\omega t}$)

$$Z_s = R_s + iZ_s = \sqrt{\frac{\mu_0\mu}{\varepsilon_0\varepsilon}}, \tag{2}$$

where μ_0 is the magnetic permeability and ε_0 the permittivity of vacuum. It follows from Eq. (2) that, specifically, the surface impedance of a nonmagnetic ($\mu \cong 1$) conductor under normal skin effect conditions ($\varepsilon = -i\sigma/\omega\varepsilon_0$, where σ is the dc conductivity and $\omega = 2\pi\nu$) is determined by the relation

$$R_s = X_s = \sqrt{\frac{\omega\mu_0}{2\sigma}}. \tag{3}$$

Figure 1 shows for the disordered alloy Pd_2AuFe the frequency dependence of the quantity $r = (R_s/\sqrt{\omega\mu_0/2\sigma})$ — the ratio of the measured surface resistance to the resistance calculated according to Eq. (3) using the static dc resistivity ($\rho = \sigma^{-1}$), i.e., actually the ratio of the total electromagnetic power absorbed in the alloy to the eddy-current losses.

Despite the lack of data in the frequency interval from $\nu \approx 150$ MHz to $\nu \approx 2$ GHz (at present this range is inaccessible to us for measurements), one can see that the disordered alloy Pd_2AuFe in the ferromagnetic state in the frequency range from $\nu \approx 1$ MHz to $\nu \approx 10$ GHz has, besides eddy-current losses, an additional contribution to electromagnetic power absorption that exhibits a resonance frequency dependence. Besides the main maximum at $\nu_0 \approx 1$ GHz the frequency dependence $r(\nu)$ for this alloy contains a less

pronounced additional maximum at $\nu_1 \approx 25$ MHz and nonmonotonic behavior in the form of a ''step'' in the region 1–5 MHz. The effective magnetic permeability μ_R, which is often employed as a parameter characterizing the electromagnetic power absorption in a ferromagnetic metal, is related with r as follows:

$$\mu_R = (\mu'^2 + \mu''^2)^{1/2} + \mu'' = r^2. \tag{4}$$

Therefore the frequency dependence of μ_R retains all the main features of $r(\nu)$ (Fig. 1).

Figure 1 also displays the frequency dependence $r(\nu)$ for the alloy Pd_2AuFe annealed at $T=720$ K for 5 h ($\rho = 2.25\ \mu\Omega\cdot$m). One can see that, within the limits of the experimental error, the relation $r=1$ holds for this alloy at all frequencies investigated, as should be the case for a nonmagnetic ($\mu \cong 1$) conductor under normal skin effect conditions. The relation (3) for R_s also holds in the case of two other partially ordered alloys with $\tau_{ann}=15$ min and 30 min in the experimental frequency range. The absence of features in the frequency dependences $r(\nu)$ for partially ordered alloys Pd_2AuFe shows that the frequency dependence $r(\nu)$ observed for the maximally disordered sample is not due to factors such as experimental error, the quality of the mechanical working, and impurity inclusions in the surface of the sample.

Since the measurements were performed at a temperature below T_c for the disordered alloy Pd_2AuFe, the observed resonance frequency dependence of r (essentially, the electromagnetic power losses) can be attributed to the frequency dispersion of the complex magnetic permeability of this alloy. It is well known from investigations of the magnetic spectra of ferrites (see, for example, Ref. 4) that in the experimental frequency range the resonance dependence of the electromagnetic power absorption in the ferromagnet in the absence of a dc external magnetic field can be due to two factors: 1) oscillations of the walls of ferromagnetic domains and 2) the natural ferromagnetic resonance.

To determine which of these two mechanisms is responsible for the appearance of the resonance in electromagnetic power absorption at $\nu_0 \approx 1$ GHz for the disordered alloy Pd_2AuFe, we performed measurements of R_s of this alloy as a function of the dc magnetic field at five frequencies in the interval 2.26–9.40 GHz (H_{dc} was directed perpendicular to the axis of the cylindrical sample). The results of these measurements are displayed in Figure 2 in the form of the frequency dependences of the ratio $R_s/\sqrt{\omega\mu_0/2\sigma}$ at fixed values of H_{dc}.

As follows from the results presented in Fig. 2, an external magnetic field shifts the resonance, which exists even at $H_{dc}=0$, to higher frequencies. The linear growth of the resonance frequency ν_H in a dc magnetic field with increasing H_{dc} (Fig. 3) agrees well with what should be observed in the case of magnetization precession in a dc magnetic field such that $H_a \ll H_{dc}$,[2] since the effect of the demagnetizing fields for samples of the shape employed is small.[2)] Moreover, the preservation of the resonance peak as $H_{dc} \to H_s$ ($H_s = 3.5$ kOe — saturation field for the disordered alloy Pd_2AuFe at $T=295$ K) rules out a possible origin of the

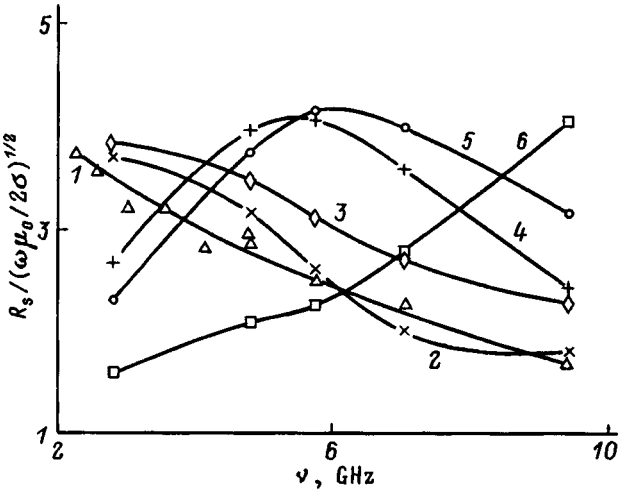

FIG. 2. Frequency dependence of $r = R_s/\sqrt{\omega\mu_0/2\sigma}$ for the disordered alloy Pd_2AuFe at $T=295$ K. $H_{dc}=0$ (*1*), 0.5 (*2*), 1.0 (*3*), 1.5 (*4*), 2.0 (*5*), and 3.5 kOe (*6*).

resonance in absorption ($\nu_0 \approx 1$ GHz) with $H_{dc}=0$ on account of oscillations of the domain walls.

The magnetomechanical ratio γ and, correspondingly, the spectroscopic splitting factor g for the disordered alloy Pd_2AuFe can be determined[2] from the slope of the curve of ν_H versus H_{dc}, presented in Fig. 3: $\gamma = (2.42 \pm 0.33) \times 10^7$ $G^{-1}\cdot s^{-1}$ and $g = 2.75 \pm 0.37$. The anisotropy field can also be estimated as $H_a = 2\pi\nu_0\gamma^{-1} \approx 260$ Oe. Since the experimental samples were polycrystalline, H_a is the value obtained by averaging over directions.

An additional argument in favor of the fact that the oscillations of domain walls cannot lead to the appearance of the main resonance peak ($\nu_0 \approx 1$ GHz) in the dependence $r(\nu)$ with $H_{dc}=0$ are simple estimates of the parameters of the domain structure for the disordered alloy Pd_2AuFe. It is known[3] that the characteristic frequency ν_{DB} of oscillations of domain walls appears in the relation

$$2\pi\nu_{DB}\sqrt{\mu_a} = \alpha\sqrt{\frac{d}{D}}\gamma I_s, \tag{5}$$

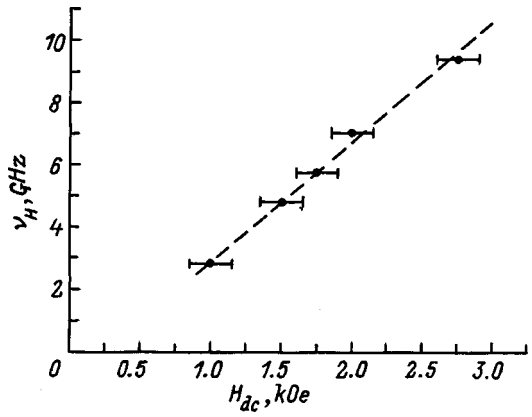

FIG. 3. Resonance frequency ν_H in the absorption of electromagnetic power versus the external dc magnetic field H_{dc} for the disordered alloy Pd_2AuFe at $T=295$ K.

where the dimensionless factor $\alpha \sim 1$; μ_a is the ''quasistatic'' initial (small field amplitudes) magnetic permeability; d is the thickness of the domain wall; D is the characteristic size of a domain; γ is the magnetomechanical ratio; and, I_s is the saturation magnetization. If in Eq. (5) $\nu_0 \approx 1$ GHz is substituted for ν_{DB} and the values presented above for γ, α, and the corresponding parameters for the disordered alloy Pd_2AuFe: $I_s(T=295\ \text{K}) = 345$ G (Ref. 16) and $\mu_a = 4.5$ are substituted, then the ratio $d/D = 2.76$. This is a physically meaningless result, since for $H_a \neq 0$ the thickness of a domain wall cannot exceed the characteristic size of a domain.[3,7] Apparently, oscillations of domain walls lead to the appearance of an additional maximum in the dependence $r(\nu)$ at $\nu_1 \approx 25$ MHz (Fig. 1). Substituting $\nu_1 \approx 25$ MHz for ν_{DB} and substituting the remaining parameters presented above into Eq. (5) gives $d/D = 1.68 \times 10^{-3}$, which is a reasonable value.

The results of measuring the frequency dependences of R_s in a dc magnetic field confirm the magnetic origin of the resonance absorption of electromagnetic power in the disordered alloy Pd_2AuFe with $H_{dc} = 0$ and give grounds for asserting that the observed effect is indeed NFR due to the existence of an internal effective-magnetic-anisotropy field H_a in this ferromagnetic metal.

It should be noted that, when a defective layer with magnetic properties different from the properties in the interior is present on the surface of a metal, additional nonuniformity of the magnetic moment (spatial dispersion of the magnetic susceptibility) and, therefore, a special anisotropy of the surface layer that can have a strong influence on the ferromagnetic resonance spectra may appear.[9,19,20] The effect of the anisotropy of a surface layer on ferromagnetic resonance is strongest when the thickness of the defect layer, which depends on the method used to prepare the sample, is of the order of the depth of the skin layer (see, for example, Ref. 21). To determine the possible influence of such an anisotropy on the NFR spectra in our case, we removed by electropolishing the most strongly deformed, ≈ 25 μm thick part of the surface of the disordered alloy Pd_2AuFe. This is obviously greater than the skin layer depth of the alloy in the frequency range 2.26–9.40 GHz, and the volume of material removed by electropolishing equals 2% of the total volume of the sample. Measurements of R_s of the electropolished alloy at several frequencies in the range 2.26–9.40 GHz showed that the removal of a surface layer of the thickness indicated does not cause the effect to vanish nor does it appreciably decrease its magnitude. Hence it can be concluded that the influence of a defective surface layer on the NFR spectrum in the disordered alloy Pd_2AuFe is negligible.

The bulk magnetic anisotropy in the disordered alloy Pd_2AuFe, from our viewpoint, could be due to two factors: 1) the existence of unique directions along which the atoms in the nearest-neighbor environment of one another become ordered (this form of anisotropy, which is the analog of magnetocrystalline anisotropy in crystalline ferromagnets, even occurs in amorphous ferromagnets[22]) and 2) induction of magnetic anisotropy by plastic deformation during the preparation of the disordered alloy. Additional investigations are required to determine the specific type of bulk magnetic anisotropy responsible for the NFR in the disordered Pd_2AuFe.

In summary, a natural ferromagnetic resonance in a metallic ferromagnet was observed in the present work for the first time. This was accomplished by means of a successful choice of sample (disordered Pd_2AuFe alloy), which at room temperature ($T \sim 295\ \text{K} < T_c$) has values of ρ, μ_a, H_s and H_a that make it possible to observe the anomalous behavior of $R_s(\nu)$ in a frequency range convenient for measurements under conditions in which the influence of the ''Kittel mechanism'' is weak.[10] The NFR is manifested experimentally as a resonance frequency-dependence of the ratio of the measured surface resistance to the computed value $\sqrt{(\omega\mu_0/2\sigma)}$, which contains a contribution to R_s only from eddy currents and does not take into account magnetic losses. It would be of interest to perform simultaneous measurements of the frequency dependences of both R_s and the imaginary part X_s of the surface impedance, since such investigations would make it possible to establish the form of the frequency dependences of μ' and μ'' for a ferromagnetic metal near the NFR.

We are grateful to V. P. Dyakina, E. G. Gerasimov, and A. V. Korolev for assisting in the measurements.

These investigations were made possible by the partial support of the International Science Fund (Grant N NMI000).

[a)]E-Mail: lowtemp@ifm.e-burg.su

[1)]For iron at room temperature $H_a = (2K_1/I_s) = 553$ Oe, while $\nu_p = (\gamma \cdot H_a/2\pi) = 0.63 \times 10^9$ s^{-1}. Here the cubic anisotropy constant $K_1 = 4.72 \times 10^5$ ergs/cm^3;[3] the saturation magnetization $I_s = 1707$ G.[11] The corresponding estimates for nickel with parameters taken from the same sources give $H_a = 157$ Oe, while $\nu_p = 4.87 \times 10^8$ s^{-1}.

[2)]For the case at hand, where the coordinate z axis is also the axis of the cylindrical sample, calculations using the geometric dimensions of the sample give[18] $N_x = N_y \approx 0.3$ and $N_z \approx 0.35$. Hence it follows that the influence of the demagnetizing fields $H_{dem} \leqslant (N_z - N_x) \cdot I_s \approx 17.25$ Oe $\ll 1$ kOe $\leqslant H_{dc}$ on the value of ν_H is negligibly small compared with H_{dc} and can be neglected (just as for a spherical sample).

[1] S. V. Vonsovskiĭ [Ed.], *Ferromagnetic Resonance* [in Russian], Moscow (1961), 343 pp.
[2] A. G. Gurevich and G. A. Melkov, *Magnetic Oscillations and Waves* [in Russian], Nauka, Moscow (1994), 464 pp.
[3] S. Tikadzumi, *The Physics of Ferromagnetism. Magnetic Characteristics and Applications* (Mir, Moscow, 1987), 420 pp.
[4] G. Zh. Rankis, *Dynamics of Magnetization of Polycrystalline Ferrites* [in Russian], Zinatne, Riga (1981), 186 pp.
[5] L. Landau and E. Lifschitz, Phys. Z. Sowjetunion **8**, 153 (1935) (in *Collected Works of L. D. Landau* [in Russian], edited by E. M. Lifshitz, Nauka, Moscow (1969), Vol. 1, p. 128).
[6] L. A. Fomenko, Usp. Fiz. Nauk **64**, 669 (1958).
[7] S. V. Vonsovskiĭ, *Magnetism* [in Russian], Nauka, Moscow (1971), 1032 pp.
[8] S. M. Bhagat, in *Techniques of Metals Research VI* (Wiley, N. Y., 1973), p. 79.
[9] Z. Frait and D. Fraitova, in *Spin Waves and Magnetic Excitations*, edited by A. S. Borovik–Romanov and S. K. Sinha (North–Holland, Amsterdam, 1988), Pt. 2, p. 1.
[10] C. Kittel, Phys. Rev. **70**, 281 (1946).
[11] C. Kittel, *Introduction to Solid State Physics* (Nauka, Moscow, 1978), 696 pp.
[12] L. D. Landau and E. M. Lifshitz, *Electrodynamics of Continuous Media* [Pergamon Press, N. Y; Nauka, Moscow, 1982, 620 pp.].
[13] I. N. Sachkov, L. S. Chemerinskaya, and V. V. Ovchinnikov, Fiz. Tverd.

Tela (St. Petersburg) **38**, 603 (1996) [Phys. Solid State **38**, 331 (1996)].
[14] A. A. Kuranov, V. P. Dyakina, Yu. G. Ignatenko *et al.*, Fiz. Met. Metalloved. **53**, 931 (1982).
[15] Yu. A. Vereshchagin, M. A. Alekseeva, S. V. Grishchenko, P. V. Gel'd, and G. P. Gasnikova, Fiz. Met. Metalloved. **68**, 697 (1989).
[16] M. A. Borozdina, Yu. A. Vereshchagin, F. A. Sidorenko, A. A. Kuranov, P. V. Gel'd, and Yu. G. Karpov, Fiz. Met. Metalloved. **56**, 80 (1983).
[17] D. N. Kourov and A. S. Shcherbakov, Rev. Sci. Instrum. **67**, 274 (1996).
[18] M. Sato and Y. Ishii, J. Appl. Phys. **66**, 983 (1989).
[19] M. I. Kaganov and Yui Lu, Izv. Akad. Nauk SSSR, Ser. Fiz. **25**, 1375 (1961).
[20] Z. Frait, D. Fraitova, and N. Zarubova, Phys. Status Solidi B **128**, 219 (1985).
[21] M. I. Kaganov and G. Paash, Fiz. Tverd. Tela (Leningrad) **17**, 2731 (1975) [Sov. Phys. Solid State **17**, 1812 (1975)].
[22] K. Handrich and S. Kobe, *Amorphous Ferro- and Ferrimagnets* (Mir, Moscow, 1982), 293 pp.

Translated by M. E. Alferieff

Effect of electric field on neutron scattering in lead magnoniobate

S. B. Vakhrushev, A. A. Naberezhnov, N. M. Okuneva

A. F. Ioffe Physicotechnical Institute, Russian Academy of Sciences, 194021 St. Petersburg, Russia

B. N. Savenko

Joint Institute for Nuclear Research, 141980 Dubna, Russia
(Submitted March 13, 1998)
Fiz. Tverd. Tela (St. Petersburg) **40**, 1905–1910 (October 1998)

The temperature dependence of the intensity of the Bragg and the transverse component of quasi-elastic neutron scattering from the single-crystal model relaxor $PbMg_{1/3}Nb_{2/3}O_3$ (PMN) has been studied for various applied electric fields. It is shown that application of a field $E>E_{th}\approx 1.6$ kV/cm increases the elastic scattering intensity and reduces the intensity of the transverse diffuse-scattering component and that, below 230 K and for $E>6$ kV/cm, the elastic-scattering intensity saturates while the temperature-dependent part of the transverse diffuse-scattering component becomes practically suppressed. The measured temperature and field dependences of the intensity of type $(h00)$ and $(hh0)$ Bragg reflections provide supportive evidence both for the presence of considerable lead-ion displacements relative to the ideal perovskite sites and for the existence in strong electric fields of an induced transition to the ferroelectric phase below 250 K. © *1998 American Institute of Physics.*
[S1063-7834(98)02910-4]

Disordered perovskite-like compounds exhibiting a diffuse phase transition (relaxors) have been attracting considerable attention and are of interest not only from the standpoint of basic science but also because they possess unique physical properties and, hence, have a promising technological potential. The lead magnoniobate $PbMg_{1/3}Nb_{2/3}O_3$ (PMN) may be considered as a model crystal to study relaxors. In PMN, the nonisovalent ions Mg^{2+} and Nb^{5+} are distributed in crystallographically equivalent positions on the *B* sublattice at the center of the oxygen tetrahedron with probabilities of 1/3 and 2/3, respectively, while the *A* sublattice sites at the corners of the cubic cell are occupied by the Pb^{2+} ions. One could expect such a random charge distribution to produce local electric fields distributed randomly both in magnitude and direction, as well as to result in a random pattern of interaction among the generated dipole moments. While there is presently a wealth of experimental material obtained in investigation of this and other similar compounds, the microscopic nature of the low-temperature phase remains a subject of heated discussion. One has recently succeeded in describing some of the observed features, such as the frequency behavior of the temperature and amplitude of the dielectric permittivity maximum,[1] the logarithmic character of dispersion of ε below the temperature of the maximum,[1,2] and acoustic anomalies[3] in terms of the model[3,4] of a phase transition (PT) to a dipole-glass-type state. It was shown (see, e.g., Refs. 4–9) that the observed features in the macroscopic behavior of PMN in dc electric fields depend on the actual regime of electric field application to the sample, the magnitude of this field, and the sample prehistory, which also is in overall agreement with the glass-like PT model. This is why studies of the changes in the pattern of x-ray and neutron scattering from single-crystal PMN as a function of the magnitude and regimes of application of the electric field to a sample are of unquestionable interest, because it is these studies that may provide an insight into the processes occurring in a sample on the microscopic scale. It is this problem that is considered in the present work, which is a continuation of our previous investigations[4,9–11] of neutron scattering from disordered objects.

1. EXPERIMENTAL METHODS

The study was carried out on two PMN single crystals, with the first being a parallelepiped measuring $3\times 3.7\times 10$ mm, and the second, a 2.2-mm thick, 12×7-mm plane-parallel plate. The quality of the single crystals was established from rocking-curve measurements on a γ diffractometer, with the width of the curve being about $1'$. In measurements performed in an electric field, vector **E** was close in direction to the [110] crystal axis. The studies were made on a triple-axis neutron spectrometer Neutron-3 at the WWR-M reactor (PNPI, Gatchina) and on a neutron time-of-flight diffractometer DN-2 at the IBR-2 pulsed reactor (LNF JINR, Dubna). In both cases, the crystal was mounted with the $[1\bar{1}0]$ axis pointing vertically up. The incident-neutron wavelength in Neutron-3 was $\lambda=1.28$ Å, the functions of monochromator and analyzer being served by copper single crystals reflecting from the (111) planes. The reciprocal space was scanned in longitudinal and transverse directions with respect to the reciprocal-lattice vector τ. The data treatment method used is described in detail elsewhere,[10] the background was assumed to be linear and was derived from the wings of the experimental Bragg- and diffuse-scattering distributions. The graphs referred to subsequently are shown with the background subtracted. The DN-2 diffractometer

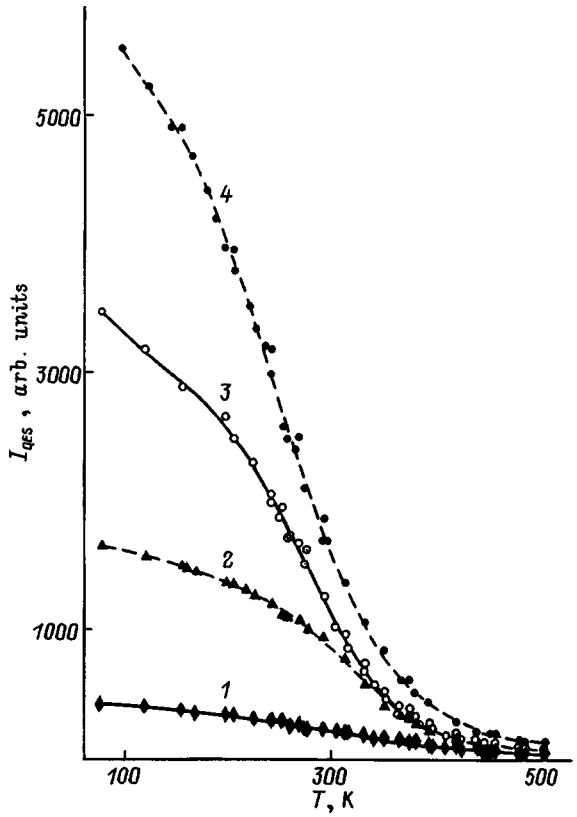

FIG. 1. Temperature dependence of quasi-elastic scattering intensity near the reciprocal-lattice point (330) for q: *1*—$0.1a^*$, *2*—$0.04a^*$, *3*—$0.03a^*$, and *4*—$0.02a^*$.

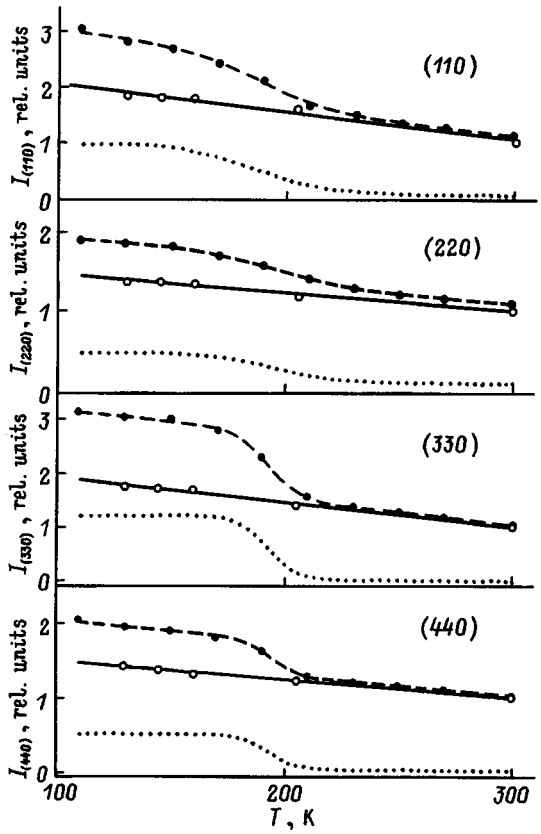

FIG. 2. Temperature dependence of Bragg scattering intensity for $(hh0)$-type reflections in zero electric field (open circles) and in a 6-kV/cm field (filled circles). Solid line—variation of scattering intensity in zero field, dotted line—variation (increment) of scattering intensity under application of a 6-kV/cm electric field.

measurements made use of a position-sensitive detector, thus permitting one to obtain simultaneously two-dimensional neutron-scattering intensity distributions in the vicinity of several reciprocal-lattice points of the same family. The studies were carried out within the temperature interval from 300 to 90 K (with the temperature determined to not worse than 1 K), the electric field was applied at room temperature, and the subsequent cooling and measurements were made in this field (an analog of the field-cooled regime employed in spin-glass investigations). After each cooling run, the crystal was heated in zero field to a temperature of $\approx$360 K, at which it was held up for about 1.5 h. The recovery to the initial state was judged from the Bragg reflection intensities.

2. MEASUREMENTS IN ZERO ELECTRIC FIELD

Neutron-scattering measurements in the vicinity of various reciprocal-lattice points revealed the existence of quasi-elastic scattering of two types. Near $(2h2k2l)$-type points [for instance, (200) and (400)] the scattering intensity increased weakly with temperature, and the isointensive contours were found to be extended along the reciprocal-lattice vector. The pattern of scattering near $(2h+1\,2k+1\,2l)$-type points had a radically different pattern, namely, its intensity grew rapidly with decreasing temperature (Fig. 1), and the isointensive diffuse-scattering contours were extended perpendicular to the scattering vector τ, in other words, the temperature-dependent part of scattering had a clearly pronounced transverse character.[12] It should also be pointed out that the isointensive contours for this scattering approached in shape the lemniscate-like curves predicted by theory[13] for scattering from critical ferroelectric fluctuations. Treatment of the data obtained both in this experiment and in earlier studies showed that the intensity of this scattering can be well fitted by the relation of Ornstein-Zernike $I(q)\propto 1/(q^2+\varkappa^2)$, where $\varkappa=1/R$ is the reciprocal correlation radius, and q is the reduced wave vector. For $q\gg\varkappa$, the $I(q)$ dependence approximates closely to a power-law relation $q^{-\alpha}$ with $\alpha=2$; thus in contrast to our earlier synchrotron study[11] we have not been able to reveal in the neutron experiment any deviation of the line shape from Lorentzian; this can probably be attributed to the insufficiently high resolution, which brings about an apparent lowering of the power in the $I(q)$ relation as a result of convolution with the instrument response function.

Thus the temperature dependence of the intensity of the observed diffuse scattering, the shape of the isointensive curves, and the character of the inverse correlation radius $\varkappa$ as a function of temperature permit a conclusion that this phenomenon originates from scattering from ferroelectric fluctuations and that, while the ''density'' of these fluctuations increases with decreasing temperature, no PT to an ordered state takes place. The first type of scattering, which is most clearly pronounced near $(2h2k2l)$-type points where critical scattering is strongly suppressed, is apparently Huang

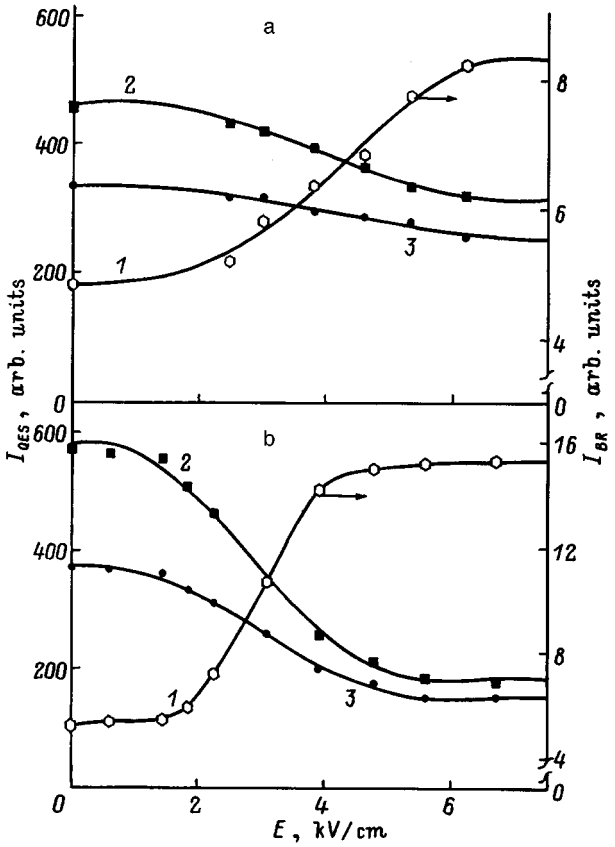

FIG. 3. Intensity of (*1*) Bragg and (*2*) diffuse scattering [for $q=0.025a^*$ (*2*) and $0.035a^*$ (*3*)] vs applied field at 260 K (a) and 180 K (b) for the (330) point.

scattering from microscopic elastic lattice strains.

The temperature dependence of the Bragg scattering intensity was studied on the DN-2 diffractometer. The temperature dependence of the intensities of $(hh0)$-type reflections is plotted in Fig. 2 (open circles) after subtraction of the diffuse-scattering contribution, and one readily sees that the intensities grow weakly and monotonically with decreasing temperature. This growth is accounted for by the variation of the Debye-Waller factor with decreasing temperature and is qualitatively in accord with x-ray scattering data[14]. The experimental points can be well fitted in this case by a linear relation.

3. MEASUREMENT OF THE BRAGG AND DIFFUSE SCATTERING IN AN ELECTRIC FIELD

Figure 3 shows the behavior of the Bragg scattering intensity at the (330) reciprocal-lattice point and of the diffuse scattering intensity in the vicinity of this point (for $q=0.025a^*$ and $0.035a^*$, where a^* is the reciprocal-lattice parameter) as functions of applied electric field for two temperatures, 260 (a) and 180 K (b). These temperatures lie, accordingly, above and below the splittings in the temperature dependences of Bragg and diffuse scattering intensity observed by us earlier[4] in FC and ZFC (zero-field cooling) regimes. The values of q^* were taken greater than $0.02a^*$, because, as follows from experimental data, Bragg scattering practically does not contribute to the diffuse process at these

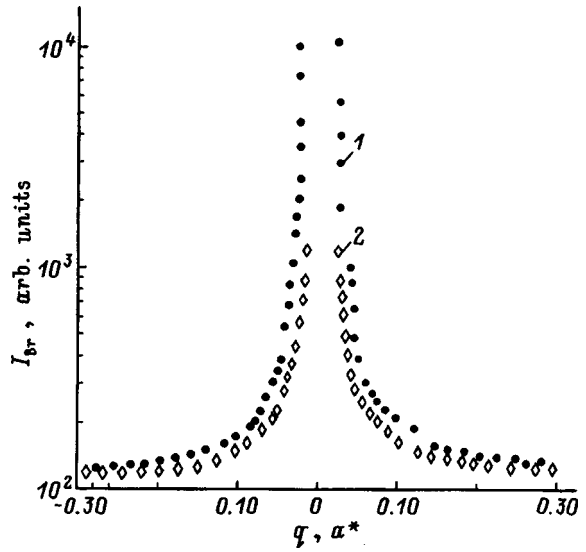

FIG. 4. q dependence of the scattering intensity observed near the (110) Bragg reflection at 210 K. E(kV/cm): *1*—0, *2*—6.5.

values of q, and our inelastic-scattering measurements established that the high resolution obtained when adjusting the instrument to the $\omega=0$ energy makes the contribution due to inelastic scattering from transverse acoustic phonons negligible. As evident from Fig. 3, an increase of the applied field gives rise to a growth of Bragg scattering, and simultaneously to suppression of a part of the observed diffuse scattering. Both effects are seen particularly well below the splitting-point temperature (see Fig. 3b). Note also that the diffuse-scattering intensity *vs* field plot obtained at 180 K shows a threshold behavior starting with $E_{th}\approx 1.6$ kV/cm (if reduced to the [111] direction). For higher applied fields (≈ 6.5 kV/cm) the experimentally observed intensity distribution changes noticeably its pattern (Fig. 4). Below the splitting point of the FC and ZFC curves the Bragg intensity saturates, the transverse diffuse-scattering intensity decreases substantially to the extent where one can no longer describe the observed scattering-curve shape by a Lorentzian, and for $q \gg \varkappa$ the $I(q)$ relation approximates to a power law $q^{-\alpha}$ with $\alpha\approx 1.5$. Thus application of an electric field changes the parameter α from two for $E=0$ to $\alpha=1.5$ for $E=6.5$ kV/cm (Fig. 5), and the intensity of the remaining component depends on q while being practically independent of the temperature and field. This value of parameter α observed in strong electric fields appears strange and is apparently associated with the above-mentioned underestimation of the exponent in the $I(q)$ relation obtained in the neutron experiment. As for the physical nature of the remaining diffuse scattering, one could suggest several possible sources, first, not fully suppressed critical fluctuations and, second, scattering from domain walls, because the appearing ferroelectric state was shown[15] not to be single-domain. Obviously enough, the question of the type of function that could be used to describe superposition of these various types of scattering is a fairly complex theoretical problem which requires further investigation.

We also measured the temperature dependence of the

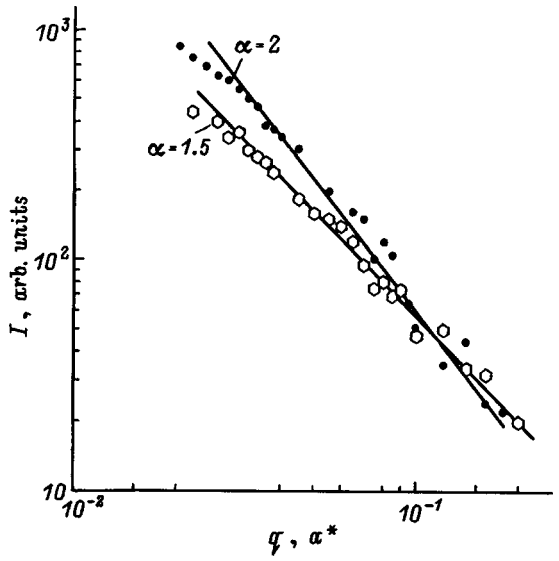

FIG. 5. Diffuse scattering intensity vs reduced wave vector in the vicinity of the (110) reciprocal lattice point measured at 210 K. E(kV/cm): 0 (filled circles) and 6.5 (open circles).

intensity of the transverse diffuse-scattering component in strong electric fields. Figure 6 presents two series of measurements made on the Neutron-3 (filled circles) and time-of-flight DN-2 diffractometer (open circles) for several values of reduced wave vector q in the vicinity of the (330) reciprocal-lattice point. As seen from the figure, the data agree for $q=0.05a^*$ and $0.03a^*$, and the slight discrepancy at $q=0.02a^*$ can be assigned to the fact that this value of q

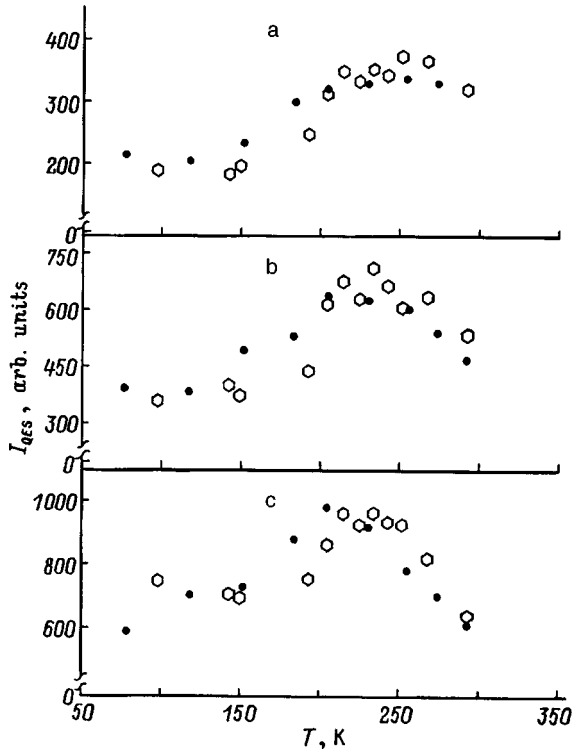

FIG. 6. Temperature dependence of diffuse scattering intensity near the (330) point in an electric field of 6 kV/cm for q: (a) $0.05a^*$, (b) $0.03a^*$, and (c) $0.02a^*$.

TABLE I. Relative integrated intensities of type $(hh0)$ and $(h00)$ reflections.

(hkl)	(200)	(400)	(600)	(300)	(500)	(110)	(330)	(220)	(440)
I_2/I_1	1.23	1.27	1.44	1.64	1.66	2.18	2.62	1.56	1.72

lies practically at the limit of DN-2 resolution. For all q one clearly observes a maximum, and its position shifts toward lower temperatures with decreasing q. This behavior of $I_{\mathrm{QES}}(q)$ indicates that the first to freeze out under field cooling are small clusters, and that the larger is a cluster, the lower is its freeze-out temperature.

Consider now possible reasons for the experimentally observed growth in the Bragg scattering intensity. One may conjecture that this growth is connected with a change in extinction caused by a rearrangement of the mosaic crystal structure under a strong applied electric field. The simplest way of testing this assumption lies in studying the behavior of Bragg reflection intensity as a function of incident neutron wavelength. With this purpose in mind, a special experiment was performed on the DN-2 diffractometer to measure the behavior of the intensities of type $(hh0)$ and $(h00)$ Bragg reflections on the $3\times3.7\times10$-mm crystal at $E=0$ and 6 kV/cm. The use of the time-of-flight technique permitted one in this case to measure the intensities of the corresponding Bragg-family reflections at various incident-neutron wavelengths in the same geometry and at the same angle 2θ [in our experiment, the angle 2θ was 118° for type $(h00)$, and about 160° for type $(hh0)$ reflections].

Table I presents integrated Bragg intensities obtained at 190 K in a field of 6 kV/cm (I_2) and normalized to their room-temperature, zero-field values (I_1). The error of the intensity ratio determination did not exceed 1% for strong reflections [$(2h2k2l)$ type], and 2% for the others.

As seen from Table I, the intensity of reflections with large (hkl) grows faster than that with smaller ones, i.e. the observed growth argues against the assumption of its having extinction nature.[16] Nevertheless, we attempted to determine the extinction parameters from the above set of integrated-intensity ratios for different reflections; this attempt did not, however, meet with success, because the fitting either failed or yielded nonphysical values of the parameters. One can thus maintain that the observed growth of integrated neutron-scattering intensity in the presence of an electric field is not due to a field-induced change in extinction. This conclusion is buttressed indirectly by a study of the variation of the cubic-phase (222) reflection intensity with time made[15] at $T=175$ K and $E=3$ kV/cm.

Another possibility of interpreting the observed growth in intensity is connected with the presence in the initial state of the crystal of large ion displacements, random both in magnitude and direction, which would distort the local cubic symmetry. In this case the magnitude of the structure factor for arbitrary reflection turns out to be smaller than that expected theoretically for the perovskite structure. Application of a strong electric field can result in an ordering of these displacements and, as a consequence, in an increase of the structure factor as a whole.

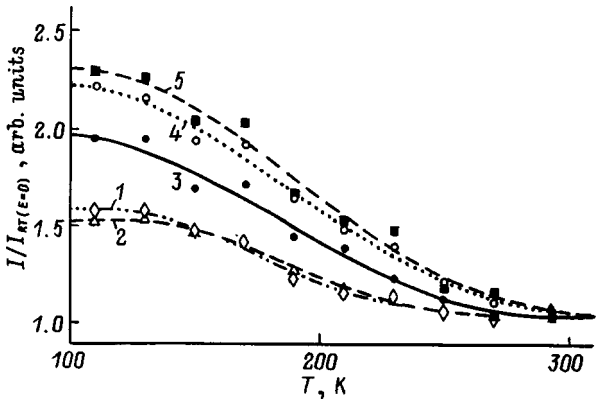

FIG. 7. Temperature dependence of Bragg intensity for $(h00)$-type reflections obtained under cooling in an electric field of 6 kV/cm. *1*—(200), *2*—(400), *3*—(600), *4*—(300), and *5*—(500).

It is well known that the structure factors for cubic perovskite-like compounds have the form

$$(2h\ 2k\ 2l) \qquad F = f_{\mathrm{Pb}} \exp(-M_{\mathrm{Pb}}) + f_{\mathrm{MN}} \exp(-M_{\mathrm{MN}}) + 3f_0 \exp(-M_0),$$

$$(2h+1\ 2k\ 2l) \qquad F = f_{\mathrm{Pb}} \exp(-M_{\mathrm{Pb}}) - f_{\mathrm{MN}} \exp(-M_{\mathrm{MN}}) - f_0 \exp(-M_0),$$

$$(2h+1\ 2k+1\ 2l) \qquad F = f_{\mathrm{Pb}} \exp(-M_{\mathrm{Pb}}) + f_{\mathrm{MN}} \exp(-M_{\mathrm{MN}}) - f_0 \exp(-M_0),$$

$$(2h+1\ 2k+1\ 2l+1) \qquad F = f_{\mathrm{Pb}} \exp(-M_{\mathrm{Pb}}) - f_{\mathrm{MN}} \exp(-M_{\mathrm{MN}}) + 3f_0 \exp(-M_0),$$

where $f_{\mathrm{MN}} = \frac{1}{3} f_{\mathrm{Mg}} + \frac{2}{3} f_{\mathrm{Nb}}$, f are the corresponding neutron-scattering amplitudes, and M_i are the Debye-Waller factors. The factor F_{hkl} is maximum for $(2h2k2l)$-type reflections and is equal to the sum of atomic amplitudes f_i multiplied by the corresponding Debye-Waller factor; one can thus readily see that F_{hkl} cannot increase in any structural rearrangement. At the same time our study of the temperature dependence of Bragg intensity in a strong (≈ 6 kV/cm) electric field revealed a clearly pronounced growth in the intensity of $(2h2k2l)$-type reflections (Fig. 7), which argues for the above-mentioned considerations of the existence of considerable ion displacements. It should also be pointed out that a decrease in temperature gives rise to a substantially larger increase in intensity for the $(2h+1\ 2k2l)$- and $(2h+1\ 2k+1\ 2l)$-type reflections than it does for the $(2h2k2l)$ reflections. This suggests that it is the contribution of lead to the structure factor that is primarily depressed in the initial state (without the field). Indeed, the thermal-neutron scattering amplitude from the lead nucleus (0.94×10^{-12} cm) is larger by a factor 1.3 than that for niobium (0.71×10^{-12} cm) and almost twice that for oxygen (0.58×10^{-12} cm) and magnesium (0.52×10^{-12} cm). Thus the contribution of lead to $(2h2k2l)$ reflections is relatively small, and its increase entails a comparatively small increase in intensity. At the same time for the $(2h+1\ 2k2l)$ and $(2k+1\ 2k+1\ 2l)$ reflections the relative contribution of lead is substantially larger, and any change in its magnitude should affect to a greater extent the reflection intensity; note also that one can expect a larger growth for $(2h+1\ 2k+1\ 2l)$-type reflections, because their structure factor contains the difference between the amplitudes for lead and the other atoms. The corresponding experimental data, presented in Figs. 2 and 7, correlate well with the above considerations. Thus the observed behavior of the intensities provides supportive evidence for the considerable displacements of lead ions from the ideal crystallographic perovskite sites cited in Ref. 17 and is in agreement with the observation[18] in PMN crystal of anomalously large rms static displacements of atoms.

As seen from Fig. 2 presenting the temperature behavior of neutron scattering intensity for $(hh0)$-type reflections obtained in a field of 6 kV/cm (filled circles), cooling the crystal down to ~ 250 K brings about a weak intensity increase compared to the zero-field values (solid line and open circles in the figure). At a lower temperature the rate of scattering-intensity growth becomes substantially larger; the change (increment) of intensity, δI, is shown in Fig. 2 with a dotted line. It should be pointed out that for ferrodistorsive transitions ($\mathbf{q}_s$) the change in Bragg intensity near T_c is proportional to η^2 (Ref. 19), where η is an order parameter, and the temperature dependence of η^2 in strong fields (for $E > E_{\mathrm{crit}}$) measured in Ref. 20 is in a good qualitative agreement with the above temperature dependence of δI. Thus it may be assumed that the observed jump in intensity is a manifestation of a field-induced transition to the ferroelectric phase, which was shown to exist, for example, in Refs. 5, and 21.

We have thus shown that application of an electric field $E > E_{\mathrm{th}} \approx 1.6$ kV/cm (reduced to the [111] direction) gives rise to a substantial change in the nature of neutron scattering. In particular, in strong fields and for $q \gg \varkappa$ the parameter α in the power-law relation $q^{-\alpha}$ describing the diffuse scattering intensity changes from two to 1.5. It has also been shown that, in an electric field ≈ 6.5 kV/cm and at temperatures below the splitting point in the FC and ZFC curves, the intensity of the transverse diffuse-scattering component decreases considerably while the Bragg intensity saturates. A study of the temperature dependence of Bragg-reflection intensity at $E \approx 6$ kV/cm supports the existence of ionic displacements in the unit cell of PMN, which become ordered by a strong electric field, and argues for the onset of an induced ferroelectric transition below ~ 250 K. The results obtained are in a good agreement with published data[12,22] on the magnitude and form of these displacements.

Support of the Russian Fund for Fundamental Research (Grant 95-02-04065) and of the ''Neutron Studies of Matter'' program (Grant 96-110) is gratefully acknowledged.

[1] E. V. Colla, E. Yu. Koroleva, N. M. Okuneva, and S. B. Vakhrushev, J. Phys.: Condens. Matter **4**, 3671 (1992).
[2] N. K. Yushin, S. N. Dorogovtsev, and S. I. Smirnov, Pis'ma Zh. Tekh. Fiz. **14**, 125 (1988) [Sov. Tech. Phys. Lett. **14**, 55 (1988)].
[3] S. N. Dorogovtsev and N. K. Yushin, Ferroelectrics **112**, 27 (1990).
[4] S. B. Vakhrushev, B. E. Kvyatkovsky, A. A. Nabereznov, N. M. Okuneva, and B. P. Toperverg, Physica B **156–157**, 90 (1989).
[5] M. Chabin, M. Malki, E. Husson, and A. Morell, J. Phys. III **4**, 1151 (1994).
[6] V. Westphal, W. Kleemann, and M. D. Glinchuk, Phys. Rev. Lett. **68**, 847 (1992).
[7] R. Sommer, N. K. Yushin, and J. van der Klink, Phys. Rev. B **48**, 13 230 (1993).

[8] E. V. Colla, E. Yu. Koroleva, A. A. Nabereznov, and N. M. Okuneva, Ferroelectrics **151**, 337 (1994).
[9] S. B. Vakhrushev, B. E. Kvyatkovsky, A. A. Naberezhnov, and N. M. Okuneva, Ferroelectrics **90**, 173 (1989).
[10] S. B. Vakhrushev, A. A. Naberezhnov, N. M. Okuneva, and B. P. Toperverg, FTI Preprint No. 1440, Leningrad (1990).
[11] S. B. Vakhrushev, A. A. Nabereznov, S. K. Sinha, Y. P. Feng, and T. Egami, J. Phys. Chem. Solids **57**, 1517 (1996).
[12] S. B. Vakhrushev, A. A. Naberezhnov, N. M. Okuneva, and B. N. Savenko, Fiz. Tverd. Tela (St. Petersburg) **37**, 3621 (1995) [Phys. Solid State **37**, 1993 (1995)].
[13] M. F. Krivoglaz, *Theory of X-Ray and Thermal Neutron Scattering by Real Crystals* [Plenum Press, New York, 1969; Nauka, Moscow, 1967].
[14] L. A. Shebanov, P. P. Kapostins, and J. A. Zvirgzds, Ferroelectrics **56**, 53 (1984).
[15] S. B. Vakhrushev, J.-M. Kiat, and B. D. Bkhil, Solid State Commun. **103**, 477 (1997).
[16] A. Guinier, *Théorie et Technique de la Radiocrystallographie* [Dunod, Paris, 1956; Fizmatgiz, Moscow, 1961].
[17] S. B. Vakhrushev, S. Zhukov, G. Fetisov, and V. Chernyshov, J. Phys.: Condens. Matter **6**, 4021 (1994).
[18] L. A. Shebanov, P. P. Kapostin'sh, É. H. Birks, and Yu. A. Zvirgzds, Kristallografiya **31**, 317 (1986) [Sov. Phys. Crystallogr. **31**, 187 (1986)].
[19] A. D. Bruce and R. A. Cowley, *Structural Phase Transitions* (Taylor & Francis, London, 1981).
[20] Yu. A. Izyumov and V. N. Syromyatnikov, *Phase Transitions and Crystal Symmetry* [in Russian], Nauka, Moscow, 1984.
[21] E. V. Colla, S. B. Vakhrushev, E. N. Koroleva, and N. M. Okuneva, Fiz. Tverd. Tela (St. Petersburg) **38**, 2183 (1996) [Phys. Solid State **38**, 1202 (1996)].
[22] N. de Mathan, E. Husson, G. Calvarin, J. R. Gavarri, A. W. Hewat, and A. Morell, J. Phys.: Condens. Matter **3**, 8159 (1991).

Translated by G. Skrebtsov

Effect of γ irradiation on the hysteresis phenomena at the incommensurate-commensurate phase transition in Rb_2ZnBr_4

A. U. Sheleg, K. V. Iodkovskaya, and N. F. Kurilovich

Institute of Solid-State and Semiconductor Physics, National Academy of Belarus, 220072 Minsk, Belarus
(Submitted March 16, 1998)
Fiz. Tverd. Tela (St. Petersburg) **40**, 1911–1914 (October 1998)

The effect of γ irradiation on the temperature hysteresis in dielectric permittivity ε and loss tangent $\tan\delta$ of crystalline Rb_2ZnBr_4 has been studied in the vicinity of the incommensurate-commensurate phase transition. The $\varepsilon(T)$ and $\tan\delta(T)$ curves were found to exhibit anomalies in the form of maxima. Hysteresis was observed in the measured properties, including the transition temperature T_c ($\Delta T = T_c^h - T_c^c$), in both unirradiated and irradiated samples. It is shown that, as the radiation dose increases the extent of the hysteresis ΔT increases, the values of $\varepsilon_{\max}$ and $\tan\delta_{\max}$ at the transition point decrease, and the anomalies wash out. © *1998 American Institute of Physics.* [S1063-7834(98)03010-X]

Rb_2ZnBr_4 crystals belong to a large group of A_2BX_4 compounds, which undergo a sequence of phase transitions (PT) with varying temperature. When cooled, Rb_2ZnBr_4 passes at $T_i \cong 347$ K through a second-order PT from the paraphase to incommensurate (IC) phase, and at $T_c \cong 200$ K, a first-order transition from the IC to ferroelectric commensurate (C) phase with a modulation wave vector $\mathbf{q}_c = \frac{1}{3}\mathbf{c}^*$ and a polarization vector $\mathbf{P}_s \| \mathbf{a}$ (with the axes chosen as $b > c > a$).[1] Besides these PTs, Rb_2ZnBr_4 crystals undergo at lower temperatures three more PTs at $T_3 \cong 108$ K, $T_4 \cong 80$ K, and $T_5 \cong 50$ K, which have presently become a subject of intensive investigation.[2] It is known that the properties of crystals with incommensurate phases are very sensitive to the presence of impurities and other lattice defects.

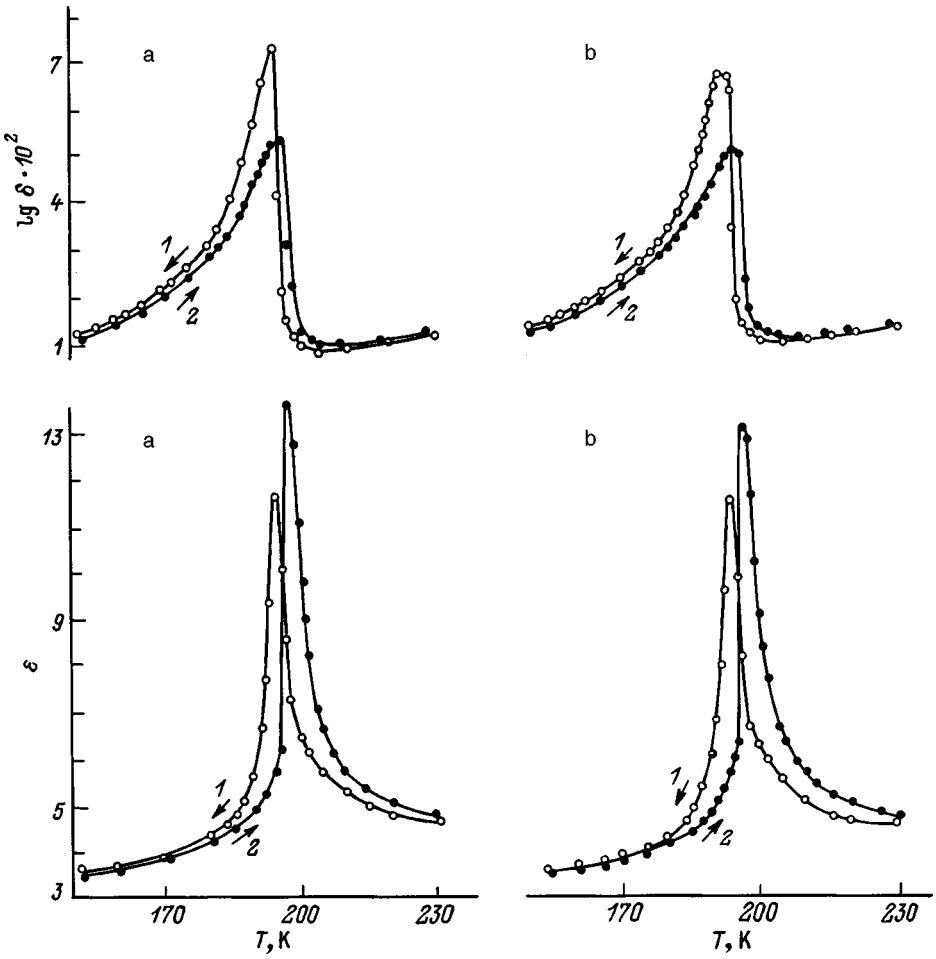

FIG. 1. Temperature dependence of the loss tangent $\tan\delta$ and dielectric permittivity ε for (a) unirradiated Rb_2ZnBr_4 crystals and (b) for crystals irradiated by a dose of 10^6 R. *1*—cooling, *2*—heating.

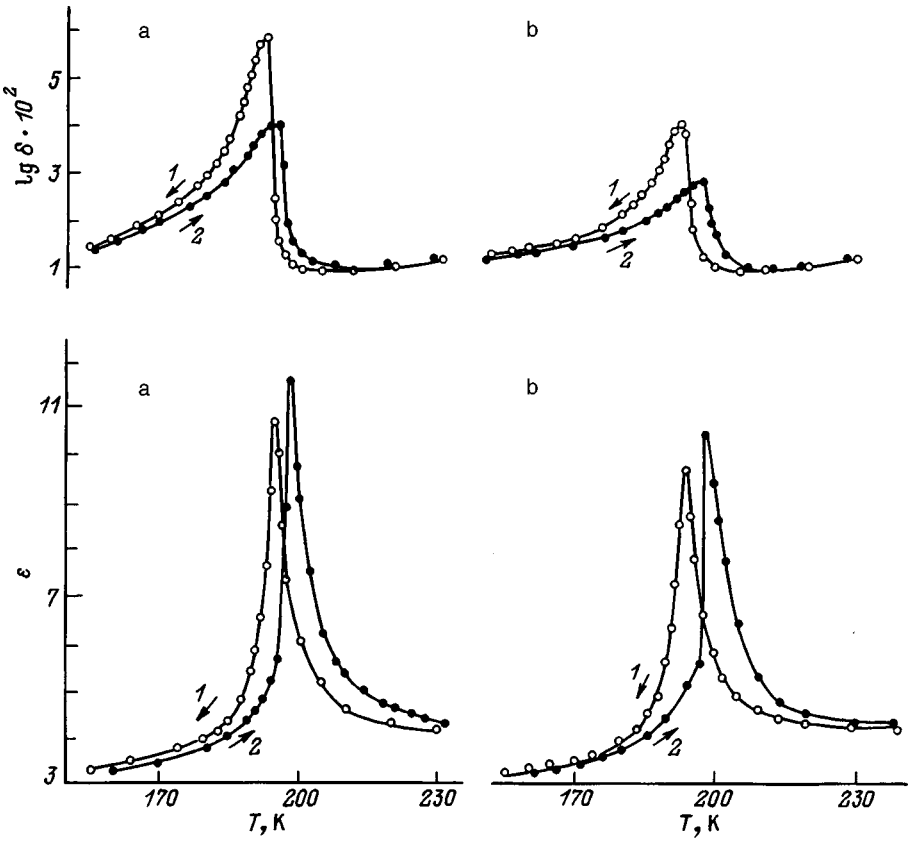

FIG. 2. Temperature dependence of tan δ and ε for Rb_2ZnBr_4 crystals irradiated by a dose of (a) 10^7 R and (b) 5×10^7 R. *1*—cooling, *2*—heating.

This is particularly true for molecular and ionic crystals, such as Rb_2ZnBr_4, where interatomic forces in the $ZnBr_4$ tetrahedra are strong enough, while the chemical bonds between Rb^+ ions and the tetrahedra are weak and extremely sensitive to changes in the crystal lattice.[3]

The effect of impurities and lattice defects, including induced ones, on the physical properties of crystals with modulated structures has been dealt with in many studies.[4–9] The influence of irradiation by ions (of hydrogen and sulfur) on the dielectric permittivity of Rb_2ZnCl_4 and Rb_2ZnBr_4 in the vicinity of the $IC\leftrightarrow C$ transition was investigated in Refs. 4 and 5. It was shown that the ε_{max} peaks decrease in amplitude at the PT, while the transition temperature T_c practically does not change with increasing irradiation dose. A study of the effect of γ irradiation on the dielectric characteristics of Rb_2ZnCl_4 revealed that the transition temperature T_c decreases slightly after the irradiation.[9] An unusual feature is the practically twofold increase of the ε_{max} peak following irradiation at all the three frequencies used in the measurements. We showed[10] that following γ irradiation, ε_{max} decreases at the T_c point for Rb_2ZnCl_4 and Rb_2ZnBr_4, and the T_c itself decreases slightly for Rb_2ZnCl_4 and increases for Rb_2ZnBr_4. It should be pointed out that these thermal studies[10] were carried out in the heating mode.

This paper reports a study of the effect of γ irradiation on the hysteresis phenomena in the temperature dependence of dielectric permittivity ε and the loss tangent tan δ of Rb_2ZnBr_4 crystals in the vicinity of the $IC\leftrightarrow C$ PT.

1. EXPERIMENTAL TECHNIQUE

Rb_2ZnBr_4 crystals were grown from aqueous solutions of rubidium bromozincate by evaporation at 298–299 K. Rubidium bromozincate was prepared of rubidium carbonate Rb_2CO_3, zinc oxide ZnO, and hydrobromic acid HBr, taken in stoichiometric ratios. The samples, cut from Rb_2ZnBr_4 single crystals, were $5\times4\times0.8$-mm plates with the faces perpendicular to the polar axis a. The contacts were prepared by firing the silver paste deposited on the plate's faces at $\sim$380 K for several hours. The special holder fixing the sample was maintained in nitrogen vapor. The temperature was varied by means of a heater mounted in the sample holder. The sample temperature was measured with a chromel-coppel thermocouple, whose junction was at the sample surface.

The dielectric permittivity ε and the loss tangent tan δ were measured within the 150–240 K temperature interval in the course of continuous cooling and heating runs at a rate of 0.5 K/min in weak fields at a frequency of 1 MHz using a E7-12 digital meter. The samples were irradiated at room temperature by a Co^{60} source of strength $\sim$180 R/s in the irradiation zone. The irradiation dose, built up by successive exposures of a sample, was 10^6, 10^7, 5×10^7, 10^8, and 2×10^8 R.

2. RESULTS AND DISCUSSION

Figures 1–3 display the temperature dependences of tan δ and ε of Rb_2ZnBr_4 samples, both unirradiated and irra-

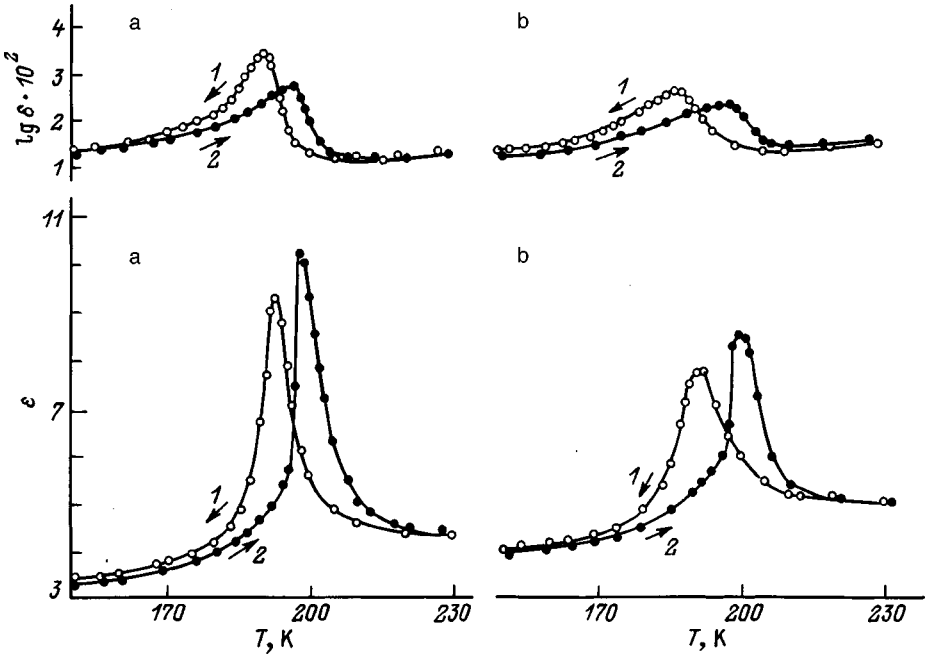

FIG. 3. Temperature dependence of tan δ and ε for Rb_2ZnBr_4 crystals irradiated by a dose of (a) 10^8 R and (b) 2×10^8 R. *1*—cooling, *2*—heating.

diated to various γ ray doses. As seen from the figures, the tan $\delta(T)$ and $\varepsilon(T)$ curves exhibit anomalies in the vicinity of the $IC\leftrightarrow C$ phase transition in the form of distinct maxima. Measurements performed in cooling-heating cycles reveal a temperature hysteresis in the properties under study, including the transition temperature T_c. The hysteresis phenomena observed in Rb_2ZnBr_4, as in other crystals where modulated structures appear under certain conditions, originate from the interaction of the modulated wave with lattice defects. As a result of this interaction, the incommensurate structure becomes pinned at the defects. Pinning interferes with changes of the modulation period as the temperature is varied and gives rise to metastable states. The hysteresis in dielectric permittivity ε is observed in the temperature region $\sim$170–240 K, whereas for tan δ this region is $\sim$170–205 K. The hysteresis in the transition temperature T_c for unirradiated samples is $T_c^h - T_c^c = \Delta T = 2$ K, where T_c^h and T_c^c are the temperatures of the maximum in tan δ observed under heating and cooling, respectively. $\Delta T = 2$ K is a comparatively small quantity for such crystals as Rb_2ZnBr_4, which attests to the fairly good quality of the samples used. As seen from Figs. 1–3, both tan $\delta(T)$ and $\varepsilon(T)$ curves obtained in the *C* phase under cooling lie substantially above the corresponding curves recorded in the heating runs, which is explained by the domain-structure state. When heated above T_c, the domain structure breaks down, and the structure forming in the course of cyclic cooling resides in an excited nonequilibrium state, which exhibits typically higher values of tan δ and ε.[11] Note the asymmetric pattern of the anomalies in the tan $\delta(T)$ curves near the $IC\leftrightarrow C$ phase transition. The tan $\delta(T)$ curves obtained within the *C* phase both under cooling and heating fall off slowly as one moves away from T_c, whereas within the *IC* phase this relation becomes steeper. When measured under heating in the $T > T_c^h$ region, i.e. in the *IC* phase, the dielectric permittivity varies smoothly and close to the Curie-Weiss law. At the same time in the *C* phase, for $T < T_c^h$, ε varies rapidly with increasing *T*. This pattern of $\varepsilon(T)$ variation is close to the theoretically predicted temperature dependence of dielectric permittivity of ferroelectric crystals in the vicinity of T_c.[12] It should be pointed out that this trend in the $\varepsilon(T)$ dependence is characteristic only of unirradiated Rb_2ZnBr_4 samples, or of samples irradiated by a comparatively small dose. The $\varepsilon(T)$ curves obtained in the $T < T_c^c$ region under cooling fall off relatively slowly, which does not agree with the theoretical $\varepsilon(T)$ behavior.[12] The cause for these anomalous hysteresis phe-

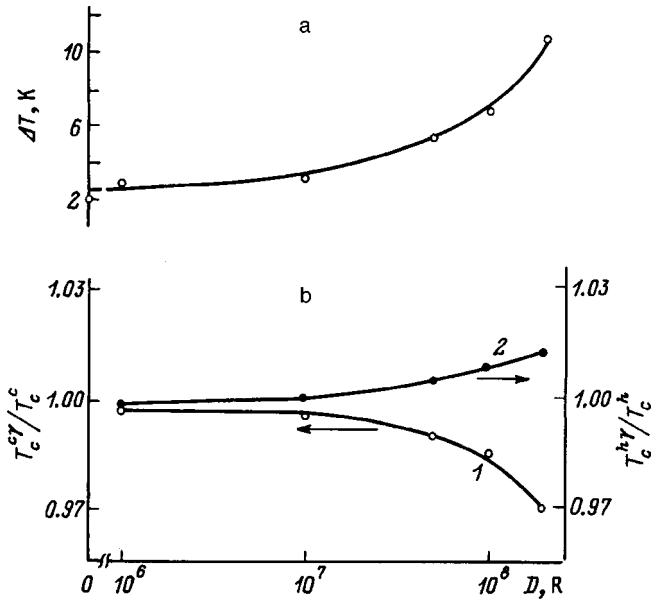

FIG. 4. Dose dependences of (a) the hysteresis ΔT in the PT temperature T_c, and relative change in transition temperature (b) under cooling, $T_c^{c\gamma}/T_c^c$ (*1*) and under heating, $T_c^{h\gamma}/T_c^h$ (*2*) where $T_c^{c\gamma}$ and $T_c^{h\gamma}$ are the transition temperatures of irradiated samples under cooling and heating, respectively, and T_c^c and T_c^h are those for unirradiated samples.

nomena was shown to lie in the formation of metastable states resulting from domain-wall pinning at lattice defects.[12–14] A theoretical analysis of modulated structures shows that, as the temperature is lowered into the region of existence of the *IC* phase, domain walls become narrow enough to allow their pinning at lattice planes, which makes domain-wall mobility dependent on the crystal-defect structure and, thus, gives rise to long-lived metastable states.[15–17]

Figure 4 presents dose dependences of the hysteresis ΔT in the transition temperature T_c and relative variations in the transition temperature observed under heating, T_c^h, and under cooling, T_c^c. As seen from Figs. 1–4, an increase in the irradiation dose D results, first, in a decrease of $\tan \delta_{\max}$ and $\varepsilon_{\max}$, both under cooling and under heating, second, an increased hysteresis in the properties under study, including the phase-transition temperature T_c, which becomes as high as $\Delta T \cong 11$ K at $D = 2 \times 10^8$ R (Fig. 4a), and, third, a washout of the anomalies. An increase in the irradiation dose brings about a growth of T_c^h under heating and a decrease of T_c^c in the cooling mode. It should be noted, however, that the change in T_c^c is somewhat larger than that in T_c^h, in other words, the increase of ΔT with dose is due mostly to the decrease of T_c^c in the cooling run (Fig. 4b).

Support of the Fund for Fundamental Research of Belarus (Grant F013.016) is gratefully acknowledged.

[1] T. Ueda, S. Iida, and H. Terauchi, J. Phys. Soc. Jpn. **51**, 3953 (1982).
[2] H. Kasano, H. Shigematsu, H. Mashiyama, Yu. Iwata, H. Kasatami, and M. Terauchi, J. Phys. Soc. Jpn. **63**, 1681 (1994).
[3] M. S. Novikova, R. A. Tamazyan, and I. P. Aleksandrova, Kristallografiya **40**, 37 (1995) [Crystallogr. Rep. **40**, 31 (1995)].
[4] M. A. R. Benyacar, E. Cattáneo, H. Ceva, H. Lanza, and L. Schmirgeld, Phys. Rev. B **37**, 3409 (1988).
[5] L. Schmirgeld, M. A. R. Benyacar, G. Carrau, H. Catau, H. Ceva, and H. Lanza, Radiat. Eff. Defects Solids **110**, 61 (1989).
[6] S. Leon-Gits, Phase Transit. **11**, 297 (1988).
[7] K. Hamano, H. Sakata, K. Yoneda, K. Ema, and S. Hirotsu, Phase Transit. **11**, 279 (1988).
[8] D. Durand and F. Denoyer, Phase Transit. **11**, 241 (1988).
[9] D. Zhang, Y. Zhu, H. Yang, W. Ma, and B. Gua, Acta Phys. Sin. **3**, 176 (1994).
[10] A. U. Sheleg, I. A. Afonskaya, K. V. Iodkovskaya, N. F. Kurilovich, and L. E. Soshnikov, Fiz. Tverd. Tela (St. Petersburg) **37**, 1492 (1995) [Phys. Solid State **37**, 807 (1995)].
[11] E. V. Peshikov, *Radiation Effects in Ferroelectrics* [in Russian], FAN, Tashkent (1986), 138 pp.
[12] B. A. Strukov, Izv. Akad. Nauk SSSR, Ser. Fiz. **51**, 1717 (1987).
[13] K. Hamano, T. Hishimuma, and K. Ema, J. Phys. Soc. Jpn. **50**, 2666 (1981).
[14] K. Hamano, Y. Ikeda, T. Fujimoto, K. Ema, and S. Hirotsu, J. Phys. Soc. Jpn. **49**, 2278 (1980).
[15] M. H. Jansen and P. Bak, Phys. Rev. B **29**, 6280 (1984).
[16] W. L. McMillan, Phys. Rev. B **14**, 1496 (1976).
[17] S. Aubry, Ferroelectrics **24**, 53 (1981).

Translated by G. Skrebtsov

Dielectric relaxation in thin-film metal–PZT-ferroelectric–metal structures

V. K. Yarmarkin and S. P. Teslenko

A. F. Ioffe Physicotechnical Institute, Russian Academy of Sciences, 194021 St. Petersburg, Russia
(Submitted February 17, 1998; resubmitted April 14, 1998)
Fiz. Tverd. Tela (St. Petersburg) **40**, 1915–1918 (October 1998)

The parameters of the Colle–Colle-type distribution function for the time constant of $Pb(Zr_{0.52}Ti_{0.48})O_3$ thin-film layers and the pattern of the bulk resistivity distribution through the film thickness have been derived from measured frequency dependences of the complex capacitance of metal–PZT-ferroelectric–metal thin-film structures within the 100 Hz to 100 MHz range. © *1998 American Institute of Physics.* [S1063-7834(98)03110-4]

Progress in the physics of thin ferroelectric films depends on obtaining reliable information on their local structure and the distribution of electrical parameters through the film thickness, which are dominated by the specific crystallization features in thin (less than 1 μm thick) films and their interaction with the substrate and the environment during preparation. Formation of near-surface pyrochlore-structure layers in thin lead-zirconate-titanate (PZT) ferroelectric films can result in a low-frequency dispersion of dielectric permittivity in films, originating from interlayer Maxwell-Wagner polarization.[1] Determination of the dielectric-relaxation parameters of films may, in its turn, provide information on the distribution of the electrical parameters in films throughout their thickness.[2] This work reports a study of this problem in thin $Pb(Zr_{0.52}Ti_{0.48})O_3$ sol-gel films prepared on platinum-coated silicon substrates.

1. EXPERIMENTAL METHOD

The study was carried out using Ni-PZT-Pt thin-film capacitor structures prepared on the surface of preoxidized Si(100) plates.[3,4] The silicon oxide layer was 500 nm thick. The lower electrode (100-nm Pt coating on a 10-nm Ti sublayer for better adhesion) was deposited by rf magnetron sputtering. We used solutions of Pb, Zr, and Ti methoxyethanolates in methoxyethanol with a concentration of 0.2 mol/l and with Pb/Zr/Ti ratios of 1.05/0.52/0.48 (a slight, 5–10 mol %, Pb excess was added to the solutions to compensate the evaporation of lead in the course of the film crystallization anneal performed at 550 °C for 20 min). The PZT film thickness was ~200 nm. As the upper electrode served dia. 0.2-mm, 100-nm-thick Ni coatings deposited on the film surface by thermal evaporation through a mask.

The frequency dependences of the complex structure capacitance were studied at frequencies from 100 Hz to 100 MHz. Below 1 MHz, one used bridges (TM-351-G, MTsE-12A, and E7-12) permitting direct measurement of the capacitance and loss tangent, within the 60–400-kHz range, the measurements were done with a *E*9-4 Q-meter, and above 0.5 MHz, with an VM 508 impedance meter. In the latter case (i.e., above approximately 1 MHz), the spurious coupling between elements of the circuit under study was taken into account by simulating the sample holder and the corresponding part of the impedance-meter measurement circuit by an equivalent circuit containing R, L, and C elements, whose magnitude was derived from the frequency dependences of the impedance under short-circuit condition. The parameters were chosen taking into account the skin effect in connecting wires by a minimum χ^2 fit in interactive mode using the Mathcad package. The impedances $Z(\omega)$ of the structures found in this way were used to calculate their capacitances, $C=\mathrm{Im}(Z)/\omega|Z|^2$, and the loss tangent, $\tan\delta=-\mathrm{Re}(Z)/\mathrm{Im}(Z)$, $Z=|Z|\exp\{j\varphi\}$, where f, $\omega=2\pi f$, and φ are

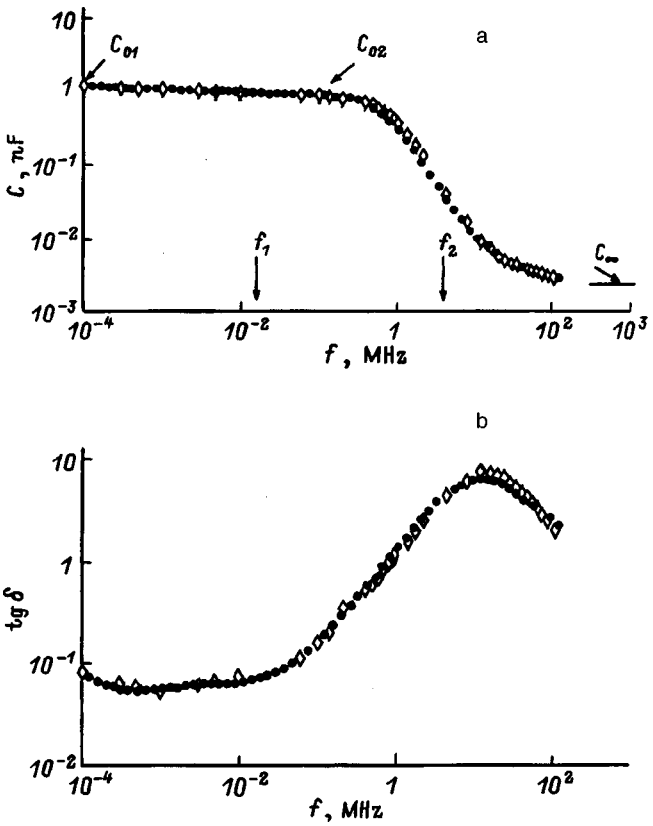

FIG. 1. Frequency dependence of (a) capacitance and (b) loss tangent for a Ni-PZT-Pt structure on silicon. C_{01} and C_{02} are, respectively, the low- and high-frequency structure capacitances for the relaxation process with characteristic frequency f_1, and C_{02} and C_∞ are the same parameters for the relaxation process with characteristic frequency f_2.

the frequency, circular frequency, and phase of the measuring voltage, respectively.

2. RESULTS AND THEIR DISCUSSION

The values of C and $\tan\delta$ over the total frequency-measurement range are presented in Fig. 1. The pattern of the frequency dependences characteristic of the structures under study here is typical of relaxation processes. The experimental values of C and $\tan\delta$ were used to calculate the complex capacitance of the structures $C^*=C(1-j\tan\delta)$ and to determine the real (C') and imaginary (C'') parts of C^* (Fig. 2), to be subsequently employed in the data treatment based on the standard Cole-Cole diagrams. The numbers in Fig. 2 identify experimental data obtained at various frequencies within the measurement range at a fixed amplitude of 20 mV. The diagram shown in Fig. 2 evidences the existence in the structures under study of at least two relaxation processes. Bearing this in mind and invoking the dc conductivity data for the structures, the frequency dependence of C^* was fitted by a function containing two relaxation-type terms and a term taking into account the dielectric losses due to the dc conductivity[5]

$$C^*=\varepsilon^* C_0, \tag{1}$$

where

$$\varepsilon^*=\varepsilon_\infty+\frac{\varepsilon_{01}-\varepsilon_{02}}{1+(j\omega\tau_1)^{1-\alpha_1}}+\frac{\varepsilon_{02}-\varepsilon_\infty}{1+(j\omega\tau_2)^{1-\alpha_2}}-\frac{j}{\varepsilon_0\omega\rho},$$

$C_0=\varepsilon_0 A/d$, ε_0 is the dielectric permittivity of vacuum, and A, d, and ρ are the area, thickness, and effective bulk resistivity of the structure, respectively.

The parameters entering Eq. (1) were found by fitting the calculated curves to experimental points in the Cole-Cole diagram (Fig. 2) using as the zero approximation for C_∞, C_{01}, C_{02}, $\tau_1=1/f_1$, and $\tau_2=1/f_2$ the values derived from the frequency dependences of the capacitance and the dielectric losses plotted in Fig. 1. The rms deviation of experimental from calculated data was 12% for the frequency dependence of the structure's capacitance, and 13% for that of the loss tangent. The parameters obtained in this calculation, which characterize the relaxation processes in the structure under study, are presented in Table I.

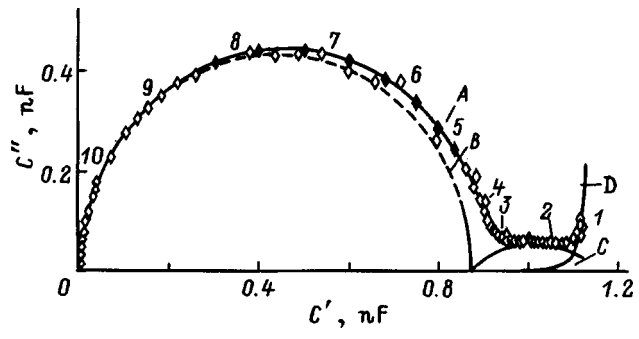

FIG. 2. Cole-Cole diagram (A) and components (B,C,D) of the relaxation process in the Ni-PZT-Pt structure on silicon. A—envelope calculated from Eq. (1), B—high-frequency relaxation process, C—low-frequency relaxation process, D—contribution due to dc conductivity. The numbers label some of the experimental data obtained at the following measurement frequencies (MHz): 0.0001 (*1*), 0.001 (*2*), 0.01 (*3*), 0.1 (*4*), 0.2 (*5*), 0.4 (*6*), 0.7 (*7*), 1.0 (*8*), 1.8 (*9*), and 4.4 (*10*).

TABLE I. Experimental values of the parameters characterizing the dielectric relaxation in Ni-PZT-Pt structures.

C, nF			τ, s		α		ρ,
C_∞	C_{01}	C_{02}	τ_1	τ_2	α_1	α_2	$\Omega\times$cm
0.002	1.15	0.875	5.56×10^{-5}	2.17×10^{-7}	0.49	0.05	5×10^8

The absence of any dispersion of ε^* in bulk ceramic PZT samples of the same composition[6] permits a conclusion that the features observed in the dielectric spectra of the thin-film structures can be assigned to interlayer Maxwell–Wagner relaxation originating from an inhomogeneous structure of the films through their thickness.[6,7] The high-frequency process characterized by a narrow distribution in relaxation times ($\alpha_2<0.1$) can be associated with the metal-electrode–ferroelectric-film interface, and the low-frequency one, exhibiting a broad relaxation-time spectrum ($\alpha_1\cong0.5$), with the presence in near-electrode regions of the film of layers with a higher conductivity due to their being oxygen deficient.[8] Taking into account the smooth variation of oxygen concentration in the near-electrode regions of sol-gel PZT films, which was demonstrated by layer-by-layer Auger spectroscopy,[9] one cannot consider the simple two-layer model used to describe the structure of such films in Refs. 1, 6, 7 as anything but a rough approximation. The model of dielectric relaxation in multilayer structures with smoothly varying parameters[2] appears to be a more adequate approach in trying to interpret the observed dispersion pattern of the complex capacitance of structures in the low-frequency domain. The main propositions of this model are as follows:

1) Each layer in a structure is characterized by a coordinate-dependent time constant $t(x)=\varepsilon_0\varepsilon(x)\rho(x)$;

2) A distribution function $g(t)$ of the layer's time constant t is introduced, which is expressed in terms of the normalized layer thickness dx/L:

$$g[t(x)]dt=\frac{\varepsilon_\infty}{\varepsilon(x)}\frac{dx}{L},$$

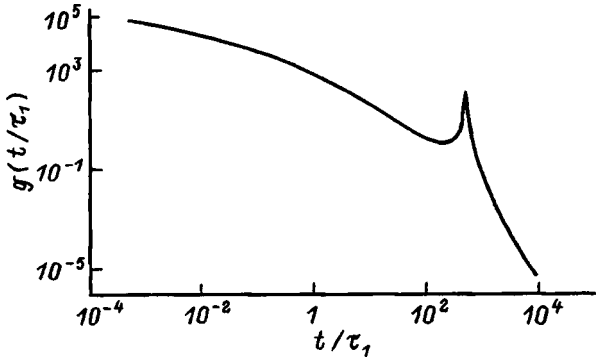

FIG. 3. Distribution function of the layer time constant for the PZT film in the Ni-PZT-Pt structure on silicon.

where L is the geometric thickness of the structure;

3) The integral

$$L(t)=\int_0^t g(u)du$$

expresses the effective normalized thickness of the structure's layer in which the time constant does not exceed t;

4) The complex dielectric permittivity of a structure can be expressed both through the distribution function of relaxation time $\varphi(\tau)$, which is conventionally used in describing such structures in the relation

$$\varepsilon^*=\varepsilon_\infty+(\varepsilon_0-\varepsilon_\infty)\int_0^\infty \frac{\varphi(\tau)}{1+j\omega\tau}d\tau-\frac{j}{\omega\rho},$$

and through function $g(t)$

$$\frac{1}{\varepsilon^*}=\frac{1}{\varepsilon_\infty}\int_0^\infty \frac{g(t)}{1+\dfrac{1}{j\omega t}}dt.$$

The analytic expression for $g(t)$ corresponding to Cole–Cole-type relaxation has the form[2]

$$g(t)=\frac{\sin[(1-\alpha)\pi]\varepsilon_\infty}{(\varepsilon_0-\varepsilon_\infty)\pi t\left[\left(\dfrac{t}{\tau}\right)^{1-\alpha}(G+1)^2+\left(\dfrac{\tau}{t}\right)^{1-\alpha}G^2+2G(G+1)\cos[(1-\alpha)\pi]\right]},$$

where

$$G=\frac{\varepsilon_\infty}{\varepsilon_0-\varepsilon_\infty}-\frac{t}{\rho(\varepsilon_0-\varepsilon_\infty)}.$$

Figure 3 plots the distribution function $g(t)$ calculated using the data in Figs. 1 and 2 for the low-frequency relaxation process. To estimate the variation of electrical resistivity $\rho(t)$ through the film thickness, the dielectric permittivity $\varepsilon(x)$ was approximated by a monotonically increasing function with only two of its values fixed, namely, on the surface, $\varepsilon_s=40$ (for the pyrochlore phase in near-surface regions), and in the bulk of the film, $\varepsilon_b=800$ (derived from layer-by-layer studies of films performed earlier by x-ray diffraction and electron-microscopy[10,11]). The $\rho(x)$ relation presented in Fig. 4 was calculated from the experimentally measured function $g(t)$ by varying the $\varepsilon(x)$ function with due account of the above restrictions; the smoothness of the $\rho(x)$ function was taken as a good-fit criterion. The $\rho(x)$ graph in Fig. 4 was used to estimate the total film thickness as ~ 0.2 μm and the thickness of the near-electrode high-conductivity transition layer as ~ 0.03 μm, which coincide, accordingly, with the film thickness determined with an interference microscope[3] and with the thickness of the oxygen-deficient near-surface layers in PZT films[8] which were similar in the composition and preparation technique. In addition, it was shown[10,11] that the 30–50-nm thick near-surface film regions directly adjoining the upper Ni electrode differ substantially in crystal structure from the material in the bulk of the films, thus implying a noticeable change of the chemical composition in these regions. This suggests that the film thickness range in Fig. 4 from $x=0.001$ to $\cong 0.03$ μm possesses a higher conductivity (compared to the $0.03 \leqslant x \leqslant 0.2$ μm region) indicating the presence in the film of a near-surface transition layer adjoining the Ni electrode in the Ni-PZT-Pt structures under study.

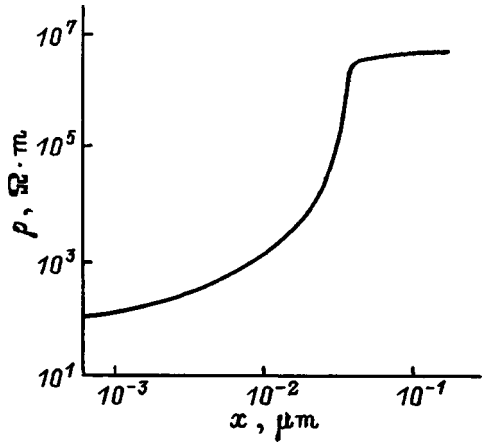

FIG. 4. Distribution of bulk resistivity through the thickness of the PZT film in a Ni-PZT-Pt structure on silicon. Thickness x is reckoned from the Ni electrode in the structure.

The authors express their gratitude to V. V. Lemanov for fruitful discussions.

Support of the Russian Fund for Fundamental Research (Grant 98-02-18164) and of the ''Physics of Solid-State Nanostructures'' (Grant 97-2017) is gratefully acknowledged.

[1] Z. Surowiak, D. Czekaj, A. A. Bakirov, E. V. Sviridov, and V. P. Dudkevich, Integr. Ferroelectrics **8**, 267 (1995).
[2] Y. Kita, J. Appl. Phys. **55**, 3747 (1984).
[3] V. K. Yarmarkin, N. V. Zaĭtseva, S. V. Shtel'makh, and A. V. Motornyĭ, Fiz. Tverd. Tela (St. Petersburg) **37**, 324 (1995) [Phys. Solid State **37**, 176 (1995)].
[4] V. V. Lemanov, N. V. Zaitseva, S. V. Shtel'makh, A. V. Motorny, and V. K. Yarmarkin, Ferroelectrics **170**, 231 (1995).
[5] N. P. Bogoroditskiĭ, Yu. M. Volokobinskiĭ, A. A. Vorob'ev, and B. M. Tareev, *Theory of Dielectrics* [in Russian], Energiya, Moscow–Leningrad (1965), 344 pp.
[6] M. Sayer, A. Mansingh, A. K. Arora, and A. Lo, Integr. Ferroelectr. **1**, 129 (1992).

[7] M. Sayer, D. S. McIntyre, M. Sedlar, A. Mansingh, R. Tandon, and V. Chivukula, Integr. Ferroelectr. **11**, 277 (1995).
[8] A. S. Carrico, C. A. Paz de Araujo, T. Michara, and H. Watanabe, Integr. Ferroelectr. **13**, 247 (1996).
[9] L. E. Sanchez, D. T. Dion, S. Y. Wu, and I. K. Naik, Ferroelectrics **116**, 1 (1991).
[10] V. V. Lemanov and V. K. Yarmarkin, Fiz. Tverd. Tela (St. Petersburg) **38**, 2482 (1996) [Phys. Solid State **38**, 1363 (1996)].
[11] V. V. Lemanov, G. N. Mosina, L. M. Sorokin, S. V. Shtel'makh, and V. K. Yarmarkin, Fiz. Tverd. Tela (St. Petersburg) **38**, 3108 (1996) [Phys. Solid State **38**, 1700 (1996)].

Translated by G. Skrebtsov

LATTICE DYNAMICS. PHASE TRANSITIONS

Formation of a bistructure of a solid in a computer experiment

V. A. Lagunov and A. B. Sinani

A. F. Ioffe Physicotechnical Institute, Russian Academy of Sciences, 194021 St. Petersburg, Russia
(Submitted April 7, 1998)
Fiz. Tverd. Tela (St. Petersburg) **40**, 1919–1924 (October 1998)

Molecular-dynamics was used to investigate the structural changes occurring in a three-dimensional solid when the solid is transferred from an amorphous into a crystalline state. Crystal cells of a new type — pentadecahedrons with five square lateral faces and ten regular triangular faces at the vertices of a cell — were found for the first time in a computer experiment. It is shown that a bistructure consisting of crystal cells of different types, including cells with five-fold symmetry axes, are stable in the solid. © *1998 American Institute of Physics.* [S1063-7834(98)03210-9]

In Ref. 1, molecular-dynamics investigations of an amorphous body were performed in a two-dimensional anharmonic model. It was of interest to expand these investigations and to go on to study the crystallization of three-dimensional solids. The same algorithm as the one in Ref. 1 was used to prepare the initial sample. According to this algorithm, a sample with a random distribution of atomic coordinates is formed in a fixed region of space. The algorithm is constructed so that only atoms located farther away than a fixed critical distance from all atoms in the model are retained. Another parameter of the algorithm is the maximum number of coordinates chosen, usually of the order of one million.

A modified Lennard–Jones potential

$$U(r)=D[(a/r)^{12}-2(a/r)^{6}]K(r) \tag{1}$$

was used to describe the force interaction between atoms. Here a is the equilibrium interatomic distance, D is the dissociation energy of a pair of atoms, r is the distance between the atoms, and $K(r)$ is a factor given by the relations

$$K(r)=1, \quad r\leqslant r_1,$$

$$K(r)=[1-((r-r_1)/(r_2-r_1))^2]^2, \quad r_1<r<r_2,$$

$$K(r)=0, \quad r\geqslant r_2. \tag{1a}$$

The choice of the values of r_1 and r_2 is determined by the following requirements: First, Eqs. (1a) are taken into account on the descending branch of the curve of the variation of the interaction force acting between atoms and, second, the cutoff radius r_2 of the potential must remain less than the radius of the second coordination sphere of a face-centered cube. In the present work r_1 and r_2 were equal to 1.11 and 1.72 (in units of the equilibrium interatomic distance a), respectively.

The equations of motion of the atoms were integrated by the method of second finite differences, while the interatomic interaction forces required for this were determined by differentiating expression (1) numerically with the increment of r equal to $0.01a$. The transition from the two- to the three-dimensional model did not radically change the properties of the interacting atoms. In the model adopted, the behavior of particles containing about 1000 atoms can be studied.

A series of computer experiments was performed on a sample obtained by randomly throwing in atoms. The aim of the experiments was to study the formation kinetics of crystalline inclusions during cooling of an amorphous material. To preserve structure, the model sample was cooled by the quenching method developed in Ref. 1. According to this method, the kinetic energy of the atoms was decreased to zero every time it reached the maximum value. This decrease of the kinetic energy (and the corresponding increase of the potential energy) was performed as long as the decrease remained above an established critical value.

The spherical sample obtained was repeatedly heat treated in order to transfer it from an amorphous into a crystalline state. Prior to each treatment, the sample was given a spherical shape of prescribed size by removing and then randomly adding atoms. Experience showed that the atoms reached only a surface layer (no closer than 96% of the radius of the sample). This shows that large pores, where the discarded atoms could end up, do not arise in the central region of the sample during the motion of the atoms. Quenching at each even numbered test was preceded by a short period (with a duration equal to approximately 20 lattice vibrations of the atoms) during which the sample was held at an average kinetic energy of the atoms equal to half the dissociation energy D. At this temperature evaporation of single atoms was observed in some cases.

The coordination number of each atom was determined using the program developed, which made it possible to estimate the number of nearest neighbors. It is known (see, for example, Ref. 2) that in face-centered cubic (fcc) and hexagonal close-packed (hcp) lattices this number equals 12. The increase in the number of ''crystal'' atoms with coordination number 12 during heat treatment of the sample is

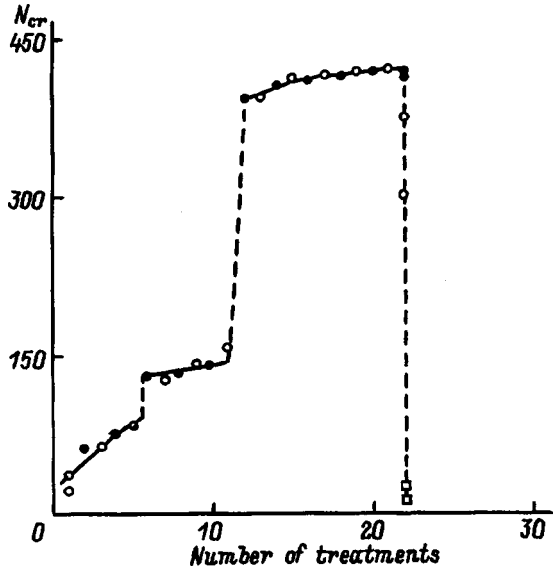

FIG. 1. Change in the number of crystal cells N_{cr} as a result of heat treatment of the sample. The open circles were obtained after quenching and the filled circles were obtained after annealing with average kinetic energy of an atom $E/n=0.5D$ followed by quenching.

shown in Fig. 1. One can see that jump-like growth of the crystal cells at the 12th treatment of the sample was observed against the background of a quite slow increase in the number of crystal cells. At this stage the number of crystal cells more than doubled and the ratio of fcc and hcp cells changed from 1.7 to 0.5. The degree of crystallinity, determined as the ratio of the number of ''crystal'' atoms to the number of all atoms in a measuring cell, increased from 32 to 81%. All calculations were performed in a cell smaller in size than the sample, not including the surface layer of the sample. An increase in the density of the sample and the average potential energy of the atoms correlating well with the number of crystal cells was observed in parallel with an increase in the crystallinity of the sample.

The initial porosity of the sample after atoms were randomly thrown in was equal to 49%, but it could not be maintained at this high value. Even after the first quench, performed to obtain an amorphous state of the material under normal conditions, it decreased to 7%. Such a sharp decrease of the porosity, as compared with the two-dimensional case, is apparently due to the larger movement of the atoms in the interior than in the two-dimensional case.

Even after the first heat treatment, crystal cells with a coordination number of 12 appear in the sample. To recognize and differentiate them, changes were made in the program analyzing the arrays of data for the coordinates of the atoms. The resulting algorithm was capable of not only revealing crystal cells but also separating them according to the type of crystal structure.

The types of crystal cells observed in the sample investigated are shown in Fig. 2. We note that, at the end of each quench, when they become immobile, the atoms from a complicated conglomerate of microparticles coupled with one another. They form with their neighbors a spatial network of regular triangles and squares. In the experiment, as one can see in the figure, four basic types of crystal cells with coordination number 12 are observed. The cells of the types *A* and *B* have in common the presence of six square faces and eight triangles. If the cells of the first type possess central symmetry, where the square faces do not have edges in common, then, in the second case, mirror symmetry with three pairs of squares and four pairs of triangular faces is observed. Type *A* cells are fcc cells characteristic for copper and aluminum structures,[2] while type *B* cells are bilayer hcp

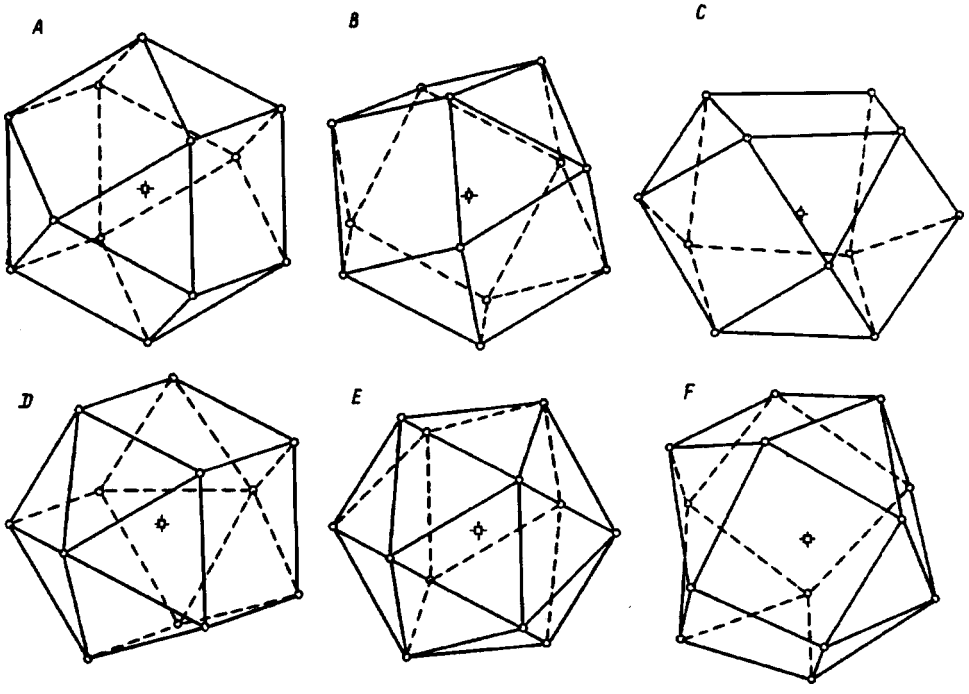

FIG. 2. Types of crystal cells observed in the computer experiment.

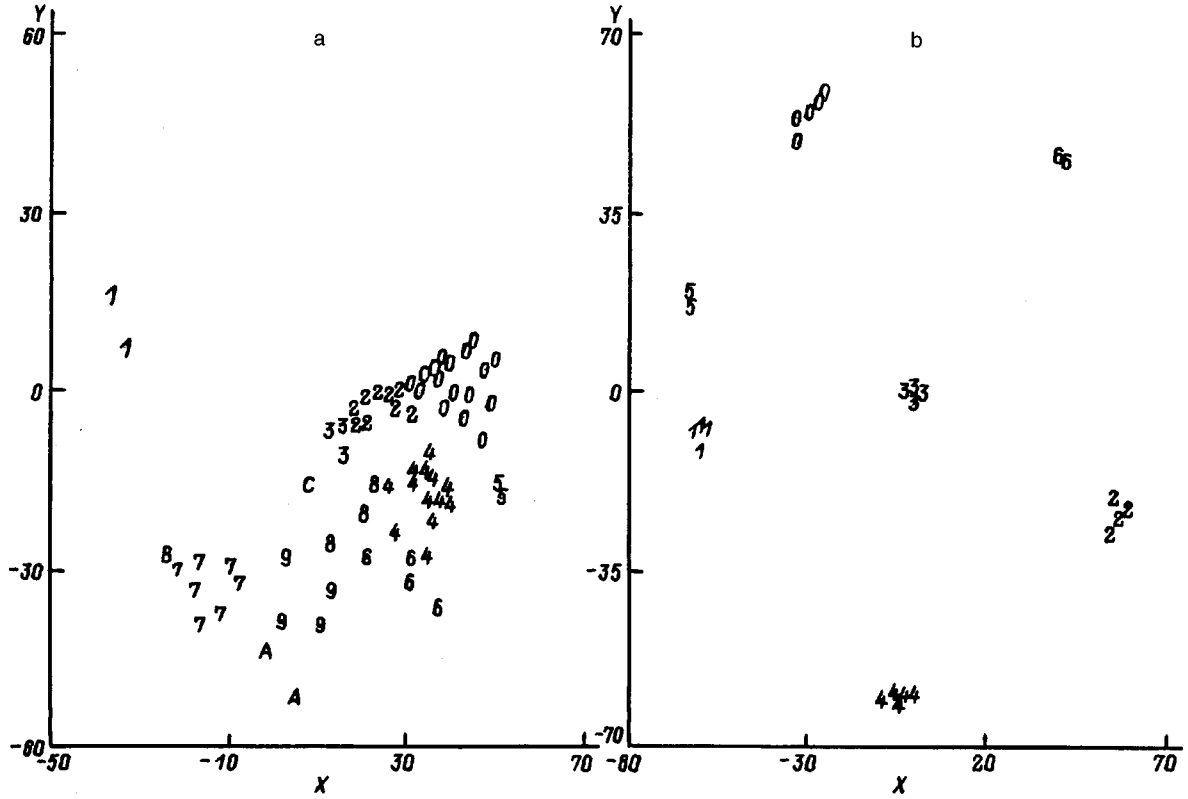

FIG. 3. Picture of the intersection of the continuations of the edges of fcc cells of a projecting plane before (a) and after (b) a critical transition.

cells characteristic of zinc.[2] The *A* and *B* cells are capable of forming crystals.

Crystal cells of the types *D* and *E*, which possess fivefold axes, also arise in the computer experiment. For the *D* cells the presence of five square and ten triangular faces, coupled with one another, is characteristic. In the *A* and *B* cells all 12 atoms are equivalent and have four identical bonds with their neighbors, whereas in the *D* cell there are two atoms which are separated from one another and possess five bonds, fixing the orientation of the cell in space. Cells of high symmetry, type *E* cells, possessing 20 triangular faces are also observed in the experiment. These are icosahedral cells. It is not difficult to show that they are obtained if one mirror-symmetric half of a *D* cell is rotated by 36° relative to the other half.

Figure 2 also shows crystal cells with coordination numbers 11 and 13. These cells possess the same number of bonds between atoms and their neighbors. The search for such cells in the sample was performed using a program. A type-*C* cell with a coordination number of 11 can be interpreted as being the result of an interaction of a vacancy with a *D* cell, where the front atom in the figure occupies an intermediate position, replacing the absent atom, while an *F* cell with a coordination number of 13 can be interpreted as being the result of an interaction of an *A* cell with an interstitial atom, strongly distorting the lower half of the cell.

As noted above, strong changes in the crystallinity of the material were observed after the 12th treatment of the sample, when the number of crystal cells in the sample immediately more than doubled. The qualitative changes which occurred in the sample make it necessary to study the relative orientation of the crystal cells. A program making it possible to investigate orientational effects was developed. It projects onto a plane located 100 interatomic distances away from the origin the emergence of the best cells, with respect to orientation of the edges, placed at the origin. Comparing Figs. 3a and 3b, where pictures of the intersection of the edges of fcc cells with this plane before and after a critical transition are shown, attest to a qualitative change in the structure of the sample and ordering of the orientation of the crystal cells as a result of the transition.

Before the transition, the orientation of neighboring cells was characterized by a quite large spots in Fig. 3a, indicating a large disorientation of the cells in a group, and there was also a large number of cells with arbitrary orietation which are not coupled with one another. After a transition, the isolated cells completely vanished. Only several groups of cells with a small disorientation angle remained. The largest group contained 54 atoms in the case of the fcc cells, and the indicated angle was less than 1 degree. A similar picture was also observed in the case of hcp cells.

A program was developed to distinguish nuclei of crystallites in the sample. The parameters of this program are the admissible disorientation angle of the cells in a crystallite and the number N_{cr} of atoms in the shell of the cell that have the same orientation as the central atom. By varying the second parameter it is possible to determine the composition of the nuclei formed in the presence of cells of different types. Figure 4 displays data for a sample before a critical transition with $N_{cr}=4$. They indicate the appearance of three spatially localized nuclei of a fcc crystallite: a single-layer crystallite 0 and three-layer crystallites 2 and 4. The nuclei of the hcp

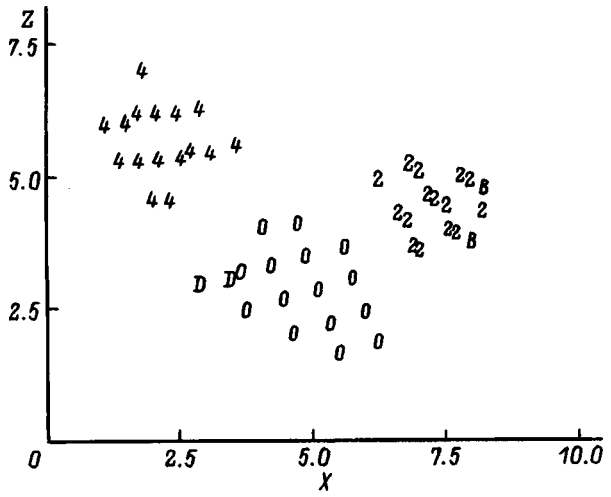

FIG. 4. Nuclei of crystallites in the sample before a critical transition period.

crystallites labelled with letters are only indicated in the figure because of their small number, and as one can see the type-*B* cells attach to crystallites 2. Indeed, as the measurements of the angle between the oriented directions of their edges, which equals only 4.4°, show they have a close orientation.

Similar crystallites can be distinguished after the critical transition only if $N_{cr} \leqslant 6$. This indicates that the sample contains cells with the same number of fcc and hcp atoms in the outer shell of the cell. This is also indicated by the data, obtained from the computer experiment, on the close orientation of some edges of these cells, which for all groups of fcc and hcp cells is less than one-half of one degree. All this gives a basis for treating the fcc and hcp cells as being of the same type when separating crystallites.

The fcc and hcp cells, which have a similar structure, are actually different in terms of their functional possibilities. Thus, our data show that fcc cells never contain atoms which have characteristic cells with five-fold symmetry axes and that the icosahedral cells consist only of type-*D* atoms. At the same time, the high predisposition of fcc and hcp cells to consolidate should be underscored.

The observed more than order-of-magnitude increase in the number of cells with a five-fold symmetry axis is of greatest interest. As already noted, cells with a coordination number of 12 which possess a five-fold symmetry axis appeared in the sample at the very start of annealing. The increase in their number after a critical transition is especially noticeable. The formation of noncubic structural units was observed earlier[3] during rapid cooling of manganese-aluminum alloy. Later,[4,5] this result was attributed to the appearance of a quasicrystalline structure with icoshedral cells. Here, relying on the computer data, we shall give a somewhat different interpretation of the observed structure with cells of five-fold symmetry.

Analysis of the array of data on the coordinates of the atoms shows that a crystal structure appears at two levels. A component part of the structural framework formed by cells of five-fold symmetry is the linear crystal shown in Fig. 5. For clarity, only half of its cells are shown in this figure. As one can see, the crystal consists of a linear formation of rigidly coupled cells, among which is present an icosahedral cell (the only one in the crystal), which changes the rotation angle of the entire segment of the crystal along the crystal axis by 36°.

The data on the arrangement of such crystals in a sample are presented in Fig. 6 in two projections. Here like symbols correspond to cells of the same orientation, which form linear crystals similar to that shown in Fig. 5. The sample was first turned so that the main linear crystal was perpendicular to the first projection. This made it possible to examine the properties of the observed structure in greater detail. It follows from the figure that the structure of the linear crystals is a complicated but symmetric formation permeating the entire sample. In our case it consists of a pair of star-shaped groups of atoms, arranged one above the other at a distance of six interatomic intervals. Each group of atoms in turn consists of an intersection of six small crystals, similar to those shown in Fig. 5, at the location of the icosahedral cell, if such a cell is observed in the experiment. In Fig. 6 it is marked with an asterisk. The fact that the projections of the upper and lower rays of the crystals coincide shows that the orientation of the entire group of atoms of five-fold symmetry is the same.

The second-level structure is created by fcc and hcp cells, filling the structure described above. According to the data obtained, the first structure plays a decisive role in setting the orientation of the cells of the rest of the atoms. Indeed, for the largest crystallite (215 atoms), consisting of fcc and hcp cells, the disorientation of the cells with the structure arising equals only 0.15°. Moreover, spatially separated crystallites are often observed to have the same orientation.

The question of defects inside a crystallite is of great interest. Defects can be seen by examining a sample in transmission with the background from the front and back surface layers of the sample removed, concentrating attention on the changes in the composition of the central cells. For this, the central part of a sample was investigated. Only cells with coordination numbers different from 12 were recorded. Figure 7 shows similar data for a sample before and after a

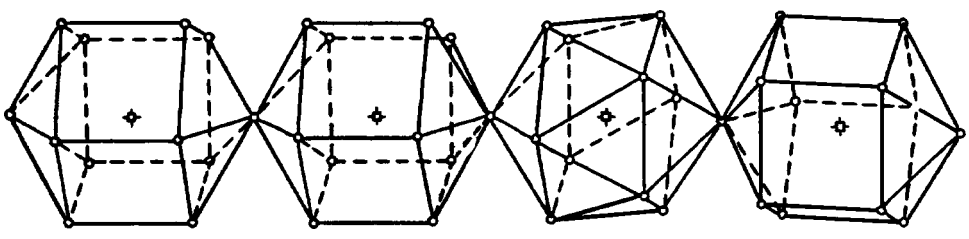

FIG. 5. Linear crystal consisting of cells with a five-fold symmetry axis.

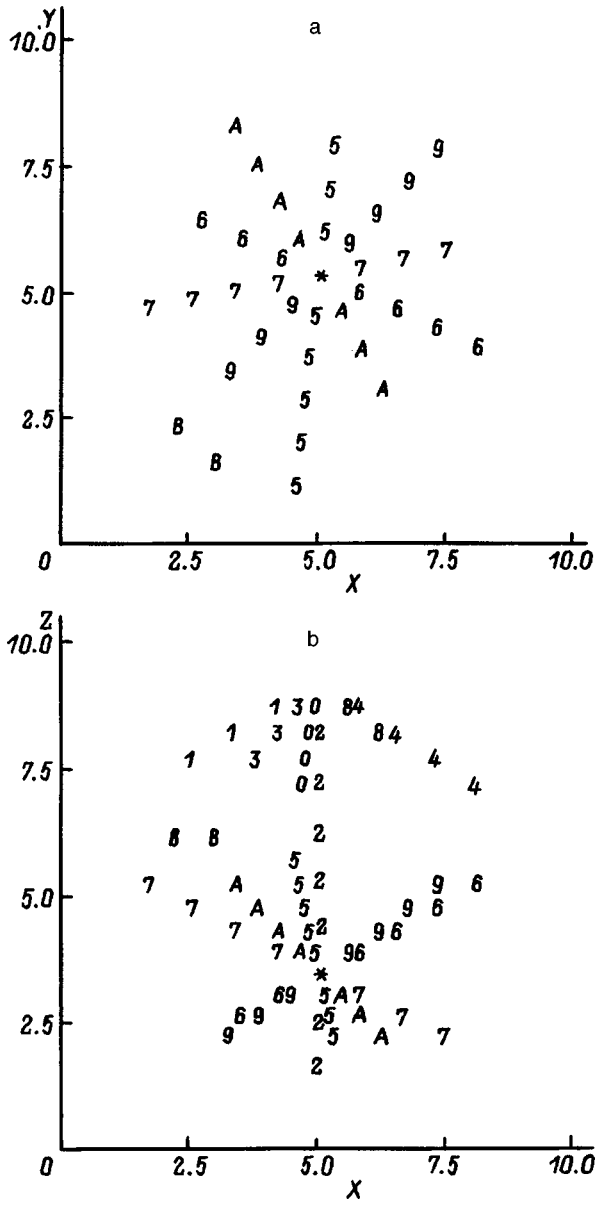

FIG. 6. Arrangement of cells which have five-fold symmetry in a sample after a critical transition in two projections.

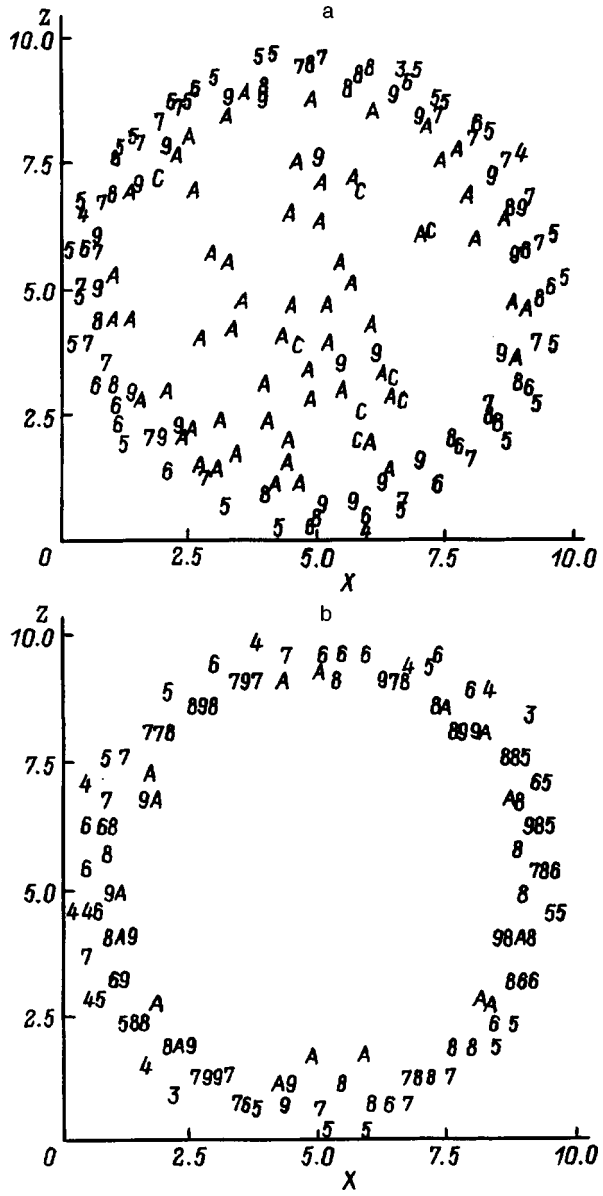

FIG. 7. Distribution of the coordination number of the atoms in the sample before (a) and after (b) a critical transition.

critical transition. Here the numbers correspond to the value of the coordination number decreased by 1; the symbol *A* corresponds to ''vacancy'' cells with a coordination number of 11, while the symbol *C* corresponds to cells with an interstitial atom. It follows from the figure that a large number of ''vacancy'' cells, aligned in chains and concentrated, most likely, along grain boundaries, were observed in the sample before a transition. There is also a small number of interstitial atoms. As a rule, these atoms are located next to the ''vacancy'' cells, which indicates that they are capable of rapid recombination.

A different picture is observed after the critical transition. In this case, only atoms with a coordination number of 12 remain inside the central part of a sample, though cells with different orientations are also present in this part, as the data from our measurements show. This means that the grain boundaries consist of only cells with 12 nearest-neighbor atoms. It is interesting that the presence of a cell structure with five-fold symmetry inside the sample does not always require a change in the orientation of the crystallites. The absence of different structural defects, which at first glance seems paradoxical, is probably attributable to the fact that fcc and hcp cells and cells with five-fold symmetry, which have different shapes, are combined in them.

The observed bistructure is a quite stable formation. At the end of the series of experiments different annealings were performed to determine the temperature at which the structure breaks down. From Fig. 1, which shows annealing data with average kinetic energy of the atoms equal to 1.0, 2.0, 2.13, 2.27, and 2.4 times the dissociation energy D of a pair of atoms, it follows that this structure vanishes when the average thermal energy of the atoms equals $2.27D$, while its

average potential energy, determining the energy of sublimation of the crystal, according to our measurements, equals $5.45D$.

In summary, this investigation showed that when a sample is quenched to preserve its amorphous structure, at a certain stage a polycrystal consisting of bilayer fcc and hcp cells, which was permeated by a symmetric structure consisting of cells with five-fold symmetry, determining the property of the entire sample, was obtained.

[1] V. A. Lagunov and A. B. Sinani, Fiz. Tverd. Tela (St. Petersburg) **38**, 1791 (1996) [Phys. Solid State **38**, 987 (1996)].
[2] H. W. King in *Physical Metallurgy*, edited by R. W. Cahn and P. Haasen [North-Holland, N. Y., 1983, 3rd edition; 1st edition, Mir, Moscow, 1967, Vol. 1, p. 11].
[3] D. Shechtman, I. Blech, D. Gratias, and J. W. Cahn, Phys. Rev. Lett. **53**, 1951 (1984).
[4] C. Janot and J. M. Dubois, Phys. F **18**, 2303 (1988).
[5] I. A. Ovid'ko, *Defects in Condensed Media* [in Russian], Znanie, St. Petersburg, (1991), 247 pp.

Translated by M. E. Alferieff

LOW-DIMENSIONAL SYSTEMS AND SURFACE PHYSICS

Interface optical anisotropy in a heterostructure with different cations and anions

E. L. Ivchenko and A. A. Toropov

A. F. Ioffe Physicotechnical Institute, Russian Academy of Sciences, 194021 St. Petersburg, Russia

P. Voisin

L'École Normal Supérieure, 75005 Paris, France

(Submitted April 21, 1998)
Fiz. Tverd. Tela (St. Petersburg) **40**, 1925–1931 (October 1998)

A theory of optical anisotropy and quantum-confined Pockels effect in CA/C′A′(001) quantum-well structures with different cations and anions, i.e. for C≠C′ and A≠A′, has been developed. The theory is based on a generalized effective-mass method, in which the boundary conditions for the envelope functions were constructed taking into account the mixing of heavy- and light-hole states under normal incidence of the hole on the interface. It is shown that an absorption anisotropy in interband transitions occurs for different mixing coefficients t_{l-h} in the boundary conditions for the right-hand (A-C′) and left-hand (A′-C) interfaces. An analysis is made of the interface contribution to the anisotropy induced by an external electric field for coinciding and different band offsets at the interfaces. The microscopic sp^3s^* tight-binding model is used to estimate the difference between the t_{l-h}(A-C′) and t_{l-h}(A′-C) coefficients. © *1998 American Institute of Physics.* [S1063-7834(98)03310-3]

Carrier quantum confinement in quantum-well structures and redistribution of electron density between adjacent layers in superlattices are the best known manifestations of band offsets at heteroboundaries in nanostructures. By lowering the translation and point symmetry of the system, the presence of interfaces can result not only in mixing of electronic states with wave vectors $\mathbf{k}=(k_x,k_y,k_z)$ and $\tilde{\mathbf{k}}=(k_x,k_y,-k_z)$ in the same subband (z is the growth axis of the structure), but in intervalley or intersubband mixing.[1,2] This work studies theoretically lateral optical anisotropy of CA/C′A′(001) quantum-well structures caused by heavy- and light-hole state mixing at the interfaces.

Figure 1 shows the arrangement of atoms at the heteroboundary in a CA/C′A(001) structure having a common anion, as is, for instance, GaAs/AlAs. The interface is the (001) plane with anions A, for which the nearest neighbors on both sides of the plane are cations C and C′. An ideal single heterojunction has point symmetry C_{2v}, which includes a two-fold axis $C_2\|[001]$ and two reflection planes (110) and $(1\bar{1}0)$. Mirror rotation through 90° about the principal axis $z\|[001]$ turns the interfaces C′-A-C (Fig. 1a) and C-A-C′ (Fig. 1b) into one another. Therefore the CA/C′A(001) quantum-well structure possesses a sufficiently high symmetry D_{2d} for which there is no optical anisotropy in the interface plane (x,y). In the case of a CA/C′A′ heteropair with unlike cations and anions, e.g. InAs/GaSb, (In, Ga)As/InP, or ZnSe/BeTe, the CA-on-C′A′ heteroboundary consists of two planes containing atoms A and C′ for the C-A-C′-A′-type interface (Fig. 2) or atoms C and A′ for the A-C-A′-C′-type interface. When growing C′A′ material on CA, there are two possibilities: C′-A′-C-A and A′-C′-A-C (the substrate is on the right). Thus for C≠C′ and A≠A′ one can conceive four variants of the quantum well (see, e.g., Refs. 3–5). In the absence of special monitoring, one usually prefers to grow the variant with the C′-A′-C-A or C-A-C′-A′ interfaces, where the plane filled by cations of one material is used as a substrate on which to grow the plane with anions of the other material. These two interfaces with different A′-C and A-C′ internal bonds are not turned into one another by any orthogonal transformation, the quantum-well structure retains C_{2v} symmetry, and its optical properties measured in the $\mathbf{e}\|[110]$ and $\mathbf{e}\|[1\bar{1}0]$ polarizations must be different. The giant optical anisotropy in heterostructures without common cations and anions was predicted by Krebs and Voisin[6] and observed[7,8] in GaInAs/InP quantum wells. A semiqualitative approach (the H_{bf} model) was developed to describe this anisotropy,[6] and a numerical calculation was performed[8] within the microscopic tight-binding model. The theory developed in this work is based on a generalized envelope-function method employed earlier[2] in studying heterostructures with a common anion.

1. OPTICAL ANISOTROPY IN THE ENVELOPE-FUNCTION METHOD

Let us calculate the lateral optical anisotropy of a quantum-well structure CA/C′A′ at the absorption edge, i.e., in *hh1-e1* interband transitions with zero two-dimensional electron wave vector ($k_x=k_y=0$, Γ point). In the envelope-function method, the electron and hole effective Hamilto-

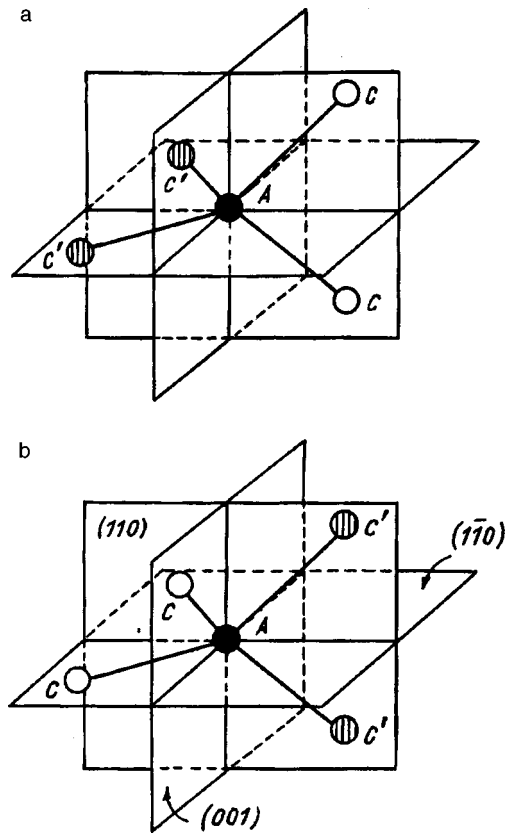

FIG. 1. Arrangement of atoms at the interface in a CA/C′A(001) heterostructure with a common anion, e.g. GaAs/AlAs. The left-hand interface C′-A-C (a) is turned into the right-hand interface C-A-C′ (b) under mirror rotation about the axis $z\|[001]$.

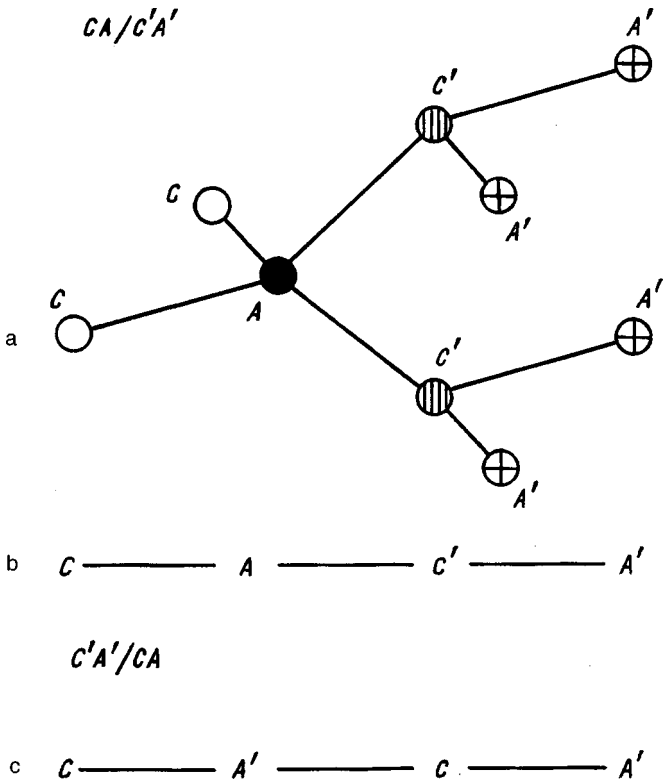

FIG. 2. Schematic presentation of the arrangement of atoms at the interface in a CA/C′A′(001) heterostructure with unlike cations and anions. (a) A-C′ interface; (b) same interface but with only atomic planes shown; (c) atomic-plane sequence at the A′-C interface.

nians within the well or in the barrier have the same form as in the corresponding bulk materials and, in particular, possess cubic symmetry T_d, and the low symmetry of the interface is taken into account by including additional terms in the boundary conditions for the wave-function envelope. Neglecting the relativistically small corrections, we shall use for the conduction-band electron such commonly accepted boundary conditions as the continuity of the envelope and of its normal derivative divided by the effective mass. In this case the electron wave function at the bottom of the $e1$ subband can be written conveniently as

$$\psi^{(e1)}_{\pm 1/2}=K(z)|\Gamma_6,\pm 1/2\rangle, \tag{1}$$

where $|\Gamma_6,\pm 1/2\rangle$ are the $\uparrow S$ and $\downarrow S$ Bloch functions, and S is the coordinate function of the Γ_1 representation of group T_d.

For the four envelope functions φ_m ($m=\pm 3/2,\pm 1/2$) of the hole wave function we shall use the boundary conditions first proposed in Ref. 2:

$$\varphi_m=\varphi'_m, \quad \nabla_m\varphi_m=\nabla'_m\varphi'_m+\frac{2}{\sqrt{3}}t_{l-h}\sum_n\{J_xJ_y\}_{mn}\varphi'_n, \tag{2}$$

and taking into account the mixing between the heavy- and light-hole states at the (001) interface, which is allowed by interface symmetry even under normal incidence of the hole, i.e., for $k_x=k_y=0$. The notation used by us in writing the boundary conditions is $m,n=\pm 3/2,\pm 1/2$

$$\nabla_{\pm 3/2}=a_0\frac{m_0}{m_{hh}}\frac{d}{dz}, \quad \nabla_{\pm 1/2}=a_0\frac{m_0}{m_{lh}}\frac{d}{dz},$$

a_0 is the lattice constant, m_0 is the free-electron mass, m_{hh},m_{lh} are the heavy- and light-hole effective masses, which are different in the CA and C′A′ materials (here and subsequently the quantities pertaining to the C′A′ material are primed), J_α are the angular-momentum matrices for $J=3/2$ in the Γ_8 basis, $\{J_xJ_y\}=(J_xJ_y+J_yJ_x)/2$, and t_{l-h} is a dimensionless parameter of heavy-light-hole mixing. For $t_{l-h}\neq 0$, the pair of the Kramers-conjugate states at the bottom of the *hh1* hole subband contains an admixture of $m=\pm 1/2$ states:

$$\psi^{(hh1)}_{\pm 3/2}=F(z)|\Gamma_8,\pm 3/2\rangle\pm iG(z)|\Gamma_8,\mp 1/2\rangle, \tag{3}$$

where $|\Gamma_8,m\rangle$ are the Bloch functions. Note that the second of the boundary conditions (2) for function $G(z)$ has the form

$$\frac{1}{m_{hh}}\frac{dG}{dz}=\frac{1}{m'_{hh}}\frac{dG'}{dz}+\frac{t_{l-h}}{a_0m_0}F'. \tag{4}$$

Within the quantum well the real envelope functions $F(z)$ and $G(z)$ can be written

$$F(z)=A\cos k_hz+B\sin k_hz,$$

$$G(z)=C\cos k_l z+D\sin k_l z, \tag{5}$$

and in the barrier layers, $z>a/2$ and $z<-a/2$, they decay exponentially

$$F(z)=F(\pm a/2)\exp[-\varkappa_h(|z|-a/2)],$$

$$G(z)=G(\pm a/2)\exp[-\varkappa_l(|z|-a/2)]. \tag{6}$$

Here a is the quantum-well thickness, A,B,C,D are z-independent coefficients, the point $z=0$ is chosen at the well center,

$$k_h=(2m_{hh}\varepsilon/\hbar^2)^{1/2},$$

$$k_l=(2m_{lh}\varepsilon/\hbar^2)^{1/2}=(m_{lh}/m_{hh})^{1/2}k_h,$$

$$\varkappa_h=[2m'_{hh}(V-\varepsilon)/\hbar^2]^{1/2},\quad \varkappa_l=(m'_{lh}/m'_{hh})^{1/2}\varkappa_h, \tag{7}$$

ε is the hole energy, and V is the barrier height, i.e. the valence band offset at the interface. Note that the barrier height for conduction-band electrons is ΔE_g-V, where ΔE_g is the difference between the band-gap widths in composite materials. In a common-anion structure the mixing coefficients t^L_{l-h} and t^R_{l-h} at the left- and right-hand interfaces, respectively, coincide, and therefore coefficients B and C in Eq. (5) vanish identically, and $F(a/2)=F(-a/2), G(a/2)=-G(-a/2)$. For $t^L_{l-h}\neq t^R_{l-h}$, the $F(z),G(z)$ functions do not possess definite parity under sign inversion of z.

According to Eqs. (1) and (5), optical transitions involving excitation of an electron-hole pair, $(e1,-1/2;hh1,3/2)$ and $(e1,1/2;hh1,-3/2)$ are allowed in the $\mathbf{e}\perp z$ light polarization. For linear polarization, the squared modulus of the matrix elements can be written

$$|M_{-1/2,3/2}(\mathbf{e})|^2=|M_{1/2,-3/2}(\mathbf{e})|^2$$

$$=M_0^2\left(I_1^2+\frac{1}{3}I_2^2+\frac{2}{\sqrt{3}}I_1I_2\cos 2\phi\right), \tag{8}$$

where M_0 is a constant, ϕ is the angle between the plane of polarization and the [110] axis, and

$$I_1=\int K(z)F(z)dz,\quad I_2=\int K(z)G(z)dz.$$

In accordance with symmetry considerations, light absorption passes through extrema at $\phi=0$ ($\mathbf{e}\|[110]$) and $\phi=\pi/2$ ($\mathbf{e}\|[1\bar{1}0]$). According to Eq. (8), the anisotropy in the absorption coefficient α in a periodic quantum-well structure is described by the relation

$$\rho\equiv\frac{\alpha_{[110]}-\alpha_{[1\bar{1}0]}}{\alpha_{[110]}+\alpha_{[1\bar{1}0]}}=\frac{2}{\sqrt{3}}\frac{I_1I_2}{I_1^2+(I_2^2/3)}\approx\frac{2}{\sqrt{3}}\frac{I_2}{I_1}. \tag{9}$$

In a quantum well grown of materials with unlike cations and anions, and with no electric field present, the optical anisotropy is dominated by the difference between heavy-light-hole mixing coefficients t_{l-h} for the CA/C′A′ and C′A′/CA heteroboundaries. It is assumed that the potential barriers at the left- and right-hand interfaces are the same. Figure 3 plots the absorption-coefficient anisotropy *vs* mixing parameters for the left-hand (t^L_{l-h}) and right-hand (t^R_{l-h}) interfaces. The calculation was done using Eq. (9) for $Ga_{0.47}In_{0.53}As/InP$ quantum wells with thicknesses of 100 Å (solid lines) and 70 Å (dashed line). The main parameters of the materials are listed in Table I, and the band offsets used in the calculations were $\Delta E_c=0.262$ eV and $\Delta E_v=0.348$ eV for the conduction and valence bands, respectively. For a fixed value of t^L_{l-h}, the t^R_{l-h} dependences presented in Fig. 3 reverse sign at $t^L_{l-h}=t^R_{l-h}$, which corresponds to a symmetric quantum well. A decrease in well thickness brings about a growth of the interface contribution and, hence, a steeper $\rho(t^R_{l-h})$ dependence for a more narrow quantum well.

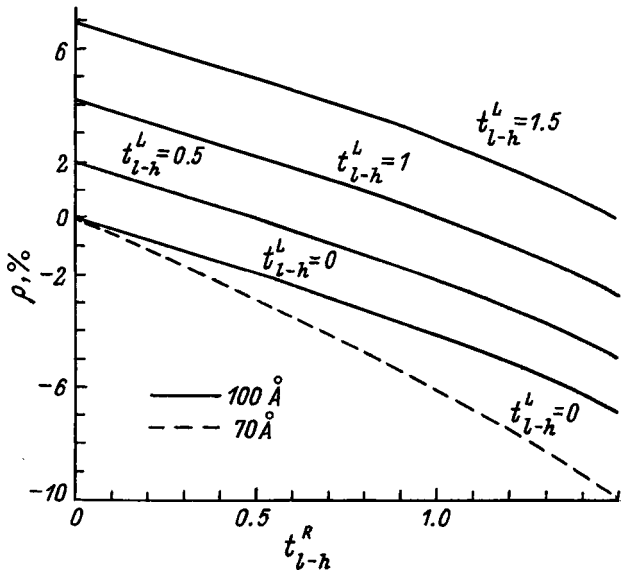

FIG. 3. Relative anisotropy of the absorption coefficient in a periodic quantum-well structure $Ga_{0.47}In_{0.53}As/InP$ vs nondimensional heavy-light-hole mixing coefficient t^R_{l-h} at the right-hand interface calculated for fixed values of t^L_{l-h}. The solid lines were calculated for wells with thickness $a=100$Å, and the dashed line, for $a=70$Å.

2. ELECTRIC-FIELD-INDUCED ANISOTROPY

Electric field $\mathbf{E}\|[001]$ applied to a bulk zincblende semiconductor results in a linear-in-field birefringence with the principal axes of the dielectric permittivity tensor oriented along the three directions $[1\bar{1}0]$, [110], and [001]. Two mechanisms of the Pockels effect in quantum-well structures were discussed in Ref. 9. One of them involves uniaxial strain $u_{xy}\propto E$ ($x\|[100], y\|[010]$) induced by the electric field (piezoelectric effect), and the mixing of heavy- and light-hole states induced by this strain, i.e., a contribution to function $G(z)$ in Eq. (3) and to the overlap integral I_2 proportional to u_{xy}. The second mechanism is purely electronic in nature, namely, one has to take into account that the interband matrix element of the momentum operator $\langle c,s,\mathbf{k}|\mathbf{ep}|v,m,\mathbf{k}\rangle$ in a semiconductor of class T_d contains terms linear in the electron wave vector $\mathbf{k}$. For $\mathbf{k}\|z$ we have

$$\langle c,1/2,k_z|\mathbf{ep}|v,3/2,k_z\rangle=-Pe_+-Qk_ze_-,$$

$$\langle c,-1/2,k_z|\mathbf{ep}|v,-3/2,k_z\rangle=Pe_--Qk_ze_+,$$

where $\mathbf{e}$ is the light-polarization unit vector, $e_\pm=e_x\pm ie_y$, and P and Q are constants. When calculating the optical anisotropy by the envelope-function method, k_z has to be

TABLE I. Parameters of the materials making up the heteropair.

	E_g, eV	m_e/m_0	m_{hh}/m_0	m_{lh}/m_0
GaInAs	0.81	0.041	0.377	0.052
lnP	1.42	0.077	0.65	0.12

replaced by operator $-id/dz$. In the lowest order in the small parameters I_2/I_1 and $Q/(aP)$ we obtain

$$\rho=\frac{2}{\sqrt{3}}\frac{I_2}{I_1}-\frac{2Q}{aP}\frac{I_3}{I_1}, \tag{10}$$

where $I_3=a\int dzKdF/dz$, and factor a is introduced for the sake of convenience so that the quantities I_1, I_2, I_3 have the same dimension. In an electric field, the envelope $F(z)$ becomes asymmetrical even for $t_{l-h}^{L,R}=0$, and the integral I_3 is not zero.

Besides the above two bulk mechanisms, there is in quantum wells with $t_{l-h}^L, t_{l-h}^R \neq 0$ an additional mechanism of the Pockels effect which involves the interfaces. Indeed, an electric field changes the values of the envelope function $G(z)$ at the interfaces, and, as follows from Eq. (4), this results in a change in Eq. (3) of the extent of admixture of the $|\Gamma_8, \mp 1/2\rangle$ to $|\Gamma_8, \pm 3/2\rangle$ states, and, hence, to a change in the overlap integral I_2. Figure 4 presents electric-field dependences of the optical anisotropy due to the interface contribution. The curves were calculated for various combinations of the values of t_{l-h}^L and t_{l-h}^R given in the caption, and the other parameters correspond to a 100-Å wide $Ga_{0.47}In_{0.53}As/InP$ quantum well.

We have been assuming until now that the potential barriers at the C′A′/CA and CA/C′A′ interfaces are the same. But in a general case for C≠C′ and A≠A′ the effective dipole moments corresponding to the C-A′ and C′-A bonds are different, so that the difference between the band offsets V_L and V_R at the left- and right-hand interfaces may be as high as 50–100 meV.[7–10] At equilibrium, this difference generates a built-in electric field which equalizes the electrochemical potential. The curves labeled *2*, *3*, and *4* in Fig. 4 were calculated for noncommutative interfaces, whereas curve *1* corresponds to a symmetric quantum well. We did not intend here to calculate precisely the built-in field, and therefore, for the sake of simplicity, the external field was augmented by a field $E_0(z)=(V_R-V_L)/(|e|a)$ in the well, and $E_0(z)=0$ in the barriers (e is the electronic charge). Positive values on the horizontal axis in Fig. 4 correspond to the external electric-field vector **E** directed from the left- to right-hand interface, which coincides with the direction of the built-in field $E_0=60$ kV/cm. Curve *3* was calculated assuming the equality $t_{l-h}^L=t_{l-h}^R=1$. Under these conditions, the nonzero anisotropy ($\approx 8\%$) observed for $E=0$ is dominated by the built-in field. Application of a negative external field compensates the built-in one and, accordingly, reduces the degree of anisotropy. Curves 2 and 4 illustrate the field-induced imbalance between the contributions due to the left- and right-hand interfaces to the anisotropy. An increase in a positive external field polarizes the electron and hole wave functions and, in this way, increases the relative contribution

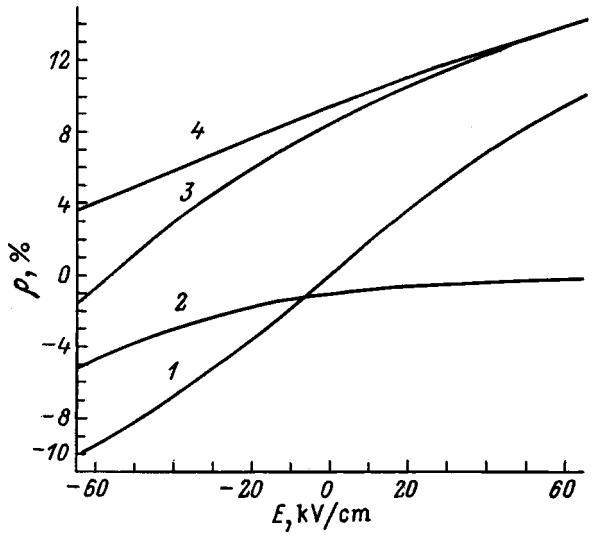

FIG. 4. Lateral absorption anisotropy as a function of external electric field in a 100-Å thick quantum-well structure $Ga_{0.47}In_{0.53}As/InP$. Curve *1*— calculation for a symmetric well with $t_{l-h}^L=t_{l-h}^R=1$ and equal band offsets $\Delta V=348$ meV, curves *2–4*—asymmetric well with $\Delta V_L=318$ meV, $\Delta V_R=378$ meV, and a built-in electric field of 60 kV/cm; the mixing coefficients t_{l-h}^L and t_{l-h}^R are chosen, respectively, to be 1, 0 (curve *2*); 1, 1 (curve *3*); and 0, 1 (curve *4*).

of the right-hand interface at which the hole functions are maximum. The contribution of the left-hand interface tends to zero with increasing field, and curves 2 ($t_{l-h}^L=1, t_{l-h}^R=0$) and 4 ($t_{l-h}^L=0, t_{l-h}^R=1$) approach asymptotically the zero value ($t_{l-h}^L=0, t_{l-h}^R=0$) and curve 3 ($t_{l-h}^L=1, t_{l-h}^R=1$), respectively. Curve *1*, calculated for a symmetric quantum well with commutative interfaces ($t_{l-h}^L=t_{l-h}^R=1, V_L=V_R$), is naturally symmetric relative to the origin.

3. RELATION BETWEEN THE TIGHT-BINDING MODEL AND THE ENVELOPE-FUNCTION METHOD

To estimate the coefficients entering the boundary conditions for the envelope functions $\hbar_m$, we shall use the empirical tight-binding model sp^3s^* in the nearest-neighbor-coupling approximation.[11] This model was employed earlier to derive the boundary conditions at the interface between common-anion semiconductors.[2,12] For $\mathbf{k}\|z$, the wave function of the valence-band electron can be expanded in planar atomic orbitals

$$\psi_\alpha(\mathbf{r})=\sum_n C_n\phi_{n\alpha}(\mathbf{r}-z_n\mathbf{e}_z), \tag{11}$$

where $z_n=na_0/4$, a_0 is the lattice constant, $\mathbf{e}_z$ is the unit vector along [001], $\phi_{n\alpha}$ is the planar orbital for a monatomic layer of cations (odd n) or anions (even n). The spin is initially not taken into account, and one derives boundary conditions for the envelopes of the Bloch functions $(|X\rangle+|Y\rangle)/\sqrt{2}$ and $(|X\rangle-|Y\rangle)/\sqrt{2}$, which transform according to the one-dimensional representations Δ_3, Δ_4 of the wave-vector group at point Δ. Therefore in Eq. (11) we have $\alpha=\Delta_3, \Delta_4$, and for the corresponding orbitals we can write $(p_x+p_y)/\sqrt{2}$ or $(p_x-p_y)/\sqrt{2}$. Consider for definiteness how the Δ_3 states are joined at the CA/C′A′ heterojunction. The

interface monolayers A and C′ are assigned the numbers $n=0$ and $n=1$. We shall use subsequently the following notation for the tight-binding model parameters: E_c, E_a are the diagonal energies for the cation or anion p orbitals, $V_{\gamma\delta}$ is the tight-binding matrix element between the anion orbital p_γ and cation orbital p_δ in the bulk semiconductor CA ($\gamma,\delta=x,y$), $E'_c, E'_a, V'_{\gamma\delta}$ are the same parameters for material C′A′, $\tilde{E}_a$ and $\tilde{E}'_c$ are the diagonal energies for the interface atoms A and C′, and $\tilde{V}_{\gamma\delta}$ is the binding matrix element for the AC′ pair.

The coefficients for solutions of Δ_3 symmetry in the bulk semiconductor CA satisfy the coupled linear equations

$$U_- C_{2l-1}+(E_a-E)C_{2l}+U_+ C_{2l+1}=0,$$
$$U_+ C_{2l}+(E_c-E)C_{2l+1}+U_- C_{2l+2}=0, \tag{12}$$

where E is the electron energy, $U_\pm=(V_{xx}\pm V_{xy})/2$, and l is an integer. Solutions Δ_4 satisfy a similar system of equations, where U_+ and U_- switch places. In the electron representation, the dispersion of the Δ_3 or Δ_4 valence states can be written

$$E(k,\mathrm{CA})=\frac{1}{2}(E_a+E_c)-D_k, \tag{13}$$

where

$$D_k=\sqrt{\Delta^2+V_k V_{-k}}, \quad \Delta=\frac{1}{2}(E_c-E_a),$$
$$V_k=U_- e^{ika_0/4}+U_+ e^{-ika_0/4}. \tag{14}$$

The values of the wave vector $\mathbf{k}=(0,0,k)$ are real within the allowed band and imaginary for an energy in the gap. For a given value of k, coefficients C_n can be presented in the form

$$C_n(k)=f_k\begin{cases}\eta_k e^{ikz_n} & \text{for even } n,\\ \xi_k e^{ikz_n} & \text{for odd } n,\end{cases} \tag{15}$$

where f_k is an arbitrary factor, and

$$\eta_k=\left(\frac{D_k+\Delta}{2D_k}\right)^{1/2}, \quad \xi_k=-\eta_k\frac{V_k}{D_k+\Delta}. \tag{16}$$

In bulk material C′A′, the equations for C_n can be obtained by replacing $E_a, E_c, V_k, \Delta, D_k, U_\pm, f_k$ with $E'_a, E'_c, V'_{k'}, \Delta', D'_{k'}, U'_\pm, f_{k'}$. The solutions for a heterostructure are constructed in the form of linear combinations of k and $-k$ waves in material CA, and $k', -k'$ waves in material C′A′, where k and k' satisfy the dispersion equations $E=E(k,\mathrm{CA})=E(k',\mathrm{C'A'})$. Accordingly, coefficients C_n become

$$C_n=\begin{cases}C_n(k,\mathrm{CA})+C_n(-k,\mathrm{CA}) & \text{for } n\leqslant 0,\\ C_n(k',\mathrm{C'A'})+C_n(-k',\mathrm{C'A'}) & \text{for } n\geqslant 1.\end{cases} \tag{17}$$

Factors $f_{\pm k}, f_{\pm k'}$ are related through two ''interface'' equations

$$U_- C_{-1}+(\tilde{E}_a-E)C_0+\tilde{U}_+ C_1=0,$$
$$\tilde{U}_+ C_0+(\tilde{E}'_c-E)C_1+U'_- C_2=0. \tag{18}$$

We have to take now into account that the envelope in the effective-mass method is the function

$$f(z)=f_k e^{ikz}+f_{-k}e^{-ikz}. \tag{19}$$

Using Eq. (18), one can derive the boundary conditions relating $f(0)=f_k+f_{-k}$ and the first derivative $df(0)/dz=ik(f_k-f_{-k})$ to $f'(0)=f_{k'}+f_{-k'}$ and $df'(0)/dz=ik'(f_{k'}-f_{-k'})$. We finally come to

$$f(0)=t_{11}f'(0)+t_{12}\dot{f}'(0),$$
$$\dot{f}(0)=t_{21}f'(0)+t_{22}\dot{f}'(0), \tag{20}$$

$\dot{f}\equiv a_0(m_0/M)(df/dz)$, the effective mass $M=\hbar^2 d(dE/dk)^{-1}$,

$$t_{11}=\frac{1}{\eta}\left(\eta'\frac{U'_+}{\tilde{U}_+}-\frac{E'_c-\tilde{E}'_c}{\tilde{U}_+U'_+}S'_+\right),$$

$$t_{12}=\frac{1}{\eta\eta'}\frac{E'_c-\tilde{E}'_c}{\tilde{U}_+U'_+}\frac{\hbar^2}{m_0a_0^2},$$

$$t_{21}=\frac{m_0a_0^2}{\hbar^2}\frac{\eta}{2}$$
$$\times\left\{[S_+-S_-+\eta(2\tilde{E}_a-E_a-E)]t_{11}-2S'_+\frac{\tilde{U}_+}{U'_+}\right\}, \tag{21}$$

$$t_{22}=\frac{\eta}{\eta'}\frac{\tilde{U}_+}{U'_+}+\frac{\eta}{2}\frac{m_0a_0^2}{\hbar^2}t_{12}[S_+-S_-+\eta(2\tilde{E}_a-E_a-E)].$$

We have used the following notation:

$$S_\pm=\frac{U_\pm(U_\pm+U_\mp\cos ka_0/2)}{\sqrt{2D(D+\Delta)}},$$

$$S'_\pm=\frac{U'_\pm(U'_\pm+U'_\mp\cos k'a_0/2)}{\sqrt{2D'(D'+\Delta')}}, \tag{22}$$

$\eta=\eta(k), \eta'=\eta'(k'), D=D_k, D'=D'_{k'}$. In deriving Eq. (22), we took into account the identity $S'_+S'_-=\eta'(E'_a-E)$. One can readily verify that matrix t_{ij} is unimodular: $t_{11}t_{22}-t_{12}t_{21}=1$. The result for a GaAs/AlAs-type heteropair is[2] as follows: in common-anion heterostructures, $\tilde{E}'_c=E'_c, \tilde{E}_a=(E_a+E'_a)/2$, $\tilde{U}_+=U'_+$, and $t_{11}=\eta'/\eta$, $t_{12}=0$, $t_{22}=\eta/\eta'$,

$$t_{21}=\frac{m_0a_0^2}{2\hbar^2}[\eta'(S_+-S_-)-\eta(S'_+-S'_-)]$$
$$=\frac{m_0a_0^2}{2\hbar^2}\left(\frac{V_{xx}V_{xy}}{D+\Delta}-\frac{V'_{xx}V'_{xy}}{D'+\Delta'}\right). \tag{23}$$

Expressions (21) permit one to relate the elements of matrix t_{ij} to the microscopic parameters of the tight-binding model. Calculations were carried out for two possible types of the interface in the $Ga_{0.47}In_{0.55}As/InP$ heterostructure:

TABLE II. Material parameters used in the calculations.

	a_0	V_{xx}	V_{xy}	E_a	E_c
lnP	5.8688	1.6888	4.1213	0.7090	3.792
GaInAs	5.8679	1.1636	4.4547	0.2331	3.8352
GaInP	5.6725	1.3812	3.6936	0.4771	3.7600
InAs	6.0583	1.3013	4.8025	0.2697	4.1464

TABLE III. Calculated coefficients t_{ij}.

	InAs (Δ_3)	InAs (Δ_4)	GaInP (Δ_3)	GaInP (Δ_4)
t_{11}	0.9415	0.6872	1.2160	0.8050
t_{12}	0.0000	0.0000	−0.0157	−0.0825
t_{21}	−2.3957	2.7657	−0.2881	1.2582
t_{22}	1.0621	1.4551	0.8261	1.1132

1) InAs type in the atomic plane sequence

-(GaIn)-As-(GaIn)-[As-In]-P-In-P-

2) GaInP type in the sequence

-In-P-In-[P-(GaIn)]-As-(GaIn)-As-,

where the interface atoms are bracketed. Table II lists the parameters used, and Table III presents the coefficients t_{ij} calculated with boundary conditions (20) for an energy E close to the top of the GaInAs valence band. The diagonal energies $\tilde{E}_a, \tilde{E}_c'$ were chosen in accordance with the tight-binding model used in Ref. 8: $\tilde{E}_a = E_a$(GaInAs), $\tilde{E}_c' = E_c$(InP) for the InAs interface, $\tilde{E}_a = E_a$(InP), $\tilde{E}_c' = E_c$(GaInAs) for the GaInP interface, and the valence-band offset was assumed to be $\delta E_v = 0.348$ eV. As seen from Table III, the diagonal coefficients t_{11} and t_{22} are close to one, and coefficient t_{12} is considerably smaller than the others. For $t_{11}, t_{22} \approx 1$, the mixing coefficient at the interface of the orbitals $|X\rangle, |Y\rangle$ is (disregarding the spin-orbit coupling) $t_{X-Y} = [t_{21}(\Delta_3) - t_{21}(\Delta_4)]/2$, and the heavy-light-hole mixing coefficient in Eq. (2) can be written $t_{l-h} = t_{X-Y}/\sqrt{3}$.[2] As follows from Table III, the coefficients t_{l-h} at InAs- and GaInP-type interfaces take the values of -2.58 and -0.77, i.e., they differ by more than a factor of three. The tight-binding model used here is somewhat approximate and serves only to estimate the absolute values of coefficients t_{l-h}^L, t_{l-h}^R and the difference between them, which is responsible for the lateral anisotropy. The precise values of these coefficients could be found from a detailed comparison with experiment, which is beyond the scope of the present work. In Fig. 3, the maximum optical anisotropy is $\approx 10\%$, in full agreement with the tight-binding calculation.[8] The experimental values of the relative absorption anisotropy ρ exceed the theoretical estimate by a factor two to three. It may be conjectured that besides the intrinsic mechanism analyzed in this work interface imperfections, such as islands, steps, or ledges, oriented predominantly along [110] or $[1\bar{1}0]$, may contribute to lateral anisotropy too. Nevertheless, a comparison with experiment shows that the contribution to ρ due to the intrinsic mechanism is not small, and in samples with more perfect interfaces it will certainly exceed the extrinsic one.

Support of the Russian Fund for Fundamental Research (Grant 98-02-18206), as well as of the Volkswagen-Stiftung, is gratefully acknowledged.

[1] Y. Fu, M. Willander, E. L. Ivchenko, and A. A. Kiselev, Phys. Rev. B **47**, 13 498 (1993), E. L. Ivchenko, A. A. Kiselev, Y. Fu, and M. Willander, Phys. Rev. B **50**, 7747 (1994).
[2] E. L. Ivchenko, A. Yu. Kaminskiĭ, and I. L. Aleĭner, Zh. Éksp. Teor. Fiz. **104**, 3401 (1993) [JETP **77**, 609 (1993)]; E. L. Ivchenko, A. Yu. Kaminski, and U. Rössler, Phys. Rev. B **54**, 5852 (1996).
[3] B. R. Bennett, B. V. Shanabrook, R. J. Wagner, J. L. Davis, and J. R. Waterman, Appl. Phys. Lett. **63**, 949 (1993).
[4] P. M. Thibado, B. R. Benett, M. E. Twigg, B. V. Shanabrook, and L. J. Whitman, Appl. Phys. Lett. **67**, 3578 (1995).
[5] A. Y. Lew, S. L. Zuo, E. T. Yu, and R. H. Miles, Appl. Phys. Lett. **70**, 75 (1997).
[6] O. Krebs and P. Voisin, Phys. Rev. Lett. **77**, 1829 (1996).
[7] O. Krebs, W. Seidel, and P. Voisin, Inst. Phys. Conf. Ser. No. 155: Chapter 12, in *Proceedings of the 23rd International Symposium on Compound Semiconductors* (St. Petersburg, Russia, 1996), edited by M. S. Shur and R. A. Suris (1997), p. 859.
[8] O. Krebs, W. Seidel, J. P. André, D. Bertho, C. Jouanin, and P. Voisin, Semicond. Sci. Technol. **12**, 938 (1997).
[9] S. H. Kwok, H. T. Grahn, K. Ploog, and R. Merlin, Phys. Rev. Lett. **69**, 973 (1992).
[10] W. Seidel, O. Krebs, P. Voisin, J. C. Harmand, F. Aristone, and J. F. Palmier, Phys. Rev. B **55**, 2274 (1997).
[11] P. Vogl, H. P. Hjalmarson, and J. D. Dow, J. Phys. Chem. Solids **44**, 365 (1983).
[12] A. Yu. Kaminskiĭ, Candidate Thesis, FTI RAN (1996).

Translated by G. Skrebtsov

Efficiency of Si $L_{2,3}$ x-ray generation in the SiO_2/Si system by electron impact

A. S. Shulakov, A. P. Braĭko, N. V. Moroz, and V. A. Fomichev

Institute of Physics, St. Petersburg State University, 198904 Petrodvorets, Russia
(Submitted March 23, 1998)
Fiz. Tverd. Tela (St. Petersburg) **40**, 1932–1936 (October 1998)

The paper reports a study of the depth profile of the generation efficiency and escape of the ultrasoft silicon $L_{2,3}$ x-ray radiation excited by electrons of various energies. The generation function describing the excitation efficiency is the kernel of an integral equation determining the dependence of x-ray emission intensity on primary-electron energy. To determine the form of this function, a study was made of the dependence of the Si $L_{2,3}$ x-ray spectral intensity and of its silicon $L_{2,3}$ component bands, from crystalline silicon and amorphous dioxide SiO_2, on primary-electron energy in samples made from dioxide layers of various thicknesses grown on crystalline silicon. These experiments permitted investigation of the generation-function cross sections at the depth of the Si-SiO_2 interface. The theoretical simulation of the generation function made use of the simplest laws governing electron interaction with solids and of the cross section of the inner-level ionization by electron impact in its most general form. A comparison of the experimentally obtained relative contributions of the Si and SiO_2 emissions with the calculations shows them to be in good agreement up to primary-electron energies of 2–3 keV. © *1998 American Institute of Physics.* [S1063-7834(98)03410-8]

Ultrasoft x-ray spectroscopy of characteristic emission bands combined with variation of the primary electron-beam energy exciting the emission has demonstrated its merits as a nondestructive method of layer-by-layer analysis of the electronic structure and chemical phase composition of near-surface regions in solids within the thickness range extending from a few nm to hundreds of nm.[1–3] A calculational model was developed for quantitative analysis, in which the excitation efficiency of characteristic x-ray emission was implicitly assumed to be uniformly distributed throughout the emitting layer.[1] The obvious incorrectness of this assumption was compensated by introducing certain corrections, but it was evident that the model should include a reliable distribution of the emission-generation efficiency in depth. This distribution is usually approximated by a generation function $G_{E0}(c_i(x),x)$, which depends on primary-electron energy and concentration gradient of the emitting atoms of the ith species and is the kernel of an integral equation determining in a general form the dependence of the x-ray spectral intensity on primary-electron energy

$$I(E_0,\omega)\sim\int_0^\infty G_{E0}(c_i(x),x/\sin\theta_0)\times\exp[-\mu(\omega)x/\sin\theta]dx, \tag{1}$$

where $c_i(x)$ is the concentration profile of the emitting atoms of species i in depth x, θ_0 and θ are the grazing angles of incidence of primary electrons and escaping x rays, respectively, $\mu(\omega)$ is the linear absorption coefficient of the outgoing radiation in the sample material, and $\exp[-\mu(\omega)x/\sin\theta]$ is the fraction of the radiation absorbed in the sample (a quantitative characteristic of the self-absorption effect). The generation function can be expressed in the most general form as

$$G_{E0}[c_i(x),x]dx\sim c_i(x)\int_{E_i}^{E_0} n_{E0}(\varepsilon,x)\sigma_i(\varepsilon)d\varepsilon, \tag{2}$$

where E_i is the ionization potential of the scanned level of atoms i, $\sigma_i(\varepsilon)$ is the ionization cross section of this level by electron impact, and $n_{E0}(\varepsilon,x)$ is the normalized distribution in energy ε of the ensemble of electrons (primary, secondary, Auger) generated by primary electrons of energy E_0 in a layer of unit thickness located at depth x. This distribution forms as a result of multiple elastic and inelastic electron scattering by electrons, plasmons, phonons, defects etc., and its first-principles calculation is extremely complex even for single-phase solids.

In our earlier work[3] we attempted to use, for a quantitative estimation of the complex multiphase system SiO_2-Si-Au, an arbitrary modification of Filiber's relation to describe the generation function for large E_0. The results of the fitting showed that, while this generation function can, in principle, adequately approximate the excitation-efficiency depth profile, it requires refinement. The present work describes a comprehensive study of the function of ultrasoft characteristic x-ray generation.

The investigation technique is as follows. Use was made of silicon dioxide layers with various thicknesses grown on single-crystal silicon (a set of samples with different depths of the SiO_2-Si interface). When such samples are bombarded by primary electrons, a dynamic distribution of the efficiency of Si $L_{2,3}$ spectrum excitation in depth sets in, which can be approximated by the generation function under study. This function should be close in shape to that forming in an isotropic sample, because the mass densities c of the coating and of the substrate are close, with only silicon atom concentrations being different. Also close are the linear absorption coefficients at the energies of the Si $L_{2,3}$ bands in SiO_2

and Si (according to Ref. 4, at a photon energy of 92 eV these coefficients are approximately 10^5 cm^{-1}). Note, however, that the shapes of the Si $L_{2,3}$ x-ray emission bands in silicon dioxide and crystalline silicon are different, which permits one to reliably deconvolute these superposed bands observed under their simultaneous excitation. This approach was successfully used before.[3,5] Thus the interface may be conceived as a cross section of the generation function at the depth of the interface (i.e., the thickness of the SiO_2 layer). The atoms located above this cross section emit the spectrum characteristic of the Si $L_{2,3}$ band in SiO_2, and those below it, the band due to crystalline silicon. Depending on the actual depth of the interface and on the primary-electron energy, one will observe either the Si $L_{2,3}$ band in SiO_2, or superposition of this band with the band of the substrate, i.e. of crystalline silicon. By deconvolving this complex feature into components, one can estimate with a good accuracy their relative intensities.

The same quantity can be calculated using a given or calculated generation function and the characteristics of the model system chosen. The quality of the fit between the calculated and experimental data will characterize primarily the degree of adequacy of the generation function selected. Because preliminary studies showed the generation functions constructed for high primary-electron energies to be close to actual distributions, we can use the results obtained in the classical work of Borovskiĭ and Rydnik[6] for microanalytical purposes in the hard x-ray energy region.

To find the energy distribution of scattered electrons in a massive target, $n_{E0}(\varepsilon,x)$, Ref. 6 used a model function $f(\varepsilon,x)$ which was a sum of two terms describing the incident and outgoing electron fluxes:

$$f(\varepsilon,x)=g_f(\varepsilon,x)+g_b(\varepsilon,x). \tag{3}$$

The function $g_f(\varepsilon,x)$ was estimated assuming exponential attenuation of the electron flux[7]

$$N(x)=N_0\ \exp[-(x/X)^p] \tag{4}$$

and a power-law slowing-down along the trajectory

$$\varepsilon^n(x)=E_0^n(1-x/x_{\max}). \tag{5}$$

In Eqs. (4) and (5), $X=\alpha E_0/\rho$; $p=(1.51n)/\log Z$; $n=2.44(Z/A)^{0.5}$; ρ, A, and Z denote the mass density, atomic weight, and atomic number, respectively; $\alpha=3.33\times10^{-6}$ for E_0 measured in keV, and x, in cm; $x_{\max}$ is the maximum penetration depth for electrons with energy E_0 into the target;[8,9] and N_0 is the number of incident electrons. Based on these simplest relations, one can readily show that using the system of dimensionless units $\chi=x/X$ and $\xi=\varepsilon/E_0$, the function $g(\xi,\chi)$ can be written in the following form

$$g(\xi,\chi)=pn\chi^p[\xi^{n-1}/(1-\xi^n)^{p+1}]\exp[-(\chi/(1-\xi^n))^p],$$

$$\int_0^1 g(\xi,\chi)d\xi=N(\chi)/N_0. \tag{6}$$

In the first approximation, we have neglected the second term describing electron backscattering from the target. This term is small compared to the first one,[10] and it should affect primarily the amplitude of the generation function, but the quantities used by us here (the intensity ratios of the contributions due to the SiO_2 layer and the Si substrate) should not be sensitive to the absolute values of the integrands in Eqs. (1) and (2).

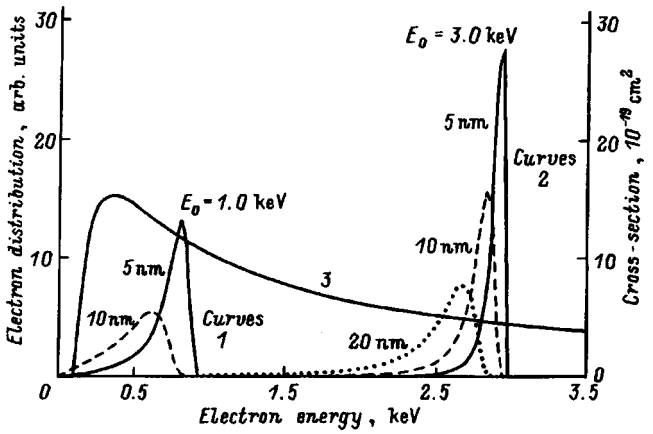

FIG. 1. Electron energy distribution at various depths from a SiO_2 target surface calculated using Eqs. (3)–(6) for the primary electron energies (*1*) $E_0=1.0$ keV and (*2*) $E_0=3.0$ keV (the depths are shown in nm); (*3*) cross section of Si $2p$-level ionization by electron impact calculated using Eq. (7) (right-hand scale).

Figure 1(a) displays the $n_{E0}(x,\varepsilon)$ profiles calculated in this way for different primary-electron energies and for different depths. One readily sees that, the maxima in the distributions shift to lower energies as the depth increases, and they decrease in amplitude and broaden. Also shown in the same figure is the electron-impact-ionization cross section for the Si $2p$ level. This curve was calculated using the universal relation of Gryzinsky, which was obtained within classical theory of atomic collisions and was found to fit well experimental data[11]

$$\sigma_{\mathrm{Si}}(\varepsilon)=(\sigma_0/E_{2p}^2y)[(y-1)/(y+1)]^{3/2}\times\{1+2/3(1-1/2y)\ln[2.7+(y-1)^{1/2}]\}, \tag{7}$$

where $\sigma_0=6.56\times10^{-14}$ eV$^2\cdot$cm^2 for electron-atom collisions, $y=\varepsilon/E_{2p}$; and E_{2p} is the Si $2p$ binding energy, which was chosen (102.3 eV) as an average between those characteristic of crystalline silicon and silicon dioxide.[12]

The form of the generation function (2) is determined by the ionization cross section and the electron energy distribution. Because far from the core-level ionization potential the ionization cross section falls off slowly, the shape of the generation function will be dominated by the character of the $n_{E0}(x,\varepsilon)$ distributions. The effect of the ionization cross-section function will be the strongest near its maximum (the values equal to the third-fourth ionization potentials). For instance, if the primary-electron energy lies near the maximum of $\sigma_i(\varepsilon)$ or to the left of it, then the low-energy part of the $n_{E0}(x,\varepsilon)$ function describing emission from deep layers will be suppressed, and the contribution due to emission from the top layer will increase, thus bringing about a noticeable increase in the sensitivity of surface measurements. The high surface sensitivity of x-ray emission spectroscopy was first revealed in near-threshold excitation of characteris-

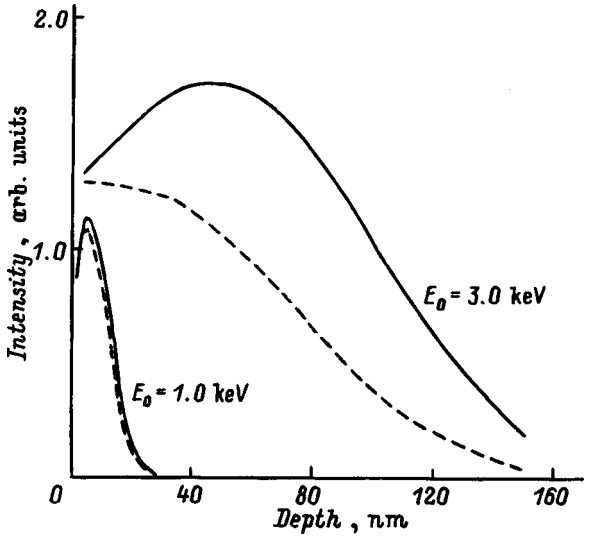

FIG. 2. Generation functions $G_{E0}(x)$ (solid lines) and output functions (dashed curves) calculated using Eqs. (1)–(7) for $E_0 = 1.0$ and 3.0 keV.

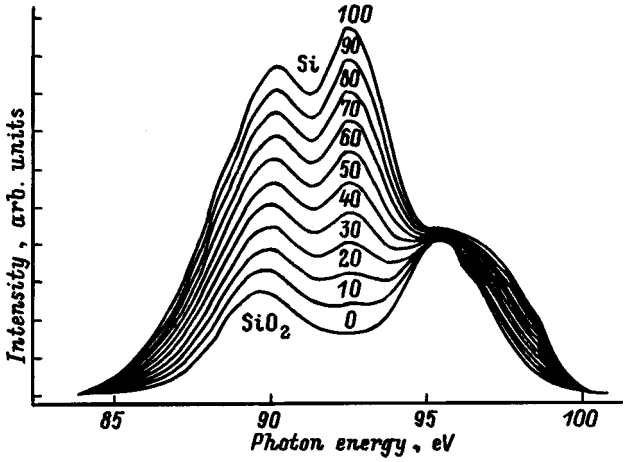

FIG. 3. Superposition of Si $L_{2,3}$ bands due to crystalline Si (c-Si) and SiO_2. The figures refer to the percentage contribution of the band intensity due to pure silicon.

tic bands of metals,[13] which supports the conclusion made by analyzing the form of the integrands in Eq. (2).

Figure 2 shows generation functions for Si $L_{2,3}$ emission in SiO_2 calculated for two different primary-electron energies. Each curve has a maximum and, as E_0 increases, the position of the maximum shifts rapidly to greater depths (by more than a factor ten for E_0 changing from 1 to 3 keV), and the width of the generation-efficiency curve increases (sevenfold at half maximum). The dashed lines in Fig. 2 show the emission output functions [the integrand in Eq. (1) is the generation function modified by absorption of the escaping radiation in the sample material]. We readily see that the output function differs only slightly from the generation function for $E_0 = 1$ keV, while self-absorption affects radically the shape of the generation function for $E_0 = 3$ keV, so that it becomes smoother and no longer has a maximum in the bulk of the target. The steepness of the right-hand slope of the generation and output functions increases with decreasing E_0 which, based on general considerations, should improve the accuracy of an analysis or resolution with depth.

Let us turn now to the SiO_2/Si system. It consisted of three samples with silicon dioxide layers 19, 26, and 121 nm thick. The samples were prepared by dry oxidation of the (111) face of a silicon single crystal. The thicknesses were determined from the oxidation time and ellipsometrically to within 3%. The generation and output functions of Si $L_{2,3}$ emission for such samples will differ from the ones displayed in Fig. 2 only in the presence of a jump at interface depth. This jump is caused by an increase in volume density of emitting Si atoms as one goes from the SiO_2 layer to the Si substrate, as well as by the change in the band intensity due to the electronic structure rearrangement.

Single-crystal samples of pure silicon and of silicon coated by a thick (200 nm) dioxide layer were used to determine the magnitude of this jump. A 7-nm-thick gold layer was deposited on the surface of each sample. The integrated intensities of the Si $L_{2,3}$ bands in Si and SiO_2 obtained for different E_0 were compared by normalizing them to the Au $N_{6,7}$ band intensity. It was found that the emission intensity ratio for silicon and SiO_2 is 4.5 ± 0.5. It is this magnitude of the jump that was used in describing the generation and output efficiency profiles for the SiO_2/Si system. The angles θ_0 and θ in Eq. (1) were set to 45°.

One could expect that the shape of the spectrum would change gradually with smoothly increasing E_0 from that characteristic of SiO_2 to the one typical of crystalline silicon (for large values of E_0, where the contribution due to emission from the layer becomes small). Figure 3 illustrates this transition through superposition of the c-Si and SiO_2 bands. Shown in Fig. 4 are Si $L_{2,3}$ spectra obtained experimentally at various primary-electron energies from a SiO_2(19 nm)/Si sample (the technique used and experimental conditions were the same as in Refs. 1–3). The observed pattern of spectral shape variation is seen to be similar to the one displayed in Fig. 3. Similar dependences were obtained for all samples. Each spectrum was decomposed by least-squares fitting into the Si $L_{2,3}$ component bands emitted by c-Si and SiO_2. One finally calculated the integrated band-intensity ra-

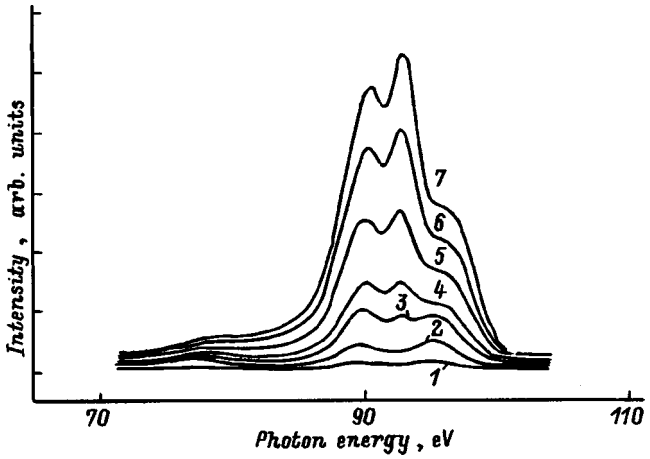

FIG. 4. Si $L_{2,3}$ spectra obtained for various primary-electron energies from a sample with a 19-nm thick SiO_2 surface layer. Primary-electron energy (keV): *1* — 0.5, *2* — 0.75, *3* — 1.0, *4* — 1.5, *5* — 2.0, *6* — 3.0, *7* — 4.0.

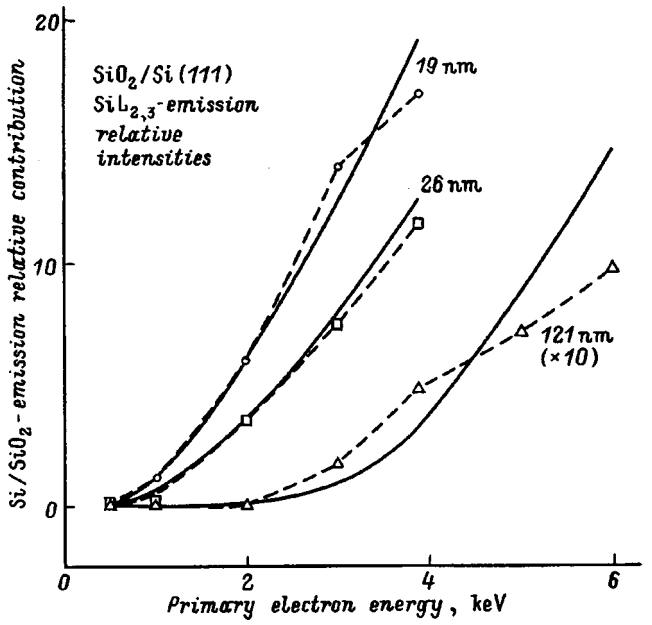

FIG. 5. Si $L_{2,3}$ band intensity ratio for single-crystal silicon and SiO_2 *vs* primary-electron energy for samples with surface SiO_2 layers 19, 26, and 121 nm thick. Calculation—solid lines, experiment—symbols connected by dashed lines.

tio of c-Si to SiO_2 for each value of E_0. The results of experimental spectrum treatment and calculations are compared in Fig. 5.

We see that for thin, 19 and 26 nm, SiO_2 layers the calculations fit satisfactorily to experimental data, with a discrepancy of not over 10% within the total E_0 variation range, and considerably less than that for $E_0<3.0$ keV. The fit for the sample with the thickest oxide film (121 nm) is substantially worse. It should, however, be pointed out that both theory and experiment show the relation to rise from zero at $E_0=2.0$ keV, which evidences the correctness of the depth scale.

Thus the depth profile of the excitation efficiency and output of Si $L_{2,3}$ emission constructed by us agrees satisfactorily with experiment for low primary-electron energies $E_0<3.0$ keV and can be used in calculations of thin-layer characteristics and distributions (a few tens of nm thick).

For layers 19 and 26 nm thick, the disagreement between theory and experiment becomes noticeable for E_0 of 2–3 keV. At these energies, the tops and left-hand slopes of the generation functions pass through the interfaces. It is possibly these regions that were described by us less adequately through neglect of electron backscattering in the target. An analysis of the results obtained for the 121-nm thick layer shows that as E_0 is increased from 2 to 6 keV the interface passes through both the right- and left-hand slopes of the $G_{E0}(x)$ curves. It might appear that the generation functions are completely wrong, but one should take into account that, for sufficiently large E_0, the self-absorption effect can result not only in a decrease of the escaping radiation intensity but in a distortion of band shape as well, even if the absorption coefficient does not have a fine structure and is instead described[14] by a smoothly sloped curve. This, in its turn, interferes with deconvolution of experimental curves into components and results in errors in intensity-ratio calculations. The influence of this effect and of other parameters on the accuracy of describing the depth profile of generation efficiency and of outgoing characteristic x-ray intensity will be reported in our subsequent publications.

Support of the Russian Fund for Fundamental Research (Grant 96-03-33319a) and RF MOPO on basic research in natural sciences (Grant 97-7.2-80) is gratefully acknowledged.

[1] A. S. Shulakov, Cryst. Res. Technol. **23**, 835 (1988).
[2] A. S. Shulakov, A. P. Stepanov, and A. P. Braĭko, Fiz. Tverd. Tela (St. Petersburg) **35**, 2135 (1993) [Phys. Solid State **35**, 1061 (1993)].
[3] A. S. Shulakov and A. P. Braĭko, Fiz. Tverd. Tela (St. Petersburg) **39**, 2101 (1997) [Phys. Solid State **39**, 1880 (1997)].
[4] A. S. Vinogradov, E. O. Filatova, and T. M. Zimkina, Fiz. Tverd. Tela (Leningrad) **25**, 1120 (1983) [Sov. Phys. Solid State **25**, 643 (1983)].
[5] A. S. Shulakov and A. P. Stepanov, Poverkhnost' No. 10, 146 (1988).
[6] I. B. Borovskiĭ and V. I. Rydnik, Izv. Akad. Nauk SSSR, Ser. Fiz. **31**, 1009 (1967).
[7] A. F. Makhov, Fiz. Tverd. Tela (Leningrad) **2**, 2161 (1960) [Sov. Phys. Solid State **2**, 1934 (1960)].
[8] G. Dupuoy, F. Perrier, G. Verdier, and F. Annal, C. R. Acad. Sci. URSS **258**, 3655 (1964).
[9] G. Dupuoy, F. Perrier, G. Verdier, and F. Annal, C. R. Acad. Sci. URSS **260**, 6055 (1965).
[10] I. M. Bronshteĭn and B. S. Fraĭman, *Secondary Electron Emission* [in Russian], Nauka, Moscow (1969), 407 pp.
[11] M. Gryzinsky, Phys. Rev. **138**, A336 (1965).
[12] V. I. Nefedov, *X-Ray Photoelectron Spectroscopy of Chemical Compounds* [in Russian], Khimiya, Moscow (1984), 255 pp.
[13] A. S. Shulakov, A. V. Fedorov, and G. Kaindl, in *Abstract of the 17th International Conference ''X-Ray and Inner-Shell Processes X-96''* (Hamburg, 1996), p. 80.
[14] A. S. Shulakov, A. Szász, H. Müller, and H. Kirchmayr, Phys. Status Solidi A **133**, 555 (1992).

Translated by G. Skrebtsov

Effect of temperature and surface coverage on the samarium interaction with Si(111)

T. V. Krachino, M. V. Kuz'min, M. V. Loginov, and M. A. Mittsev

A. F. Ioffe Physicotechnical Institute, Russian Academy of Sciences, 194021 St. Petersburg, Russia
(Submitted March 27, 1998)
Fiz. Tverd. Tela (St. Petersburg) **40**, 1937–1944 (October 1998)

The interaction of Sm atoms with Si(111) has been studied. The study was carried out by low-energy electron diffraction, Auger-electron spectroscopy, and contact-potential difference method over a broad range of temperatures (from room temperature to 1140 K) at which samarium was deposited on the silicon sample surface. The surface coverage varied from zero to 55 monolayers. It was shown that the shape of the low-energy Auger spectrum of samarium depends on coverage, and that its variation correlates with that of the Sm atom valence state. It was established that no ordered structures form when samarium is deposited on silicon at room temperature, and that partial mixing of the metal and semiconductor atoms takes place in the initial stages of this process. If samarium is deposited on heated silicon (900 and 1140 K), an adsorbed film (transition layer), whose structure is determined by the coverage and temperature, is the first to form. After that, three-dimensional silicide crystallites begin to grow on this transition layer. Their shape depends on the substrate temperature. This dependence accounts for the relation between temperature and the coverage at which the crystallites coalesce.
 [S1063-7834(98)03510-2]

Our previous publications described an investigation into the formation mechanisms of the interfaces Eu-Si(111) (Ref. 1) and Yb-Si(111) (Refs. 2 and 3) and their physicochemical properties. This investigation showed that further progress in understanding the character of the processes occurring on the Si(111) surface under deposition on it of rare-earth (RE) metal atoms can be reached, in particular, by studying the interaction of silicon with other RE elements. Our first step in this direction was to study the formation of the Sm–Si(111) interface. Some of the results obtained in the work were summarized in Ref. 4, with the remainder being presented in this communication. The difference between these two works lies primarily in the experimental techniques employed. Ref. 4 made use of low-energy electron diffraction (LEED), thermal desorption spectroscopy, atomic-beam modulation, and mass spectrometry (MS). This communication describes the results obtained by Auger-electron spectroscopy (AES), LEED, contact-potential difference (CPD), and MS. These methods were applied in the same experimental arrangement as in the preceding work.[4] The Auger spectra were measured in differential form. The substrates were phosphorus-doped *n*-silicon samples cut parallel to the (111) plane and having resistivity of $1-10\ \Omega\cdot$cm.

EXPERIMENTAL RESULTS AND THEIR DISCUSSION

The experimental method used in this work differed from the commonly accepted procedure. Usually, the metal is deposited on a silicon sample maintained at room temperature. After this, the substrate is heated to the desired temperature, and the measurements are performed subsequently at room temperature. In this work, samarium was deposited on samples heated to a certain temperature (which will be specified when describing the experimental conditions). The measurements were carried out at room temperature. Such a procedure was chosen for the following two reasons. First, deposition of an RE metal on a heated crystal produces a more-ordered silicide films.[5] Second, this growth technique may initiate as yet unknown mechanisms of RE-Si(111) interface formation.

We chose two temperatures, 900 and 1140 K. The choice of the first temperature was motivated by the observation that near it the $(\sqrt{3}\times\sqrt{3})R30°$ structure forms within the coverage interval $0.5\leqslant\theta\leqslant 25$. For $\theta>25$, it is replaced by the (1×1) structure. At the same time if experiments are carried out by the conventional method, the (1×1) structure will be observed for all $\theta\geqslant 2$.

As for 1140 K, it is the maximum temperature at which Sm does not start to evaporate from the surface. This temperature produces within the coverage interval $0.35\leqslant\theta\leqslant 45$ only (5×1) reflections. The same structure is observed if samarium first is deposited on the crystal maintained at $T=700-900$ K, after which the temperature is raised to 1140 K. In this case, however, its reflections are very weak.

The results of these structural studies formed a basis for developing the program of the present work. This program included, first, investigation of the dependence of the samarium Auger-line shape on the number of samarium atoms deposited on the silicon surface. This investigation was stimulated by the results of Refs. 6 and 7, which indicate that the valence state of Sm atoms depends on coverage θ. And a change in the valence state may, in principle, be accompanied by transformation of the samarium Auger lines.

The second objective was to study the concentration dependences of the amplitudes of Sm and Si Auger peaks for different temperatures of Sm deposition on silicon surface. These data could yield information on the mechanism of interface formation and on how it is affected by experimental conditions. Samarium was deposited on silicon at three tem-

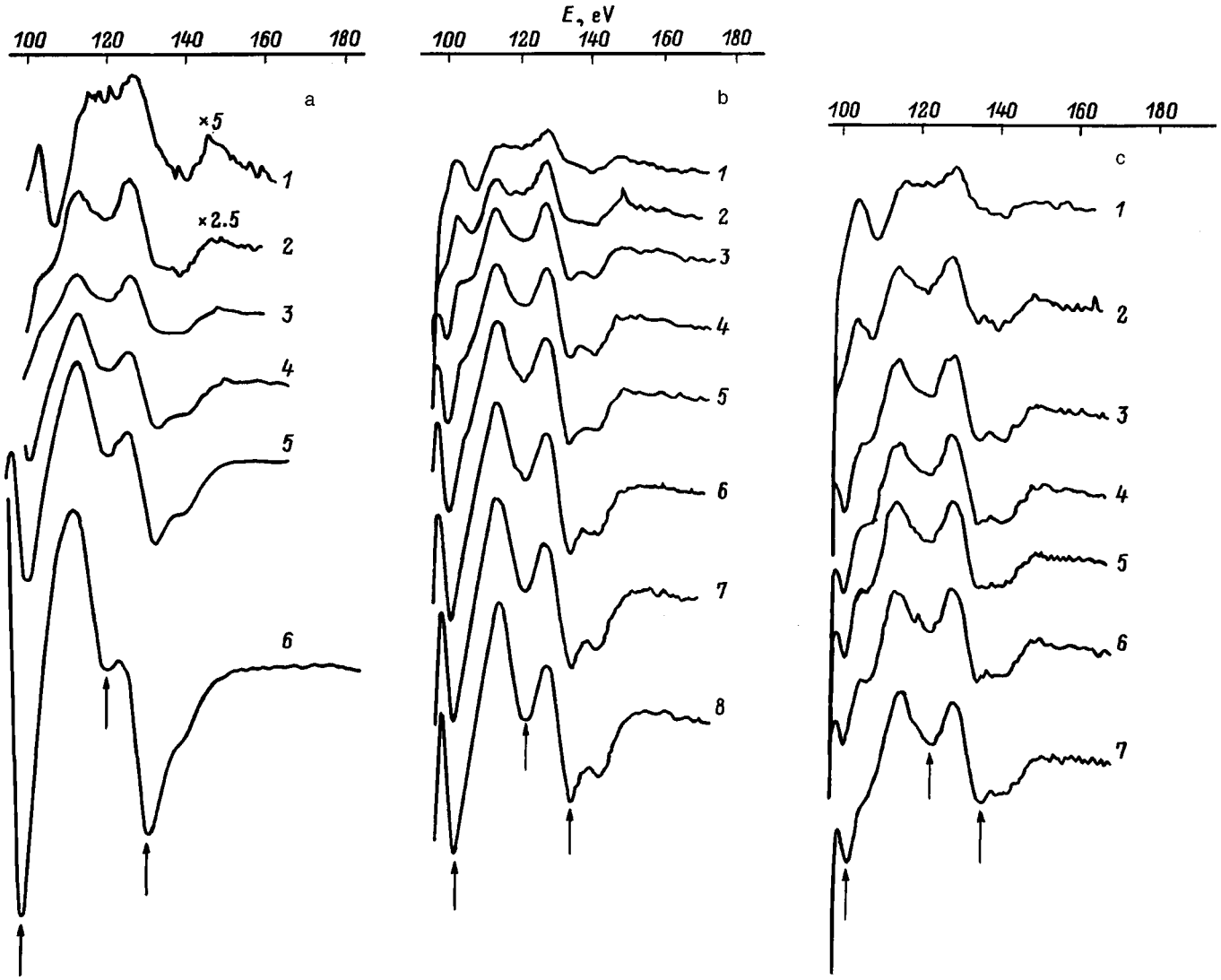

FIG. 1. Low-energy samarium spectra including $N_{4,5}O_{2,3}N_{6,7}$ (101 eV), $N_{4,5}N_{6,7}V$ (121 eV), and $N_{4,5}VV$ (134 eV) peaks obtained for different coverages. Parts *a*, *b*, and *c* correspond to different silicon temperatures at which samarium was deposited. The samarium atom concentration on the surface, $N=7.84\times10^{14}$ cm^{-2}, was taken for $\theta=1$. (a) $T=300$ K. θ: *1*—0.13, *2*—0.40, *3*—0.67, *4*—1.47, *5*—2.95, *6*—11.0. (b) $T=900$ K. θ: *1*—0.13, *2*—0.27, *3*—0.40, *4*—0.54, *5*—0.67, *6*—1.07, *7*—2.68, *8*—8.04. (c) $T=1140$ K. θ: *1*—0.13, *2*—0.27, *3*—0.40, *4*—0.54, *5*—0.67, *6*—1.07, *7*—2.68, *8*—8.04.

peratures of the substrate, at room temperature, 900, and 1140 K.

Finally, the third purpose of the study was to see how the silicon-surface work function depends on the amount of the deposited Sm atoms. Data obtained in such measurements provide information on the electronic state of adsorbed Sm films or of the silicide film surface. In the investigation of the concentration dependences of Auger peak amplitudes, samarium was deposited on silicon maintained at three temperatures: room temperature, 900, and 1140 K.

The results obtained in this investigation are presented in graphical form in Figs. 1–5. Consider them in sequence.

1) *Shape of samarium Auger spectra (Fig. 1).* The shape of the low-energy part of the room-temperature samarium Auger spectrum including the $N_{4,5}O_{2,3}N_{6,7}$ (101 eV), $N_{4,5}N_{6,7}V$ (121 eV), and $N_{4,5}VV$ (134 eV) peaks depends on coverage (Fig. 1(a)). The shape begins to change already at submonolayer coverages. It continues to change for $\theta>1$ as well until, finally, at $\theta=11$ this part of the spectrum takes on the form typical of three-dimensional samples of samarium. After that, further increase of the coverage no longer affects its shape.

All these observations can be easily explained by considering the studies[6,7] of samarium valency. It was found that the valency of Sm atoms adsorbed on the Si(111)7×7 face at room temperature increases within the coverage interval $0<\theta<1$ from $2+$ to larger values with increasing surface concentration. This growth becomes still more pronounced for $1<\theta<2$. For $\theta>2$, the soft x-ray absorption spectra used to determine the valence state practically coincide with those for bulk samarium metal.[7] Because in the bulk of the metal samarium is trivalent, this coincidence implies that for $\theta=2$ samarium atoms deposited on silicon are predominantly trivalent.

It thus follows that the above-mentioned change in the shape of the low-energy part of the Auger spectrum is apparently due to the valence state of Sm atoms increasing from $2+$ at low coverages to close to $3+$ for large θ, and, hence,

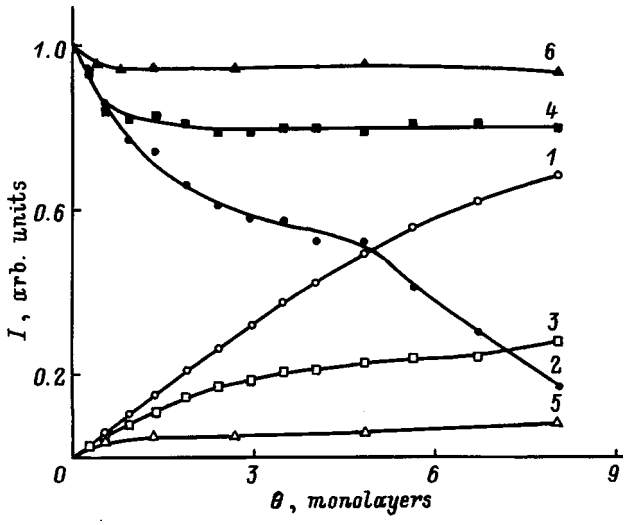

FIG. 2. Auger-peak amplitudes for Sm $M_5N_{4,5}N_{4,5}$ (816 eV) (curves *1,3,5*) and Si L_3VV (92 eV) (curves *2,4,6*) *vs* samarium atom concentration on the silicon surface (coverage interval $0<\theta\leqslant 8$). Samarium was deposited at T(K): *1,2*—300, *3,4*—900, *5,6*—1140.

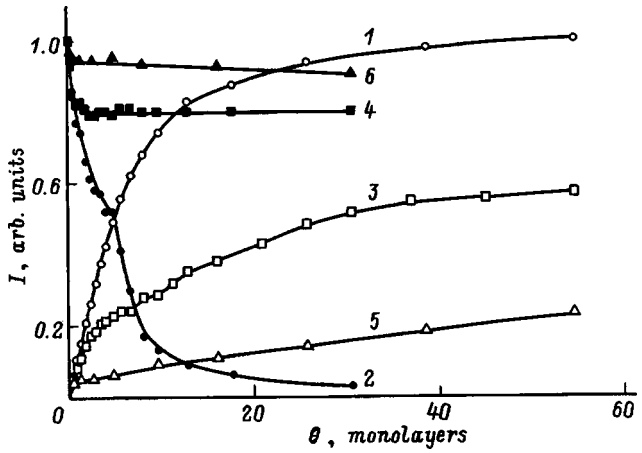

FIG. 3. Auger-peak amplitudes for Sm $M_5N_{4,5}N_{4,5}$ (816 eV) (curves *1,3,5*) and Si L_3VV (92 eV) (curves *2,4,6*) *vs* samarium atom concentration on the silicon surface (coverage interval $0<\theta\leqslant 55$). Samarium was deposited at T(K): *1,2*—300, *3,4*—900, *5,6*—1140.

that this spectral shape can indeed serve as an indication of the samarium valency.

Below 900 K, the change in the low-energy Auger spectrum of samarium with increasing coverage is about the same as that observed at room temperature (Fig. 1(b)). This implies, in particular, that Sm atoms in the silicide formed at an elevated temperature has a valence of $3+$.

The pattern observed at 1140 K is qualitatively different. In this case the growth of coverage for $\theta\leqslant 8$ is accompanied only by an insignificant change in shape of the corresponding part of the Auger spectrum (Fig. 1(c)). It would thus seem that the valence state of samarium in the silicide film starting to form at $\theta=0.4$ is close to two. An analysis of the concentration dependences of the Auger peak amplitude (see below) showed, however, that the constancy of Auger spectral shape for silicide films grown at 1140 K is due to other reasons. These reasons will be considered in the next section.

2) *Auger-peak intensity vs samarium concentration on the silicon surface.* These dependences were obtained using the 92-eV L_3VV Si Auger peak. For samarium we had to take the weak high-energy $M_5N_{4,5}N_{4,5}$ Auger line at 816 eV, because the strongest samarium line, $N_{4,5}O_{2,3}N_{6,7}$ at 101 eV, partly overlaps the silicon Auger spectrum and, thus, is unsuitable for quantitative measurements. The other, weaker samarium Auger peaks, $N_{4,5}N_{6,7}V$ (121 eV) and $N_{4,5}VV$ (134 eV), lie, as already mentioned, in the low-energy region, where the spectrum changes its shape with increasing coverage. Therefore they are likewise unsuitable for measuring the concentration
dependences. As for the shape of the $M_5N_{4,5}N_{4,5}$ peak at 816 eV, it remains constant throughout the coverage range studied.

The concentration dependences obtained by us at $T=300$ K (curves *1* and *2* in Figs. 2 and 3) are in full agreement with those reported in Ref. 8. They argue for the mixing of Sm and Si atoms for $\theta<8$. For $\theta>8$, a film of metallic samarium grows on the surface. When combined with the data presented in the preceding section, these results show that samarium is predominantly trivalent both in the samarium-silicon mixing stage and after its completion.

In the cases where samarium is deposited onto heated samples, the concentration dependences of Auger-signal intensity exhibit a number of significant features. First, one observes a substantial difference in the behavior of the curves for silicon and samarium (Figs. 2 and 3). Indeed, for silicon they saturate already at low coverages, $\theta=2$ for $T=900$ K and $\theta=0.8$ for $T=1140$ K. The same dependences measured for samarium do not, strictly speaking, reach saturation for any coverage. At the same time while the samarium Auger signal at 1140 K grows linearly with concentration for all $\theta>10$ (curve *5* in Fig. 3), the silicon signal at 900 K shows a tendency to saturate for coverages $\theta>37$ (curve *3* in Fig. 3). Second, the Auger signal intensity depends on temperature. For instance, the Auger peak amplitude for samarium at 900 K exceeds considerably that obtained for 1140 K. In the case of silicon, the peak intensities are in the opposite relation.

Correct interpretation of the above relations requires their comparison with the data of our structure studies (briefly discussed above) and with the results obtained both in our preceding work[4] and in studies of other authors dealing with the Sm–Si(111) system. According to these results, the Sm–Si(111) film structure forms by a mechanism close to that of Stransky-Krastanov. It is essentially as follows. At low coverages, the samarium film adsorbed on silicon reconstructs the sample surface (this film, together with the reconstructed surface, is called in what follows the reconstruction or transition layer). There may be more than one such reconstruction and, in one of them, 3D samarium-silicide crystallites grow. Obviously, this film structure should become manifest in AES and LEED measurements. Indeed, the samarium Auger-peak amplitude I for the coverage region where the silicide crystallites have not yet coalesced can be written approximately

$$I=I_1+I_2=xI_{10}+(1-x)I_{20}, \tag{1}$$

where I_1 is the Auger signal produced by the fraction x of the transition layer which is not covered by crystallites, I_2 is that due to the crystallites, and I_{10} and I_{20} are the corresponding Auger signals for unit surface area. Equation (1) assumes the crystallite height h exceeds the Auger-electron mean-free path λ and, therefore, the part of the transition layer under the crystallites does not contribute to I_1. Despite its obviously approximate nature, Eq. (1) can be used for a qualitative analysis of experimental results. One immediately sees, in particular, that the signal I should decrease with increasing coverage if $I_{10}>I_{20}$, and increase if $I_{20}>I_{10}$. The latter case is apparently most probable, because the thickness of the transition layer is less than the mean free path of the Auger electrons, whereas the height h may exceed it. The results obtained in this work for Sm-Si(111) (Figs. 2 and 3) suggest that in this system $I_{20}>I_{10}$. The value of x entering Eq. (1) is obviously dependent on the crystallite shape, so that the larger is the $k=h/s$ ratio (s is the crystallite base area), the larger will be x for a given coverage, and vice versa.

For coverages large enough to allow the crystallites to coalesce, $x=0$. For these values of θ, which are functions of parameter k, the Auger signal I will no longer depend on the number of the metal atoms deposited on the surface. Its amplitude will be $I=I_{20}$. A similar qualitative analysis can be made for the silicon Auger peak as well.

The LEED pattern for the transition layer accommodating isolated 3D silicide layers should be a superposition of two patterns, namely, those of the layer and of the islands. After the latter have coalesced, the first pattern will disappear leaving only the second one in place. The brightness of its reflections at coverages below the level of coalescence should depend on the shape of the crystallites and on the extent to which their arrangement on the surface is matched. For example, if the crystallites resemble thin long whiskers oriented normal to the sample surface, the silicide reflection intensity will most likely be very low.

The above considerations permit one to analyze our results obtained by AES (Figs. 1–3) and LEED for two temperatures, 900 and 1140 K. In the first case, the diffraction pattern of the $(\sqrt{3}\times\sqrt{3})R30°$ reconstruction on which the silicide film grows begins to disappear at $\theta\cong 25$, with only the (1×1) structure remaining for $\theta>30$. At about the same coverages the concentration dependence $I(\mathrm{Sm})=f(\theta)$ approaches saturation asymptotically. This suggests that 3D silicide crystallites coalesce at coverages above $\theta=25$, and that silicide arranges in the (1×1) structure.

The pattern observed for 1140 K is radically different. In this case the silicide film grows on a reconstructed (5×1) structure. Its diffraction pattern does not vanish even for $\theta=45$. This may imply that either the silicide has the (5×1) structure or the 3D silicide islands have not yet coalesced. The second possibility is argued for by the fact that the samarium-Auger-peak amplitude does not show a tendency to saturation throughout the coverage range studied (Fig. 3). It thus becomes clear that the experimental AES and LEED data do not provide an answer to the question of the structure of the silicide films forming at 1140 K. We have succeeded in finding the answer by studying the concentration dependences of the work function (section 3). These studies showed that the silicides forming at 900 and 1140 K most likely have the same structure, (1×1). At first glance this conclusion is at odds with the Auger-signal-intensity measurements (Figs. 1 and 3). Indeed, the latter suggest that, for equal coverages, the Auger peak of samarium obtained at 1140 K is always substantially smaller than that for 900 K. These differences in signal intensity can, however, result not only from the change in silicide stoichiometry occurring with increasing temperature. They could be due also to different ratios $k=h/s$ for the crystallites forming at 900 and 1140 K. For instance, the above difference in Auger-signal intensity will be observed if $k(1140\ \mathrm{K})>k(900\ \mathrm{K})$. Indeed, for the same coverage the area occupied by crystallites will decrease in going from $T=900$ to 1140 K, and the value of x in Eq. (1) will increase. And if at the same time $I_{20}>I_{10}$, as is the case with the Sm-Si(111) system, these changes will tend to reduce the signal I. This decrease will, however, be not the only consequence of the change in shape of the 3D crystallites. The increase in the $k=h/s$ ratio in going from 900 to 1140 K should be accompanied also by an increase of the coverage at which the crystallites start to coalesce. This conclusion is in full agreement with the concentration dependences of the Auger signals (Figs. 2 and 3).

In this way, the approach used in this Section offers an explanation for the above results. Moreover, it sheds light on some of the observations reported in the preceding Section. In particular, one can now readily explain why the low-energy Auger spectrum of samarium undergoes a transformation with increasing coverage if the RE metal is deposited on a crystal heated to 900 K, while changing very little if this is done at $T=1140$ K (Fig. 1). This difference in the spectral pattern is due to the fact that for $\theta\leqslant 8$ (Fig. 1) the value of I_2 in Eq. (1) is comparable to I_1 for $T=900$ K and $I_2\ll I_1$ for 1140 K because the crystallites assume different 3D shapes at these temperatures. Thus, because of the specific shape of the crystallites, the Auger signal observed at 1140 K is dominated by electrons from the transition layer with the (5×1) structure. As already mentioned, Sm atoms in such a layer are divalent.

3) *Work function vs samarium concentration on the silicon surface.* The pattern of these dependences (Figs. 4 and 5) changes with increasing temperature of samarium deposition on the silicon surface. These changes reflect the relation of the mechanism of interface formation to temperature. Therefore an analysis of the results obtained in this study can help in understanding this mechanism.

The $\Delta\varphi=f(\theta)$ relation obtained at room temperature is generally similar to those observed in cases where atoms of electropositive adsorbates were deposited on the surface of metals and some semiconductors. For coverages below the level at which the minimum is observed, the absolute value of $\Delta\varphi$ grows monotonically, without any features. This monotonic course may indicate that the adsorbate-substrate system is in a metastable state at room temperature. This conclusion is buttressed by a comparison of room-temperature results with similar data obtained by us with samarium (curves *2* and *3* in Fig. 4) and ytterbium[3] deposited on heated silicon. The $\Delta\varphi=f(\theta)$ relations measured in the

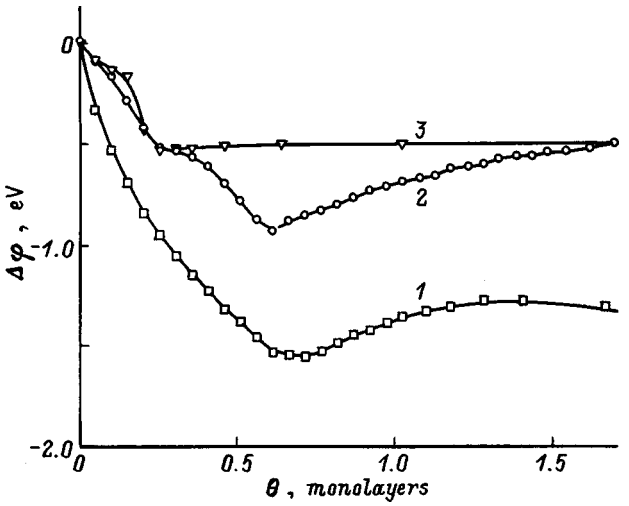

FIG. 4. Work function *vs* coverage (coverage interval $0<\theta\leqslant 1.7$) plotted for different temperatures of samarium deposition on silicon T(K): *1*—300, *2*—900, *3*—1140.

latter case exhibit a number of features such as steps, inflection points, and breaks; their positions on the concentration scale correlate with structural transitions in the intermediate layer, so that they originate from these transitions.

There is presently no information on the structure of the metastable state we have been discussing. In spite of this, one can put forward some conjectures concerning the origin of the minimum in the $\Delta\varphi=f(\theta)$ relation. These conjectures are based on determination of the Sm concentration on the surface at this point, and on the above-mentioned study[7] of the valence state of samarium atoms. The concentration at the minimum ($\theta=0.73$) is 5.64×10^{14} cm^{-2}. The average distance between atoms in such an adsorbed film is 4.2 Å. Such a short distance suggests that, for $\theta>\theta_{\min}$, the adsorbed film undergoes metallization and, as a result, after the minimum, the work function starts to grow (as it does in the case of metal-film systems). Based on the metallization concepts alone one cannot, however, explain why this growth stops at $\theta_{\max}=1.5$, and the work function starts to decrease again thereafter. In order to understand the nature of this feature in

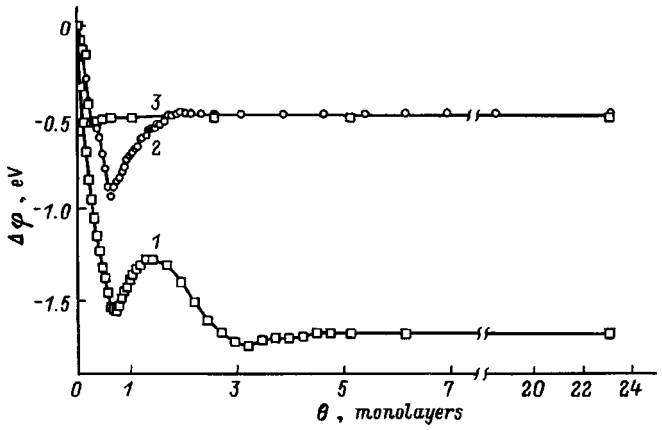

FIG. 5. Work function *vs* coverage (coverage interval $0<\theta\leqslant 23$) plotted for different temperatures of samarium deposition on silicon T(K): *1*—300, *2*—900, *3*—1140.

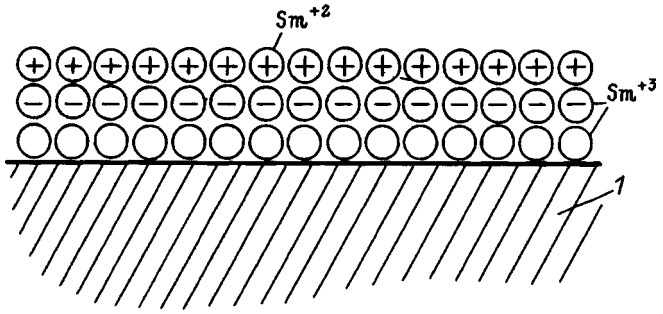

FIG. 6. Schematic picture of the double electric layer forming in an adsorbed samarium film. *1*—substrate.

the work-function behavior, one has to invoke additional data bearing on the effect of the surface concentration of samarium atoms on the state of their electronic shells. These data can be derived from Refs. 6, 7, and 9. The latter publication dealt with the concentration dependences of the work function and valence of samarium adatoms for the Sm–W(100) system. For that system, the $\varphi=f(\theta)$ relation obtained at $T=300$ K follows the same pattern as that for Sm–Si(111). It was established[9] that the point at which the work function starts to decrease after reaching a maximum for $\theta>2$ coincides with the appearance in x-ray photoelectron spectra of the component corresponding to divalent Sm atoms. This correlation implies that the above decrease in the work function is caused by divalent samarium atoms localized in the outermost monolayer of the adsorbed film. Its mechanism can be readily conceived if one assumes their electronegativity to be less than that of trivalent atoms. In this case the Sm^{2+} atoms in the topmost monolayer of the adsorbed film will be charged positively, and the Sm^{3+} atoms in the lower layer, negatively (Fig. 6). It is the double electric layer produced in this way that will cause a decrease in the work function.

A similar correlation exists between the concentration dependence of the work function obtained in this work for the Sm–Si(111) system and the change in valence state of the Sm atoms adsorbed on Si(111), which was observed in Refs. 6 and 7 (see Sec. A). It permits us to describe the effect of Sm valence on the concentration dependence of the work function in the following way. At low coverages, the growth in the number of Sm atoms is accompanied by an increase of their average valence and a considerable decrease of the work function. The former inhibits a change in the work function, in other words, if there were no $Sm^{2+}\rightarrow Sm^{3+}$ transition, φ would decrease still more. At $\theta=0.73$ the work function reaches a minimum, to start growing thereafter. As already mentioned, this growth can be caused by metallization of the film. As the number of Sm atoms on the surface increases, such a film will progressively approach in its properties three-dimensional samarium samples, on whose surface divalent states are known[10] to exist. The latter means that, starting with a certain coverage, a double electric layer will begin to form in the two topmost monolayers of the film (Fig. 6), after which the growth of the work function should be replaced by its decrease. This is indeed observed to occur within the $1.5<\theta<3$ coverage interval (curve *1* in Fig. 4).

This is approximately the same interval in which the soft x-ray absorption spectra of samarium films were found[7] to undergo the most pronounced changes eventually resembling those of bulk Sm samples. This coincidence gives us grounds to believe that the double electric layer on a samarium film starts to form at a coverage $\theta=1.5$. Thus metallization first causes an increase in the work function, which is followed by its decrease after the appearance of Sm^{2+} atoms in the topmost monolayer of the film. It should be pointed out that the model in Fig. 6 permits one not only to describe correctly the concentration dependences of the work function for the Sm–W(100) and Sm–Si(111) systems but also to explain why samarium possesses one of the lowest work functions among all RE metals.

The $\Delta\varphi=f(\theta)$ relations obtained at 900 and 1140 K differ considerably from that measured at room temperature. They differ from one another as well. The difference from the room-temperature concentration relation has primarily a clearly pronounced quantitative character. Indeed, for $\theta>3$ it becomes as large as 1.2 eV. The second difference consists in that when samarium is deposited on a heated crystal, the $\varphi=f(\theta)$ relations exhibit distinct features for $\theta<0.5$, which indicate structural changes in the transition layer.

The $\varphi=f(\theta)$ relations obtained for 900 and 1140 K differ in that the former exhibits a minimum at $\theta=0.62$, while in the latter there is no such minimum. The nature of this minimum can be readily understood if one compares the concentration dependences of the work function with the results of our structure studies.[4] These studies established for $T=900$ K the following sequence of reconstructions occurring with increasing Sm concentration: (3×1), (5×1), (7×1), and $(\sqrt{3}\times\sqrt{3})R30°$, with the latter observed within the coverage interval $0<\theta\leqslant25$. Now for 1140 K the sequence is different: (3×1) and (5×1) $(0.35<\theta\leqslant45)$. A comparison of the above sequences immediately suggests that the minimum in the $\Delta\varphi=f(\theta)$ relation for 900 K is connected with the formation of the $(\sqrt{3}\times\sqrt{3})R30°$ structure. Based on their experimental data, the authors of Ref. 6 believe that this structure consists of two layers, with the upper one formed by divalent Sm atoms, and the lower one, by Sm^{3+} atoms. Considered within the concept used by us (Fig. 6) in explaining the nature of the minimum in the room-temperature $\Delta\varphi=f(\theta)$ relation, such a two-layer formation should reduce the work function. A decrease in the work function is indeed observed exactly in the submonolayer-coverage region where the $(\sqrt{3}\times\sqrt{3})R30°$ structure starts to form. At $\theta=0.62$, however, the work function reaches a minimum and begins to grow until $\theta=2$. At this coverage, the work function takes the value equal to that for thick silicide films (Fig. 5). This pattern of the $\varphi=f(\theta)$ relation for $\theta>\theta_{\min}$ gives us grounds to maintain that the increase in the work function after its minimum is caused by the growth on the surface of the transition layer of silicide crystallites, and that for $T=900$ K this growth starts at $\theta=0.62$. Whence it follows that the contact-potential-difference method is capable of determining fairly accurately the coverage at which the silicide film starts to form. The significance of this finding can be readily assessed if we recall that for the Sm–Si(111) system, for instance, only very few of the experimental methods used by us and other researchers could provide such quantitative data.

The dependence of the work function on coverage for samarium films obtained by deposition on silicon heated to 1140 K differs substantially from that grown at 900 K. This difference is clearly seen in Figs. 4 and 5. From among the characteristic features of the $\Delta\varphi=f(\theta)$ relation obtained for 1140 K, two deserve particular attention. First, the work function depends on the amount of deposited samarium only within the coverage interval $0<\theta\leqslant0.26$. Second, the work function for $\theta\geqslant0.26$ coincides with that for thick silicide films forming when samarium is deposited on silicon heated to 900 K. The figure $\theta=0.26$ is very close to the coverage $\theta=0.33$ at which we succeeded in establishing[4] the onset of the (5×1) reconstruction. It thus follows that the corresponding work function coincides with that for the silicide. As for the equal values of φ for 900 and 1140 K, this gives us grounds to assume that the silicides formed at the two temperatures have the same stoichiometry and the same structure, (1×1).

The results displayed in Figs. 4 and 5 offer a possibility of determining the work function of metallic samarium films, φ(Sm), and of silicide films a few tens of monolayers thick, φ(sil.), as well as that of the (5×1) reconstruction, $\varphi(5\times1)$, if one takes for the work function of $Si(111)7\times7$ the value $\varphi(Si)=4.6$ eV (Ref. 11). We then obtain $\varphi(Sm)=2.9$ eV, $\varphi[\text{sil.}(900\text{ K})]=\varphi[\text{sil.}(1140\text{ K})]=\varphi(5\times1)=4.1$ eV.

The silicide work function is remarkably high. A possible explanation for this is suggested by experimental data described in section 2. By these data, the silicon Auger signal for thick silicide films approaches that for the substrate at $\theta=0$. The difference between them does not exceed 20% for $T=900$ K and 10% for 1140 K. Taking this into account, as well as the layered nature of three-dimensional silicide films,[12] it appears only natural to assume that their surface is coated by an array of silicon atoms. Silicon atoms and the underlying Sm atoms, which possess a larger electronegativity than the Si atoms, will be charged negatively, and the metal atoms, positively. Obviously enough, such a surface double layer, which increases the work function, is capable of explaining the larger value of φ for the silicide.

Support of the Russian Fund for Fundamental Research (Grant 96-02-16898) is gratefully acknowledged.

[1] M. V. Kuz'min, M. V. Loginov, M. A. Mittsev, and T. V. Krachino, Fiz. Tverd. Tela (St. Petersburg) **37**, 1030 (1995) [Phys. Solid State **37**, 559 (1995)].
[2] T. V. Krachino, M. V. Kuz'min, M. V. Loginov, and M. A. Mittsev, Fiz. Tverd. Tela (St. Petersburg) **39**, 256 (1997) [Phys. Solid State **39**, 224 (1997)].
[3] T. V. Krachino, M. V. Kuz'min, M. V. Loginov, and M. A. Mittsev, Fiz. Tverd. Tela (St. Petersburg) **39**, 1672 (1997) [Phys. Solid State **39**, 1493 (1997)].
[4] T. V. Krachino, M. V. Kuz'min, M. V. Loginov, and M. A. Mittsev, Fiz. Tverd. Tela (St. Petersburg) **40**, 371 (1998) [Phys. Solid State **40**, 341 (1998)].
[5] F. P. Netzer, J. Phys.: Condens. Matter **7**, 991 (1995).
[6] C. Wigren, J. N. Andersen, R. Nyholm, M. Göthelid, M. Hammar, C. Törnevik, and U. O. Karlsson, Phys. Rev. B **48**, 11 014 (1993).

[7] O. Sakho, M. Sacchi, F. Sirotti, and G. Rossi, Phys. Rev. B **47**, 3797 (1993).
[8] C. Wigren, J. N. Andersen, R. Nyholm, and U. O. Karlsson, Surf. Sci. **293**, 254 (1993).
[9] S. E. Efimovskiĭ, M. V. Loginov, N. V. Mamro, and M. A. Mittsev, Pis'ma Zh. Tekh. Fiz. **13**, 1013 (1987) [Sov. Tech. Phys. Lett. **13**, 423 (1987)].
[10] G. K. Wertheim and G. Crecelius, Phys. Rev. Lett. **40**, 813 (1978).
[11] W. Mönch, *Semiconductor Surfaces and Interfaces* (Springer, Berlin, 1993), 366 pp.
[12] G. Rossi, Surf. Sci. Rep. **7**, 1 (1987).

Translated by G. Skrebtsov

POLYMERS. LIQUID CRYSTALS

Effect of a bounding surface on the rotational viscosity of liquid crystals

A. V. Zakharov*

Institute of Machine Engineering, Russian Academy of Sciences, 199178 St. Petersburg, Russia
(Submitted December 17, 1997; resubmitted April 9, 1998)
Fiz. Tverd. Tela (St. Petersburg) **40**, 1945–1949 (October 1998)

The effect of a surface, bounding a nematic-liquid phase, on the rotational viscosity γ_1 is investigated on the basis of a statistical approach employing direct correlation functions. Specific calculations are performed for a model system consisting of ellipsoidal molecules interacting via a Gay–Berne potential near the bounding surface. © *1998 American Institute of Physics.* [S1063-7834(98)03610-7]

The theoretical description of dissipation processes in liquid crystals (LCs) is once again attracting investigators.[1] Despite the fact that certain qualitative advances have been made in the construction of a molecular theory of the rheological properties of nematic-liquid crystals (NLCs), it is still too early to talk about the development of a theory which would make it possible to describe the rheological processes from first principles, based only on the form of the Hamiltonian.

But, since the coefficient of rotational viscosity γ_1 is one of the parameters determining the dynamics of LCs, and extensive experimental data on the viscosity of LCs have now been accumulated,[2] the question of a theoretical interpretation of these data inevitably arises.

For the most part, this problem was solved on the one hand on the basis of either a simplified molecular model of the free volume[3] or a theory based on the Fokker-Planck equation for a model of NLCs in a polymer solution[4] or by using the same Fokker–Planck kinetics to estimate the coefficient of rotational viscosity,[5] and on the other hand by the nonequilibrium statistical operator (NSO) method,[6] taking account of different correlations to describe the rheological processes in NLCs.[7]

These approaches to describing rotational viscosity in NLCs have the serious drawback that the approximations introduced into the theory do not fall into a definite hierarchy and they serve only to resolve particular difficulties. Ultimately, this even precludes making comparisons of the final results. Another weak point of all approaches, without exception, is the large number of adjustable parameters.

The objective of the present work is to investigate the effect of a bounding surface on the rotational viscosity of liquid crystals on the basis of a treatment combining the Nemtsov model[7] and the Brook–Levinson–Zakharov model.[8] The orientational distribution function required for the final calculations of γ_1 can be obtained on the basis of an independent statistical theory[9] or by molecular-dynamics methods.[10] The theoretically established relation between γ_1 and the order parameters of the LC system, in turn, makes it possible to describe the temperature dependence of the coefficient of rotational viscosity.

1. BASIC RESULTS OF THE STATISTICAL THEORY OF VISCOSITY

The dissipation energy of nematic-liquid crystals is determined by the viscous-stress tensor

$$\sigma=\alpha_1(\mathbf{nn}:A)nn+\alpha_2\mathbf{nN}+\alpha_3\mathbf{Nn}+\alpha_4A+\alpha_5\mathbf{nn}A+\alpha_6A\mathbf{nn}, \tag{1}$$

where $A=1/2(\partial_i\nu_j+\partial_j\nu_i)$ is the symmetric part of the tensor of the gradients of the flow velocity of the NLC, $\mathbf{N}=d\mathbf{n}/dt-(\Omega\times\mathbf{n})$, where $\Omega=1/2(\partial_i\nu_j-\partial_j\nu_i)$, $\mathbf{n}$ is the unit vector of the director in the NLC, and the α_i $(i=1,...,6)$ are the coefficients of viscosity, known as the Leslie coefficients.[1]

The Leslie coefficients satisfy the Parodi relation[1]

$$\alpha_2+\alpha_3=\alpha_6-\alpha_5, \tag{2}$$

so that only five of the six coefficients α_i are independent. In the isotropic phase all α_i, except α_4, equal zero, and α_4 is the shear viscosity of an isotropic liquid.

In the case of a liquid-crystal phase the coefficient that plays the role of the coefficient of rotational viscosity $\gamma_1=\alpha_3-\alpha_2$ is of greatest interest, since it determines in the absence of hydrodynamic flow the dissipation of energy on account of only the rotation of the director $\mathbf{n}$ under the action of external forces.

The first microscopic description of the rotational viscosity of NLCs (and all other Leslie coefficients) was given by Diogo and Martins[3] who advanced idea that the coefficient of rotational viscosity

$$\gamma_1\sim S^2\ \exp[S^2E/[k(T-T_{NI})]] \tag{3}$$

is proportional to the characteristic relaxation time of the NLC, associated with the probability of overcoming a potential barrier in a molecular reorientation process. The magnitude of the barrier is determined both by the average orienting field acting on a molecule and by the parameters of the free volume of the NLC that is required for molecular reori-

entation. An essential point is that the activation energy associated with the average molecular field is proportional to the squared order parameter S and varies appreciably near the transition point T_{NI} into the isotropic phase. Here $S \equiv \langle P_2(\cos\theta_i)\rangle$ is the order parameter, $\cos\theta_i = \mathbf{n}\cdot\mathbf{k}$, $\mathbf{k}$ is a unit vector directed along the major axis of the i-th molecule, P_2 is a second-order Legendre polynomial,[1] and the brackets denote a statistical average.

This approach has the considerable drawback that it is impossible to describe the difference between the Leslie coefficients, since they are all assumed to be determined by the same relaxation time. At the same time, it is known from experiments that Leslie coefficients differ considerably not only in absolute magnitude but also in sign.[1]

An interesting approach to the description of rotational viscosity of LCs of polymer solutions has been proposed by Doi and Kuzuu (DK).[1] However, this approach is limited primarily to polymer systems characterized by a high viscosity and small volume fraction of the molecules. Another drawback of this approach is the absence of an exponential temperature dependence, observed in experiments,[2] of the Leslie coefficients and the fact that the coefficient of rotational viscosity,

$$\gamma_1 \sim \frac{\rho kTS}{D_R \xi}, \tag{4}$$

can be calculated only once the rotational self-diffusion coefficient D_R and the parameter $\xi = 1/\cos(2\varphi_0)$, associated with the maximum angle φ_0 of the orientations of the axes of the nematic order by the hydrodynamic flow, have been calculated. Here there arises an independent problem—the calculation of the rotational self-diffusion coefficient or ''microscopic friction.''

Several years ago Brook–Levinson and Zakharov (BLZ)[8] proposed a simple molecular model for calculating the rotational self-diffusion coefficient of liquid-crystal systems. The model is based on the random-walk theory combined with some statistical-mechanical ideas. The result is an expression for the rotational self-diffusion coefficient

$$D_R = \pi^3 [kT/2\pi I]^{1/2} F\left(\frac{\pi}{2}\right) \tag{5}$$

presented in the form of a function of temperature T, the molecular moment of inertia I, and the value of the orientational distribution function $F(\theta)$ at the point $\theta = \pi/2$, which corresponds to a molecular orientation perpendicular to the director. As is well known, in a liquid crystal $F(\theta)$ possesses a fairly sharp maximum at $\theta = 0$, rapidly decreasing to the point $\theta = \pi/2$, where it has a small but finite value. The quantity $F(\pi/2)$ determines the width of the ''gates'' through which molecules diffuse in orientational space. If $F(\pi/2) = 0$, then $D_R = 0$, i.e., there is no rotational diffusion, which corresponds to a completely ordered crystal. This *a priori* unknown factor $F(\pi/2)$ can be taken, for example, from computational results obtained by molecular-dynamics[10] or from a statistical theory.[9] All this makes it possible to give the DK theory a logically comlete form.

The next step in constructing a molecular theory of viscosity was taken by Osipov and Terent'ev (OT),[5] who estimated, on the basis of molecular-field theory using the Fokker–Planck equation, the coefficient of rotational viscosity as

$$\gamma_1 \sim \frac{\rho\lambda}{6} [J/kT]^{1/2} \exp[J/kT], \tag{6}$$

where $\rho = N/V$ is the density of a system of N particles in a volume V, while $J = J_0 S$, where J_0 is the height of the Maier–Saupe potential. But even in this theory the basic difficulty is to estimate the coefficient of ''microscopic friction'' of the molecules $\lambda = kT/D_R$. In the OT work an estimate of the coefficient λ was given in the form $\lambda \sim \eta l^3$ on the basis of general dimensional considerations, where η is a certain initial coefficient of viscosity which is of the order of the isotropic viscosity α_4, while l is the molecular length. Adding to this the fact that the values of the adjustable parameter J lie in the range $4.0 < J/kT < 7.0$, a reasonable choice of the other parameters in the OT theory gives order-of-magnitude agreement with experimental data for the coefficient of rotational viscosity of *p*-azoxyanisole.[2]

Another approach to describing the rotational viscosity in NLCs was developed by Nemtsov[7] on the basis of the NSO method.[6] In contrast to the investigations mentioned above, this approach takes account of not only the autocorrelation of the microscopic stress tensor but also the correlations of this quantity with the fluxes of the tensor order parameter and director. A calculation of these correlations shows the importance of the contribution of the interaction between the flow of the medium and the molecular orientation to the coefficient of viscosity. The nonequilibrium averaging of the microscopic stress tensor and the equations of motion for the order parameter and director [see Eqs. (30)–(36) in Ref. 11], performed on the basis of the NSO method, taking account of the fact that the temporal correlation functions determining the viscosity coefficients are calculated approximately using the Fokker–Planck equation [see Eqs. (37)–(40) in Ref. 11], made it possible to obtain an expression, of interest to us, for the rotational viscosity coefficient γ_1 in the form

$$\gamma_1 = \frac{6\rho}{D_R} f(S), \tag{7}$$

where

$$f(S) = \frac{(3.181 + 0.757S)S^2}{2.881 + S12.36S^2 + 4.69S^3 - 0.743S^4}.$$

But even in this approach the main difficulty is to calculate the rotational self-diffusion coefficient D_R.

Several years ago a comparative analysis was made of the computational results for γ_1, obtained on the basis of the DM and OT models, and the experimental data for a number of LC compounds.[12] The results appear to be quite encouraging at first glance, but the large number of adjustable parameters employed in the calculations decreases somewhat the value of these approaches and makes it impossible to

calculate the rotational viscosity from first principles, based only on the form of the Hamiltonian of the system.

2. INFLUENCE OF THE BOUNDING SURFACE ON THE ROTATIONAL VISCOSITY

The main problem studied in the present paper is to investigate the effect of an interacting surface on the rotational viscosity on the basis of the already-developed statistical approach[7] using the tools of direct correlation functions.[7,11]

Preference is given to the Nemtsov approach[7] for a variety of reasons: In the first place, the correlations of the microscopic stress tensor with the fluxes of the tensor order parameter and the director are taken into account more completely and, in the second place, the contributions due to the interaction between the flow of the medium and the molecular orientations are taken into account. Using the BLZ theory[8] to describe rotational self-diffusion processes makes it possible to express the coefficient γ_1 in a form convenient for direct calculations

$$\gamma_1=\frac{6\rho}{\pi^3}\,[2\pi I/kT]^{1/2}\,\frac{1}{F(\pi/2)}\,f(S). \tag{8}$$

Another possible representation of γ_1 is provided by the well-known expansion of the orientational distribution function in a series in Legendre polynomials

$$F(\theta)=\sum_l\ \frac{2l+1}{2}\,\langle P_l(\cos\,\theta)\rangle P_l(\cos\,\theta), \tag{9}$$

where l is an even number. Setting here $\theta=\pi/2$ we obtain

$$F(\pi/2)=\sum_l\ \frac{2l+1}{2}\,\langle P_l(\cos\,\theta)\rangle P_l(\cos\,\pi/2). \tag{10}$$

Since most experimental methods permit finding only the first few coefficients in Eq. (10), limiting the series to the first few terms up to $l=3$ we obtain

$$F(\pi/2)=\frac{1}{2}\left[1-\frac{5}{2}\,\langle P_2\rangle+\frac{27}{8}\,\langle P_4\rangle-\frac{65}{16}\,\langle P_6\rangle\right]. \tag{11}$$

Substituting the expression (11) into Eq. (8) we find that the coefficient of rotational viscosity can be expressed in terms of the temperature T, the molecular moment of inertia I, the order parameters $\langle P_l\rangle$, and the density ρ of the system.

We shall estimate D_R and γ_1 for the nematic *p*-azoxyanisole. According to Ref. 9, $F(\pi/2)\approx 0.05$; for $T=390$ K, $I=20\times10^{-44}$ kg·m^2, and $k=1.38\times10^{-23}$ J/K Eq. (5) gives the estimate $D_R\approx 1.1\times10^{10}$ s^{-1}, which is quite close to both the molecular-dynamics estimate[13] ($D_R=0.4\times10^{10}$ s^{-1}) and the experimental estimates[14] ($D_R\approx10^{10}-10^{11}$ s^{-1}), while Eq. (8) gives $\gamma_1\approx 0.0536$ ps. This value agrees quite well with the experimental estimate $\gamma_1^{\exp}\approx 0.067$ ps.[15]

In the case of a nematic phase bounded by a flat wall, the order parameters $\langle P_2\rangle$, $\langle P_4\rangle$, and $\langle P_6\rangle$ are functions of the distance from the surface. The computational results show that, irrespective of the nature of the interacting surface, the effect of the wall extends only to several molecular layers and is determined mainly by intermolecular correlations.[9]

Using the order parameters $\langle P_2\rangle$, $\langle P_4\rangle$, and $\langle P_6\rangle$, calculated using the single-particle molecular-orientational-distribution function determined in Ref. 9, we shall calculate the coefficient of rotational viscosity γ_1 as a function of the distance from the bounding surface on the basis of the Nemtsov, Brook–Levinson, and Zakharov approach according to Eq. (8) and expression (11). As already mentioned, the orientational distribution function $F(\theta)$ appearing in expression (8) for the coefficient of rotational viscosity can be calculated either on the basis of an independent statistical theory or using molecular-dynamics.

One such approach to calculating the function $F(\theta)$ on the basis of the method of conditional distributions[16–18] is presented in detail in Ref. 9. In this approach, the interaction potential of ellipsoidal molecules forming a nematic phase was chosen in the Gay–Berne form[16]

$$\Phi(\mathbf{q}_{ij},\mathbf{e}_i,\mathbf{e}_j)=4\epsilon_0\epsilon(\mathbf{e}_i,\mathbf{e}_j,\mathbf{e}_{ij})\{(\sigma_0/r_{ij})^{12}-(\sigma_0/r_{ij})^6\}, \tag{12}$$

where $r_{ij}=|\mathbf{q}_{ij}|-\sigma(\mathbf{e}_i,\mathbf{e}_j,\mathbf{e}_{ij}+\sigma_0)$. Here $\mathbf{e}_i$ and $\mathbf{e}_j$ are, respectively, unit vectors directed along the major axes of the ellipsoidal *a*-th and *j*-th molecules, $\mathbf{q}_{ij}$ is a vector connecting the centers of the molecules, and $\mathbf{e}_{ij}=\mathbf{q}_{ij}/|\mathbf{q}_{ij}|$. The parameters of the potential energy $\epsilon(\mathbf{e}_i,\mathbf{e}_j,\mathbf{e}_{ij})$ and the size $\sigma(\mathbf{e}_i,\mathbf{e}_j,\mathbf{e}_{ij})$ are functions of the relative orientation of the molecules i and j. They are determined by Eqs. (3), (4), and (8)–(10) from Ref. 16, respectively. These functions also depend on the molecular shape, determined by the molecular ellipticity parameter $\sigma_\parallel/\sigma_\perp$, where $\sigma_\parallel$ is the length of the major semiaxis of an ellipsoidal molecule and $\sigma_\perp$ is the length of the minor semiaxis, and on the energy parameter ϵ_l/ϵ_s (in the notations of Ref. 16).

The presence of a solid wall presupposes that the molecules forming the nematic phase occupy the half-space $x\geqslant 0$ (the coordinate system is chosen in a manner such that the x axis is directed along the normal to the surface, while the z axis is oriented so that the director lies in the xz plane). The wall also interacts with the molecules of the nematic through the potential

$$\Phi(\mathbf{e}_i,x_i)=\frac{2\pi}{3}\,\frac{\epsilon_w}{\sigma_w^2}\left[\frac{2}{15}\,(\sigma_0/\sigma_w x_i)^9-(\sigma_0/\sigma_w x_i)^3\right]. \tag{13}$$

The energy ϵ_w and size σ_w parameters depend on the orientation of the *i*-th molecule and are determined by the expression (20) and (21) of Ref. 9, respectively. The energy parameter $\epsilon_w=\epsilon\epsilon_0$ determines the strength of the interaction of the wall with the molecules in the system; x_i is the distance between a molecule and the wall; and, $\mathbf{e}_i=(e_{i,x},e_{i,y},e_{i,z})$.

In what follows, we shall employ ϵ_0 as the unit of energy and $\sigma_\perp$ as the unit of length. In this system of units the proposed theory contains several independent parameters: the dimensionless volume $\nu^*=\nu/\sigma_\perp^3$ and the temperature $\theta=kT/\epsilon_0$ as well as the parameters ϵ_w and $\sigma_\parallel/\sigma_\perp$, reflecting the degree of interaction of the wall with the molecules in the system and the character of the ellipticity of the molecules themselves, respectively. The latter parameter was chosen as $\sigma_\parallel/\sigma_\perp=3$.

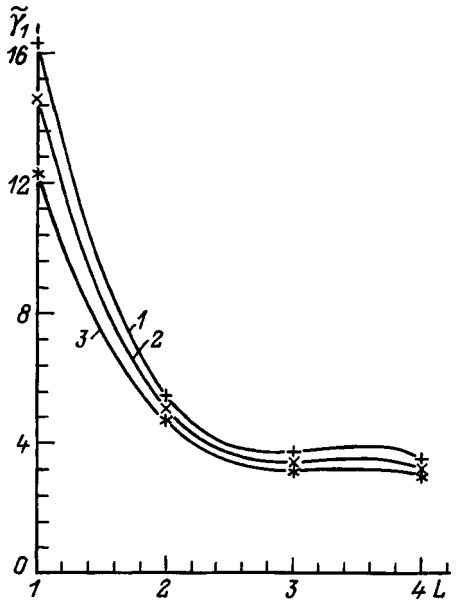

FIG. 1. Dimensionless coefficient of rotational viscosity γ_1 versus the distance L from the wall with $\nu^*=4.0$, $\sigma_\parallel/\sigma_\perp=3.0$, $\epsilon_w=5.0\epsilon_0$ and dimensionless temperatures $\theta=0.75$ (*1*), 0.7885 (*2*), and 0.827 (*3*). The values of the parameters μ and ν (in the notations of Ref. 16) were chosen equal to 1 and 2, respectively.

The computational results obtained using the model potentials (12) and (13) showed that the dimensionless coefficient of rotational viscosity $\tilde{\gamma}_1=\gamma_1\sigma_\perp^3/(\epsilon_0 I)^{1/2}$ decreases as temperature θ increases and depends strongly on the distance to the bounding surface $L=x/\sigma_\perp$ (see Fig. 1). Ordinarily, γ_1 decreases rapidly within the first two molecular volumes and rapidly reaches the bulk value γ_b. This behavior of the coefficient of rotational viscosity can be explained by the fact that molecules tend to be more strongly ordered near a strongly acting surface ($\epsilon_w=5.0\epsilon_0$) than in the interior of the nematic. This is confirmed by the results of calculations of the order parameter $S(L)=\langle P_2^{(L)}(\cos\theta_i)\rangle$ as a function of the distance L to the bounding surface. The quantity $S(L)$ also decreases rapidly within the first two molecular layers and rapidly reaches the bulk value (see Fig. 1 in Ref. 9). Alternative calculations by the molecular-dynamics methods, using the intermolecular potentials (12) and the interaction potentials (13) between the nematic molecules and a bounding surface, give good quantitative agreement (see Fig. 1 in Ref. 9). Since the order parameter $S(L)$ has the highest absolute value among the order parameters, it determines the behavior of the orientational function $F(\theta)$ and the coefficient of rotational viscosity. This explains the sharp decrease in γ_1 as a function of distance from the bounding surface.

The main result of this work is that a new model description has been proposed for the rotational viscosity of a NLC on the basis of a statistical-mechanics approach, combining the ideas of the nonequilibrium statistical-operator method[6] and the conditional-distributions method.[18] The coefficient of rotational viscosity γ_1 is determined by the moment of inertia of the molecules comprising the nematic phase, the density and temperature of the phase, and also the order parameters, to calculate which it is necessary to know only the intermolecular interaction potentials. The theory contains no adjustable parameters and gives good quantitative agreement with both the experimental results for *p*-azoxyanisole and the results obtained by alternative methods, for example, molecular dynamics. The proposed model was used to investigate the effect of a bounding surface on the rotational viscosity of NLCs. The character of the influence of the surface is in many respects similar to the influence of a bounding surface on the shear viscosity of an isotropic liquid,[19] since this surface promotes the formation of oriented layers near the walls.

In closing, I thank the Russian Fund for Fundamental Research (Grant No. 98-03-32448a) and the Fund for Natural Sciences (Grant No. 97-0-9.3-37) for financial support.

*E-Mail: alex@microm.ipme.ru

[1] G. Vertogen and W. de Jue, in *Thermotropic Liquid Crystals. Fundamentals*, Springer Series in Chemical Physics, edited by V. Goldanskii, F. Shafer, and J. Toennies, 1988, Vol. 45.
[2] V. V. Belyaev, Usp. Khim. **58**, 1601 (1989).
[3] A. C. Diogo and A. F. Martins, Mol. Cryst. Liq. Cryst. **66**, 133 (1981); J. Phys. (Paris) **43**, 779 (1982).
[4] N. Kuzuu and M. Doi, J. Phys. Soc. Jpn. **52**, 3486 (1983); **53**, 1031 (1984).
[5] M. A. Osipov and E. M. Terentjev, Nuovo Cimento **12**, 1223 (1990); Phys. Lett. A **134**, 301 (1989).
[6] D. N. Zubarev, *Nonequilibrium Statistical Thermodynamics* [in Russian], Nauka, Moscow (1971), 415 pp.
[7] V. B. Nemtsov, Teoreticheskaya i prikladnaya mekhanika (Minsk), No. 12, 111 (1985).
[8] E. T. Brook-Levinson and A. V. Zakharov, Europhys. Lett. **22**, 439 (1993).
[9] A. V. Zakharov, Phys. Rev. E **51**, 5880 (1995).
[10] D. Sandstrom, A. Komolkin, and A. Maliniak, J. Chem. Phys. **104**, 9620 (1996); A. Komolkin, A. Laaksonen, A. Maliniak, *ibid.* **101**, 4103 (1994).
[11] A. V. Zakharov, Phys. Lett. A **193**, 471 (1994).
[12] Wu Shin-Tsou and C. Wu, Phys. Rev. A **42**, 2219 (1990).
[13] A. L. Tsykalo and A. D. Bagmet, Fiz. Tverd. Tela (Leningrad) **20**, 1326 (1978) [Sov. Phys. Solid State **20**, 762 (1978)].
[14] J. Topler, B. Alefeld, and T. Springer, Mol. Cryst. Liq. Cryst. **26**, 297 (1974).
[15] H. Gasparoux and J. Prost, J. Phys. (Paris) **32**, 9539 (1971).
[16] J. B. Gay and B. J. Berne, J. Chem. Phys. **74**, 3316 (1981).
[17] L. A. Tsykalo and A. D. Bagmet, Acta Phys. Pol. A **55**, 111 (1979).
[18] L. A. Rott, *Statistical Theory of Molecular Systems* [in Russian], Nauka, Moscow (1978), 280 pp.
[19] N. V. Churaev, V. D. Sobolev, and Z. M. Zorin, in *Thin Liquid Films and Boundary Layers* (Academic Press, N.Y., 1971), 213 pp.

Translated by M. E. Alferieff

FULLERENES AND ATOMIC CLUSTERS

Magnetic susceptibility of multilayered carbon nanotubes

A. A. Ovchinnikov and V. V. Atrazhev

N. M. Émanuél' Institute of Biochemical Physics, 117334 Moscow, Russia
(Submitted January 8, 1998; resubmitted April 7, 1998)
Fiz. Tverd. Tela (St. Petersburg) **40**, 1950–1954 (October 1998)

A theoretical study of the magnetic susceptibility of multilayered carbon nanotubes in fields both parallel, $\mathbf{H}_{\|}$, and perpendicular, $\mathbf{H}_{\perp}$, to the tube axis has been carried out disregarding electron-electron interaction. The temperature dependences of the magnetic susceptibility obtained exhibit a nontrivial form for $\mathbf{H}_{\|}$, which is related to the quasi-one-dimensionality of such a system as the nanotube. The dependences of the magnetic susceptibility on chemical potential $\chi(\mu)$ have also been derived. At low temperatures, $\chi(\mu)$ has sharp peaks in fields $\mathbf{H}_{\|}$, which is connected with the presence of $1/\sqrt{E}$-type singularities in the density of states of nanotubes. The effect of interlayer coupling on magnetic susceptibility of small-radius tubes has been investigated numerically. © *1998 American Institute of Physics.* [S1063-7834(98)03710-1]

This work deals with an investigation of the magnetic susceptibility of carbon nanotubes in magnetic fields both parallel and perpendicular to the tube axis. Carbon nanotubes are actually graphite networks rolled up into tubes with radii varying from to 10 to 150 Å. Nanotubes form as a by-product of fullerene preparation in an arc discharge maintained between graphite electrodes.[1] Tubes with larger radii (above 10 Å) are multilayered, i.e., they are sets of tubes nested in one another. The interlayer distance is approximately the same as in graphite, i.e., about 3.5 Å.

Carbon nanotubes are of considerable interest as natural one-dimensional objects with the length to diameter ratio as high as 10^4-10^5. Present-day technology permits one to obtain one-layer nanotubes with a radius of 10 to 30 Å. The band structure of such tubes depends on their symmetry determined by the chirality vector C_h.[2–4] Depending on the actual symmetry of the tubes, they can be metals or semiconductors, with the magnetic field affecting the gap between the valence and conduction band. A nonmetallic tube may become metallic in a magnetic field. This gives rise to a very unusual behavior of magnetoresistance.[5,6]

Pure graphite is known to possess anisotropic diamagnetic susceptibility. The susceptibility in a field parallel to the graphite plane is approximately equal to the intrinsic susceptibility of the carbon atom ($\approx -5\times10^{-7}$ emu/g). The susceptibility in a field perpendicular to this plane is very large ($\approx -5\times10^{-5}$ emu/g). This property of graphite was studied in considerable detail.[7,8] In this connection the interest in the magnetic susceptibility of such a modification of graphite as the nanotube appears justified. A large number of publications dealing with this subject, both experimental[9,10] and theoretical,[11,12] have appeared in the literature. The magnetic susceptibility of a single-layer nanotube in a field $\mathbf{H}_{\|}$ as a function of magnetic flux Φ through the tube cross section was studied in quantitative detail.[11,12] In this case the problem simplifies considerably, because an analytical expression is available for the electronic spectrum for $\mathbf{H}_{\|}$. By contrast, the present work studies large-radius multilayered nanotubes.

1. MAGNETIC SUSCEPTIBILITY IN A FIELD PARALLEL TO THE NANOTUBE AXIS

It was shown[13] that the diamagnetic susceptibility of doped nanotubes ($E_F \neq 0$) can be as high as 10^{-3} emu/g at zero temperature, if the magnetic field is aligned with the tube axis. In experiments, however, the diamagnetic susceptibility of nanotubes was found to be even less than that of graphite. Even a very low temperature[14] ($T \approx 1$ K) was shown to reduce dramatically the diamagnetic susceptibility in $\mathbf{H}_{\|}$.

Consider the π electrons of a nanotube in the approximation of tightly bound, noninteracting electrons. It is assumed that 1) the atomic wave function is localized at lattice sites, and 2) magnetic field changes very weakly on a length scale equal to the lattice period. The π-electron Hamiltonian can be written

$$H=\beta_0\sum\ (a_m^+ a_m\ \exp(iS_{n,m})+\text{h.c.})$$

$$+\sum\ (\beta_{n,m}a_n^+ a_m\ \exp(iS_{n,m})+\text{h.c.}), \qquad (1)$$

where a^+, a are the electron creation and annihilation operators, and $S_{n,m}$ is a phase factor connected with the magnetic field[15]

$$S_{n,m}=\frac{1}{\Phi_0}\int_{R_n}^{R_m} A(\xi)\,d\xi, \qquad (2)$$

where $\mathbf{A}(\xi)$ is the vector potential of the magnetic field, and $\Phi_0=\hbar c/e$.

In the first term of the Hamiltonian, the summation is performed over the nearest neighbors in the same layer. The

second term takes into account atomic coupling between the adjacent layers in a nanotube. The resonance integral $\beta_0 = 2$ eV, and $\beta_{n,m}$ depends on the distance between atoms n and m and is chosen in the following way:

$$\beta_{n,m}=\beta(|R_n-R_m|)=\gamma\exp\left(-\frac{|R_n-R_m|}{r_0}\right),$$

$$|R_n-R_m|\leqslant 5\ \text{Å},$$

$$\beta_{n,m}=0,\quad |R_n-R_m|\geqslant 5\ \text{Å}. \tag{3}$$

If one neglects interlayer coupling in the nanotube, the π-electron spectrum in a field parallel to the tube axis $\mathbf{H}_\parallel$ can be found analytically;[11] it depends on the chirality vector C_h. We consider here zigzag-type tubes, whose unit cell is a cylinder of height $3a$ (a is the carbon-atom spacing in the graphite network). The analytical spectrum of such tubes has the simplest form:

$$E(k_x,k_y,H)=\pm\beta_0\left[1+4\cos\left(\frac{3ak_y}{2}\right)\cos\left(\frac{\sqrt{3}ak_x}{2}\right)\times 4\cos^2\left(\frac{\sqrt{3}ak_x}{2}\right)\right]^{1/2}, \tag{4}$$

where $a=1.4$ Å, k_y is the wave vector along the tube axis, $k_x=2\pi/\sqrt{3}aM_0(J+\Phi/\Phi_0)$, $J=1,2,\ldots,2M_0$, M_0 is the number of hexagons fitting into the tube perimeter, and Φ is the magnetic flux through the tube cross section.

We are interested in the differential susceptibility $\chi_\parallel$ in zero field, which can be calculated from the expression

$$\chi(T)=-\frac{\partial^2F(H,T)}{\partial H^2}=\frac{1}{V}\sum_k\left[-\frac{\partial^2E}{\partial H^2}f_e+\frac{1}{kT}\left(\frac{\partial E}{\partial H}\right)^2 f_e(1-f_e)\right], \tag{5}$$

where $F(H,T)$ is the free energy per unit volume, V is the nanotube volume, and f_e is the Fermi–Dirac distribution. The wave vector for a nanotube considered as an open cylinder of finite length is $k_y=(\pi/N_0+1)n$, $n=1,\ldots,N_0$.

For $T=0$, only the first term is left in Eq. (5). The summation over the quasi-momentum was performed numerically. When constructing multilayered tubes, the tube of the minimum radius was assigned the indices (11.0), with the perimeter of each subsequent tube being increased by 10 hexagons to (21.0), (31.0), and so on. The susceptibility of a nanotube depends on its radius and the Fermi energy E_F, i.e. on the amount of impurities. At zero temperature, the susceptibility of a doped multilayered nanotube varies as the square of its radius (Fig. 1), and for a tube of radius 150 Å doped to 1% by an acceptor impurity it is approximately -5×10^{-4} emu.

As the temperature increases to an extent where kT becomes of the order of the distance between energy levels at the Fermi surface, the diamagnetic susceptibility drops rapidly, because the second (paramagnetic) term in Eq. (5) becomes nonzero. This term is connected with different filling of the magnetic field-split levels with $k_x=\pm k$. Only the levels lying near the Fermi surface within an energy interval of order kT contribute to this term. It does not, however, vanish in the thermodynamic limit. If one goes to the thermodynamic limit in N_0, the function $(1/kT)f(1-f)$ may be considered a δ function at low temperatures. Then the second term in Eq. (5) takes on the form

$$\frac{1}{V}\sum_k\frac{1}{kT}\left(\frac{\partial E}{\partial H}\right)^2 f(1-f)=\alpha\sum_{k_x}\left(\frac{\partial E}{\partial k_x}\right)^2\rho(E,k_x), \tag{6}$$

$$\rho(E,k_x)\frac{N_0}{k_x}=\frac{N_0}{\pi}\left|\frac{\partial E(k_x,k_y)}{\partial k_y}\right|^{-1}\Bigg|_{E(k_x,k_y)=E}. \tag{7}$$

For real nanotubes, i.e. when N_0 is finite, the susceptibility approximates $\chi(+0)$ for $kT_c\approx\Delta E$ (ΔE is the level spacing near the Fermi surface). The magnetic susceptibility $\chi_\parallel$ for two-layer tubes of various lengths calculated for low temperatures is shown in Fig. 2.

As seen from Eq. (6), for $T\geqslant T_c$ the magnetic susceptibility depends on the density of states on the Fermi surface

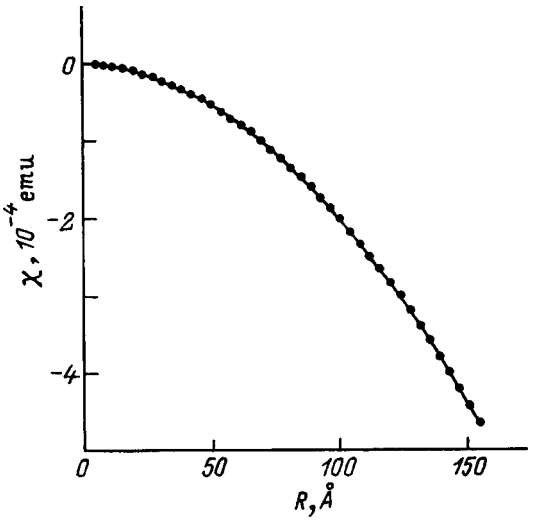

FIG. 1. Dependence of susceptibility $\chi_\parallel$ on nanotube radius R. Acceptor concentration 1%, temperature $T=0$ K.

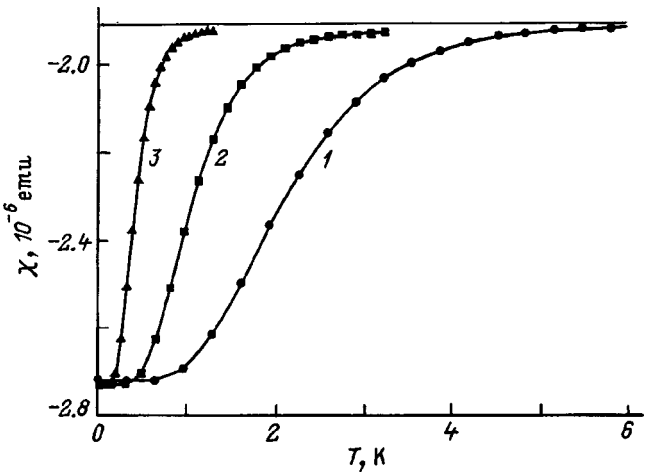

FIG. 2. Temperature dependence of susceptibility $\chi_\parallel$ of two-layered doped nanotubes of length (μm): *1*—0.42, *2*—0.84, *3*—2.1. Acceptor concentration 1%.

$\rho(E)$, which has $1/\sqrt{E}$-type singularities. The density of states of a multilayered tube is a sum of several functions with different periods, i.e. a function with quasi-randomly spaced peaks. Hence $\chi(E_F)$ of a single multilayered nanotube at a fixed temperature should vary strongly under doping. Averaging over the sample will, however, smooth the $\chi(E_F)$ function.

Consider now the effect of interlayer atomic coupling in a nanotube ($\beta_{n,m} \neq 0$). The coupling parameters are chosen such that

$$\gamma \exp\left(-\frac{1.4}{r_0}\right) = 2 \text{ eV},$$

$$\gamma \exp\left(-\frac{\Delta R}{r_0}\right) = \beta_1, \tag{8}$$

where ΔR is the layer spacing in Å, and β_1 is an energy parameter determining the interlayer coupling. We shall vary β_1 from zero to 0.4 eV. The coupled equations (8) can be used to find γ and r_0. We can no longer find analytically the spectrum of Hamiltonian (1) and will have to look for its eigenvalues numerically.

We shall treat two- and three-layered tubes as infinitely long one-dimensional objects. A three-layer tube is actually three (10.0), (20.0), (30.0) zigzag tubes nested one into another as the radius increases. The unit cell of such a tube is a cylinder of height $3a$ and contains 240 atoms. The vector potential is chosen in the form $A=(-Hy/2, Hx/2, 0)$ (the z axis is aligned with the tube axis). With the vector potential chosen in this way, the wave vector k_z remains the translational quantum number ($-\pi \leqslant k_z 3a \leqslant \pi$). Now for each fixed value of vector k_z we have to diagonalize a 120×120 matrix for a two-layer nanotube, and a matrix of size 240×240 for a three-layer tube to obtain 120 and 240 energy bands, respectively. After this, we can find the free energy of such a nanotube in the presence of a magnetic field:

$$F(H) = -kT \sum_i \int \ln\left[1+\exp\left(-\frac{E_i(k_z)-\mu}{kT}\right)\right] dk_z + \mu N_e, \tag{9}$$

where μ is the chemical potential, and N_e is the number of electrons. The summation is performed over all spectral branches of a one-dimensional system.

Having calculated the free energy for three different fields 0, H, and $2H$, one can find the differential susceptibility from the expression

$$\chi = \frac{F(0)+F(2H)-2F(H)}{VH^2}. \tag{10}$$

In a real numerical calculation, k_z runs through a discrete spectrum of values (we took 1000 values) from $-\pi/3a$ to $+\pi/3a$, and integration over k_z in Eq. (9) is replaced by summation over this discrete spectrum.

Figure 3 plots $\chi(\beta_1)/\chi(0)$ as a function of β_1/β_0 for $E_F=0$. Because in a real system $\beta_1/\beta_0 \approx 0.1$, interlayer coupling is seen to affect only weakly the magnetic susceptibility of nanotubes in a field parallel to the tube axis. Plotted in Fig. 4 are the $\chi(E_F)$ relations for doped nanotubes, which were calculated for the temperature $T=10$ K for $\beta_1=0$ and $\beta_1=0.2$ eV. We readily see that interlayer coupling does not result in noticeable flattening of the peaks where the density of states has $1/\sqrt{E}$ singularities.

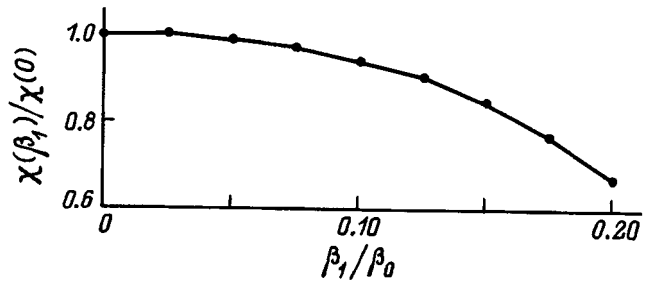

FIG. 3. Effect of interlayer coupling on susceptibility $\chi_\parallel$ for a two-layer tube calculated for $E_F=0$ eV and $T=0$ K.

2. MAGNETIC SUSCEPTIBILITY IN A FIELD PERPENDICULAR TO TUBE AXIS

If the magnetic field is perpendicular to the tube axis, we can choose the vector potential in the form $A=(0,0,Hy)$ (the z axis is along the tube axis). In a perpendicular field we can no longer find an analytical spectrum even in the case where there is no interaction between atoms in different nanotube

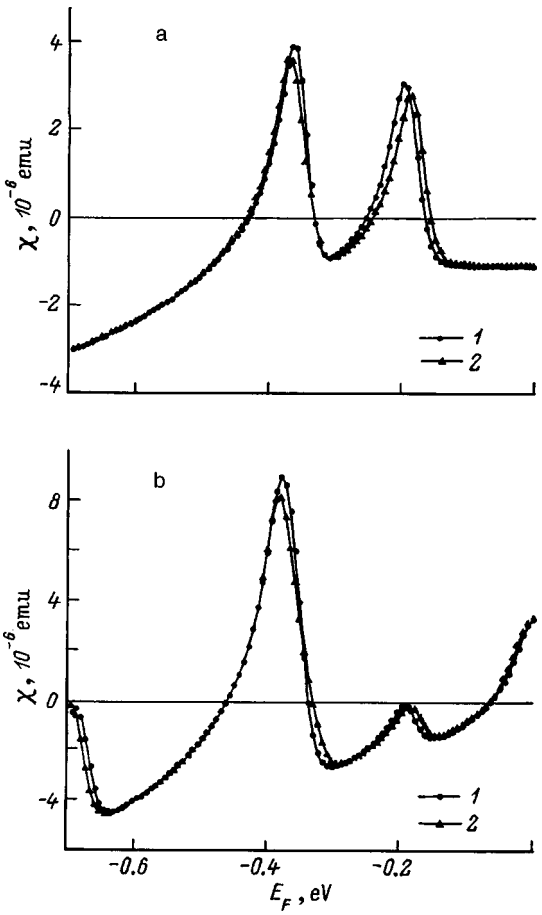

FIG. 4. Dependence of susceptibility $\chi_\parallel$ of (a) two-layered and (b) three-layered nanotube on Fermi energy E_F calculated for $T=100$ K, (*1*) $\beta_1=0$, and (*2*) $\beta_1=0.2$ eV.

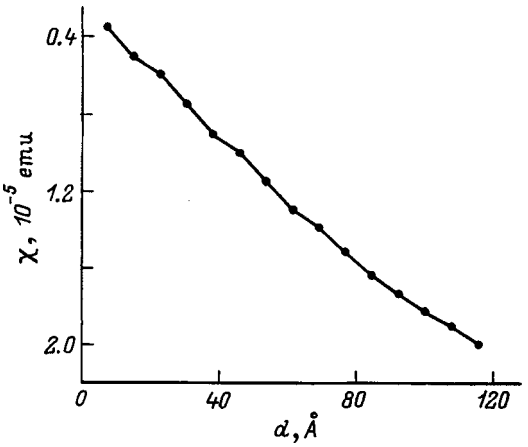

FIG. 5. Dependence on tube diameter d of susceptibility $\chi_\perp$ in a field perpendicular to the tube axis, calculated neglecting interlayer coupling.

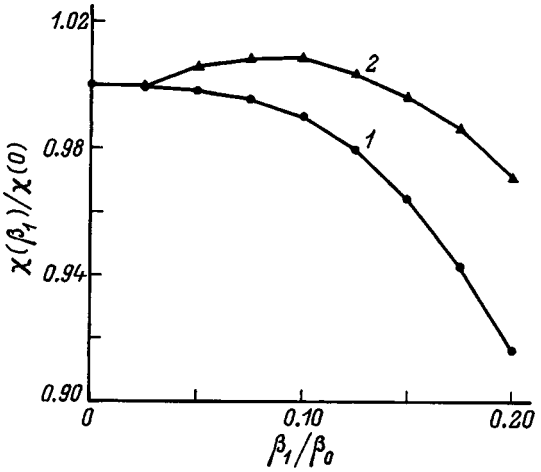

FIG. 7. Effect of interlayer coupling on susceptibility $\chi_\perp$ for (*1*) two-layered and (*2*) three-layered nanotubes calculated for $E_F=0$ eV and $T=0$ K.

layers. Therefore, we shall have to calculate the spectrum numerically, as we did in the preceding Section.

Consider first the case where all $\beta_{n,m}=0$, i.e., when there is no interlayer coupling. In this case we can find the electron spectrum and the free energy of each layer separately and then perform summation over the layers. The unit cell of each layer is a cylinder of height $3a$ (for zigzag tubes). With the vector potential chosen as above, the wave vector k_z remains a translational quantum number ($-\pi \leqslant k_z 3a \leqslant \pi$). In a one-layer tube ($N$,0) the number of atoms in a unit cell is $4N$, which yields $4N$ energy levels for each fixed value of k_z.[16] As in the case of a parallel field, we replace the continuous variable k_z with a discrete set of 1000 values of k_z. The free energy is found by replacing integration over k_z by summation over the discrete set.

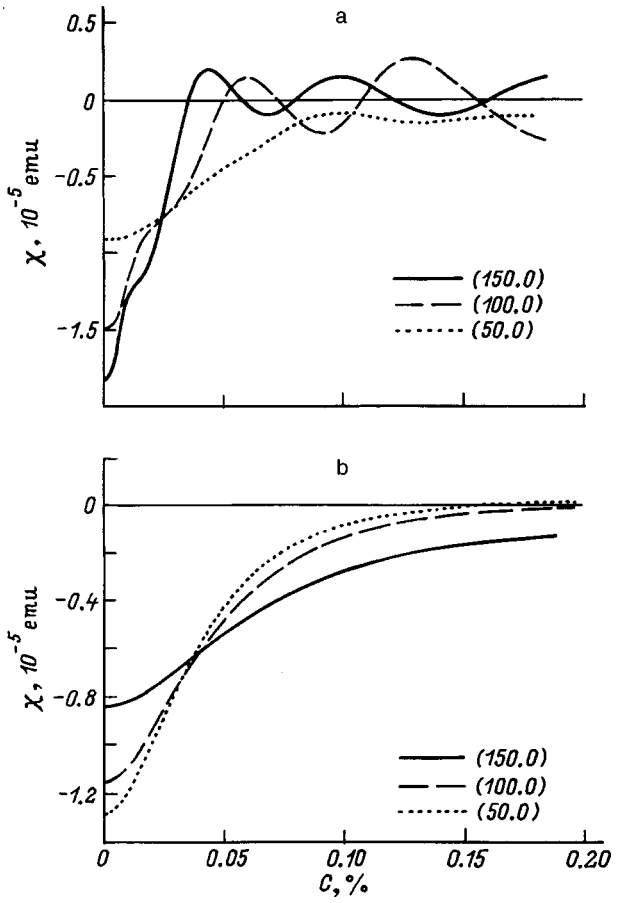

FIG. 6. Dependence of susceptibility $\chi_\perp$ of multilayered doped nanotubes of various diameters on acceptor concentration C calculated for (a) $T=100$ K and (b) $T=300$ K.

The construction of filled tubes was started by taking a tube of the minimum radius (10.0), with increasing the perimeter of each subsequent tube by 10 hexagons to (20.0), (30.0), and so on. The outermost layer of the tube with the maximum radius was (150.0). The diameter of this nanotube is approximately 110 Å. We proceed next as we did in the preceding Section, namely, we find numerically from Eq. (9) the free energy of each layer for three values of the field, 0, H, and $2H$. Summation over all nanotube layers yields the free energy $F(H)$, which can be used to calculate $\chi_\perp$ from Eq. (10). Figure 5 plots $\chi_\perp$ as a function of nanotube radius for $E_F=0$. One readily sees that the diamagnetic susceptibility $\chi_\perp$ for nanotubes of a large enough radius is lower than it is for graphite.

Figure 6 displays $\chi_\perp$ as a function of impurity concentration C (in per cent) for doped tubes. We see that even a small amount of a donor or acceptor impurity results in a strong drop of the diamagnetic susceptibility. Whence it follows that if the experimentally obtained susceptibility of nanotubes is of the order of 10^{-5} emu, they practically do not contain impurities, i.e., their chemical potential is close to zero.

Consider now the effect of interlayer coupling on $\chi_\perp$. We used the procedure employed with $\chi_\parallel$ to study the effect of interaction among atoms located in different layers on $\chi_\perp$ for $0<\beta_1/\beta_0<0.2$. The results of the calculations made for $E_F=0$ are plotted in Fig. 7. Because in real systems $\beta_1/\beta_0 \approx 0.1$, the magnetic susceptibility in a field perpendicular to tube axis is seen to be practically insensitive to interlayer coupling.

Support of the International Research & Development Center (Grant 015-94) is gratefully acknowledged.

[1] G. Dresselhaus and P. C. Eklund, J. Mater. Res. **8**, 2054 (1993).
[2] M. S. Dresselhaus, G. Dresselhaus, and R. Saito, Phys. Rev. B **45**, 6234 (1992).
[3] R. Saito, M. Fujita, G. Dresselhaus, and M. S. Dresselhaus, Phys. Rev. B **46**, 1804 (1992).
[4] R. Saito, M. Fujita, G. Dresselhaus, and M. S. Dresselhaus, Appl. Phys. Lett. **60**, 2204 (1992).
[5] L. Langer, L. Stockman, J. P. Heremans, V. Bayot, C. H. Olk, C. van Haesendonck, Y. Bruynseraede, and J.-P. Issi, J. Mater. Res. **9**, 927 (1994).
[6] M. F. Lin and Kenneth W.-K. Shung, Phys. Rev. B **51**, 7592 (1994).
[7] J. W. McClure, Phys. Rev. **104**, 666 (1956).
[8] J. W. McClure, Phys. Rev. **119**, 606 (1960).
[9] J. Heremans, C. H. Olk, and D. T. Morelli, Phys. Rev. B **49**, 15 122 (1994).
[10] X. K. Wang, R. P. H. Chang, A. Patashinski, and J. B. Ketterson, J. Mater. Res. **9**, 1578 (1994).
[11] M. F. Lin and Kenneth W.-K. Shung, Phys. Rev. B **52**, 8423 (1995).
[12] H. Ajiki and T. Ando, J. Phys. Soc. Jpn. **62**, 1255 (1993).
[13] A. A. Ovchinnikov, Phys. Lett. A **195**, 95 (1994).
[14] A. A. Ovchinnikov and V. V. Atrazhev, Dok. Akad. Nauk **356**, 182 (1997) [Phys. Doklady **42**, 467 (1997)].
[15] J. M. Luttinger, Phys. Rev. **84**, 814 (1951).
[16] R. Saito, G. Dresselhaus, and M. S. Dresselhaus, Phys. Rev. B **50**, 14 698 (1994).

Translated by G. Skrebtsov

INFORMATION FOR AUTHORS

Information for authors of the journal ''Fizika tverdogo tela''

Fiz. Tverd. Tela (St. Petersburg) **40** (October 1998)

[S1063-7834(98)03810-6]

The editorial board of the journal requests authors submitting articles for publication to adhere to the following rules.

Articles ignoring these rules will be rejected.

• The article should contain the address of the institution where the work was performed. The manuscript should be signed by the author (coauthors), whose last name, name, patronymic, home address, place of employment, and telephone numbers should be indicated. The individual(s) to whom correspondence should be directed should be indicated. Proofs are not provided.

• The journal publishes original articles and invited reviews on various aspects of solid-state physics. Two copies of the article, typed double-spaced and one-sided with a 12- or 14-point font, should be submitted. The left-hand margin should be at least 4 cm. Handwritten insertions are not allowed. All pages should be numbered.

The following should be indicated on a separate sheet:

—the title of the article;

—the initials and last names of the authors (the initials placed before the last name);

—the name of institution (no abbreviations or acronyms) submitting the article and the address of the institution: postal code, city, country;

—e-mail address.

The text of the article should be preceded by an abstract not exceeding 0.5 typed pages in length. The abstract should not repeat the introductory and concluding sections.

• The exposition of the material should be clear and succinct without intermediate equations and calculations and complicated mathematical expressions. Data given in tables, plots, and figure captions should not be repeated in the text of the article. Presentation of numerical results in tables and figures simultaneously should also be avoided. If sections are not provided with headings, they should be numbered. Abbreviations used by the authors should be defined in the text.

Latin letters should be used for dimensions of quantities and notations (in the text, tables, and figures).

• Two copies of each figure should be submitted. The minimum number of figures with a limited number of details should be used. Inscriptions in the figures should be in English.

Line drawings should be drawn using India ink on white or tracing paper.

Half-tones should be submitted in the form of glossy photographs. The second copy of the photographs should not contain letter or numerical labels (only the picture). The notation ''top'' should be written on the back using a soft pencil. Photographs should not be glued on. Clips should not be used.

Figures *composed on a computer* should be of high quality.

The last names of the authors, the title of the article, and the figure number should be indicated on the back of the figures.

Figure captions should be presented on a separate sheet of paper. Graphical elements (circles, crosses, and so on) are not allowed in captions.

• Tables should be printed on separate sheets of paper and should have headings. The units of measurement should be indicated.

• Equations should be inserted in large type, loosely, and clearly. They should be numbered continuously throughout the article (not by sections).

In the first copy of the manuscript the *equations and notations* should be marked according to the following rules:

—Greek letters should be underlined in red;

—handwritten letters should be circled using a green pencil;

—Gothic letters should be circled using a yellow pencil;

—vectors should be underscored with a blue bar (and not with an overarrow!);

—indices and exponents should be indicated by carats on the top and bottom using an ordinary pencil;

—upper- and lower-case letters having similar outlines ($C,c;K,k;P,p;O,o$), the letters I (i) and J (j), the letter I and the Roman numeral 1, and also the Arabic number 1 and the Roman numeral I, the vertical bar ($|$), 1 and a stroke in indices, l (Latin ell), and e, should be indicated clearly;

—upper-case letters should be marked, using a pencil, with two underbars ($\underline{\underline{C}}$), while lower-case letters should be marked with two overbars ($\bar{\bar{c}}$).

In in-line equations a slash should be used to indicate division. The notation exp should be used for the exponential function.

• Special attention should be given to composing the list of references:

for books—the initials and last names of *all* authors, the title of the book, publisher, location of publication, year of publication, volume, edition, total number of pages (54 p.). If a citation is made to a specific page, the number of this page

should be indicated after the year of publication: p. 54 (not 54 p.);

for periodicals—the initials and last names of all authors, the name of the journal, volume, issue, number of the first page of the article, year of publication.

Example:

1. B. P. Aduev, É. D. Aluker, V. V. Gavrilov, R. G. Deĭch, and S. A. Chernov, Fiz. Tverd. Tela **38**, 12, 3521 (1996).
2. V. J. Emery, Phys. Rev. B **14**, 3,2989 (1976).
3. L. D. Landau and E. M. Lifshitz, *Quantum Mechanics*, Nauka, M. (1989).

Citations to Russian editions are given in Russian.

The references should be numbered in the order in which they appear in the text.

• In accordance with an agreement between the editorial board of the journal ''Fizika tverdogo tela'' and the American Institute of Physics, the journal is translated into English and distributed abroad.

Authors desiring to publish their article in the journal ''Fizika tverdogo tela'' should send a letter to the editorial board in the following form:

We, the undersigned authors, . . . give the founders and the editorial board of the journal ''Fizika tverdogo tela'' the right to publish the article . . . in Russian and in English.

We affirm that this publication does not violate any copyrights of other individuals or organizations.

Signatures

Date

The authors retain their rights as owners of the article.

1. ATTENTION AUTHORS

To obtain the author's remuneration for publication of the journal abroad, authors should file an information return with the Division of Currency Exchange of the Office of Finance of the Russian Society of Authors (RSA).

2. INFORMATION RETURN

1. Last name, name, and patronymic.
2. Date of birth (day, month, year).
3. Address (registration) with postal code.
4. Passport information (series, number, name of government body issuing the passport, location and date of issuance).
5. Telephone numbers at work and at home.
6. List of works (name of journal, year of publication, volume, issue, pages).
7. I request that the monies due me be paid out in US dollars.
8. I will obtain the royalty personally (indicate one of the methods indicated below):

a) at the Russian Society of Authors;

b) in St. Petersburg at the bank ''Baltika'' (a division of the bank ''Rossiĭskiĭ kredit'');

c) in Novosibirsk at a division of the bank ''Rossiĭskiĭ kredit;''

d) at a location desired by the author, in a bank with a correspondent's account at the bank ''Rossiĭskiĭ kredit.''

Date (day, month, year) Signature of author

Payment of the remuneration to the author is made on presentation of the passport.

The author's remuneration can also be paid out by proxy.

The proxy should contain information on the registration and passport information for the principal and for the individual to whom the proxy is issued. Servicemen should indicate the information on their military pass.

The proxy can be certified by a notary, the organization employing the principal, living-working organization according to the principal's domicile.

To receive the author's remuneration by proxy, the principal should present the information return signed by the author and his or her passport.

Address of the RSA: 103670 Moscow, ul. B. Bronnaya, 6a, Division of Currency Exchange of the Office of Finance. Telephone of the Inquiries Office of the Division of Currency Exchange—(095) 203 35 33.

Translated by M. E. Alferieff